



HAL
open science

Formation of large-scale structure in various cosmological scenarios

Luca Alberto Rizzo

► **To cite this version:**

Luca Alberto Rizzo. Formation of large-scale structure in various cosmological scenarios. *Cosmology and Extra-Galactic Astrophysics [astro-ph.CO]*. Université Paris Saclay (COMUE), 2017. English. NNT : 2017SACLS166 . tel-01593509

HAL Id: tel-01593509

<https://theses.hal.science/tel-01593509v1>

Submitted on 26 Sep 2017

HAL is a multi-disciplinary open access archive for the deposit and dissemination of scientific research documents, whether they are published or not. The documents may come from teaching and research institutions in France or abroad, or from public or private research centers.

L'archive ouverte pluridisciplinaire **HAL**, est destinée au dépôt et à la diffusion de documents scientifiques de niveau recherche, publiés ou non, émanant des établissements d'enseignement et de recherche français ou étrangers, des laboratoires publics ou privés.

NNT : **2017SACL5166**

THÈSE DE DOCTORAT
DE
L'UNIVERSITÉ PARIS-SACLAY
PRÉPARÉE À
"INSTITUT DE PHYSIQUE THÉORIQUE, CEA SACLAY"

ECOLE DOCTORALE N° 564
Physique de l'Ile-de-France

Spécialité de doctorat Physique

Par

LUCA ALBERTO RIZZO

COSMOLOGIE DES THÉORIES
DE GRAVITE MODIFIÉES

Thèse présentée et soutenue à Saclay, le 04/07/2017

Composition du Jury :

Prof. Christian Marinoni	Universite Aix-Marseille, Marseille	Président
Prof. Baojiu Li	Durham University, Durham, UK	Rapporteur
Prof. David Langlois	Universite Paris 7, France	Rapporteur
Dr. Valeria Pettorino	SAP-CEA SACLAY	Examinatrice
Dr. Patrick Valageas	IPhT-CEA SACLAY	Directeur de thèse

Titre : COSMOLOGIE DES THÉORIES DE GRAVITE MODIFIÉES

Mots clés : cosmologie, gravité modifiée, structure à grande échelle

Résumé : La cosmologie a atteint une ère passionnante. Pour la première fois dans l'histoire humaine, un modèle quantitatif pour la formation et l'évolution de l'Univers existe, expliquant une gamme très variée de phénomènes et ayant été testé avec une impressionnante. De plus, nous sommes à l'aube d'une époque dans laquelle nous aurons à notre disposition une abondance de données de grande qualité, ce qui nous permettra d'utiliser la cosmologie comme un outil pour tester la physique fondamentale.

En particulier, comme les structures de grandes échelles de l'Univers sont gouvernées par la force de gravité, la cosmologie peut être utilisée pour tester la théorie de la relativité générale d'Einstein. Cette idée a inspiré la plupart des travaux décrits dans ce manuscrit, dans lequel j'ai étudié des théories alternatives au modèle standard de la cosmologie et des tests à grandes échelles pour la relativité générale.

Dans la première partie de ma thèse, je me suis concentré sur les "théories tenseur-scalaire" de la gravité. Ce sont des théories alternatives de la gravité, dans lesquelles un champ scalaire, qui est responsable de l'accélération de l'expansion de l'Univers, est ajouté à l'action de Einstein-Hilbert. Dans le deuxième chapitre, j'ai décrit le modèle de K-mouflage, une "théorie tenseur-scalaire" dans laquelle le champ scalaire possède un terme cinétique non-standard, en montrant son effet non négligeable sur la dynamique des amas des galaxies. J'ai aussi montré comment cet effet peut être utilisé pour contraindre le modèle de "K-mouflage" en utilisant des observations en rayon X.

En particulier, j'ai montré que le cisaillement cosmique a un pouvoir assez limité actuellement pour contraindre ces théories, à cause de la faible précision des observations actuelles et des dégénérescences avec les processus baryoniques.

Dans le cinquième chapitre, j'ai donné une description de mon étude des relations de cohérence. Ce sont des relations entre les fonctions de corrélation des champs cosmiques à $(n + 1)$ et n points, valables aussi dans le régime non-linéaire.

Leur intérêt vient du fait que leur dérivation dépend seulement du

Principe d'Équivalence et de l'hypothèse de conditions initiales Gaussiennes, et donc elles peuvent être utilisées pour tester ces hypothèses fondamentales du modèle standard de la cosmologie.

Des relations similaires ont été étudiées auparavant, mais j'ai montré comment il est possible d'obtenir des relations qui ne s'annulent pas lorsque tous les champs sont considérés au même instant. J'ai utilisé ce résultat pour obtenir des relations de cohérence entre fonctions de corrélation de quantités observables, notamment le champ de densité des galaxies et la fluctuation de température du fond diffus cosmologique donnée par l'effet Sachs-Wolfe. Ces relations peuvent être utilisées pour des tests de la relativité générale, reposant sur des observations par satellites, sans avoir besoin de modéliser la physique des baryons aux petites échelles.

Enfin, j'ai donné un aperçu des quelques perspectives possibles pour poursuivre le travail décrit dans ce manuscrit.

En particulier, j'ai souligné comment des simulations numérique sont nécessaires pour mieux comprendre la formation des structures dans le contexte des modèles "K-mouflage" et "ultra-local". En outre, elles peuvent être aussi utilisées pour tester les hypothèses sous-tendant l'analyse des lentilles gravitationnelles faibles présentée dans ce manuscrit, surtout pour distinguer l'effet de la physique des baryons et des neutrinos de l'effet des théories de gravité modifiée sur le cisaillement cosmique. En ce qui concerne les relations de cohérence, une étude de faisabilité de leur mesure avec les "surveys" cosmologiques est nécessaire, pour comprendre si elles peuvent donner des contraintes compétitives sur les théories alternatives de la gravité.



Title : Formation of large-scale structure in various cosmological scenarios

Keywords : cosmology, modified gravity, large-scale structure

Abstract : The study of physical cosmology has reached an exciting era. For the first time in human history, a quantitative model for the formation and the evolution of the Universe exists, which explains a wide range of phenomena and has been tested with incredible accuracy during the last century. Moreover, we are approaching a time when a bounty of high quality cosmological data will be available, allowing us to use cosmology as a tool to test fundamental physics.

In particular, as the large-scale structures of the Universe are governed by gravity, cosmology can help us to assess the correctness of Albert Einstein's general relativity. This idea fueled most of the work described in this manuscript, in which we study alternative theories to the standard cosmological model and large-scale structure tests for general relativity.

In particular, we focus on two scalar-tensor theories of gravity, the K-mouflage models described in Chapter 2 and the ultra-local models of gravity presented in Chapter 3. The K-mouflage theories are k-essence models with a non-standard kinetic term that were already studied at the linear and background levels. In this manuscript, we extend this description showing how the scalar field, which is responsible for the late time acceleration of the Universe, has a non-negligible impact on cluster dynamics, arguing that future surveys may have the power of constraining K-mouflage models via X-ray observations. Next, we study the ultra-local models of gravity, where a scalar field with a negligible kinetic term is added to the Einstein-Hilbert action, investigating how the latter modifies cosmological structure formation and how these models can be related to super-chameleon models.

In Chapter 4, we present a cosmic shear data analysis in the context of $f(R)$ and Dilaton models, and we show how current data can accommodate most of the theories considered, once baryonic and neutrino physics degeneracies are taken into account.

Finally, in Chapter 5 we present an analysis of consistency relations for large-scale structures, which are non-perturbative relations among correlations of cosmic fields. They are also valid in the non-linear regime, where very few analytical results are known, and only rely on the Equivalence Principle and primordial Gaussian initial conditions. This makes them a powerful tool to test general relativity and inflationary models using the cosmological large-scale structures.

We provide here the first non-vanishing equal-time consistency relations, which we use to obtain consistency relations involving observational quantities.

In this Thesis manuscript, we highlight the major results of the full analysis done in the articles that are appended to the main text, where the reader can quench any thirst for technical details.



Contents

Abbreviations	6
Notations	7
1 Introduction	3
1.1 Dark energy problem and Λ -CDM model	3
1.2 Λ -CDM model	4
1.3 Strong equivalence principle	5
1.4 Dark energy	5
1.5 Modified-gravity theories	6
1.5.1 Scalar-tensor theory of gravity	6
1.5.2 Screening mechanisms	7
1.6 Tests of gravity	9
1.7 Conclusions	10
2 K-mouflage	11
2.1 Introduction	11
2.2 Description of the model	11
2.3 Large- and small-scale constraints	14
2.4 Background cosmology	15
2.5 Large scale structure formation	16
2.6 Lack of screening of clusters in K-mouflage models	18
2.7 Cluster dynamics	20
2.7.1 Halo mass function	20
2.7.2 Cluster concentration	21
2.7.3 Hydrostatic equilibrium	21
2.7.4 Scaling laws	23
2.7.5 Cluster temperature function	24
2.7.6 Dynamical and weak lensing masses	25
2.8 Conclusions	25
3 Ultra-local models of gravity	27
3.1 Introduction	27
3.2 Description of the models	27

3.3	Background and perturbations in Jordan frame	29
3.4	Constraints on A	30
3.5	Characteristic transition scales of ULMs	33
3.6	Spherical collapse and halo mass function	33
3.7	Screening mechanism	34
	3.7.1 Clusters and galaxies	36
	3.7.2 Solar System	37
3.8	Thermodynamical analysis	39
3.9	Super-chameleons and ultra-local models	41
3.10	Conclusions	42
4	Testing modified gravity with cosmic shear	44
4.1	Introduction	44
4.2	Dilation and $f(R)$ theory of gravity	44
4.3	Weak lensing	45
4.4	Results	46
4.5	Conclusions	47
5	Consistency relations for large-scale structure	51
5.1	Introduction	51
5.2	Correlation and response function	52
5.3	Consistency relations for velocities and momenta	55
5.4	Consistency relations for observables	56
5.5	Conclusions	58
6	Conclusions	60
7	Résumé	62
A	K-mouflage effects on clusters of galaxies	70
B	Ultra local models of gravity without the kinetic term	105
C	Supersymmetric chameleons and ultra-local models	146
D	Testing Modified Gravity with Cosmic Shear	170
E	Nonzero Density-Velocity Consistency Relations for Large Scale Structures	184
F	Consistency relations for large-scale structures: applications to the integrated Sachs-Wolfe effect and the kinematic Sunyaev-Zeldovich effect	190

Abbreviations

GR	G eneral R elativity
MGT	M odified G ravity T heorys
FLRW	F riedmann- L emaître- R oberston- W alker
QFTG	Q uantum F ield T heory of G ravity
EHA	E instein H ilbert A ction
DEM	D ark E nergy M odel
SEP	S trong E quivalence P rinciple
BAO	B aryonic A coustic O scillations
ISW	I ntegrated S achs W olfe
kSZ	k inetic S unyaev Z eldovich
NFW	N avarro F renck W hite
ULM	U ltra- L ocal M odel
SMC	S uper- C hameleon M odel
CR	C onsistency R elations

Notations

\mathcal{G}	Newton's Constant
z	cosmological redshift
a	scale factor
$\bar{\rho}_m$	background matter density of the Universe
$\delta = \rho/\bar{\rho} - 1$	matter density contrast
$G(z)$	time dependent Newton's parameter
$H(z)$	Hubble parameter
$\tilde{M}_{\text{Pl}} = 1/\sqrt{8\pi\mathcal{G}}$	Planck mass
Φ	00 part of the metric
Ψ	trace of the spatial metric

Abstract

The study of physical cosmology has reached an exciting era. For the first time in human history, a quantitative model for the formation and the evolution of the Universe exists, which explains a wide range of phenomena and has been tested with incredible accuracy during the last century. Moreover, we are approaching a time when a bounty of high quality cosmological data will be available, allowing us to use cosmology as a tool to test fundamental physics.

In particular, as the large-scale structures of the Universe are governed by gravity, cosmology can help us to assess the correctness of Albert Einstein's general relativity. This idea fueled most of the work described in this manuscript, in which we study alternative theories to the standard cosmological model and large-scale structure tests for general relativity.

In particular, we focus on two scalar-tensor theories of gravity, the K-mouflage models described in Chapter 2 and the ultra-local models of gravity presented in Chapter 3. The K-mouflage theories are k-essence models with a non-standard kinetic term that were already studied at the linear and background levels. In this manuscript, we extend this description showing how the scalar field, which is responsible for the late time acceleration of the Universe, has a non-negligible impact on cluster dynamics, arguing that future surveys may have the power of constraining K-mouflage models via X-ray observations. Next, we study the ultra-local models of gravity, where a scalar field with a negligible kinetic term is added to the Einstein-Hilbert action, investigating how the latter modifies cosmological structure formation and how these models can be related to super-chameleon models.

In Chapter 4, we present a cosmic shear data analysis in the context of $f(R)$ and Dilaton models, and we show how current data can accommodate most of the theories considered, once baryonic and neutrino physics degeneracies are taken into account.

Finally, in Chapter 5 we present an analysis of consistency relations for large-scale structures, which are non-perturbative relations among correlations of cosmic fields. They are also valid in the non-linear regime, where very few analytical results are known, and only rely on the Equivalence Principle and primordial Gaussian initial conditions. This makes them a powerful tool to test general relativity and inflationary models using the cosmological large-scale structures.

We provide here the first non-vanishing equal-time consistency relations, which we use to obtain consistency relations involving observational quantities.

In this Thesis manuscript, we highlight the major results of the full analysis done in the articles that are appended to the main text, where the reader can quench any thirst for technical details.

f

Chapter 1

Introduction

1.1 Dark energy problem and Λ -CDM model

Before discussing possible modifications to Einstein's General Relativity (GR), it is worth stressing which astonishing accomplishment GR is, both in terms of its profound theoretical foundations and of the huge variety of phenomena that it can describe. On the first hand, its description of a Lorentz invariant space-time couched in the language of differential geometry it is meaningful and elegant and remains unchanged after more than one century from its first formulation. On the other hand, GR has proven to be spectacularly successful [1] when tested against experiments and observations, which range from millimeter scale laboratory tests to Solar System tests, including also strong regime tests such as binary pulsars dynamics. Within the standard model, GR governs the expansion of the Universe, the behavior of black holes, the propagation of gravitational waves, and cosmological structure formation from planets and stars to the galaxy clusters.

Having such an outstanding theory of gravity, one may wonder why there is such a huge number of alternative theories in the literature, and why there are different experimental and observational projects to test GR. Despite its success, there are (at least) two major reasons why it is interesting to study possible modifications of GR : the first one is the lack of a widely accepted quantum field theory of gravity (QFTG). In fact, even if different proposals for a QFTG exist, none of them has proven to be completely satisfactory in reconciling GR to quantum field theory [2] . Secondly, most of our current results in cosmology are based on a huge extrapolation of our knowledge of gravity up to scales where GR has never been tested.

In particular, it became extremely important to test the validity of our extrapolation on the nature of gravity at large scales, after the discovery of the late time accelerated expansion of the Universe [3, 4]. This is currently explained assuming the existence of a new component of the Universe called “dark energy”, whose nature is still unknown and accounts for around 70 % of the energy budget of the Universe today.

This scenario, i.e our current lack of knowledge about the main component of the Universe which drives its late time expansion, is usually referred as the “dark energy problem” and it can be addressed in several ways. In this chapter, we will focus on two approaches, the “Dark Energy” models (DEMs), where a new species is added to the Universe stress-energy tensor, and “modified gravity” theories (MGTs), alternative models for the gravitational interaction, since they are of particular importance for the work outlined in this manuscript.

1.2 Λ -CDM model

The simplest way to explain the accelerated expansion of the Universe is to introduce a cosmological constant (often referred to as Λ) into the Einstein-Hilbert Action (EHA)

$$S = \int d^4x \left[\sqrt{-\tilde{g}} \left(\tilde{M}_{\text{Pl}}^2 \frac{\tilde{R}}{2} - \Lambda^4 \right) + \mathcal{L}_m(\psi_m^{(i)}, \tilde{g}_{\mu\nu}) \right], \quad (1.1)$$

where \tilde{R} is the Ricci scalar, $\tilde{g}_{\mu\nu}$ is the metric tensor and \mathcal{L}_m is the Lagrangian of the matter fields $\psi_m^{(i)}$. This solution, known as the Λ -CDM model, assumes GR validity at all scales and introduces an energy scale, associated to Λ , which has to be set “by hand” in order to mimic the late-time acceleration of the Universe.

Applying the Λ -CDM model to the study of large scale structures of the Universe puts us in the somewhat unpleasant situation of having a successful theory to describe a large class of phenomena, while lacking a deeper understating of the nature of the cosmological constant itself. For this reason, some attempts at explaining Λ in terms of the quantum vacuum energy have been made[5], but the value of the cosmological constant predicted by quantum field theory is many orders of magnitude higher than the one observed. These considerations lead to the so-called cosmological constant problems, which can be stated as:

- why Λ is so small as compared to the quantum field theory prediction?
- can Λ be understood by means of a more general theory which involves a dynamical model for the evolution of dark energy?

Even though these problems could probably be related, in the following we will not concentrate on the first one and we will address just the second one, i.e we will assume that the contribution to the cosmological constant due to the vacuum energy can be set to zero due to some unknown mechanism, as it is done in most of the studies of modified-gravity theories in the context of cosmology[6].

1.3 Strong equivalence principle

The theoretical problems delineated above, along with some discrepancies between observations and Λ -CDM model predictions [7–10], have motivated the study of a plethora of alternatives to Λ -CDM, which are often categorized in two broad classes, “Dark Energy” models (DEMs) and MGTs.

Broadly speaking, one could say that DEMs modify the Universe stress-energy tensor by adding a new species, whose equation of state is $w = p_{\text{DE}}/\rho_{\text{DE}} \simeq -1$, which is responsible for the late time acceleration of the Universe. On the other hand, MGTs modify the coupling between matter and gravity, introducing new degrees of freedom. It is possible to draw a more precise line between this two classes of models using the strong equivalence principle (SEP) [11], i.e. the assumption that there exists only one metric field to which all the massive bodies couple, independently from their composition. We can in fact describe DEMs as modifications to Λ -CDM which are compatible with the SEP, while MGTs are not and they are often described by the means of a “fifth force”. This classification cannot be considered completely satisfactory, since there are models for which choosing between DEMs and MGTs is somewhat a matter of personal tastes. However this approach will be used here, since it is sufficient for the scope of this manuscript.

1.4 Dark energy

DEMs are one of the most natural directions to explore, while researching on dynamical mechanisms to explain the current value of the cosmological constant. One of the simplest examples of DEM is the so-called quintessence models [12], in which a scalar field drives the cosmic evolution at late times. The action for these models reads

$$S = \int d^4x \sqrt{-\tilde{g}} \left[\frac{\tilde{R} \tilde{M}_{\text{Pl}}^2}{2} - \frac{1}{2} (\partial\varphi)^2 - V(\varphi) + \mathcal{L}_m(\psi_m^{(i)}, \tilde{g}_{\mu\nu}) \right], \quad (1.2)$$

where \tilde{R} is the Ricci scalar, φ is the scalar field and $V(\varphi)$ is its potential, often a free function of the theory. In quintessence models the scalar field behaves as a perfect fluid, whose equation of state is given by:

$$w = \frac{\frac{1}{2}\dot{\varphi}^2 - V(\varphi)}{\frac{1}{2}\dot{\varphi}^2 + V(\varphi)} \quad (1.3)$$

where $\dot{\varphi}$ is the partial time derivative of the scalar field. Since observations suggest at late times $w \simeq -1$, in quintessence models the potential energy dominates over the kinetic energy, i.e we must have $V(\varphi) \gg \dot{\varphi}^2$. This means that the potential has to be chosen to fulfill this requirement, along with other ones to provide theoretical stability and observational viability [13, 14]. From Eq.(1.2), it

is possible to explicitly see that DEMs do not violate SEP, as the gravitational sector is not modified.

It is possible to construct a very large class of models generalizing Eq.(1.2), which are of great importance and have been studied extensively both on theoretical and observational levels. We will not discuss them here, since it is far beyond the scope of this manuscript, which mostly focuses on MGTs, but we refer the reader to [13, 14] for an overview of this topic.

1.5 Modified-gravity theories

In GR the gravitational force is mediated by a single 2-rank tensor, namely the metric $g_{\alpha\beta}$. This is inspired by the original Einstein's idea that matter moves along geodesics evaluated using $g_{\alpha\beta}$, which is deformed by the presence of any form of energy, including massive objects. It has been shown that GR is the only possible gravitational theory mediated by a single 2-rank tensor [15] and then any MGT must include some extra field. The simplest scenario other than GR is to consider the presence of an additional scalar field to the EHA, which we will describe with some detail in this section since it is of vital importance for most part of this Thesis. Moreover, it is possible to consider also some other extra fields such as vectors, tensors and higher-rank fields [16, 17], but we will not discuss these scenarios here, since this is beyond the scope of this manuscript.

However, any effect due to the presence of an additional scalar field must be suppressed in all the environments where GR is well tested, such as the Solar system and laboratories. This can be achieved by weakly coupling the extra scalar field to matter at all scales, but also, as we will discuss in more details in sec 1.5.2, via a scale-dependent mechanism that provides convergence to GR when necessary.

1.5.1 Scalar-tensor theory of gravity

MGTs in which a scalar field is added to the EHA are often called **scalar-tensor theories of gravity**. They are of particular interest because their simple structure allows us to obtain analytical results, which can be used to test GR. Thus, they can be seen as toy-models which can shed some light on possible signatures of a more profound theory for gravitational interactions.

It is possible to write down a general form for the scalar-tensor theories action as[18]

$$S = \int d^4x \sqrt{-\tilde{g}} \left[\tilde{R} + \mathcal{L}(\varphi, \tilde{g}_{\mu\nu}) \right] + \int d^4x \sqrt{-g} \mathcal{L}_m(\psi_m^{(i)}, g_{\mu\nu}), \quad (1.4)$$

where $\mathcal{L}(\varphi, \tilde{g}_{\mu\nu})$ is the scalar-field Lagrangian density and \mathcal{L}_m is the Lagrangian of the matter fields $\psi_m^{(i)}$, which are coupled to the gravitational sector of the theory

via a transformation of the metric [19]

$$g_{\mu\nu} = A^2(\varphi)\tilde{g}_{\mu\nu} + B(\varphi)\tilde{\nabla}_\mu\varphi\tilde{\nabla}_\nu\varphi \quad (1.5)$$

where $\tilde{\nabla}_\mu$ is the covariant derivative (with respect to metric $\tilde{g}_{\mu\nu}$) and $A(\varphi)$ and $B(\varphi)$ are free functions of the scalar field. Eq.(1.5) shows that, counter to what is dictated by GR, in scalar-tensor theories there exist two different metrics, one for the Einstein-Hilbert action and the other one for the dynamics of all matter particles. As we will see in sec.2.2 and 3.2, matter particles follow geodesics due to $g_{\mu\nu}$, which are in general different from the ones obtained from $\tilde{g}_{\mu\nu}$. This means that *physics looks different* using the two different metrics and leads to the definition of two different frames : the Einstein frame, associated to the metric $\tilde{g}_{\mu\nu}$, where matter fields are minimally coupled to the gravity sector, and the Jordan frame, associated to $g_{\mu\nu}$, where matter is non-minimally coupled to gravity sector. For this reason, in the Einstein frame we recover the EHA but the equations of motion of matter are non-standard (e.g., the continuity equation shows a source term and matter density is not conserved), while in the Jordan frame the equations of motion of matter take the usual form (matter density is conserved and radiative processes are given by the standard results and do not vary with time or space), but gravity is modified (e.g., the Friedmann equations are modified). For reasons delineated above, choosing conveniently between Einstein and Jordan frame can give great advantages while comparing theoretical expectations with observational results [20]. In this manuscript, we will often choose the Jordan frame, since it is more convenient for our work.

Moreover, along all this Thesis we will restrain ourselves to a particular case of Eq.(1.5),

$$g_{\mu\nu}(x) = A^2(\varphi(x))\tilde{g}_{\mu\nu}(x), \quad (1.6)$$

which describes a transformation function of the particular space-point considered, via the space-time dependency of the scalar field. Eq.(1.6) represents an isotropic expansion (or contraction) at the same rate along any direction and so it is often called a **conformal transformation**.

It is possible with an adequate choice of $A(\varphi)$ and $\mathcal{L}(\varphi)$, and throughout this manuscript we will give some explicit examples, to provide MGTs with a dynamical mechanism for the late time acceleration of the Universe and a convergence mechanism to GR at small scales.

1.5.2 Screening mechanisms

As we already discussed above, any viable modification to GR must provide a screening mechanism, i.e. a mechanism which provides convergence to GR at Solar system and laboratory scales. One can rephrase this statement by noticing that the matter density field in the Universe varies over several orders of magnitude, ranging from $\rho_{\text{crit}} \simeq 10^{-29} \text{ g cm}^{-3}$ to $\rho_{\text{Solar System}} \simeq 3 \text{ g cm}^{-3}$, and assuring that the screening mechanism provides convergence to GR in high-density environments.

This is of crucial importance since the background value of the scalar field $\bar{\varphi}$ often depends on the local matter density ρ . If so happens, it can be much easier to express the screening mechanism in terms of ρ than in terms of a particular scale, unless the considered system possesses a particular symmetry.

For a scalar-tensor theory, one can classify the possible screening mechanisms, using a second-order Lagrangian for the scalar field

$$\delta\mathcal{L}_\varphi = -\frac{1}{2}Z(\bar{\varphi})(\partial\delta\varphi)^2 - \frac{m^2(\bar{\varphi})}{2}(\delta\varphi)^2 - \beta(\bar{\varphi})\delta\varphi\delta\rho \quad (1.7)$$

where we defined the scalar field perturbation as $\delta\varphi(x, t) = \varphi(x, t) - \bar{\varphi}(t)$, $Z(\bar{\varphi})$ represents the self-derivatives interactions of the scalar field, $\beta(\varphi)$ is the coupling function between the scalar and the matter field and $m^2(\bar{\varphi}) = \partial^2 V/\partial\varphi^2$ is the scalar field mass squared, with $V(\varphi)$ the scalar field potential.

In this context the screening mechanism can be realized in 3 different ways, each associated with a different term of Eq.(1.7):

- **high mass** : the scalar field does not propagate beyond the Compton wavelength m^{-1} and so the force mediated by the latter is suppressed above this scale. By making $m \rightarrow +\infty$ in high-density environments, the force associated to the scalar field can be suppressed with respect to the Newtonian one. This kind of mechanism is often referred to as **the chameleon-type screening mechanism** [21, 22].
- If the coupling to matter $\beta(\varphi)$ is small in regions of high density, the strength of the fifth force generated by the scalar field is weak and modifications of gravity are suppressed. This screening mechanism is realized in **dilaton and symmetron** MGTs [23].
- If $Z(\bar{\varphi})$ becomes large in dense environments, the coupling to matter is effectively suppressed, because the gradients of the scalar field become much smaller than would be predicted by the linear theory. This can be achieved in (at least) two ways, i.e. with a screening mechanism controlled either by $|\nabla^2\varphi|$ (**Vainshtein mechanism** [24]) or by $|\nabla\varphi|$ (**K-mouflage** [25]).

As outlined in this section, the fifth force becomes negligible with respect to the Newtonian one when the screening mechanism occurs. In the next sections, we will discuss how this transition regime can be used to probe the viability of (some) MGTs, studying astrophysical objects, such as galaxies or galaxy clusters, dynamics. It is worth noticing that this transition occurs at different scales for different MGTs and thus screening mechanisms could be used to discriminate among them.

1.6 Tests of gravity

In this section, we discuss how MGTs, in particular scalar-tensor theories of gravity, can be tested using cosmological and astrophysical probes. We will focus on the impact of MGTs on cosmological structure formation in a quite broad sense, i.e without specifying a particular theory ¹ but relying on phenomenological parametrizations to highlight the effects of the presence of a scalar field.

Broadly speaking, MGTs can have two effects on the formation of large scale structures in the Universe. On the first hand, they can modify the expansion history of the Universe, e.g. modifying the time dependence of $H(z)$ or $G(z)$. However, the former has been measured using several techniques such as supernovae [26], baryonic acoustic oscillation (BAO) [27] and early-type galaxies [28] and was found to be consistent with Λ -CDM model at percent level. For this reason most of MGTs are crafted in such a way that they reproduce exactly Λ -CDM at the background level but some exceptions exist, e.g. the K-mouflage model, which induce modifications to the expansion history that are used to put constraints on these models. On the other hand, almost any scalar-tensor theory of modified gravity induces modifications at the perturbation level. In the Newtonian gauge perturbed metric $ds^2 = a^2 [-(1 + 2\Phi) d\tau^2 + (1 - 2\Psi) d\mathbf{x}^2]$, these modifications are often parametrized for linear perturbations as [29]

$$\begin{aligned} k^2\Psi &= 4\pi\mathcal{G}\mu(k, z)a^2\bar{\rho}_m\delta \\ \frac{\Phi}{\Psi} &= \eta(k, z) \end{aligned} \tag{1.8}$$

where the two function $\mu(k, z)$ and $\eta(k, z)$ are peculiar to each model of modified gravity. They can be in principle computed from the Lagrangian of the model, and are equal to 1 in Λ -CDM. In particular, $\mu(k, z)$ describes how the growth of structure is modified and it might have an impact, depending on the considered theory, in a variety of cosmological observables such as the galaxy power spectrum or the halo temperature function. On the other hand, $\eta(k, z)$ expresses the possible differences between the time and space perturbation potentials and it can be constrained using a combination of probes, including weak lensing $\Phi + \Psi$ and temperature anisotropies due to integrated Sachs-Wolfe (ISW) [30, 31] or kinetic Sunyaev-Zeldovich (kSZ) effect [32].

Moreover, at Solar System scales, a modification to the Newtonian law of gravitation, due to the presence of the scalar field, can perturb the orbits of satellites around massive objects. In particular, this can happen for the Moon's orbit around the Earth, causing an anomalous angular advance of the perihelion ² of the orbit. However, the latter was measured with exquisite precision [33], imposing very tight constraints on modified gravity theories with a time and space dependent effective Newtonian coupling.

¹We will focus on some particular theories in sec.2.5,3.3, where we describe K-mouflage and ultra-local models of gravity.

²More details will be given for K-mouflage model in sec.2.3.

Beside these observational probes, any early time modification of gravity is constrained by the CMB observations of the Planck satellite [34, 35], which endorsed the current picture that CMB physics is governed by the Λ -CDM model. However, these results usually impose poor constraints on MGTs, with respect to late-times probes, due to the small impact of dark energy at early times.

To summarize, all these tests of gravity give us a picture which is consistent with Λ -CDM so far, with room for possible extensions of GR that must satisfy a substantial number of constraints. However, it is highly probable that next-generation large-scale structure surveys will impose very stringent constraints on MGTs at the cosmological level [36–40], possibly ruling out some MGTs or in the best-case scenario measuring some deviations from GR.

1.7 Conclusions

In this chapter, we gave a very short introduction on the vast topic of the dark energy problem, i.e. the lack of understanding beyond the late time acceleration of the Universe.

We also briefly introduced DEMs and MGTs, seen as modifications to the standard Λ -CDM model that are useful to address the dark energy problem. In this context, we focused on scalar-tensor theories, because of their simplicity and their importance for this manuscript.

We then moved on to discuss the screening mechanism, highlighting how it can be achieved in high-density regions, such as the Solar System where GR is very well tested.

Finally, we described how MGTs affect cosmological and small-scale observables, and how the latter can be used to put constraints on the viability of MGTs.

In the next chapters, using some of the results of this chapter, we will focus on two modified-gravity theories, namely the K-mouflage and ultra-local models of gravity. These are scalar-tensor theories, which we studied in depth in arts. [A](#), [B](#), [C](#). They show two different screening mechanisms and several different possible signatures, which will be recalled in this manuscript.

Chapter 2

K-mouflage

2.1 Introduction

In this chapter, we will discuss K-mouflage models. They are k-essence models of modified gravity, universally coupled to matter by a conformal rescaling of the metric. For the scope of this manuscript, K-mouflage models will serve as a benchmark to introduce MGTs, since they are complex enough to be an interesting alternative to GR (they possess a dynamical mechanism responsible for the late time acceleration of the Universe, a screening mechanism and modify the dynamics of astrophysical objects) but they are simple enough to be treated using semi-analytical techniques, at least in particular cases which are of great interest for cosmology.

K-mouflage models were studied at the background and linear levels in the literature [41, 42], and here we will extend the analysis to situations where the scalar field responsible for the modification of gravity is coupled to a perfect fluid with pressure. Within this framework, it is possible to study the impact of K-mouflage models on galaxy cluster dynamics, which are unscreened in this theory, and to study how it is possible to constrain them using cluster observations.

Most of the results shown in this chapter were found in art.A, which is appended to this manuscript for the reader's convenience, along with most technical details of the calculations.

2.2 Description of the model

K-mouflage models are described by an action of the form

$$S = \int d^4x \sqrt{-\tilde{g}} \left[\frac{\tilde{M}_{\text{Pl}}^2}{2} \tilde{R} + \mathcal{M}^4 K(\tilde{\chi}) \right] + \int d^4x \sqrt{-g} \mathcal{L}_m(\psi_m^{(i)}, g_{\mu\nu}) \quad (2.1)$$

where we denoted with a tilde the Einstein-frame quantities, to distinguish them from Jordan frame ones.

The Lagrangian of the scalar field is composed by two terms: firstly \mathcal{M}^4 , an energy scale which can be set of the order of the current dark energy density to recover the late-time acceleration of the Universe; and secondly $K(\tilde{\chi})$, a non-standard kinetic term, which is a free function of the standard kinetic term

$$\tilde{\chi} = -\frac{1}{2\mathcal{M}^4} \tilde{\nabla}^\mu \varphi \tilde{\nabla}_\mu \varphi. \quad (2.2)$$

The functional form of $K(\chi)$ is subject to several viability constraints, which we will discuss in sec.2.3.

From Eq.(2.2), it is possible to understand how $\tilde{\chi}$ behaves in the cosmological and the small-scale regime, which are crucial to put constraints on $K(\chi)$:

- in the cosmological regime, the scalar field is time dependent and uniform, its spatial gradients can be neglected with respect to its time derivatives, and $\chi > 0$;
- in the small-scale regime, the scalar field is quasi-static and non-uniform, its gradients are much greater than its time derivatives, making $\chi < 0$.

As discussed in sec.1.5.1, we will couple the scalar with the matter field via a conformal transformation of the type of Eq.(1.6), setting the coupling function $A(\varphi)$ as

$$A(\varphi) = \exp\left(\frac{\beta\varphi}{\tilde{M}_{\text{Pl}}}\right), \quad (2.3)$$

where β is a coupling constant that can be chosen to be positive, without loss of generality, since this simply corresponds to a redefinition of the sign of the scalar field. Along this chapter, we will restrict to the case in which β is a constant, both in space and time.

Using the relation $\sqrt{-g} = A^4 \sqrt{-\tilde{g}}$ and the relation between Ricci scalars in Jordan and Einstein frames [15]

$$\tilde{R} = A^2 [R + 6\Box \ln A - 6g^{\mu\nu} \partial_\nu \ln A \partial_\mu \ln A], \quad (2.4)$$

it is possible to obtain

$$G(z) = \bar{A}^2 \mathcal{G} \simeq \left(1 + \frac{2\beta\bar{\varphi}}{\tilde{M}_{\text{Pl}}}\right) \mathcal{G}, \quad (2.5)$$

where we used (2.3) to obtain the last result. Eq.(2.5) implies a time variation of the Newton coupling due to the time variation of the scalar field. This is of particular importance for K-mouflage since $|\bar{A} - 1| \lesssim 1$, and leads to percent variations in the background cosmology with respect to the Λ -CMD case. As a matter of example, we show in Fig.2.1 the redshift evolution of Ω_m and Ω_{de} for the

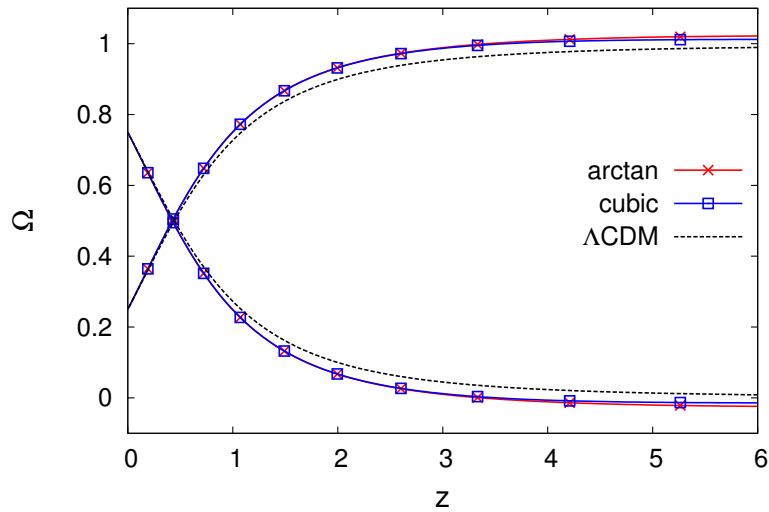


FIGURE 2.1: Redshift evolution of the matter and dark-energy cosmological parameters Ω_m and Ω_{de} . In red we show the K-mouflage model of Eq.(71), in blue the one defined by Eq.(74) of art.A, and in black the Λ -CDM model.

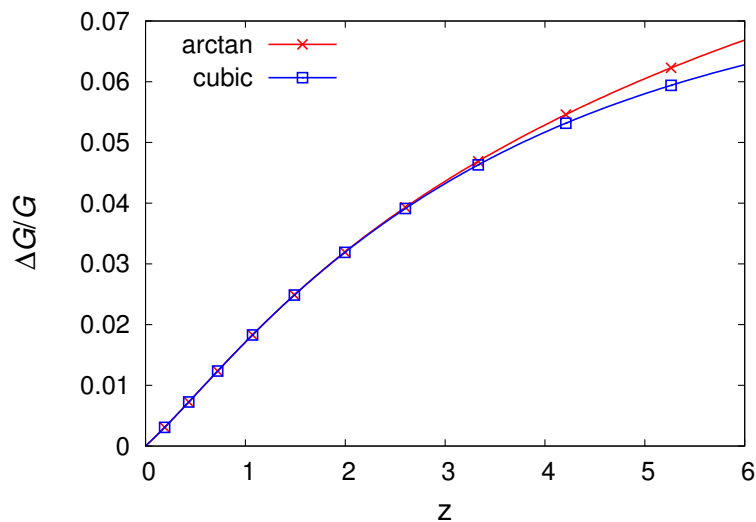


FIGURE 2.2: Relative drift with redshift of the Newton's coupling for the K-mouflage models.

two K-mouflage models used in art.A, which we normalized by their Einstein-frame values today. Ω_{de} differs from its Λ -CDM counterpart because of the evolution of the scalar field, which is dictated by its Klein-Gordon equation. This implies that Ω_m also differs from the Λ -CDM prediction, as in both cosmologies we assumed a flat universe. Furthermore, the percent time variation of $G(z)$, which we show in Fig.2.2, results in severe constraints on the value of the coupling constant, as we will show in sec.2.3.

2.3 Large- and small-scale constraints

Since we are aiming at constructing a MGT which provides a dynamical mechanism to mimic late time acceleration of the Universe, the kinetic function must converge to a cosmological constant at late times and large scales. This can be achieved by imposing:

$$\begin{aligned} \mathcal{M}^4 &= \tilde{\rho}_\Lambda, \\ \tilde{\chi} \rightarrow 0 : K(\tilde{\chi}) &= -1 + \tilde{\chi} + \dots \end{aligned} \quad (2.6)$$

where the zeroth order factor -1 corresponds to the late-time acceleration. We can choose the normalization of the first two terms of $K(\chi)$ without a loss of generality, since they just set the normalization of \mathcal{M}^4 and φ .

The functional form of $K(\chi)$ can be constrained by several theoretical arguments and observations. These constraints can be (roughly) divided in two categories, the large-scale ones (when $\chi > 0$)

- $K' > 0$ (with $K' = dK/d\tilde{\chi}$): to avoid ghosts in the theory;
- $\bar{K}' + 2\chi\bar{K}'' > 0$: this ensures that we have a well-defined and unique scalar field profile for any value of the matter density. This is of particular importance at high redshifts when the matter density becomes increasingly large;
- $\beta^2/\bar{K}' < 0.05$: to satisfy the Big Bang Nucleosynthesis constraint. If it was not the case, $H(z)$ would deviate too much from the Λ -CDM counterpart, causing a non-viable abundance of primordial elements. Since $\bar{K}' \sim 1$ in the cosmological context (Eq.(2.6)), the constraint on β^2/\bar{K}' can be recast as a constraint on the coupling, which turns out to be $\beta \lesssim 0.22$;
- $\tilde{\chi}\bar{K}' \ll \bar{K}$ to recover the DE equation of state (see Eq.(17) of A),

and the small-scale ones (when $\chi < 0$)

- $\beta < 0.1$: the time dependence of Newton coupling affects the trajectories of planets and moons. In particular, the Lunar Laser Ranging experiment [33] observed the Earth-Moon system, allowing a maximum time variation of $|d \ln G/dt| \simeq 10^{-12} \text{yr}^{-1}$. This can be recast as a constraint on $|d \ln \bar{A}/d \ln a| \simeq \beta^2/\bar{K}' \simeq \beta^2$, which leads to $\beta \lesssim 0.1$ [43]. This constraint is tighter than the one due to BBN and sets the value of $\beta = 0.1$ that we used for all plots shown in this chapter;
- $|\delta\pi \frac{\beta^2}{K'} \chi \frac{K''}{K'} \frac{K'+2\chi K''}{K'}| < 2 \times 10^{-11}$. The fifth force associated to the K-mouflage scalar field perturbs the lunar orbit around the Earth, causing an advance in the anomalous perihelion. However, the latter is severely bounded by the Lunar Ranging experiment, resulting in a constraint on both β and $K(\chi)$.

If we assume that $\beta \simeq 0.1$, the only way in fulfilling such a requirement is to diminish $\chi K''/K'$ when $\chi < 0$, giving a severe constraint on the shape of $K(\chi)$ in the static regime.

- laboratory tests, such as atom interferometers, constrain the amplitude of the fifth force, which is proportional to β^2/K' , to a 10^{-4} level. However, this happens well inside the region where screening occurs, making these bounds much less severe than the previous ones.

When all these constraints on the shape of $K(\chi)$ are enforced, it is still possible to find analytical expressions for the kinetic function, such as the one of Eq.(71) of art.A ¹, which leaves us with 4 additional parameters other than the usual cosmological ones, namely

$$\{\beta, \chi_*, K_*, \mathcal{M}\} \quad (2.7)$$

which have to be chosen to fulfill all the constraints aforementioned. (But note that \mathcal{M} merely replaces the usual cosmological constant parameter Ω_{de} .)

2.4 Background cosmology

If we assume a FLRW metric $ds^2 = a^2(-d\tau^2 + d\mathbf{x}^2)$, we obtain the Jordan frame Friedmann equation

$$3M_{\text{Pl}}^2 H^2 = \bar{\rho} + \bar{\rho}_{(r)} + \bar{\rho}_{de} \quad (2.8)$$

where we defined the Jordan-frame time dependent Planck mass $M_{\text{Pl}} = \tilde{M}_{\text{Pl}}/\bar{A}$, and

$$\bar{\rho}_{de} = \bar{\rho}_\varphi + \frac{2\epsilon_2 - \epsilon_2^2}{(1 - \epsilon_2)^2} (\bar{\rho} + \bar{\rho}_{(r)} + \bar{\rho}_\varphi), \quad (2.9)$$

where $\bar{\rho}_\varphi = \mathcal{M}^4 (2\bar{\chi}\bar{K}' - \bar{K})$ and $\epsilon_2 = d \ln \bar{A} / d \ln a$. We defined the dark energy density as the density that is missing in the Friedmann equation to match the Hubble rate, after taking into account radiation and matter densities.

The Klein-Gordon equation for the scalar field in Jordan frame reads,

$$\frac{d}{dt} \left(\bar{A}^{-2} a^2 \frac{d\bar{\varphi}}{dt} \bar{K}' \right) = -a^3 \bar{\rho} \frac{d \ln \bar{A}}{d\varphi}, \quad (2.10)$$

which dictates the evolution of $\bar{\varphi}$, shown in Fig.2.3. The scalar field φ is negative, grows with time (we choose the normalization $\varphi = 0$ at $z \rightarrow +\infty$) and $|\beta\bar{\varphi}/M_{\text{Pl}}| \ll 1$ until $z = 0$.

¹The model defined by Eq.(74) of art.A does not satisfy Solar System constraints. However it can be seen as an effective model for the semiaxis $\chi > -1$, which is sufficient for the purposes of this chapter.

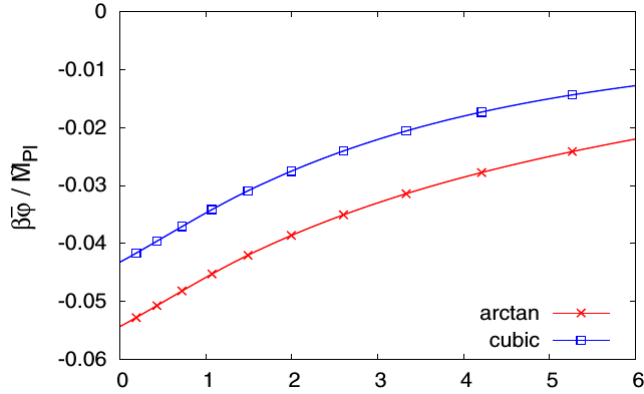


FIGURE 2.3: background scalar field $\bar{\varphi}$ as a function of redshift.

2.5 Large scale structure formation

As pointed out in sec.2.2, K-mouflage models change the expansion history of the Universe (in Jordan frame), modifying the background cosmological quantities with respect to their Λ -CDM counterparts. Additionally, these models enhance the growth rate of cosmological structure, both at linear and non-linear levels (sec. III-B of A). This can be seen as the effect of the presence of a scalar field potential, due to the conformal coupling, which modifies the 00 component and the trace of the perturbed FRLW metric as:

$$\Phi = \Psi_N + \frac{\delta A}{\bar{A}}, \quad \Psi = \Psi_N - \frac{\delta A}{\bar{A}}. \quad (2.11)$$

We can connect $\delta A/\bar{A}$ to $\delta\rho$, using Klein-Gordon equation of motion for the scalar field

$$\frac{1}{a^2} \nabla^2 \varphi = \frac{\beta \bar{A}}{K' M_{\text{Pl}}} \delta\rho, \quad (2.12)$$

which, at the first order, gives

$$\frac{1}{a^2} \nabla^2 \frac{\delta A}{\bar{A}} = \frac{\beta^2}{M_{\text{Pl}}^2 K'} \delta\rho. \quad (2.13)$$

Eq.(2.13) can be used to write the Jordan frame Poisson equation

$$\frac{1}{a^2} \nabla^2 \Phi = \frac{1 + \epsilon_1}{2M_{\text{Pl}}^2} \delta\rho, \quad (2.14)$$

where $\epsilon_1 = 2\beta^2/K'$. Additionally, the Jordan frame continuity and Euler equations read

$$\frac{\partial \rho}{\partial \tau} + \nabla \cdot (\rho \mathbf{v}) + 3\mathcal{H}\rho = 0 \quad (2.15)$$

$$\frac{\partial \mathbf{v}}{\partial \tau} + (\mathbf{v} \cdot \nabla) \mathbf{v} + \mathcal{H}\mathbf{v} = -\nabla \Psi. \quad (2.16)$$

Using the results obtained above, at the linear level it is possible to write down the evolution equation of the linear growing mode

$$\frac{d^2 D}{d(\ln a)^2} + \left(2 + \frac{1}{H^2} \frac{dH}{dt} \right) \frac{dD}{d \ln a} - \frac{3}{2} \Omega_m (1 + \epsilon_1) D = 0, \quad (2.17)$$

which differs from the Λ -CDM one for two reasons: the different values of Ω_m and H and the time-dependent amplification factor $(1 + \epsilon_1)$ that comes from the modified Poisson equation. These result in the enhancement of $D(a)$ at the percent level (Fig.2.4) at late times, when $\epsilon_1 \simeq 0.02$ (Fig.2.5). On the other hand, we recover a Λ -CDM cosmology at late times, since $\epsilon_1 \rightarrow 0$ (along as Ω_m and H tend to their Λ -CDM counterparts).

It is also possible to study the spherical collapse, using Eq.(2.16) in spherical symmetry

$$\frac{d^2 \mathbf{r}}{dt^2} - \frac{1}{a} \frac{d^2 a}{dt^2} \mathbf{r} = -\nabla \Psi. \quad (2.18)$$

Let us introduce the normalized radius

$$y(t) = \frac{r(t)}{a(t) q} \quad \text{with} \quad q = \left(\frac{3M}{4\pi \bar{\rho}_0} \right)^{1/3}, \quad (2.19)$$

where q is the Lagrangian radius of a spherical structure of mass M and it is related to the matter density within $r(t)$ as

$$1 + \delta(< r) = y(t)^{-3}. \quad (2.20)$$

Using Eq.(2.19) into Eq.(2.18) we obtain

$$\frac{d^2 y}{d(\ln a)^2} + \left(2 + \frac{1}{H^2} \frac{dH}{dt} \right) \frac{dy}{d \ln a} + \frac{\Omega_m}{2} (1 + \epsilon_1) (y^{-3} - 1) = 0, \quad (2.21)$$

which can be used to obtain the evolution of $\delta(< r)$ via Eq.(2.20). Eq.(2.21) differs from the Λ -CDM case through the different values of H and Ω_m , and the amplification factor $(1 + \epsilon_1)$, which comes from the Poisson equation as for Eq.(2.17). In Fig.2.6, we show the linear density contrast $\delta_{L(\Lambda)}$ that corresponds to a nonlinear density contrast $\delta[\delta_L] = \Delta_m$, where $\Delta_m = \Delta_c / \Omega_m(z)$ is the nonlinear threshold that we choose to define halos and Δ_c is a free parameter that we choose to be equal to 200. Since the K-mouflage models accelerate the growth of large-scale structures, a smaller density contrast in the linear regime is needed to reach the same non-linear density Δ_c . This has an impact on the halo mass function, as we will see in sec.2.7.1.

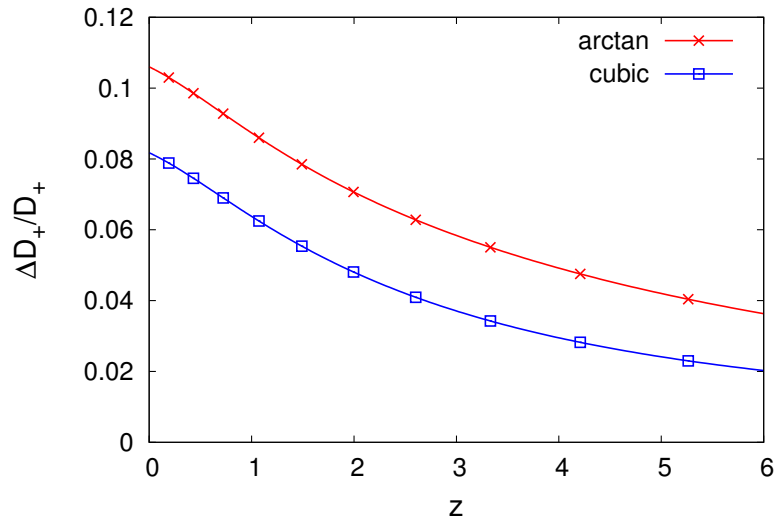


FIGURE 2.4: Relative deviation $D_+/D_{\Lambda\text{-CDM}} - 1$ as a function of redshift.

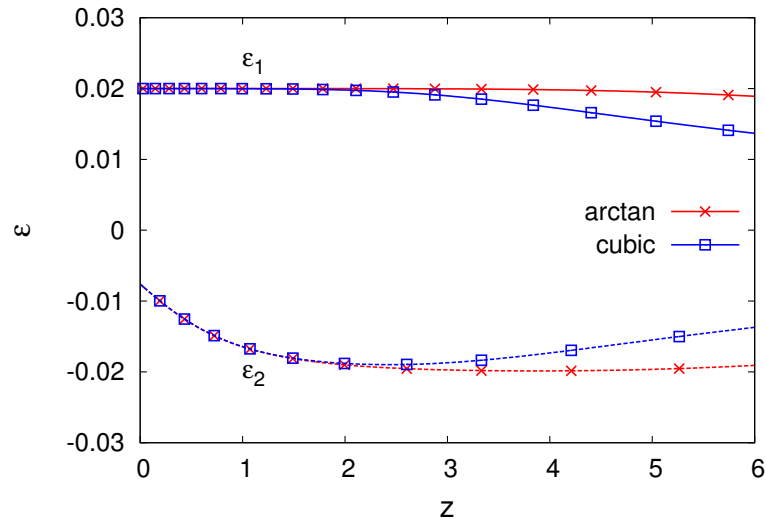


FIGURE 2.5: Redshift evolution of the coefficients ϵ_1 and ϵ_2 .

2.6 Lack of screening of clusters in K-mouflage models

In K-mouflage models of modified gravity, clusters of galaxies are not screened from the fifth force, even far inside the cluster boundaries (sec V-B of ref.A). This can be seen using the Klein-Gordon equation for the scalar field, applied to a spherically symmetric system

$$\frac{d\varphi}{dr} K' = \frac{\beta \bar{A} M(r)}{c^2 M_{\text{Pl}} 4\pi r^2}, \quad (2.22)$$

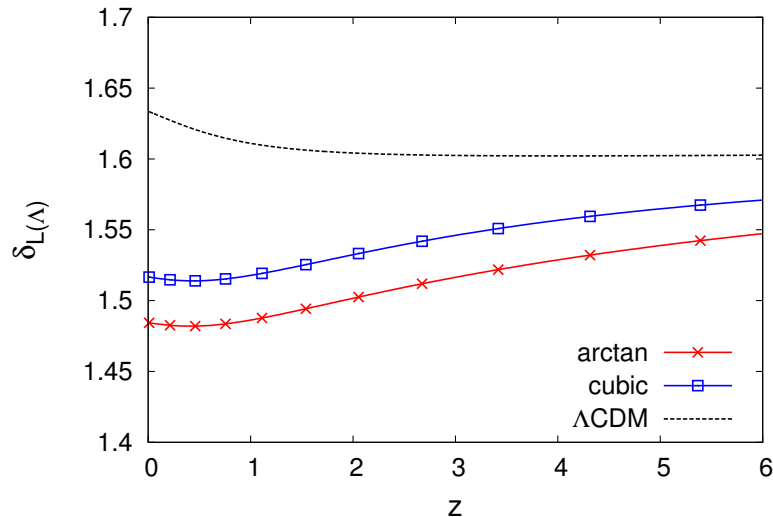


FIGURE 2.6: Linear density contrast threshold $\delta_{L(\Lambda)}$, associated with the non-linear density contrast $\Delta_c = 200$ with respect to the critical density ρ_{crit} , for the K-mouflage models and the Λ -CDM reference.

where $M(< r)$ is the mass enclosed within the radius r . It is possible to recast Eq.(2.22) by introducing the so-called “K-mouflage screening radius” R_K

$$R_K(M) = \left(\frac{\beta \bar{A}^2 M}{4\pi c M_{\text{Pl}} \mathcal{M}^2} \right)^{1/2}, \quad (2.23)$$

where $M = M(R)$ is the total mass of the object of radius R , the rescaled dimensionless variables $x = r/R_K$, $m(x) = M(< r)/M$, $\phi(x) = \varphi(r)/\varphi_K$, with $\varphi_K = \mathcal{M}^2 R_K / c \bar{A}$, to obtain

$$\frac{d\phi}{dx} K' = \frac{m(x)}{x^2}, \quad \text{with} \quad \tilde{\chi} = -\frac{1}{2} \left(\frac{d\phi}{dx} \right)^2. \quad (2.24)$$

It is possible to give an estimate of R_K , using that $\mathcal{M}^4 \sim \bar{\rho}_{\text{de}0}$ and that $\bar{A} \sim 1$, obtaining

$$R_K(M) \simeq \sqrt{\frac{\beta M}{10^{14} M_{\odot}}} 0.12 h^{-1} \text{Mpc}. \quad (2.25)$$

With $\beta = 0.1$ and a cluster mass $10^{14} M_{\odot}$, we obtain a K-mouflage screening radius of $R_K \simeq 0.04 h^{-1} \text{Mpc}$. This is much smaller than the size of a typical cluster of mass $M = 10^{14} M_{\odot}$, leaving much of the cluster unscreened. Moreover, $M(< r)$ decreases as we move inside the cluster, delaying the beginning of the screened region. For this reason, clusters are not screened in K-mouflage theories, and the fifth force has a non-negligible impact on their dynamics, as we will show in sec.2.7.

At this stage, one may wonder about the impact of the fifth force on the non-linear

substructures present in the cluster. Because of the non-linearities of the Klein-Gordon equation of the scalar field, the solution obtained for the averaged halo profile may greatly differ from the “exact solution” obtained by taking into account substructures. In particular, galaxies in clusters, whose density is much higher than the one of the intra-cluster medium, are screened in K-mouflage models [44], and this may have an effect on the cluster dynamics. For this reason, around each galaxy j we must cut a patch where the Klein-Gordon equation must be solved in the fully-nonlinear regime, giving rise to a screened region around the galaxy of size $R_{j,gal}$. In practice, since $R_{j,gal} \ll R$, we can patch all galaxy solutions within the global cluster solution. Assuming a reasonable number and distribution of galaxies in a cluster (sec.VI-B of art.A), we can show that galaxies occupy only 10^{-6} of the total volume of the cluster and we can safely assume that the global solution is a good approximation to study the cluster dynamics. More precisely, K-mouflage models do not bring any other restriction than Λ -CDM models in the study of the intracluster medium or the X-ray properties of the clusters, which are already studied using global solutions.

2.7 Cluster dynamics

As shown in the previous section, clusters of galaxies are unscreened in K-mouflage. Hence, we can hope to put some constraints on K-mouflage models using cluster dynamics. In this section, we will summarize some of the results obtained in art.A, to describe the impact of the fifth force on gravitational and thermodynamical properties of the clusters.

2.7.1 Halo mass function

As shown in Fig.2.7, the halo mass function of dark matter halos in K-mouflage models gets higher in the high-mass tail, with respect to the Λ -CDM one, due to the enhancement of gravity and the faster growth of structures. On the contrary, the halo mass function gets lower at small masses, due to the normalization of both the Λ -CDM and K-mouflage halo mass functions, since the matter in the halos is bounded by the total matter content of the Universe. With respect to other MGTs, like $f(R)$, dilaton or ultra-local models [45–47], K-mouflage models show a scale independent enhancement, since there is no other particular scale introduced by the model (in the unscreened regime).

2.7.2 Cluster concentration

To estimate the impact of the K-mouflage model on the internal cluster dynamics, we assumed a NFW profile for the dark matter in halos [48]

$$\rho_{DM}(r) = \frac{\rho_s}{(r/r_s)(1+r/r_s)^2}, \quad (2.26)$$

which is characterized by r_s and ρ_s , respectively the scale radius and density. The scale density ρ_s can be expressed in terms of the concentration $c = R_{\Delta_c}/r_s$, where R_{Δ_c} is the radius such that $\rho_{DM}(< R_{\Delta_c}) = \Delta_c \rho_{\text{crit}}$ and Δ_c is the halos overdensity threshold, as

$$\rho_s = \rho_{\text{crit}} \frac{\Delta_c}{3} \frac{c^3}{\ln(1+c) - c/(1+c)}. \quad (2.27)$$

We assumed ρ_s to be proportional (up to a free parameter) to the critical density of the Universe at the formation redshift z_f , estimated by computing

$$\sigma(q, z_f) = \sigma_f, \quad (2.28)$$

where q is the halo Lagrangian radius and σ_f a free parameter. As shown in Fig.2.8, in K-mouflage models halos are more concentrated than the ones in Λ -CDM, due to the faster growth of gravitational clustering, which gives a slightly greater ρ_s . In Fig.2.8, we also show $c(M)$ for Λ -CDM and K-mouflage models compared to 19 x-ray observations obtained by the Cluster Lensing and Supernova Survey using the Hubble telescope [49], at mean redshift of $\bar{z} \simeq 0.37$. Both models agree quite well with observations, and the discrepancies between them are quite modest when compared to the error bars of current observations. Hence we do not expect to put any competitive constraints on K-mouflage models using this kind of observations in the near future, even though a more detailed study of cluster dynamics may be needed, probably involving numerical simulations, to shed more light on how K-mouflage models impact the internal structure of the clusters.

2.7.3 Hydrostatic equilibrium

From the Euler equation, it is possible to write down the hydrostatic equilibrium equation for a perfect fluid, which reads

$$\nabla\Phi = \nabla \left(\Psi_N + \frac{\beta c^2 \varphi}{\tilde{M}_{\text{Pl}}} \right) = -\frac{\nabla p_g}{\rho_g} \quad (2.29)$$

where p_g and ρ_g are respectively the gas pressure and density and Ψ_N is the Newtonian potential fixed by the dark matter. Assuming isothermal equilibrium and spherical symmetry, it is possible to obtain an expression for the gas density profile

$$\rho_g(r) \propto e^{-(1+\epsilon_1)\mu m_p \Psi_N(r)/k_B \bar{T}_g} \quad (2.30)$$

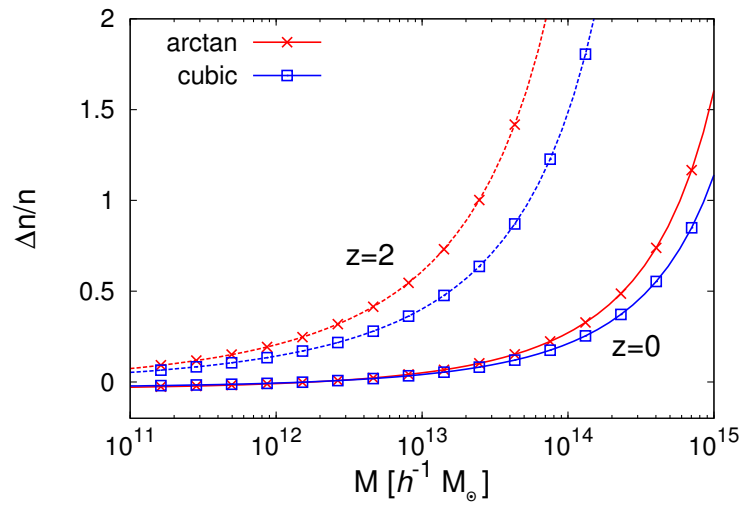


FIGURE 2.7: Relative deviation of the halo mass function $n/n_{\Lambda\text{-CDM}} - 1$ of K-mouflage models from the $\Lambda\text{-CDM}$ reference, at $z = 0$ (solid lines) and $z = 2$ (dashed lines)

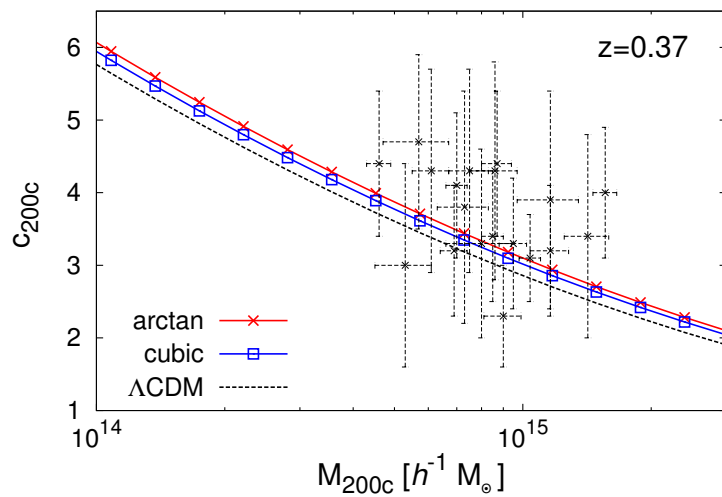


FIGURE 2.8: Mass-concentration relation for NFW halos in K-mouflage models and $\Lambda\text{-CDM}$, at $z = 0.37$. The observational measures, shown with black points, are taken from [50].

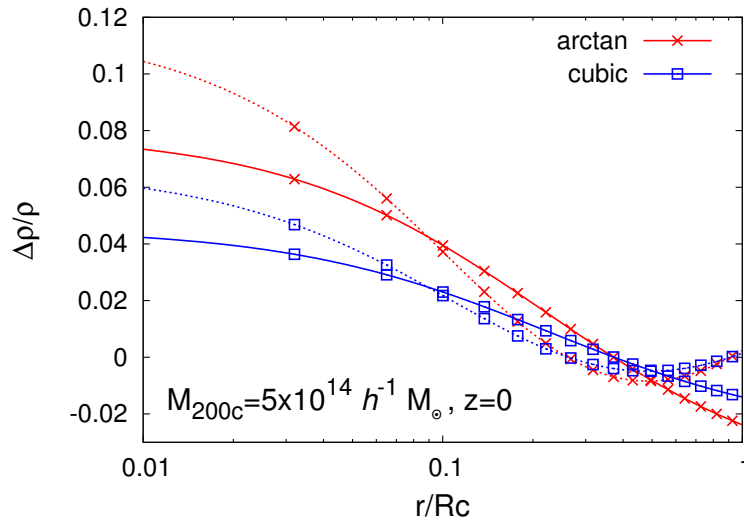


FIGURE 2.9: Relative deviation from the Λ -CDM reference of the dark matter (solid lines) and gas (dotted lines) density profiles for a cluster mass $M = 5 \times 10^{14} h M_{\odot}$.

where μm_p is the mean molecular weight of the gas and \bar{T}_g is the mean gas temperature. We estimated \bar{T}_g assuming it to be proportional to the dark matter velocity dispersion σ_{DM}^2 evaluated using Jeans equation at equilibrium. In Fig.(2.9), we show the dark matter and gas profiles both for K-mouflage and Λ -CDM: as expected from the results of sec.2.7.2, the scalar field makes the profile slightly more compact, even though this effect is quite modest.

2.7.4 Scaling laws

Among the most used methods to study cluster dynamics, there are the so-called scaling laws, i.e. relations among cluster observables such as mass, temperature or X-ray luminosity. These have been observed by numerous cosmological surveys [51, 52] and can be estimated using analytical techniques.

It is possible to reconstruct the X-ray luminosity $L_X(< R)$ within the radius R , integrating the cluster gas density over the cluster size and assuming a X-ray emissivity function, which expresses the X-ray flux at given halo temperature. To avoid complications due to the cluster internal structures and to closely resemble the procedure used by observations, we decide to compute the X-ray luminosity outside a certain core radius $R_{\text{core}} = f_{\text{core}} R$, with R the cluster radius and $f_{\text{core}} \simeq 0.15$. In Fig.2.10, we show this $L_X - T$ relation, without contributions from the cores. At fixed temperature, the K-mouflage models give a slightly lower X-ray luminosity. This is because a smaller mass is needed to have a cluster temperature T , because the fifth force enhances the velocity dispersion of clusters. Since the X-ray luminosity scales as $L_X \propto \rho_s M \sqrt{T}$, a lower mass implies a lower luminosity since the effect of the scalar fields on ρ_s is negligible.

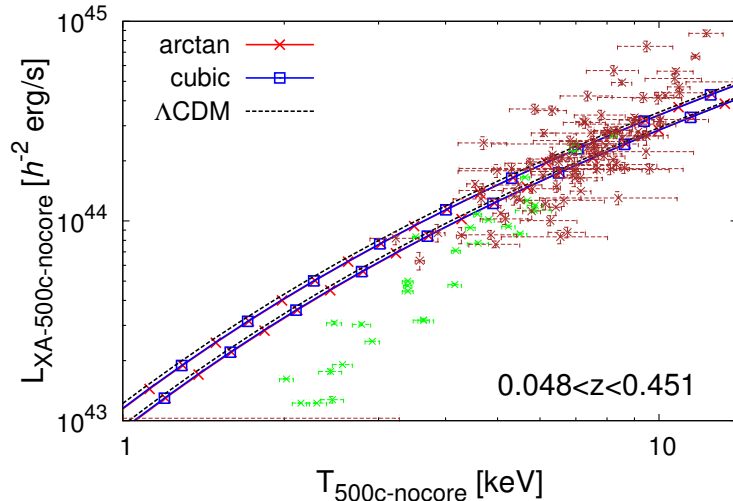


FIGURE 2.10: Temperature-luminosity relation for the K-mouflage models and Λ -CDM at $z = 0.048$ (lower curves) and $z = 0.451$ (upper curves). The data points are taken from observations made by [52] (in green) and [51] (in brown), with clusters in the redshift range $0.048 < z < 0.451$.

To summarize, we found percent deviations in cluster scaling relations (we found similar results for $M - T$ and $Y - M$ relations, see art.A) for K-mouflage models, with respect to Λ -CDM. However, these deviations are far too small to be used as competitive constraints for K-mouflage models, due to large uncertainties in current observations and to the very stringent constraints which come from Solar System and cosmological dynamics.

2.7.5 Cluster temperature function

The results of previous sections, in particular the halo mass function and the mass-temperature relation, can be used to compute the X-ray cluster temperature function as

$$n(T) = n(M) \frac{d \ln M}{d \ln T} \quad (2.31)$$

which can be measured using X-ray surveys, as was done in [53].

As shown in Fig.2.11, K-mouflage models are in good agreement with observations and predict a deviation in the high-mass tail of the order of unity. This is mostly due to the amplification of the halo mass function in the high-mass tail since, as discussed in sec.2.7.4, the effect of K-mouflage on cluster scaling laws is modest. However, deviations of $n(T)$ are large enough that we may expect to put some constraints on K-mouflage using next-generation surveys. This may require the study of degeneracies between the fifth force and baryonic physics, probably by means of numerical simulations.

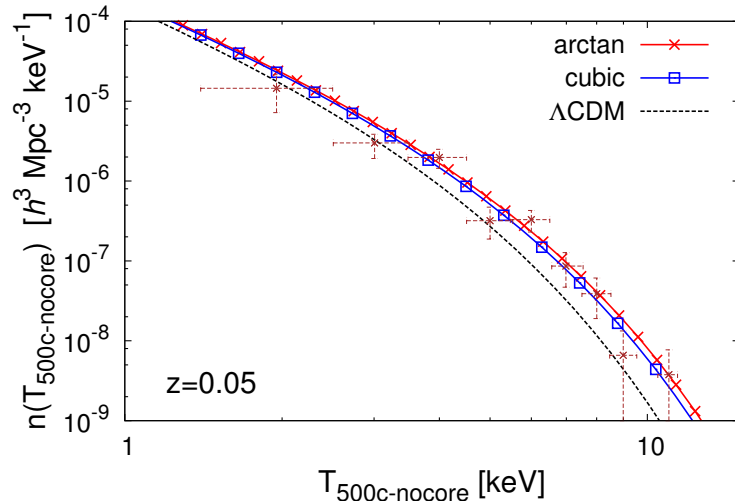


FIGURE 2.11: Cluster temperature function for K-mouflage and Λ -CDM models at $z = 0.05$. The observational data points are taken from [53] from a sample of cluster at $z \simeq 0.05$.

2.7.6 Dynamical and weak lensing masses

As shown in Eq.(2.11), in the K-mouflage models Ψ and Φ differ by a factor $2\delta A/A$ but their sum is still equal to Ψ_N . For this reason, the only difference for weak lensing signals comes from the different evolution of matter fields, but baryons fall in potential wells due to Φ and hence feel the fifth force. This leads, as in other MGTs, to different estimates for the cluster mass using either weak lensing or cluster dynamics probes. In particular, for K-mouflage we can write

$$\frac{M_{\text{dyn}}}{M_{\text{lens}}} = 1 + \epsilon_1(t) \quad (2.32)$$

where M_{dyn} and M_{lens} are respectively the mass inferred from cluster dynamics and from weak lensing. This leads to a deviation of about 2%, set by the value of β because clusters of galaxies are unscreened. However, β is severely constrained by cosmological and Solar system observations, and so the ratio $M_{\text{dyn}}/M_{\text{lens}}$ can just give an upper bound to constrain K-mouflage models.

2.8 Conclusions

In this chapter, we presented the K-mouflage models of modified-gravity theories, focusing in particular on their effects on cluster dynamics, the main topic of art.A.

For this reason, we focused on results in the Jordan frame, which differs from the Einstein frame at percent level in K-mouflage, since it is better suited to describe radiative phenomena.

Before studying cluster dynamics, we recalled some results from background cosmology and structure formation. In particular, we showed that, within K-mouflage models, the Newton coupling assumes a time dependency which can be used to impose constraints on the coupling strength β of the theory. Moreover, we showed that cosmological structure formation is enhanced at percent level, with respect to the Λ -CDM one. This enhancement is scale-independent in the unscreened regime, since K-mouflage models do not provide an additional scale in the theory, as other MGTs do.

Next, we moved to the study of cluster dynamics, showing that K-mouflage models make clusters more compact and their X-ray luminosity and temperature deviate from the Λ -CDM ones at percent level. These deviations are unfortunately too small to put competitive constraints on K-mouflage models, even in the light of future surveys. More promisingly, we found deviations in the cluster temperature function which are large enough to hope that they will be within the sensitivity limits of future large-scale surveys.

To further understand the (possible) impact of K-mouflage models on cosmology, at least two lines of research can be pursued. Firstly, along this chapter we focused on few $K(\chi)$ functions in order to give an estimate of the effects on cluster dynamics. However, a more detailed MCMC analysis may be more suited to explore the parameter space of K-mouflage models. On the other hand, dedicated K-mouflage cosmological simulations could be well suited to study the impact of screening on mildly non-linear scales, which could be of crucial importance to understand the screening mechanism. We leave to future works the detailed study using the two techniques, which we will improve our understating of K-mouflage models.

Chapter 3

Ultra-local models of gravity

3.1 Introduction

In this chapter, we present a class of MGTs called ultra-local model (ULMs), where a scalar field with a negligible kinetic term is added to the EHA. This class of theories gives rise to a new type of screening mechanism, not entirely due to the non-linearity of the scalar field, which relies on the absence of the kinetic term.

We show that the cosmological background evolution in ULMs differs from the Λ -CMD one at most at the 10^{-6} level, but these models can have a great impact on structure formation at small scales. We also present a thermodynamic analysis of the non-linear and inhomogeneous fifth-force regime, showing that the latter does not lead to the existence of clumped matter on very small scales, which would put severe constraints on these theories.

Finally, we show that these models are similar to chameleon-type theories with a large mass down to their Compton scale, and we test their viability at the cosmological level.

The results presented in this chapter were found in art.[B](#) and [C](#), which are appended to this manuscript.

3.2 Description of the models

ULMs are scalar-tensor theories, defined by the following action

$$S = \int d^4x \sqrt{-\tilde{g}} \left[\frac{\tilde{M}_{\text{Pl}}^2}{2} \tilde{R} + \tilde{\mathcal{L}}_\varphi(\varphi) \right] + \int d^4x \sqrt{-g} \mathcal{L}_m(\psi_m^{(i)}, g_{\mu\nu}), \quad (3.1)$$

where, as for K-mouflage models, the scalar field is coupled to matter by a conformal coupling of the metric. We define the Lagrangian of the scalar field $\tilde{\mathcal{L}}_\varphi(\varphi)$

as

$$\tilde{\mathcal{L}}_\varphi(\varphi) = -V(\varphi), \quad (3.2)$$

so that the scalar field has a negligible kinetic term and its dynamics are dominated by the potential.

As we will see in more details in sec.3.7, the absence of the kinetic term plays a pivotal role in the screening mechanism for these models, in particular screening with 100 % efficiency the orbits of planets in the Solar System.

If we assume that the potential can be inverted, we can make a change of variables of the type:

$$\tilde{\Xi} \equiv -\frac{V(\varphi)}{\mathcal{M}^4}, \quad \text{and} \quad A(\tilde{\Xi}) \equiv A(\varphi), \quad (3.3)$$

where we introduced an energy scale \mathcal{M}^4 , a free parameter of the model that can be chosen to be $\mathcal{M}^4 \simeq \bar{\rho}_{\text{de}0}$, since it just defines the $\tilde{\Xi}$ normalization.

Using Eq.(3.3), we can recast Eq.(3.2) and Eq.(1.6) as

$$\tilde{\mathcal{L}}_{\tilde{\Xi}}(\tilde{\Xi}) = \mathcal{M}^4 \tilde{\Xi} \quad \text{and} \quad g_{\mu\nu} = A^2(\tilde{\Xi}) \tilde{g}_{\mu\nu}, \quad (3.4)$$

leaving the functional form of $\tilde{\mathcal{L}}$ completely fixed when expressed in terms of $\tilde{\Xi}$, and we are left with a single free function for the model, the coupling $A(\tilde{\Xi})$. For this reason, there is a broad degeneracy between $A(\varphi)$ and $V(\varphi)$, since we recover the same physics for any couple of these functions which gives the same $A(\tilde{\Xi})$ (see sec.V of art.B). Thus, we will work with the $\tilde{\Xi}$ variable, and $A(\tilde{\Xi})$ will be the free function of our model, similarly to $K(\tilde{\chi})$ in K-mouflage.

From Eq.(3.1), it is possible to obtain the Klein-Gordon equation for the scalar field, which reads in Jordan frame

$$\mathcal{M}^4 + T A^4 \frac{d \ln A}{d \tilde{\Xi}} = 0, \quad (3.5)$$

where T is the trace of the matter energy-momentum tensor. Eq.(3.5) is a constraint equation (it contains no derivative terms), which gives the $\Xi(\mathbf{x})$ field as a function of the the local matter density $\rho(\mathbf{x})$.

Finally, the energy-momentum tensor of the scalar field reads

$$\tilde{T}_\nu^\mu(\tilde{\Xi}) = \mathcal{M}^4 \tilde{\Xi} \delta_\nu^\mu, \quad (3.6)$$

leading to the expressions for the scalar field energy density and pressure

$$\tilde{\rho}_{\tilde{\Xi}} = -\mathcal{M}^4 \tilde{\Xi}, \quad \tilde{p}_{\tilde{\Xi}} = \mathcal{M}^4 \tilde{\Xi} = -\tilde{\rho}_{\tilde{\Xi}}. \quad (3.7)$$

3.3 Background and perturbations in Jordan frame

If we assume a background metric (in Jordan frame) of the form $ds^2 = a^2(-d\tau^2 + d\mathbf{x}^2)$, we obtain the Friedmann equation

$$3M_{\text{Pl}}^2 \mathcal{H}^2 = a^2(\bar{\rho} + \bar{\rho}_{\text{rad}} + \bar{\rho}_{\text{de}}), \quad (3.8)$$

where $\mathcal{H} = d \ln a / d\tau$ and we defined the the Jordan-frame Planck mass as

$$M_{\text{Pl}}^2(t) = \bar{A}^{-2}(t) \tilde{M}_{\text{Pl}}^2, \quad (3.9)$$

and the effective dark energy density as

$$\bar{\rho}_{\text{de}} = \bar{\rho}_{\Xi} + \frac{2\epsilon_2 - \epsilon_2^2}{(1 - \epsilon_2)^2} (\bar{\rho} + \bar{\rho}_{\text{rad}} + \bar{\rho}_{\Xi}), \quad (3.10)$$

with $\epsilon_2 = d \ln \bar{A} / d \ln a$, as we did for the K-mouflage model.

At the perturbation level, if we compare the Einstein-frame Newtonian gauge perturbed metric to its Jordan-frame counterpart (i.e Eq.(14) with Eq.(25) of art.B), we obtain a relation among the potentials which reads

$$1 + 2\Phi = \frac{A^2}{\bar{A}^2}(1 + 2\tilde{\Phi}), \quad 1 - 2\Psi = \frac{A^2}{\bar{A}^2}(1 - 2\tilde{\Psi}). \quad (3.11)$$

Since observations tell us that deviations from Λ -CDM in the matter dynamics have to be small, at most ten per cent, we want that the Jordan-frame potentials do not deviate too much from the Newtonian one Ψ_N . This means that we can linearize Eq.(3.11) to obtain

$$\Phi = \Psi_N + \delta \ln A, \quad \Psi = \Psi_N - \delta \ln A, \quad (3.12)$$

which can be used to obtain the Jordan-frame Poisson equation

$$\frac{\nabla^2}{a^2} \Psi_N = \frac{\delta\rho + \delta\rho_{\Xi}}{2M_{\text{Pl}}^2}. \quad (3.13)$$

To fulfill observational constraints, we also require that $|\delta\rho_{\Xi}| \lesssim |\delta\rho|$, which means that we can linearize Eq.(3.7) to obtain

$$\delta\rho_{\Xi} = -\bar{A}^{-4} \mathcal{M}^4 \delta\Xi. \quad (3.14)$$

In ULMs the Jordan-frame Euler equation reads

$$\frac{\partial \mathbf{v}}{\partial \tau} + (\mathbf{v} \cdot \nabla) \mathbf{v} + \mathcal{H} \mathbf{v} = -\nabla \Psi_N - \frac{\nabla p_A}{\rho}, \quad (3.15)$$

with

$$p_A = \frac{\mathcal{M}^4 c^2}{\bar{A}^4} \Xi, \quad (3.16)$$

where we used the Klein-Gordon equation Eq.(3.5) to relate the potential $\ln A$ to $\tilde{\Xi}$. Since $\tilde{\Xi}$ only depends on the matter density, the pressure-term p_A depends solely on ρ , similarly to what happens for polytropic equations of state.

To summarize, at the level of matter dynamics, the ULMs have two effects, a modification of the Poisson equation, due to the additional source associated to the scalar field, and a pressure-like term in the Euler equation.

At the linear level in the matter density perturbation δ , it is possible, using Eq.(3.5), to relate the density perturbations to the matter ones

$$\delta\tilde{\Xi} = -\frac{\beta_1}{\beta_2}\delta, \quad (3.17)$$

where $\beta_n(t) = d^n \ln \bar{A}/d\tilde{\Xi}^n$. Using this result, we obtain the linear growth rate equation of motion

$$\frac{\partial^2 D}{\partial(\ln a)^2} + \left(2 + \frac{1}{H^2} \frac{dH}{dt}\right) \frac{\partial D}{\partial \ln a} - \frac{3\Omega_m}{2}(1 + \epsilon)D = 0, \quad (3.18)$$

where $\epsilon(k, t)$ is a factor which describes the deviation from the Λ -CDM cosmology, given by

$$\epsilon(k, t) = \epsilon_1(t) \left(1 + \frac{2}{3\Omega_m} \frac{c^2 k^2}{a^2 H^2}\right), \quad (3.19)$$

with $\epsilon_1(t) = \beta_1^2/\beta_2$. The presence of $\epsilon(k, t)$ in Eq.(3.19) makes the growth rate scale-dependent and can enhance or diminish the growth rate of structure depending on the sign of ϵ_1 . The k -dependence scales as k^2 and becomes important when $ck/aH > 1$, i.e. at sub-horizon scales. This can be visualized in Figs.3.1, 3.2 and 3.3, where we solve the growth rate of structure for the three functional forms of $A(\tilde{\Xi})$ defined by Eqs.(55), (63) and (70) of art.B ¹, which we will call model (I), (II) and (III) respectively. As expected, for these models the growth rate of structure is strongly enhanced (or diminished) for $k > 1 h \text{ Mpc}^{-1}$ with respect to the Λ -CDM case. In particular, as shown by Fig.3.3, in ULMs with negative ϵ_1 the growth rate of structure develops oscillations when the factor $(1 + \epsilon)$ becomes negative. However, this rather peculiar behavior is associated to a model which should be discarded, for reasons that will be discussed in sec.3.4.

3.4 Constraints on A

Similarly to what happens for the K-mouflage models free function $K(\chi)$, several constraints can be imposed on the coupling function $A(\tilde{\Xi})$. We summarize here the most important ones :

¹These functions were chosen in order to fulfill the constraints that we will discuss in sec.3.4.

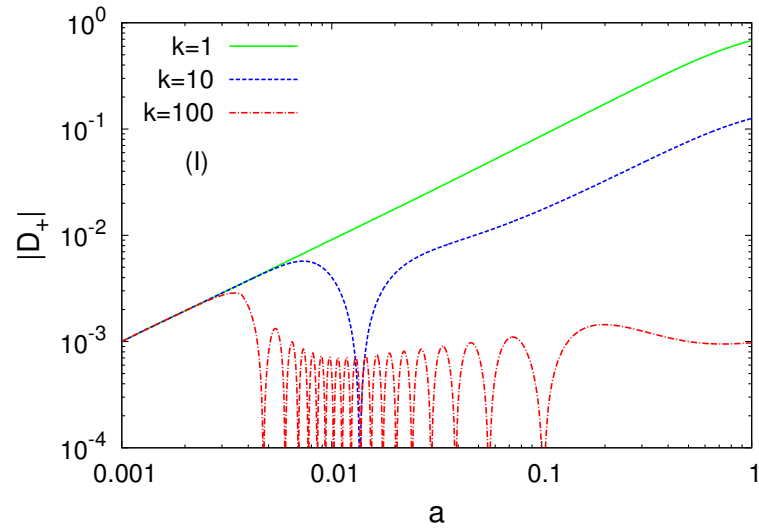


FIGURE 3.1: Absolute value of the linear growing mode $D(k, a)$ for the model (I) as a function of the scale factor for $k = 1, 10$ and $100 h \text{ Mpc}^{-1}$ respectively in green, blue and red

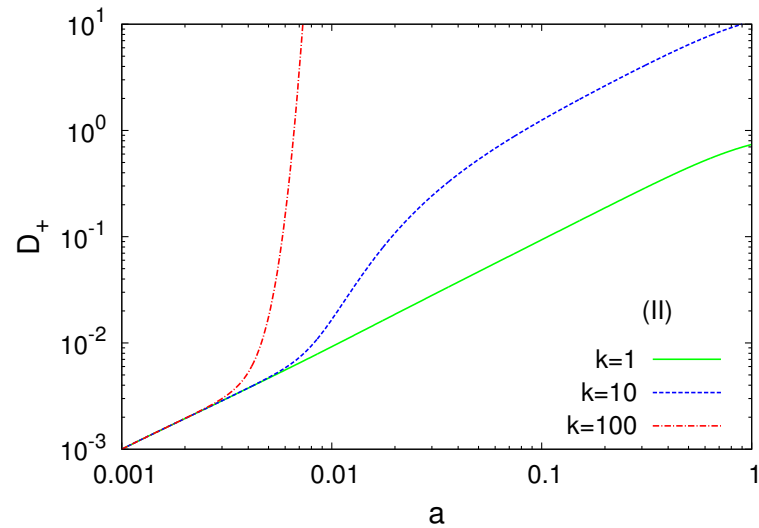


FIGURE 3.2: Linear growing mode $D(k, a)$ for the model (II) as a function of the scale factor for $k = 1, 10$ and $100 h \text{ Mpc}^{-1}$ respectively in green, blue and red.

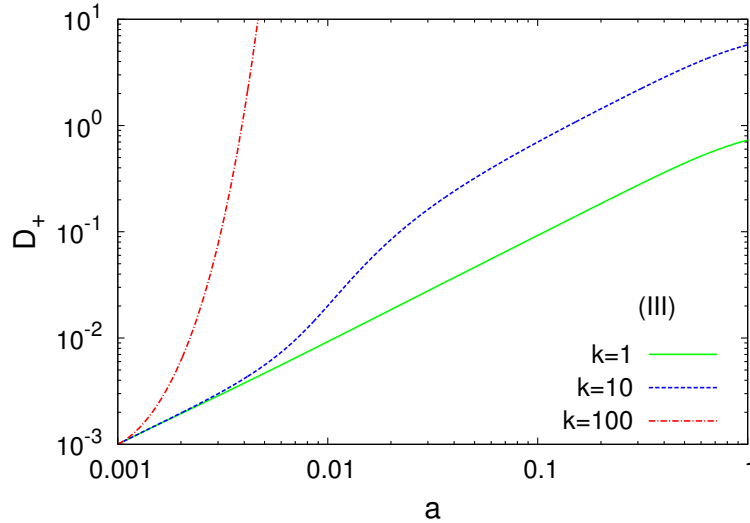


FIGURE 3.3: Linear growing mode $D(k, a)$ for the model (III) as a function of the scale factor for $k = 1, 10$ and $100 h \text{ Mpc}^{-1}$ respectively in green, blue and red.

- $|\ln A| \lesssim 10^{-6}$, hence $|A - 1| \lesssim 10^{-6}$: in ULMs the screening mechanism does not rely on the suppression due to the derivative terms, since the Klein-Gordon equation is a constraint one. $\ln A$ only depends on the value of the local matter density, and the latter varies over several orders of magnitude from the intergalactic medium to the atmospheres and cores of planets and stars. For these reasons, we must bound $\ln A$ below 10^{-6} , to avoid large modifications to the matter dynamics. This allows deviations of the background with respect to the Λ -CDM counterpart at most at the 10^{-6} level, ensuring that all the bounds related to the time variation of the Newton's coupling are satisfied;
- $|\epsilon_1| \lesssim 10^{-7}$: the linear growth rate of structure in ULMs cannot differ too much from the Λ -CDM one. This bound can be obtained by imposing that $|\epsilon| \lesssim 1$ for all wave numbers up to $k = 1 h \text{ Mpc}^{-1}$. For smaller scales, we enter the non-linear regime where Eq.(3.18) does not hold and a more careful analysis is needed. Finally, it is possible to show that $\epsilon_2 \sim \epsilon_1$ (Eq.(41) of art.B), which also gives a constraint on the value of ϵ_2 ;
- $\tilde{\Xi}_0 < 0$: using the aforementioned constraint on ϵ_2 and Eq.(3.10), we obtain $\tilde{\rho}_{\text{de}0} = -\mathcal{M}^4 \tilde{\Xi}_0$. To impose that the scalar field drives the acceleration of the Universe at late times, we must impose $\tilde{\Xi}_0 < 0$;
- $d \ln A / d \tilde{\Xi}$ is a monotonic function of $\tilde{\Xi}$ which goes from 0 to $+\infty$: this is to ensure that the Klein-Gordon equation for the scalar field has a well-defined and unique solution for every value of the matter density;
- $\ln A(\tilde{\Xi})$ must be a convex function: in realistic scenarios, ULMs may correspond to cases in which the kinetic term is negligible with respect to the potential, but non-zero. It is possible to show (sec.V-A of art.B) that the

Klein-Gordon equation (3.5) remains a good description of the evolution of the scalar field, once a small kinetic term is added to the $\mathcal{L}_{\tilde{\Xi}}$, only if $\beta_2 > 0$, i.e. when $\ln A(\tilde{\Xi})$ is a convex function. It is worth noticing here that model (I) of art.B does not satisfy this condition and hence should be discarded (but this scenario can be made viable within the related class of the Goldstone models).

3.5 Characteristic transition scales of ULMs

The Klein-Gordon equation can be recast as:

$$\frac{d\lambda}{d\tilde{\Xi}} = \frac{1}{\hat{\rho}} \quad (3.20)$$

where we defined

$$\begin{aligned} \ln A(\tilde{\Xi}) &= \alpha \lambda(\tilde{\Xi}), \text{ with } \alpha \sim 10^{-6} \\ \hat{\rho} &= \frac{\alpha \rho}{\mathcal{M}^4} \equiv \frac{\rho}{\rho_\alpha}. \end{aligned} \quad (3.21)$$

From Eq.(3.20), we expect a cosmological transition when $\bar{\rho} \sim \rho_\alpha$, which defines a ‘‘transition’’ redshift z_α

$$z_\alpha \sim \alpha^{-1/3} \sim 100, \quad a_\alpha \sim \alpha^{1/3} \lesssim 0.01, \quad (3.22)$$

when we expect that the impact of the scalar field on matter dynamics becomes important.

In Fig.3.4, we show the time evolution of $\epsilon_1(t)$, which influences the growth rate of structure. As expected from Eq.(3.22), ϵ_1 has a peak around $a = a_\alpha \sim 0.01$ meaning that ULMs of gravity have the characteristic property that the main modification to the gravitational dynamics occurs at early times.

3.6 Spherical collapse and halo mass function

In ULMs the spherical collapse is modified by the presence of the scalar field potential $\Psi_A = c^2 \ln A$. Under the spherical approximation, we can write

$$\frac{\partial \Psi_A}{\partial r} = \frac{c^2}{r} \frac{d \ln A}{\ln \rho} \frac{d \ln \rho}{d \ln r} \quad (3.23)$$

where r is the physical coordinate. Eq.(3.23) introduces a term in the equation of motion for $r(t)$, that depends on the density profile $\rho(r)$, which couples different shells before shell crossing, in contrast with what happens in the Λ -CDM case.

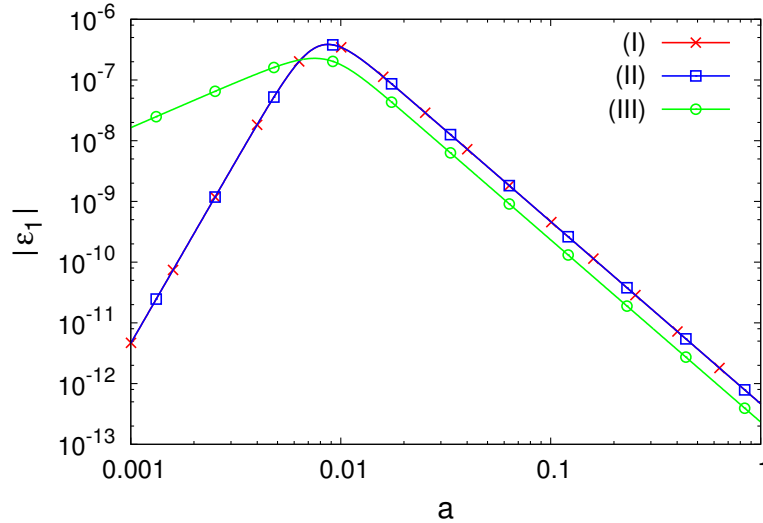


FIGURE 3.4: Absolute value of the factor ϵ_1 as a function of the scale factor. We show our results for model (I), (II) and (III) with red, blue and green lines respectively.

It is possible to give an estimate for the time evolution of the non-linear density contrast given by the spherical dynamics, $\delta_{<}(a) = y(a)^{-3} - 1$, using

$$\frac{d^2 y}{d(\ln a)^2} + \left(2 + \frac{1}{H^2} \frac{dH}{dt}\right) \frac{dy}{d \ln a} = -\frac{y}{H^2 r} \frac{\partial}{\partial r} (\Psi_N + \Psi_A) \quad (3.24)$$

and an ansatz for the density profile that corresponds to the typical density profile around a spherical overdensity for a Gaussian field (Eq.(135) of art.B). The results are shown for model II in Fig.3.5: the collapse is accelerated for small-mass halos and occurs as early as $a \sim 0.01$, while remaining close to Λ -CDM one for $M > 10^{14} h^{-1} M_{\odot}$. For this reason, as shown in Fig.3.6, the linear density contrast needed to collapse into a halo of mass M at $z = 0$ is much smaller than the Λ -CDM one at small masses and converges to $\delta_{<L}^{\Lambda\text{-CDM}} \simeq 1.6$ for higher masses.

These results also reflect in the halo mass functions $n(M)$, which are shown for model (II) and (III) in Figs.3.7 and 3.8. $n(M)$ shows an enhancement in the formation of small-mass halos with respect to the Λ -CDM cosmology counterpart, due a large range of masses collapsed before $z_{\alpha} \sim 100$. However, at small masses $n(M)$ is not dominated by its Gaussian tail and we do not expect the results presented here to be accurate, but we still expect to have an enhancement in the number of small-scale halos in ULMs, even though a more detailed study of the spherical collapse is needed, possibly by means of numerical simulations.

3.7 Screening mechanism

We describe here the screening mechanism in ULMs, in particular emphasizing its difference at Solar System scales with the screening mechanisms discussed in

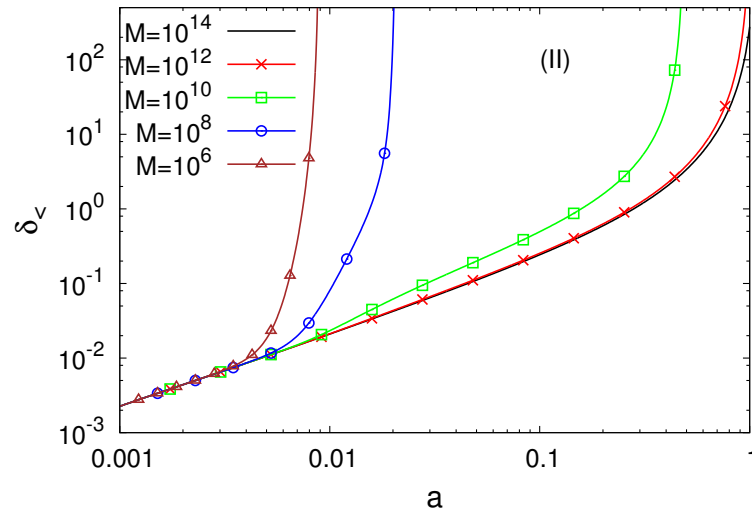


FIGURE 3.5: Time evolution of the nonlinear density contrast $\delta_{<}$ given by the spherical dynamics, as a function of the scale factor for mass $M = 10^{14}$ to $10^6 h M_{\odot}$ from bottom to top, with the same initial condition that corresponds to the Λ -CDM linear density threshold.

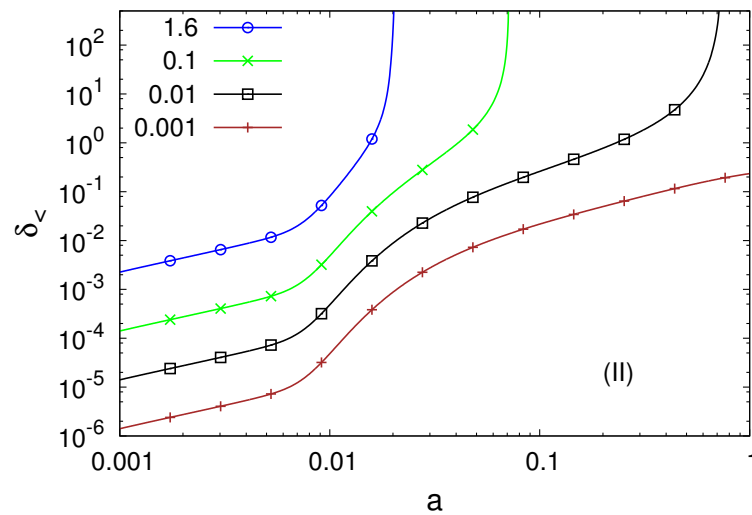


FIGURE 3.6: Time evolution of the nonlinear density contrast $\delta_{<}(a)$ for several Λ -CDM conditions, from $\delta_L = 1.6$ to 0.001 from top to bottom, for a mass of $M = 10^8 h^{-1} M_{\odot}$.

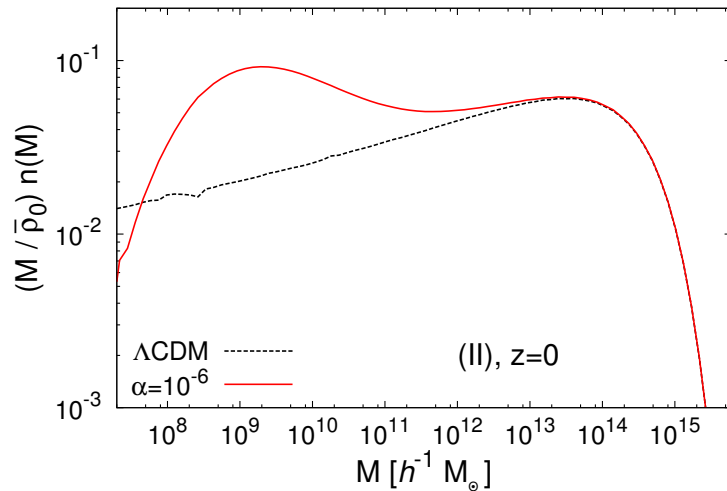


FIGURE 3.7: Halo mass function at $z = 0$ for the model (II) (solid line) and the Λ -CDM reference (dashed line).

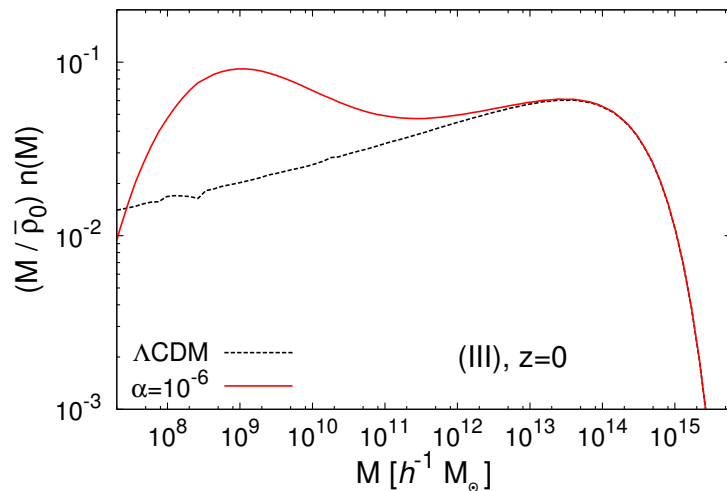


FIGURE 3.8: Halo mass function at $z = 0$ for the model (III) (solid line) and the Λ -CDM reference (dashed line).

sec.1.5.2.

3.7.1 Clusters and galaxies

We can estimate the impact of ULMs on the dynamics of astrophysical objects, like galaxy clusters or galaxies, by computing the ratio η between the fifth force F_A and the Newtonian one F_N . Assuming spherical symmetry, at the boundary of clusters we have

$$\frac{F_N}{c^2} \sim \frac{\mathcal{G}M}{c^2 R^2}, \quad \frac{F_A}{c^2} \sim \frac{d \ln A}{dr} \sim \frac{1}{R} \frac{d \ln A}{d \ln \rho} \sim \frac{1}{R} \alpha^2 \Delta \quad (3.25)$$

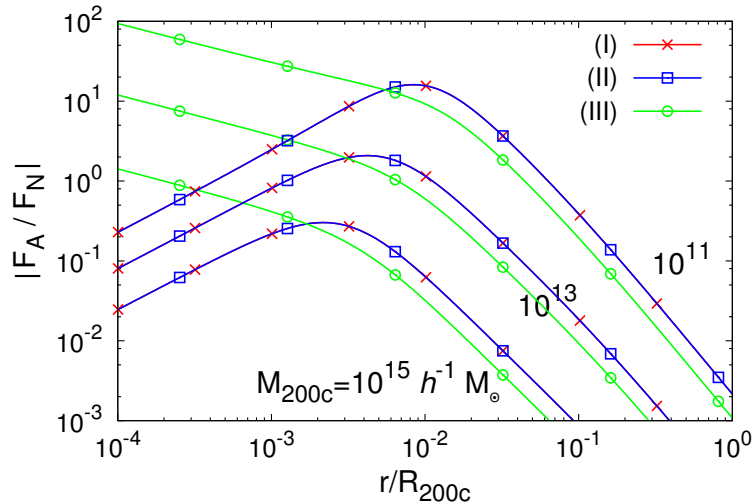


FIGURE 3.9: Absolute value of the ratio $\eta = F_A/F_N$ as a function of the radius within spherical halos. We display the halo masses $M = 10^{15}, 10^{13}$ and $10^{11} h^{-1} M_{\odot}$, from bottom to top. The models (I), (II) and (III) are shown respectively by red, blue and green line.

where in the last passage we used the Klein-Gordon equation in the low density regime (with respect to $\hat{\rho}$). Combining the results obtained in Eq.(3.25), we obtain $F_A/F_N \simeq (10^4\alpha)^2 \ll 1$, which means that the fifth force is negligible at cluster scales. Using a similar argument for galaxies, we obtain $F_A/F_N \simeq (10^6\alpha)^2 \sim 1$, which indicates the fifth force is comparable to the Newtonian one at galaxy scales, and hence galactic dynamics could be used to test ULMs.

In Fig.3.9, we show the absolute value of η as a function of the radius r in a spherical NFW halo. For some models, in particular the model III, η keeps growing as we approach the center of the halo. Observations may severely constrain this model since the latter would lead to very different halos than the one obtained in Λ -CDM. However, a more detail study of internal dynamics of the halos in ULMs it is needed, which we leave for a future study.

3.7.2 Solar System

In ULMs, objects in the Solar System are screened with 100 % efficiency. Because the fifth force depends only on the the local density and its gradient, the impact of the Sun onto planets' motion is exactly zero, unless distant gradients are created by other means (as can happen because of Newtonian gravity). However, the impact of the Sun's Newtonian gradient onto the Earth matter distribution is negligible, as compared to those from local sources, such as the radial structure of the Earth or mountains and oceans. For this reason, the Sun is completely screened as viewed from Earth and similarly this happens for all other planets or moons of the Solar System. Hence, the trajectories of all astrophysical objects in the Solar

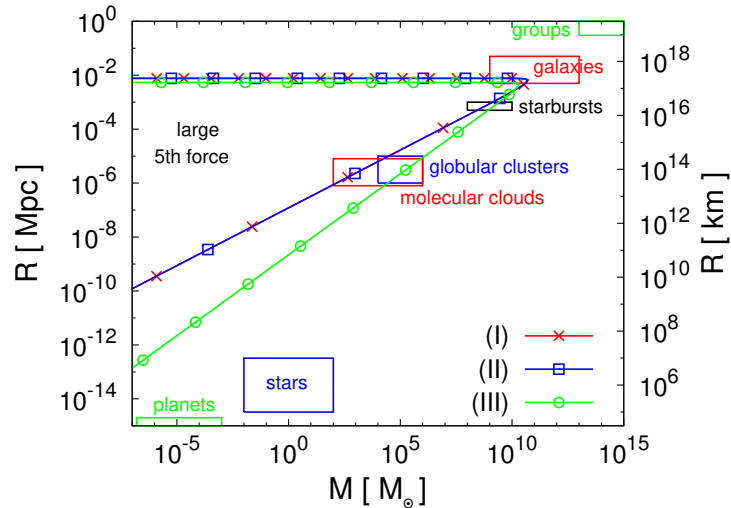


FIGURE 3.10: Domain in the mass-radius plane where the fifth force is greater than Newtonian gravity. The horizontal axis is the typical mass of the structure, M , given in units of the solar mass. The vertical axis is the typical radius of the structure, R , given in Mpc in the left border scale and in km in the right-border scale. The rectangles show the typical scales of various astrophysical structures.

System are given by GR and ULMs pass all the Solar System tests described in sec.2.3, which often severely constrain other MGTs such as K-mouflage.

On smaller scales, one can expect that there exists a small-scale cut-off ℓ_s of the theory, below which the scalar field acquires a kinetic term and a screening mechanism similar to the one in Dilaton modified-gravity theories. This scale can be taken to be of the order of the mean interparticle distance in the inter-galactic medium (see sec.V-B of art.B), i.e. on the meter scale, thus much smaller than any scale of interest for cosmological or Solar System dynamics. Moreover, ℓ_s can be introduced into the model without the need of a new parameter, simply expressing the latter as combination of the parameters of the theory, like $\ell_s \sim \alpha \mathcal{M}^4 \sim 100$ m. In any case, a small-scale regulation of the theory is needed to have a complete picture of ULMs and requires further study.

In Fig.3.10, we show the mass-radius plane where the fifth force is greater than the Newtonian one, that we computed assuming an NFW density profile [48]. The lines are obtained evaluating $R_\eta(M)$, i.e. for any given mass, the radius at which $\eta = 1$. The rectangles represent the typical scales of various astrophysical objects showing that some of them, like galaxies or globular clusters, lie at the boundary $R_\eta(M)$ and they may be used to test ULMs. We leave a detailed analysis on these possible constraints for a future work.

3.8 Thermodynamical analysis

In the previous sections, we computed the fifth force assuming that the density ρ was a homogeneous field on cosmological scales. However, in ULMs the fifth force can enhance the formation of structure at early times, $a < a_\alpha$, and this may develop very strong inhomogeneities in the density field. In this scenario, the Universe would be made of small clumps of matter built at high z , which are screened as planets in the Solar System, while perturbations evolve according to GR.

In sec.XI of art.B, we addressed this issue by using a thermodynamical analysis, suited to study this highly non-linear problem. We described domains in the early Universe as a grand canonical ensemble of particles, which act solely under the influence of the fifth force potential $\ln A$. This approximation is possible since we studied the structure formation at early times, when the Newtonian force is negligible with respect to the fifth force. We also assumed that such a system reaches an equilibrium with a process similar to the violent relaxation [54] for gravitational systems. In particular, we obtained the phase-space diagram of the system and we checked if the early time Universe was in a one-phase state, i.e. in a homogeneous state, or was undergoing a phase transition, i.e. was in a highly inhomogeneous phase.

To study the equilibrium of the system, we minimized the grand-canonical potential Ω , which is given by

$$\Omega = E - S/\beta - \mu M \quad (3.26)$$

where E, S and M are respectively the energy, the entropy and the mass of the system and β and μ are the inverse temperature and chemical potential. The phase-space equilibrium distribution $f(\mathbf{x}, \mathbf{v})$ can be obtained by $\mathcal{D}\Omega/\mathcal{D}f = 0$ and yields

$$f(\mathbf{x}, \mathbf{v}) = f_0 e^{-\beta(v^2/2 + c^2 \ln A + c^2 d \ln A/d \ln \rho) + \beta\mu - 1}, \quad (3.27)$$

which can be used to compute the density at the equilibrium

$$\rho(\mathbf{x}) = f_0 \left(\frac{2\pi}{\beta} \right)^{3/2} e^{-\beta c^2 (\ln A + d \ln A/d \ln \rho) + \beta\mu - 1}. \quad (3.28)$$

This equilibrium condition can be recast as

$$\hat{\mu} = \theta + \hat{\beta}\nu(\theta), \quad (3.29)$$

where we introduced

$$\begin{aligned} \hat{\beta} &= \alpha c^2 \beta, \quad \hat{\mu} = \ln \left[\frac{\alpha f_0 c^3}{\mathcal{M}^4} \left(\frac{2\pi}{\beta c^2} \right)^{3/2} \right] + \beta\mu - 1 \\ \theta &= \ln \hat{\rho}, \quad \nu(\theta) = \lambda + \frac{d\lambda}{d\theta}. \end{aligned} \quad (3.30)$$

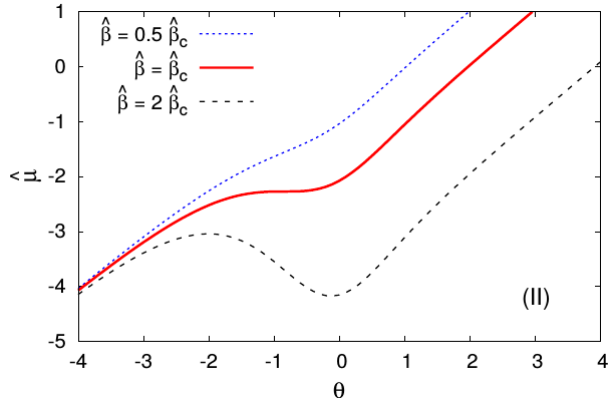


FIGURE 3.11: Thermodynamic equilibrium relation $\hat{\mu} = \hat{\mu}(\theta, \hat{\beta})$ as a function of θ , at fixed values of $\hat{\beta}$.

The equilibrium density can be found as the solution (in terms of θ) of Eq.(3.29), for fixed values of $\hat{\beta}$. In Fig.3.11 we show $\hat{\mu}(\theta)$ function for model (II) for 3 values of $\hat{\beta}$ around $\hat{\beta}_c$, the inverse temperature where the phase transition occurs (see Eq.(190) of art.B). At low $\hat{\beta}$ (i.e., high temperature) the function is monotonic and the system is in a homogeneous phase while for high $\hat{\beta}$ (i.e., at low temperature) $\mu(\theta)$ is non-monotonic and the system is inhomogeneous since two different phases, with two different values for θ , coexist.

The results of this analysis for model (II) can be summarized by Fig.(3.12) where we show the phase diagram of the system. The red line in the plot represents the cosmological trajectory, i.e. the typical density ρ_{coll} and typical inverse velocity β_{coll} at the collapse, which we estimated as

$$\rho_{\text{coll}}(z) = \bar{\rho}(z), \quad \beta_{\text{coll}} = \frac{1}{c_{\text{coll}}^2}, \quad (3.31)$$

where c_{coll} is the effective velocity at the collapse

$$c_{\text{coll}}^2 = c_s^2 + c_N^2, \quad (3.32)$$

which is the sum of the “sound speed” c_s^2 that comes from the pressure-like term of the Euler equation and the Newtonian c_N^2 term which comes from its right-hand side (see sec. XI-A for more details).

Fig.(3.12) shows that the high-density region of the cosmological trajectory, which is associated to the early-times Universe, lies almost at the boundary between the homogeneous and the inhomogeneous regions and so the system does not develop strong inhomogeneities. At later times, Newtonian gravity becomes dominant and the system behaves like a Λ -CDM Universe, not developing unusual inhomogeneities. Similar results are obtained for model (III) as shown in Fig.(20) and (21) of art.B.

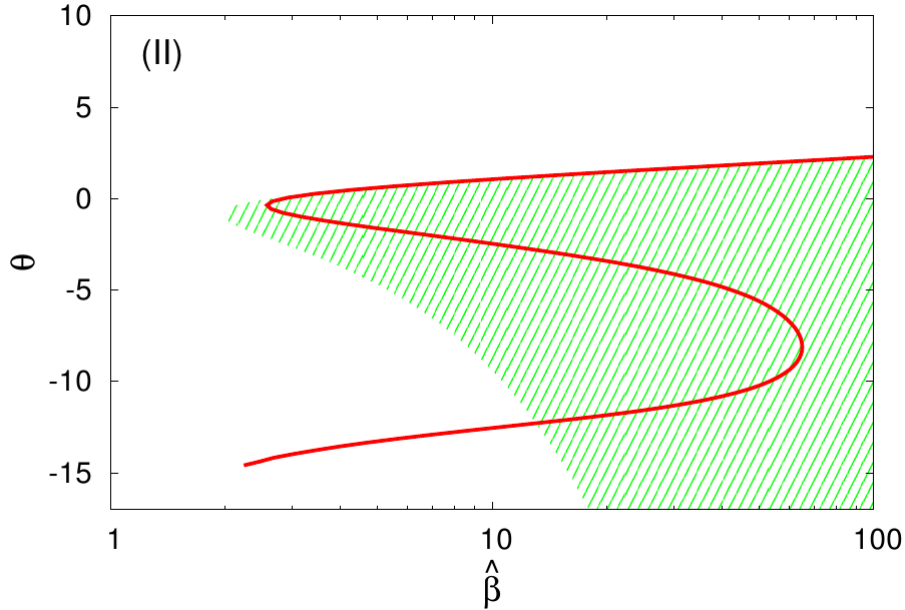


FIGURE 3.12: Thermodynamic phase diagram of model (II). The shaded area represents the region where the system is in an inhomogeneous phase, while the white area corresponds to the homogeneous one. The red line is the cosmological trajectory $(\beta_{\text{coll}}(z), \theta_{\text{coll}}(z))$.

3.9 Super-chameleons and ultra-local models

The super-chameleon models (SCMs) [55, 56] are chameleon models embedded in a supersymmetric setting, with three separate sectors, the dark one where dark matter and energy live, the matter one for standard model particles, and a supersymmetry sector for supersymmetric partners. Here, as we did in art.C, we will describe a supersymmetric setting at low energy for the SCMs assuming that the three sectors only interact via gravity.

At energies comparable to the cosmological ones, these models can be seen as a scalar-tensor theory of gravity, whose scalar field is responsible for the acceleration of the Universe at late times (see sec.I and II of art.C). Moreover, it is possible to show that the super-chameleon scalar field has an extremely short range interaction with the matter fields, on scales smaller than $r_{\text{SCMs}} \ll m_{3/2}^{-1}$ with $m_{3/2}$ the gravitino mass. As the gravitino mass is always greater than 10^{-5} eV in realistic models of supersymmetry breaking [57], the range of the scalar interaction mediated by φ is very small, at most at the cm level. Even at very early times, this scale is sufficiently small that we can treat SCMs as ultra-local models for cosmological purposes.

For these models, the functional form of $A(\Xi)$ is fixed ² by the supersymmetric interactions

$$A(\tilde{\Xi}) = 1 + \alpha \left(1 + \sqrt{-1 - \tilde{\Xi}} \right)^{-2\sigma/n} \quad (3.33)$$

²Up to the choice of two numerical parameters.

and for $k/a \ll m_{\text{eff}}$ the linear density contrast obeys

$$\frac{\partial^2 \delta}{\partial \tau^2} + \mathcal{H} \frac{\partial \delta}{\partial \tau} - \frac{3}{2} \Omega_m(\tau) \mathcal{H}^2 \left(1 + \frac{2k^2 \beta^2(\varphi)}{m_{\text{eff}}^2 a^2} \right) \delta = 0, \quad (3.34)$$

with

$$m_{\text{eff}}^2(\varphi) = \frac{\rho \beta_1 \beta^2}{M_{\text{Pl}}^2 \beta_1^2}. \quad (3.35)$$

On sub-horizon scales this equation is the same as for the ultra-local models, since we can neglect the unity factor in Eq.(3.19). Then, it is possible to test the viability of SCMs with the same techniques used for ultra-local models.

We may notice that in the usual chameleon models such as $f(R)$, for which we have $\beta \sim 1$, a large mass would lead to a negligible deviation from Λ -CDM. This is not the case for the SCMs models, since it is possible to show that

$$\frac{\beta^2}{m_{\text{eff}}^2} = \frac{\alpha^2 M_{\text{Pl}}^2}{\Lambda^4} \quad (3.36)$$

and so $\beta^2 k^2 / m_{\text{eff}}^2 a^2$ can be order of unity at cosmological scales even with $\alpha \ll 1$.

The coupling function for SCMs resembles the model (III) studied above and most of the results obtained for the latter are valid also for SCMs. One important difference is shown in Fig.3.13, where we show the mass-radius plane for SMCs. In this plot, we only show astrophysical objects whose dynamics is due to the presence of dark matter, since in SMCs the coupling between baryons and the scalar field is negligible. Hence, we found that only galaxies can be used to test SMCs since they are the only class of objects that lie on the boundary of R_η .

This leads to the conclusion that, at this preliminary level, superchameleons are found to be globally consistent with current observational constraints. As for the ultra-local models, we leave to a future work a more detailed study of galactic dynamics in SCMs, which could be useful to put constraints on SCM parameters.

3.10 Conclusions

In this chapter, we introduced ULMs, a class of MGTs where a scalar field with a negligible kinetic term is added to EHA. We showed that ULMs give rise to a new screening mechanism, which is due to the absence of the kinetic term, making the Solar System screened with 100 % efficiency. Moreover, we showed that galaxies are unscreened, making galactic dynamics a promising tool to test ULMs.

The predictions of ULMs only depend on a single free function, which we constrained using theoretical and observational arguments. We showed that for these models deviations of the background are at most at the 10^{-6} level, while structure formation is strongly enhanced at small scales, leading to an excess in the formation of small-mass halos as compared to the Λ -CDM cosmology. This could lead

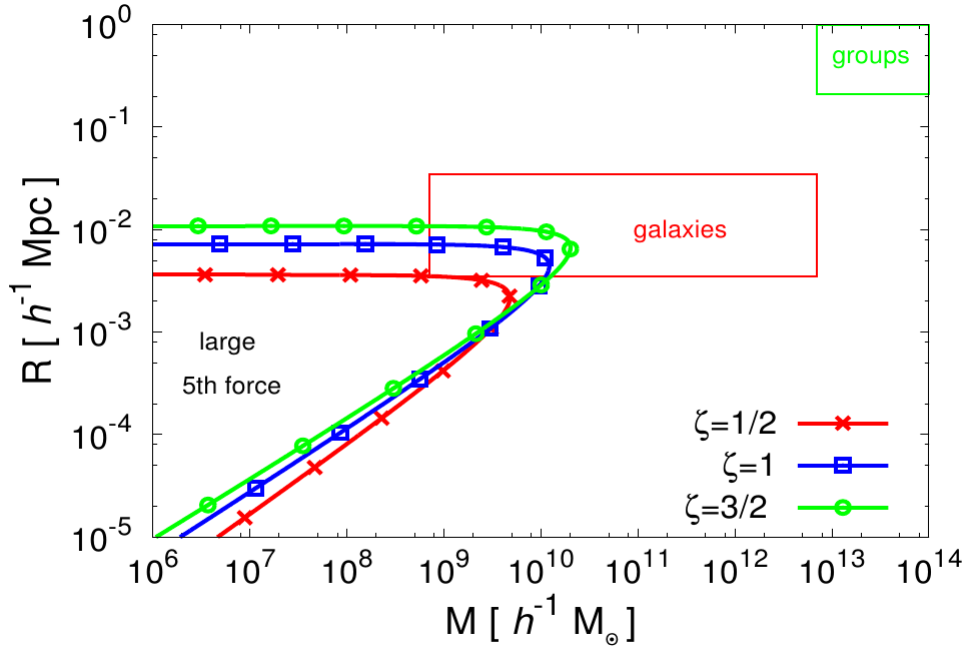


FIGURE 3.13: Domain in the mass-radius plane where the fifth force is greater than Newtonian gravity for SCMs. The rectangles show the typical scales of astrophysical structures whose dynamics is dominated by the presence of dark matter.

to severe constraints on ULMs, even though more detailed studies are needed in order to give a robust quantitative estimate.

To study the non-linear and inhomogeneous regime of the fifth force, which requires to go beyond perturbation theory or the spherical collapse, we have presented a thermodynamic analysis, showing that inhomogeneous transition had not occurred at early time, validating our cosmological analysis, which assumes a smooth density field.

Finally, we briefly introduced SCMs, super-chameleon models embedded in a supersymmetric setting, that act as ultra-local model at scales larger than their very short Compton length. We found that these theories are compatible with current observational constraints and we expect them to have an impact on galactic dynamics.

To conclude, to study in deeper details the impact of ULMs and SCMs on cosmology dedicated numerical simulations are required. In particular, the ultra-local force may alter significantly the internal structure of small-mass halos, and numerical methods are well suited to understand sub-halo dynamics. Moreover, an accurate comparison with data on galaxy scales can be useful to constrain both ULMs and SCMs. As for K-mouflage models, a MCMC analysis is needed to explore the full parameter space of ultra-local models without focusing on particular functions for $\ln A(\tilde{\Xi})$, which we leave for detailed studies.

Chapter 4

Testing modified gravity with cosmic shear

4.1 Introduction

In this chapter, we give an example of how MGTs can be constrained using weak lensing data taken from cosmological surveys.

In particular, we will describe how Dilaton and $f(R)$ models of gravity can be tested using cosmic shear data. After briefly reviewing them, we will study their impact on the cosmic shear two-point correlation functions, and we will discuss degeneracies with neutrino and baryonic physics.

Finally, we will use data taken from the Canada-France-Hawaii Telescope Lensing Survey (CFHTLenS) ¹, a ground-based multi-color optical survey with a 154 deg^2 sky coverage optimized for the study of weak gravitational lensing [58], to constrain some parameters associated to Dilaton and $f(R)$ models.

4.2 Dilation and $f(R)$ theory of gravity

In this section, we review the models of modified-gravity theories constrained in art.D, namely the Dilaton and $f(R)$ models.

The Dilaton is a class of scalar-tensor theory of gravity defined by

$$S = \int d^4x \sqrt{-\tilde{g}} \left[\frac{\tilde{M}_{\text{Pl}}^2}{2} \tilde{R} + \frac{1}{2} (\tilde{\nabla} \varphi)^2 - V(\varphi) - \Lambda_0^4 \right] + \int d^4x \sqrt{-g} \mathcal{L}_{\text{m}}(\psi_{\text{m}}^{(i)}, g_{\mu\nu}) \quad (4.1)$$

¹CFHTLenS : www.cfhtlens.org

where we explicitly added the cosmological constant contribution Λ_0^4 , and the matter is coupled to the scalar field via a conformal rescaling of the metric. In the original Dilaton model, the potential and the coupling function read

$$\begin{aligned} V(\varphi) &= V_* \exp\left(-\frac{\varphi}{\tilde{M}_{\text{Pl}}}\right) \\ A(\varphi) &= 1 + \frac{1}{2} \frac{A_2}{\tilde{M}_{\text{Pl}}^2} \varphi^2 \end{aligned} \quad (4.2)$$

where $\{A_2, V_*\}$ are free parameters of the theory. At the background level, the scalar-field energy density is dominated by its potential term, which is negligible as compared with the matter density and the Dilaton theories recover the Λ -CDM background cosmology within a 10^{-6} accuracy. Hence, the main modification to structure formation is not due to a different background evolution, but to the effect of the fifth force on matter dynamics (see sec.2.1 of art.D).

On the other hand, $f(R)$ theories are MGTs defined by

$$S = \int d^4x \sqrt{-g} \left[\frac{\tilde{M}_{\text{Pl}}^2}{2} [R + f(R)] - \Lambda_0^4 + \mathcal{L}_m(\psi_m^{(i)}) \right]. \quad (4.3)$$

In the Hu & Sawicki parametrization [59], the functional form for $f(R)$ is chosen to be

$$f(R) = -\frac{f_{\text{R0}}}{n} \frac{R_0^{n+1}}{R^n} \quad (4.4)$$

where $\{f_{\text{R0}}, n\}$ are free parameters of the theory. $f(R)$ theories recover Λ -CDM background cosmology at 10^{-4} accuracy, while at the perturbation level the modified Einstein's equations lead to a modification of the metric potentials Ψ and Φ which introduces a new source in the Poisson equation (see sec.2.2 of art.D).

4.3 Weak lensing

Weak lensing is a powerful tool to test GR at cosmological scales [60], since it directly probes the so-called weak-lensing potential

$$\Phi_{\text{wl}} = \frac{\Phi + \Psi}{2} \quad (4.5)$$

which is sensible to modifications of gravity.

In particular, the integrated convergence field at the point $\vec{\theta}$ on the sky reads as

$$\kappa(\vec{\theta}) = \int_0^{+\infty} d\tau \frac{\tau}{c^2} g(\tau) \nabla^2 \Phi_{\text{wl}}(\tau, \tau\vec{\theta}) \quad (4.6)$$

where $g(\tau)$ is a kernel function which takes into account the contributions coming from several sources along the line of sight. Expanding $\kappa(\vec{\theta})$ in multipoles, we obtain the convergence power spectrum

$$C_\ell^\kappa = \int_0^{+\infty} d\tau \frac{g(\tau)}{c^2} \frac{\ell^4}{\tau^4} P_{\text{wl}}(\ell/\tau, \tau). \quad (4.7)$$

where P_{wl} is the weak-lensing power spectrum. From Eq.(4.7), it is possible to obtain the cosmic shear two-point correlation functions

$$\xi_\pm(\theta) = \frac{1}{2\pi} \int C_\ell^\kappa J_{0/4}(\ell\theta) \ell d\ell, \quad (4.8)$$

which can be reconstructed from survey data, as was done in sec.3.3 of art.D. Moreover, due to their dependence on P_{wl} , $\xi_\pm(\theta)$ are sensitive to modifications of gravity, and thus can be used to constrain modified-gravity parameters, as we will see in sec.4.4. In particular, for all MGTs for which the expansion rate H and comoving distances can be approximated with the Λ -CDM ones, it is possible to show that P_{wl} can be expressed as

$$P_{\text{wl}}(k, z) = \left(\frac{3\Omega_0 H_0^2}{2ak^2} \right)^2 P(k, z), \quad (4.9)$$

which connects the matter power spectrum to the weak-lensing one.

4.4 Results

We model the impact of massive neutrinos, baryon feedback and MGTs on the matter power spectrum by using multiplicative feedback biases, namely

$$P^{\text{DM}+\nu+b(m)+\text{MG}} = P^{\text{DM}} \times b_{M_\nu}^2 \times b_m^2 \times b_{\text{MG}(\alpha)}^2 \quad (4.10)$$

where P^{DM} is dark matter power spectrum and the M_ν , m and $\text{MG}(\alpha)$ stand respectively for the contributions from the massive neutrinos, the baryons physics and MGTs. We estimate the the neutrino feedback bias $b_{M_\nu}^2$ as

$$b_{M_\nu}^2 \equiv \frac{P_{\text{CAMB}}^{\text{DM}+M_\nu}(k, z)}{P_{\text{CAMB}}^{\text{DM}}(k, z)} \quad (4.11)$$

with $M_\nu = (0.0, 0.2, 0.4, 0.6)$ eV is the total neutrino mass and CAMB indicates that we computed the power spectra using the CAMB code [61]. Similarly, we compute the baryon bias feedback as

$$b_m^2 \equiv \frac{P_{\text{OWL}}^{\text{DM}+b(m)}(k, z)}{P_{\text{OWL}}^{\text{DM}}(k, z)} \quad (4.12)$$

where OWL indicates that power spectra were computed using the data from a suite of simulations [62] which studied the effects of baryon physics on the matter power spectrum, in particular the impact of different AGN feedback models.

In Fig.4.1, we show $P(k, z)$ at $z = 1$ when massive neutrinos and AGN feedbacks are taken into account. AGN and neutrino feedbacks can suppress more than 50 % of the power at mildly non-linear scales, depending on the model and neutrino total masses.

Finally, we take into account the MGTs contribution via the MGT bias

$$b_{\text{MG}(\alpha)}^2 \equiv \frac{P_{\text{VNT}}^{\text{MG}(\alpha)}(k, z)}{P_{\text{VNT}}^{\text{DM}}(k, z)} \quad (4.13)$$

where $\text{MG}(\alpha)$ labels different gravity models (see sec.3.2.3 of art.D for more details) and VNT means that we computed the MGT power spectra as in [63]. This leads to a 10-20 % enhancement in the matter power spectrum, which we show with thick and dotted lines in Fig.4.1, respectively for the Dilaton and $f(R)$ model. It is worth noticing here that maximal modifications to Λ -CDM occur at $k \sim 1 h \text{Mpc}^{-1}$, in a region where degeneracies with baryon and neutrino physics are strong.

Once all these contributions are considered, Eq.(4.10) can be used to compute ξ_{\pm} and MGTs can be tested against data. As an example, we display in Figs.4.3 and 4.4 ξ/ξ_{DM} for a particular combination of MGT, neutrino mass and AGN feedbacks, along with data taken from the CFHTLenS. Moreover, we performed a rejection analysis using the χ^2 method (see sec.4.2 of art.D) to study the viability of $f(R)$ and Dilaton models. As a main result, which is summarized in table 2 of art.D, we show that with current data it is possible to accommodate most of MGTs considered, once that neutrino and baryonic physics are taken into account, with the notable exception of the $f(R)$ theory with $\{f_{R_0}, n\} = \{10^{-4}, 1\}$.

4.5 Conclusions

In this chapter, we introduced the cosmic shear as a way to constrain MGT parameters and to study degeneracies among neutrino, baryonic physics and MGTs at mildly non-linear scales.

We focused on the Dilaton and $f(R)$ models of gravity, which we briefly reviewed in sec.4.2. We took into account their impact on the cosmic two-point correlation functions, along with the one from massive neutrinos and AGN feedbacks, by using multiplicative bias factors to compute the matter power spectrum.

We showed that it is not possible to find a preferred model among the ones considered, i.e. that the current data have very few constraining power, once that neutrino and AGN feedbacks are taken into account.

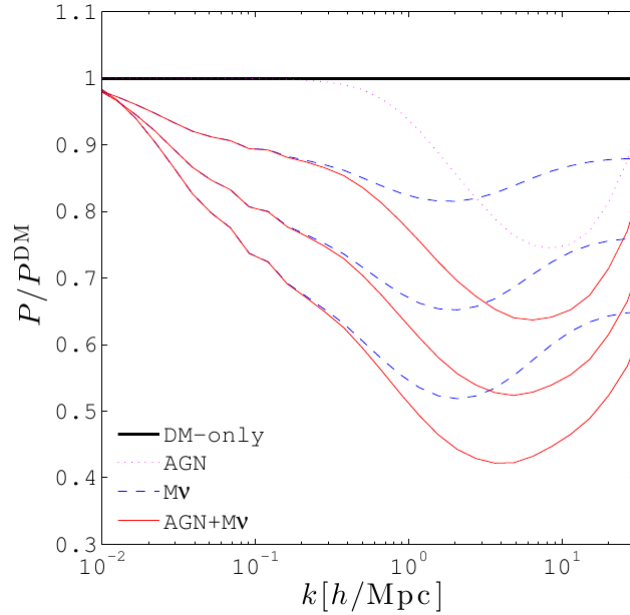


FIGURE 4.1: Ratio between the matter power spectrum $P(k)$, including baryon and massive neutrinos feedbacks and the dark matter one P^{DM} , evaluated at $z = 1$. The blue dashed lines represents the effect of massive neutrinos with $M_\nu = 0.2, 0.4$ and 0.6 eV from top to bottom, the pink dotted line represents the AGN feedback effect and the red solid lines represent the combined effect of massive neutrinos and AGN feedback.

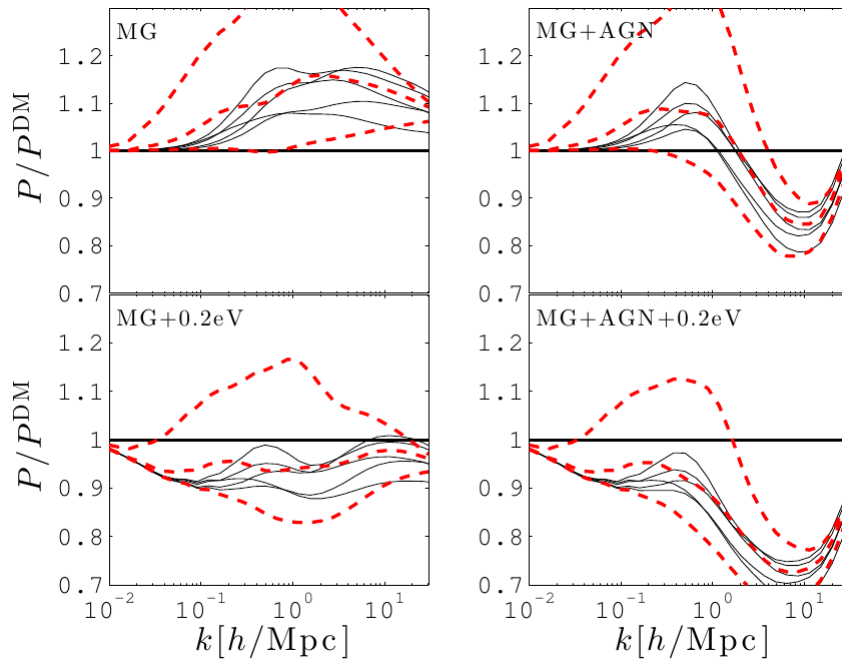


FIGURE 4.2: Ratio between the matter power spectrum $P(k)$, including baryon, massive neutrinos and MGT feedbacks and the dark matter one P^{DM} , evaluated at $z = 1$. From top to bottom at $k = 0.2h\text{Mpc}^{-1}$, the solid lines represent Dilaton models B4, A3, E3,D1 and C1 respectively (see table 1 of art.D for details). The thick red dashed lines correspond to $f(R)$ gravity with $n = 1$. Top to bottom are for $|f_{R0}| = 10^{-4}, 10^{-5}$ and 10^{-6} respectively.

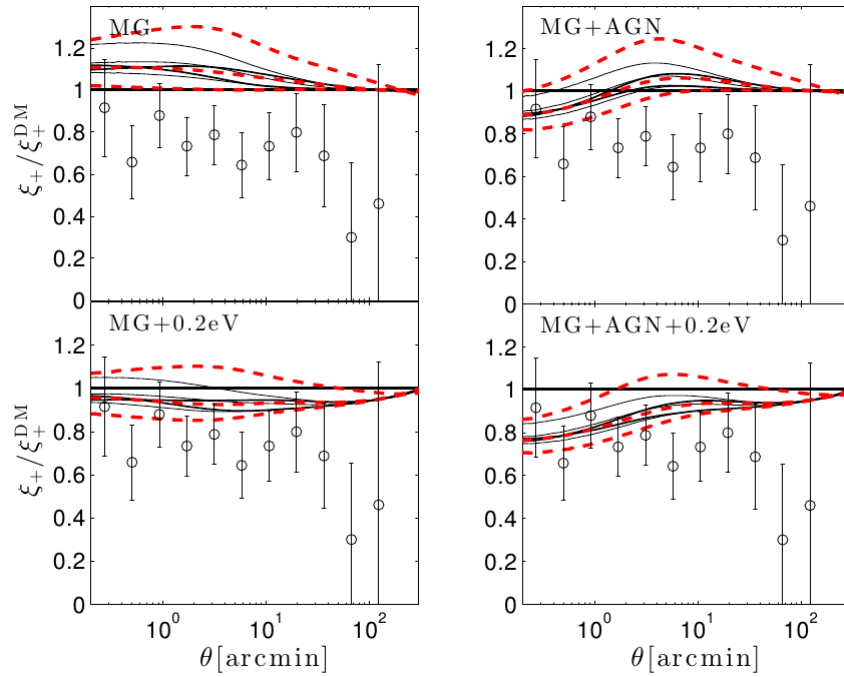


FIGURE 4.3: Same as Fig.4.2, but for ξ_+ . The open symbols represent our measurements from the CFHTLenS data with 1σ error bars.

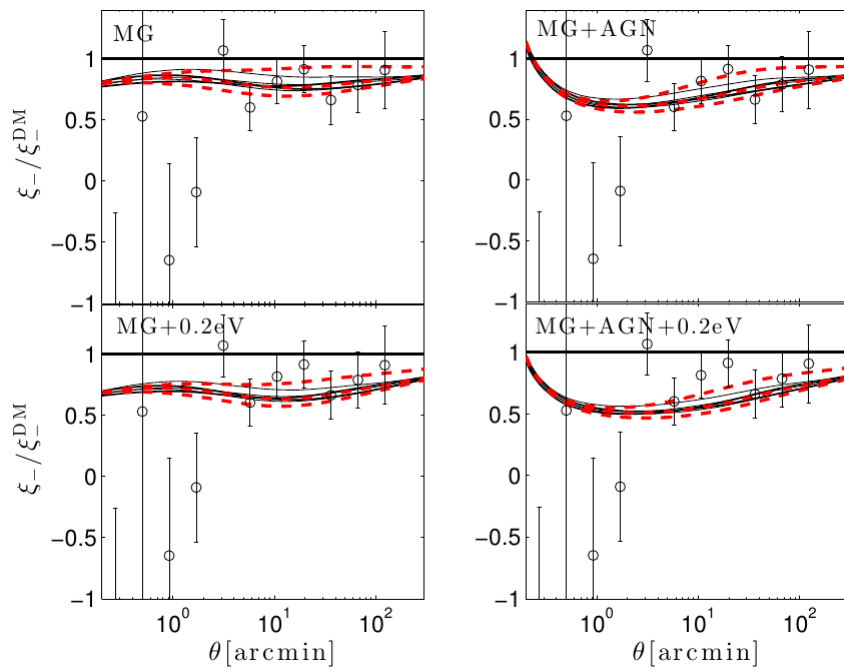


FIGURE 4.4: Same as Fig.4.2, but for ξ_- . The open symbols represent our measurements from the CFHTLenS data with 1σ error bars.

We however showed that cosmic shear studies can be used as a powerful tool to test GR, especially when neutrino and baryonic physics will be understood with greater precision and observational systematics will be reduced.

To further improve this analysis one might think to test the simplifying assumption of the uncorrelated biases used to compute $P(k, z)$, which will require suites of dedicated cosmological simulations. Moreover, since several MGTs can accommodate similar phenomenological effects, applying this analysis within the framework of model-independent parametrizations for the weak lensing convergence power spectrum [64], can be useful to test a larger class of theories than the one presented in this chapter.

Chapter 5

Consistency relations for large-scale structure

5.1 Introduction

The cosmological large-scale structure is one of the main probes to measure the properties of the Universe and to test the validity of the Λ -CDM model. On large scales, cosmological structures are described by perturbative methods, which can be improved by resummation schemes [63, 65–70]. On small scales, the theoretical modeling of gravitational dynamics becomes much more difficult since we aim at describing a non-linear system in which baryonic physics plays an important role. For these reasons, small-scale structure formation is often studied by the means of numerical simulations or phenomenological models [71] and exact results are very rare.

However, recently some exact non-linear results have been obtained [72–74], among which we find the so called “kinematic consistency relations” (CRs) for large-scale structures, i.e., a factorization of $(\ell + n)$ -cosmological fields correlators, with ℓ linear and n small-scale (even non-linear) modes, in terms of n -point correlators and ℓ linear power spectrum factors. CRs arise from the equivalence principle, making them a promising tool to test GR, and describe the response of a small-scale structure to a large-scale perturbation, namely an uniform displacement at leading order. When applied to the density fields, these relations express a kinematic effect which vanishes at equal times, as an uniform displacement has no effect on their statistics. This property make the CRs for the density fields very hard to measure, since different-time correlators would be needed.

In this chapter, we present an extension of CRs, based on the work of art.E and F, which involves cross-correlators between the density and the velocity fields. These CRs are sensitive to the transportation of the small-scale structure because of the shift in the velocity fields, and thus do not vanish at equal times. Moreover, we show how to relate CRs to observational probes such as the galaxy density

contrast and the integrated Sachs-Wolfe effect, to obtain a test of the equivalence principle and of primordial non Gaussianity valid also at non-linear scales.

5.2 Correlation and response function

To obtain CRs, we assume that the primordial fluctuations can be considered Gaussian and thus the dynamic are fully determined by the initial Gaussian linear growing mode $\delta_{L0}(\mathbf{x})$. For this reason, any dependent quantity $\{\rho_1, \dots, \rho_n\}$ is a functional of the field δ_{L0} and we can write the mixed correlation function as a Gaussian average

$$C^{1,n}(\mathbf{x}) = \langle \delta_{L0}(\mathbf{x}) \rho_1 \dots \rho_n \rangle = \int \mathcal{D}\delta_{L0} e^{-\delta_{L0} \cdot C_{L0}^{-1} \cdot \delta_{L0}/2} \delta_{L0}(\mathbf{x}) \rho_1 \dots \rho_n, \quad (5.1)$$

where $C_{L0} = \langle \delta_{L0}(\mathbf{x}_1) \delta_{L0}(\mathbf{x}_2) \rangle$ is the two-point correlation function for the field δ_{L0} . Integrating by parts Eq.(5.1) over δ_{L0} yields

$$C^{1,n}(\mathbf{x}) = \int d\mathbf{x}' C_{L0}(\mathbf{x}, \mathbf{x}') R^{1,n}(\mathbf{x}'), \quad (5.2)$$

where we defined the mean response function

$$R^{1,n}(\mathbf{x}) = \left\langle \frac{\mathcal{D}[\rho_1 \dots \rho_n]}{\mathcal{D}\delta_{L0}(\mathbf{x})} \right\rangle, \quad (5.3)$$

which describes the dependence of $\{\rho_i\}$ on the variation of the initial density field δ_{L0} . Eq.(5.2) can be expressed in Fourier space as

$$\tilde{C}^{1,n}(\mathbf{k}') = P_{L0}(k') \tilde{R}^{1,n}(-\mathbf{k}'), \quad (5.4)$$

where we defined the Fourier-space correlation and response functions as

$$\tilde{C}^{1,n}(\mathbf{k}') = \langle \tilde{\delta}_{L0}(\mathbf{k}') \rho_1 \dots \rho_n \rangle, \quad \tilde{R}^{1,n}(\mathbf{k}') = \left\langle \frac{\mathcal{D}[\rho_1 \dots \rho_n]}{\mathcal{D}\tilde{\delta}_{L0}(\mathbf{k}')} \right\rangle. \quad (5.5)$$

and P_{L0} is the linear matter power spectrum.

Let us now consider the quantities $\{\rho_1, \dots, \rho_n\}$ to be the non-linear density contrast $\tilde{\delta}(\mathbf{k}_i, t_i)$, which can be expressed as

$$\tilde{\delta}(\mathbf{k}, t) = \int \frac{d\mathbf{x}}{(2\pi)^3} e^{-i\mathbf{k} \cdot \mathbf{x}} \delta(\mathbf{x}, t) = \int \frac{d\mathbf{q}}{(2\pi)^3} e^{-i\mathbf{k} \cdot \mathbf{x}} \quad (5.6)$$

where we introduced the Lagrangian coordinate \mathbf{q} , we used the matter conservation equation $(1 + \delta)d\mathbf{x} = d\mathbf{q}$ and we discarded the term $\delta_D(\mathbf{k})$ that does not contribute for $\mathbf{k} \neq 0$. We can now compute the response function, substituting Eq.(5.6) in

Eq.(5.5), to obtain

$$R^{1,n} = \left\langle \int \frac{d\mathbf{q}_1 \cdots \mathbf{q}_n}{(2\pi)^{3n}} \sum_n^{i=1} \mathbf{k}_i \cdot \frac{\mathcal{D}\Psi}{\mathcal{D}\tilde{\delta}(\mathbf{k}', \tau)} e^{-\mathbf{k}_1 \cdot (\mathbf{q}_1 + \Psi_1) - \cdots - \mathbf{k}_n \cdot (\mathbf{q}_n + \Psi_n)} \right\rangle, \quad (5.7)$$

where we introduced the displacement field $\Psi(\mathbf{q}, t) = \mathbf{x}(\mathbf{q}, t) - \mathbf{q}$. We now wish to compute $\mathcal{D}\Psi/\mathcal{D}\tilde{\delta}(\mathbf{k}', \tau)$ in order to obtain the response function. In the linear regime this can be easily done by means of the continuity equation, which gives

$$k' \rightarrow 0 : \frac{\mathcal{D}\Psi_L}{\mathcal{D}\tilde{\delta}(\mathbf{k}', \tau)} \rightarrow i \frac{\mathbf{k}'}{k'^2} D(\tau), \quad (5.8)$$

and we want to show that this result is still valid at the non-linear level if we are in the squeezed limit for $n+1$ density correlators (i.e., the limit $k' \rightarrow 0$). To do so, we consider an infinitesimal change of the initial condition $\Delta\delta_{L0}$ which leads, from the definition of functional derivative, to a change of the non-linear displacement field

$$\Delta\Psi(\mathbf{q}) = \int d\mathbf{k}' \frac{\mathcal{D}\Psi(\mathbf{q})}{\mathcal{D}\tilde{\delta}(\mathbf{k}', \tau)} \Delta\tilde{\delta}_{L0}. \quad (5.9)$$

To obtain the low- k limit of the functional derivative we can look at a perturbation $\Delta\delta_{L0}$ that is restricted to $k < k_c$ and $k_c \rightarrow 0$. For instance, we can choose a Gaussian perturbation of size $R \rightarrow +\infty$ centered in \mathbf{q}_c far away from the point \mathbf{q} , which corresponds to adding a mass ΔM around the point \mathbf{q}_c . This modifies the linear density field δ_L as

$$\delta_L(\mathbf{q}, \tau) \rightarrow \hat{\delta}_L = \delta_L + D(\tau)\Delta\delta_{L0} \quad (5.10)$$

and also the velocity field v_{L0} by the precise amount that corresponds to the relation between velocity and density in the growing mode

$$\mathbf{v}_L(\mathbf{q}, \tau) \rightarrow \hat{\mathbf{v}}_L = \mathbf{v}_L - \frac{dD}{d\tau} \nabla_{\mathbf{q}}^{-1} \cdot \Delta\delta_{L0}. \quad (5.11)$$

At the linear level, this means that the small-scale region around \mathbf{q} is falling towards the large-scale mass ΔM centered on \mathbf{q}_c , as stated by Eq.(5.8). Since we are aiming at describing results at the non-linear level, we must show that the impact of a mass ΔM is still to attract the small-scale region with the same acceleration as in the linear regime, even when the small-scale region around \mathbf{q} is non-linear.

This can be seen from the equation of motion of the trajectories

$$\frac{\partial^2 \mathbf{x}}{\partial \tau^2} + \mathcal{H} \frac{\partial \mathbf{x}}{\partial \tau} = -\nabla\Phi = -\mathbf{F} \quad (5.12)$$

where Φ and \mathbf{F} are the Newtonian potential and force. If we add a perturbation ΔM , the trajectories are modified following Eq.(5.12) giving rise to the perturbed

trajectories $\hat{\mathbf{x}}$. To compute $\hat{\mathbf{x}}$ we can consider the auxiliary trajectory

$$\mathbf{x}'(\mathbf{q}, \tau) \equiv \mathbf{x}(\mathbf{q}, \tau) + D(\tau)\Delta\Psi_{L0}(\mathbf{q}), \quad (5.13)$$

where $\Delta\Psi_{L0}(\mathbf{q}) = -\nabla_{\mathbf{q}}^{-1}\Delta\delta_{L0}$ is the displacement due to the $\Delta\delta_{L0}$. These auxiliary trajectories satisfy

$$\frac{\partial^2 \mathbf{x}'}{\partial \tau^2} + \mathcal{H} \frac{\partial \mathbf{x}'}{\partial \tau} = -\mathbf{F} + \left(\frac{\partial^2 D}{\partial \tau^2} + \mathcal{H} \frac{\partial D}{\partial \tau} \right) = \mathbf{F}(\mathbf{x}', \tau) + \Delta\mathbf{F}_L(\mathbf{q}, \tau) \quad (5.14)$$

where we used $\mathbf{F}'(\mathbf{x}') = \mathbf{F}(\mathbf{x})$ because the uniform translation only gives rise to the same translation of the Newtonian force, since $\mathbf{F} \propto \nabla^{-1}\delta$. The last term follows from Eq.(5.12), which implies that at linear level the displacement field obeys to

$$\frac{\partial^2 \Psi_L}{\partial \tau^2} + \mathcal{H} \frac{\partial \Psi_L}{\partial \tau} = -\nabla_{\mathbf{q}} \Phi = -\mathbf{F}. \quad (5.15)$$

We then notice that the trajectories \mathbf{x}' satisfy the same initial conditions of the perturbed ones and they follow the same equation of motion if we can write $\Delta\mathbf{F}' = \Delta\mathbf{F}_L$. This is valid when $R \rightarrow +\infty$ since ΔM produces a Newtonian force that varies over the scale R and can be approximated as a constant for the small-scale region \mathbf{q} . Moreover, since we consider a regime when $k' \rightarrow 0$, the force is set by the Poisson equation sourced by $\Delta\delta_L$ and hence it is in the linear regime. We can conclude that $\mathbf{x}' = \hat{\mathbf{x}}$ and ΔM produced a uniform translation also in the non-linear regime. This allows us to write

$$k' \rightarrow 0 : \frac{\mathcal{D}\Psi}{\mathcal{D}\tilde{\delta}(\mathbf{k}', \tau)} \rightarrow i \frac{\mathbf{k}'}{k'^2} D(\tau), \quad (5.16)$$

from which we obtain

$$R_{k' \rightarrow 0}^{1,n} = \left\langle \tilde{\delta}(\mathbf{k}_1, \tau_1) \cdots \tilde{\delta}(\mathbf{k}_n, \tau_n) \right\rangle \sum_{i=1}^n \frac{\mathbf{k} \cdot \mathbf{k}'}{k'^2} D(\tau_i), \quad (5.17)$$

which can be substituted in Eq.(5.4) to obtain the CRs for the density fields

$$\left\langle \tilde{\delta}_{L0}(\mathbf{k}') \tilde{\delta}(\mathbf{k}_1, t_1) \cdots \tilde{\delta}(\mathbf{k}_n, t_n) \right\rangle'_{k' \rightarrow 0} = - \sum_{i=1}^n \frac{\mathbf{k}_i \cdot \mathbf{k}'}{k'^2} D(\tau_i) P_{L0}(k') \left\langle \tilde{\delta}(\mathbf{k}_1, t_1) \cdots \tilde{\delta}(\mathbf{k}_n, t_n) \right\rangle' \quad (5.18)$$

where $\langle \cdots \rangle'$ denotes that we removed the Dirac factor $\delta_D(\sum \mathbf{k}_i)$. As stated above, the main property of Eq.(5.18) is that it does not require $\tilde{\delta}$ to be in the linear or perturbative regime and we can check directly that it does vanish at equal time (i.e., when $\tau_1 = \cdots = \tau_n$), since in the squeezed limit we have $\mathbf{k}_1 + \cdots + \mathbf{k}_n \simeq \mathbf{k} + \mathbf{k}_1 + \cdots + \mathbf{k}_n = 0$.

At this stage, it is worth highlighting the connection between Eq.(5.18) and the equivalence principle. As we saw, a change $\Delta\delta_{L0}$ in the initial density gives rise to the same displacement for all scales and this is a direct consequence of the equivalence principle since all scales feel the same effect regardless of their size.

For this reason, CRs rely on the equivalence principle and provide a way to test GR in the non-perturbative regime.

5.3 Consistency relations for velocities and momenta

The main effect of a long wavelength perturbation is to move small structures with a uniform shift, hence we expect that CRs involving velocity fields may detect this effect. It is in fact possible to show (see sec.3 of art.E) that the transformation law for velocities reads

$$\tilde{\mathbf{v}}(\mathbf{k}, \tau) \rightarrow \hat{\tilde{\mathbf{v}}}(\mathbf{k}, \tau) = \tilde{\mathbf{v}}(\mathbf{k}, \tau) - \imath D(\mathbf{k} \cdot \Delta\Psi_{L0}) \tilde{\mathbf{v}}(\mathbf{k}, \tau) + \frac{dD}{d\tau} \Delta\Psi_{L0} \delta_D(\mathbf{k}), \quad (5.19)$$

where the last factor is a term associated with the shift of the amplitude. Eq.(5.19) can be used to obtain the CRs for velocity (and density) fields

$$\begin{aligned} & \langle \tilde{\delta}(\mathbf{k}', \tau') \prod_{j=1}^n \tilde{\delta}(\mathbf{k}_j, \tau_j) \prod_{j=n+1}^{n+m} \tilde{\mathbf{v}}(\mathbf{k}_j, \tau_j) \rangle'_{k' \rightarrow 0} = -P_L(k', \tau') \\ & \times \left\{ \left\langle \prod_{j=1}^n \tilde{\delta}(\mathbf{k}_j, \tau_j) \prod_{j=n+1}^{n+m} \tilde{\mathbf{v}}(\mathbf{k}_j, \tau_j) \right\rangle' \sum_{i=1}^{n+m} \frac{D(\tau_i) \mathbf{k}_i \cdot \mathbf{k}'}{D(\tau')} \frac{1}{k'^2} \right. \\ & \left. + \sum_{i=n+1}^{n+m} \left\langle \prod_{j=1}^n \tilde{\delta}(\mathbf{k}_j, \tau_j) \prod_{j=n+1}^{i-1} \tilde{\mathbf{v}}(\mathbf{k}_j, \tau_j) \times \left(\frac{(dD/d\tau)(\tau_i)}{D(\tau')} \imath \frac{\mathbf{k}'}{k'^2} \delta_D(\mathbf{k}_i) \right) \prod_{j=i+1}^{n+m} \tilde{\mathbf{v}}(\mathbf{k}_j, \tau_j) \right\rangle' \right\}. \end{aligned} \quad (5.20)$$

If we take $\mathbf{k}_i \neq 0$, as usual for studies of Fourier-space spectra, the last term vanishes and we recover the same form as CRs of the density fields. However, this new Dirac term gives a nonzero contribution in configuration space and real-space correlators obey consistency relations that differ from those of the density fields. One may obtain scalar relations by taking for instance the divergence of the velocity field, $\theta = \nabla \cdot \mathbf{v}$ (see Eq.(15) of art.E or [75]), but this obeys CRs similar to the density fields ones because the new Dirac term disappears as $\tilde{\theta}_i = \mathbf{k}_i \cdot \tilde{\mathbf{v}}_i$.

One simple way to obtain scalar non-vanishing CRs at equal times is to consider the divergence of the weighted momentum $\mathbf{p} = (1 + \delta)\mathbf{v}$, i.e $\tilde{\lambda} \equiv \nabla \cdot (1 + \delta)\mathbf{v}$. For $\tilde{\lambda} = \imath \mathbf{k} \cdot \mathbf{p}$, the transformation law reads

$$\frac{\mathcal{D}\tilde{\lambda}(\mathbf{k})}{\mathcal{D}\tilde{\delta}_{L0}(\mathbf{k}')} = \frac{\mathbf{k} \cdot \mathbf{k}'}{k'^2} \left(D\tilde{\lambda}(\mathbf{k}) + \imath \frac{dD}{d\tau} \tilde{\delta}(\mathbf{k}) \right), \quad (5.21)$$

from which we obtain

$$\begin{aligned}
& \langle \tilde{\delta}(\mathbf{k}', \tau') \prod_{j=1}^n \tilde{\delta}(\mathbf{k}_j, \tau_j) \prod_{j=n+1}^{n+m} \tilde{\lambda}(\mathbf{k}_j, \tau_j) \rangle'_{k' \rightarrow 0} = -P_L(k', \tau') \times \\
& \left\{ \langle \prod_{j=1}^n \tilde{\delta}(\mathbf{k}_j, \tau_j) \prod_{j=n+1}^{n+m} \tilde{\lambda}(\mathbf{k}_j, \tau_j) \rangle' \sum_{i=1}^{n+m} \frac{D(\tau_i)}{D(\tau')} \frac{\mathbf{k}_i \cdot \mathbf{k}'}{k'^2} \right. \\
& \left. - \sum_{i=n+1}^{n+m} \langle \tilde{\delta}(\mathbf{k}_i, \tau_i) \prod_{j=1}^n \tilde{\delta}(\mathbf{k}_j, \tau_j) \prod_{\substack{j=n+1 \\ j \neq i}}^{n+m} \tilde{\lambda}(\mathbf{k}_j, \tau_j) \rangle' \times \frac{(dD/d\tau)(\tau_i)}{D(\tau')} \frac{\mathbf{k}_i \cdot \mathbf{k}'}{k'^2} \right\}, \tag{5.22}
\end{aligned}$$

which at equal times read

$$\begin{aligned}
& \langle \tilde{\delta}(\mathbf{k}') \prod_{j=1}^n \tilde{\delta}(\mathbf{k}_j) \prod_{j=n+1}^{n+m} \tilde{\lambda}(\mathbf{k}_j) \rangle'_{k' \rightarrow 0} = P_L(k') \frac{d \ln D}{d\tau} \\
& \times \sum_{i=n+1}^{n+m} \frac{\mathbf{k}_i \cdot \mathbf{k}'}{k'^2} \langle \tilde{\delta}(\mathbf{k}_i) \prod_{j=1}^n \tilde{\delta}(\mathbf{k}_j) \prod_{\substack{j=n+1 \\ j \neq i}}^{n+m} \tilde{\lambda}(\mathbf{k}_j) \rangle' \tag{5.23}
\end{aligned}$$

where we did not write the common time τ . The second term of Eq.(5.22) comes from the second term of Eq.(5.21), does not vanish at equal times and transforms the momentum divergences $\tilde{\lambda}$ into density perturbations $\tilde{\delta}$. The simplest relation that does not vanish at equal times is the bispectrum with two $\tilde{\delta}$ fields and one $\tilde{\lambda}$ field

$$\langle \tilde{\delta}(\mathbf{k}') \tilde{\delta}(\mathbf{k}) \tilde{\lambda}(-\mathbf{k}) \rangle'_{k' \rightarrow 0} = -\frac{\mathbf{k} \cdot \mathbf{k}'}{k'^2} \frac{d \ln D}{d\tau} P_L(k') P(k). \tag{5.24}$$

with $P(k)$ the non-linear power spectrum. Eq.(5.24) can be extended to galaxy fields

$$b_g \langle \tilde{\delta}_g(\mathbf{k}') \tilde{\delta}_g(\mathbf{k}) \tilde{\lambda}_g(-\mathbf{k}) \rangle'_{k' \rightarrow 0} = -\frac{\mathbf{k} \cdot \mathbf{k}'}{k'^2} \frac{d \ln D}{d\tau} P_{\delta_g \delta_g}(k') \times P_{\delta_g \delta_g}(k), \tag{5.25}$$

where $\tilde{\delta}_g$ is the galaxy density contrast, $P_{\delta_g \delta_g}$ is the galaxy density power spectrum and we assumed a deterministic large-scale limit bias b_g for galaxy bias.

CRs such as Eq.(5.25) are very useful, as we will see sec.5.4, since they provide a way to connect theoretical non-perturbative results to observational probes in order to test GR and primordial non-Gaussianity.

5.4 Consistency relations for observables

In this section, we apply some of the results obtained above to observational probes, focusing on the galaxy number density contrast and the ISW effect.

From galaxy survey, we can typically measure the galaxy density contrast within some redshift bin smoothed with some finite-size window

$$\delta_g^s(\vec{\theta}) = \int d\vec{\theta}' W_\Theta(|\vec{\theta}' - \vec{\theta}|) \int d\tau I_g(\eta) \delta_g[r, r\vec{\theta}'; \tau], \quad (5.26)$$

where $W_\Theta(|\theta| \leq \Theta)$ is a 2D symmetric window function centered on the direction on the sky of angular radius Θ , $r = \tau_0 - \tau$ is the radial comoving distance along the line of sight and

$$I_g(\eta) = \left| \frac{dz}{d\tau} \right| n_g(z), \quad (5.27)$$

is a weight associated with the normalized galaxy selection function $n_g(z)$. Eq.(5.26) can be expanded in Fourier space to obtain

$$\delta_g^s(\vec{\theta}) = \int d\eta I_g(\eta) \int d\mathbf{k} \tilde{W}_\Theta(k_\perp r) e^{ik_\parallel r + i\mathbf{k}_\perp \cdot r\vec{\theta}} \tilde{\delta}_g(\mathbf{k}, \tau), \quad (5.28)$$

when we defined

$$\tilde{W}_\Theta(|\vec{\ell}|) = \int d\vec{\theta}' e^{-i\vec{\ell} \cdot \vec{\theta}'} W_\Theta(|\vec{\theta}'|), \quad (5.29)$$

and $\mathbf{k} = (k_\parallel, \mathbf{k}_\perp)$ are respectively the parallel and the perpendicular components of \mathbf{k} .

Similarly, cosmological surveys can measure the secondary CMB anisotropy due to ISW along the direction $\vec{\theta}$

$$\Delta_{\text{ISW}}(\vec{\theta}) = \int d\eta e^{-\tau_{\text{opt}}(\tau)} \left(\frac{\partial \Psi}{\partial \tau} + \frac{\partial \Phi}{\partial \tau} \right) [r, r\vec{\theta}; \tau] = 2 \int d\tau e^{-\tau_{\text{opt}}(\tau)} \frac{\partial \Psi}{\partial \tau} [r, r\vec{\theta}; \tau], \quad (5.30)$$

where τ_{opt} is the optical depth and we assumed no anisotropic stress. It is possible to relate $\tilde{\lambda}$ to $\tilde{\Psi}$ via the Fourier space Poisson equation as

$$\frac{\partial \tilde{\Psi}}{\partial \tau} = \frac{4\pi \mathcal{G} \bar{\rho}_0}{k^2 a} (\tilde{\lambda} + \mathcal{H} \tilde{\delta}), \quad (5.31)$$

which gives

$$\Delta_{\text{ISW}}^s(\vec{\theta}) = \int d\tau I_{\text{ISW}}(\tau) \int d\mathbf{k} \tilde{W}_\Theta(k_\perp r) e^{ik_\parallel r + i\mathbf{k}_\perp \cdot r\vec{\theta}} \times \frac{\tilde{\lambda} + \mathcal{H} \tilde{\delta}}{k^2}, \quad (5.32)$$

with

$$I_{\text{ISW}}(\tau) = 8\pi \mathcal{G} \bar{\rho}_0 \frac{e^{-\tau_{\text{opt}}}}{a}. \quad (5.33)$$

These two results can be used to compute the cross-correlation between two galaxy density contrasts and an ISW temperature anisotropy

$$\xi_3(\delta_g^s, \delta_{g_1}^s, \Delta_{\text{ISW}_2}^s) = \langle \delta_g^s(\vec{\theta}) \delta_{g_1}^s(\vec{\theta}_1) \Delta_{\text{ISW}_2}^s(\vec{\theta}_2) \rangle. \quad (5.34)$$

where $\vec{\theta}, \vec{\theta}_1, \vec{\theta}_2$ are the directions along which we measure the observables. Since we want to apply the CRs obtained in sec.5.3, we must ensure that we fulfill the linear conditions and the squeezed limit, i.e. k , the wavelength associated to the first δ_g , has to be both linear and much smaller than k_1, k_2 associated to δ_{g1} and $\Delta_{\text{ISW}2}$. These conditions in configuration space correspond to

$$\Theta \gg \Theta_L, \quad \Theta \gg \Theta_j, \quad |\vec{\theta} - \vec{\theta}_j| \gg |\vec{\theta}_1 - \vec{\theta}_2|, \quad (5.35)$$

and once fulfilled, ξ_3 reads (see sec.4.1 of art.F)

$$\begin{aligned} \xi_3 = & \frac{(\vec{\theta} - \vec{\theta}_2) \cdot (\vec{\theta}_1 - \vec{\theta}_2)}{|\vec{\theta} - \vec{\theta}_2| |\vec{\theta}_1 - \vec{\theta}_2|} (2\pi)^4 \int d\eta b_g I_g I_{g1} I_{\text{ISW}2} \frac{d \ln D}{d\tau} \times \\ & \int_0^\infty dk_\perp dk_{1\perp} \tilde{W}_\Theta(k_\perp r) \tilde{W}_{\Theta_1}(k_{1\perp} r) \tilde{W}_{\Theta_2}(k_{1\perp} r) \\ & \times P_L(k_\perp, \tau) P_{g1,m}(k_{1\perp}, \tau) J_1(k_\perp r |\vec{\theta} - \vec{\theta}_2|) \times J_1(k_{1\perp} r |\vec{\theta}_1 - \vec{\theta}_2|), \end{aligned} \quad (5.36)$$

where $P_{g1,m}$ is the galaxy-matter power spectrum and J_1 is the first-order Bessel function of the first kind. Eq.(5.36) expresses the response of the small-scale two-point correlation function $\langle \delta_{g1}^s(\vec{\theta}_1) \Delta_{\text{ISW}2}^s(\vec{\theta}_2) \rangle$ to a change in the large-scale mode $\delta_g^s(\vec{\theta})$ and represents the motion of the small-scale structures $\tilde{\delta}_1, \tilde{\lambda}_2$ towards (or away from) $\tilde{\delta}$. This explains why Eq.(5.36) vanishes when $(\vec{\theta} - \vec{\theta}_2) \perp (\vec{\theta}_1 - \vec{\theta}_2)$: in fact, when this happens, there is a reflection symmetry, from the point of view of $\vec{\theta}_2$ and $\vec{\theta}_1$, along the $\vec{\theta} - \vec{\theta}_2$ axis. Hence we have a positive $\tilde{\lambda}_2$ for both an increase and a decrease of δ_g . Then, at the leading order, there is no effect on the small scale structures motion changing δ_g and hence the kinematic effect vanishes.

Eq.(5.36) represents an example of CRs which can be directly observed by galaxy surveys and its angular dependence could provide a test for the equivalence principle, even without computing its right-hand side. Other CRs can be obtained evaluating different probes (see sec.4 and 5 of art.F) such as the weak lensing convergence field or the CMB anisotropies due to the kinematic Sunyaev-Zeldovich effect, however they do not show an angular dependence or involve galaxy-free electron spectra, making them harder to measure.

5.5 Conclusions

In this chapter, we introduced the kinematic consistency relations for large-scale structure, i.e., non-perturbative relations among correlators of the density and velocity fields in the squeezed limit. CRs rely on the equivalence principle and Gaussian initial conditions, and thus their violation would signal a modification of GR or non-Gaussian initial conditions.

After presenting a simple non-relativistic derivation of CRs, we extended this result to velocity and momentum fields to obtain CRs which do not vanish at equal times. Finally, we showed how to relate CRs with observational probes,

such as galaxy density contrast and ISW temperature CMB anisotropies, and we obtained a relation which can be directly measured and shows a particular angular dependence as a function of the relative angular positions.

For these reasons, the CRs obtained in this chapter can become a powerful tool to test MGTs in the light of future surveys, even though the study of the feasibility of this kind of observations in actual surveys will require additional study, which may include a signal-to-noise analysis, that we leave for a future work.

Chapter 6

Conclusions

In this manuscript, we have highlighted the physical intuitions and the main results obtained in the appended articles.

In Chapter 1, we gave a short introduction to the vast domain of alternatives to Λ -CDM, focusing on dark energy models and modified gravity theories.

In Chapter 2, we presented the K-mouflage model of modified gravity, studying its impact on cluster dynamics and showing how these theories modify at a non-negligible level the halo temperature function as compared to the Λ -CDM one, leaving cluster scaling relations indistinguishable using current data.

In Chapter 3, we introduced the ultra-local models of gravity, scalar-tensor theories of gravity with a scalar field which possesses a negligible kinetic term. We showed how these theories have a great impact on structure formation at small scales and how they show a novel screening mechanism which relies on the lack of kinetic term. Moreover, we demonstrated that super-chameleon theories can be seen at cosmological scales as ultra-local model of gravity (up to their Compton scales) and we found them to be globally consistent with current observations.

In Chapter 4, we gave a glimpse on how cosmic data can be used to constrain modified-gravity theories, in particular focusing on the impact of $f(R)$ and Dilaton model on cosmic shear data. We showed that degeneracies among baryons, neutrinos and modified-gravity theories are essential to give reasonable constraints using cosmic shear data and how, once these are taken into account, current cosmic shear data can accommodate most of the theories considered due to the large uncertainties in measurements and baryonic feedback.

In Chapter 5, we presented consistency relations for large-scale structures, factorizations of $(n + 1)$ -points correlators in terms of the n -points ones valid at the non-linear level, that only rely on the equivalence principle and Gaussian initial conditions. We presented here the first non-vanishing consistency relations at equal times, which we connected to observable quantities. In particular, we presented a practical result, involving the cross-correlation between δ_g and Δ_{ISW} fields, which can be used to test the Λ -CDM model using survey observations.

Outlooks

As often happens when one tries to study cosmological structure formation at non-linear scales[76–79], numerical simulations are what is mostly needed to give a clearer picture of the modified-gravity theories presented in this manuscript. In particular, the K-mouflage model screening mechanism occurs well inside cluster of galaxies and numerical simulations can help to understand the impact of the scalar field on the internal structure of the cluster and its degeneracies with baryonic physics. For the ultra-local models (and super chameleon ones), numerical simulations can help to understand their impact on galaxy formation, possibly to use them to constrain the coupling function of the model. Finally, investigating degeneracies between baryonic physics and $f(R)$ and Dilaton models may have a strong impact on the underlying assumption of uncorrelated biases that we used in the cosmic-shear data analysis presented in this manuscript, which can be tested using dedicated numerical simulations.

On another note, for both K-mouflage and ultra-local models, a Montecarlo analysis is needed to explore a larger parameter space than the ones presented here, using different functional forms for the free functions of the models.

Finally, the feasibility of measurement of consistency relations involving observables has to be addressed in a detailed way and numerical methods will probably be needed due to the complex modeling of survey observations. On a more theoretical side, consistency relations valid for alternative theories to Λ -CDM are necessary to understand if/how consistency relations can be used to discriminate among different modified-gravity theories.

Chapter 7

Résumé

La cosmologie a atteint une ère passionnante. Pour la première fois dans l'histoire humaine, un modèle quantitatif pour la formation et l'évolution de l'Univers existe, expliquant une gamme très variée de phénomènes et ayant été testé avec une précision impressionnante. De plus, nous sommes à l'aube d'une époque dans laquelle nous aurons à notre disposition une abondance de données de grande qualité, ce qui nous permettra d'utiliser la cosmologie comme un outil pour tester la physique fondamentale.

En particulier, comme les structures de grandes échelles de l'Univers sont gouvernées par la force de gravité, la cosmologie peut être utilisée pour tester la théorie de la relativité générale d'Einstein. Cette idée a inspiré la plupart des travaux décrits dans ce manuscrit, dans lequel j'ai étudié des théories alternatives au modèle standard de la cosmologie et des tests à grandes échelles pour la relativité générale.

Dans la première partie de ma thèse, je me suis concentré sur les "théories tenseur-scalaire" de la gravité. Ce sont des théories alternatives de la gravité, dans lesquelles un champ scalaire, qui est responsable de l'accélération de l'expansion de l'Univers, est ajouté à l'action de Einstein-Hilbert. Dans le deuxième chapitre, j'ai décrit le modèle de K-mouflage, une "théorie tenseur-scalaire" dans laquelle le champ scalaire possède un terme cinétique non-standard, en montrant son effet non négligeable sur la dynamique des amas des galaxies. J'ai aussi montré comment cet effet peut être utilisé pour contraindre le modèle de "K-mouflage" en utilisant des observations en rayon X.

Dans le troisième chapitre, j'ai présenté le modèle "ultra-local" de la gravité, une "théorie tenseur-scalaire" dont le champ scalaire possède un terme cinétique négligeable. J'ai étudié sa faisabilité en tant que théorie alternative à la relativité générale aux échelles cosmologiques, en montrant comment la formation des structures est très accélérée aux petites échelles. De plus, j'ai prouvé comment les modèles "super-chaméléons" peuvent être vus comme des modèles "ultra-locaux" jusqu'à leur échelle de Compton, et j'ai utilisé les résultats obtenus pour

ces derniers pour montrer leur faisabilité en tant que théories alternatives de la gravité.

Dans le quatrième chapitre, j’ai décrit comment les théories de la gravité “ $f(R)$ ” et “Dilaton” modifient le signal qui provient des lentilles gravitationnelles faibles. En particulier, j’ai montré que le cisaillement cosmique a un pouvoir assez limité actuellement pour contraindre ces théories, à cause de la faible précision des observations actuelles et des dégénérescences avec les processus baryoniques.

Dans le cinquième chapitre, j’ai donné une description de mon étude des relations de cohérence. Ce sont des relations entre les fonctions de corrélation des champs cosmiques à $(n + 1)$ et n points, valables aussi dans le régime non-linéaire. Leur intérêt vient du fait que leur dérivation dépend seulement du Principe d’Équivalence et de l’hypothèse de conditions initiales Gaussiennes, et donc elles peuvent être utilisées pour tester ces hypothèses fondamentales du modèle standard de la cosmologie. Des relations similaires ont été étudiées auparavant, mais j’ai montré comment il est possible d’obtenir des relations qui ne s’annulent pas lorsque tous les champs sont considérés au même instant. J’ai utilisé ce résultat pour obtenir des relations de cohérence entre fonctions de corrélation de quantités observables, notamment le champ de densité des galaxies et la fluctuation de température du fond diffus cosmologie donnée par l’effet Sachs-Wolfe. Ces relations peuvent être utilisées pour des tests de la relativité générale, reposant sur des observations par satellites, sans avoir besoin de modéliser la physique des baryons aux petites échelles.

Enfin, j’ai donné un aperçu des quelques perspectives possibles pour poursuivre le travail décrit dans ce manuscrit. En particulier, j’ai souligné comment des simulations numérique sont nécessaires pour mieux comprendre la formation des structures dans le contexte des modèles “K-mouflage” et “ultra-local”. En outre, elles peuvent être aussi utilisées pour tester les hypothèses sous-tendant l’analyse des lentilles gravitationnelles faibles présentée dans ce manuscrit, surtout pour distinguer l’effet de la physique des baryons et des neutrinos de l’effet des théories de gravité modifiée sur le cisaillement cosmique. En ce qui concerne les relations de cohérence, une étude de faisabilité de leur mesure avec les “surveys” cosmologiques est nécessaire, pour comprendre si elles peuvent donner des contraintes compétitives sur les théories alternatives de la gravité.

Bibliography

- [1] C. M. Will, “The Confrontation between General Relativity and Experiment,” *Living Reviews in Relativity* **17** (Dec., 2014) 4, [1403.7377](#).
- [2] R. P. Woodard, “How far are we from the quantum theory of gravity?,” *Reports on Progress in Physics* **72** (Dec., 2009) 126002, [0907.4238](#).
- [3] **Supernova Cosmology Project** Collaboration, S. Perlmutter *et. al.*, “Cosmology from Type Ia supernovae,” *Bull.Am.Astron.Soc.* **29** (1997) 1351, [astro-ph/9812473](#).
- [4] **Supernova Cosmology Project** Collaboration, S. Perlmutter *et. al.*, “Measurements of Omega and Lambda from 42 high redshift supernovae,” *Astrophys.J.* **517** (1999) 565–586, [astro-ph/9812133](#).
- [5] S. E. Rugh and H. Zinkernagel, “The Quantum Vacuum and the Cosmological Constant Problem,” *ArXiv High Energy Physics - Theory e-prints* (Dec., 2000) [hep-th/0012253](#).
- [6] K. Koyama, “Cosmological Tests of Modified Gravity,” *Rept. Prog. Phys.* **79** (2016), no. 4 046902, [1504.04623](#).
- [7] R. A. Battye, T. Charnock, and A. Moss, “Tension between the power spectrum of density perturbations measured on large and small scales,” *Phys. Rev.* **D91** (2015), no. 10 103508, [1409.2769](#).
- [8] S.-H. Oh, W. J. G. de Blok, E. Brinks, F. Walter, and R. C. Kennicutt, Jr, “Dark and luminous matter in THINGS dwarf galaxies,” *Astron. J.* **141** (2011) 193, [1011.0899](#).
- [9] M. Boylan-Kolchin, J. S. Bullock, and M. Kaplinghat, “The Milky Way’s bright satellites as an apparent failure of LCDM,” *Mon. Not. Roy. Astron. Soc.* **422** (2012) 1203–1218, [1111.2048](#).
- [10] J. P. Ostriker and P. J. Steinhardt, “New light on dark matter,” *Science* **300** (2003) 1909–1913, [astro-ph/0306402](#).
- [11] A. Joyce, L. Lombriser, and F. Schmidt, “Dark Energy Versus Modified Gravity,” *Ann. Rev. Nucl. Part. Sci.* **66** (2016) 95–122, [1601.06133](#).

- [12] R. R. Caldwell, R. Dave, and P. J. Steinhardt, “Cosmological imprint of an energy component with general equation of state,” *Phys. Rev. Lett.* **80** (1998) 1582–1585, [astro-ph/9708069](#).
- [13] P. J. E. Peebles and B. Ratra, “The Cosmological constant and dark energy,” *Rev. Mod. Phys.* **75** (2003) 559–606, [astro-ph/0207347](#).
- [14] E. J. Copeland, M. Sami, and S. Tsujikawa, “Dynamics of dark energy,” *Int. J. Mod. Phys. D* **15** (2006) 1753–1936, [hep-th/0603057](#).
- [15] Y. Fujii and K. ichi Maeda, “The scalar-tensor theory of gravitation,” *Classical and Quantum Gravity* **20** (2003), no. 20 4503.
- [16] M. A. Vasiliev, “Consistent equations for interacting gauge fields of all spins in 3+1 dimensions,” *Physics Letters B* **243** (July, 1990) 378–382.
- [17] E. S. Fradkin and M. A. Vasiliev, “On the gravitational interaction of massless higher-spin fields,” *Physics Letters B* **189** (Apr., 1987) 89–95.
- [18] I. L. Shapiro and H. Takata, “Conformal transformation in gravity,” *Physics Letters B* **361** (Feb., 1995) 31–37, [hep-th/9504162](#).
- [19] J. D. Bekenstein, “Relation between physical and gravitational geometry,” *Physical Review D* **48** (Oct., 1993) 3641–3647, [gr-qc/9211017](#).
- [20] V. Faraoni and E. Gunzig, “Einstein frame or Jordan frame ?,” *ArXiv Astrophysics e-prints* (Oct., 1999) [astro-ph/9910176](#).
- [21] J. Khoury and A. Weltman, “Chameleon cosmology,” *Physical Review D* **69** (Feb., 2004) 044026, [astro-ph/0309411](#).
- [22] J. Khoury and A. Weltman, “Chameleon Fields: Awaiting Surprises for Tests of Gravity in Space,” *Physical Review Letters* **93** (Oct., 2004) 171104, [astro-ph/0309300](#).
- [23] P. Brax, C. van de Bruck, A.-C. Davis, and D. Shaw, “Dilaton and modified gravity,” *Physical Review D* **82** (Sept., 2010) 063519, [1005.3735](#).
- [24] A. Vainshtein, “To the problem of nonvanishing gravitation mass,” *Phys.Lett.* **B39** (1972) 393–394.
- [25] E. Babichev, C. Deffayet, and R. Ziour, “k-Mouflage gravity,” *Int.J.Mod.Phys.* **D18** (2009) 2147–2154, [0905.2943](#).
- [26] N. e. a. Suzuki, “The Hubble Space Telescope Cluster Supernova Survey. V. Improving the Dark-energy Constraints above $z > 1$ and Building an Early-type-hosted Supernova Sample,” *Astrophys. J.* **746** (Feb., 2012) 85, [1105.3470](#).
- [27] F. Beutler, C. Blake, M. Colless, D. H. Jones, L. Staveley-Smith, L. Campbell, Q. Parker, W. Saunders, and F. Watson, “The 6dF Galaxy Survey: baryon acoustic oscillations and the local Hubble constant,” *Mon. Not. R. Astr. Soc.* **416** (Oct., 2011) 3017–3032, [1106.3366](#).

- [28] M. e. a. Moresco, “Improved constraints on the expansion rate of the Universe up to $z \sim 1.1$ from the spectroscopic evolution of cosmic chronometers,” *JCAP* **8** (Aug., 2012) 006, [1201.3609](#).
- [29] L. Amendola, M. Kunz, and D. Sapone, “Measuring the dark side (with weak lensing),” *JCAP* **4** (Apr., 2008) 013, [0704.2421](#).
- [30] S. P. Boughn and R. G. Crittenden, “A detection of the integrated Sachs Wolfe effect,” *NAR* **49** (May, 2005) 75–78, [arXiv:astro-ph/0404470](#).
- [31] Y.-C. Cai, B. Li, S. Cole, C. S. Frenk, and M. Neyrinck, “The integrated SachsWolfe effect in $f(R)$ gravity,” *Mon. Not. Roy. Astron. Soc.* **439** (2014), no. 3 2978–2989, [1310.6986](#).
- [32] A. Cooray, “Large scale pressure fluctuations and the Sunyaev-Zel’dovich effect,” *Physical Review D* **62** (Nov., 2000) 103506–+, [arXiv:astro-ph/0005287](#).
- [33] J. G. Williams, S. G. Turyshev, and D. H. Boggs, “Lunar laser ranging tests of the equivalence principle,” *Classical and Quantum Gravity* **29** (Sept., 2012) 184004, [1203.2150](#).
- [34] Planck Collaboration, P. A. R. Ade, N. Aghanim, M. Arnaud, M. Ashdown, J. Aumont, C. Baccigalupi, A. J. Banday, R. B. Barreiro, J. G. Bartlett, and et al., “Planck 2015 results. XIII. Cosmological parameters,” *Astr. & Astrophys.* **594** (Sept., 2016) A13, [1502.01589](#).
- [35] Planck Collaboration, P. A. R. Ade, N. Aghanim, M. Arnaud, M. Ashdown, J. Aumont, C. Baccigalupi, A. J. Banday, R. B. Barreiro, N. Bartolo, and et al., “Planck 2015 results. XIV. Dark energy and modified gravity,” *Astr. & Astrophys.* **594** (Sept., 2016) A14, [1502.01590](#).
- [36] L. Amendola *et. al.*, “Cosmology and Fundamental Physics with the Euclid Satellite,” [1606.00180](#).
- [37] L. Perenon, F. Piazza, C. Marinoni, and L. Hui, “Phenomenology of dark energy: general features of large-scale perturbations,” *JCAP* **1511** (2015), no. 11 029, [1506.03047](#).
- [38] H. Steigerwald, J. Bel, and C. Marinoni, “Probing non-standard gravity with the growth index: a background independent analysis,” *JCAP* **1405** (2014) 042, [1403.0898](#).
- [39] F. Piazza, H. Steigerwald, and C. Marinoni, “Phenomenology of dark energy: exploring the space of theories with future redshift surveys,” *JCAP* **1405** (2014) 043, [1312.6111](#).
- [40] S. Casas, M. Kunz, M. Martinelli, and V. Pettorino, “Linear and non-linear Modified Gravity forecasts with future surveys,” [1703.01271](#).
- [41] P. Brax and P. Valageas, “K-mouflage Cosmology: Formation of Large-Scale Structures,” *Phys. Rev.* **D90** (2014), no. 2 023508, [1403.5424](#).

- [42] P. Brax and P. Valageas, “K-mouflage Cosmology: the Background Evolution,” *Phys. Rev.* **D90** (2014), no. 2 023507, [1403.5420](#).
- [43] A. Barreira, P. Brax, S. Clesse, B. Li, and P. Valageas, “K-mouflage gravity models that pass Solar System and cosmological constraints,” *Phys. Rev.* **D91** (2015), no. 12 123522, [1504.01493](#).
- [44] P. Brax and P. Valageas, “The effective field theory of K-mouflage,” *JCAP* **1601** (2016), no. 01 020, [1509.00611](#).
- [45] A. Terukina and K. Yamamoto, “Gas density profile in dark matter halo in chameleon cosmology,” *Phys. Rev.* **D86** (2012) 103503, [1203.6163](#).
- [46] C. Arnold, E. Puchwein, and V. Springel, “Scaling relations and mass bias in hydrodynamical $f(R)$ gravity simulations of galaxy clusters,” *Mon. Not. Roy. Astron. Soc.* **440** (2014), no. 1 833–842, [1311.5560](#).
- [47] A. Terukina, L. Lombriser, K. Yamamoto, D. Bacon, K. Koyama, and R. C. Nichol, “Testing chameleon gravity with the Coma cluster,” *JCAP* **1404** (2014) 013, [1312.5083](#).
- [48] J. F. Navarro, C. S. Frenk, and S. D. M. White, “The Structure of Cold Dark Matter Halos,” *Astrophysical Journal* **462** (May, 1996) 563, [astro-ph/9508025](#).
- [49] M. Postman *et. al.*, “Cluster Lensing And Supernova survey with Hubble (CLASH): An Overview,” *Astrophys. J. Suppl.* **199** (2012) 25, [1106.3328](#).
- [50] J. Merten *et. al.*, “CLASH: The Concentration-Mass Relation of Galaxy Clusters,” *Astrophys. J.* **806** (2015), no. 1 4, [1404.1376](#).
- [51] A. Mantz, S. W. Allen, H. Ebeling, D. Rapetti, and A. Drlica-Wagner, “The Observed Growth of Massive Galaxy Clusters II: X-ray Scaling Relations,” *Mon. Not. Roy. Astron. Soc.* **406** (2010) 1773–1795, [0909.3099](#).
- [52] G. W. Pratt, J. H. Croston, M. Arnaud, and H. Boehringer, “Galaxy cluster X-ray luminosity scaling relations from a representative local sample (REXCESS),” *Astron. Astrophys.* **498** (2009) 361, [0809.3784](#).
- [53] Y. Ikebe, T. H. Reiprich, H. Boehringer, Y. Tanaka, and T. Kitayama, “A new measurement of the x-ray temperature function of clusters of galaxies,” *Astron. Astrophys.* **383** (2002) 773, [astro-ph/0112315](#).
- [54] D. Lynden-Bell, “Statistical mechanics of violent relaxation in stellar systems,” *Mon. Not. Roy. Astron. Soc.* **136** (1967) 101–121.
- [55] P. Brax, A.-C. Davis, and J. Sakstein, “SUPER-Screening,” *Phys. Lett.* **B719** (2013) 210–217, [1212.4392](#).
- [56] P. Brax, A.-C. Davis, and J. Sakstein, “Dynamics of Supersymmetric Chameleons,” *JCAP* **1310** (2013) 007, [1302.3080](#).

- [57] P. Fayet, “Lower Limit on the Mass of a Light Gravitino from e^+e^- Annihilation Experiments,” *Phys. Lett.* **B175** (1986) 471–477.
- [58] C. Heymans *et. al.*, “CFHTLenS: The Canada-France-Hawaii Telescope Lensing Survey,” *Mon. Not. Roy. Astron. Soc.* **427** (2012) 146, [1210.0032](#).
- [59] W. Hu and I. Sawicki, “Models of $f(R)$ Cosmic Acceleration that Evade Solar-System Tests,” *Phys. Rev.* **D76** (2007) 064004, [0705.1158](#).
- [60] D. Munshi, P. Valageas, L. Van Waerbeke, and A. Heavens, “Cosmology with Weak Lensing Surveys,” *Phys. Rept.* **462** (2008) 67–121, [astro-ph/0612667](#).
- [61] A. Lewis and S. Bridle, “Cosmological parameters from CMB and other data: A Monte Carlo approach,” *Phys. Rev.* **D66** (2002) 103511, [astro-ph/0205436](#).
- [62] M. P. van Daalen, J. Schaye, C. M. Booth, and C. Dalla Vecchia, “The effects of galaxy formation on the matter power spectrum: a challenge for precision cosmology,” *MNRAS* **415** (Aug., 2011) 3649–3665, [1104.1174](#).
- [63] P. Valageas, T. Nishimichi, and A. Taruya, “Matter power spectrum from a Lagrangian-space regularization of perturbation theory,” *Phys. Rev.* **D87** (2013) 083522, [1302.4533](#).
- [64] C. D. Leonard, T. Baker, and P. G. Ferreira, “Exploring degeneracies in modified gravity with weak lensing,” *Phys. Rev.* **D91** (2015), no. 8 083504, [1501.03509](#).
- [65] A. Taruya, F. Bernardeau, T. Nishimichi, and S. Codis, “RegPT: Direct and fast calculation of regularized cosmological power spectrum at two-loop order,” *Phys. Rev.* **D86** (2012) 103528, [1208.1191](#).
- [66] P. Valageas, “Large- N expansions applied to gravitational clustering,” *Astron. Astrophys.* **465** (2007) 725, [astro-ph/0611849](#).
- [67] M. Crocce and R. Scoccimarro, “Renormalized cosmological perturbation theory,” *Phys. Rev.* **D73** (2006) 063519, [astro-ph/0509418](#).
- [68] D. Langlois and F. Vernizzi, “A geometrical approach to nonlinear perturbations in relativistic cosmology,” *Class. Quant. Grav.* **27** (2010) 124007, [1003.3270](#).
- [69] D. Langlois and F. Vernizzi, “Nonlinear perturbations of cosmological scalar fields,” *JCAP* **0702** (2007) 017, [astro-ph/0610064](#).
- [70] D. Langlois and F. Vernizzi, “Evolution of non-linear cosmological perturbations,” *Phys. Rev. Lett.* **95** (2005) 091303, [astro-ph/0503416](#).
- [71] A. Cooray and R. K. Sheth, “Halo models of large scale structure,” *Phys. Rept.* **372** (2002) 1–129, [astro-ph/0206508](#).

-
- [72] A. Kehagias and A. Riotto, “Symmetries and Consistency Relations in the Large Scale Structure of the Universe,” *Nucl. Phys.* **B873** (2013) 514–529, [1302.0130](#).
- [73] M. Peloso and M. Pietroni, “Galilean invariance and the consistency relation for the nonlinear squeezed bispectrum of large scale structure,” *JCAP* **1305** (2013) 031, [1302.0223](#).
- [74] P. Valageas, “Kinematic consistency relations of large-scale structures,” *Phys. Rev.* **D89** (2014), no. 8 083534, [1311.1236](#).
- [75] P. Creminelli, J. Norea, M. Simonovi, and F. Vernizzi, “Single-Field Consistency Relations of Large Scale Structure,” *JCAP* **1312** (2013) 025, [1309.3557](#).
- [76] B. Falck, K. Koyama, G.-b. Zhao, and B. Li, “The Vainshtein Mechanism in the Cosmic Web,” *JCAP* **1407** (2014) 058, [1404.2206](#).
- [77] B. Li and H. Zhao, “Structure Formation by Fifth Force I: N-Body vs. Linear Simulations,” *Phys. Rev.* **D80** (2009) 044027, [0906.3880](#).
- [78] B. Li, D. F. Mota, and J. D. Barrow, “N-body Simulations for Extended Quintessence Models,” *Astrophys. J.* **728** (2011) 109, [1009.1400](#).
- [79] C. De Boni, K. Dolag, S. Ettori, L. Moscardini, V. Pettorino, and C. Baccigalupi, “Hydrodynamical simulations of galaxy clusters in dark energy cosmologies: I. general properties,” *Mon. Not. Roy. Astron. Soc.* **415** (2011) 2758, [1008.5376](#).

Article A

K-mouflage effects on clusters of galaxies

K-mouflage effects on clusters of galaxies

Philippe Brax, Luca Alberto Rizzo, and Patrick Valageas

*Institut de Physique Théorique, Université Paris-Saclay CEA,
CNRS, F-91191 Gif-sur-Yvette, Cédex, France*

(Received 26 May 2015; published 26 August 2015)

We investigate the effects of a K-mouflage modification of gravity on the dynamics of clusters of galaxies. We extend the description of K-mouflage to situations where the scalar field responsible for the modification of gravity is coupled to a perfect fluid with pressure. We describe the coupled system at both the background cosmology and cosmological perturbations levels, focusing on cases where the pressure emanates from small-scale nonlinear physics. We derive these properties in both the Einstein and Jordan frames, as these two frames already differ by a few percents at the background level for K-mouflage scenarios, and next compute cluster properties in the Jordan frame that is better suited to these observations. Galaxy clusters are not screened by the K-mouflage mechanism and therefore feel the modification of gravity in a maximal way. This implies that the halo mass function deviates from Λ -CDM by a factor of order 1 for masses $M \gtrsim 10^{14} h^{-1} M_{\odot}$. We then consider the hydrostatic equilibrium of gases embedded in galaxy clusters and the consequences of K-mouflage on the x-ray cluster luminosity, the gas temperature, and the Sunyaev–Zel’dovich effect. We find that the cluster temperature function, and more generally number counts, are largely affected by K-mouflage, mainly due to the increased cluster abundance in these models. Other scaling relations such as the mass-temperature and the temperature-luminosity relations are only modified at the percent level due to the constraints on K-mouflage from local Solar System tests.

DOI: [10.1103/PhysRevD.92.043519](https://doi.org/10.1103/PhysRevD.92.043519)

PACS numbers: 98.80.-k

I. INTRODUCTION

K-mouflage [1,2] is one of the four types of screening mechanisms, together with the chameleon [3,4], the Damour–Polyakov [5], and the Vainshtein [6] ones, which are compatible with second-order equations of motion for single scalar-field models [7]. The properties of K-mouflage have already been thoroughly studied both at the background cosmology Brax:2014a and perturbation levels [8,9]; see also Ref. [10] for a more general analysis within an “imperfect-fluid” formalism. The small-scale dynamics have been studied in Ref. [11], and models that satisfy both cosmological and Solar System constraints have been devised in Ref. [12].

In this paper, we extend these studies by including fluids with pressure as befitting the description of gases in galaxy clusters. We do so for both the background and perturbations. We also present the dynamics of the system in both the Einstein frame (used in previous works) and the Jordan frame and discuss the relations between both frames. Because the properties of gases, such as the x-ray luminosity or the Sunyaev–Zel’dovich effect [13], or the wavelength of atomic emission or absorption lines, are tied to the frame in which atomic physics is described without any modification due to the scalar field, we work in the Jordan frame to describe clusters of galaxies. We use the fact that galaxy clusters are not screened by the K-mouflage mechanism and that their number would be increased as compared with Λ -cold dark matter (CDM) in this scenario.

As a result, clusters appear as a useful testing ground for K-mouflage and its effects on the growth of structure.

We take into account the modification of the hydrostatic equilibrium in K-mouflage models, together with the change of the matter density profiles, which we find to become slightly more compact. This allows us to investigate the x-ray luminosity as a function of the gas temperature. The deviation from Λ -CDM is at the percent level and is set by the tests of gravity in the Solar System, which strongly constrain the coupling constant that defines these models. In a similar fashion, the temperature-mass relation is affected at the same level. As particular examples, we focus on a simple “cubic” K-mouflage model (that agrees with cosmological constraints) and on an “arctan” model which satisfies cosmological constraints as well as all Solar System tests, including the advance of the perihelion of the Moon [12]. The latter gives slightly amplified results as compared to the former, but both remain at the percent level. The only observable which deviates significantly from Λ -CDM is the cluster temperature function (or more generally, number counts) due to the increased abundance of clusters for masses $M \gtrsim 10^{14} h^{-1} M_{\odot}$.

The paper is arranged as follows. In Sec. II, we define the K-mouflage models and detail some of their properties for a fluid with pressure coupled to K-mouflage at the background and perturbation levels, working in the Einstein frame. In Sec. III, we reformulate the dynamics in terms of the Jordan-frame quantities. In Sec. IV, we present our numerical results for the background and the growth of

structure for two K-mouflage models: the cubic and arctan models. In Sec. V, we turn to galaxy clusters and their properties, focusing on the physics of the gas embedded in the clusters. In Sec. VI, we discuss in details the similarity and differences between the K-mouflage scenarios and other modified-gravity theories. We conclude in Sec. VII.

A derivation of the equations of motion in the Einstein frame is given in Appendix A, while details on the Einstein–Jordan connection can be found in Appendix B. We discuss unitarity constraints in Appendix C.

II. DEFINITION OF K-MOUFFLAGE MODELS

A. Jordan-frame and Einstein-frame metrics

We consider scalar-field models where the action has the form [1,2]

$$S = \int d^4x \sqrt{-\tilde{g}} \left[\frac{\tilde{M}_{\text{Pl}}^2}{2} \tilde{R} + \tilde{\mathcal{L}}_\varphi(\varphi) \right] + \int d^4x \sqrt{-g} \mathcal{L}_m(\psi_m^{(i)}, g_{\mu\nu}), \quad (1)$$

which involves two metrics, the Jordan-frame metric $g_{\mu\nu}$, with determinant g , and the Einstein-frame metric $\tilde{g}_{\mu\nu}$, with determinant \tilde{g} . The matter Lagrangian density, \mathcal{L}_m , where $\psi_m^{(i)}$ are various matter fields, is given in the Jordan frame, where it takes the usual form without explicit coupling to the scalar field (although one could add explicit couplings to build more complex models). The gravitational sector is described by the usual Einstein–Hilbert action, but in terms of the Einstein-frame metric $\tilde{g}_{\mu\nu}$ and the associated reduced Planck mass $\tilde{M}_{\text{Pl}} = 1/\sqrt{8\pi\tilde{\mathcal{G}}}$. The Lagrangian density $\tilde{\mathcal{L}}_\varphi(\varphi)$ of the scalar field is also given in the Einstein frame.

Throughout this paper, we denote Einstein-frame quantities with a tilde, to distinguish them from their Jordan-frame counterparts (when they are not identical). We choose this notation, which is the opposite to the one used in our previous papers [7,8,11,12] where we mostly worked in the Einstein frame, as here we mostly work in the Jordan frame.

If the two metrics were identical, this model would be a simple quintessence scenario [14,15], with an additional scalar field to the usual matter and radiation components but with standard electrodynamics and gravity (General Relativity). In this paper, we consider modified-gravity models where the two metrics are related by the conformal transformation [16]

$$g_{\mu\nu} = A^2(\varphi)\tilde{g}_{\mu\nu}. \quad (2)$$

This gives rise to an explicit coupling between matter and the scalar field. In the Einstein frame, we recover General Relativity (e.g., the Friedmann equations), but the equations of motion of matter are nonstandard (e.g., the

continuity equation shows a source term, and matter density is not conserved). In the Jordan frame, the equations of motion of matter take the usual form (e.g., matter density is conserved), but gravity is modified (e.g., the Friedmann equations are modified). In this paper, we compute the properties of astrophysical objects such as clusters of galaxies, including their temperature and x-ray luminosity, and it is more convenient to work in the Jordan frame. Then, radiative processes, such as bremsstrahlung, are given by the standard results and do not vary with time or space. Moreover, matter density is conserved. This simplifies the analysis, as the only difference from a Λ -CDM scenario will be a change of gravity laws, which can be explicitly derived from the action (1).

The conformal transformation (2) actually means that the line elements are transformed as $ds^2 = A^2 d\tilde{s}^2$. Using conformal time τ and comoving coordinates \mathbf{x} , this local change of distance can be absorbed in the scale factor for the background universe as

$$ds^2 = a^2(-d\tau^2 + d\mathbf{x}^2), \quad d\tilde{s}^2 = \tilde{a}^2(-d\tau^2 + d\mathbf{x}^2), \quad (3)$$

with

$$a = \bar{A} \tilde{a}, \quad \tau = \tilde{\tau}, \quad \mathbf{x} = \tilde{\mathbf{x}}. \quad (4)$$

[Throughout this paper, we denote with an overbar mean background quantities, such as $\bar{A} = A(\bar{\varphi})$.] However, physical time t and distances \mathbf{r} , with $ds^2 = -dt^2 + d\mathbf{r}^2$, are changed as

$$dt = \bar{A} d\tilde{t}, \quad \mathbf{r} = a\mathbf{x} = \bar{A} \tilde{\mathbf{r}}. \quad (5)$$

In particular, the cosmic times t and \tilde{t} are not the same in both frames.

B. K-mouflage kinetic function

In this paper, we consider K-mouflage models [1,2,7], which correspond to cases where the scalar-field Lagrangian has a nonstandard kinetic term,

$$\tilde{\mathcal{L}}_\varphi(\varphi) = \mathcal{M}^4 K(\tilde{\chi}) \quad \text{with} \quad \tilde{\chi} = -\frac{1}{2\mathcal{M}^4} \tilde{\nabla}^\mu \varphi \tilde{\nabla}_\mu \varphi. \quad (6)$$

Throughout this paper, $\tilde{\nabla}_\mu(\nabla_\mu)$ is the covariant derivative associated with the metric $\tilde{g}_{\mu\nu}(g_{\mu\nu})$ (hence, $\chi = A^{-2}\tilde{\chi}$, but we work with $\tilde{\chi}$ in the following). Here, \mathcal{M}^4 is an energy scale that is of the order of the current dark-energy density (i.e., set by the cosmological constant) to recover the late-time accelerated expansion of the Universe. Thus, the canonical cosmological behavior, with a cosmological constant $\tilde{\rho}_\Lambda = \mathcal{M}^4$, is recovered at late time in the weak- $\tilde{\chi}$ limit if we have

$$\tilde{\chi} \rightarrow 0: K(\tilde{\chi}) \simeq -1 + \tilde{\chi} + \dots, \quad (7)$$

where the dots stand for higher-order terms, the zeroth-order factor -1 corresponding to the late-time cosmological constant \mathcal{M}^4 . The normalization of the first two terms in Eq. (7) defines the normalizations of the constant \mathcal{M}^4 and of the field φ , and hence it does not entail any loss of generality (within this class of models). We only consider models that satisfy this low- $\tilde{\chi}$ expansion in this article, and where $\tilde{\chi} \rightarrow \infty$ for $\tilde{t} \rightarrow 0$ and $\tilde{\chi} \rightarrow 0$ for $\tilde{t} \rightarrow \infty$.

Well-behaved K-mouflage scenarios have $K' > 0$, where we denote $K' = dK/d\tilde{\chi}$, and $W_{\pm}(y) = yK'(\pm y^2/2)$ must be monotonically increasing functions up to $+\infty$ over $y \geq 0$. This ensures that the cosmological dynamics are well defined up to arbitrarily high redshift, where the matter density becomes increasingly large, and that small-scale static solutions exist for any matter density profile [11]. Moreover, there are no ghosts around the cosmological background nor small-scale instabilities [7].

We must point out that the kinetic functions $K(\tilde{\chi})$ that we use for numerical computations and illustrative purposes in this paper are defined by fully nonlinear expressions, namely Eqs. (71) and (74) below, and as such go beyond the low- $\tilde{\chi}$ expansion (7). As explained above, the latter expansion is very general and holds for well-behaved models, where $K' > 0$ for all $\tilde{\chi}$ and $W_{\pm}(y) = yK'(\pm y^2/2)$ are monotonically increasing functions of y . The expansion (7) would only be violated if K' diverges at low $\tilde{\chi}$, e.g., $K(\tilde{\chi}) = -1 + \tilde{\chi}^{3/4} + \dots$, but we do not consider such singular cases here.

Then, it happens that at low redshifts, in the dark-energy era, $\tilde{\chi}$ [with its normalization defined by the first two coefficients in the expansion (7)] is small on cosmological scales, which implies $K' \approx 1$. This holds both for the homogeneous background and for the cosmological large-scale structures. This property is related to the fact that at low redshifts, in the dark-energy era, we require the cosmological evolution to remain close to the Λ -CDM behavior. From the expressions (17), we can see that this implies $\tilde{\chi}\bar{K}' \ll \bar{K}$ (to recover a dark-energy equation of state $\bar{p}_{\text{de}} \approx -\bar{\rho}_{\text{de}}$) whence $\tilde{\chi} \ll 1$. In fact, at low z , we have the scaling $\tilde{\chi} \sim \beta^2$, where β is the coupling strength defined in Eq. (9) below, so that $\tilde{\chi} \sim 0.01$ as we take $\beta = 0.1$. We shall check this behavior in Fig. 4 below.

We shall also check in Sec. VB and Fig. 13 below that this also applies to clusters of galaxies at low redshifts, which are not screened by the nonlinearities of the scalar-field Lagrangian, in spite of their large mass. This would not be the case for a coupling $\beta \gg 0.1$, but this would violate some Solar System and cosmological constraints, and we do not consider such models here.

Nevertheless, the nonlinearities of the kinetic function $K(\tilde{\chi})$ come into play at high redshift and are taken into account in our computations, using the explicit nonlinear examples (71) and (74). This ensures in particular that the dark-energy density becomes subdominant at high z and that we recover the Einstein–de Sitter cosmology in the

early matter era [7]. Moreover, the background solution can be shown to be stable and is a tracker solution [7]. The nonlinearities on the far negative semiaxis, $-\tilde{\chi} \gg 1$, also play a critical role to ensure that Solar System tests of gravity are satisfied by the K-mouflage model, but we do not consider this regime in this paper.

Although K-mouflage theories involve high-order derivative interactions, they do not suffer from quantum-mechanical problems such unitarity violation in their interaction with matter [17,18], as explained in Appendix C.

C. K-mouflage coupling function

The coupling function $A(\varphi)$ has the low- φ expansion

$$A(\varphi) = 1 + \frac{\beta\varphi}{\tilde{M}_{\text{Pl}}} + \dots, \quad (8)$$

where the dots stand for higher-order terms. The normalization of the first term does not entail any loss of generality and only corresponds to a normalization of coordinates. At early times, $\tilde{t} \rightarrow 0$, we have $\tilde{\varphi} \rightarrow 0$ and $g_{\mu\nu} \rightarrow \tilde{g}_{\mu\nu}$. More generally, we define the coupling β as

$$\beta(\varphi) = \tilde{M}_{\text{Pl}} \frac{d \ln A}{d\varphi}. \quad (9)$$

It is constant for exponential coupling functions, $A(\varphi) = \exp[\beta\varphi/\tilde{M}_{\text{Pl}}]$. Without loss of generality, we take $\beta > 0$ (which simply defines the sign of the scalar field φ).

Cosmological and Solar System constraints imply $\beta \lesssim 0.1$; see Ref. [12]. Moreover, we have the scaling $|\beta\tilde{\varphi}/\tilde{M}_{\text{Pl}}| \sim \beta^2 \ll 1$, see Ref. [7], as we shall check in Fig. 4 below (see also Ref. [9]). Therefore, in realistic models, we have $|\bar{A} - 1| \lesssim 0.1$, and the higher-order terms in the expansion (8) only have a small quantitative impact. We shall also check in Fig. 13 below that the fluctuations of the scalar field are small, $|\varphi - \tilde{\varphi}| \ll |\tilde{\varphi}|$, so that the coupling function $A(\varphi)$ remains dominated by the low-order terms of the expansion (8) in clusters of galaxies (and at smaller scales). This can be readily understood from the fact that realistic models should have a fifth force that is not greater than the standard Newtonian force. This typically implies $|\delta A/A| \lesssim |\Psi_{\text{N}}|$, where Ψ_{N} is the Newtonian potential, whence $|\beta\delta\varphi/\tilde{M}_{\text{Pl}}| \lesssim 10^{-5}$.

D. Equations of motion in the Einstein frame

Observable effects, such as lensing or two point correlations that can be measured, are independent of the choice of frame, so that we can work in either the Einstein or the Jordan frame. As explained in the Introduction, for our purposes, the Jordan frame is more convenient and more transparent. Indeed, in this frame, both the matter and radiation components obey their usual equations of motion; e.g., the matter energy-momentum tensor satisfies

$\nabla_\mu T_\nu^\mu = 0$ so that the matter density obeys the usual conservation equation. Moreover, particle masses and atomic emission or absorption lines do not evolve with the cosmic time (whereas they do in the Einstein frame). Then, the only effect of the scalar field is to change the gravitational sector, that is, the Friedmann equations that determine the background cosmological expansion rate and the relation between the metric gravitational potentials and the matter density fluctuations (i.e., it leads to modified Poisson equations that can be interpreted as a fifth force).

Therefore, in this article, we work in the Jordan frame and compute observable effects, in particular the properties of clusters of galaxies, in this frame. However, to simplify the derivation of the equations of motion, it is convenient to first derive the Friedmann equations and the equations that govern the growth of cosmological large-scale structures in the Einstein frame, where gravity takes the standard form. In a second step, we will use these results to obtain the equations of motion in the Jordan frame through a change of variables, in Sec. III. Afterward, all our computations will remain in the Jordan frame.

Thus, we describe in Appendix A the derivation of the equations of motion of the scalar field and of the matter component in the Einstein frame, for a cosmological fluid with a nonzero pressure. In this section, we only give the main results, which will be needed to obtain the equations of motion in the Jordan frame in Sec. III.

We consider three components of the energy density of the Universe, a matter fluid with nonzero pressure, radiation, and the scalar field. The Einstein-frame and Jordan-frame matter energy-momentum tensors are given by

$$\tilde{T}_{\mu\nu} = \frac{-2}{\sqrt{-\tilde{g}}} \frac{\delta S_m}{\delta \tilde{g}^{\mu\nu}}, \quad T_{\mu\nu} = \frac{-2}{\sqrt{-g}} \frac{\delta S_m}{\delta g^{\mu\nu}}, \quad (10)$$

where we dropped the subscript ‘‘m.’’ The conformal transformation (2) gives

$$T_{\mu\nu} = A^{-2} \tilde{T}_{\mu\nu}, \quad T_\nu^\mu = A^{-4} \tilde{T}_\nu^\mu, \quad T^{\mu\nu} = A^{-6} \tilde{T}^{\mu\nu}, \quad (11)$$

where we use $g^{\mu\nu}(\tilde{g}^{\mu\nu})$ to raise indices in $T(\tilde{T})$ and the relation $g^{\mu\nu} = A^{-2} \tilde{g}^{\mu\nu}$. In particular, the Einstein-frame and Jordan-frame densities and pressures are related by

$$\tilde{\rho} = A^4 \rho, \quad \tilde{p} = A^4 p. \quad (12)$$

We work in the nonrelativistic limit, $v^2 \ll 1$, where v is the mean fluid peculiar velocity, and in the weak field regime, $\tilde{\Psi}_N \ll 1$, where $\tilde{\Psi}_N$ is the Newtonian gravitational potential. Moreover, assuming the usual cold dark matter scenario for the dark matter, the matter pressure \tilde{p} is negligible on cosmological scales, and it arises from the small-scale nonlinear processes, such as the collapse of gas clouds which generate shocks or the virialization of of

dark matter halos (which generate an effective pressure through the velocity dispersion of the matter particles). Then, $\tilde{p} \sim \tilde{\rho} c_s^2$, where c_s is the speed of sound or the velocity dispersion, and $c_s^2 \sim \tilde{\Psi}_N$ because it is generated by the gravitational collapse (as in hydrostatic equilibrium where pressure gradients balance the gravitational force). In addition, we consider the small-scale (subhorizon) limit, $k/\tilde{a}\tilde{H} \gg 1$, where spatial gradients dominate over time derivatives and quasistatic approximations apply. Thus, we focus on the regime defined by

$$v^2 \ll 1, \quad \tilde{\Psi}_N \ll 1, \quad \frac{\tilde{p}}{\tilde{\rho}} \sim c_s^2 \sim \tilde{\Psi}_N \ll 1, \quad \frac{k}{\tilde{a}\tilde{H}} \gg 1. \quad (13)$$

As the background level, the matter background pressure is zero, $\tilde{p} = 0$, and the Einstein-frame Friedmann equations read as

$$3\tilde{M}_{\text{Pl}}^2 \tilde{H}^2 = \tilde{\rho} + \tilde{\rho}_{(r)} + \tilde{\rho}_\phi, \quad (14)$$

$$-2\tilde{M}_{\text{Pl}}^2 \frac{d\tilde{H}}{d\tilde{t}} = \tilde{\rho} + \tilde{\rho}_{(r)} + \tilde{p}_{(r)} + \tilde{\rho}_\phi + \tilde{p}_\phi, \quad (15)$$

where $\tilde{\rho}$, $\tilde{\rho}_{(r)}$ and $\tilde{p}_{(r)} = \tilde{\rho}_{(r)}/3$ are the background matter and radiation densities and pressure, which evolve as

$$\frac{d\tilde{\rho}}{d\tilde{t}} = -3\tilde{H}\tilde{\rho} + \tilde{\rho} \frac{d \ln \tilde{A}}{d\tilde{t}}, \quad \frac{d\tilde{\rho}_{(r)}}{d\tilde{t}} = -4\tilde{H}\tilde{\rho}_{(r)}, \quad (16)$$

while $\tilde{\rho}_\phi$ and \tilde{p}_ϕ are the background scalar-field density and pressure, given by

$$\tilde{\rho}_\phi = \mathcal{M}^4 (2\tilde{\chi}\tilde{K}' - \tilde{K}), \quad \tilde{p}_\phi = \mathcal{M}^4 \tilde{K}, \quad (17)$$

with

$$\tilde{\chi} = \frac{1}{2\mathcal{M}^4} \left(\frac{d\tilde{\varphi}}{d\tilde{t}} \right)^2. \quad (18)$$

(Throughout this paper, we consider a flat universe with zero background curvature.) The background scalar field obeys the Klein–Gordon equation

$$\frac{d}{d\tilde{t}} \left[\tilde{a}^3 \frac{d\tilde{\varphi}}{d\tilde{t}} \tilde{K}' \right] = -\tilde{a}^3 \tilde{\rho} \frac{d \ln \tilde{A}}{d\tilde{\varphi}}. \quad (19)$$

For the matter perturbations, the continuity and Euler equations are written as

$$\frac{\partial \tilde{\rho}}{\partial \tau} + \nabla \cdot (\tilde{\rho} \mathbf{v}) + 3\tilde{\mathcal{H}}\tilde{\rho} = \tilde{\rho} \frac{d \ln \tilde{A}}{d\tau}, \quad (20)$$

$$\begin{aligned} \frac{\partial \mathbf{v}}{\partial \tau} + (\mathbf{v} \cdot \nabla) \mathbf{v} + \left(\tilde{\mathcal{H}} + \frac{d \ln \bar{A}}{d\tau} \right) \mathbf{v} \\ = -\nabla(\tilde{\Psi}_N + \ln A) - \frac{\nabla \tilde{\rho}}{\tilde{\rho}}, \end{aligned} \quad (21)$$

where the Einstein-frame Newtonian potential is given by the Poisson equation

$$\frac{1}{\bar{a}^2} \nabla^2 \tilde{\Psi}_N = \frac{1}{2\tilde{M}_{\text{Pl}}^2} \delta \tilde{\rho}. \quad (22)$$

In the small-scale (quasistatic) limit, the Klein–Gordon equation for the scalar field becomes

$$\frac{1}{\bar{a}^2} \nabla \cdot (\nabla \varphi \bar{K}') = \frac{d \ln \bar{A}}{d\bar{\varphi}} \delta \tilde{\rho}. \quad (23)$$

Here we also used the fact that the fluctuations of φ can be neglected in the factor \bar{K}' , so that the Klein–Gordon equation can actually be linearized in the scalar field, while keeping the matter density fluctuations nonlinear. See Ref. [8] for a detailed discussion and an explicit computation of the matter power spectrum, up to one-loop order, that includes up to the cubic term in φ in Eq. (23), which is checked to make no quantitative difference for cosmological large-scale structures of cluster sizes and beyond. This corresponds to the fact that clusters are not screened by the nonlinear K-mouflage mechanism, which comes into play at much smaller scales and higher densities, as in the Solar System.

III. EQUATIONS OF MOTION IN THE JORDAN FRAME

We now derive the equations of motion of the scalar field and of the matter component in the Jordan frame. To do so, we use the results obtained in Sec. IID in the Einstein frame and express these equations in terms of Jordan-frame variables.

A. Background dynamics

The Jordan-frame metric $g_{\mu\nu}$ is related to the Einstein-frame metric $\tilde{g}_{\mu\nu}$ by the conformal transformation (2). As seen in Eqs. (3)–(5), this leads to a rescaling of the scale factor and of physical time and distance, while the conformal coordinates are unchanged. The Hubble expansion rates, $H = d \ln a / dt$ and $\tilde{H} = d \ln \tilde{a} / d\tilde{t}$, are also different and related by

$$H = \frac{\tilde{H}(1 + \tilde{\epsilon}_2)}{\bar{A}} = \frac{\tilde{H}}{\bar{A}(1 - \epsilon_2)}, \quad (24)$$

where $\tilde{\epsilon}_2(t)$ was defined in Eq. (A45) and verifies $d \ln \bar{A} / d\tilde{t} = \tilde{\epsilon}_2 \tilde{H}$, and we introduced its Jordan-frame counterpart,

$$\epsilon_2(t) = \frac{d \ln \bar{A}}{d \ln a}, \quad e_2 = \frac{\tilde{\epsilon}_2}{1 + \tilde{\epsilon}_2}, \quad \tilde{\epsilon}_2 = \frac{\epsilon_2}{1 - \epsilon_2}. \quad (25)$$

The Einstein-frame and Jordan-frame densities and pressures are related as in Eq. (12), so that the Friedman equation (14) gives

$$3M_{\text{Pl}}^2 H^2 = (1 - \epsilon_2)^{-2} (\bar{\rho} + \bar{\rho}_{(r)} + \bar{\rho}_{\varphi}), \quad (26)$$

where we introduced the Jordan-frame reduced Planck mass,

$$M_{\text{Pl}}^2(t) = \tilde{M}_{\text{Pl}}^2 / \bar{A}(t)^2. \quad (27)$$

Thus, in the Jordan frame, Newton’s constant, $\mathcal{G} = 1/8\pi M_{\text{Pl}}^2$, varies with time, as $\mathcal{G}(t) = \tilde{\mathcal{G}} \bar{A}^2 \propto \bar{A}^2$. Equation (26) shows how the Friedmann equation is modified in the Jordan frame, as compared with the usual General Relativity result, because the gravitational Einstein–Hilbert action is defined in terms of the auxiliary metric $\tilde{g}_{\mu\nu}$. Substituting for $g_{\mu\nu}$, this effectively corresponds to a change of the Einstein–Hilbert action. At the background level, this simply introduces the time-dependent functions $\bar{A}(t)$ and $\epsilon_2(t)$ in Eq. (26).

We can also write Eq. (26) in the standard form (albeit with a time-dependent reduced Planck mass) as

$$3M_{\text{Pl}}^2 H^2 = \bar{\rho} + \bar{\rho}_{(r)} + \bar{\rho}_{\text{de}}, \quad (28)$$

by defining the dark-energy component as the energy density that is “missing” in the Friedmann equation to match the Hubble rate, after we sum over the other matter and radiation components. This yields

$$\bar{\rho}_{\text{de}} \equiv \bar{\rho}_{\varphi} + \frac{2\epsilon_2 - \epsilon_2^2}{(1 - \epsilon_2)^2} (\bar{\rho} + \bar{\rho}_{(r)} + \bar{\rho}_{\varphi}). \quad (29)$$

This interpretation corresponds to the case where measurements of the Hubble rate and of the matter and radiation densities are performed in the Jordan frame, and the remaining part, which explains the accelerated expansion, is ascribed to the dark-energy component [as in the usual Λ -CDM case, where the background dark energy is also measured from the missing energy density that is required to account for $H(z)$]. This is a natural configuration, as $a(t)$ and $H(t)$ are obtained from redshift measurements of standard candles, which assumes that atomic absorption and emission lines are the same at distant redshifts as in the laboratory. By definition, this is the case in the Jordan frame but not in the Einstein frame (where particle masses are actually time dependent). On the other hand, these standard candles must not depend on the local gravity, because in the Jordan frame, Newton’s constant becomes time dependent, so that these candles are no longer standard (i.e., similar to those at $z = 0$). This rules out supernovae

(which involve both local gravity and electrodynamics, within the star) but allows one to use geometric candles such as baryon acoustic oscillations [19,20] or the Alcock–Paczynski test [21].

Using Eq. (16), the matter and radiation densities now evolve as

$$\frac{d\bar{\rho}}{dt} = -3H\bar{\rho}, \quad \frac{d\bar{\rho}_{(r)}}{dt} = -4H\bar{\rho}_{(r)}. \quad (30)$$

Thus, we recover the usual conservation equations for matter and radiation in the Jordan frame, whence comes

$$\bar{\rho}(t) = \frac{\bar{\rho}_0}{a^3}, \quad \bar{\rho}_{(r)}(t) = \frac{\bar{\rho}_{(r)}}{a^4}, \quad \text{with } a_0 = 1, \quad (31)$$

where $\bar{\rho}_0$ are the mean Jordan-frame energy densities today, at $z = 0$, and we normalized the Jordan-frame scale factor by $a_0 = 1$.

From Eq. (A11), with $\tilde{p} = 0$, and Eq. (29), the Jordan-frame dark-energy density evolves as

$$\frac{d\bar{\rho}_{\text{de}}}{dt} = -3H(\bar{\rho}_{\text{de}} + \bar{p}_{\text{de}}), \quad (32)$$

where we defined the Jordan-frame dark-energy pressure as

$$\begin{aligned} \bar{p}_{\text{de}} = & \bar{p}_\varphi + \frac{\epsilon_2}{1-\epsilon_2}(\bar{p}_{(r)} + \bar{p}_\varphi) + \left(\epsilon_2 - \frac{2}{1-\epsilon_2} \frac{d\epsilon_2}{d \ln a} \right) \\ & \times \frac{\bar{\rho} + \bar{\rho}_{(r)} + \bar{\rho}_\varphi}{3(1-\epsilon_2)^2}. \end{aligned} \quad (33)$$

On the other hand, from Eq. (19), the Klein–Gordon equation reads as

$$\frac{d}{dt} \left[\bar{A}^{-2} a^3 \frac{d\bar{\varphi}}{dt} \bar{K}' \right] = -a^3 \bar{\rho} \frac{d \ln \bar{A}}{d\bar{\varphi}}. \quad (34)$$

This can be integrated as

$$\frac{d\bar{\varphi}}{dt} \bar{K}' = -\bar{A}^2 a^{-3} \int_0^t dt' \frac{\bar{\rho}_0 \beta(t')}{\bar{M}_{\text{Pl}}}, \quad (35)$$

because the integration constant must vanish to recover a realistic early-time cosmology [7].

Finally, we define the Jordan-frame cosmological parameters as

$$\Omega_{\text{m}} = \frac{\bar{\rho}}{\rho_{\text{crit}}}, \quad \Omega_{(r)} = \frac{\bar{\rho}_{(r)}}{\rho_{\text{crit}}}, \quad \Omega_{\text{de}} = \frac{\bar{\rho}_{\text{de}}}{\rho_{\text{crit}}}, \quad (36)$$

where $\rho_{\text{crit}} = 3M_{\text{Pl}}^2 H^2 = \bar{A}^{-4} (1-\epsilon_2)^{-2} \tilde{\rho}_{\text{crit}}$ is the Jordan-frame critical density. This gives

$$\Omega_{\text{m}} = (1-\epsilon_2)^2 \tilde{\Omega}_{\text{m}}, \quad \Omega_{(r)} = (1-\epsilon_2)^2 \tilde{\Omega}_{(r)}, \quad (37)$$

and

$$\Omega_{\text{de}} = \tilde{\Omega}_\varphi + (2\epsilon_2 - \epsilon_2^2)(\tilde{\Omega}_{\text{m}} + \tilde{\Omega}_{(r)}). \quad (38)$$

We can check that $\Omega_{\text{m}} + \Omega_{(r)} + \Omega_{\text{de}} = \tilde{\Omega}_{\text{m}} + \tilde{\Omega}_{(r)} + \tilde{\Omega}_\varphi = 1$. The effective dark-energy equation of state in the Jordan frame is simply defined as

$$w_{\text{de}} = \bar{p}_{\text{de}}/\bar{\rho}_{\text{de}}. \quad (39)$$

B. Perturbations

The dynamics of large-scale perturbations in the Jordan frame are also obtained from the equations derived in the Einstein frame in Sec. IID.

In the Einstein frame, the Newtonian gauge metric (A16) reads as $d\tilde{s}^2 = \tilde{a}^2 [-(1+2\tilde{\Psi}_{\text{N}})d\tau^2 + (1-2\tilde{\Psi}_{\text{N}})d\mathbf{x}^2]$, where we used Eq. (A31). In the Jordan frame, we write

$$ds^2 = a^2 [-(1+2\Phi)d\tau^2 + (1-2\Psi)d\mathbf{x}^2]. \quad (40)$$

Then, using $ds^2 = A^2 d\tilde{s}^2$ and $a = \bar{A} \tilde{a}$, we obtain, up to first order in $\delta A = A - \bar{A}$,

$$\Phi = \Psi_{\text{N}} + \frac{\delta A}{\bar{A}}, \quad \Psi = \Psi_{\text{N}} - \frac{\delta A}{\bar{A}}, \quad (41)$$

where we introduced the Jordan-frame Newtonian potential, given by

$$\frac{1}{a^2} \nabla^2 \Psi_{\text{N}} = \frac{1}{2M_{\text{Pl}}^2} \delta\rho, \quad \text{whence comes } \Psi_{\text{N}} = \tilde{\Psi}_{\text{N}}. \quad (42)$$

The last equality follows from Eqs. (22) and (27). Therefore, in the Jordan frame, the two metric potentials are no longer equal, but their sum remains equal to $2\Psi_{\text{N}}$. This is related to the fact that photons do not feel the effect of the fifth force; see also Eq. (A7). Therefore, weak lensing statistics show the same dependence on the matter density fluctuations as in General Relativity, and the impact of the modified gravity only arises through the different evolution of the density field and the time-dependent Newton constant; see also Sec. V H below.

The Klein–Gordon equation (23) reads as

$$\frac{1}{a^2} \nabla^2 \varphi = \frac{\beta \bar{A}}{\bar{K}' M_{\text{Pl}}} \delta\rho, \quad (43)$$

and, up to first order over $\delta\varphi$, we obtain

$$\frac{\delta A}{\bar{A}} = \frac{\beta}{M_{\text{Pl}} \bar{A}} \delta\varphi, \quad \frac{1}{a^2} \nabla^2 \frac{\delta A}{\bar{A}} = \frac{\beta^2}{M_{\text{Pl}}^2 \bar{K}'} \delta\rho. \quad (44)$$

This also gives

$$\frac{1}{a^2} \nabla^2 \Phi = \frac{1 + \epsilon_1(t)}{2M_{\text{Pl}}^2(t)} \delta\rho \quad \text{and} \quad \Phi = (1 + \epsilon_1) \Psi_N, \quad (45)$$

where ϵ_1 is defined by

$$\epsilon_1(t) = \frac{2\beta^2}{\bar{K}'}, \quad (46)$$

and we recover the same factor as in the first relation (A45).

The continuity equation (20) and the Euler equation (21) become

$$\frac{\partial \rho}{\partial \tau} + \nabla \cdot (\rho \mathbf{v}) + 3\mathcal{H}\rho = 0 \quad (47)$$

and

$$\frac{\partial \mathbf{v}}{\partial \tau} + (\mathbf{v} \cdot \nabla) \mathbf{v} + \mathcal{H} \mathbf{v} = -\nabla \Phi - \frac{\nabla p}{\rho}. \quad (48)$$

Therefore, in contrast with the Einstein frame, in the Jordan frame, the continuity and Euler equations take the same form as in Λ -CDM, and the coupling to the scalar field φ only gives rise to the modified Poisson equation (45), in terms of the formation of large-scale structures. There is no longer a nonconservation term in the continuity equation nor an additional friction term in the Euler equation. However, in contrast with the Einstein frame and the Λ -CDM cosmology, the two gravitational potentials Φ and Ψ that enter the Newtonian gauge metric are now different.

C. Formation of large-scale structures

Introducing the Jordan-frame matter density contrast,

$$\delta = \delta\rho/\bar{\rho}, \quad (49)$$

the continuity equation (47) is also written as

$$\frac{\partial \delta}{\partial \tau} + \nabla \cdot [(1 + \delta) \mathbf{v}] = 0. \quad (50)$$

This is the same equation as (A40), and we have

$$\delta = \hat{\delta} = \tilde{\delta}. \quad (51)$$

Indeed the matter density contrasts in the Einstein frame, whether we consider the density $\tilde{\rho}$ or the ‘‘conserved’’ density $\hat{\rho}$ of Eq. (A13) (in case of zero pressure), and in the Jordan frame are equal within the approximations described in the previous sections.

On perturbative scales, we again set the pressure term to zero, and we introduce the two-component vector

$$\psi \equiv \begin{pmatrix} \psi_1 \\ \psi_2 \end{pmatrix} \equiv \begin{pmatrix} \delta \\ -(\nabla \cdot \mathbf{v})/(da/dt) \end{pmatrix}. \quad (52)$$

Equations (A42) and (A43) become

$$\begin{aligned} \frac{\partial \psi_1}{\partial \ln a} - \psi_2 &= \int d\mathbf{k}_1 d\mathbf{k}_2 \delta_D(\mathbf{k}_1 + \mathbf{k}_2 - \mathbf{k}) \hat{\alpha}(\mathbf{k}_1, \mathbf{k}_2) \\ &\quad \times \psi_2(\mathbf{k}_1) \psi_1(\mathbf{k}_2), \end{aligned} \quad (53)$$

$$\begin{aligned} \frac{\partial \psi_2}{\partial \ln a} - \frac{3}{2} \Omega_m (1 + \epsilon_1) \psi_1 + \left(2 + \frac{1}{H^2} \frac{dH}{dt} \right) \psi_2 \\ = \int d\mathbf{k}_1 d\mathbf{k}_2 \delta_D(\mathbf{k}_1 + \mathbf{k}_2 - \mathbf{k}) \hat{\beta}(\mathbf{k}_1, \mathbf{k}_2) \psi_2(\mathbf{k}_1) \psi_2(\mathbf{k}_2). \end{aligned} \quad (54)$$

We recover the same form as for the Λ -CDM cosmology, except for the factor ϵ_1 that corresponds to a time-dependent amplification of Newton’s gravity, from the modified Poisson equation (45).

On large scales or at early times, we can again linearize the equations of motion, and the evolution equation (A46) for the linear modes becomes

$$\frac{d^2 D}{d(\ln a)^2} + \left(2 + \frac{1}{H^2} \frac{dH}{dt} \right) \frac{dD}{d \ln a} - \frac{3}{2} \Omega_m (1 + \epsilon_1) D = 0. \quad (55)$$

Again, as compared with the Einstein-frame Eq. (A46), we find that the coefficient ϵ_2 has disappeared and the only difference from the Λ -CDM case is the time-dependent amplification of the gravitational term by $(1 + \epsilon_1)$.

As in Galileon models, but in contrast with $f(R)$, dilaton and symmetron models, the linear growing modes remain scale independent as in the Λ -CDM cosmology. This is because we did not include a potential $V(\varphi)$ in the scalar-field Lagrangian (6) and the field is massless. Thus, the amplification of gravity extends up to the Hubble scale and is only damped on galactic and smaller scales by the nonlinear K-mouflage mechanism. See Sec. VI for a discussion and comparison with other modified-gravity theories.

D. Spherical collapse dynamics

As can be derived from Eq. (48), on large scales where the pressure is negligible, the particle trajectories $\mathbf{r}(t)$ read as

$$\frac{d^2 \mathbf{r}}{dt^2} - \frac{1}{a} \frac{d^2 a}{dt^2} \mathbf{r} = -\nabla_{\mathbf{r}} \Phi, \quad (56)$$

where $\mathbf{r} = a\mathbf{x}$ is the physical coordinate and $\nabla_{\mathbf{r}} = \nabla/a$ the gradient operator in physical coordinates. To study the spherical collapse before shell crossing, it is convenient to label each shell by its Lagrangian radius q or enclosed mass M and to introduce its normalized radius $y(t)$ by

$$y(t) = \frac{r(t)}{a(t)q} \quad \text{with} \quad q = \left(\frac{3M}{4\pi\bar{\rho}_0} \right)^{1/3}, \quad y(t=0) = 1. \quad (57)$$

In particular, the matter density contrast within radius $r(t)$ reads as

$$1 + \delta(< r) = y(t)^{-3}. \quad (58)$$

Since the Poisson equation (46) is only modified by the time-dependent prefactor $1 + \epsilon_1(t)$ and the time dependence of Newton's constant, for a spherical system, the gravitational force is still set by the total mass within radius r ,

$$\frac{d\Phi}{dr} = (1 + \epsilon_1) \frac{\mathcal{G}\delta M}{r^2}, \quad (59)$$

where $\delta M = 4\pi\delta(< r)\bar{\rho}r^3/3$. Then, Eq. (56) gives for the evolution of the normalized radius y , or density contrast $\delta(< r) = y^{-3} - 1$,

$$\frac{d^2y}{d(\ln a)^2} + \left(2 + \frac{1}{H^2} \frac{dH}{dt} \right) \frac{dy}{d \ln a} + \frac{\Omega_m}{2} (1 + \epsilon_1)(y^{-3} - 1)y = 0. \quad (60)$$

Again, as in the Λ -CDM cosmology but in contrast with $f(R)$, dilaton and symmetron models, the spherical collapse is scale invariant so that the dynamics of different mass shells decouple. This applies to the unscreened regime, from clusters of galaxies up to the Hubble radius.

E. Halo mass function

As usual, we can write the halo mass function $n(M)dM/M$ as

$$n(M) \frac{dM}{M} = \frac{\bar{\rho}_0}{M} f(\nu) \frac{d\nu}{\nu}, \quad \text{with} \quad \nu = \frac{\delta_L}{\sigma(M)}, \quad (61)$$

where we used the fact that the linear growing modes are scale independent [so that $\delta_L/\sigma(M) = \delta_{Li}/\sigma_i(M)$, where the subscript ‘‘i’’ refers to the high redshift z_i where the Gaussian initial conditions are defined, far before the dark-energy era]. Here $\sigma(M)$ is the root mean square of the linear density contrast at scale M , and δ_L is the linear density contrast associated with the nonlinear density threshold Δ_m that defines the virialized halos. The mapping $\delta_L \rightarrow \delta$ is obtained by solving the spherical collapse dynamics (60), with the initial condition $y_i = 1 - \delta_{Li}/3$ at a very high redshift z_i . Inverting this relation gives the linear density threshold δ_L that is associated with a given nonlinear density threshold $\delta = \Delta_m$, where the subscript m denotes that $\delta = y^{-3} - 1$ is the density contrast with respect to the mean density of the Universe.

The scaling variable ν directly measures the probability of density fluctuations in the Gaussian initial conditions. Then, we take for the scaling function $f(\nu)$ the fit to Λ -CDM simulations obtained in Ref. [22], which obeys the exponential tail $f(\nu) \sim e^{-\nu^2/2}$ at large ν . This means that the mass function (61) shows the correct large-mass tail, which is set by the Gaussian initial conditions.

F. Planck masses

It is interesting to note that, depending on the physical process that is considered, one can define several effective Planck masses. In other words, if we assume General Relativity and measure the reduced Planck mass or Newton's constant from different sets of observations, we would obtain different values. This could be used as a signature of the modified-gravity theory.

From Eq. (26), the effective Planck mass that would be read from the Friedmann equation, at the background level, is

$$M_{\text{Pl(Friedmann)}}^2(t) = \frac{\tilde{M}_{\text{Pl}}^2(1 - \epsilon_2(t))^2}{\tilde{A}^2(t)}. \quad (62)$$

On the other hand, with respect to large-scale density fluctuations in the cosmological unscreened regime, where the Klein–Gordon equation can be linearized over the scalar field, the effective Planck mass that would be read from the modified Poisson equation (45) is

$$M_{\text{Pl(unscreened)}}^2(t) = \frac{\tilde{M}_{\text{Pl}}^2}{\tilde{A}^2(t)(1 + \epsilon_1(t))}. \quad (63)$$

On small astrophysical scales, within the highly nonlinear screened regime, the effective Planck mass is instead the one defined in Eq. (27),

$$M_{\text{Pl(screened)}}^2(t) = \frac{\tilde{M}_{\text{Pl}}^2}{\tilde{A}(t)^2}. \quad (64)$$

The difference between these various definitions is a signature of the modification of gravity associated with the scalar-field models (1), as seen from the Jordan frame.

G. Symmetry of large-scale gravitational clustering

On large scales, where we neglect shell crossing and pressure, the dynamics of gravitational clustering is given by Eqs. (50), (48) (with $\tilde{p} = 0$), and (45). It is convenient to define the rescaled velocity and metric potential by

$$\mathbf{v} = \frac{da}{dt} f \mathbf{u}, \quad \Phi = \left(\frac{da}{dt} f \right)^2 \phi, \quad (65)$$

where we introduced the linear growth rate

$$f = \frac{d \ln D_+}{d \ln a}, \quad (66)$$

and to change the time variable from t to $\ln D_+$. Then, the equations of motion are written as

$$\frac{\partial \delta}{\partial \ln D_+} + \nabla \cdot [(1 + \delta)\mathbf{u}] = 0, \quad (67)$$

$$\frac{\partial \mathbf{u}}{\partial \ln D_+} + (\mathbf{u} \cdot \nabla)\mathbf{u} + (\kappa - 1)\mathbf{u} = -\nabla\phi, \quad (68)$$

$$\nabla^2\phi = \kappa\delta, \quad (69)$$

where we introduced the time-dependent factor $\kappa(t)$, defined by

$$\kappa(t) = \frac{4\pi\mathcal{G}\bar{\rho}(1 + \epsilon_1)}{\left(\frac{d \ln D_+}{dt}\right)^2} = \frac{3\Omega_m}{2f^2}(1 + \epsilon_1). \quad (70)$$

Therefore, after the change of time coordinate $t \rightarrow \ln D_+$ and the rescaling (65), the only dependence on cosmology that is left in large-scale gravitational clustering is encapsulated in the function $\kappa(t)$. This remains valid beyond shell crossing, but it breaks down on small scales where baryonic effects become important and introduce new characteristic scales, which cannot be absorbed by the change of variables (65). Nevertheless, on large scales where gravity is the dominant process, this symmetry means that all cosmological scenarios with the same function $\kappa(D_+)$ show the same density and velocity fields $\{\delta, \mathbf{u}\}$. In particular, this means that quintessence models, where only the background dynamics is modified [i.e., the Hubble expansion rate $H(z)$], and modified-gravity models or dark-energy models (with dark-energy fluctuations) that only give rise to a modification of Poisson equation by a time-dependent Newton's constant are equivalent with respect to gravitational clustering, if they show the same function $\kappa(D_+)$. In the context of Λ -CDM cosmology, this property has also been used to derive approximate consistency relations satisfied by the matter correlation functions [valid at the nonlinear level within the approximation where the dependence on cosmology of $\kappa(D_+)$ can be neglected] [23–25].

In the case of the K-mouflage scenarios, this symmetry only holds on large scales (down to cluster scales) where the Klein–Gordon equation can be linearized over φ , as in Eq. (43). On smaller scales (galactic scales and below), higher-order terms over φ become important, and the nonlinear K-mouflage screening mechanism comes into play. Then, the modified Poisson equation no longer takes the linear form (45), and the symmetry (70) breaks down. On even smaller scales, we actually recover General Relativity as $\Phi \approx \Psi_N$, because the fifth force is screened. In hierarchical scenarios, where smaller scales collapse first, larger scales are not very sensitive to the details of the clustering on smaller scales, while small collapsed scales are sensitive to the clustering up to the largest scale that has turned nonlinear. Therefore, we expect the symmetry (70)

to apply to scales that are greater than the transition to the K-mouflage screening regime, and not to smaller scales (even though we recover General Relativity far inside the nonlinear screening regime). Besides, on such small scales, nongravitational baryonic effects come into play (such as active galaxy nuclei (AGN) feedback), and the symmetry no longer holds.

For our purposes in this paper, the formulation (67)–(70) explicitly shows that, from cluster scales up to the Hubble scale, K-mouflage cosmologies belong to the same family as the Λ -CDM and quintessence scenarios, with respect to matter clustering. The equations that govern the gravitational dynamics in these rescaled variables take the same form, except for a time-dependent function $\kappa(D_+)$. However, the shape of this function is similar for realistic scenarios (we shall see in Fig. 5 that ϵ_1 is about 2%). Therefore, we can expect that gravitational clustering shows the same qualitative properties in these cosmologies and only small quantitative deviations. In particular, semianalytical methods should work equally well for all these cosmologies, and phenomenological observations, such as the fact that virialized halos are well described by Navarro–Frenk–White (NFW) profiles [26] in Λ -CDM cosmology, should remain valid in other cases. This justifies our modelization of clusters, described in Sec. V below, where we treat Λ -CDM and K-mouflage cosmologies in the same manner.

IV. NUMERICAL RESULTS FOR LARGE-SCALE STRUCTURES

In this paper, we consider two simple models for $K(\tilde{\chi})$. The first one, which we call the “arctan model” in the following, is defined by

$$K_{\text{arctan}}(\tilde{\chi}) = -1 + \tilde{\chi} + K_*[\tilde{\chi} - \chi_* \arctan(\tilde{\chi}/\chi_*)], \quad (71)$$

with the low- $\tilde{\chi}$ expansion

$$\tilde{\chi} \rightarrow 0: K_{\text{arctan}}(\tilde{\chi}) = -1 + \tilde{\chi} + \frac{K_*\tilde{\chi}^3}{3\chi_*^2} - \frac{K_*\tilde{\chi}^5}{5\chi_*^4} + \dots \quad (72)$$

and the choice of parameters

$$K_* = 10^3, \quad \chi_* = 10^2. \quad (73)$$

This gives a K-mouflage model that is consistent with both Solar System and cosmological constraints (with $\beta = 0.1$). For comparison, we also consider the model used in Refs. [7,8], which we call the “cubic model” in the following, in which $K(\tilde{\chi})$ is a low-order polynomial:

$$K_{\text{cubic}}(\tilde{\chi}) = -1 + \tilde{\chi} + K_0\tilde{\chi}^m \quad (74)$$

and the choice of the parameters

$$m = 3, \quad K_0 = 1. \quad (75)$$

Here Eq. (74) should not be understood as a perturbative expansion around $\tilde{\chi} = 0$. It is rather a simple model that interpolates between the low- $\tilde{\chi}$ behavior (7) and a large- $\tilde{\chi}$ power-law behavior $\propto \tilde{\chi}^m$. The cubic model is consistent with cosmological constraints, but its form at large negative χ , $-\chi \gg 1$, is not consistent with Solar System constraints. Therefore, this is an effective model that applies to the semiaxis $\chi \geq -1$ while the large-negative domain is left unspecified. This is sufficient for our purposes, since the cosmological background and large-scale perturbations correspond to $\chi > 0$ and clusters correspond to $\chi > -1$ (more precisely, $|\chi| \ll 1$).

For both models, we choose an exponential form for the coupling function,

$$A(\varphi) = e^{\beta\varphi/\tilde{M}_{\text{Pl}}}, \quad \text{with } \beta = 0.1. \quad (76)$$

We also consider a reference Λ -CDM model for comparison.

All the cosmological scenarios are normalized to the same background cosmological parameters today, $\{\Omega_{\text{m}0}, \Omega_{(r)0}, \Omega_{\text{de}0}, H_0\}$. In addition, we normalize the Planck mass (27) to the same value $M_{\text{Pl}0}^2$ today, as measured by Solar System experiments. This means that we renormalize the Einstein-frame Planck mass by a factor \tilde{A}_0^2 , where $\tilde{A}_0 = \tilde{A}(z=0)$,

$$M_{\text{Pl}}^2(t) = M_{\text{Pl}0}^2 \frac{\tilde{A}_0^2}{\tilde{A}(t)^2}, \quad \text{whence comes } \tilde{M}_{\text{Pl}}^2 = M_{\text{Pl}0}^2 \tilde{A}_0^2. \quad (77)$$

On the other hand, the matter density power spectrum $P(k)$ is normalized to the same value at high redshift, when dark energy is subdominant and both cosmologies almost coincide. However, these different scenarios do not exactly converge in terms of the background expansion rate at a given matter density, because of the different high-redshift reduced Planck masses. Therefore, the normalization to the same power spectrum for the matter density contrast at high z is somewhat arbitrary, since the K-mouflage and Λ -CDM models do not coincide. Nevertheless, for our purposes, this is a convenient choice as it illustrates how the difference in the gravitational clustering dynamics that appear at low z , because of the fifth force mediated by the scalar field, affect the late-time density field. (For other normalization choices, it would be difficult to distinguish the effects due to the different normalizations at high z , before the dark-energy era and when the fifth force was negligible, and to the late-time dynamics characterized by different growth rates.) This normalization also corresponds to the case where we can measure the density contrast field, i.e., the patterns of large-scale structures (e.g., the scale associated with the nonlinear transition $\sigma^2 = 1$) at high z , independently of accurate measures of the background density and expansion rate. In practice, this normalization ambiguity does not appear because one compares each

cosmological scenario with the data, rather than comparing with a theoretical reference cosmology (in particular, the best fits associated with different theories will typically have slightly different cosmological parameters and expansion rates at both $z = 0$ and $z \rightarrow \infty$).

In the following, we present our results for the choice of cosmological parameters today given by $\Omega_{\text{m}0} = 0.25$, $\Omega_{\text{de}0} = 0.75$, $h = 0.70$, and $\sigma_8 = 0.7$.

A. Background dynamics

We consider the density parameters $\Omega_{\text{m}}(z)$ and $\Omega_{\text{de}}(z)$ in Fig. 1 for the two K-mouflage models defined in Eqs. (71) and (74) and for the reference Λ -CDM universe. Since we normalize the density and dark-energy parameters to be equal to the ones observed today, all models coincide at $z = 0$ in terms of background quantities. The deviations from the Λ -CDM scenario are slightly greater for the arctan model (71) than for the cubic model (74), in agreement with Ref. [12]. This is due to the fact that $K'(\tilde{\chi})$ is slightly smaller in the former case over the range of redshifts of interest, $z \lesssim 6$, and that deviations from the Λ -CDM scenario typically scale as β^2/K' ; see for instance Eq. (46) and Ref. [7].

As for studies performed in the Einstein frame [7] (where the cosmological parameters are normalized by their Einstein-frame values today), we find that the dark-energy density becomes negative (and subdominant) at high redshift. This gives $\Omega_{\text{m}} > 1$ at high z for the two K-mouflage models (71) and (74) (but as in the Λ -CDM case, $\Omega_{\text{m}} \rightarrow 1$ at high redshift).

In Fig. 2, we consider the relative deviation, $H(z)/H_{\Lambda\text{-CDM}}(z) - 1$, of the Hubble rate with respect to the Λ -CDM reference. The deviation is slightly larger for the cubic model (74) at $z \sim 6$, but this is only a transient effect

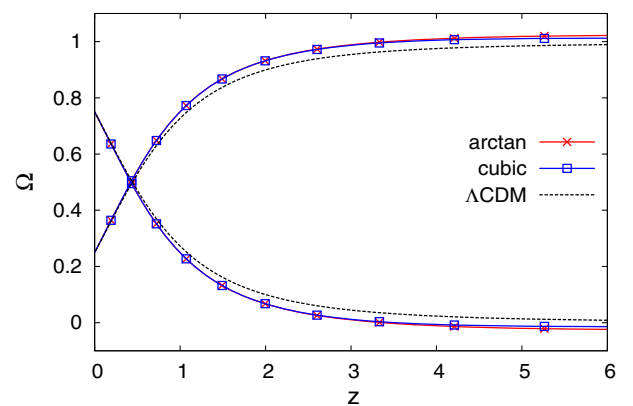


FIG. 1 (color online). Evolution with redshift of the matter and dark-energy cosmological parameters $\Omega_{\text{m}}(z)$ and $\Omega_{\text{de}}(z)$. We display the two K-mouflage models of Eqs. (71) (arctan model, red crosses) and (74) (cubic model, blue squares) and the reference Λ -CDM universe (black dashed lines). The two scalar-field models almost coincide in this figure.

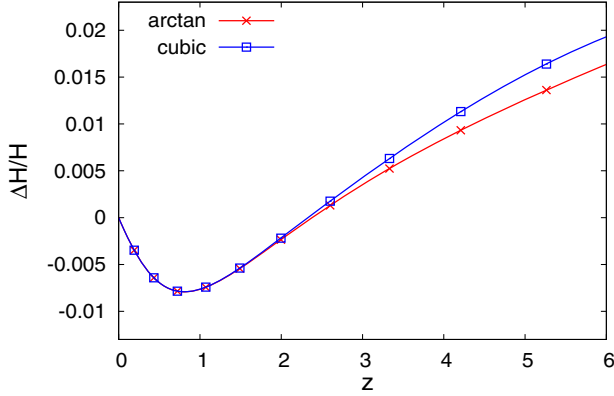


FIG. 2 (color online). Relative deviation of the Hubble expansion rate with respect to the Λ -CDM reference, $\Delta H/H = H/H_{\Lambda\text{-CDM}} - 1$, for the same K-mouflage models as in Fig. 1.

because at $z > 12$ the deviation is slightly greater for the arctan model (71), as expected. At moderate redshifts, the Hubble expansion rates differ by less than 2% between the three cosmologies that we consider here. This amplitude is mostly set by our choice of coupling constant $\beta = 0.1$, because as recalled above, deviations from the Λ -CDM scenario scale as β^2/\bar{K}' and at low z we have $\bar{K}' \approx 1$. Therefore, $\beta = 0.1$ typically leads to percent deviations from the Λ -CDM scenario. This value of β (or lower values) is required to satisfy observational constraints on cosmological and Solar System scales [12], in particular from the expansion rate at the time of big bang nucleosynthesis and from the bounds on the current time derivative of the gravitational coupling \mathcal{G} provided by the Lunar Ranging experiment.

The deviation from the Λ -CDM reference does not vanish at high redshift because the reduced Planck masses are different; see Eq. (77). Indeed, in the K-mouflage models, $M_{\text{pl}}^2(t)$ becomes time dependent, and we choose to normalize all scenarios by their Planck mass today (when Solar System measurements and laboratory experiments are performed). Note that in studies performed in the Einstein frame [7], where the reduced Planck mass is constant, one can recover the Λ -CDM expansion rate at both $z = 0$ and at high redshift. However, this requires normalizing the matter density today by the conserved density $\hat{\rho}$ of Eq. (A13) instead of the Einstein-frame density $\tilde{\rho}$.

In Fig. 3, we display the effective equation of state parameter for the dark energy, $w_{\text{de}} = \bar{p}_{\text{de}}/\bar{\rho}_{\text{de}}$, evaluated using Eqs. (29) and (33) for $\bar{\rho}_{\text{de}}$ and \bar{p}_{de} . For both models, $w_{\text{de}} \rightarrow -1$ at late times, mimicking the presence of a cosmological constant. As in studies performed in the Einstein frame, the effective equation of state parameter is beyond -1 at low z and changes sign at a moderate redshift while going through $\pm\infty$ (this does not correspond to a singularity in terms of the Hubble rate or dark-energy density but to the vanishing and change of sign of $\bar{\rho}_{\text{de}}$).

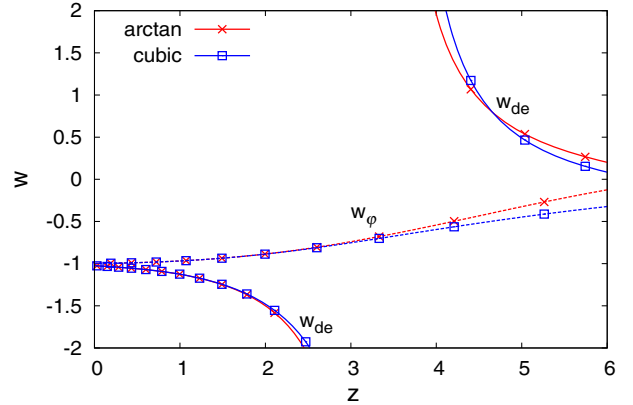


FIG. 3 (color online). Effective equation of state parameters $w_{\text{de}}(z)$ (solid lines with a divergence and change of sign at $z \approx 3$) and $w_{\phi}(z)$ (dashed lines with a smooth behavior), for the same K-mouflage models as in Fig. 1.

We also show in Fig. 3 the equation of state parameter w_{ϕ} defined as

$$w_{\phi} = \frac{\bar{p}_{\phi}}{\bar{\rho}_{\phi}} = \frac{\bar{K}}{2\bar{\chi}\bar{K}' - \bar{K}}, \quad (78)$$

where we used Eq. (17). In contrast to w_{de} , w_{ϕ} remains negative over $z \leq 6$ and shows no divergence. The difference between the behaviors of w_{de} and w_{ϕ} shows the impact of the coupling between the matter and scalar-field components. This makes the dark-energy density and pressure significantly different from the bare scalar-field ones, see Eqs. (29) and (33), and can even make $\bar{\rho}_{\text{de}}$ and $\bar{\rho}_{\phi}$ have different signs.

B. Background scalar field

We show in Fig. 4 the background values $\bar{\varphi}$ and $\bar{\chi}$ of the scalar field and of its kinetic term. The scalar field $\bar{\varphi}$ is negative, and its amplitude grows with redshift (we chose the normalization $\bar{\varphi} = 0$ at high redshift, $z \rightarrow \infty$). We can see that $|\beta\bar{\varphi}/\tilde{M}_{\text{pl}}| \ll 1$ until $z = 0$. Thus, the coupling function $A(\varphi)$ is dominated by its low-order terms in the expansion (8), and choosing for instance $A(\varphi) = (1 + \beta\varphi/n\tilde{M}_{\text{pl}})^n$, with $n > 0$, would give similar results to the exponential choice (76).

The kinetic term $\bar{\chi}$ decreases with time. It goes to infinity at high redshift, $z \rightarrow \infty$, and we can check that at low z it is significantly smaller than unity. Then, the kinetic function $K(\bar{\chi})$ is dominated by its low-order terms in the expansion (7). This explains why the two K-mouflage models converge at low z in the lower panel of Fig. 4.

C. Modified gravitational potentials, gravitational slip and effective Newton's constant

As seen in Sec. III, both for the background quantities and the large-scale perturbative structures, the deviations

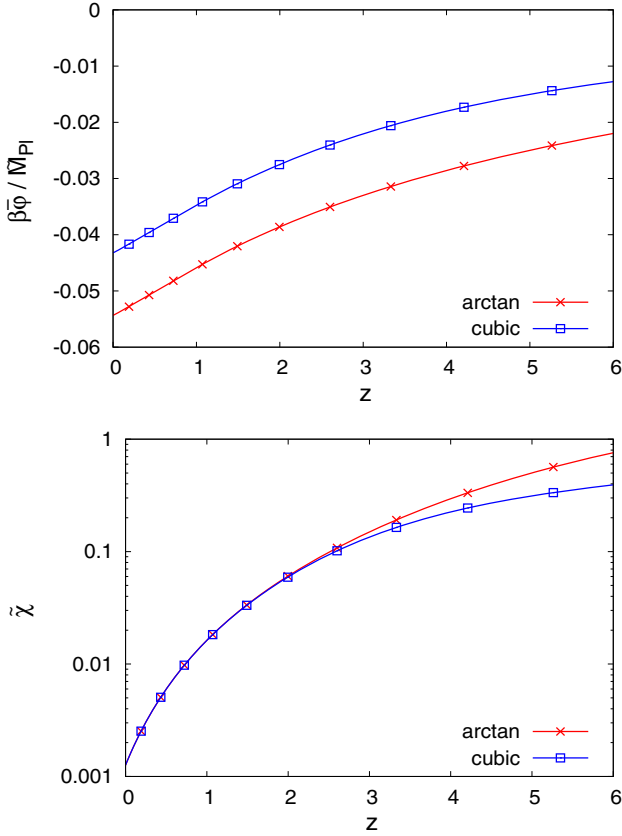


FIG. 4 (color online). *Upper panel:* background scalar field $\bar{\varphi}$ as a function of redshift. *Lower panel:* background kinetic term $\tilde{\chi}$ as a function of redshift.

from the Λ -CDM universe can be measured by the two coefficients $\epsilon_1(t)$ and $\epsilon_2(t)$, defined in Eqs. (46) and (25). In particular, from Eqs. (41) and (44), the two gravitational potentials Φ and Ψ of the Jordan-frame metric (40) read for large-scale unscreened structures as

$$\Phi = (1 + \epsilon_1)\Psi_N, \quad \Psi = (1 - \epsilon_1)\Psi_N, \quad (79)$$

and the normalized gravitational slip is written as

$$\eta \equiv \frac{\Psi - \Phi}{\Psi + \Phi} = -\epsilon_1. \quad (80)$$

We show both coefficients $\epsilon_1(t)$ and $\epsilon_2(t)$ in Fig. 5. We can see that they are of order 2% at low z . Again, as can be seen from Eq. (46), this amplitude is set by our choice $\beta = 0.1$ (to satisfy observational constraints) as $\bar{K}' \approx 1$ at low z and deviations from the Λ -CDM reference then scale as β^2 . This also sets the amplitude of the gravitational slip η . At high z , the coefficients $\epsilon_i(t)$ go to zero, as \bar{K}' goes to infinity and we enter a cosmological nonlinear screening regime that also ensures that the dark-energy component becomes subdominant at early times. This decrease of ϵ_i appears faster for the cubic model, because of its stronger growth of

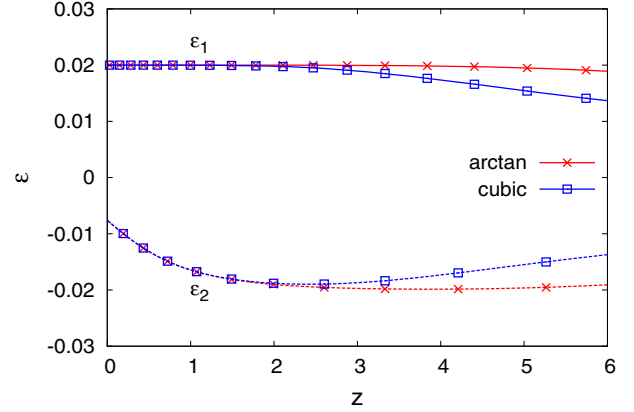


FIG. 5 (color online). Coefficients ϵ_1 and ϵ_2 , defined in Eqs. (46) and (25) for the K-mouflage models, as functions of redshift.

$K'(\chi)$ at large positive χ . As noticed above, this means that departures from the Λ -CDM scenario are greater for the arctan model than for the cubic model (with our choice of parameters).

The Jordan-frame coefficient ϵ_1 is always positive, and the gravitational slip η defined in Eq. (80) is negative. From Eq. (25), the coefficient ϵ_2 also reads as

$$\epsilon_2(t) = \frac{\beta(t)}{\tilde{M}_{\text{Pl}}} \frac{d\bar{\varphi}}{d \ln a} = \frac{\beta(t)}{\tilde{M}_{\text{Pl}} H(t)} \frac{d\bar{\varphi}}{dt}, \quad (81)$$

which is negative from Eq. (35) and of order β^2 / \bar{K}' .

In Fig. 6, we show the evolution with redshift of the effective Newton constant, defined from Eq. (77) as

$$\mathcal{G}(t) = \mathcal{G}_0 \frac{\bar{A}^2(t)}{A_0^2}. \quad (82)$$

Because of the dependence of the effective Newton coupling strength on the background value of the scalar field, \mathcal{G} is a few percent higher at $z \sim 6$ than today.

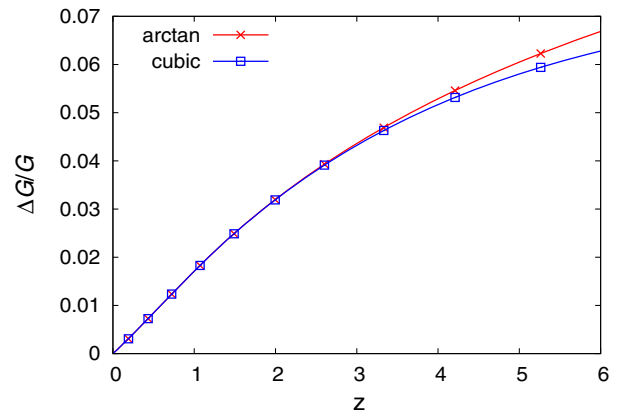


FIG. 6 (color online). Relative drift with redshift of the effective Newton constant for the K-mouflage models.

D. Linear theory

In Fig. 7, we show the relative deviation, $D_+/D_{+\Lambda\text{-CDM}} - 1$, of the linear growing mode, obtained by solving Eq. (55), from the Λ -CDM reference case, and the linear growth rates $f(z)$. Again, the relative deviation of the growing mode is greater for the arctan model (71) than for the cubic model (74), because of the lower value of \bar{K}' over relevant redshifts; see Eq. (46) for the coefficient e_1 that modifies the linear growing mode equation (55). All linear growing modes converge at high redshift, despite the slightly different Planck masses and Hubble expansion rates. Indeed, far in the early matter-dominated era, we recover an Einstein–de Sitter cosmology, and the Hubble term in the parenthesis in Eq. (55) converges to $H^{-2}dH/dt \rightarrow -3/2$. Moreover, the factor e_1 goes to zero because of the nonlinear K-mouflage screening mechanism, see Eq. (46), as at high redshift $\tilde{\chi}$ and \bar{K}' become large. This large- K' behavior is also required to ensure that the background dark-energy density becomes subdominant.

We show the relative deviation of the linear growth rates $f(z)$ in Fig. 8. Overall, $f(z)$ is greater for the K-mouflage scenarios, in agreement with the higher value of the linear growing mode shown in Fig. 7. The deviation is again of the order of a few percent. The deviation for the linear modes D_+ shown in Fig. 7 could reach 10% at $z = 0$ because of the cumulative effect due to the integration over time. The growth rates $f(z)$ converge to unity at high redshift, but we can see that there remains a noticeable difference between the K-mouflage models and the Λ -CDM reference up to $z \sim 6$.

This rather slow decrease of the deviations from the Λ -CDM reference at higher redshift is a characteristic signature of K-mouflage models, as many other modified-gravity models, such as $f(R)$ theories, lead to a faster convergence to the Λ -CDM scenario at $z \gtrsim 2$. This is related to the fact that in the linear subhorizon regime the K-mouflage effects are scale independent, as the factors $e_1(t)$ and $e_2(t)$ only depend on time. In contrast, in $f(R)$

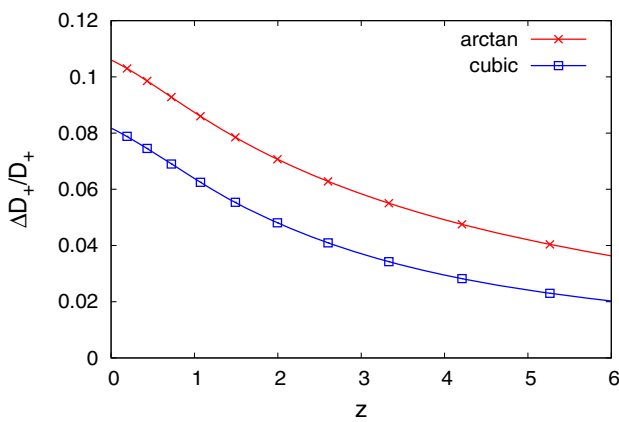


FIG. 7 (color online). Relative deviation, $D_+/D_{+\Lambda\text{-CDM}} - 1$, of the linear growing mode D_+ from the Λ -CDM reference.

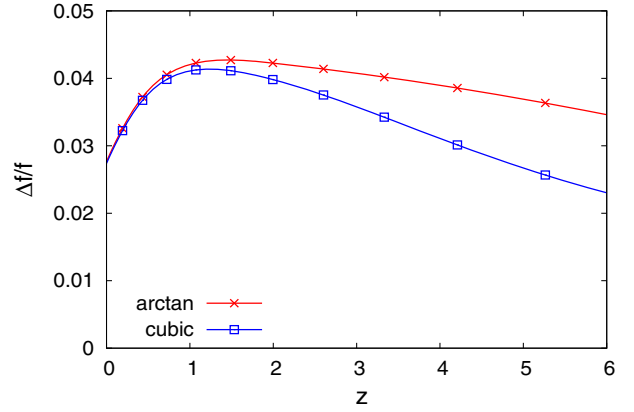


FIG. 8 (color online). Relative deviation, $f/f_{\Lambda\text{-CDM}} - 1$, of the linear growth rate, $f(z) = d \ln D_+ / d \ln a$, from the Λ -CDM reference.

theories or dilaton models, the factor $e(k, t)$ that appears in the modified Euler or Poisson equations, or in the evolution equation for the linear density modes, takes the form $e(k, t) \propto \beta^2 k^2 / (a^2 m^2 + k^2)$, with a characteristic physical scale $2\pi/m$ beyond which the theory converges to General Relativity. At high redshift, this scale typically goes to zero, so that at a fixed physical (or also comoving) scale, deviations from the Λ -CDM scenario vanish because the coupling β decreases or one enters the unmodified regime beyond $2\pi/m$. In the K-mouflage models that we consider in this paper, because there is no such characteristic scale, the convergence to General Relativity is only due to the vanishing of the effective coupling strength β^2/K' , with β being constant (in our case) and K' increasing at high z because of the nonlinear K-mouflage mechanism itself. However, this decrease of β^2/K' at high z is rather slow for generic kinetic functions $K(\chi)$, as seen from the curve obtained for $e_1(t)$ in Fig. 5 for the simple cubic model.

E. Halo mass function

Solving the spherical collapse equation (60), we can compute the linear density contrast threshold $\delta_L(z)$ that corresponds to a nonlinear density contrast of $\delta[\delta_L] = \Delta_m$, where Δ_m is the nonlinear threshold that we choose to define halos. As discussed in Ref. [8], we are not interested in $\delta_L(z)$ at the observation redshift, because it is not an observable quantity. Instead, we wish to evaluate the linear threshold δ_{L_i} , at a given high redshift z_i , that is required to produce at later time z a nonlinear density contrast Δ_m . In other words, we want to estimate the initial density fluctuation associated with a given nonlinear density contrast at the observed redshift. To avoid the introduction of an arbitrary high redshift z_i , following what it is done in Ref. [8] and usual practice, we translate all the initial thresholds δ_{L_i} to redshift z by multiplying them by $D_{+\Lambda\text{-CDM}}(z)/D_{+\Lambda\text{-CDM}}(z_i)$ [instead of using $D_+(z)/D_+(z_i)$, i.e., the linear growing mode associated with each K-mouflage scenario], and we denote

this quantity the linear density contrast threshold $\delta_{L(\Lambda)}$. This common multiplicative factor enables a meaningful comparison between the different scenarios.

In Fig. 9, we display $\delta_{L(\Lambda)}$ when we define halos by a constant density contrast threshold $\Delta_c = 200$ with respect to the critical density ρ_{crit} . This corresponds to a density contrast with respect to the mean density $\bar{\rho}$ of $\Delta_m = \Delta_c / \Omega_m(z)$. We choose a constant Δ_c rather than Δ_m because observational cluster surveys usually define cluster halos by a constant overdensity with respect to the critical density ρ_{crit} . At high redshift, both definitions coincide, as $\Omega_m \rightarrow 1$, while at low redshift or far in the dark energy-dominated era, one can argue that Δ_c makes more physical sense. Indeed, during an exponential acceleration phase, the growth of large-scale structures freezes out, and one obtains isolated halos among increasingly large voids. Then, the mean universe density $\bar{\rho}$ decreases as a^{-3} , following the dilution due to the expansion, and it does not correspond to the typical density of halos (nor voids). In contrast, we can assume that the isolated halos keep a roughly constant physical radius and density, like the critical density ρ_{crit} (in an exponential phase where the Hubble rate is constant), so that it is more meaningful to express halo densities in terms of ρ_{crit} .

Both K-mouflage models accelerate the growth of large-scale structures as compared with the Λ -CDM reference, as seen from the linear growing modes of Fig. 7. Therefore, we find in Fig. 9 that a smaller linear density contrast is required to reach the same nonlinear overdensity of 200 (with respect to the critical density). Again, the deviation from the Λ -CDM prediction is greater for the arctan model (71).

From the linear threshold displayed in Fig. 9, we obtain the halo mass function as in Eq. (61) (note that $\nu = \delta_L / \sigma = \delta_{L(\Lambda)} / \sigma_{(\Lambda)} = \delta_{L_i} / \sigma_i$). In Fig. 10, we show the relative deviation $n(M) / n_{\Lambda\text{-CDM}}(M) - 1$ of the halo

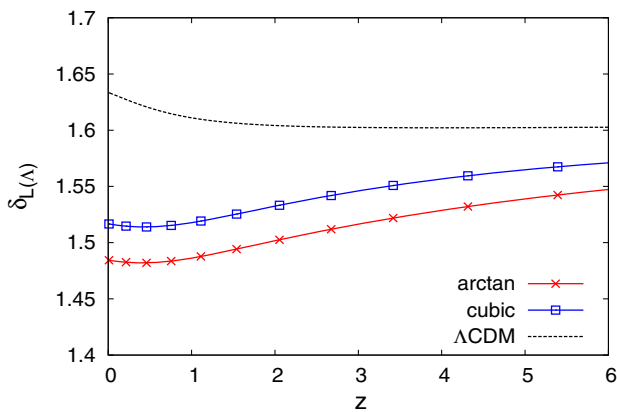


FIG. 9 (color online). Linear density contrast threshold $\delta_{L(\Lambda)}$ associated with the nonlinear density contrast $\Delta_c = 200$ with respect to the critical density ρ_{crit} , for the K-mouflage models and the Λ -CDM reference.

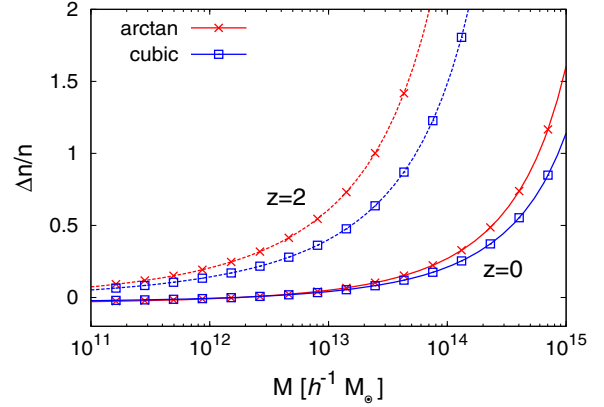


FIG. 10 (color online). Relative deviation, $n(M) / n_{\Lambda\text{-CDM}}(M) - 1$, of the halo mass function of the K-mouflage models from the Λ -CDM reference, at $z = 0$ (solid lines) and $z = 2$ (dashed lines). Halos are defined by the density contrast $\Delta_c = 200$ with respect to the critical density.

mass function from the Λ -CDM reference case, at $z = 0$ and $z = 2$. As for the case of $\delta_{L(\Lambda)}$, since the scalar field enhances gravitational clustering, we find that the mass functions for the two K-mouflage models are higher than the Λ -CDM reference in the high-mass tail, with the greater deviation obtained for the arctan model (71). As usual, the deviation increases at high mass because the exponential falloff amplifies the sensitivity to slight departures of the growth of structures. (The deviation becomes slightly negative at low mass because all mass functions obey the same normalization to unity: there cannot be more matter in halos than the matter content of the universe.)

At fixed mass, $M \sim 10^{14} h^{-1} M_{\odot}$, the deviation from the Λ -CDM reference is greater at $z = 2$ than at $z = 0$, despite the difference in linear density thresholds being lower, as seen in Fig. 9. This is because at fixed mass we are further into the rare high-mass tail, which amplifies the dependence on the linear density threshold and more than compensates the slow convergence between the K-mouflage and Λ -CDM thresholds.

F. Matter density power spectrum and correlation function

We show in Fig. 11 the matter density power spectra and correlation functions at $z = 0$ and $z = 2$. The computation of this power spectrum $P(k)$ combines perturbation theory up to one-loop order with a halo model, as described in Ref. [8] in the case of Einstein-frame studies and following the approach introduced in Ref. [27]. The two-point correlation function $\xi(x)$ is obtained from the Fourier transform of the power spectrum. On large scales, we obtain the same constant relative deviation for the power spectra and the correlation functions, as the linear growing modes $D_+(t)$ are scale independent in both K-mouflage and Λ -CDM cosmologies (much below the horizon).

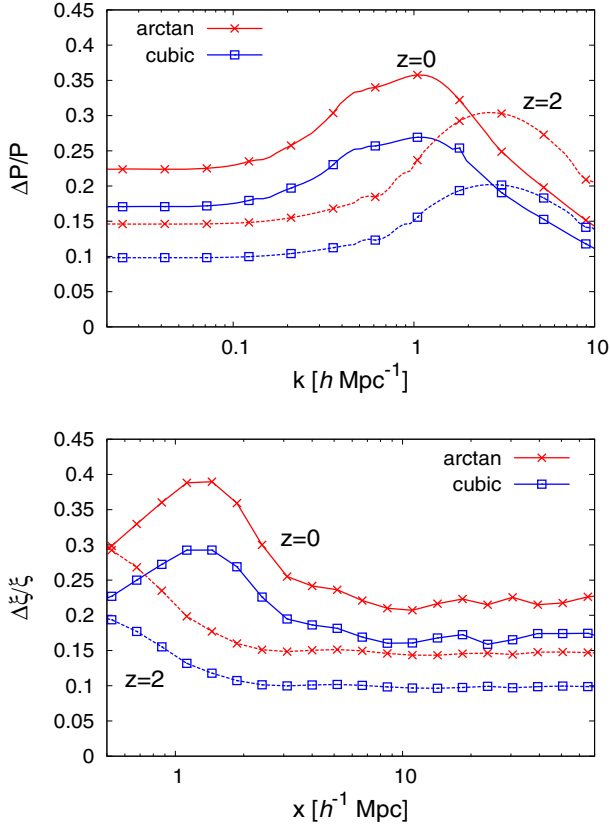


FIG. 11 (color online). *Upper panel*: relative deviation of the matter density power spectrum from the Λ -CDM reference, at $z = 0$ (solid lines) and $z = 2$ (dashed lines), for the K-mouflage models. *Lower panel*: relative deviation of the matter density correlation function from the Λ -CDM reference.

This deviation of 20% is consistent with the deviation of 10% obtained for the linear growing modes in Fig. 7. The deviation from the Λ -CDM reference grows on mildly nonlinear scales, as nonlinearities amplify the effects of the fifth force. This is related to the increase of the large-mass tail of the halo mass function shown in Fig. 10, because on these scales, the power spectrum and the correlation function probe the formation of massive halos, as can be clearly seen in a halo model approach. The deviation decreases on smaller scales because the power spectrum now probes the inner regions of halos, and we assume similar NFW profiles [26] for all cosmologies (but this regime shows a greater theoretical inaccuracy, and numerical simulations would be needed to measure the impact of the modified gravity on small highly nonlinear scales and halo profiles). However, in the nonlinear range shown in Fig. 11, the impact of changes to the mass function is greater than that of halo profiles; see also Ref. [28] for a detailed study of these various contributions.

The deviation from the Λ -CDM reference slowly decreases at high z , as the fifth force mediated by the scalar field becomes negligible (as seen from the vanishing

of the key factor β^2/\bar{K}' as $\bar{K}' \rightarrow \infty$). This decrease of the deviations of large-scale clustering from the Λ -CDM reference is slower than what is found in many other modified-gravity scenarios, such as the $f(R)$ theories, and is characteristic of these K-mouflage models.

V. CLUSTERS OF GALAXIES

To go beyond background quantities and the large-scale perturbative regime, we investigate in this section the impact of K-mouflage scenarios on the largest collapsed structures that we observe, that is, clusters of galaxies. This provides another probe of modified-gravity models, which is complementary with background and perturbative studies, as it corresponds to the nonlinear regime of the matter density field and to the well-defined objects measured in actual surveys.

For our purposes, clusters present two advantages as compared with galaxies. First, they are unscreened objects [8], so that the impact of the modification to gravity is very simple and corresponds to a time-dependent effective Newton constant (we shall check that this holds down to the cluster cores in Sec. V B below). Therefore, one does not expect dramatic qualitative changes from the Λ -CDM case, and the same semiquantitative models can be applied to both K-mouflage and Λ -CDM cosmologies. This is also illustrated by the symmetry described in Sec. III G, which shows that in this unscreened regime, from the point of view of nonlinear gravitational clustering, the Λ -CDM cosmology, quintessence models, and K-mouflage scenarios, belong to the same class. They obey the same equations of motion (67)–(68), with only slightly different time-dependent functions $\kappa(t)$ from Eq. (70). Second, at first order, clusters can be described by simple physical laws, such as hydrostatic equilibrium for the gas profile and bremsstrahlung emission for the x-ray luminosity, giving rise to the so-called cluster scaling laws [29]. This is especially true for the most massive clusters that we focus on.

In contrast, galaxies probe the transition from the unscreened to screened regimes and also involve many complex astrophysical phenomena, such as cooling processes, star formation, supernovae, and AGN winds and feedback. Therefore, although they would be very interesting probes, they are much more difficult to model, both for the modified-gravity sector and for the usual galaxy formation processes that also appear in the Λ -CDM cosmology.

In this paper, our goal is to estimate the magnitude of the impact of K-mouflage models on clusters of galaxies rather than building a very accurate description of clusters. Therefore, we consider the simplest possible modelling of clusters with only few physical parameters. This may not provide the highest-accuracy cluster model, but we can expect that it captures the main physical processes and provides a robust estimate of the impact of modifications to gravity. Moreover, we check that our predictions show a reasonable agreement with observations.

A. Halo density profiles

To study the effects of K-mouflage scenarios on clusters of galaxies, we need their dark matter profile. Because in the unscreened regime gravitational clustering proceeds in the same fashion in K-mouflage and Λ -CDM cosmologies, as described in Sec. III G, we assume in all cases NFW profiles [26],

$$\rho_{\text{DM}}(r) = \frac{\rho_s}{(r/r_s)(1+r/r_s)^2}. \quad (83)$$

This profile is characterized by a scaling radius and density, respectively, r_s and ρ_s , which can be expressed in terms of the concentration parameter $c = R_{\Delta_c}/r_s$. Here R_{Δ_c} is the radius such that the mean density within R_{Δ_c} is Δ_c times the critical density, $\rho(< R_{\Delta_c}) = \Delta_c \rho_{\text{crit}}$, as we again define the extension of the halos by an overdensity threshold with respect to the critical density. From the definition of c , it is possible to express ρ_s as

$$\rho_s = \rho_{\text{crit}} \frac{\Delta_c}{3} \frac{c^3}{\ln(1+c) - c/(1+c)}, \quad (84)$$

which can be inverted to give c as a function of ρ_s .

To consider the effects of the presence of the scalar field on the shape of the dark matter profile, we consider a simple model for the halo concentration. We assume that halos of mass M typically form at a redshift $z_f(M)$ determined by

$$\sigma(q, z_f) = \sigma_f, \quad (85)$$

where $q = (3M/4\pi\bar{\rho}_0)^{1/3}$ is the halo Lagrangian radius and σ_f is a free parameter, and that the density of the newly formed halo is proportional to $\rho_{\text{crit}}(z_f)$,

$$\rho_s(M) = \Delta_f \rho_{\text{crit}}(z_f), \quad (86)$$

with Δ_f a second free parameter. Equation (85) means that halos of a given mass typically form when density fluctuations at this mass scale reach the nonlinear regime, while Eq. (86) assumes that the core of the cluster keeps a roughly constant density after its formation, which is set by the critical density at the formation time. As discussed in Sec. IV E, we choose to rescale ρ_s in terms of the critical density rather than the mean density at redshift z_f because the former is more physical at late times (whereas they coincide at high redshift) and it also corresponds to our definition of halos. Next, using Eq. (84), we compute $c(M)$, and we define the dark matter density profile using (83).

In Fig. 12, we display the mass-concentration relation obtained with the choice of parameters $\sigma_f = 0.2$ and $\Delta_f = 500$ (halos are again defined by $\Delta_c = 200$). As is well known [30], the concentration c (and the scaling density ρ_s) is larger for smaller mass, because in hierarchical scenarios, smaller mass scales turned nonlinear at higher redshift

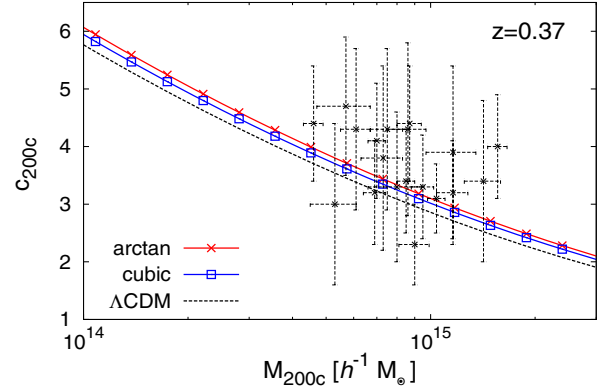


FIG. 12 (color online). Mass-concentration relation for NFW halos, for the K-mouflage models and the Λ -CDM reference, at $z = 0.37$. The black points (with their error bars) are observational measures taken from Ref. [31].

when the critical (and the mean) density of the Universe was greater. This is of course consistent with our model (85)–(86). We compare these results with the mass-concentration relation obtained by Ref. [31], from the analysis of 19 x-ray selected galaxy clusters from the Cluster Lensing and Supernova Survey with Hubble, with a mean redshift $z \approx 0.37$. We can see that reasonable choices of the parameters σ_f and Δ_f (we naturally expect $\sigma_f \lesssim 1$ and $\Delta_f \gtrsim 200$) allow us to obtain a reasonable match to observations. This suggests that this simple modelling captures the main features of the gravitational formation of halos. Therefore, we do not consider here more sophisticated models, which involve the past accretion history and merging trees of virialized halos. These could provide more accurate modelling, at the price of additional complexity (and often additional parameters), but it is not clear if their estimate of the dependence on the underlying gravity theory would be much more accurate. Such studies are left for future works, where N-body simulations would be needed to check detailed models.

As expected, we find a small increase of the concentration $c(M)$ in the K-mouflage models, as compared with the Λ -CDM reference. This is due to the faster growth of gravitational clustering, which implies a slightly greater scaling density $\rho_s(M)$. However, we can see that the effect is rather modest.

B. Clusters are not screened

As noticed in Refs. [7,8], clusters are unscreened, and the Klein–Gordon equation (23) can be kept at the linear level over the fluctuations of the scalar field, as in Eq. (43). In this section, we check that this property extends far inside the cluster profile.

In the small-scale static limit, which corresponds for instance to high-density astrophysical objects, the Klein–Gordon equation (A3) becomes

$$\nabla_{\mathbf{r}} \cdot (\nabla_{\mathbf{r}} \phi K') = \frac{\beta \bar{A}}{c^2 M_{\text{Pl}}} \rho, \quad (87)$$

where \mathbf{r} is the Jordan-frame physical coordinate and we assumed $\delta\rho \approx \rho$ (i.e., $\delta \gg 1$). As compared with Eq. (43), here we do not make the approximation $K' \approx \bar{K}'$. Instead we consider the small-scale regime where $\tilde{\chi} \approx \delta\tilde{\chi} < 0$. For a spherically symmetric halo, using the Stokes theorem, this gives

$$\frac{d\phi}{dr} K' = \frac{\beta \bar{A} M(r)}{c^2 M_{\text{Pl}} 4\pi r^2}. \quad (88)$$

As in Refs. [7,8,12] (but in Jordan-frame coordinates), defining the ‘‘K-mouflage screening radius’’ R_K by

$$R_K(M) = \left(\frac{\beta \bar{A}^2 M}{4\pi c M_{\text{Pl}} \mathcal{M}^2} \right)^{1/2}, \quad (89)$$

where $M = M(R)$ is the total mass of the object of radius R , and introducing the rescaled dimensionless variables $x = r/R_K$, $m(x) = M(<r)/M$, $\phi(x) = \phi(r)/\phi_K$, with $\phi_K = \mathcal{M}^2 R_K / c \bar{A}$, the integrated Klein–Gordon equation (88) reads as

$$\frac{d\phi}{dx} K' = \frac{m(x)}{x^2}, \quad \text{with} \quad \tilde{\chi} = -\frac{1}{2} \left(\frac{d\phi}{dx} \right)^2. \quad (90)$$

As pointed out in Ref. [7], in the small-scale static regime, we have $\tilde{\chi} < 0$, whereas the cosmological background value satisfies $\tilde{\chi} > 0$. Using that $\mathcal{M}^4 \sim \bar{\rho}_{\text{de}0}$ is roughly the dark-energy density today and that $\bar{A} \sim 1$, we obtain

$$R_K(M) \approx \sqrt{\frac{\beta M}{1 M_{\odot}}} 3470 \text{ a.u.} \approx \sqrt{\frac{\beta M}{10^{14} M_{\odot}}} 0.12 h^{-1} \text{ Mpc}. \quad (91)$$

The first equality shows that the Solar System is screened by the Sun, which allows these K-mouflage scenarios to satisfy Solar System constraints [12]. On the other hand, for $\beta = 0.1$, the K-mouflage screening radius of a cluster of mass $10^{14} M_{\odot}$ is $R_K \approx 0.04 h^{-1} \text{ Mpc}$. This is much smaller than the radius of the cluster, which means that most of the cluster is unscreened. Moreover, as we move inside the halo, the enclosed mass $M(<r)$ decreases, which further delays the onset of K-mouflage screening. When $|\tilde{\chi}| \ll 1$ we have $K' \approx 1$, and we obtain

$$|\tilde{\chi}| \ll 1: \tilde{\chi}(r) \approx -\frac{m(x)^2}{2x^4}, \quad (92)$$

which gives inside the halo

$$|\tilde{\chi}| \ll 1, \quad r < R: \tilde{\chi}(r) \approx -\frac{\rho_{\text{crit}}}{6\mathcal{M}^4} \left(\beta \bar{A}^2 \Delta_c(<r) \frac{Hr}{c} \right)^2. \quad (93)$$

We show the radial profiles of $-\tilde{\chi}(r)$ in the lower panel in Fig. 13, for $M = 10^{15} h^{-1} M_{\odot}$ and $10^{13} h^{-1} M_{\odot}$. In both cases, we can check that $|\tilde{\chi}| \ll 1$ over the full halo profile [as seen from Eq. (92), $\tilde{\chi}(r)$ goes to a finite value at $r \rightarrow 0$ for NFW density profiles, because $\rho \propto 1/r$ and $m \propto x^2$ in the core]. This means that clusters are not screened and that we can use the background value \bar{K}' for the kinetic function. In fact, at low z , we also have $\tilde{\chi} \ll 1$ and $\bar{K}' \approx 1$, so that the kinetic function is dominated by the low-order terms in the expansion (7) and the results are not very sensitive to the precise nonlinear form of $K(\tilde{\chi})$. Then, the Klein–Gordon equation can be linearized in the scalar field as in Eq. (43), and the gravitational potential Φ that governs the dynamics of matter is again given by Eq. (45).

From the kinetic factor $\tilde{\chi}(r)$, we can obtain the radial profile of the scalar field, $\phi(r)$, by integrating $d\phi/dx = \sqrt{-2\tilde{\chi}}$ and using $\phi = \phi_K \phi$. The boundary condition is

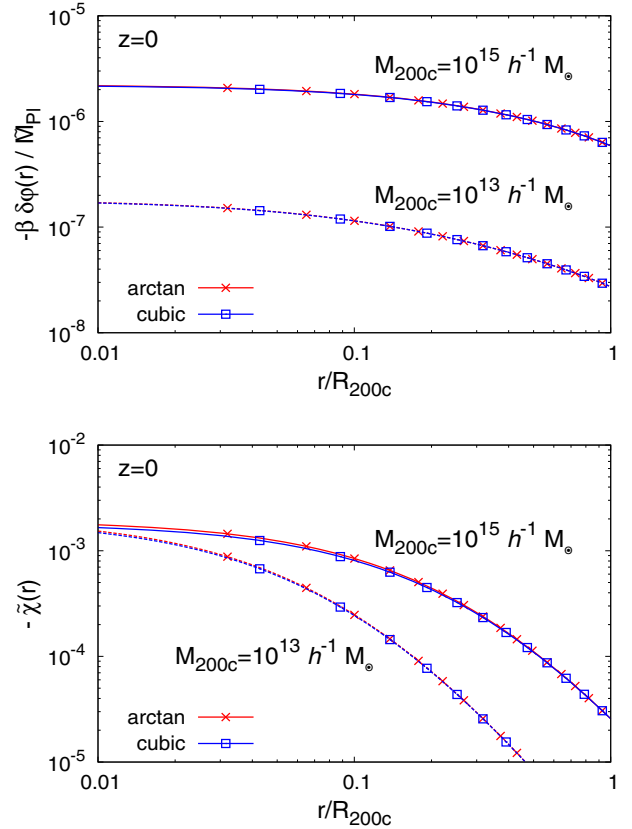


FIG. 13 (color online). *Upper panel:* scalar-field radial profile, $\delta\phi(r) = \phi(r) - \bar{\phi}$, for halos of mass $10^{15} h^{-1} M_{\odot}$ (upper solid lines) and $10^{13} h^{-1} M_{\odot}$ (lower dashed lines). The scalar-field fluctuation is negative as the scalar field ϕ is minimum at the center of the halo. *Lower panel:* radial profile of the ‘‘kinetic energy’’ $-\tilde{\chi}(r)$ of the scalar field, for halos of mass $10^{15} h^{-1} M_{\odot}$ (upper solid lines) and $10^{13} h^{-1} M_{\odot}$ (lower dashed lines). Here $\tilde{\chi} < 0$ because we consider the static limit, which is dominated by spatial gradients. The arctan and cubic K-mouflage models give almost identical results in this figure.

$\varphi \rightarrow \bar{\varphi}$ at infinity. We show the radial profile of the fluctuation $\delta\varphi = \varphi - \bar{\varphi}$ in the lower panel in Fig. 13. We can check from the comparison with Fig. 4 that $|\delta\varphi| \ll |\bar{\varphi}|$, in agreement with the scaling $\delta\varphi/\bar{\varphi} \sim (aH/ck)^2 \delta\rho/\bar{\rho}$ obtained from Eq. (A35) and $\bar{\varphi}/\bar{M}_{\text{pl}} \sim \beta/\bar{K}'$. In particular, this explicitly shows that the coupling function $A(\varphi)$ remains dominated by its low-order terms in the expansion (8), both for the background and for large-scale structures such as clusters of galaxies.

The magnitude of $\delta\varphi$ can also be read from the modified Poisson equations (41). In realistic models, the fifth force should not have a magnitude greater than the Newtonian force, which implies $|\delta A/\bar{A}| \approx |\beta\delta\varphi/\bar{M}_{\text{pl}}| \lesssim |\Psi_{\text{N}}|$, whence $|\beta\delta\varphi/\bar{M}_{\text{pl}}| \lesssim 10^{-5}$.

C. Impact of nonlinear substructures

The Klein–Gordon equation (87) that determines the scalar field φ is nonlinear, because of the factor $K'(\tilde{\chi})$. This means that substructures could have a strong impact on the solution $\varphi(\mathbf{r})$ as there is no longer a linear superposition property and the solution obtained for the averaged halo profile is not identical to the average of the exact solutions obtained by taking into account substructures. In this section, we check that this nonlinearity does not play a significant role and does not invalidate our approach described in Sec. V B.

First, we note that for an object that is exactly spherically symmetric the integrated Klein–Gordon equation (88) holds and the scalar-field profile only depends on the integrated mass $M(r)$ within radius r . This smoothes out radial substructures. However, in practice, clusters are not exactly spherically symmetric, and individual cluster galaxies also break any overall spherical symmetry. We have seen in Sec. V B that clusters are unscreened as the kinetic factor, $\tilde{\chi}_{\text{clus}}(r)$, associated with the mean cluster density profile (83), is much smaller than unity. Then, if galactic halos only form a small fraction of the total cluster volume, throughout most of the cluster volume, we can linearize Eq. (87), as in Eq. (43), which gives

$$\text{unscreened region: } \nabla_{\mathbf{r}}^2 \varphi = \frac{\beta \bar{A}}{\bar{K}' c^2 \bar{M}_{\text{pl}}} \rho, \quad (94)$$

where \bar{K}' is the background value, with $\bar{K}' \approx 1$ at low z . This equation breaks down around each cluster galaxy, where the high matter density, which is much greater than the NFW mean density $\rho_{\text{DM}}(r)$ of Eq. (83) at that radius, makes the scalar field enter the nonlinear screening regime. Thus, around each galaxy “ i ,” $i = 1, \dots, N_{\text{gal}}$, we must cut a patch V_{K_i} where the equation (94) must be replaced by the fully nonlinear equation (87). By definition, the volume V_{K_i} is given by the K-mouflage radius R_{K_i} of the galaxy. In practice, if $R_{K_i} \ll R_{\text{clus}}$, we can build an approximate solution by patching the solutions within each galaxy volume V_{K_i} with the global solution (94) that holds in

between galaxies. Around each galaxy, using an approximate spherical symmetry around the galaxy center, we obtain the local profile by solving Eq. (88), where M is replaced by the galaxy mass $m_{\text{gal}}(r)$, and the boundary condition at R_{K_i} is approximated as a constant obtained from the global solution (94).

This scenario holds provided the regions V_{K_i} do not extend far beyond the galaxy volumes V_i (defined for instance by their stellar content or by the region where matter is gravitationally bound to the galaxy) and do not cover most of the cluster volume. From Eq. (89), we have $R_K(m_{\text{gal}}) \propto m_{\text{gal}}^{1/2}$. Defining the mass function $n(m)dm$ of the cluster galaxies, the total volume built by the nonlinear regions V_{K_i} reads as

$$V_{K_{\text{gal}}} = \int_0^\infty dm \frac{dn}{dm} V_K(m) \propto \int_0^\infty dm \frac{dn}{dm} m^{3/2}. \quad (95)$$

The mass function of the cluster galaxies or of dark matter subhalos is typically a power law at low mass with an exponential cutoff at high mass [32]. In any case, the integral $\int dm (dn/dm) m = M_{\text{gal}}$ is necessarily finite and equal to the total mass associated with the galaxies, which is smaller than the total cluster mass. Therefore, the integral (95) converges at low mass and is dominated by the galaxies around the knee of the galaxy multiplicity function, which typically corresponds to $M \sim 10^{12} M_\odot$. From Eq. (91), we have $R_K(10^{12} M_\odot) \approx 4h^{-1}$ kpc, with $\beta = 0.1$, which gives a volume fraction of the order of $(0.004)^3 \sim 5 \times 10^{-8}$. Even if we have ~ 20 such galaxies in the cluster, this only makes a fraction of order 10^{-6} of the cluster volume.

Moreover, we can see that R_{K_i} is typically smaller than the actual radius R_i of the galaxy (by a factor of a few). In the Λ -CDM cosmology itself, the analysis of the hot gas that makes most of the intracluster medium and gives rise to the cluster x-ray luminosity (based on hydrostatic equilibrium and scaling laws) only applies outside of the cluster galaxies, where cooling and star formation processes play a major role. Therefore, the nonlinearities of the Klein–Gordon equation (87) do not bring further restrictions as compared with the standard Λ -CDM case, as they are “hidden” within the galaxies, and the impact of the fifth force on the intracluster medium can be obtained from the linearized equation (94) associated with the unscreened regime. They do not modify global properties either, such as the cluster correlation function, as the dynamics and formation of the clusters remain governed by the linearized Klein–Gordon equation (94).

D. Hydrostatic equilibrium

From Eq. (48), the equation of hydrostatic equilibrium for the gas density ρ_g and pressure p_g reads as

$$\nabla \Phi = \nabla \left(\Psi_{\text{N}} + \frac{\beta c^2 \varphi}{\bar{M}_{\text{pl}}} \right) = - \frac{\nabla p_g}{\rho_g}, \quad (96)$$

where we used Eqs. (41) and (44). This explicitly shows how the pressure gradient is amplified, at a fixed density profile, by the fifth force. Assuming spherical symmetry, this leads to

$$\frac{dp_g}{dr} = -\rho_g(1 + \epsilon_1) \frac{d\Psi_N}{dr}, \quad (97)$$

where we used the fact that clusters are unscreened, so that $K' \simeq \bar{K}'$ and the Klein–Gordon equation can again be linearized as in Eq. (94). In the Λ -CDM cosmology, we simply have $\epsilon_1 = 0$. To obtain the gas profile from Eq. (97), we also need an equation of state that gives the pressure as a function of the gas density or temperature. We consider an isothermal gas with $p_g = \rho_g k_B \bar{T}_g / (\mu m_p)$, where k_B is Boltzmann’s constant and μm_p is the mean molecular weight of the gas. This yields the gas density profile

$$\rho_g(r) \propto e^{-(1+\epsilon_1)\mu m_p \Psi_N(r)/k_B \bar{T}_g}, \quad (98)$$

where the Newtonian potential Ψ_N is fixed by the dark matter profile.

To evaluate \bar{T}_g , we assume that the gas temperature is proportional to the mean value of the dark matter “temperature,” $T_{\text{DM}}(r)$, which we define from the velocity dispersion $\sigma_{\text{D}}^2(r)$ as

$$k_B T_{\text{DM}}(r) = \mu m_p \sigma_{\text{DM}}^2(r). \quad (99)$$

The dark matter being collisionless, it is not described by a thermodynamical temperature. However, we can expect the virialization processes associated with the formation of the halo to scale in the same fashion for the dark matter, as measured by its velocity dispersion, and for the gas, as measured by its temperature. In particular, the dark matter velocity dispersion obeys the Jeans equation, which can be written at equilibrium as [33]

$$\frac{1}{\rho_{\text{DM}}} \frac{d[\rho_{\text{DM}} \sigma_{\text{DM}}^2]}{dr} = -\frac{d\Phi}{dr} = -(1 + \epsilon_1) \frac{d\Psi_N}{dr}. \quad (100)$$

For a given dark matter halo profile, set by the NFW profile (83) and concentration parameter $c(M)$, the Jeans equation (100) determines the velocity dispersion profile $\sigma_{\text{DM}}^2(r)$, whence comes the effective dark matter temperature $T_{\text{DM}}(r)$ defined in Eq. (99). Then, we set the gas temperature \bar{T}_g as

$$\bar{T}_g = \frac{1}{\beta_g} \bar{T}_{\text{DM}} = \frac{1}{\beta_g} \frac{\int dr 4\pi r^2 \rho_{\text{DM}}(r) T_{\text{DM}}(r)}{\int dr 4\pi r^2 \rho_{\text{DM}}(r)}, \quad (101)$$

where β_g is a free parameter that we fix to be equal to 0.6, which is of the same order as the values used in studies of clusters of galaxies [34]. In other words, we assume that the kinetic and thermal energies of the dark matter and the gas

are proportional, because they are generated by the same process, the formation and virialization of the halo.

Finally, to fully specify the gas density profile (98), we normalize it as

$$M_g = \int_0^{R_{\Delta c}} dr 4\pi r^2 \rho_g(r) = \frac{\Omega_b}{\Omega_{\text{DM}}} M_{\text{DM}}. \quad (102)$$

Thus, we consider that the baryon and dark matter mass fractions in clusters are given by the cosmological abundance. This assumes that there is no significant redistribution and segregation of matter on scales greater than cluster radii, which should be a reasonable approximation for massive clusters.

Therefore, in terms of the intracluster medium, the differences between the K-mouflage and Λ -CDM scenarios only arise through three effects, in our framework. First, the dark matter profiles (83) are slightly different because of the small change of the halo concentration shown in Fig. 12, which comes from the different growth rates of large-scale structures. Second, the equation of hydrostatic equilibrium (96) is modified by the factor $\epsilon_1(t)$, which corresponds to the amplification of gravity by the fifth force in the unscreened regime. This implies slightly greater pressure gradients for the gas. Third, the gas (and dark matter) temperature itself is also amplified by the same factor $(1 + \epsilon_1)$, at a fixed dark matter profile, because it also arises from the gravitational collapse; see Eqs. (100) and (101). The second and third effects compensate in terms of the gas density profile, as the greater potential depth is balanced by the greater gas temperature, so that we can expect rather modest deviations between the different cosmological scenarios.

In Fig. 14, we show the dark matter and gas density profiles for a cluster of mass $M = 5 \times 10^{14} h^{-1} M_{\odot}$ at $z = 0$, for the K-mouflage models and the Λ -CDM reference. The presence of the scalar field makes the density profiles more compact, in agreement with Fig. 12. As expected, the deviations from the Λ -CDM reference are of the order of a few percent.

E. Scaling laws

From the gas density profile $\rho_g(r)$ and temperature \bar{T}_g , we obtain the x-ray cluster luminosity within radius R as [35]

$$L_X(< R) = 4\pi \epsilon_X(\bar{T}_g) \int_0^R n_g^2(r) r^2 dr, \quad (103)$$

where $n_g(r) = \rho_g(r)/\mu m_p$ is the cluster gas density and $\epsilon_X(T)$ is the x-ray emissivity, which can be expressed in terms of the temperature as [32]

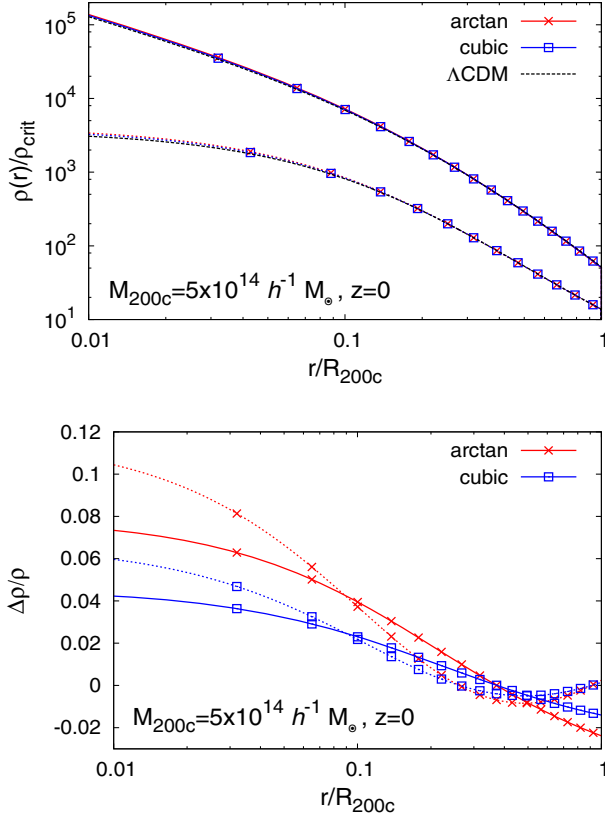


FIG. 14 (color online). *Upper panel:* density profiles for a cluster of mass $M_{200c} = 5 \times 10^{14} h^{-1} M_{\odot}$. The upper solid lines refer to the dark matter density profiles and the lower dotted lines to the gas density profiles. The K-mouflage models and the Λ -CDM reference cannot be distinguished in this figure. *Lower panel:* relative deviation from the Λ -CDM reference of the dark matter (solid lines) and gas (dotted lines) density profiles.

$$\epsilon_X(T) = 4.836 \times 10^{-24} \frac{4 - 2Y}{(4 - Y)^2} \left(\frac{T}{1 \text{ KeV}} \right)^{1/2} \text{ erg.s}^{-1} \text{ .cm}^3. \quad (104)$$

Here Y is the helium mass fraction, and $\mu = 2/(4 - Y)$, $n_e/n_g = (2 - Y)/(4 - Y)$, and $(n_H + 4n_{\text{He}})/n_g = 2/(4 - Y)$, where we assume complete ionization. This applies to high temperatures of order 1 keV and above, where the x-ray emissivity is dominated by bremsstrahlung. Equation (103), with the emissivity (104), gives the total bolometric luminosity. In practice, one measures the radiation from x-ray clusters within finite frequency bands. Therefore, we also define the luminosity within frequency bands, denoted for instance as bands “ $A = [\nu_1^A, \nu_2^A]$,” “ $B = [\nu_1^B, \nu_2^B]$,” ..., by

$$L_{XA}(< R) = L_X(< R) (e^{-h\nu_1^A/k_B \bar{T}_g} - e^{-h\nu_2^A/k_B \bar{T}_g}). \quad (105)$$

Observational studies often measure the x-ray properties of galaxy clusters within a radius R_X that is smaller than

R_{200c} , because the luminosity scales as the squared density [see Eq. (103)] so that inner high-density regions are easier to measure. A popular choice is the radius set by the density threshold $\Delta_c = 500$ with respect to the critical density. In the following, keeping our definition of halos by the threshold $\Delta_c = 200$ as in Figs. 10 and 12–14, we use the density profile obtained from Eq. (98) and displayed in Fig. 14 to compute x-ray properties within R_X defined by $\Delta_c = 500$ (hence, $R_X < R_{\text{halo}}$).

To avoid the complications due to the internal structures of the clusters (presence of massive galaxies in the center, importance of dissipative processes, cooling cores, ...) and also to follow the observational procedures, we define a core radius R_{core} outside of which we evaluate the quantities of interest. As in many observational analyses, we simply define R_{core} as a fixed fraction of the cluster radius R_X (as defined by the threshold $\Delta_c = 500$ with respect to the critical density), with $R_{\text{core}} = f_{\text{core}} R_X$ and typically $f_{\text{core}} \sim 0.15$. Then, we obtain for instance the luminosity in the outer cluster shells, between $R_{\text{core}} < r < R_X$, as

$$L_{XA \text{ no-core}} = L_{XA}(< R_X) - L_{XA}(< R_{\text{core}}). \quad (106)$$

In Figs. 15 and 16, we show, respectively, the $M_{500c} - T_{500c\text{-nocore}}$ and $T_{500c\text{-nocore}} - L_{XA-500c\text{-nocore}}$ relations compared to observations of clusters of galaxies in the x ray, with the choice of parameter $f_{\text{core}} = 0.15$ and the frequency “A band” [0.1–2.4] keV. For the $M - T$ relation, we obtain a good agreement with observations, while our prediction for the slope of the $T - L$ relation is too shallow. This is a well-known problem associated with a noticeable breakdown of the naive “scaling laws” for the x-ray luminosity, especially for small clusters [35]. This is usually explained by a decrease of the gas fraction and a greater importance of nonthermal effects, or departures from hydrostatic equilibrium, in small clusters. However, because our goal is only to estimate the magnitude of the effects due to modifications of gravity, we do not try to build a more accurate and more complex model in this paper. Moreover, our simple model is sufficient to recover the typical x-ray luminosity in the range $4 < T < 15$ keV, which corresponds to massive bright clusters.

At fixed mass, the temperature in the K-mouflage scenarios is greater than in the Λ -CDM reference by about 2%. This is mostly set by the factor ϵ_1 , which is about 2% as seen in Fig. 5. Indeed, from Eq. (100), we can see that at a fixed dark matter density profile the fifth-force enhancement of gravity by the factor $(1 + \epsilon_1)$ yields an increase of the dark matter velocity dispersion and of the gas temperature by the same factor. The small deviations from this 2% value, which depend on mass, that appear in Fig. 15 correspond to the small changes of the dark matter profile through the modification of the concentration parameter shown in Fig. 12.

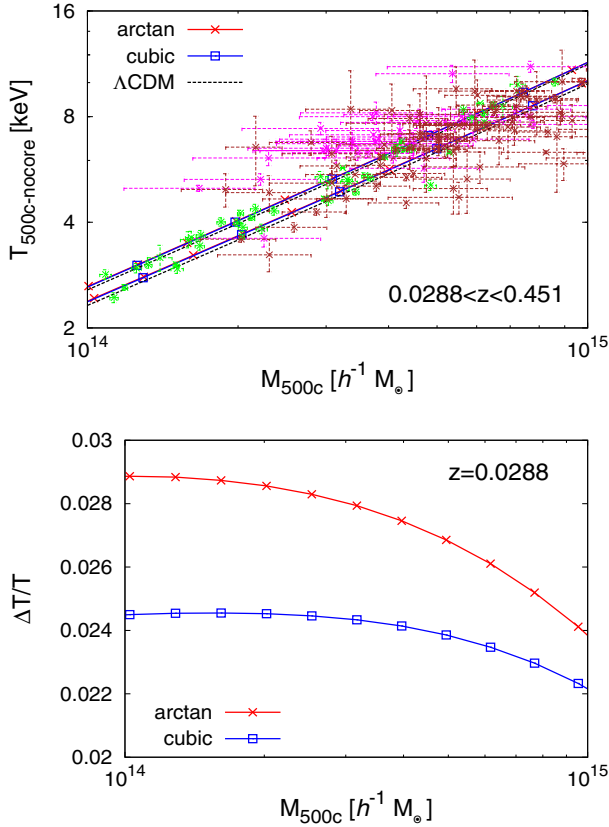


FIG. 15 (color online). *Upper panel*: mass-temperature relation for the K-mouflage models and the Λ -CDM reference, at $z = 0.0288$ (lower curves) and $z = 0.451$ (upper curves). The data points are taken from observations made by Refs. [36] (in green), [37] (in magenta), and [38] (in brown), with clusters in the redshift range $0.0288 \leq z \leq 0.451$. *Lower panel*: relative deviation of the cluster mass-temperature relation from the Λ -CDM reference, at $z = 0.0288$.

At fixed temperature, the K-mouflage models give a slightly lower x-ray luminosity. This is because at fixed mass K-mouflage models give a higher temperature, as seen in Fig. 15. Therefore, they give a lower mass at a fixed temperature. Since the x-ray luminosity scales as $L_X \sim \rho_s M \sqrt{T}$, a lower mass implies a lower luminosity (disregarding the impact on ρ_s). As expected, we find percent deviations as for the $M - T$ scaling law.

Thus, as for the quantities studied in previous sections, we obtain percent deviations from the Λ -CDM scaling laws. Unfortunately, this is probably too small to be used as a meaningful constraint on these modified-gravity scenarios, in view of the observational and theoretical uncertainties. Therefore, it is unlikely that cluster scaling laws can provide competitive constraints on such modified-gravity models, that must also pass very tight Solar System bounds and satisfy larger-scale cosmological constraints associated with the growth of large-scale structures or the evolution of the Hubble expansion rate (e.g., constraints from big bang nucleosynthesis).

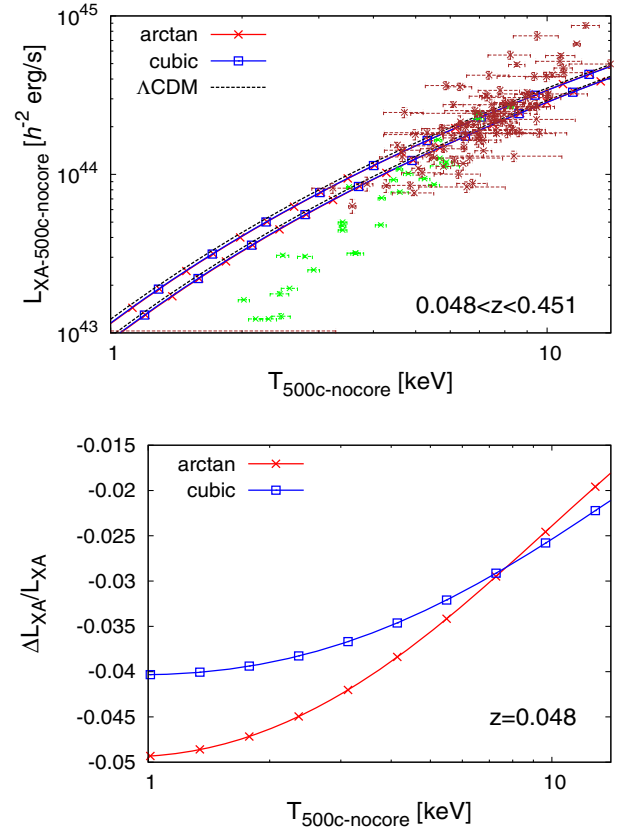


FIG. 16 (color online). *Upper panel*: temperature-luminosity relation for the K-mouflage models and the Λ -CDM reference, at $z = 0.048$ (lower curves) and $z = 0.451$ (upper curves). The data points are taken from observations made by Refs. [39] (in green) and [38] (in brown), with clusters in the redshift range $0.048 \leq z \leq 0.451$. *Lower panel*: relative deviation of the cluster temperature-luminosity relation from the Λ -CDM reference, at $z = 0.048$.

F. Cluster temperature function

Neglecting the scatter of the mass-temperature relation, by combining the halo mass function described in Sec. IV E with the mass-temperature relation obtained in Sec. V D and Fig. 15, we obtain the x-ray cluster temperature function

$$n(T) = n(M) \frac{d \ln M}{d \ln T}. \quad (107)$$

In Fig. 17, we show the temperature functions computed for the K-mouflage models together with the Λ -CDM case, evaluated at $z = 0.05$, to compare them with the observations obtained by Ref. [40].

We obtain a reasonable agreement with observations. As is well known, this also means that the cluster temperature is a rather robust quantity (as compared for instance with the x-ray luminosity) and that it is not necessary to build very sophisticated models to recover the right order of magnitude. As shown in the lower panel, we now obtain deviations for the cluster number counts that are of order

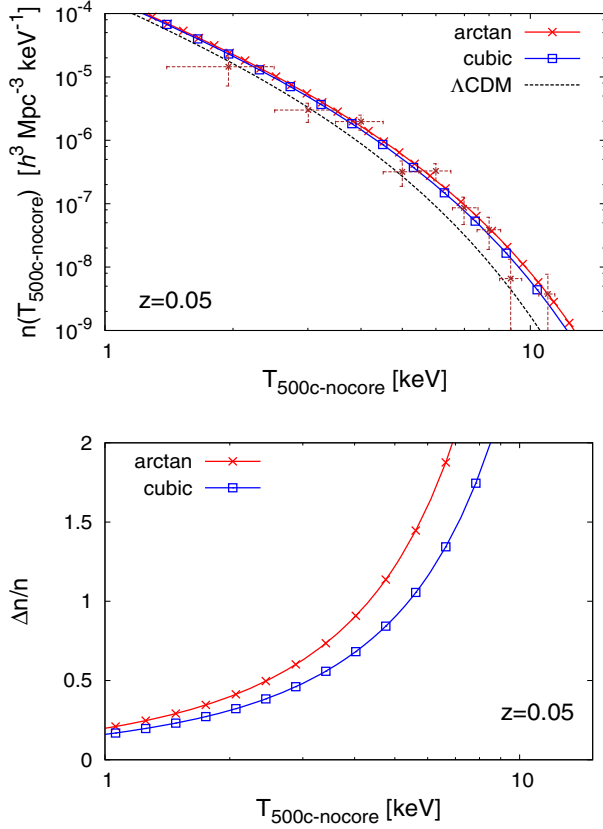


FIG. 17 (color online). *Upper panel:* cluster temperature function for the K-mouflage models and the Λ -CDM reference, at $z = 0.05$. The data points are taken from observations made by Ref. [40] from a sample of clusters with $z \approx 0.05$. *Lower panel:* relative deviation of the cluster temperature function from the Λ -CDM reference at $z = 0.05$.

unity: the K-mouflage models can predict twice or three times more high- T clusters than the Λ -CDM reference. As we have seen, this difference is not due to deviations in the cluster scaling laws, that is, in the intracluster medium, which are quite small, but to the amplification of the high-mass tail of the halo mass function already shown in Fig. 10. Therefore, this result should be rather robust as it is directly related to the faster growth of large-scale structures in the K-mouflage scenarios.

G. Sunyaev–Zel’dovich effect

An indirect method to infer the properties of the clusters is to use the Sunyaev–Zel’dovich effect (hereafter SZE) [13]. It occurs when photons from the cosmic microwave background (CMB) inverse Thompson scatter in the intracluster medium. The measured CMB temperature is then distorted with an amplitude proportional to the so-called Compton parameter (see, e.g., Ref. [41]),

$$y = \int n_e \sigma_T \frac{k_B T_g}{m_e c^2} dl, \quad (108)$$

where n_e is the electron number density, T_g is the gas temperature, m_e is the electron mass, $\sigma_T = 6.65 \times 10^{-25} \text{cm}^2$ is the Thompson cross section, and dl denotes the integration along the line of sight. Following a common observational practice, by integrating over the angular area of the cluster, defined for instance by the radius R_{500c} associated with the density contrast of 500 with respect to the critical density, we define the integral Compton parameter

$$Y_{500c} \equiv \int y d\Omega = r_d^{-2}(z) \int_0^{R_{500c}} 4\pi r^2 n_e(r) \sigma_T \frac{k_B T_g}{m_e c^2} dr, \quad (109)$$

where $r_d(z)$ is the angular distance of the cluster located at redshift z .

In Fig. 18, we show the relations $M_{g500c} - Y_{500c} r_d^2(z)$ and $T_{500c-nocore} - Y_{500c} r_d^2(z)$ for the K-mouflage models and the Λ -CDM reference, and we compare them to the

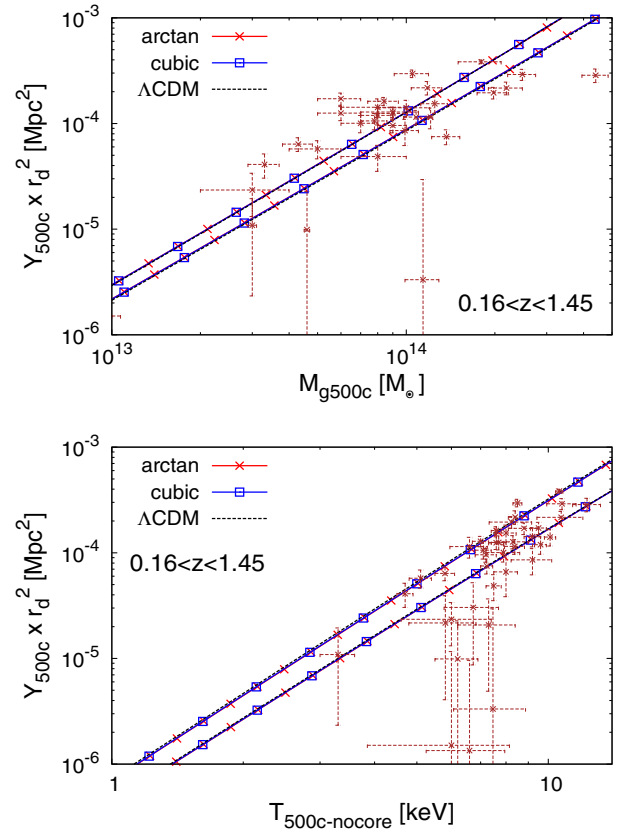


FIG. 18 (color online). Integrated Comptonization within R_{500c} as a function of the gas mass (upper panel) and gas temperature (lower panel) for the K-mouflage models and the Λ -CDM reference. These different models cannot be distinguished in these figures. We show our results for $z = 0.16$ (lower curves in the upper panel and upper curves in the lower panel) and $z = 1.45$ (upper curves in the upper panel and lower curves in the lower panel). The data points are measures from a sample of clusters in the range $0.16 \leq z \leq 1.45$ [41].

observations made by Ref. [41]. Again, we obtain a reasonable agreement with observations and a small deviation between the different scenarios. The agreement is better for the $M_g - Y$ relation than for the $T - Y$ relation, but the latter shows a very large scatter and is probably contaminated by large observational errors.

In any case, as in Sec. V E, it appears that deviations of cluster scaling laws associated with modified-gravity scenarios are too small as compared with observational error bars and theoretical uncertainties to be competitive. However, number counts, whether in terms of the cluster temperature or SZE parameter Y , could provide useful constraints.

H. Dynamical and weak lensing masses

Finally, we briefly comment on the dynamical and weak lensing masses of clusters and massive halos. In the unscreened regime, which applies to clusters and larger scales, the dynamics of matter particles (dark matter and the gas) is governed by the metric potential Φ , as in Eqs. (48) and (56). This gravitational potential is related to the matter density through the modified Poisson equation (45), and it is equal to the standard Newtonian potential (but with a time-dependent Newton constant) multiplied by the factor $1 + \epsilon_1$. From observations of the dynamics in clusters, one would then measure the dynamical mass

$$M_{\text{dyn}} \equiv [1 + \epsilon_1(t)] \frac{\mathcal{G}(t)}{\mathcal{G}_0} M, \quad (110)$$

assuming General Relativity (GR) gravity with today's Newton's constant. On the other hand, the weak lensing potential Φ_{wl} that governs the deflection of light rays by the perturbations of the metric is

$$\Phi_{\text{wl}} = \frac{\Phi + \Psi}{2} = \Psi_{\text{N}}, \quad (111)$$

where we used Eq. (41). Therefore, weak lensing observations of clusters would give the weak lensing mass

$$M_{\text{lens}} \equiv \frac{\mathcal{G}(t)}{\mathcal{G}_0} M, \quad (112)$$

and the ratio between the dynamical and weak lensing masses reads as

$$\frac{M_{\text{dyn}}}{M_{\text{lens}}} = 1 + \epsilon_1(t). \quad (113)$$

We have shown the factor ϵ_1 in Fig. 5. Thus, we find that the dynamical mass is greater than the lensing mass by about 2%. As explained above, this is set by the value of $2\beta^2$, which is constrained to be of order 2% or below because of cosmological and Solar System constraints [12]

(the big bang nucleosynthesis constraint and bound on the time dependence of \mathcal{G}). Therefore, this result on the ratio $M_{\text{dyn}}/M_{\text{lens}}$ gives an upper bound for its deviation from GR for all realistic K-mouflage models.

I. Cluster correlation function

In the previous sections, we considered the internal and integrated properties of clusters, as well as their abundance. Another probe of cosmology is provided by the cluster correlation function. Following Refs. [42,43], we write the halo bias as

$$b(M) = 1 + \frac{\nu^2 - 1}{\delta_L}. \quad (114)$$

More accurate fitting formulas have been proposed for Λ -CDM cosmologies [44], but they involve free parameters that might vary for different modified-gravity scenarios. Moreover, numerical simulations find that the spherical collapse model (114) provides reasonably good predictions that can fare better than more sophisticated models for rare and massive halos [45], which we focus on here. Therefore, Eq. (114) should be sufficient for our purposes and provide a simple estimate of the impact of K-mouflage models. Note that, because clusters are not screened, the reasoning that leads to Eq. (114) in the Λ -CDM cosmology remains valid for K-mouflage scenarios, as the only change is the time-dependent effective Newton constant as it would be defined from Eq. (63). This enters the bias (114) through the different values of $\nu(M)$ and δ_L , that we compute from the spherical collapse described in Secs. III D and IV E.

Combining the halo bias (114) with the matter correlation function $\xi(x)$ shown in Fig. 11, we obtain the cluster correlation function $\xi_{\text{cl}}(x)$ displayed in Fig. 19. The comparison with Fig. 11 shows that the cluster correlation function is much less affected by K-mouflage than the matter correlation and it can actually be slightly lower than

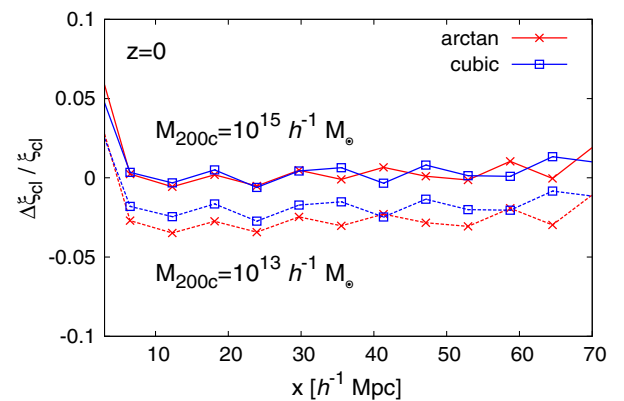


FIG. 19 (color online). Relative deviation of the cluster correlation function from the Λ -CDM reference for the K-mouflage models. We consider halos of mass $10^{15} h^{-1} M_{\odot}$ (upper solid lines) and $10^{13} h^{-1} M_{\odot}$ (lower dashed lines).

in the reference Λ -CDM cosmology. This is because the amplification of gravity, associated with the greater effective Newton constant $(1 + \epsilon_1(t))\mathcal{G}(t)/\mathcal{G}_0$, merely accelerates the growth of large-scale structures. This amplifies the matter density power spectrum and correlation function, as well as the large-mass tail of the halo mass function, as seen in Figs. 11 and 10. However, this same phenomenon also implies that, at a fixed mass M , massive halos are less rare and have a smaller bias $b(M)$ [in particular, $\nu(M)$ becomes smaller in Eq. (114)]. This effect almost cancels the increase of the underlying matter density correlation function. Therefore, it appears that the matter correlation function, measured for instance from weak lensing observations or galaxy surveys (using typical halos with a bias of order unity that is not significantly changed by K-mouflage), is a better probe of such modified-gravity scenarios than the cluster correlation function (or more generally the correlation of rare objects).

VI. COMPARISON WITH OTHER MODIFIED-GRAVITY MODELS

A. Some other modified-gravity theories

Before we conclude this study of K-mouflage models, it is interesting to compare our results with other modified-gravity models that have been investigated in the literature. The main scenarios that have led to detailed analytical and numerical studies are the $f(R)$ theories, scalar-field models such as dilaton and symmetron models, and Galileon models [46–48].

The $f(R)$ models [4,49–53] can be recast as scalar-field models with an Einstein-frame action of the form (1), with a standard kinetic term, an exponential coupling function $A(\varphi)$, and a scalar-field potential $V(\varphi)$ [54]. The dilaton [55–57] and symmetron [58,59] models are also scalar-tensor theories of this form, but with different coupling functions $A(\varphi)$ and potentials $V(\varphi)$ (and standard kinetic terms). Finally, Galileon models [60–63] also involve a scalar field, with a nonstandard kinetic term (the scalar-field Lagrangian contains higher-order terms in $\nabla\varphi$ and $\nabla^2\varphi$), but there is no coupling function $A(\varphi)$ (i.e., $g_{\mu\nu} = \tilde{g}_{\mu\nu}$). (Of course, it is possible to build more complex models that combine these various ingredients.)

These different scenarios show different nonlinear screening mechanisms that ensure convergence to GR in the Solar System, chameleon [3] (for $f(R)$ models), Damour–Polyakov [5] (for dilaton and symmetron models), and Vainshtein [6] (for Galileon models) mechanisms. The theories that are closest to K-mouflage scenarios are the Galileon models, as their screening mechanism also relies on the nonlinear derivative terms of the scalar-field Lagrangian; but they also involve $\nabla^2\varphi$ instead of $\nabla\varphi$ only, which gives rise to different scaling exponents, for instance for the Vainshtein and K-mouflage screening radii as a function of the mass M of compact objects.

B. Einstein and Jordan frames

A first important difference between the K-mouflage scenario and these other modified-gravity models is the distinction between the Einstein and Jordan frames. As recalled above, this distinction does not apply to the (simplest) Galileon models, but the $f(R)$, dilaton, and symmetron models also naturally give rise to distinct Einstein and Jordan frames. However, it turns out that in these scenarios the coupling function is constrained to remain very close to unity. Thus, $|A - 1| \lesssim 10^{-4}$ for $f(R)$ models, because the “mass” of the scalar field must be sufficiently large, $m \gtrsim 10^3 H/c$, to ensure an efficient screening of the fifth force by a chameleon mechanism in the Solar System. For dilaton and symmetron models, we have $|A - 1| \lesssim 10^{-6}$ as the coupling strength β must vanish sufficiently fast in high-density regions to screen the fifth force through a Damour–Polyakov mechanism. This means that, in terms of background quantities (e.g., the Hubble expansion rate and the scale factor), one can identify the Einstein and Jordan frames, which also become almost identical to the Λ -CDM reference. However, at the level of the metric perturbations Φ and Ψ , this is no longer the case, and the Einstein and Jordan gravitational potentials differ by terms set by δA , and the dynamics of perturbations deviate from the Λ -CDM reference because of the fifth force.

In the K-mouflage case, this identification already breaks down at the background level. Indeed, $|A - 1|$ can reach values of the order of a few percents (see Fig. 6) while being consistent with Solar System and cosmological constraints [12]. For the same reason, the background dynamics (in both Einstein and Jordan frames) show percent deviations from the Λ -CDM reference. Therefore, we must pay attention to the distinction between Einstein and Jordan frames already at the background level. In particular, in this paper, as we study clusters of galaxies that involve atomic or radiative processes (both for the definition of their redshift, from atomic lines, and for their properties such as x-ray emission), the Jordan frame is the one that is more directly connected to observations, and we work in this frame. Another advantage of the Jordan frame is that the equations of motion take their usual form; in particular matter is conserved, which permits a clear and simple physical interpretation, and only gravity is modified. In contrast, in the Einstein frame, gravity takes a standard form, but the equations of motion are modified, and the matter density is usually not conserved.

C. Scale dependence and screening regime

A second important difference between the K-mouflage scenario and some other modified-gravity models is that the deviations from the Λ -CDM reference are scale independent on perturbative scales (from cluster scales to the horizon). This is most easily seen from the fact that the factor $\epsilon_1(t)$ that enters the evolution equation (55) of the linear growing mode only depends on time, so that the linear growing mode $D_+(t)$ remains scale independent

as in the Λ -CDM cosmology. This is due to the fact that in the scalar-field Lagrangian (6) we focused on the non-standard kinetic term and neglected a possible potential term $V(\varphi)$. Of course, in the highly nonlinear regime, a new scale dependence appears, as the fluctuations of the scalar field themselves become nonlinear and give rise to the K-mouflage screening mechanism, which ensures the convergence to GR in the Solar System. However, it happens that the screening transition appears at galaxy scales, so that clusters remain unscreened and fully feel the effect of the fifth force.

The same behavior is obtained in the Galileon models, where linear scales below the horizon show scale-independent growing modes and the Vainshtein screening mechanism applies to cluster scales and below [64,65]; but in the K-mouflage case, the nonlinear screening only applies to galaxy scales and below, as clusters remain unscreened. In contrast, in $f(R)$ and dilaton/symmetron models, there is a characteristic scale dependence, as we recover GR both on very large scales $x \gg 1h^{-1}$ Mpc (because of the finite mass of the scalar field) and on very small scales $x \ll 1h^{-1}$ Mpc (because of nonlinear screening mechanisms, here chameleon or Damour–Polyakov mechanisms [3,5]). Then, the linear growing mode $D_+(k, t)$ shows a clear scale dependence on quasilinear scales, and nonlinear screening effects also add a further scale dependence around $x \sim 1h^{-1}$ Mpc [66]. Thus, in these models, clusters probe a scale-dependent regime and the transition between the unscreened and screened regimes.

Therefore, clusters of galaxies are especially well-suited probes of K-mouflage scenarios because they are unscreened (hence they feel the full amplitude of the fifth force). Moreover, the modification of gravity is still scale independent on these scales so that cluster properties should not be too difficult to model (the same modelizations should apply equally well to the Λ -CDM and K-mouflage cosmologies).

D. Clusters

1. Cluster profiles

The effect of the fifth force on the cluster matter and gas profiles within the context of modified-gravity scenarios with chameleon mechanisms [mostly for $f(R)$ models] has been investigated in Refs. [67–70].

As recalled above, the fifth force effect is somewhat different between $f(R)$, dilaton and symmetron models, and K-mouflage scenarios. In the former cases, clusters are typically at the transition between the screened and unscreened regimes. Then, massive clusters are screened by the chameleon or Damour–Polyakov mechanisms (the deviations from GR being most efficiently suppressed in the symmetron models), while for low-mass clusters, only a small core is efficiently screened. In particular, for $f(R)$ and symmetron models, the amplification of gravity is

localized in the outskirts of massive clusters. This gives a distinct scale dependence of the modified-gravity effect in these theories [71,72], but the efficient screening also decreases the overall deviation from GR. See, for instance, Ref. [66] for a detailed analysis and comparison of these different models and Refs. [71,73–76] for numerical simulations of various models. In Galileon scenarios, depending on the model, clusters may be fully screened (and their profiles are similar to those of a quintessence model with no fifth force and the same expansion history) or only partly screened (which gives rise to complex effects) [65]. In the K-mouflage case, clusters still are in the unscreened regime. Therefore, there is no characteristic scale dependence that can be used to distinguish them from Λ -CDM cosmologies, but the amplitude of the smooth deviation is greater (as compared with screened scenarios).

There have been no specific simulations of K-mouflage models so far, but we can recall here some results from simulations of other modified-gravity models.

Reference [76] develops hydrodynamic N-body simulations to investigate the impact on dark matter and gas profiles of $f(R)$ and symmetron scenarios. In agreement with the discussion above, the authors find that the dark matter density is increased as compared with the Λ -CDM reference in the outskirts of massive halos. This is because the fifth force applies to outer radii, which are unscreened, and this also yields a greater velocity to the particles, which cannot cluster as strongly within inner radii. They also find a lower deviation from Λ -CDM for the gas density profile than for the dark matter density profile. They note that this may be due to delays in the collapse of the dark matter and the gas, with the screening of the halos taking place after dark matter collapse and before gas collapse. As explained above, for K-mouflage scenarios, we do not expect such a localized enhancement in the matter densities and different behaviors for the dark matter and the gas, because clusters are unscreened and the dynamics remains similar to the Λ -CDM cosmology, as illustrated by the explicit symmetry described in Sec. III G. In fact, in Fig. 14, we find that within our very simple model the deviation from Λ -CDM is slightly greater for the gas than for the dark matter [because of the small change in the concentration parameter and the higher sensitivity for the gas that arises from the exponential equilibrium distribution (98)].

We can note that N-body simulations of $f(R)$ models also find that in the case $f_{R_0} = -10^{-4}$, where chameleon screening is not efficient, deviations from Λ -CDM are smooth and the velocity dispersion σ_v^2 and gas temperature T_g are about 4/3 times the GR value [68,74], due to the 4/3 increase of the effective Newton constant. In our case, this corresponds to the $(1 + \epsilon_1)$ enhancement in Eq. (100), but with $\epsilon_1 \simeq 2\%$ instead of 1/3. These simulations also find that dark matter halos remain well described by NFW profiles [77]. These results suggest that our approach for

the density profiles and the gas temperature described in Secs. VA and VD should fare reasonably well.

For chameleon scenarios, Ref. [67] considers the effect of the fifth force on the cluster gas profile, which becomes more compact for a given dark matter profile [in our case, we also include the effect on the dark matter profile, through the modification of the concentration parameter shown in Fig. 12, and we assume an isothermal gas (i.e., $\gamma = 1$) instead of a polytropic equation of state $p_g \propto \rho_g^\gamma$ with $\gamma \sim 1.2$]. However, they find that observational error bars are too large to give useful constraints on $f(R)$ models. We reach the same conclusion for the K-mouflage models studied in this paper.

References [69,70] combine x-ray observations (which probe the temperature and electron number density profiles) and weak lensing signals (which probe the total matter profile) to constrain deviations from General Relativity. Indeed, while the gas profile is sensitive to the fifth force, the lensing deflection of light rays remains the same as in GR. This allows them to derive the upper bound $|f_{R_0}| \leq 6 \times 10^{-5}$. The same behavior applies to the K-mouflage scenario. In this paper, we found a few percent deviations from GR, which should apply to all realistic K-mouflage models that satisfy cosmological and Solar System constraints [as this is due to the constraint on the coupling β , independently of the details of the kinetic function $K(\chi)$]. We leave a more general Markov chain Monte Carlo (MCMC) analysis of K-mouflage scenarios, combining different probes, to future works.

2. Cluster scaling relations

The impact of $f(R)$ gravity on the cluster scaling relations has been studied in Ref. [68] with numerical simulations. Again, we find similar behaviors for the K-mouflage models as for the $f(R)$ model with $f_{R_0} = -10^{-4}$, where clusters are not screened. In particular, the dark matter velocity dispersion and gas temperature are increased, at fixed mass, and the x-ray luminosity is decreased, at fixed temperature, as compared with the Λ -CDM reference. However, whereas in $f(R)$ theories the deviations from Λ -CDM can reach a factor 1/3 in the unscreened regime, and deviations of order unity can also be expected in dilaton or symmetron models, realistic K-mouflage models can only deviate by a few percent at most. Indeed, the magnitude of these deviations is set by the factor ϵ_1 , which itself is set by $2\beta^2$ (at $z = 0$), and the coupling strength must satisfy $\beta \leq 0.1$ because of cosmological and Solar System constraints [12].

3. Cluster lensing; Dynamical and lensing masses

In $f(R)$, dilaton, and symmetron scenarios, the weak lensing potential Φ_{wl} that governs the deflection of light rays, given by $\Phi_{\text{wl}} = (\Phi + \Psi)/2$, is equal to the Newtonian potential Ψ_N [using $|f_{R_0}| \ll 1$ in the case of $f(R)$ theories] [78]. Then, for weak lensing observations, the only

difference from the Λ -CDM scenario comes from the different evolution of the matter density fields. In contrast, the motions of matter particles or of small halos (e.g., satellite halos or small galaxies), which fall toward massive clusters, feel the fifth force. This gives rise to different lensing and dynamical masses. This has been investigated in semianalytical models and N-body simulations [74,79] and used in Refs. [69,70] in combination with x-ray observations, for $f(R)$ theories, and in Ref. [80], using the galaxy infall kinematics onto massive clusters, for $f(R)$ and Galileon models.

In the K-mouflage scenario, we again have $\Phi_{\text{wl}} = \Psi_N$, as the factor $\delta A/\bar{A}$ cancels from the sum over the two metric potentials; see Eq. (41). However, in contrast with the former theories, the effective Newton constant [which enters the Newtonian potential (42)] now depends on time, as in Eq. (77). (This effect does not appear in the other scenarios because they have \bar{A} very close to unity, within 10^{-4} or better.) On the other hand, this time-dependent prefactor cancels from the ratio between the dynamical and lensing potentials or masses; see Eq. (113). However, whereas in $f(R)$ theories this ratio can again deviate from unity by a factor 1/3 in the unscreened regime, and deviations of order unity can also be reached in dilaton or symmetron models, in realistic K-mouflage models, this ratio can only deviate from unity by 2% at most because of observational constraint on the scalar-field coupling, $\beta \leq 0.1$. Therefore, K-mouflage models cannot significantly decrease the tension between measures of x-ray and lensing clusters masses.

4. Cluster number counts

In most modified-gravity scenarios, the growth of large-scale perturbations differs from the GR evolution. This typically leads to a new scale dependence of the linear growth rates (e.g., in $f(R)$, dilaton, and symmetron models), as one goes from the very large scales (beyond the Compton wavelength of the scalar field) where GR is recovered to the quasilinear scales where the fifth force is unscreened and gives its maximum amplification of the gravitational interaction (at smaller scales, nonlinear screening leads again to a convergence to GR). This amplification typically yields a faster growth of matter density perturbations on scales $1h^{-1}$ to $10h^{-1}$ Mpc, whence come a greater abundance of massive halos and clusters as compared with the Λ -CDM cosmology; see Refs. [65,73,81–84] for numerical studies of various models. As explained above, a similar enhancement is found in the K-mouflage scenarios, with the important difference that all clusters are unscreened and that the modification of gravity extends up to the horizon (so that the linear modes grow faster than in Λ -CDM but remain scale independent). In Galileon scenarios, the screening mechanism has a strong impact, and, depending on the models, the tail of the halo mass function can be either increased or decreased, as

compared with a quintessence scenario with the same expansion history [65].

The abundance of massive clusters has been used within $f(R)$ theories to constrain f_{R_0} [85–87]. In combination with CMB, baryon acoustic oscillations, and SNeIa Type Ia supernovae observations, one can obtain an upper bound $|f_{R_0}| \lesssim 1.7 \times 10^{-5}$ [86,87], but most of the constraint comes from the cluster data. We can expect that for K-mouflage models similar results should be obtained, especially since clusters are unscreened so that their abundance should provide useful constraints. In this paper, we presented the physics of K-mouflage scenarios on cluster scales, highlighting the difference between the Einstein and Jordan frames (which can be neglected in most other scenarios) and investigating both the modified growth of structures and halo mass functions and the modified cluster scaling laws. We leave a detailed MCMC analysis of the K-mouflage parameter space to future works.

5. Cluster correlation function

In modified-gravity scenarios, the correlation function and the power spectrum of the matter density field are often increased as the growth of large-scale structures is amplified by the fifth force. This also enhances the large-mass tail of the halo mass function and decreases the bias of massive halos as they become less rare. In the K-mouflage models that we considered in this paper, this decrease of the cluster bias mostly cancels the increase of the underlying matter density correlation, and the cluster correlation function is much closer to the Λ -CDM reference than the matter correlation itself. Therefore, the correlation of the matter density field, which can be measured from weak lensing observations, for instance, is a better probe of modified cosmology than the clustering of massive halos. The same effects, with a similar compensation between the smaller bias and the higher matter correlation (but the compensation may only be partial, depending on the model) appear in other modified-gravity scenarios; see, for instance, Ref. [88] for $f(R)$ theories.

E. Other tests

On slightly larger scales than those probed by clusters of galaxies, modified-gravity models have also been tested from galaxy surveys, using redshift-space distortions of the galaxy power spectrum [89], the clustering of Luminous Red Galaxies [65], or the shape of the galaxy correlation function itself [90]. Similar studies could be performed for K-mouflage models, as they can lead to 20% deviations for the matter power spectrum and correlation function, as seen in Fig. 11. This will be investigated in future works.

In between the cluster and cosmological scales (e.g., the formation of large-scale structures and the background dynamics) and the Solar System scales (where we must recover GR up to a very high accuracy), modified-gravity

theories have also been tested on intermediate galaxy scales. In particular, within chameleon scenarios, low-mass galaxies should be unscreened so that the rotation curve of their diffuse gas component probes the fifth force, while their stars, being compact high-density objects, are screened and move as in GR [91]. This can provide constraints as tight as $|f_{R_0}| \leq 10^{-6}$ for $f(R)$ theories [92]. The same behaviors apply to K-mouflage models, and we can expect that such tests could also provide useful constraints on these scenarios. We leave this task to future studies.

Numerical simulations have also been used to investigate the impact of $f(R)$ theories on Lyman- α forest observations (the transmitted flux fraction and the flux power spectrum) [93]. They find changes that are too small as compared with observational error bars and do not provide competitive constraints. Although this study does not distinguish the impact of screening effects, screening can be expected to be rather inefficient for such moderate density fluctuations. Therefore, it is likely that similar conclusions would be reached for K-mouflage models, but we leave a detailed study for future works.

VII. CONCLUSIONS

We have extended previous works on K-mouflage models by deriving the equations of motion in both the Einstein and Jordan frames for a fluid with pressure and next focusing on the usual case where the pressure arises from small-scale nonlinear processes. In contrast with many modified-gravity scenarios, the Einstein and Jordan frames already differ by a few percent at the background level, for K-mouflage models that are consistent with cosmological and Solar System constraints. Therefore, one must take into account these deviations and use the correct quantities when comparing with observations.

We focused on the Jordan frame, which is better suited to cosmological probes that involve atomic processes, such as x-ray clusters. We show that, even though K-mouflage models only differ from the Λ -CDM reference by a few percent at the background level, the linear growing modes can deviate by 10%, and the matter density power spectrum and correlation function by 30%. The tail of the halo mass function is enhanced by factors of order unity for $M \gtrsim 10^{14} h^{-1} M_\odot$ at $z = 0$.

Galaxy clusters are not screened by the K-mouflage mechanism, contrary to what happens for chameleon models like $f(R)$ in the large curvature limit or Galileon models subject to the Vainshtein screening. For this reason, we investigate the effects of the K-mouflage modification of gravity on clusters. We take into account the impact of the fifth force mediated by the K-mouflage scalar field on both the dark matter and gas profiles, through the modifications to the growth of large-scale structures and to the hydrostatic equilibrium. We find that K-mouflage makes

clusters slightly more compact. Similarly, the gas temperature and the x-ray luminosity differ from their Λ -CDM counterparts by a few percent, an order of magnitude which follows directly from the constraints on K-mouflage (especially on the coupling strength β) due to Solar System tests. The only deviation of noticeable order appears in the cluster temperature function, as the number of clusters is larger than in the Λ -CDM scenario for K-mouflage models, because of the faster growth of large-scale structures. This appears to be large enough that one can hope that this will be within the reach of the future large-scale surveys. On the other hand, the cluster correlation function only deviates by a few percent from the Λ -CDM case because the increase of the underlying matter density correlation function is compensated by the lower cluster bias, as massive halos become less rare at fixed mass, due to the enhanced structure formation.

In this paper, we only considered two kinetic functions $K(\tilde{\chi})$ to illustrate the K-mouflage scenarios and to estimate the amplitude of the effects that can be reached by realistic models, which are consistent with cosmological and Solar System constraints. We leave to future works a more detailed MCMC analysis of K-mouflage scenarios, which would provide the parameter space of K-mouflage models that is allowed by cluster observations and combinations with other observational probes.

ACKNOWLEDGMENTS

This work is supported in part by the French Agence Nationale de la Recherche under Grant No. ANR-12-BS05-0002. P.B. acknowledges partial support from the European Union FP7 ITN INVISIBLES (Marie Curie Actions, Grant No. PITN-GA-2011-289442) and from the Agence Nationale de la Recherche under Contract No. ANR 2010 BLANC 0413 01.

APPENDIX A: EQUATIONS OF MOTION IN THE EINSTEIN FRAME

In this Appendix, we derive the equations of motion of the scalar field and of the matter component in the Einstein frame, for a cosmological fluid with a nonzero pressure. The derivation is similar to the one presented in previous papers [7,8], where we studied the background cosmological dynamics and the formation of large-scale cosmological structures, but with the addition of the pressure terms.

1. Energy-momentum tensors and equations of motion

We consider three components of the energy density of the Universe, a matter fluid with nonzero pressure, radiation, and the scalar field. The Einstein-frame and Jordan-frame matter energy-momentum tensors are given by Eq. (10), and they satisfy the relations (11). Assuming a perfect fluid, the matter energy-momentum tensor is written as

$$\tilde{T}_\nu^\mu = (\tilde{\rho} + \tilde{p})\tilde{u}^\mu\tilde{u}_\nu + \tilde{p}\delta_\nu^\mu, \quad (\text{A1})$$

where \tilde{u}^μ is the velocity 4-vector, normalized such that $\tilde{u}^\mu\tilde{u}_\mu = -1$, and $\tilde{\rho}$ and \tilde{p} are the Einstein-frame density and pressure, which are related to their Jordan-frame counterparts by Eq. (12).

For the radiation component, we neglect perturbations and only consider the contribution to the background, with the mean density and pressure $\tilde{\rho}_{(r)}$ and $\tilde{p}_{(r)} = \tilde{\rho}_{(r)}/3$. Their Jordan-frame counterparts are again given as in Eq. (12).

The Einstein-frame energy-momentum tensor of the scalar field reads as

$$\tilde{T}_{\mu\nu(\varphi)} = \frac{-2}{\sqrt{-\tilde{g}}}\frac{\delta S_\varphi}{\delta \tilde{g}^{\mu\nu}} = K'\tilde{\nabla}_\mu\varphi\tilde{\nabla}_\nu\varphi + \mathcal{M}^4 K\tilde{g}_{\mu\nu}. \quad (\text{A2})$$

The Klein–Gordon equation that governs the dynamics of the scalar field φ is obtained from the variation of the action (1) with respect to φ . This yields

$$\tilde{\nabla}_\mu[\tilde{\nabla}^\mu\varphi K'] = (\tilde{\rho} - 3\tilde{p})\frac{d\ln A}{d\varphi}. \quad (\text{A3})$$

Here we used the fact that the trace of the matter energy-momentum tensor is $\tilde{T}_\mu^\mu = -\tilde{\rho} + 3\tilde{p}$, from Eq. (A1), while it is zero for the radiation component as $\tilde{p}_{(r)} = \tilde{\rho}_{(r)}/3$. Combining with Eq. (A2), we find for the scalar field the “nonconservation” equation

$$\tilde{\nabla}_\mu\tilde{T}_{\nu(\varphi)}^\mu = (\tilde{\rho} - 3\tilde{p})\tilde{\nabla}_\nu\ln A. \quad (\text{A4})$$

The matter energy-momentum tensor is conserved in the Jordan frame,

$$\nabla_\mu T_\nu^\mu = 0, \quad (\text{A5})$$

which gives in the Einstein frame the nonconservation equation

$$\tilde{\nabla}_\mu\tilde{T}_\nu^\mu = -(\tilde{\rho} - 3\tilde{p})\tilde{\nabla}_\nu\ln A. \quad (\text{A6})$$

On the other hand, the radiation energy-momentum tensor is conserved in both frames,

$$\nabla_\mu T_{\nu(r)}^\mu = 0, \quad \tilde{\nabla}_\mu\tilde{T}_{\nu(r)}^\mu = 0. \quad (\text{A7})$$

The sum of all energy-momentum tensors is also conserved in both frames, and $\tilde{\nabla}_\mu[\tilde{T}_\nu^\mu + \tilde{T}_{\nu(r)}^\mu + \tilde{T}_{\nu(\varphi)}^\mu] = \nabla_\mu[T_\nu^\mu + T_{\nu(r)}^\mu + T_{\nu(\varphi)}^\mu] = 0$.

Finally, in the Einstein frame, the Einstein equations take the usual form, $\tilde{M}_{\text{Pl}}^2\tilde{G}_\nu^\mu = \tilde{T}_\nu^\mu + \tilde{T}_{\nu(r)}^\mu + \tilde{T}_{\nu(\varphi)}^\mu$.

2. Background dynamics

At the level of the cosmological background, the Friedmann equations take the usual form in the Einstein frame,

$$3\tilde{M}_{\text{Pl}}^2\tilde{H}^2 = \tilde{\rho} + \tilde{\rho}_{(r)} + \tilde{\rho}_\varphi, \quad (\text{A8})$$

$$-2\tilde{M}_{\text{Pl}}^2\frac{d\tilde{H}}{d\tilde{t}} = \tilde{\rho} + \tilde{p} + \tilde{\rho}_{(r)} + \tilde{p}_{(r)} + \tilde{\rho}_\varphi + \tilde{p}_\varphi, \quad (\text{A9})$$

where $\tilde{\rho}_\varphi$ and \tilde{p}_φ are the background scalar-field energy density and pressure (in the Einstein frame), given by Eq. (17).

The Klein–Gordon equation (A3) gives

$$\frac{d}{d\tilde{t}} \left[\tilde{a}^3 \frac{d\tilde{\varphi}}{d\tilde{t}} \tilde{K}' \right] = -\tilde{a}^3 (\tilde{\rho} - 3\tilde{p}) \frac{d \ln \tilde{A}}{d\tilde{t}}, \quad (\text{A10})$$

and the scalar-field energy density satisfies

$$\frac{d\tilde{\rho}_\varphi}{d\tilde{t}} = -3\tilde{H}(\tilde{\rho}_\varphi + \tilde{p}_\varphi) - (\tilde{\rho} - 3\tilde{p}) \frac{d \ln \tilde{A}}{d\tilde{t}}. \quad (\text{A11})$$

The nonconservation equation (A6) gives for the matter density the evolution equation

$$\frac{d\tilde{\rho}}{d\tilde{t}} = -3\tilde{H}(\tilde{\rho} + \tilde{p}) + (\tilde{\rho} - 3\tilde{p}) \frac{d \ln \tilde{A}}{d\tilde{t}}. \quad (\text{A12})$$

In particular, we have $d(\tilde{\rho} + \tilde{\rho}_\varphi)/d\tilde{t} = -3\tilde{H}(\tilde{\rho} + \tilde{p} + \tilde{\rho}_\varphi + \tilde{p}_\varphi)$. When the pressure is zero, we can define a conserved density $\hat{\rho}$ by

$$\hat{\rho} = \tilde{\rho}/A, \quad \hat{p} = \tilde{p}/A. \quad (\text{A13})$$

Indeed, substituting into Eq. (A12) gives

$$\frac{d\hat{\rho}}{d\tilde{t}} = -3\tilde{H}(\hat{\rho} + \hat{p}) - 3\tilde{p} \frac{d \ln \tilde{A}}{d\tilde{t}}. \quad (\text{A14})$$

Thus, if $\hat{p} = 0$, we obtain a conservation of the standard form in the Einstein frame, $d\hat{\rho}/d\tilde{t} = -3\tilde{H}\hat{\rho}$. However, if $\hat{p} \neq 0$, it is no longer possible to cancel the nonconservation term of Eq. (A12) by such a simple redefinition of the density.

The background radiation density obeys the usual conservation equation,

$$\frac{d\tilde{\rho}_{(r)}}{d\tilde{t}} = -3\tilde{H}(\tilde{\rho}_{(r)} + \tilde{\rho}_{(r)}) = -4\tilde{H}\tilde{\rho}_{(r)}, \quad (\text{A15})$$

in agreement with the second Eq. (A7).

3. Perturbations

In the conformal Newtonian gauge, the Einstein-frame metric can be written as

$$d\tilde{s}^2 = \tilde{a}^2 [-(1 + 2\tilde{\Phi})d\tau^2 + (1 - 2\tilde{\Psi})d\mathbf{x}^2], \quad (\text{A16})$$

where $\tau = \int d\tilde{t}/\tilde{a}$ is the conformal time and $\tilde{\Phi}$ and $\tilde{\Psi}$ are the two metric gravitational potentials. Throughout this paper, we consider the nonrelativistic and weak-gravitational-fields regime, with $\tilde{\Phi} \ll 1$, $\tilde{\Psi} \ll 1$, $v^2 \ll 1$ (where $\mathbf{v} = d\mathbf{x}/d\tau$ is the peculiar velocity of the particles), and we expand up to first order in $\{\tilde{\Phi}, \tilde{\Psi}, v^2\}$. Then, in the final equations, we only keep zeroth-order terms, $1 + \tilde{\Psi} \simeq 1$ and $1 + v^2 \simeq 1$, except when the potentials or the velocity arises with a gradient operator, as in Eqs. (A24) and (A27). In particular, we have for the matter velocity 4-vector

$$\begin{aligned} \tilde{u}^\mu &= \tilde{a}^{-1}(1 - \tilde{\Phi} + v^2/2, v^i), \\ \tilde{u}_\mu &= -\tilde{a}(1 + \tilde{\Phi} + v^2/2, -v_i), \end{aligned} \quad (\text{A17})$$

where we denote

$$v_i = v^i = \frac{dx^i}{d\tau} \quad (\text{A18})$$

the peculiar velocity.

The nonconservation equation (A6) gives

$$\begin{aligned} (\dot{\tilde{\rho}} + \dot{\tilde{p}})\tilde{u}_\nu + 3\tilde{h}(\tilde{\rho} + \tilde{p})\tilde{u}_\nu + (\tilde{\rho} + \tilde{p})\dot{\tilde{u}}_\nu + \tilde{\nabla}_\nu\tilde{p} \\ = -(\tilde{\rho} - 3\tilde{p})\tilde{\nabla}_\nu(\ln A), \end{aligned} \quad (\text{A19})$$

where we have introduced

$$\dot{\tilde{\rho}} \equiv \tilde{u}^\mu \tilde{\nabla}_\mu \tilde{\rho}, \quad \dot{\tilde{u}}_\nu \equiv \tilde{u}^\mu \tilde{\nabla}_\mu \tilde{u}_\nu, \quad 3\tilde{h} \equiv \tilde{\nabla}_\mu \tilde{u}^\mu. \quad (\text{A20})$$

Contracting with \tilde{u}^ν and using $\tilde{u}^\nu \tilde{u}_\nu = -1$, we get

$$\dot{\tilde{\rho}} + 3\tilde{h}(\tilde{\rho} + \tilde{p}) = (\tilde{\rho} - 3\tilde{p}) \frac{\dot{A}}{A}. \quad (\text{A21})$$

It is easy to see that $\dot{\tilde{\rho}} = \tilde{a}^{-1}[\partial_\tau \tilde{\rho} + (\mathbf{v} \cdot \nabla)\tilde{\rho}]$, where $\nabla \equiv \partial/\partial \mathbf{x}$ is the standard 3D spatial gradient, and $3\tilde{h} = \tilde{a}^{-1}[3\tilde{\mathcal{H}} + (\nabla \cdot \mathbf{v})]$, where $\tilde{\mathcal{H}} = d \ln \tilde{a}/d\tau$ is the conformal expansion rate in the Einstein frame. Therefore, this is explicitly

$$\begin{aligned} \frac{\partial \tilde{\rho}}{\partial \tau} + (\mathbf{v} \cdot \nabla)\tilde{\rho} + (3\tilde{\mathcal{H}} + \nabla \cdot \mathbf{v})(\tilde{\rho} + \tilde{p}) \\ = (\tilde{\rho} - 3\tilde{p}) \left[\frac{\partial \ln A}{\partial \tau} + (\mathbf{v} \cdot \nabla) \ln A \right]. \end{aligned} \quad (\text{A22})$$

Next, the nonconservation equation (A19) can be simplified by subtracting Eq. (A21) multiplied by \tilde{u}_ν . This leads to

$$\dot{\tilde{u}}_\nu = -\frac{\tilde{\nabla}_\nu \tilde{p} + \tilde{u}_\nu \dot{\tilde{p}}}{\tilde{\rho} + \tilde{p}} - \frac{\tilde{\rho} - 3\tilde{p}}{\tilde{\rho} + \tilde{p}} \frac{\tilde{\nabla}_\nu A + \tilde{u}_\nu \dot{A}}{A}. \quad (\text{A23})$$

This is the generalized geodesic equation. Specializing to $\mu = i$, we get the Euler equation of K-mouflage hydrodynamics,

$$\begin{aligned} \frac{\partial \mathbf{v}}{\partial \tau} + (\mathbf{v} \cdot \nabla) \mathbf{v} + \left(\tilde{\mathcal{H}} + \frac{1}{\tilde{\rho} + \tilde{p}} \frac{\partial \tilde{p}}{\partial \tau} + \frac{\tilde{\rho} - 3\tilde{p}}{\tilde{\rho} + \tilde{p}} \frac{\partial \ln A}{\partial \tau} \right) \mathbf{v} \\ = -\nabla \tilde{\Phi} - \frac{\nabla \tilde{p}}{\tilde{\rho} + \tilde{p}} - \frac{\tilde{\rho} - 3\tilde{p}}{\tilde{\rho} + \tilde{p}} \nabla \ln A. \end{aligned} \quad (\text{A24})$$

From Eq. (A24), we can see that $(\mathbf{v} \cdot \nabla) \ln A \sim \partial_\tau v^2 + v^2 (\nabla \cdot \mathbf{v})$, and hence this term can be neglected in the continuity equation (A22) in the nonrelativistic limit $v^2 \ll 1$. This simplifies as

$$\frac{\partial \tilde{\rho}}{\partial \tau} + (\mathbf{v} \cdot \nabla) \tilde{\rho} + (3\tilde{\mathcal{H}} + \nabla \cdot \mathbf{v})(\tilde{\rho} + \tilde{p}) = (\tilde{\rho} - 3\tilde{p}) \frac{\partial \ln A}{\partial \tau}. \quad (\text{A25})$$

The Klein–Gordon equation (A3) is written as

$$\frac{1}{\tilde{a}^3} \frac{\partial}{\partial \tilde{t}} \left(\tilde{a}^3 \frac{\partial \varphi}{\partial \tilde{t}} K' \right) - \frac{1}{\tilde{a}^2} \nabla \cdot (\nabla \varphi K') = -(\tilde{\rho} - 3\tilde{p}) \frac{d \ln A}{d \varphi}. \quad (\text{A26})$$

The (0,0) component of Einstein equations, $\tilde{M}_{\text{Pl}}^2 \tilde{G}_0^0 = \tilde{T}_0^0 + \tilde{T}_{0(\varphi)}^0$, gives

$$\tilde{\Psi} = \tilde{\Psi}_N \quad \text{with} \quad \frac{1}{\tilde{a}^2} \nabla^2 \tilde{\Psi}_N = \frac{1}{2\tilde{M}_{\text{Pl}}^2} (\delta \tilde{\rho} + \delta \tilde{\rho}_\varphi), \quad (\text{A27})$$

where $\delta \tilde{\rho} = \tilde{\rho} - \bar{\rho}$ and $\delta \tilde{\rho}_\varphi = \tilde{\rho}_\varphi - \bar{\rho}_\varphi$, with $\tilde{\rho}_\varphi = -\mathcal{M}^4 K + K' (\partial \varphi / \partial \tilde{t})^2$. Here we denoted $\tilde{\Psi}_N$ the usual Newtonian potential. The (i, j) components of the Einstein equations give (focusing on the part that is not proportional to δ_j^i)

$$\frac{\tilde{M}_{\text{Pl}}^2}{\tilde{a}^2} \partial_i \partial_j (\tilde{\Psi} - \tilde{\Phi}) = (\tilde{\rho} + \tilde{p}) v_i v_j + \frac{K'}{\tilde{a}^2} \partial_i \varphi \partial_j \varphi. \quad (\text{A28})$$

From Eq. (A27), we can see that on the left-hand side in Eq. (A28) we have $\tilde{M}_{\text{Pl}}^2 \tilde{a}^{-2} \partial_i \partial_j \tilde{\Psi} \sim \delta \tilde{\rho} \sim \tilde{\rho}$. Therefore, the first term on the right-hand side, $(\tilde{\rho} + \tilde{p}) v_i v_j$, is negligible as $v^2 \ll 1$. Next, from the Klein–Gordon equation (A26), we obtain, on scales that are much smaller than the horizon,

$$k/\tilde{a} \tilde{H} \gg 1: \delta \varphi \sim \frac{\beta}{\tilde{M}_{\text{Pl}}} \frac{\tilde{a}^2 \delta \tilde{\rho} - 3\delta \tilde{p}}{k^2 K'}, \quad (\text{A29})$$

where k is the typical comoving wave number of interest. Then, the second term in the right-hand side in Eq. (A28) is of order

$$\frac{K'}{\tilde{a}^2} \partial_i \varphi \partial_j \varphi \sim \delta \tilde{\rho} \frac{\delta \tilde{\rho}}{\tilde{\rho}} \frac{\beta^2}{K'} \frac{\tilde{a}^2 \tilde{H}^2}{k^2} \ll \delta \tilde{\rho}, \quad (\text{A30})$$

which is again negligible compared to $\tilde{M}_{\text{Pl}}^2 \tilde{a}^{-2} \partial_i \partial_j \tilde{\Psi}$. Therefore, the Einstein equations (A28) give

$$\tilde{\Phi} = \tilde{\Psi} = \tilde{\Psi}_N, \quad (\text{A31})$$

within the approximations that we use in this paper.

To close the system formed by the equations of motion obtained above, we must specify the pressure, for instance, through an (effective) equation of state such as $\tilde{p} = w\tilde{\rho}$ with some parameter w .

4. Pressure due to small-scale nonlinear physics

In the previous sections, we derived the equations of motion for a cosmological fluid with a nonzero pressure, in the nonrelativistic limit $v^2 \ll 1$ for the mean fluid velocity and in the weak field regime $\tilde{\Psi}_N \ll 1$. We made no approximation for the pressure, and the equations of motion also apply to fluids with a pressure of the same order as the density, such as $\tilde{p} = w\tilde{\rho}$ where w is a parameter of order unity. However, in the usual CDM context, the pressure is negligible on cosmological scales, and it is built on small scales by nonlinear processes, such as the collapse of gas clouds that generate shocks or the virialization of dark matter halos (which generate an effective pressure through the velocity dispersion of the particles). Then, the pressure is of the order $\tilde{p} \sim \tilde{\rho} c_s^2$, where c_s is the speed of sound or the velocity dispersion, and $c_s^2 \sim \tilde{\Psi}_N$ because it is generated by the gravitational collapse (for instance, if we have hydrostatic equilibrium, we typically have $\nabla \tilde{\Psi}_N \sim \nabla \tilde{p}/\tilde{\rho}$ as the pressure balances gravity).

Then, in the regime $\tilde{p}/\tilde{\rho} \sim \tilde{\Psi}_N \sim v^2 \ll 1$, the background pressure is zero, $\bar{\tilde{p}} = 0$, and we recover the cosmological dynamics studied in Ref. [7] for a pressureless fluid. Thus, the Friedmann equations read as Eqs. (14) and (15), and the matter and radiation densities evolve as in Eq. (16). The Klein–Gordon equation becomes as in Eq. (19).

For the perturbations, the continuity and Euler equations (A25) and (A24) simplify as

$$\frac{\partial \tilde{\rho}}{\partial \tau} + \nabla \cdot (\tilde{\rho} \mathbf{v}) + 3\tilde{\mathcal{H}} \tilde{\rho} = \tilde{\rho} \frac{\partial \ln A}{\partial \tau}, \quad (\text{A32})$$

and

$$\begin{aligned} \frac{\partial \mathbf{v}}{\partial \tau} + (\mathbf{v} \cdot \nabla) \mathbf{v} + \left(\tilde{\mathcal{H}} + \frac{\partial \ln A}{\partial \tau} \right) \mathbf{v} \\ = -\nabla (\tilde{\Psi}_N + \ln A) - \frac{\nabla \tilde{p}}{\tilde{\rho}}, \end{aligned} \quad (\text{A33})$$

while the Poisson equation remains identical to Eq. (A27) and the Klein–Gordon equation (A26) becomes

$$\frac{1}{\tilde{a}^3} \frac{\partial}{\partial \tilde{t}} \left(\tilde{a}^3 \frac{\partial \varphi}{\partial \tilde{t}} K' \right) - \frac{1}{\tilde{a}^2} \nabla \cdot (\nabla \varphi K') = -\tilde{\rho} \frac{d \ln A}{d \varphi}. \quad (\text{A34})$$

Therefore, in this regime, the only effect of the pressure is to add the usual pressure term in the Euler equation, without mixed terms involving the coupling function $A(\varphi)$.

5. Subhorizon regime

To simplify the Einstein equations (A28), we already used the small-scale limit, $k/\tilde{a}\tilde{H} \gg 1$, which corresponds to scales that are much below the Hubble scale $\tilde{r}_H = 1/\tilde{H}$. This is the regime that is relevant for the formation of cosmological large-scale structures, such as clusters of galaxies. Then, the continuity and Euler equations (A32)–(A33) and the Poisson equation (A27) can be further simplified. Indeed, as in Eq. (A29), we obtain the estimates

$$k/\tilde{a}\tilde{H} \gg 1: \frac{\delta\varphi}{\tilde{M}_{\text{Pl}}} \sim \frac{\beta}{K'} \frac{\tilde{a}^2 \tilde{H}^2}{k^2} \frac{\delta\tilde{\rho}}{\tilde{\rho}} \ll \frac{\delta\tilde{\rho}}{\tilde{\rho}}, \quad (\text{A35})$$

$$\delta A \sim \frac{\beta\delta\varphi}{\tilde{M}_{\text{Pl}}} \sim \frac{\beta^2}{K'^2} \frac{\tilde{a}^2 \tilde{H}^2}{k^2} \frac{\delta\tilde{\rho}}{\tilde{\rho}} \ll \frac{\delta\tilde{\rho}}{\tilde{\rho}}, \quad (\text{A36})$$

$$\delta\tilde{\chi} \approx -\frac{(\nabla\delta\varphi)^2}{2\mathcal{M}^4\tilde{a}^2} \sim \frac{\beta^2}{K'^2} \frac{\tilde{a}^2 \tilde{H}^2}{k^2} \frac{(\delta\tilde{\rho})^2}{\tilde{\rho}^2} \ll \frac{(\delta\tilde{\rho})^2}{\tilde{\rho}^2}, \quad (\text{A37})$$

$$\frac{\delta\tilde{\rho}_\varphi}{\delta\tilde{\rho}} \sim \frac{\beta^2}{K'} \frac{\tilde{a}^2 \tilde{H}^2}{k^2} \left(1 + \frac{\delta\tilde{\rho}}{\tilde{\rho}}\right) \ll 1. \quad (\text{A38})$$

Then, in the continuity and Euler equations (A32) and (A33), we can write $\partial \ln A / \partial \tau \approx d \ln \bar{A} / d\tau$, which leads to Eqs. (20) and (21). In the Poisson equation (A27), we can neglect $\delta\tilde{\rho}_\varphi$, which gives Eq. (22). In the Klein–Gordon equation (A34), we can neglect the fluctuations of A and only keep the spatial gradients. This leads to Eq. (23), which also corresponds to the quasistatic approximation.

6. Formation of large-scale structures

Introducing the Einstein-frame matter density contrast,

$$\tilde{\delta} = \delta\tilde{\rho}/\tilde{\rho}, \quad (\text{A39})$$

the continuity equation (20) is also written as

$$\frac{\partial\tilde{\delta}}{\partial\tau} + \nabla \cdot [(1 + \tilde{\delta})\mathbf{v}] = 0. \quad (\text{A40})$$

Thus, in terms of the density contrast, we recover the usual continuity equation, without any A -term left. This is related to the fact that $\tilde{\delta} = \hat{\delta}$, where $\hat{\delta} = \delta\hat{\rho}/\hat{\rho}$ is the conserved matter density introduced in Eq. (A13), within our set of approximations ($\tilde{\rho} \ll \hat{\rho}$ and $A \approx \bar{A}$, so that the factor \bar{A} cancels out in the ratio $\delta\hat{\rho}/\hat{\rho}$).

On perturbative scales, we set the pressure term to zero, as in standard perturbation theory, because it is generated by nonperturbative effects such as shell crossing and virialization (shocks). Then, the formation of large-scale structures can be tackled through a perturbative approach, as in the usual Λ -CDM case. Introducing the two-component vector $\tilde{\psi}$,

$$\tilde{\psi} \equiv \begin{pmatrix} \tilde{\psi}_1 \\ \tilde{\psi}_2 \end{pmatrix} \equiv \begin{pmatrix} \tilde{\delta} \\ -(\nabla \cdot \mathbf{v}) / (d\tilde{a}/d\tilde{t}) \end{pmatrix}, \quad (\text{A41})$$

equations (A40) and (21) read in Fourier space as

$$\frac{\partial\tilde{\psi}_1}{\partial \ln \tilde{a}} - \tilde{\psi}_2 = \int d\mathbf{k}_1 d\mathbf{k}_2 \delta_D(\mathbf{k}_1 + \mathbf{k}_2 - \mathbf{k}) \hat{\alpha}(\mathbf{k}_1, \mathbf{k}_2) \times \tilde{\psi}_2(\mathbf{k}_1) \tilde{\psi}_1(\mathbf{k}_2), \quad (\text{A42})$$

$$\begin{aligned} \frac{\partial\tilde{\psi}_2}{\partial \ln \tilde{a}} - \frac{3}{2} \tilde{\Omega}_m(1 + \tilde{\epsilon}_1) \tilde{\psi}_1 + \left(2 + \frac{1}{\tilde{H}^2} \frac{d\tilde{H}}{d\tilde{t}} + \tilde{\epsilon}_2\right) \tilde{\psi}_2 \\ = \int d\mathbf{k}_1 d\mathbf{k}_2 \delta_D(\mathbf{k}_1 + \mathbf{k}_2 - \mathbf{k}) \hat{\beta}(\mathbf{k}_1, \mathbf{k}_2) \tilde{\psi}_2(\mathbf{k}_1) \tilde{\psi}_2(\mathbf{k}_2), \end{aligned} \quad (\text{A43})$$

with

$$\begin{aligned} \hat{\alpha}(\mathbf{k}_1, \mathbf{k}_2) &= \frac{(\mathbf{k}_1 + \mathbf{k}_2) \cdot \mathbf{k}_1}{k_1^2}, \\ \hat{\beta}(\mathbf{k}_1, \mathbf{k}_2) &= \frac{|\mathbf{k}_1 + \mathbf{k}_2|^2 (\mathbf{k}_1 \cdot \mathbf{k}_2)}{2k_1^2 k_2^2}. \end{aligned} \quad (\text{A44})$$

The two differences from the equations of motion obtained in the Λ -CDM cosmology are the two time-dependent factors $\tilde{\epsilon}_i(t)$, defined by

$$\tilde{\epsilon}_1(\tilde{t}) \equiv \frac{2\beta^2}{\tilde{K}'}, \quad \tilde{\epsilon}_2(\tilde{t}) \equiv \frac{d \ln \bar{A}}{d \ln \tilde{a}} = \frac{\beta}{\tilde{M}_{\text{Pl}}} \frac{d\tilde{\varphi}}{d \ln \tilde{a}}. \quad (\text{A45})$$

In Eq. ((A43)) the factor $\tilde{\Omega}_m(1 + \tilde{\epsilon}_1)$ can also be written as $\hat{\Omega}_m(1 + \hat{\epsilon}_1)$, where $\hat{\Omega}_m$ is the cosmological parameter associated with the conserved density $\hat{\rho}$ defined in Eq. ((A13)), [$\hat{\Omega}_m = \hat{\rho}/\hat{\rho}_{\text{crit}} = \tilde{\Omega}_m/\bar{A}$, with $\hat{\rho}_{\text{crit}} = 3\tilde{M}_{\text{Pl}}^2 \tilde{H}^2$ the Einstein-frame critical density], and $\hat{\epsilon}_1 = \bar{A}(1 + \tilde{\epsilon}_1) - 1 = \bar{A} - 1 + 2\bar{A}\beta^2/\tilde{K}'$.

On large scales or at early times, we can linearize the equations of motion (A42), (A43). This gives for the linear growing and decaying modes $\tilde{D}_\pm(\tilde{t})$ the evolution equation

$$\frac{d^2\tilde{D}}{d(\ln \tilde{a})^2} + \left(2 + \frac{1}{\tilde{H}^2} \frac{d\tilde{H}}{d\tilde{t}} + \tilde{\epsilon}_2\right) \frac{d\tilde{D}}{d \ln \tilde{a}} - \frac{3}{2} \tilde{\Omega}_m(1 + \tilde{\epsilon}_1) \tilde{D} = 0. \quad (\text{A46})$$

APPENDIX B: COMPARISON OF EINSTEIN-FRAME AND JORDAN-FRAME BACKGROUNDS

In this Appendix, we compare the Einstein-frame background quantities with their Jordan-frame counterparts. We show in Fig. 20 the relative deviation of the Einstein-frame Hubble rate from the Jordan-frame Hubble rate. From Eq. (24), this is given by

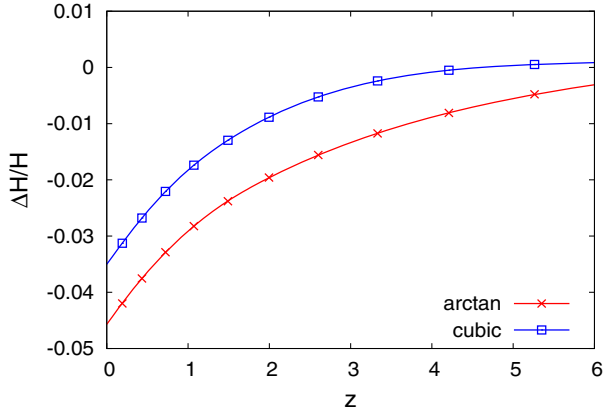


FIG. 20 (color online). Relative deviation, $\tilde{H}/H - 1$, of the Einstein-frame Hubble rate from the Jordan-frame Hubble rate, as a function of the Jordan-frame redshift.

$$\frac{\tilde{H} - H}{H} = \bar{A}(1 - \epsilon_2) - 1. \quad (\text{B1})$$

We can see that at low redshift the Einstein-frame Hubble rate is typically lower than its Jordan-frame counterpart, at a fixed Jordan-frame redshift. The comparison with Fig. 2 shows that at $z \lesssim 4$ the deviation between these two expansion rates is greater than the deviation between the Jordan-frame expansion and its Λ -CDM reference. As expected, this deviation is again of the order of a few percent, set by the value of β^2 . This clearly shows that for the K-mouflage scenario one cannot treat both frames as approximately identical, contrary to what happens in many modified-gravity theories such as $f(R)$ models or dilaton models. At high z , the relative difference between both Hubble rates vanishes, as can be seen from Eq. (24) as $\bar{A} \rightarrow 1$ and $\epsilon_2 \rightarrow 0$.

We show in Fig. 21 the deviation between the Einstein-frame and Jordan-frame density cosmological parameters. More precisely, for the Einstein frame, we consider the cosmological conserved matter density $\hat{\rho}$ introduced in Eq. (A13). Using Eq. (37), this is given by

$$\hat{\Omega}_m = \frac{\tilde{\Omega}_m}{\bar{A}} = \frac{\Omega_m}{\bar{A}(1 - \epsilon_2)^2}. \quad (\text{B2})$$

On the other hand, the radiation density parameter in the Einstein frame is $\hat{\Omega}_{(r)} = \Omega_{(r)}/(1 - \epsilon_2)^2$, from Eq. (37), and the Einstein-frame dark-energy density is then

$$\hat{\Omega}_{\text{de}} \equiv 1 - \hat{\Omega}_m - \hat{\Omega}_{(r)} = \frac{\bar{A} - 1}{\bar{A}} \tilde{\Omega}_m + \tilde{\Omega}_\varphi. \quad (\text{B3})$$

Again, we find in Fig. 21 that the differences between the Einstein-frame and Jordan-frame cosmological parameters are of the order of 1%.

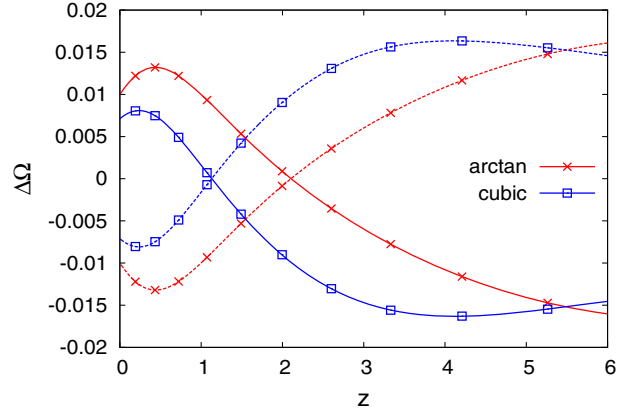


FIG. 21 (color online). Deviation of the Einstein-frame cosmological parameters from their Jordan-frame counterparts, $\hat{\Omega} - \Omega$, as a function of the Jordan-frame redshift. We show the matter density parameters (solid lines) and the dark-energy density parameters (dashed lines). In the Einstein frame, we consider the effective matter and dark-energy densities as given by Eqs. (B2) and (B3).

APPENDIX C: UNITARITY CONSTRAINTS

The K-mouflage models involve higher-order operators in the derivatives of φ and a coupling of the scalar field to matter β . This coupling induces a Yukawa interaction of the scalar field with fermions,

$$\mathcal{L}_I = \beta \frac{m_f}{M_{\text{Pl}}} \bar{\psi} \psi \delta\varphi, \quad (\text{C1})$$

where $\delta\varphi = \varphi - \bar{\varphi}$ are the fluctuations around a background $\bar{\varphi}$. Interaction terms in the scalar Lagrangian of the type $\mathcal{M}^4 \tilde{\chi}^n$ in a background field configuration $\tilde{\chi}$ imply the existence of the two-body scattering processes $f\bar{f} \rightarrow \varphi\varphi$ at tree level, with the exchange of one scalar field φ . In quantum mechanics, unitarity of the scattering matrix requires that the scattering amplitude $\mathcal{M}_{f\bar{f} \rightarrow \varphi\varphi}$ for this process should satisfy $\mathcal{M}_{f\bar{f} \rightarrow \varphi\varphi} \leq 16\pi$. In the clusters that we consider in the main body of the paper, the background value of $\tilde{\chi} \lesssim 10^{-3}$ is small, and the background value of $\bar{K}' \approx 1$ implies that clusters are unscreened. We focus on processes that can happen inside the hot gas of the clusters and consider the two-body scattering processes involving either electrons or nuclei. For temperatures of the gas less than $T_g \lesssim 10$ keV, the particles are nonrelativistic. We only consider K-mouflage functions $K(\tilde{\chi})$ of which the small $\tilde{\chi}$ expansion starts at the cubic order. In this case, the three-point self-interaction of the scalar field is of order

$$\mathcal{L}_3 \sim \mathcal{M}^4 \tilde{\chi} \frac{(\partial_{\mathbf{r}} \bar{\varphi})(\partial_{\mathbf{r}} \delta\varphi)(\partial \delta\varphi)^2}{\mathcal{M}^4 \mathcal{M}^4}, \quad (\text{C2})$$

where we consider a quasistatic background configuration. The energies of the two outgoing scalars are $E_{1,2} \sim m_f$,

whereas the spatial 3-momentum of the particles is $p_r \sim \sqrt{m_f T_g}$. The scalar propagator gives a factor of $1/m_f^2$ in the nonrelativistic limit, and finally we get that the scattering amplitude can be estimated as

$$\mathcal{M}_{f\bar{f} \rightarrow \varphi\varphi} \sim \beta \frac{m_f^2}{M_{\text{Pl}} \mathcal{M}^2} \bar{\chi}^{3/2} \sqrt{m_f T_g}. \quad (\text{C3})$$

For protons and neutrons at temperatures $T_g \lesssim 10$ keV for $\beta = 0.1$ and using $\bar{\chi} \lesssim 10^{-3}$, we find that $\mathcal{M}_{f\bar{f} \rightarrow \varphi\varphi} \lesssim 10^{-2}$, implying that unitarity is respected in the two-body processes.

Terms of higher order in $\bar{\chi}$ can lead to processes such as $f\bar{f} \rightarrow n\varphi$ involving n scalars in the final state. The scattering cross section grows fast with the number of outgoing particles and can exceed the Froissart bound on the

$\sigma_{\text{total}} \lesssim \frac{1}{m_f^2}$. This violation is relaxed by classicalization [94,95] in the same fashion as in Galileon models [18], where a classical lump sourced by the incoming energy of the two fermions in the center-of-mass frame is created. For K-mouflage models, this classical configuration has a typical size given by the K-mouflage radius R_K [11], and the scattering cross section becomes equal to the geometrical cross section proportional to R_K^2 . This process is analogous to the creation of black holes in high-energy collisions.

K-mouflage models also satisfy a nonrenormalization theorem analogous to the one for Galileons [96]. The quantum corrections going beyond the K-mouflage Lagrangian are negligible when $r \gtrsim \mathcal{M}_K^{-1}$, where $\mathcal{M}_K = \bar{K}^{1/4} \mathcal{M}$. Inside galaxy clusters, this is a short scale around 1 mm, and we can completely neglect quantum corrections on cluster scales.

-
- [1] E. Babichev, C. Deffayet, and R. Ziour, *Int. J. Mod. Phys. D* **18**, 2147 (2009).
- [2] P. Brax, C. Burrage, and A.-C. Davis, *J. Cosmol. Astropart. Phys.* **01** (2013) 020.
- [3] J. Khoury and A. Weltman, *Phys. Rev. Lett.* **93**, 171104 (2004).
- [4] J. Khoury and A. Weltman, *Phys. Rev. D* **69**, 044026 (2004).
- [5] T. Damour and A. M. Polyakov, *Nucl. Phys.* **B423**, 532 (1994).
- [6] A. Vainshtein, *Phys. Lett. B* **39**, 393 (1972).
- [7] P. Brax and P. Valageas, *Phys. Rev. D* **90**, 023507 (2014).
- [8] P. Brax and P. Valageas, *Phys. Rev. D* **90**, 023508 (2014).
- [9] A. Barreira, P. Brax, S. Clesse, B. Li, and P. Valageas, *Phys. Rev. D* **91**, 063528 (2015).
- [10] I. Sawicki, I. D. Saltas, L. Amendola, and M. Kunz, *J. Cosmol. Astropart. Phys.* **01** (2013) 004.
- [11] P. Brax and P. Valageas, *Phys. Rev. D* **90**, 123521 (2014).
- [12] A. Barreira, P. Brax, S. Clesse, B. Li, and P. Valageas, *Phys. Rev. D* **91**, 123522 (2015).
- [13] R. A. Sunyaev and Y. B. Zeldovich, *Comments Astrophys. Space Phys.* **4**, 173 (1972).
- [14] R. R. Caldwell, R. Dave, and P. J. Steinhardt, *Phys. Rev. Lett.* **80**, 1582 (1998).
- [15] P. J. Steinhardt, L. Wang, and I. Zlatev, *Phys. Rev. D* **59**, 123504 (1999).
- [16] G. Esposito-Farèse and D. Polarski, *Phys. Rev. D* **63**, 063504 (2001).
- [17] P. Brax and C. Burrage, *Phys. Rev. D* **90**, 104009 (2014).
- [18] P. Brax and C. Burrage, *Phys. Rev. D* **91**, 043515 (2015).
- [19] D. J. Eisenstein, W. Hu, and M. Tegmark, *Astrophys. J. Lett.* **504**, L57 (1998).
- [20] D. J. Eisenstein *et al.*, *Astrophys. J.* **633**, 560 (2005).
- [21] A. C. and B. Paczynski, *Nature (London)* **281**, 358 (1979).
- [22] P. Valageas, *Astron. Astrophys.* **508**, 93 (2009).
- [23] P. Valageas, *Phys. Rev. D* **89**, 123522 (2014).
- [24] T. Nishimichi and P. Valageas, *Phys. Rev. D* **90**, 023546 (2014).
- [25] A. Kehagias, H. Perrier, and A. Riotto, *Mod. Phys. Lett. A* **29**, 1450152 (2014).
- [26] J. F. Navarro, C. S. Frenk, and S. D. M. White, *Astrophys. J.* **462**, 563 (1996).
- [27] P. Valageas, T. Nishimichi, and A. Taruya, *Phys. Rev. D* **87**, 083522 (2013).
- [28] P. Valageas, *Phys. Rev. D* **88**, 083524 (2013).
- [29] N. Kaiser, *Mon. Not. R. Astron. Soc.* **222**, 323 (1986).
- [30] J. F. Navarro, C. S. Frenk, and S. D. M. White, *Astrophys. J.* **490**, 493 (1997).
- [31] J. Merten *et al.*, *Astrophys. J.* **806**, 4 (2015).
- [32] H. Mo, F. C. van den Bosch, and S. White, *Galaxy Formation and Evolution* (Cambridge University Press, Cambridge, England, 2010).
- [33] J. Binney and S. Tremaine, *Galactic Dynamics* (Princeton University, Princeton, NJ, 1987).
- [34] A. Cavaliere and R. Fusco-Fermiano, *Astron. Astrophys.* **49**, 137 (1976).
- [35] M. Plionis, *Lect. Notes Phys.* **740** (2008).
- [36] A. Vikhlinin *et al.*, *Astrophys. J.* **692**, 1033 (2009).
- [37] Y.-Y. Zhang, A. Finoguenov, H. Böhringer, J.-P. Kneib, G. P. Smith, R. Kneissl, N. Okabe, H. Dahle, and T. H. Reiprich, in *The X-ray Universe 2008* (2008), p. 222, http://xmm.esac.esa.int/external/xmm_science/workshops/2008symposium/.
- [38] A. Mantz, S. W. Allen, H. Ebeling, D. Rapetti, and A. Drllica-Wagner, *Mon. Not. R. Astron. Soc.* **406**, 1773 (2010).
- [39] G. W. Pratt, J. H. Croston, M. Arnaud, and H. Böhringer, *Astron. Astrophys.* **498**, 361 (2009).
- [40] Y. Ikebe, T. H. Reiprich, H. Böhringer, Y. Tanaka, and T. Kitayama, *Astron. Astrophys.* **383**, 773 (2002).
- [41] A. N. Bender *et al.*, *arXiv:1404.7103*.

- [42] S. Cole and N. Kaiser, *Mon. Not. R. Astron. Soc.* **237**, 1127 (1989).
- [43] H. J. Mo and S. D. M. White, *Mon. Not. R. Astron. Soc.* **282**, 347 (1996).
- [44] R. K. Sheth, H. J. Mo, and G. Tormen, *Mon. Not. R. Astron. Soc.* **323**, 1 (2001).
- [45] J. L. Tinker, B. E. Robertson, A. V. Kravtsov, A. Klypin, M. S. Warren, G. Yepes, and S. Gottlöber, *Astrophys. J.* **724**, 878 (2010).
- [46] P. Brax, A.-C. Davis, B. Li, and H. A. Winther, *Phys. Rev. D* **86**, 044015 (2012).
- [47] J. Khoury, [arXiv:1312.2006](https://arxiv.org/abs/1312.2006).
- [48] P. Brax, *Classical Quantum Gravity* **30**, 214005 (2013).
- [49] W. Hu and I. Sawicki, *Phys. Rev. D* **76**, 064004 (2007).
- [50] P. Brax, C. van de Bruck, A.-C. Davis, and D. J. Shaw, *Phys. Rev. D* **78**, 104021 (2008).
- [51] T. P. Sotiriou and V. Faraoni, *Rev. Mod. Phys.* **82**, 451 (2010).
- [52] A. de Felice and S. Tsujikawa, *Living Rev. Relativity* **13**, 3 (2010).
- [53] R. Gannouji, M. Sami, and I. Thongkool, *Phys. Lett. B* **716**, 255 (2012).
- [54] T. Chiba, *Phys. Lett. B* **575**, 1 (2003).
- [55] M. Gasperini, F. Piazza, and G. Veneziano, *Phys. Rev. D* **65**, 023508 (2002).
- [56] P. Brax, C. van de Bruck, A.-C. Davis, and D. Shaw, *Phys. Rev. D* **82**, 063519 (2010).
- [57] P. Brax, C. van de Bruck, A.-C. Davis, B. Li, and D. J. Shaw, *Phys. Rev. D* **83**, 104026 (2011).
- [58] K. Hinterbichler and J. Khoury, *Phys. Rev. Lett.* **104**, 231301 (2010).
- [59] P. Brax, A.-C. Davis, B. Li, H. A. Winther, and G.-B. Zhao, *J. Cosmol. Astropart. Phys.* **10** (2012) 002.
- [60] A. Nicolis, R. Rattazzi, and E. Trincherini, *Phys. Rev. D* **79**, 064036 (2009).
- [61] C. Deffayet, G. Esposito-Farèse, and V. A., *Phys. Rev. D* **79**, 084003 (2009).
- [62] C. Deffayet, D. S., and G. Esposito-Farèse, *Phys. Rev. D* **80**, 064015 (2009).
- [63] A. De Felice and S. Tsujikawa, *Phys. Rev. Lett.* **105**, 111301 (2010).
- [64] A. De Felice and S. Tsujikawa, *J. Cosmol. Astropart. Phys.* **03** (2012) 025.
- [65] A. Barreira, B. Li, W. A. Hellwing, L. Lombriser, C. M. Baugh, and S. Pascoli, *J. Cosmol. Astropart. Phys.* **04** (2014) 029.
- [66] P. Brax and P. Valageas, *Phys. Rev. D* **88**, 023527 (2013).
- [67] A. Terukina and K. Yamamoto, *Phys. Rev. D* **86**, 103503 (2012).
- [68] C. Arnold, E. Puchwein, and V. Springel, *Mon. Not. R. Astron. Soc.* **440**, 833 (2014).
- [69] A. Terukina, L. Lombriser, K. Yamamoto, D. Bacon, K. Koyama, and R. C. Nichol, *J. Cosmol. Astropart. Phys.* **04** (2014) 013.
- [70] H. Wilcox *et al.*, [arXiv:1504.03937](https://arxiv.org/abs/1504.03937).
- [71] L. Lombriser, F. Schmidt, T. Baldauf, R. Mandelbaum, U. Seljak, and R. E. Smith, *Phys. Rev. D* **85**, 102001 (2012).
- [72] J. Clampitt, B. Jain, and J. Khoury, *J. Cosmol. Astropart. Phys.* **01** (2012) 030.
- [73] F. Schmidt, M. Lima, H. Oyaizu, and W. Hu, *Phys. Rev. D* **79**, 083518 (2009).
- [74] C. C. Moran, R. Teyssier, and B. Li, *Mon. Not. R. Astron. Soc.* **448**, 307 (2015).
- [75] M. Gronke, C. Llinares, D. F. Mota, and H. A. Winther, *Mon. Not. R. Astron. Soc.* **449**, 2837 (2015).
- [76] A. Hammami, C. Llinares, D. F. Mota, and H. A. Winther, *Mon. Not. R. Astron. Soc.* **449**, 3635 (2015).
- [77] L. Lombriser, K. Koyama, G.-B. Zhao, and B. Li, *Phys. Rev. D* **85**, 124054 (2012).
- [78] S. Tsujikawa and T. Tatekawa, *Phys. Lett. B* **665**, 325 (2008).
- [79] T. Y. Lam, F. Schmidt, T. Nishimichi, and M. Takada, *Phys. Rev. D* **88**, 023012 (2013).
- [80] Y. Zu, D. H. Weinberg, E. Jennings, B. Li, and M. Wyman, *Mon. Not. R. Astron. Soc.* **445**, 1885 (2014).
- [81] G.-B. Zhao, B. Li, and K. Koyama, *Phys. Rev. D* **83**, 044007 (2011).
- [82] S. Ferraro, F. Schmidt, and W. Hu, *Phys. Rev. D* **83**, 063503 (2011).
- [83] B. Li, G.-B. Zhao, and K. Koyama, *Mon. Not. R. Astron. Soc.* **421**, 3481 (2012).
- [84] L. Lombriser, B. Li, K. Koyama, and G.-B. Zhao, *Phys. Rev. D* **87**, 123511 (2013).
- [85] F. Schmidt, A. Vikhlinin, and W. Hu, *Phys. Rev. D* **80**, 083505 (2009).
- [86] M. Cataneo, D. Rapetti, F. Schmidt, A. B. Mantz, S. W. Allen, D. E. Applegate, P. L. Kelly, A. von der Linden, and R. G. Morris, [arXiv:1412.0133](https://arxiv.org/abs/1412.0133).
- [87] L. Boubekour, E. Giusarma, O. Mena, and H. Ramírez, *Phys. Rev. D* **90**, 103512 (2014).
- [88] D. S. Y. Mak, E. Pierpaoli, F. Schmidt, and N. Macellari, *Phys. Rev. D* **85**, 123513 (2012).
- [89] H. Okada, T. Totani, and S. Tsujikawa, *Phys. Rev. D* **87**, 103002 (2013).
- [90] J. Bel, P. Brax, C. Marinoni, and P. Valageas, *Phys. Rev. D* **91**, 103503 (2015).
- [91] B. Jain and J. VanderPlas, *J. Cosmol. Astropart. Phys.* **10** (2011) 032.
- [92] V. Vikram, J. Sakstein, C. Davis, and A. Neil, [arXiv:1407.6044](https://arxiv.org/abs/1407.6044).
- [93] C. Arnold, E. Puchwein, and V. Springel, *Mon. Not. R. Astron. Soc.* **448**, 2275 (2015).
- [94] G. Dvali, G. F. Giudice, C. Gomez, and A. Kehagias, *J. High Energy Phys.* **08** (2011) 108.
- [95] L. Keltner and A. J. Tolley, [arXiv:1502.05706](https://arxiv.org/abs/1502.05706).
- [96] C. de Rham, *C.R. Phys.* **13**, 666 (2012).

Article B

Ultra local models of gravity without the kinetic term

Ultra-local models of modified gravity without kinetic term

Philippe Brax, Luca Alberto Rizzo, and Patrick Valageas

Institut de Physique Théorique,

CEA, IPhT, F-91191 Gif-sur-Yvette, Cédex, France

CNRS, URA 2306, F-91191 Gif-sur-Yvette, Cédex, France

(Dated: May 20, 2016)

We present a class of modified-gravity theories which we call ultra-local models. We add a scalar field, with negligible kinetic terms, to the Einstein-Hilbert action. We also introduce a conformal coupling to matter. This gives rise to a new screening mechanism which is not entirely due to the non-linearity of the scalar field potential or the coupling function but to the absence of the kinetic term. As a result this removes any fifth force between isolated objects in vacuum. It turns out that these models are similar to chameleon-type theories with a large mass when considered outside the Compton wave-length but differ on shorter scales. The predictions of these models only depend on a single free function, as the potential and the coupling function are degenerate, with an amplitude given by a parameter $\alpha \lesssim 10^{-6}$, whose magnitude springs from requiring a small modification of Newton's potential astrophysically and cosmologically. This singles out a redshift $z_\alpha \sim \alpha^{-1/3} \gtrsim 100$ where the fifth force is the greatest. The cosmological background follows the Λ -CDM history within a 10^{-6} accuracy, while cosmological perturbations are significantly enhanced (or damped) on small scales, $k \gtrsim 2h\text{Mpc}^{-1}$ at $z = 0$. The spherical collapse and the halo mass function are modified in the same manner. We find that the modifications of gravity are greater for galactic or sub-galactic structures. We also present a thermodynamic analysis of the non-linear and inhomogeneous fifth-force regime where we find that the Universe is not made more inhomogeneous before z_α when the fifth force dominates, and does not lead to the existence of clumped matter on extra small scales inside halos for large masses while this possibility exists for masses $M \lesssim 10^{11} M_\odot$ where the phenomenology of ultra-local models would be most different from Λ -CDM.

PACS numbers: 98.80.-k

I. INTRODUCTION

Since the discovery of the accelerated expansion of the Universe [1, 2], explaining its nature has become a major problem in modern cosmology. Most of the possible solutions for this problem rely either on the inclusion of a dark energy component and/or on modifications of General Relativity (GR) [3]. These alternative theories of gravitation, which go beyond a simple cosmological constant, usually imply the presence of at least one additional low-mass scalar field in the theory and induce the presence of a fifth force on cosmological scales. However, the presence of the scalar field must have a very small impact on the dynamics of the Solar System and on any laboratory test due to very stringent constraints imposed by observations (e.g. [4]). One possible solution, which was recently explored in [5], is to construct modified gravity theories with a screening mechanism that provides convergence to GR in dense environments [6, 7] such as the Solar System.

In this paper we investigate a particular type of modification of gravity with a new screening mechanism, that we will call “ultra-local models”. We add to the Einstein-Hilbert action a scalar field whose Lagrangian has a zero (or negligible) kinetic term. For this reason, the equation of motion for the scalar field of this theory, which gives the relation between the scalar and the matter fields, is a “constraint” equation with no time derivatives, contrary to what happens in the case of other scalar tensor theories. In the ultra-local models, the scalar field is coupled

to the matter field via a non-linear conformal transformation function of the field itself and depends on the local value of the matter density. In such a way the fifth force associated to the scalar field is proportional to the local gradient of the matter density. This provides an automatic screening mechanism as it implies that there is no fifth force between isolated compact objects, independently of the parameters of the model. This ultra-local property ensures that astrophysical systems like the Solar System are perfectly screened.

Thus, although these models can be seen as the limit of chameleon scenarios with a scalar field mass or potential that is much greater than its kinetic energy, outside the Compton wave-length, they differ from the chameleon scenarios on smaller scales. This gives rise to new features for both the definition of the theory and its phenomenology. In particular, because the scalar field potential and coupling function are degenerate, we find it convenient to choose (without loss of generality) a linear potential, so that the physics arises from the non-linearity of the coupling function. This is somewhat similar to what happens in the Damour-Polyakov mechanism [8], although here we have no potential and the field is not attracted to the minimum of the coupling function (the screening does not arise from the vanishing of the coupling but from its locality). In contrast, other screening mechanisms studied in the literature are associated to non-linearities of the scalar Lagrangian of the scalar field (e.g. chameleon [9], Vainshtein [10] or K-mouflage [11]) either in the kinetic terms or the potential.

The non-linear coupling function is the only free function of the theory, which can be constrained using theoretical and cosmological results. In particular, we require the coupling function to be severely bounded so that its contribution to the metric potential does not exceed the Newtonian one, associated with typical cosmological perturbations and astrophysical objects. These ultra-local models correspond to modified source models [12] where the coupling to matter has a magnitude of order $|\ln A| \lesssim 10^{-6}$ to guarantee that the contribution of modified gravity to Newton's potential is at most of order one. This implies that the Λ -CDM expansion history is recovered up to a 10^{-6} accuracy. At the linear level, the scalar field in this theory acts as a scale and time dependent modification of the growth rate which can either enhance or diminish it, depending on the shape of the coupling function. On astrophysical scales, the modification of gravity is the largest on galactic scales while no effects are expected in the Solar System and on cluster scales. On the other hand, this is not the case inside halos, in particular for masses below $10^{12}h^{-1}M_\odot$. The effects of the ultra-local interaction can be so drastic for smaller masses inside the Navarro-Frenk-White profile that the system can undergo a thermodynamic phase transition with the presence of small clumps. We expect that the fifth force on these small scales is eventually screened by the ultra-locality of the scalar interaction. This would lead to a different landscape of inhomogeneities for small mass objects $M \lesssim 10^{11}M_\odot$ deep inside their cores. A more precise analysis would require numerical simulations and this is left for future work.

The paper is organised as follows. In section II we introduce the ultra-local models and in section III we study the equations of motion, both in Einstein and Jordan frames. In section IV we consider some generic constraints on the form of such theories and we present some explicit models, while in section V we study the validity and the self-consistency of the theory. We study the evolution of the cosmological background in section VI, of cosmological linear perturbations in section VII, the dynamics of the spherical collapse in section VIII and the halo mass function in section IX. We consider the screening properties of the theory, from clusters of galaxies down to the Solar System and the Earth, in section X. We investigate the formation of non-linear structures and the fifth-force non-linear regime in section XI, considering the stability of both cosmological and astrophysical inhomogeneities. In section XII we study the dependence of the previous results under the variation of the free parameter α of the coupling function and in section XIII we compare the ultra-local models to other modified gravity theories. Finally we conclude in section XIV.

II. SCALAR-FIELD MODEL WITH NEGLIGIBLE KINETIC TERM

We consider scalar field models with actions of the form

$$S = \int d^4x \sqrt{-\tilde{g}} \left[\frac{\tilde{M}_{\text{Pl}}^2}{2} \tilde{R} + \tilde{\mathcal{L}}_\varphi(\varphi) \right] + \int d^4x \sqrt{-g} \mathcal{L}_m(\psi_m^{(i)}, g_{\mu\nu}), \quad (1)$$

where the various matter fields follow the Jordan-frame metric $g_{\mu\nu}$, with determinant g , which is related to the Einstein-frame metric $\tilde{g}_{\mu\nu}$, with determinant \tilde{g} , by [10]

$$g_{\mu\nu} = A^2(\varphi)\tilde{g}_{\mu\nu}. \quad (2)$$

In this paper, we investigate models where the scalar field Lagrangian is dominated by its potential term, so that we write

$$\tilde{\mathcal{L}}_\varphi(\varphi) = -V(\varphi), \quad (3)$$

where we set the kinetic term to zero. Then, assuming that the potential $V(\varphi)$ can be inverted (i.e., that it is a monotonic function over the range of φ of interest), we can make the change of variable from φ to V . More precisely, introducing the characteristic energy scale \mathcal{M}^4 of the potential we define the dimensionless field $\tilde{\chi}$ as

$$\tilde{\chi} \equiv -\frac{V(\varphi)}{\mathcal{M}^4}, \quad \text{and} \quad A(\tilde{\chi}) \equiv A(\varphi). \quad (4)$$

Therefore, in terms of the field $\tilde{\chi}$ the scalar field Lagrangian and the conformal metric transformation read as

$$\tilde{\mathcal{L}}_{\tilde{\chi}}(\tilde{\chi}) = \mathcal{M}^4\tilde{\chi} \quad \text{and} \quad g_{\mu\nu} = A^2(\tilde{\chi})\tilde{g}_{\mu\nu}. \quad (5)$$

Thus, these models are fully specified by a single function, $A(\tilde{\chi})$, which is defined from the initial potential $V(\varphi)$ and coupling function $A(\varphi)$ through Eq.(4). This means that there is a broad degeneracy in the action (1) as different couples $\{V(\varphi), A(\varphi)\}$ with the same rescaled coupling $A(\tilde{\chi})$ give rise to the same physics. Therefore, in the following we work with the field $\tilde{\chi}$ and with Eq.(5). The energy scale \mathcal{M}^4 is arbitrary and only defines the normalization of the field $\tilde{\chi}$. We can choose without loss of generality $\mathcal{M}^4 > 0$ and we shall typically have $\mathcal{M}^4 \sim \bar{\rho}_{\text{de}0}$, where $\bar{\rho}_{\text{de}0}$ is the mean dark energy density today, if we require the accelerated expansion of the Universe at low z to be driven by the scalar field potential $V(\varphi)$, without adding an extra cosmological constant.

III. EQUATIONS OF MOTION

Because the matter fields follow the geodesics set by the Jordan frame and satisfy the usual conservation equations in this frame, we mostly work in the Jordan frame.

This is also the frame that is better suited to make the connection with observations as atomic physics remains the same throughout cosmic evolution in this frame [13]. However, because the gravitational sector is simpler in the Einstein frame, we first derive the Einstein equations in the Einstein frame, and next translate these equations in terms of the Jordan tensors.

A. Einstein frame

1. Scalar-field and Einstein equations

The scalar-field Lagrangian (5) is given in the Einstein frame, where the equation of motion of the scalar field reads as

$$\mathcal{M}^4 + \tilde{T} \frac{d \ln A}{d \tilde{\chi}} = 0, \quad (6)$$

where $\tilde{T} = \tilde{T}^\mu_\mu$ is the trace of the matter energy-momentum tensor in the Einstein frame. From the conformal coupling (5) the energy-momentum tensors in the Einstein and Jordan frames are related by

$$\tilde{T}^\mu_\nu = A^4 T^\mu_\nu \quad \text{and} \quad \tilde{T} = A^4 T. \quad (7)$$

As there is no kinetic term in the scalar-field Lagrangian (5), the ‘‘Klein-Gordon’’ equation (6) contains no derivative term and it is a constraint equation, which gives the field $\tilde{\chi}(\mathbf{x})$ as a function of the matter density field $\tilde{\rho}(\mathbf{x})$. The energy-momentum tensor of the scalar field also reads as

$$\tilde{T}^\mu_{\nu(\tilde{\chi})} = \mathcal{M}^4 \tilde{\chi} \delta^\mu_\nu, \quad (8)$$

so that the scalar-field energy density and pressure are

$$\tilde{\rho}_{\tilde{\chi}} = -\mathcal{M}^4 \tilde{\chi}, \quad \tilde{p}_{\tilde{\chi}} = \mathcal{M}^4 \tilde{\chi} = -\tilde{\rho}_{\tilde{\chi}}. \quad (9)$$

In the Einstein frame, the Einstein equations take their standard form, $\tilde{G}^\mu_\nu = \tilde{T}^\mu_\nu$.

2. Cosmological background in the Einstein frame

Using the conformal time τ and comoving coordinates \mathbf{x} , the background metrics in both frames are given by $d\tilde{s}^2 = \tilde{a}^2(-d\tau^2 + d\mathbf{x}^2)$ and $ds^2 = a^2(-d\tau^2 + d\mathbf{x}^2)$, with

$$a = \tilde{A}\tilde{a} \quad \text{and} \quad dt = \tilde{A}d\tilde{t}, \quad \mathbf{r} = \tilde{A}\tilde{\mathbf{r}}, \quad (10)$$

where we denote background quantities with a bar. Thus, the cosmic times and physical distances are different in the two frames. From Eq.(7) the densities and pressures are also related by

$$\bar{\rho} = \tilde{A}^4 \tilde{\rho}, \quad \bar{p} = \tilde{A}^4 \tilde{p}, \quad (11)$$

while the Friedmann equation takes the standard form,

$$3\tilde{M}_{\text{Pl}}^2 \tilde{\mathcal{H}}^2 = \tilde{a}^2(\tilde{\rho} + \tilde{\rho}_{\text{rad}} + \tilde{\rho}_{\tilde{\chi}}), \quad (12)$$

with $\tilde{\mathcal{H}} = d \ln \tilde{a} / d\tau$ the conformal expansion rate in the Einstein frame. From Eq.(9) the background scalar field energy density and pressure are given by

$$\tilde{\rho}_{\tilde{\chi}} = -\mathcal{M}^4 \tilde{\chi}, \quad \tilde{p}_{\tilde{\chi}} = \mathcal{M}^4 \tilde{\chi} = -\tilde{\rho}_{\tilde{\chi}}. \quad (13)$$

3. Perturbations in the Einstein frame

Taking into account the perturbations from the homogeneous background, the Einstein-frame metric reads in the Newtonian gauge as

$$d\tilde{s}^2 = \tilde{a}^2[-(1 + 2\tilde{\Phi})d\tau^2 + (1 - 2\tilde{\Psi})d\mathbf{x}^2], \quad (14)$$

and the Einstein equations yield, at linear order over the metric potentials and in the quasi-static approximation (for scales much below the Hubble radius),

$$\tilde{\Phi} = \tilde{\Psi} = \tilde{\Psi}_{\text{N}} \quad \text{with} \quad \frac{\nabla^2}{\tilde{a}^2} \tilde{\Psi}_{\text{N}} \equiv \frac{\delta\tilde{\rho} + \delta\tilde{\rho}_{\tilde{\chi}}}{2\tilde{M}_{\text{Pl}}^2}. \quad (15)$$

Here we use the non-relativistic limit $v^2 \ll c^2$, so that the gravitational slip $\tilde{\Phi} - \tilde{\Psi}$ vanishes, and $\delta\tilde{\rho} = \tilde{\rho} - \bar{\rho}$ and $\delta\tilde{\rho}_{\tilde{\chi}} = \tilde{\rho}_{\tilde{\chi}} - \bar{\rho}_{\tilde{\chi}}$ are the matter and scalar-field density fluctuations. In particular, we have

$$\delta\tilde{\rho}_{\tilde{\chi}} = -\mathcal{M}^4 \delta\tilde{\chi}. \quad (16)$$

B. Jordan frame

1. Cosmological background in the Jordan frame

From Eq.(10) the conformal expansion rates in the two frames are related by

$$\tilde{\mathcal{H}} = (1 - \epsilon_2)\mathcal{H} \quad \text{with} \quad \epsilon_2(t) \equiv \frac{d \ln \tilde{A}}{d \ln a}, \quad (17)$$

while the densities and pressures are related as in Eq.(11). Therefore, the Friedmann equation (12) yields

$$3\tilde{M}_{\text{Pl}}^2 \mathcal{H}^2 = (1 - \epsilon_2)^{-2} a^2 (\bar{\rho} + \bar{\rho}_{\text{rad}} + \bar{\rho}_{\tilde{\chi}}), \quad (18)$$

where the Jordan-frame Planck mass is

$$\tilde{M}_{\text{Pl}}^2(t) = \tilde{A}^{-2}(t) \tilde{M}_{\text{Pl}}^2. \quad (19)$$

Then, we can define an effective dark energy density by

$$3\tilde{M}_{\text{Pl}}^2 \mathcal{H}^2 = a^2 (\bar{\rho} + \bar{\rho}_{\text{rad}} + \bar{\rho}_{\text{de}}), \quad (20)$$

which gives

$$\bar{\rho}_{\text{de}} = \bar{\rho}_{\tilde{\chi}} + \frac{2\epsilon_2 - \epsilon_2^2}{(1 - \epsilon_2)^2} (\bar{\rho} + \bar{\rho}_{\text{rad}} + \bar{\rho}_{\tilde{\chi}}). \quad (21)$$

In the Jordan frame the matter obeys the standard conservation equations, $\nabla_\mu T^\mu_\nu = 0$, and the background matter and radiation densities evolve as

$$\bar{\rho} = \frac{\bar{\rho}_0}{a^3}, \quad \bar{\rho}_{\text{rad}} = \frac{\bar{\rho}_{\text{rad}0}}{a^4}. \quad (22)$$

The scalar-field equation of motion (6) gives

$$\mathcal{M}^4 = \bar{A}^4 \bar{\rho} \frac{d \ln \bar{A}}{d \tilde{\chi}} \quad \text{and} \quad \frac{d \tilde{\chi}}{d \tau} = \bar{A}^4 \frac{\bar{\rho}}{\mathcal{M}^4} \epsilon_2 \mathcal{H}, \quad (23)$$

hence

$$\bar{\rho}_{\tilde{\chi}} = -\bar{A}^{-4} \mathcal{M}^4 \tilde{\chi}, \quad \frac{d \bar{\rho}_{\tilde{\chi}}}{d \tau} = -4 \epsilon_2 \mathcal{H} \bar{\rho}_{\tilde{\chi}} - \epsilon_2 \mathcal{H} \bar{\rho}. \quad (24)$$

2. Perturbations in the Jordan frame

In the Jordan frame we write the Newtonian gauge metric as

$$ds^2 = a^2 [-(1 + 2\Phi)d\tau^2 + (1 - 2\Psi)d\mathbf{x}^2], \quad (25)$$

so that the Einstein- and Jordan-frame metric potentials are related by

$$1 + 2\Phi = \frac{A^2}{\bar{A}^2} (1 + 2\tilde{\Phi}), \quad 1 - 2\Psi = \frac{A^2}{\bar{A}^2} (1 - 2\tilde{\Psi}), \quad (26)$$

while the Einstein-frame Newtonian potential (15) is also the solution of

$$\frac{\nabla^2}{a^2} \tilde{\Psi}_N = \frac{\delta(A^4 \rho) + \delta(A^4 \rho_{\tilde{\chi}})}{2\bar{A}^4 M_{\text{Pl}}^2}. \quad (27)$$

Since we wish the deviations from General Relativity and the Λ -CDM cosmology to be small, at most of the order of ten percent, the potentials Φ and Ψ cannot deviate too much from the Jordan-frame Newtonian potential defined by

$$\frac{\nabla^2}{a^2} \Psi_N \equiv \frac{\delta\rho + \delta\rho_{\tilde{\chi}}}{2M_{\text{Pl}}^2}, \quad (28)$$

where the scalar field density fluctuations must also remain modest as compared with the matter density fluctuations. Therefore, Eqs.(26) and (27) lead to the constraints

$$\left| \frac{\delta A}{\bar{A}} \right| \lesssim |\Psi_N|, \quad |\delta\rho_{\tilde{\chi}}| \lesssim |\delta\rho|. \quad (29)$$

Then, since $|\Psi_N|$ is typically of order 10^{-5} , we can linearize in δA as we did for the metric potentials, and within a 10^{-5} relative accuracy we obtain

$$\Phi = \Psi_N + \delta \ln A, \quad \Psi = \Psi_N - \delta \ln A, \quad (30)$$

and

$$\delta\rho_{\tilde{\chi}} = -\bar{A}^{-4} \mathcal{M}^4 \delta\tilde{\chi}. \quad (31)$$

The equation of motion of the scalar field reads as

$$\mathcal{M}^4 = \bar{A}^4 \rho \frac{d \ln A}{d \tilde{\chi}}. \quad (32)$$

The matter and radiation components obey the standard equations of motion, which gives for the matter component the continuity and Euler equations

$$\frac{\partial \rho}{\partial \tau} + (\mathbf{v} \cdot \nabla) \rho + (3\mathcal{H} + \nabla \cdot \mathbf{v}) \rho = 0, \quad (33)$$

and

$$\frac{\partial \mathbf{v}}{\partial \tau} + (\mathbf{v} \cdot \nabla) \mathbf{v} + \mathcal{H} \mathbf{v} = -\nabla \Phi. \quad (34)$$

From Eq.(30) we have $\nabla \Phi = \nabla \Psi_N + \nabla \ln A$, and the scalar-field equation (32) gives

$$\nabla \ln A = \frac{d \ln A}{d \tilde{\chi}} \nabla \tilde{\chi} = \frac{\mathcal{M}^4}{\bar{A}^4 \rho} \nabla \tilde{\chi}, \quad (35)$$

so that the Euler equation (34) also reads as

$$\frac{\partial \mathbf{v}}{\partial \tau} + (\mathbf{v} \cdot \nabla) \mathbf{v} + \mathcal{H} \mathbf{v} = -\nabla \Psi_N - \frac{\nabla p_A}{\rho}, \quad (36)$$

with

$$p_A = \frac{\mathcal{M}^4 c^2}{\bar{A}^4} \tilde{\chi}, \quad (37)$$

where we explicitly wrote the factor c^2 .

Thus, in terms of the matter dynamics, the scalar-field or modified-gravity effects appear through two factors, a) the modification of the Poisson equation (28), because of the additional source associated with the scalar-field energy density fluctuations and of the time dependence of the Jordan-frame Planck mass, and b) the new pressure term p_A in the Euler equation (36). This pressure p_A corresponds to a polytropic equation of state, as it only depends on the matter density (the sum of cold dark matter and baryons).

3. Linear regime in the Jordan frame

On large scales or at early times we may linearize the equations of motion. Expanding the coupling function $A(\tilde{\chi})$ as

$$\ln A(\tilde{\chi}) = \ln \bar{A} + \sum_{n=1}^{\infty} \frac{\beta_n(t)}{n!} (\delta\tilde{\chi})^n, \quad (38)$$

the scalar field equation (32) gives at the background and linear orders

$$\mathcal{M}^4 = \bar{A}^4 \bar{\rho} \beta_1, \quad \delta\tilde{\chi} = -\frac{\beta_1}{\beta_2} \delta, \quad (39)$$

where we note $\delta \equiv \delta\rho/\bar{\rho}$ the matter density contrast. This also yields

$$\delta p_A = -\epsilon_1(t) \bar{\rho} c^2 \delta \quad \text{and} \quad \delta\rho_{\tilde{\chi}} = \epsilon_1(t) \bar{\rho} \delta, \quad (40)$$

with

$$\epsilon_1(t) \equiv \frac{\beta_1 \mathcal{M}^4}{\beta_2 \bar{A}^4 \bar{\rho}} = \frac{\beta_1^2}{\beta_2} = \frac{\epsilon_2}{3 - 4\epsilon_2}, \quad (41)$$

where to obtain the last relation we took the time derivative of the first relation in (39) and used the second expression in (17).

The continuity equation (33) reads as $\partial_\tau \delta + \nabla \cdot [(1 + \delta)\mathbf{v}] = 0$ in terms of the density contrast. Combining with the Euler equation at linear order, this gives

$$\frac{\partial^2 \delta}{\partial \tau^2} + \mathcal{H} \frac{\partial \delta}{\partial \tau} + \epsilon_1 c^2 \nabla^2 \delta = \frac{\bar{\rho} a^2}{2M_{\text{Pl}}^2} (1 + \epsilon_1) \delta. \quad (42)$$

As compared with the Λ -CDM cosmology, the pressure term $\nabla^2 \delta$ introduces an explicit scale dependence. Going to Fourier space, the linear growing modes $D(k, t)$ now depend on the wave number k and obey the evolution equation

$$\frac{\partial^2 D}{\partial (\ln a)^2} + \left(2 + \frac{1}{H^2} \frac{dH}{dt} \right) \frac{\partial D}{\partial \ln a} - \frac{3\Omega_m}{2} (1 + \epsilon) D = 0, \quad (43)$$

where $H = d \ln a / dt$ is the Jordan-frame expansion rate (with respect to the Jordan-frame cosmic time t) and the factor $\epsilon(k, t)$, which describes the deviation from the Λ -CDM cosmology, is given by

$$\epsilon(k, t) = \epsilon_1(t) \left(1 + \frac{2}{3\Omega_m} \frac{c^2 k^2}{a^2 H^2} \right). \quad (44)$$

Thus, the two effects of the scalar field, the contribution to the gravitational potential of $\delta\rho_{\tilde{\chi}}$ and the pressure term due to the conformal transformation between the Einstein and Jordan frames, modify the growth of structures in the same direction, given by the sign of ϵ_1 . A positive ϵ_1 gives a scale dependent amplification of the gravitational force and an acceleration of gravitational clustering. The k -dependent pressure term dominates when $ck/aH > 1$, that is, on sub-horizon scales. Moreover, we have $(ck/aH)^2 \sim 10^7$ today at scales of about $1 h^{-1} \text{Mpc}$. Therefore, we must have

$$|\epsilon_1| \lesssim 10^{-7} \quad (45)$$

to ensure that the growth of large-scale structures is not too significantly modified. This also ensures that the first condition in (29) is satisfied on cosmological scales. Moreover, the fluctuations of the scalar field energy density in the Poisson equations are negligible and ϵ_2 is very small, of order 10^{-7} , from the last relation in Eq.(41).

IV. EXPLICIT MODELS

A. Constraints

1. Small parameter α

In usual scalar-field models with a kinetic term, the Klein-Gordon equation for the scalar field that corresponds to Eq.(32) contains a derivative term $\nabla^2 \varphi$, which

suppresses the fluctuations of the scalar field on small scales. This mechanism is absent in our case and the scalar field $\tilde{\chi}$ only follows the variations of the local matter density. However, we wish the fluctuations of $\ln A$ to remain small and of order 10^{-6} from cosmological scales down to astrophysical objects such as stars and planets, to comply with the first constraint in Eq.(29) and to ensure that the metric potentials remain close the Newtonian potential. Because the density varies by many orders of magnitude from the intergalactic medium to the atmospheres and cores of stars and planets, and to the typical densities found in the laboratory on Earth, and we cannot rely on the small-scale suppression due to derivative terms, the function $\ln A$ must be bounded within a small interval over its full domain,

$$|\ln A| \lesssim 10^{-6}, \quad \text{hence } |A - 1| \lesssim 10^{-6}. \quad (46)$$

Therefore, the conformal factor A always remains very close to unity (we can renormalize A by a constant multiplicative factor without loss of generality). On the other hand, from Eq.(32) we have $d \ln A / d\tilde{\chi} = \mathcal{M}^4 / \bar{A}^4 \rho$, hence

$$\frac{d \ln A}{d\tilde{\chi}} > 0, \quad (47)$$

and

$$\rho \rightarrow 0 : \frac{d \ln A}{d\tilde{\chi}} \rightarrow +\infty, \quad \rho \rightarrow \infty : \frac{d \ln A}{d\tilde{\chi}} \rightarrow 0. \quad (48)$$

The small range of the function $A(\tilde{\chi})$ in Eq.(46) also implies that the Jordan-frame Planck mass (19) does not vary by more than 10^{-6} . This ensures that the bounds on the variation with time of Newton's constant obtained from the BBN constraints [14, 15] or the Lunar Ranging measurements [16] are satisfied. It also means that at the background level the Einstein and Jordan frames are identical up to 10^{-6} .

The small range of $\ln A$ also leads to a small amplitude for the factor ϵ_2 defined in Eq.(17), of order 10^{-6} . In fact, from Eqs.(45) and (41) we have seen that we also require ϵ_1 and ϵ_2 of order 10^{-7} , so that both constraints give about the same condition (46) on the coupling function $A(\tilde{\chi})$. Then, we recover a standard Λ -CDM cosmology up to this order. Indeed, with $\epsilon_2 \simeq 0$ we recover the usual Friedmann equation in Eq.(18), the dark energy density $\bar{\rho}_{\text{de}}$ is almost identical to the scalar field energy density $\bar{\rho}_{\tilde{\chi}}$ in Eq.(21), and the latter is almost constant at low z from Eq.(24). From Eq.(24) we find that the value of the scalar field today must satisfy

$$\bar{\rho}_{\text{de}0} = -\bar{A}_0^{-4} \mathcal{M}^4 \bar{\chi}_0 \simeq -\mathcal{M}^4 \bar{\chi}_0, \quad (49)$$

if the scalar field drives the accelerated expansion of the Universe at low z without an additional cosmological constant. In particular, this implies $\bar{\chi}_0 < 0$. Finally, we must check that ϵ_1 , defined in Eq.(41), remains small, as in Eq.(45), and vanishes at high redshift if we wish to recover the standard clustering growth in the early matter era.

In the following we use the approximation $\bar{A} \simeq 1$ to simplify the expressions and we present several explicit models for the coupling function $A(\tilde{\chi})$ that satisfy the conditions (46)-(49). In particular, the equation of motion of the scalar field (32) becomes

$$\frac{d \ln A}{d \tilde{\chi}} = \frac{\mathcal{M}^4}{\rho}, \quad (50)$$

which implicitly defines the functions $\tilde{\chi}(\rho)$ and $\ln A(\rho)$ for each coupling function $\ln A(\tilde{\chi})$. To obtain a unique and well-defined solution $\tilde{\chi}(\rho)$ and $A(\rho)$ to the scalar-field equation (50), we require that $d \ln A/d \tilde{\chi}$ be a monotonic function that goes from 0 to $+\infty$ over a range of $\tilde{\chi}$, which will define the domain of the scalar field values. Then $\tilde{\chi}(\rho)$ and $\ln A(\rho)$, defined by the values that are solutions of Eq.(50) for a given ρ , are also monotonic functions of ρ .

2. Derived characteristic density ρ_α and redshift z_α

From Eq.(46) we write

$$\ln A(\tilde{\chi}) = \alpha \lambda(\tilde{\chi}), \quad \alpha \lesssim 10^{-6}, \quad (51)$$

where α is a small parameter that ensures the condition (46) is satisfied, whereas $\lambda(\tilde{\chi})$ is a bounded function of order unity and $\tilde{\chi}$ is also typically of order unity. Then, the equation of motion (50) reads as

$$\frac{d \lambda}{d \tilde{\chi}} = \frac{1}{\hat{\rho}} \quad \text{with} \quad \hat{\rho} = \frac{\alpha \rho}{\mathcal{M}^4}. \quad (52)$$

This implicitly defines the functions $\lambda(\hat{\rho})$ and $\tilde{\chi}(\hat{\rho})$, from the value of $\tilde{\chi}$ that solves Eq.(52) for a given density. The changes of variables $\ln A \rightarrow \lambda$ and $\rho \rightarrow \hat{\rho}$ have removed the explicit parameters $\mathcal{M}^4 \sim \bar{\rho}_{\text{de}0}$ and $\alpha \lesssim 10^{-6}$, so that the functions $\lambda(\tilde{\chi})$, $\lambda(\hat{\rho})$ and $\tilde{\chi}(\hat{\rho})$ do not involve small nor large parameters. Therefore, in addition to the density $\mathcal{M}^4 \sim \bar{\rho}_{\text{de}0}$, which is associated with the current dark energy density from Eq.(49), these models automatically introduce another higher density scale ρ_α given by

$$\rho_\alpha = \frac{\mathcal{M}^4}{\alpha} \sim \frac{\bar{\rho}_{\text{de}0}}{\alpha} \gtrsim 10^6 \bar{\rho}_{\text{de}0}. \quad (53)$$

This implies that, from the point of view of the coupling function $\ln A$, the low-redshift mean density of the Universe is within its very low density regime. Moreover, we can expect a cosmological transition between low-density and high-density regimes at the redshift z_α where $\bar{\rho} \sim \rho_\alpha$, which corresponds to

$$a_\alpha \sim \alpha^{1/3} \lesssim 0.01, \quad z_\alpha \sim \alpha^{-1/3} \gtrsim 100. \quad (54)$$

B. Model (I): $\tilde{\chi}$ is a bounded increasing function of ρ

We first consider the case where $\tilde{\chi}(\rho)$ is a monotonic increasing function of ρ , with $\tilde{\chi}_- < \tilde{\chi} < \tilde{\chi}_+$. From Eq.(48)

we find that $d \ln A/d \tilde{\chi}$ must decrease from $+\infty$ to 0 as $\tilde{\chi}$ grows from $\tilde{\chi}_-$ to $\tilde{\chi}_+$. Moreover, the boundary $\tilde{\chi}_-$ will correspond to the late dark energy era while the boundary $\tilde{\chi}_+$ will correspond to the early matter era. From Eq.(49) we have $\tilde{\chi}_- < 0$ and to avoid introducing another parameter we can take $\tilde{\chi}_+ = 0$, which corresponds to a vanishing dark energy density at early times from Eq.(24) (but we could also take any finite value, or an infinite boundary $\tilde{\chi}_+ \rightarrow +\infty$ that is reached sufficiently slowly to ensure that the dark energy component is subdominant at high redshift). A simple model that obeys these properties and the constraint (46), which also reads as Eq.(51), is

$$\text{model (I):} \quad -1 < \tilde{\chi} < 0, \quad \ln A = \alpha \sqrt{1 - \tilde{\chi}^2}, \quad (55)$$

with

$$\alpha > 0, \quad \alpha \sim 10^{-6}. \quad (56)$$

Here we set $\tilde{\chi}_-$ to -1 without loss of generality, as this merely defines the normalization of \mathcal{M}^4 and α . Instead of the square root we could have chosen a more general exponent, $\ln A = \alpha(1 - \tilde{\chi}^2)^\nu$ with $0 < \nu < 1$, but $\nu = 1/2$ simplifies the numerical computations. Then, the scalar-field equation (50) gives

$$\tilde{\chi}(\rho) = - \left(1 + \frac{\alpha^2 \rho^2}{\mathcal{M}^8} \right)^{-1/2}, \quad (57)$$

$$\ln A(\rho) = \alpha \left(1 + \frac{\mathcal{M}^8}{\alpha^2 \rho^2} \right)^{-1/2}, \quad (58)$$

and

$$p_A(\rho) = -\mathcal{M}^4 c^2 \left(1 + \frac{\alpha^2 \rho^2}{\mathcal{M}^8} \right)^{-1/2}. \quad (59)$$

We recover the fact that the system depends on the density through the dimensionless ratio $\hat{\rho} = \rho/\rho_\alpha$ introduced in Eqs.(52)-(53). In terms of the scale factor $a(t)$, using $\bar{\rho} = \bar{\rho}_0/a^3$, this gives (at leading order)

$$\epsilon_2(a) = 3\epsilon_1(a) \quad \text{and} \quad \epsilon_1(a) = -\alpha \frac{\alpha \bar{\rho}/\mathcal{M}^4}{(1 + \alpha^2 \bar{\rho}^2/\mathcal{M}^8)^{3/2}} \quad (60)$$

and we can check that $|\epsilon_2| = 3|\epsilon_1| \lesssim \alpha \ll 1$ at all redshifts, while we have $\tilde{\chi}_0 \simeq -1$ and $\mathcal{M}^4 \simeq \bar{\rho}_{\text{de}0}$. At low redshift, $z \simeq 0$, we actually have $|\epsilon_2| = 3|\epsilon_1| \sim \alpha^2$, which is much smaller than the maximum value of order α that is reached at a redshift $z_\alpha \sim \alpha^{-1/3}$. Therefore, in this model the modification to the growth of large-scale structures is the greatest at high redshifts, $z \sim z_\alpha$, much before the dark energy era.

As explained in Sec. II, this choice of $A(\tilde{\chi})$ corresponds to an infinite number of couples $\{V(\varphi), A(\varphi)\}$. In particular, from Eq.(4) this corresponds for instance to

$$\text{(Ia):} \quad V(\varphi) = \mathcal{M}^4 \sqrt{1 - \left(\frac{\beta \varphi}{\alpha M_{\text{Pl}}} \right)^2}, \quad A(\varphi) = e^{\beta \varphi/M_{\text{Pl}}} \quad (61)$$

with $\beta > 0$ and $0 < \beta\varphi/M_{\text{Pl}} < \alpha$, where we assumed an exponential coupling function $A(\varphi)$, or to

$$\text{(Ib)} : V(\varphi) = \mathcal{M}^4 e^{-\gamma\varphi/M_{\text{Pl}}}, \quad A(\varphi) = e^{\alpha\sqrt{1-e^{-2\gamma\varphi/M_{\text{Pl}}}}}, \quad (62)$$

with $\gamma > 0$ and $0 < \varphi < +\infty$, where we assumed an exponential potential $V(\varphi)$.

C. Model (II): $\tilde{\chi}$ is a bounded decreasing function of ρ

We next consider the case where $\tilde{\chi}$ is a monotonic decreasing function of ρ , over $\tilde{\chi}_- < \tilde{\chi} < \tilde{\chi}_+$. Thus, $d \ln A/d\tilde{\chi}$ must increase from 0 to $+\infty$ as $\tilde{\chi}$ grows from $\tilde{\chi}_-$ to $\tilde{\chi}_+$. Now $\tilde{\chi}_-$ corresponds to the early matter era whereas $\tilde{\chi}_+$ corresponds to the late dark energy era, hence $\tilde{\chi}_+ < 0$. A simple choice that satisfies these conditions is

$$\text{model (II)}: \quad \tilde{\chi}_* < \tilde{\chi} < -1, \\ \ln A = -\alpha\sqrt{(1+\tilde{\chi})(1+2\tilde{\chi}_*-\tilde{\chi})}, \quad (63)$$

where again α is a small positive parameter as in Eq.(51) and we set $\tilde{\chi}_- = \tilde{\chi}_*$ and $\tilde{\chi}_+ = -1$ without loss of generality. Then, the scalar-field equation (50) gives

$$\tilde{\chi}(\rho) = \tilde{\chi}_* - \frac{1+\tilde{\chi}_*}{\sqrt{1+\alpha^2\rho^2/\mathcal{M}^8}}, \quad (64)$$

$$\ln A(\rho) = \alpha\frac{1+\tilde{\chi}_*}{\sqrt{1+\mathcal{M}^8/\alpha^2\rho^2}}, \quad (65)$$

$$p_A(\rho) = \mathcal{M}^4 c^2 \tilde{\chi}_* - \mathcal{M}^4 c^2 \frac{1+\tilde{\chi}_*}{\sqrt{1+\alpha^2\rho^2/\mathcal{M}^8}}, \quad (66)$$

which again makes explicit the dependence on the dimensionless ratio $\hat{\rho} = \rho/\rho_c$ introduced in Eqs.(52)-(53). In terms of the scale factor $a(t)$ this gives $\epsilon_2(a) = 3\epsilon_1(a)$ and

$$\epsilon_1(a) = -\alpha(1+\tilde{\chi}_*)\frac{\alpha\bar{\rho}/\mathcal{M}^4}{(1+\alpha^2\bar{\rho}^2/\mathcal{M}^8)^{3/2}}. \quad (67)$$

Again, we can check that $|\epsilon_2| = 3|\epsilon_1| \lesssim \alpha \ll 1$ at all redshifts, with $\tilde{\chi}_0 \simeq -1$ and $\mathcal{M}^4 \simeq \bar{\rho}_{\text{de}0}$. We also have $|\epsilon_2| = 3|\epsilon_1| \sim \alpha^2$ at low z and the maximum value of order α is reached at a redshift $z_\alpha \sim \alpha^{-1/3}$.

This choice of $A(\tilde{\chi})$ corresponds for instance to

$$\text{(IIa)} : V(\varphi) = -\mathcal{M}^4 \left[\tilde{\chi}_* + \sqrt{(1+\tilde{\chi}_*)^2 - \left(\frac{\beta\varphi}{\alpha M_{\text{Pl}}}\right)^2} \right], \\ A(\varphi) = e^{\beta\varphi/M_{\text{Pl}}} \quad (68)$$

with $\beta > 0$ and $\alpha(1+\tilde{\chi}_*) < \beta\varphi/M_{\text{Pl}} < 0$, for an exponential coupling, or to

$$\text{(IIb)} : V(\varphi) = \mathcal{M}^4 e^{-\gamma\varphi/M_{\text{Pl}}}, \\ A(\varphi) = e^{-\alpha\sqrt{1+2\tilde{\chi}_*-2\tilde{\chi}_*e^{-\gamma\varphi/M_{\text{Pl}}}-e^{-2\gamma\varphi/M_{\text{Pl}}}}}, \quad (69)$$

with $\gamma > 0$ and $-\ln(-\tilde{\chi}_*) < \gamma\varphi/M_{\text{Pl}} < 0$, for an exponential potential.

D. Model (III): $\tilde{\chi}$ is an unbounded decreasing function of ρ

As a variant of the model (II) of Eq.(63), where $\tilde{\chi}(\rho)$ is a bounded decreasing function of ρ , we can consider the model

$$\text{model (III)}: \quad -\infty < \tilde{\chi} < -1, \quad \ln A = -\alpha\sqrt{1+\frac{1}{\tilde{\chi}}}, \quad (70)$$

where $\tilde{\chi}$ is unbounded from below. This avoids introducing a finite lower bound $\tilde{\chi}_*$. Equation (50) gives

$$\tilde{\chi}^3(\tilde{\chi}+1) = \frac{\alpha^2\rho^2}{4\mathcal{M}^8}, \quad (71)$$

which is a fourth-order algebraic equation for $\tilde{\chi}$. We can easily solve it in two different regimes, namely when $\chi \rightarrow -1$ ($\rho \rightarrow 0$) and $\chi \rightarrow -\infty$ ($\rho \rightarrow +\infty$). In the former case, we obtain

$$\chi \rightarrow -1, \quad \frac{\alpha\rho}{\mathcal{M}^4} \ll 1: \quad \tilde{\chi}(\rho) \simeq -1 - \frac{\alpha^2\rho^2}{4\mathcal{M}^8}, \quad (72)$$

$$\ln A(\rho) \simeq -\alpha^2\frac{\rho}{2\mathcal{M}^4}, \quad (73)$$

$$p_A(\rho) \simeq -\mathcal{M}^4 c^2 - \mathcal{M}^4 c^2 \frac{\alpha^2\rho^2}{4\mathcal{M}^8}. \quad (74)$$

At leading order this gives

$$\epsilon_2 = 3\epsilon_1 \quad \text{with} \quad \epsilon_1(a) = \frac{\alpha^2\bar{\rho}}{2\mathcal{M}^4}, \quad (75)$$

and again we can check that $\epsilon_1(a) \sim \alpha^2$ at low z . On the other hand, in the high-density limit we obtain:

$$\chi \rightarrow -\infty, \quad \frac{\alpha\rho}{\mathcal{M}^4} \gg 1: \quad \tilde{\chi}(\rho) \simeq -\sqrt{\frac{\alpha\rho}{2\mathcal{M}^4}}, \quad (76)$$

$$\ln A(\rho) \simeq -\alpha + \sqrt{\frac{\alpha\mathcal{M}^4}{2\rho}}, \quad (77)$$

$$p_A(\rho) \simeq -\mathcal{M}^4 c^2 \sqrt{\frac{\alpha\rho}{2\mathcal{M}^4}}, \quad (78)$$

and

$$\epsilon_2 = 3\epsilon_1 \quad \text{with} \quad \epsilon_1(a) \simeq \sqrt{\frac{\alpha\mathcal{M}^4}{8\rho}}, \quad (79)$$

which again shows that $|\epsilon_1(a)| \ll \alpha$ in this limit.

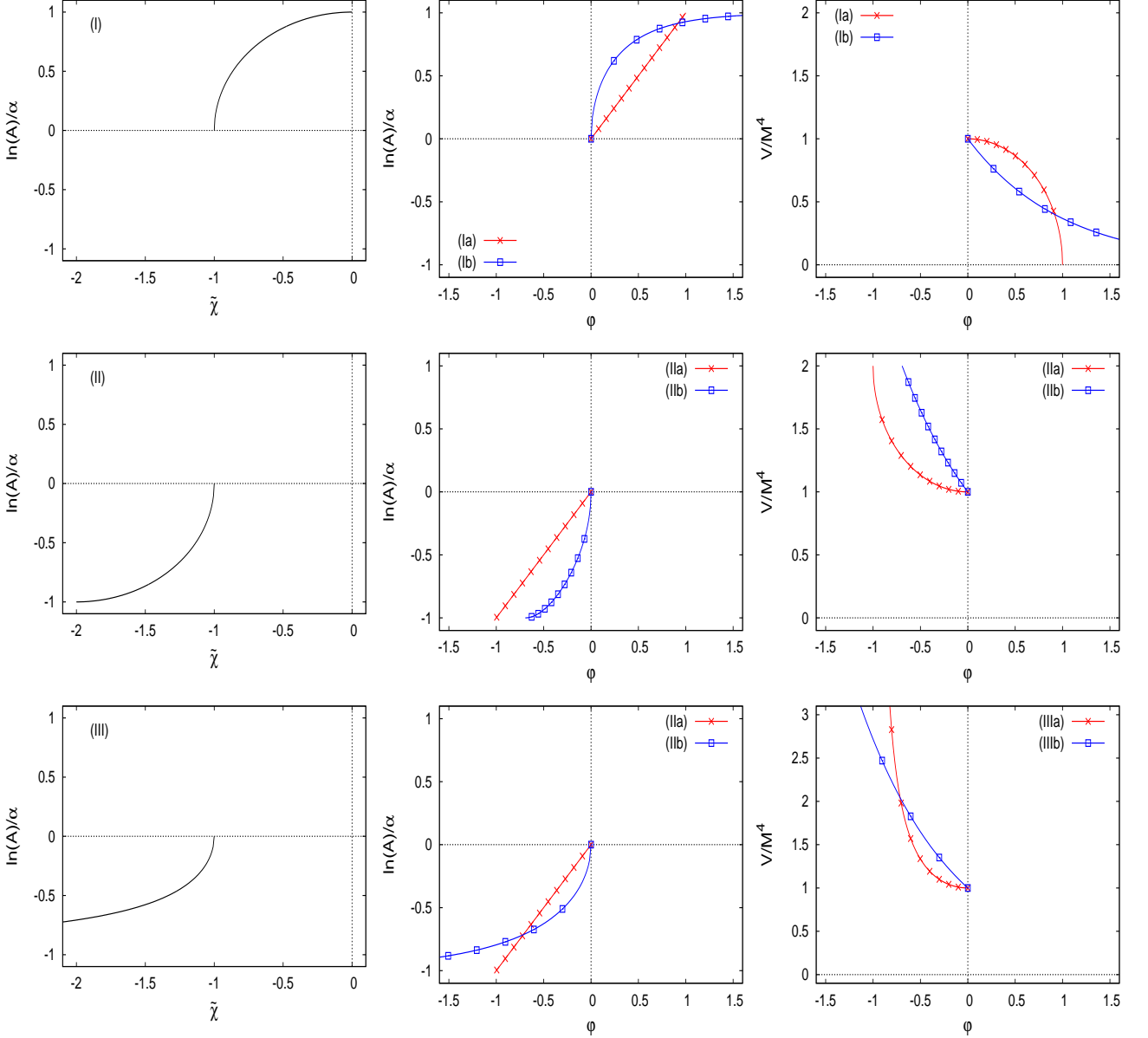


FIG. 1: Coupling functions and scalar field potentials for the model (I) of Eq.(55) (*upper row*), the model (II) of Eq.(63) (*middle row*) and the model (III) of Eq.(70) (*lower row*). *Left column*: coupling function $A(\tilde{\chi})$ [the plot shows $\ln(A)/\alpha$]. *Middle column*: coupling function $A(\varphi)$ for the examples (a) (red lines with crosses, in units of $\beta\varphi/\alpha M_{\text{Pl}}$), and (b) (blue lines with squares, in units of $\gamma\varphi/\alpha M_{\text{Pl}}$). *Right column*: potential $V(\varphi)/\mathcal{M}^4$ for the examples (a) (red lines with crosses, in units of $\beta\varphi/\alpha M_{\text{Pl}}$), and (b) (blue lines with squares, in units of $\gamma\varphi/\alpha M_{\text{Pl}}$).

As in the previous cases this coupling function $A(\tilde{\chi})$ corresponds to an infinite number of pairs $\{V(\varphi), A(\varphi)\}$. In particular, the case of an exponential coupling or an exponential potential are described by

$$\text{(IIIa)}: V(\varphi) = \frac{\mathcal{M}^4}{1 - \left(\frac{\beta\varphi}{\alpha M_{\text{Pl}}}\right)^2}, \quad A(\varphi) = e^{\beta\varphi/M_{\text{Pl}}} \quad (80)$$

with $\beta > 0$ and $-\alpha < \beta\varphi/M_{\text{Pl}} < 0$, and

$$\text{(IIIb)}: V(\varphi) = \mathcal{M}^4 e^{-\gamma\varphi/M_{\text{Pl}}}, \quad A(\varphi) = e^{-\alpha\sqrt{1 - e^{\gamma\varphi/M_{\text{Pl}}}}}, \quad (81)$$

with $\gamma > 0$ and $-\infty < \gamma\varphi/M_{\text{Pl}} < 0$.

E. Common low-redshift and low-density behavior

In the following, we consider the case $\alpha = 10^{-6}$ and $\chi_* = -2$ for the parameters that define the models (I), (II) and (III). In all cases we normalized the low-density limit of the scalar field $\tilde{\chi}$ to -1 and the derivative $d \ln A / d \tilde{\chi}$ must go to $+\infty$ in this limit, from Eq.(50). For a power-law divergence, $d \ln A / d \tilde{\chi} \sim \alpha |\tilde{\chi} + 1|^{-\nu}$, with $0 < \nu < 1$, this gives $|\tilde{\chi} + 1| \sim (\alpha \rho / \mathcal{M}^4)^{1/\nu}$ in the low-density regime. In the explicit models (55), (63) and (70) we have $\nu = 1/2$, so that in all three cases we have:

$$\frac{\alpha \rho}{\mathcal{M}^4} \ll 1: \quad |\tilde{\chi} + 1| \sim \left(\frac{\alpha \rho}{\mathcal{M}^4} \right)^2, \quad (82)$$

and

$$\frac{\alpha \bar{\rho}}{\mathcal{M}^4} \ll 1: \quad \beta_1 = \frac{\mathcal{M}^4}{\bar{\rho}} \sim \frac{\alpha}{|\tilde{\chi} + 1|^{1/2}}, \quad (83)$$

$$|\beta_2| \sim \frac{\alpha}{|\tilde{\chi} + 1|^{3/2}} \sim \alpha^{-2} \left(\frac{\mathcal{M}^4}{\bar{\rho}} \right)^3, \quad (84)$$

$$|\epsilon_1| = \frac{\beta_1^2}{|\beta_2|} \sim \alpha |\tilde{\chi} + 1|^{1/2} \sim \alpha^2 \frac{\bar{\rho}}{\mathcal{M}^4}. \quad (85)$$

For future use, writing $d \ln A / d \ln \rho = (d \ln A / d \tilde{\chi})(d \tilde{\chi} / d \ln \rho)$, we also obtain in this low-density regime

$$\frac{\alpha \rho}{\mathcal{M}^4} \ll 1: \quad \left| \frac{d \ln A}{d \ln \rho} \right| \sim \alpha^2 \frac{\rho}{\mathcal{M}^4}. \quad (86)$$

In models (I) and (II), since the scalar field $\tilde{\chi}$ has a finite range of order unity, Eq.(49) implies $\mathcal{M}^4 \sim \bar{\rho}_{\text{de}0} \sim \bar{\rho}_0$. Therefore, at low redshifts we have from Eq.(82):

$$a \gg a_\alpha \sim \alpha^{1/3}: \quad |\tilde{\chi} + 1| \sim \alpha^2 a^{-6}, \quad (87)$$

where we normalized the scale factor to unity today, $a(z=0) = 1$. In particular, we have $|\tilde{\chi} + 1| \sim \alpha^2 \sim 10^{-12}$ at low z , so that Eq.(49) implies

$$\mathcal{M}^4 = \bar{\rho}_{\text{de}0}, \quad (88)$$

up to a 10^{-12} accuracy, and this parameter is completely set by the reference Λ -CDM cosmology. Moreover, the dark energy density is almost constant, along with $\tilde{\chi}$, up to a redshift $z_\alpha \sim \alpha^{-1/3} \sim 100$, which means that the background cosmology cannot be distinguished from the Λ -CDM reference, in agreement with the analysis in Sec. IV A. For the model (III) we also take $\mathcal{M}^4 = \bar{\rho}_{\text{de}0}$, which gives the same behaviors. Then, the scalar-field equation (50) reads as

$$\beta_1(a) = \frac{d \ln \bar{A}}{d \tilde{\chi}} = \frac{\Omega_{\text{de}0}}{\Omega_{\text{m}0}} a^3. \quad (89)$$

Thus, the first derivative of the coupling function, $d \ln A / d \tilde{\chi}$, at the background level, is of order unity at low z (despite the prefactor α of $\ln A$, which means that at low z we are close to the divergence of $d \ln A / d \tilde{\chi}$) and decreases with redshift as $(1+z)^{-3}$.

Thus, these models involve two free parameters that must be set to match observations: the usual dark energy scale $\mathcal{M}^4 = \bar{\rho}_{\text{de}0}$, as in most cosmological models including Λ -CDM, and the parameter $\alpha \lesssim 10^{-6}$ that is needed to make sure that the fifth force never becomes too large as compared with Newtonian gravity. Of course, this is only an upper bound and we can take α as small as we wish, as we recover the Λ -CDM scenario and General Relativity in the limit $\alpha \rightarrow 0$ [where the coupling function $A(\tilde{\chi})$ becomes identical to unity and the non-minimal coupling between matter and the scalar field vanishes].

In Fig. 1, we show the coupling and potential functions of the models (I) (upper row), (II) (middle row) and (III) (lower row). The left column shows $\lambda(\tilde{\chi}) = \alpha^{-1} \ln A(\tilde{\chi})$ from Eqs.(55), (63) and (70). The middle column shows $\lambda(\varphi) = \alpha^{-1} \ln A(\varphi)$ for the variants (a) and (b). The right column shows $-\tilde{\chi} = V(\varphi) / \mathcal{M}^4$ for the same cases.

In models (Ia,Ib) φ is positive whereas in models (IIa,IIb,IIIa,IIIb) it is negative. It has a finite range in models (Ia) ($0 < \beta\varphi / \alpha M_{\text{Pl}} < 1$), (IIa) ($1 + \tilde{\chi}_* < \beta\varphi / \alpha M_{\text{Pl}} < 0$), (IIb) ($-\ln(-\tilde{\chi}_*) < \gamma\varphi / M_{\text{Pl}} < 0$) and (IIIa) ($-1 < \beta\varphi / \alpha M_{\text{Pl}} < 0$), while it extends from zero to $+\infty$ in model (Ib) and from zero to $-\infty$ in model (IIIb).

In all cases, the late-time dark energy era, $t \rightarrow +\infty$, corresponds to $\tilde{\chi} \rightarrow -1$, $\varphi \rightarrow 0$, $V / \mathcal{M}^4 \rightarrow 1$ (i.e. the endpoint at the center of the plots). It is the maximum of the potential $V(\varphi)$ in model (I) and the minimum in models (II) and (III). This low-density limit corresponds to $d \ln A / d \tilde{\chi} \rightarrow +\infty$, which implies $(d \ln A / d \varphi)(d \varphi / d V) \rightarrow -\infty$. In models (a), this is achieved by $dV / d\varphi \rightarrow 0$, while in models (b) this is achieved by $d \ln A / d \varphi \rightarrow +\infty$.

The early-time or high density limit corresponds to $\tilde{\chi} \rightarrow 0$ in model (I), $\tilde{\chi} \rightarrow -2$ in model (II) and $\tilde{\chi} \rightarrow -\infty$ in model (III). It also corresponds to $d \ln A / d \tilde{\chi} \rightarrow 0$, which implies $(d \ln A / d \varphi)(d \varphi / d V) \rightarrow 0$. In models (a), this is achieved by $dV / d\varphi \rightarrow -\infty$, while in models (b) this is achieved by $d \ln A / d \varphi \rightarrow 0$.

V. SELF-CONSISTENCY AND REGIME OF VALIDITY OF THE THEORY

Before we investigate the properties of the models introduced in this paper, from cosmological to Solar System scales, we consider in this section the self-consistency and the range of validity of theories defined by the Lagrangian (3).

A. Stability with respect to a nonzero kinetic term

In the Lagrangian (3) we set the kinetic term of the scalar field to zero. However, in realistic scenarios the models studied in this paper may rather correspond to cases where the scalar field Lagrangian is merely dominated by its potential term with a negligible but non-zero kinetic term. Then, we must check whether the solution (23) obtained in the previous sections remains meaningful for a small non-zero kinetic term. Thus, we generalize the Lagrangian (5) to

$$\tilde{\mathcal{L}}_{\tilde{\chi}}(\tilde{\chi}) = -\frac{\kappa}{2}\tilde{\nabla}_{\mu}\tilde{\chi}\tilde{\nabla}^{\mu}\tilde{\chi} + \mathcal{M}^4\tilde{\chi} \quad \text{with } \kappa \rightarrow 0. \quad (90)$$

Using $\bar{A} \simeq 1$, so that the Einstein and Jordan frames are identical at the background level, the equations of motion (6) or (50) of the scalar field generalize to

$$-\kappa a^{-4} \frac{\partial}{\partial \tau} \left(a^2 \frac{\partial \tilde{\chi}}{\partial \tau} \right) + \kappa a^{-2} c^2 \nabla^2 \tilde{\chi} + \mathcal{M}^4 = \rho \frac{d \ln A}{d \tilde{\chi}}. \quad (91)$$

1. Quasi-static cosmological background

At the background level, considering a scalar field that only depends on time, we expand the solution of the Klein-Gordon equation (91) around the solution $\tilde{\chi}_0$ of Eq.(23), obtained in the previous sections with a zero kinetic term,

$$\tilde{\chi} = \tilde{\chi}_0 + \bar{\phi} \quad \text{with } \mathcal{M}^4 = \bar{\rho} \frac{d \ln A}{d \tilde{\chi}}(\tilde{\chi}_0). \quad (92)$$

Using the expansion (38) of $\ln A$ around $\ln A(\tilde{\chi}_0)$, this gives at linear order over $\bar{\phi}$,

$$\kappa a^{-4} \frac{d}{d \tau} \left(a^2 \frac{d \bar{\phi}}{d \tau} \right) + \bar{\rho} \beta_2 \bar{\phi} = -\kappa a^{-4} \frac{d}{d \tau} \left(a^2 \frac{d \tilde{\chi}_0}{d \tau} \right). \quad (93)$$

In the limit $\kappa \rightarrow 0$, the particular solution reads at linear order in κ as

$$\bar{\phi}_0 = -\frac{\kappa}{a^4 \bar{\rho} \beta_2} \frac{d}{d \tau} \left(a^2 \frac{d \tilde{\chi}_0}{d \tau} \right). \quad (94)$$

As expected, it vanishes in the limit $\kappa \rightarrow 0$. More precisely, the correction $\bar{\phi}_0$ is negligible as compared to the quasi-static solution $\tilde{\chi}_0$ if

$$|\kappa| \ll |\beta_2| \frac{\bar{\rho}}{H^2} \sim |\beta_2| M_{\text{Pl}}^2. \quad (95)$$

From the expressions given in section IV and as we will check in Fig. 2 and Eq.(108) below, β_2 is of order $\alpha^{-2} \gg 1$ today and decreases at higher redshift until $z_{\alpha} \sim 100$, where it is of order α . At higher redshift it typically remains of order α [because of the prefactor α in the coupling function $\ln A(\tilde{\chi})$], or decays to zero in models such as (III) where $\bar{[\chi]}$ is not bounded and goes to infinity

at high z . Thus, for practical purposes the condition (95) is satisfied if

$$|\kappa| \ll \alpha M_{\text{Pl}}^2 \sim 10^{-6} M_{\text{Pl}}^2. \quad (96)$$

For models such as (III), the condition (95) will be violated at very high z , $z \gg z_{\alpha}$, if κ does not go to zero. Then, one must take into account the kinetic terms in the scalar field equation to obtain the background solution $\tilde{\chi}$. However, at these high redshifts the scalar field should not play an important role and our results should be independent of this early-time modification. On the other hand, in such cases the kinetic prefactor κ generically depends on time, through the factor $(d\varphi/dV)^2$ introduced by the change of variable (4), and we expect for instance κ to decrease as fast as β_2 , as $1/V^2$, for models where V goes to infinity while φ remains bounded, so that the condition (95) remains satisfied.

So far we have only introduced two parameters in the models, the dimensional dark-energy density today, $\bar{\rho}_{\text{de}0} = \mathcal{M}^4 \simeq (2.296 \times 10^{-12} \text{GeV})^4$ [17], and the dimensionless parameter $\alpha \sim 10^{-6}$. Since \mathcal{M} is smaller than the reduced Planck mass, $M_{\text{Pl}} \simeq 2.44 \times 10^{18} \text{GeV}$, by 30 orders of magnitude, we can see that we do not need to introduce additional small parameters to satisfy Eq.(96). Apart from $\kappa = 0$, the choices $\kappa \sim \mathcal{M}^2$, $\kappa \sim \mathcal{M} M_{\text{Pl}}$ or $\kappa \sim \mathcal{M}^{1/2} M_{\text{Pl}}^{3/2}$, satisfy the constraint.

The homogeneous solutions of Eq.(93) obey

$$\frac{d^2 \bar{\phi}}{d \tau^2} + \frac{a^2 \bar{\rho} \beta_2}{\kappa} \bar{\phi} = 0, \quad (97)$$

in the high-frequency limit (i.e., over time scales much below $1/H$). From the condition (95) we have $a^2 \bar{\rho} \beta_2 / \kappa \gg \mathcal{H}^2$, so that the homogeneous solution evolves indeed on time scales much shorter than the Hubble time. For the solution $\tilde{\chi}_0$ to be stable the homogeneous solutions (97) must not show exponential growth but only fast oscillations, of frequency $\omega \propto \kappa^{-1/2}$. This leads to the constraint

$$\frac{\beta_2}{\kappa} > 0. \quad (98)$$

As the field $\tilde{\chi}$ typically arises through the change of variable (4), the kinetic coefficient κ introduced in Eq.(90) depends on time. However, its sign is not modified by the change of variable and it is positive for standard well-behaved models. Then, the constraint (98) leads to $\beta_2 > 0$, which means that $\ln A(\tilde{\chi})$ must be a convex function. This rules out the model (I) introduced in Sec. IV B. More generally, from the definition of the coefficients β_1 and β_2 and the scalar-field equation (50), the condition $\beta_2 > 0$ implies that $d\rho/d\tilde{\chi} < 0$ and the function $\tilde{\chi}(\rho)$ is a monotonic decreasing function of ρ . At the background level, this implies that $\tilde{\chi}$ increases with time, hence the potential $V(\bar{\varphi})$ defined from the change of variable (4) decreases with time. As expected, the stable case corresponds to scenarios where the background scalar field $\bar{\varphi}$ rolls down its potential $V(\bar{\varphi})$ [as in models

(II) and (III) of Secs. IV C and IV D], whereas the unstable case corresponds to a background scalar field that climbs up its potential [as in model (I) of Sec. IV B].

Models with $\beta_2 < 0$ could be made stable, with respect to the classical background perturbations analyzed here, by choosing a non-standard sign $\kappa < 0$ for the small kinetic term. However, such models are typically plagued by ghost instabilities, as the kinetic energy is unbounded from below, unless one sets a high-energy cutoff of the theory at a sufficiently low energy to tame down these instabilities. In the following we also present our results for the model (I) of Sec. IV B to keep this work as general as possible, even though this is unlikely to correspond to realistic and natural scenarios.

2. Cosmological large-scale structures

To apply the equations of motion derived in Sec. III to the formation of large-scale structures, we must also check that the kinetic term plays no role on these scales. Thus, we now take into account the Laplacian term in Eq.(91) and the perturbations of the scalar field, $\phi = \delta\tilde{\chi} - \tilde{\chi}$, obey at linear order

$$-\kappa a^{-4} \frac{\partial}{\partial \tau} \left(a^2 \frac{\partial \phi}{\partial \tau} \right) + \kappa a^{-2} c^2 \nabla^2 \phi - \bar{\rho} \beta_2 \phi = \beta_1 \delta \rho. \quad (99)$$

As for the background case, the time derivatives are negligible when the condition (95) is satisfied. The spatial Laplacian can be neglected at comoving scale $1/k$, where k is the wave number of interest, if we have

$$|\kappa| \ll \frac{\bar{\rho} |\beta_2| a^2}{c^2 k^2} \sim \left(\frac{aH}{ck} \right)^2 |\beta_2| M_{\text{Pl}}^2. \quad (100)$$

This constraint is tighter than the background condition (95) as we require the theory to remain valid down to sub-horizon scales, $ck/aH \gg 1$. If we wish to apply the model without kinetic term down to $1 h^{-1} \text{kpc}$, below the galaxy-halo scale, we must have

$$k \sim 1 h \text{kpc}^{-1} : \quad \kappa \ll 10^{-19} M_{\text{Pl}}^2, \quad (101)$$

where we used again $|\beta_2| \sim \alpha \sim 10^{-6}$. We can still choose for instance $\kappa \sim \mathcal{M}^2$ or $\kappa \sim \mathcal{M} M_{\text{Pl}}$. Thus, we do not need to introduce a new low-energy scale to build a small-enough kinetic term that can be neglected for both the background and the cosmological structures.

Of course, on scales $1 h^{-1} \text{kpc}$ the density and scalar fields are in the nonlinear regime, which modifies Eq.(99). If we expand around the local solution, $\tilde{\chi}_0[\rho(\mathbf{x})]$, the factors $\bar{\rho} \beta_2(\bar{\rho})$ and $\beta_1(\bar{\rho})$ must be replaced by $\rho \beta_2(\rho)$ and $\beta_1(\rho)$. For models such as (I) and (II), where β_2 remains of order α at high densities the upper bound in Eq.(101) is simply multiplied by a factor $\rho/\bar{\rho}$. Then, nonlinearities actually loosen up the constraint (101) and the kinetic term in the scalar-field Lagrangian becomes even more negligible. In practice, the coefficient

κ will depend on the local value of the scalar field, and hence on the local density, but the relatively high upper bound $(\rho/\bar{\rho})10^{-19} M_{\text{Pl}}^2$, as compared with \mathcal{M}^2 or $\mathcal{M} M_{\text{Pl}}$, suggests that the scale \mathcal{M} will be sufficient to construct small-enough coefficients κ without introducing additional finely tuned parameters.

B. Small-scale cutoff

Independently of a possible kinetic term, the local model (5) considered so far is not expected to apply down to arbitrarily small scales. In the previous sections and through most of this paper, we implicitly assume that we can work with a continuous density field $\rho(\mathbf{x})$ defined by some coarse-graining procedure, instead of a singular field made of Dirac peaks (in the limit of classical point-like particles) or of isolated density peaks (finite-size classical particles). Therefore, we assume the models studied in this paper to be effective theories that only apply beyond some small-scale cutoff ℓ_s , so that the density field is defined by a coarse-graining at scale ℓ_s .

If we consider for instance the mean inter-particle distance, $\lambda = (m/\rho)^{1/3}$, we obtain on the Earth, with $\rho \sim 1 \text{ g/cm}^3$ and $m \sim m_p$, the proton mass,

$$\lambda_{\text{Earth}} \sim 10^{-8} \text{ cm}, \quad (102)$$

and in the intergalactic medium (IGM), using the mean density of the Universe,

$$\lambda_{\text{IGM}} \sim \left(\frac{m}{m_p} \right)^{1/3} 100 \text{ cm}, \quad (103)$$

where m can be taken as the largest among the proton and the dark matter particle mass. This typically gives a distance of the order of a meter. In fact, in our study of the cosmological background and of cosmological structures, we assume some coarse-graining of the density field on scales at least as large as λ_{IGM} , so that we can use the density ρ associated with the continuum limit.

In terms of energy scales, this corresponds to $\lambda_{\text{IGM}} \sim 1 \text{ m} = (1.973 \times 10^{-16} \text{ GeV})^{-1}$. On the other hand, the mean dark-energy density today is $\bar{\rho}_{\text{de}0} = \mathcal{M}^4 = 2.778 \times 10^{-47} \text{ GeV}^4$, which gives $\lambda_{\text{IGM}} \sim 1 \text{ m} \sim 10^4 \mathcal{M}^{-1}$. Therefore, the small-scale cutoff, ℓ_s , which defines the smoothing scale of the density field in such an effective approach, does not require the introduction of a new fundamental scale. For instance, it is sufficient to set $\ell_s = \alpha^{-1} \mathcal{M}^{-1} \sim 100 \text{ m}$, using the two parameters \mathcal{M} and α that have already been introduced to characterize the model, or $\ell_s = M_{\text{Pl}}^{1/2} \mathcal{M}^{-3/2} \sim 1 \text{ A.U.}$, using a combination with the Planck mass.

A natural way to introduce a smoothing cutoff on small scales is to have a nonzero kinetic term in the scalar-field Lagrangian (5), as considered in Sec. V A. Using again the Lagrangian (90), the fluctuations ϕ of the scalar field around the cosmological background obey Eq.(99)

and the smoothing associated with the Laplacian term becomes important at the physical scale ℓ_s if we have

$$|\kappa| \sim \frac{\bar{\rho}|\beta_2|\ell_s^2}{c^2} \sim \left(\frac{\ell_s H}{c}\right)^2 |\beta_2| M_{\text{Pl}}^2. \quad (104)$$

We can check that this constraint is not contradictory with the conditions (95) and (100), associated with the validity of the solution without kinetic term for the background and cosmological structures, because the small-scale cutoff ℓ_s can be taken to be much smaller than cosmological scales. At $z = 0$, using $|\beta_2| \sim \alpha^{-2} \sim 10^{12}$, the condition (104) reads as

$$z = 0: |\kappa| \sim \left(\frac{\ell_s}{1 \text{ m}}\right)^2 6 \times 10^{-41} M_{\text{Pl}}^2, \quad (105)$$

and for $\ell_s > 1 \text{ m}$ we can take for instance $\kappa \sim \mathcal{M} M_{\text{Pl}}$.

Such a Laplacian term is also sufficient to regularize the theory at the atomic scale (102) on the Earth if we have

$$|\kappa| > \frac{m_p |\beta_2|_{\text{Earth}}}{\lambda_{\text{Earth}} c^2}, \quad (106)$$

where $|\beta_2|_{\text{Earth}}$ is the value obtained for $\rho \sim 1 \text{ g.cm}^{-3}$. Using $|\beta_2|_{\text{Earth}} \sim \alpha \sim 10^{-6}$, as appropriate for the high-density regime (see for instance Fig. 2 below), this yields

$$\text{Earth: } |\kappa| > 3 \times 10^{-49} M_{\text{Pl}}^2. \quad (107)$$

This is a looser bound than the cosmological constraint (105). However, because of the change of variable (4) the kinetic prefactor κ generically depends on the environment through the local value of the scalar field, so that usually Eq.(107) cannot be directly compared to Eq.(105). Nevertheless, in any case the estimates (105) and (107) show that it is not difficult to regularize the theory on very small scales through a small kinetic term in the scalar-field Lagrangian, without violating the condition (95).

VI. EVOLUTION OF THE COSMOLOGICAL BACKGROUND

A. Evolution of the background scalar field

As explained in section IV A, we require the function $\ln A$ to be bounded within a small interval of order 10^{-6} , see Eq.(46), so that contributions of the fifth force to the metric potentials do not exceed the Newtonian potential by several orders of magnitude. As pointed out in section IV A, this implies that $|\bar{A} - 1| \lesssim 10^{-6} \ll 1$. This implies in turn that we recover a Λ -CDM cosmology at the background level up to a 10^{-6} accuracy. We also have $|\epsilon_1|$ and $|\epsilon_2|$ of order $\alpha \sim 10^{-6}$, and $\bar{\chi}$ and $\bar{\rho}_{\text{de}}$ are almost constant in the dark energy era, see Eq.(24).

The factor $\beta_1(a)$ is always positive and decreases with redshift as in Eq.(89), independently of the details of the

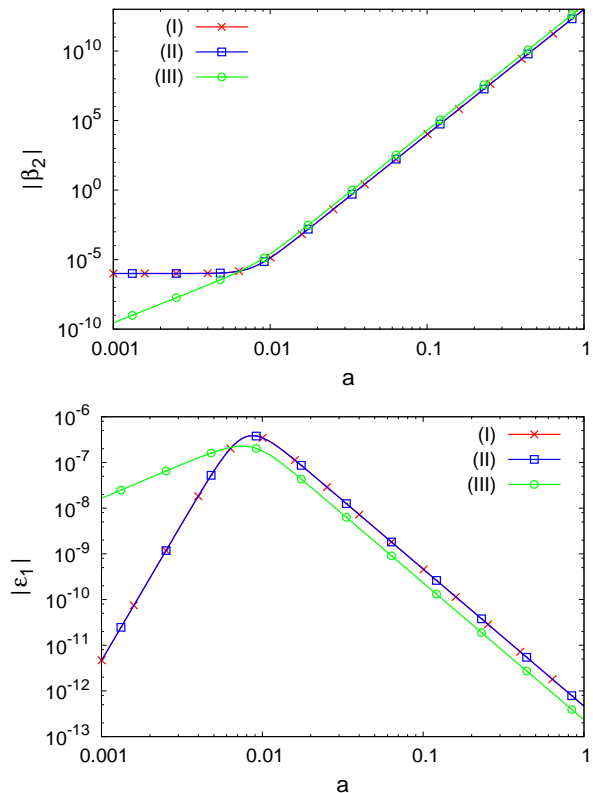


FIG. 2: Absolute value of the factors β_2 (upper panel) and ϵ_1 (lower panel) as a function of the scale factor. We show $|\beta_2|$ and $|\epsilon_1|$ for models (I) (red line with crosses), (II) (blue line with squares) and (III) (green line with circles); $\beta_2 < 0$ and $\epsilon_1 < 0$ for model (I); $\beta_2 > 0$ and $\epsilon_1 > 0$ for models (II) and (III). The absolute values $|\beta_2|$ and $|\epsilon_1|$ of models (I) and (II) are equal.

coupling function $\ln A(\bar{\chi})$, because it is directly set by the scalar-field equation of motion (50).

We show the factors $\beta_2(a)$ and $\epsilon_1(a)$ in Fig. 2. These factors are positive for models (II) and (III), where the fifth force amplifies Newtonian gravity, while they are negative for model (I), where the fifth force decreases Newtonian gravity. It happens that for our explicit choices (55) and (63) (with $\bar{\chi}_* = -2$) the factors β_2 and ϵ_1 of models (I) and (II) have the same amplitude, but opposite signs, so that their curves coincide in Fig. 2.

From Eqs.(84) and (85), we have at low redshifts

$$a \gg a_\alpha \sim \alpha^{1/3}: |\beta_2| \sim \alpha^{-2} a^9, \quad |\epsilon_1| \sim \alpha^2 a^{-3}. \quad (108)$$

Thus, $|\beta_2|$ is maximum today, with $|\beta_2|_0 \sim \alpha^{-2} \sim 10^{12}$, and decreases with redshift until $z_\alpha \sim \alpha^{-1/3} \sim 100$, where it is of order $|\beta_2|_{z_\alpha} \sim \alpha \sim 10^{-6}$. At higher redshift $|\beta_2|$ typically remains of order α , or goes to zero with a rate that depends on the details of the model.

The factor $|\epsilon_1|$ reaches a maximum of order α at a high redshift, $z_\alpha \sim \alpha^{-1/3} \sim 100$, and later decays as a^{-3} to

reach a value of order α^2 today. Therefore, the scenarios considered in this paper have the characteristic property that the main modification to the gravitational dynamics actually occurs at a high redshift $z_\alpha \sim 100$, much before the dark energy era. This is related to the small parameter $\alpha \ll 1$, in agreement with Eq.(54) and the characteristic density ρ_α of Eq.(53). At higher redshift, $z \gg z_\alpha$, $|\epsilon_1|$ decreases again, as we have seen that $\epsilon_1 = \epsilon_2/3$ (in the approximation $\bar{A} \simeq 1$) and $\epsilon_2 = d \ln \bar{A} / d \ln a$ must vanish because \bar{A} converges to a constant close to unity at early times. For models (I) and (II) we have $|\epsilon_1| \sim a^6/\alpha$ while for model (III) we have $\epsilon_1 \sim \alpha^{1/2} a^{3/2}$. Thus, the decay of ϵ_1 is much slower at very high redshift for model (III). Indeed, using the scalar-field equation (50) we can also write ϵ_2 as $\epsilon_2 = (\mathcal{M}^4/\bar{\rho}) d\tilde{\chi}/d \ln a$. Then, $d\tilde{\chi}/d \ln a$ goes to zero at high redshift for models (I) and (II), as $\tilde{\chi}$ converges to a finite value, whereas $d\tilde{\chi}/d \ln a$ goes to infinity as $\tilde{\chi}$ goes to $-\infty$. We can check these behaviors in Fig. 2.

B. Negligible backreaction of small-scale nonlinearities onto the cosmological background

We have seen in Sec. III B 3 that for small enough ϵ_1 and ϵ_2 the cosmological behavior remains close to the Λ -CDM scenario at the background and linear levels. However, the nonlinearities associated with the scalar field could jeopardize this result. In this section, we check that the nonlinearity of the scalar-field energy density does not give rise to a significant backreaction onto the background dynamics.

We have seen that the scalar field energy density reads as $\rho_{\tilde{\chi}} = -\mathcal{M}^4 \tilde{\chi}$ (using again $\bar{A} \simeq 1$). Because $\tilde{\chi}(\rho)$ is a nonlinear function of ρ , its volume average is not identical to the background value $\bar{\tilde{\chi}} \equiv \tilde{\chi}(\bar{\rho})$. This implies that the mean Hubble expansion rate over a large volume, as large as the Hubble radius today, could significantly differ from the background expansion obtained from the background Friedmann equation (18), especially if the volume average is actually dominated by the highest-density regions.

In the models described in Sec. IV, the background value $\bar{\tilde{\chi}}$ at low redshift, in the dark energy era, is very close to the value $\tilde{\chi}(0) = -1$ associated with a zero density, as $|\bar{\tilde{\chi}} + 1| \sim \alpha^2 \ll 1$, see Eq.(87). This is because of the small parameter α that was introduced to ensure a cosmological behavior that is close to the Λ -CDM predictions. Then, we simply check that $\langle \tilde{\chi} \rangle \simeq \tilde{\chi}(0)$ too, where the volume average $\langle \tilde{\chi} \rangle$ is given by

$$\langle \tilde{\chi} \rangle = \int_V \frac{d\mathbf{x}}{V} \tilde{\chi}(\rho) = \int_0^\infty d\rho \mathcal{P}(\rho) \tilde{\chi}(\rho). \quad (109)$$

Here V is a large volume, with a size of the order of the Hubble radius, while $\mathcal{P}(\rho)$ is the probability distribution of the density within this volume. It obeys the two normalization properties:

$$\int_0^\infty d\rho \mathcal{P}(\rho) = 1, \quad \int_0^\infty d\rho \mathcal{P}(\rho) \rho = \bar{\rho}. \quad (110)$$

For any density threshold $\rho_s > 0$, the second property (110) implies the Bienaymé-Tchebychev inequality

$$\rho_s > 0 : \quad \int_{\rho_s}^\infty d\rho \mathcal{P}(\rho) \leq \frac{\bar{\rho}}{\rho_s}. \quad (111)$$

For monotonic functions $\tilde{\chi}(\rho)$ we have $|\langle \tilde{\chi} \rangle - \tilde{\chi}(0)| = \int_0^\infty d\rho \mathcal{P}(\rho) |\tilde{\chi}(\rho) - \tilde{\chi}(0)|$. Splitting the integral over the two domains $\rho \leq \rho_s$ and $\rho \geq \rho_s$, and using Eq.(111), gives

$$|\langle \tilde{\chi} \rangle - \tilde{\chi}(0)| \leq |\tilde{\chi}_s - \tilde{\chi}(0)| + \frac{\bar{\rho}}{\rho_s} |\tilde{\chi}(\infty) - \tilde{\chi}(0)|, \quad (112)$$

where we assumed that $\tilde{\chi}(\rho)$ is bounded.

Let us first consider the model (I) described in Sec. IV B, where $\tilde{\chi}$ is a bounded increasing function of ρ . This gives $\tilde{\chi}(\infty) = 0$, $\tilde{\chi}_s \simeq -1 + \alpha^2 \rho_s^2 / 2\mathcal{M}^8$, for densities $\rho_s \lesssim \bar{\rho}/\alpha$, and the two terms in Eq.(112) are of the same order for $\rho_s \sim \bar{\rho}\alpha^{-2/3}$. This choice provides an upper bound $|\langle \tilde{\chi} \rangle - \tilde{\chi}(0)| \lesssim \alpha^{2/3} \ll 1$.

The model (II) described in Sec. IV C, where $\tilde{\chi}$ is a bounded decreasing function of ρ , gives similar results and again $|\langle \tilde{\chi} \rangle - \tilde{\chi}(0)| \lesssim \alpha^{2/3} \ll 1$.

The model (III) described in Sec. IV D, where $\tilde{\chi}$ is an unbounded decreasing function of ρ , remains similar to the model (II). To handle the infinite range of $\tilde{\chi}$, we split the integral (109) over three domains, $[0, \rho_s]$, $[\rho_s, \rho_\alpha]$ and $[\rho_\alpha, +\infty[$, where $\rho_\alpha = \mathcal{M}^4/\alpha$ is also the density scale where the model departs from the bounded model (II) and probes the infinite tail (76). The first two terms are of order $\alpha^{2/3}$ as for the model (II), with the same choice $\rho_s \sim \bar{\rho}\alpha^{-2/3}$. Using the Cauchy-Schwarz inequality $\int_{\rho_\alpha}^\infty d\rho \mathcal{P}(\rho) \sqrt{\rho} \leq \bar{\rho} / \sqrt{\rho_\alpha}$, the last term is found to be of order α at most.

Therefore, in all cases we have $|\langle \tilde{\chi} \rangle - \tilde{\chi}(0)| \lesssim \alpha^{2/3} \ll 1$ and the small-scale nonlinearities do not produce a significant backreaction onto the overall expansion rate of the Universe in the dark energy era.

VII. LINEAR PERTURBATIONS

A. Regime of validity

We study in more details the growth of large-scale structures at linear order in this section. We first investigate the regime of validity of the linear theory. The standard cosmological linear theory applies to large scales where the matter density fluctuations δ are small. This yields the transition scale to nonlinearity x_δ^{NL} defined by $\sigma^2(x_\delta^{\text{NL}}) = 1$, where $\sigma(x)$ is the root-mean-square (rms) density contrast at scale x , $\sigma^2 = \langle \delta_x^2 \rangle$. In addition to the perturbative expansion in δ , within the context of the scalar-field models that we study in this paper the perturbative approach involves an additional expansion in the scalar field fluctuation $\delta\tilde{\chi}$. Then, it could happen that this second expansion has a smaller range of validity, $x_{\tilde{\chi}}^{\text{NL}}$, so that linear theory applies to a smaller range than in the Λ -CDM cosmology.

Therefore, we need to investigate the range of validity of the linear regime for the fifth force. From the Euler equation (34) and the expression of the metric potential (30), the linear approximation is valid for the fifth force as long as we can linearize $\delta \ln A$ in the density contrast δ . In Sec. III B 3 we obtained the linear regime by expanding $\ln A$ in $\delta \tilde{\chi}$ and next solving for $\delta \tilde{\chi}$ from the scalar field equation (50). However, this formulation can underestimate the range of validity of the linear regime for the fifth force. Indeed, because of the factor $1/\rho$ in the right-hand side a perturbative expansion of Eq.(50) in powers of $\delta = (\rho - \bar{\rho})/\bar{\rho}$ cannot extend beyond $|\delta| \sim 1$. This artificial limitation can be removed at once by writing instead the scalar-field equation as

$$\frac{d\tilde{\chi}}{d \ln A} = \frac{\rho}{\mathcal{M}^4}. \quad (113)$$

If the function $\tilde{\chi}(\ln A)$ were quadratic the linear theory would be exact for the fifth force. In the general case, the range of validity x_A^{NL} of the linear theory for the fifth force will be determined by the nonlinearities of the function $d\tilde{\chi}/d \ln A$ but it can exceed x_δ^{NL} .

In the models described in Sec. IV we have $\ln A = \alpha \lambda(\tilde{\chi})$, where the function λ and $\tilde{\chi}$ are of order unity (or more precisely, do not involve small or large parameters), whereas $\alpha \lesssim 10^{-6} \ll 1$, as noticed in Eq.(51). Then, the scalar-field equation (113) reads as

$$\frac{d\tilde{\chi}}{d\lambda} = \frac{\alpha \bar{\rho}}{\mathcal{M}^4} (1 + \delta), \quad (114)$$

which we must solve for $\lambda(\delta)$. In the low-density regime, following the same analysis as for Eq.(82), we have in the general case $\ln A \sim \pm \alpha |\tilde{\chi} + 1|^{1-\nu}$, with $0 < \nu < 1$, and

$$\frac{\alpha \rho}{\mathcal{M}^4} \ll 1: \quad \tilde{\chi} \simeq -1 \pm |\lambda|^{1/(1-\nu)}, \quad \lambda \simeq \pm \left(\frac{\alpha \rho}{\mathcal{M}^4} \right)^{(1-\nu)/\nu}. \quad (115)$$

Then, for generic ν , at low densities the function $\lambda(\rho)$ can be linearized in δ in the range $|\delta| \lesssim 1$. For the specific case $\nu = 1/2$, which corresponds to the models introduced in Sec. IV, the last relation (115) happens to be linear so that the linear regime for $\lambda(\rho)$ applies up to $\alpha \rho / \mathcal{M}^4 \sim 1$, that is, $\delta \lesssim \mathcal{M}^4 / \alpha \bar{\rho} \sim \alpha^{-1} \gg 1$, which yields a much greater range. At high densities, $\alpha \rho / \mathcal{M}^4 \gg 1$, we have a power-law divergence of the form $d\tilde{\chi}/d\lambda \sim |\lambda + \lambda_*|^{-\mu}$, with $\mu > 0$. This yields $\lambda \simeq -\lambda_* \pm (\alpha \rho / \mathcal{M}^4)^{-1/\mu}$, which can be linearized for $|\delta| \lesssim 1$.

Therefore, we find that in all cases the regime of validity of the linear regime for the fifth force is at least as broad as that for the matter fluctuations δ . In the specific case of the models introduced in in Sec. IV, which have a square-root singularity in the low-density regime, the linear regime for the fifth force applies to a much greater range at low z , $|\delta| \lesssim \alpha^{-1}$.

B. Model (I)

We first consider the case of the model (I) introduced in Eq.(55), where $\tilde{\chi}$ is an increasing function of ρ . This leads to a negative ϵ_1 and the fifth force decreases Newtonian gravity. The linear modes $D_\pm(a)$ of the matter density contrast satisfy the evolution equation (43), where the departure from the Λ -CDM cosmology only comes from the factor $\epsilon(k, a)$. Because $|\epsilon_1| \lesssim \alpha \ll 1$, the factor 1 in Eq.(44) gives a negligible contribution to $(1 + \epsilon)$ and we can write

$$\epsilon(k, a) = \epsilon_1(a) \frac{2}{3\Omega_m} \left(\frac{ck}{aH} \right)^2. \quad (116)$$

On Hubble scales we have $\epsilon \sim \epsilon_1$, hence $|\epsilon| \lesssim \alpha \ll 1$ and we recover the Λ -CDM growth of structures. However, on smaller scales $|\epsilon(k, a)|$ grows as k^2 and it reaches unity at a wave number

$$k_\alpha(a) \simeq \frac{aH}{c\sqrt{|\epsilon_1|}} \simeq \frac{3 \times 10^{-4}}{\sqrt{a|\epsilon_1|}} h \text{ Mpc}^{-1}, \quad (117)$$

where we used $H^2 \propto a^{-3}$ in the matter era. We have seen in Sec. VI A and Fig. 2 that $|\epsilon_1|$ is maximum at redshift $z_\alpha \sim \alpha^{-1/3}$, with an amplitude $|\epsilon_1|_{\text{max}} \sim \alpha$. More precisely, from Eq.(60) we obtain

$$a \ll a_\alpha: \quad |\epsilon_1| \sim \alpha^{-1} a^6, \quad a \gg a_\alpha: \quad |\epsilon_1| \sim \alpha^2 a^{-3}. \quad (118)$$

Therefore, $k_\alpha(a)$ is minimum at $a \simeq a_\alpha$, with

$$k_\alpha^{\text{min}} \equiv k_\alpha(a_\alpha) \sim 3 \times 10^{-4} \alpha^{-2/3} h \text{ Mpc}^{-1}, \quad (119)$$

which yields $k_\alpha^{\text{min}} \sim 3 h \text{ Mpc}^{-1}$ for $\alpha = 10^{-6}$. Thus, wave numbers below k_α^{min} never probe the fifth force, while higher wave numbers feel the fifth force over a finite time range, $[a_-(k), a_+(k)]$, around the scale factor a_α . From Eq.(118) we obtain, for $k > k_\alpha^{\text{min}}$,

$$a_-(k) \sim \alpha^{1/7} \left(\frac{ck}{H_0} \right)^{-2/7}, \quad a_+(k) \sim \alpha \frac{ck}{H_0}. \quad (120)$$

In the time interval $[a_-, a_+]$, the factor $(1 + \epsilon)$ in the linear evolution equation (43) is dominated by ϵ and becomes negative. This means that the density fluctuations no longer feel an attractive gravity but a pressure-like force. Then, the linear growing mode $D_+(a)$ stops growing, as in the Λ -CDM cosmology, but develops an oscillatory behavior. In the matter era, the evolution equation (43) simplifies as

$$D'' + \frac{1}{2}D' - \frac{3}{2}(1 + \epsilon)D = 0, \quad (121)$$

where we denote with a prime the derivative with respect to $\ln a$. Rescaling the linear modes as

$$D(k, a) = a^{-1/4} y(k, a), \quad (122)$$

we obtain

$$y'' - \left(\frac{25}{16} + \frac{3\epsilon}{2} \right) y = 0. \quad (123)$$

Then, defining $\omega = \sqrt{-25/16 - 3\epsilon/2}$, we obtain in the limit $-\epsilon \gg 1$ the WKB solutions

$$y = \frac{c}{\sqrt{\omega}} \cos \left[\int_{a_-}^a \frac{da}{a} \omega(a) \right] + \frac{s}{\sqrt{\omega}} \sin \left[\int_{a_-}^a \frac{da}{a} \omega(a) \right], \quad (124)$$

where the coefficients c and s are obtained from the matching at a_- .

We show the linear growing mode $D_+(k, a)$ as a function of the scale factor in the upper panel in Fig. 3. We can check that we recover the behaviors predicted above. For $k \lesssim 3h\text{Mpc}^{-1}$ the linear growing mode follows the same growth as in the Λ -CDM cosmology (which cannot be distinguished from the upper curve in the plot). At higher k it develops oscillations, in the range $[a_-, a_+]$ around $a_\alpha \sim 0.01$. Because the number of oscillations is not very large in practice we do not need to use the WKB approximation (124) and we simply solve the exact evolution equation (43).

We show the dependence on k of the linear growing mode in the middle panel in Fig. 3. The oscillatory behavior found for the time evolution at high k gives rise to a decay of the growing mode at high wave number. Indeed, for high k the linear mode $D_+(k, a)$ stops growing in the increasingly broader interval $[a_-, a_+]$, which leads to an increasing delay for $D_+(k, a)$ as compared with the Λ -CDM reference. From the WKB approximation (124) we can see that $a^{1/4}D_+(k, a)$ has about the same amplitude at the boundaries a_- and a_+ , where $\omega \sim 1$, while it decreases as $1/\sqrt{\omega(a)}$ in-between with a minimum at a_α . Therefore, in the matter era after the oscillatory phase, $a > a_+$, we have $D_+(a) \sim D_+(a_+)a/a_+ \sim D_+(a_-)(a_+/a_-)^{-1/4}(a/a_+) \sim (a_+/a_-)^{-5/4}a$, where we normalized the Λ -CDM growing mode as $D_+^{\Lambda\text{CDM}} = a$ in the matter era. Thus, at high k the linear growing mode is damped by a factor $(a_+/a_-)^{-5/4}$. From Eq.(120) this gives:

$$k > k_\alpha^{\min} : \frac{D_+(k, a)}{D_+^{\Lambda\text{CDM}}(a)} \sim \left(\frac{k}{k_\alpha^{\min}} \right)^{-45/28}, \quad (125)$$

which is consistent with the middle panel in Fig. 3.

We display the logarithmic linear power spectrum, $\Delta_L^2(k) = 4\pi k^3 P_L(k)$, in the lower panel in Fig. 3. Its ratio to the Λ -CDM linear power is given by $(D_+/D_+^{\Lambda\text{CDM}})^2$ and shows a steep falloff with oscillations at high k , as follows from the middle panel. The lower panel shows that at $z = 0$ the decay of the linear power spectrum appears inside the nonlinear regime, at $k \gtrsim 2h\text{Mpc}^{-1}$, but at higher z it would fall in the linear regime.

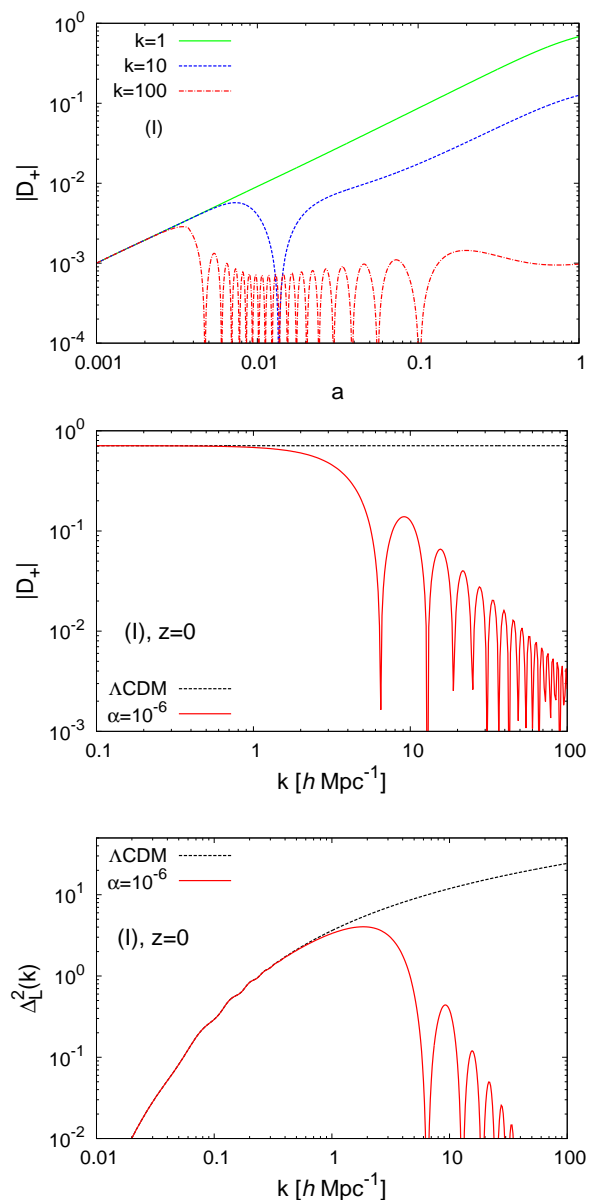


FIG. 3: Linear growing mode $D_+(k, a)$ and logarithmic power spectrum $\Delta_L^2(k, a)$ for the model (I) (we show the absolute value $|D_+|$). *Upper panel*: $D_+(k, a)$ as a function of the scale factor for $k = 1, 10$ and $100h\text{Mpc}^{-1}$, from top to bottom. *Middle panel*: $D_+(k, a)$ as a function of the wave number, at redshift $z = 0$. We also show the Λ -CDM result as the upper dashed line. *Lower panel*: linear logarithmic power spectrum $\Delta_L^2(k, a)$ at redshift $z = 0$.

C. Model (II)

We now consider the case of model (II) introduced in Eq.(63), where $\tilde{\chi}$ is a decreasing function of ρ . This leads to a positive ϵ_1 and the fifth force amplifies Newtonian gravity. Again, the linear modes $D_\pm(a)$ satisfy the evo-

lution equation (43) and the factor $\epsilon(k, a)$ is given by Eq.(116). We recover the Λ -CDM growth on Hubble scales while ϵ reaches unity at the wave number $k_\alpha(a)$ of Eq.(117). The amplitude of ϵ_1 verifies the same scalings (118) as for model (I) and this again defines the minimum wave number k_α^{\min} of Eq.(119) for which the fifth force ever had a significant impact. For $k > k_\alpha^{\min}$ the fifth force is significant in the time interval $[a_-, a_+]$ given by Eq.(120).

Because $\epsilon > 0$ the linear modes do not show oscillations in the range $[a_-, a_+]$ but faster growth and decay as compared with the Λ -CDM evolution. Neglecting the time dependence of ϵ , Eq.(121) leads to the growing and decaying modes

$$D_\pm(a) \sim a^{\gamma_\pm}, \quad \gamma_\pm = \frac{\pm\sqrt{25+24\epsilon}-1}{4}. \quad (126)$$

We show our results for the linear growing mode $D_+(k, a)$ and the linear logarithmic power spectrum $\Delta_L^2(k, a)$ in Fig. 4. We can see that low wave numbers, $k \lesssim 1h\text{Mpc}^{-1}$, follow the same growth as in the Λ -CDM cosmology whereas high wave numbers, $k \gtrsim 10h\text{Mpc}^{-1}$, follow a phase of accelerated growth around $a_\alpha \sim 0.01$. This leads to a steep increase of $D_+(k)$ at high k , at low redshift. This means that high wave numbers, $k \gg 10h\text{Mpc}^{-1}$, enter the nonlinear regime at $a \lesssim a_\alpha$, much before than in the Λ -CDM cosmology. As seen in the lower panel in Fig. 4, at $z = 0$ this strong amplification with respect to Λ -CDM is restricted to nonlinear scales, but at higher z it would also apply to scales that would be linear in the Λ -CDM cosmology.

D. Model (III)

The behaviors obtained for the model (III) are similar to those of the model (II), as $\epsilon > 0$ and the fifth force accelerates the growth of structures at high k , in a time interval $[a_-(k), a_+(k)]$. At a given time, the lowest wave number $k_\alpha(a)$ where the fifth force is significant is still given by Eq.(117). The lowest wave number k_α^{\min} where the fifth force ever played a role (at $a_\alpha \sim \alpha^{1/3}$) is also given by Eq.(119). From Eqs.(75) and (79) we now obtain, for $k > k_\alpha^{\min}$,

$$a_-(k) \sim \alpha^{-1/5} \left(\frac{ck}{H_0} \right)^{-4/5}, \quad a_+(k) \sim \alpha \frac{ck}{H_0}. \quad (127)$$

Thus, the upper boundary $a_+(k)$ behaves as for models (I) and (II), because all three models have the same low-density or late-time behavior (82) (up to a sign), but the lower boundary $a_-(k)$ decreases faster at high k . This increases the time span where the fifth force is dominant and it leads to a stronger impact on the growth of structure at high k than for model (II). This is due to the slower decrease of $\epsilon_1(a)$ at high redshift found in Fig. 2. We show our results for the linear growing mode in Fig. 5 and we can check that we recover these properties. The

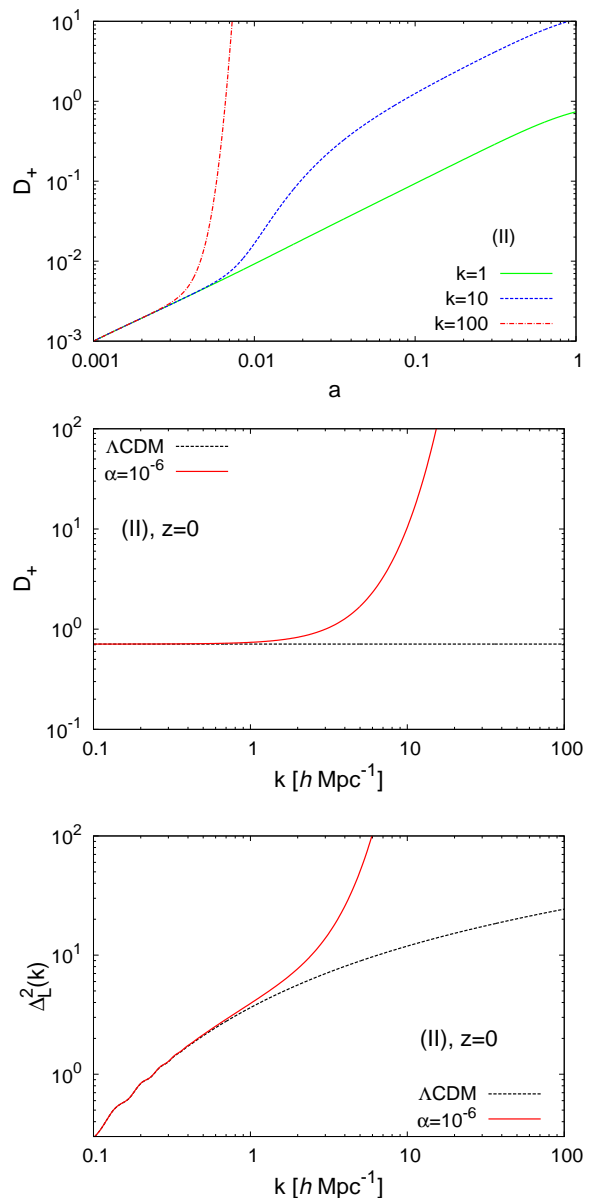


FIG. 4: Linear growing mode $D_+(k, a)$ and logarithmic power spectrum $\Delta_L^2(k, a)$ for the model (II). *Upper panel:* $D_+(k, a)$ as a function of the scale factor for $k = 1, 10$ and $100h\text{Mpc}^{-1}$, from bottom to top. *Middle panel:* $D_+(k, a)$ as a function of the wave number, at redshift $z = 0$. We also show the Λ -CDM result as the lower dashed line. *Lower panel:* linear logarithmic power spectrum $\Delta_L^2(k, a)$ at redshift $z = 0$.

linear power spectrum is very close to the one obtained from the model (II) in Fig. 4, hence we do not show it in the figure.

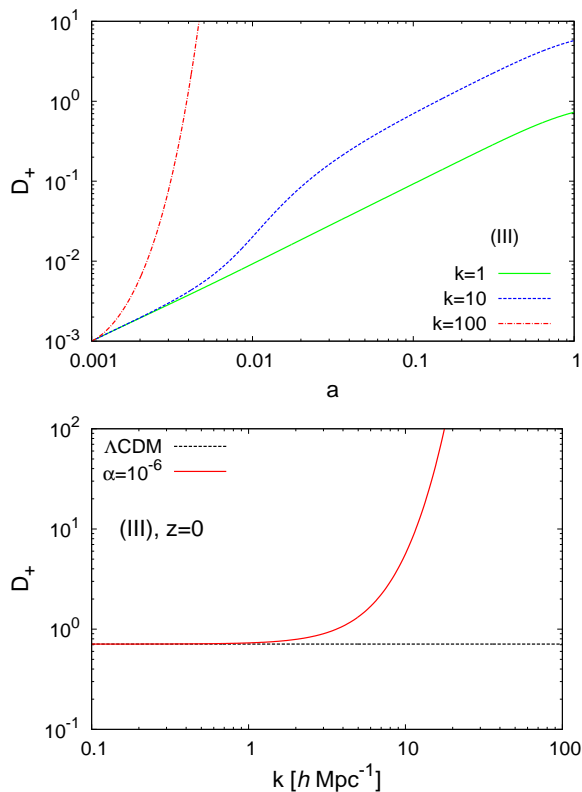


FIG. 5: Linear growing mode $D_+(k, a)$ for the model (III). *Upper panel:* $D_+(k, a)$ as a function of the scale factor for $k = 1, 10$ and $100 h\text{Mpc}^{-1}$, from bottom to top. *Lower panel:* $D_+(k, a)$ as a function of the wave number, at redshift $z = 0$. We also show the Λ -CDM result as the lower dashed line.

VIII. SPHERICAL COLLAPSE

A. Equation of motion

As can be derived from Eq.(34), on large scales where the baryonic pressure is negligible, the particle trajectories $\mathbf{r}(t)$ read as

$$\frac{d^2 \mathbf{r}}{dt^2} - \frac{1}{a} \frac{d^2 a}{dt^2} \mathbf{r} = -\nabla_{\mathbf{r}} (\Psi_{\text{N}} + \Psi_{\text{A}}), \quad (128)$$

where $\mathbf{r} = a\mathbf{x}$ is the physical coordinate, $\nabla_{\mathbf{r}} = \nabla/a$ the gradient operator in physical coordinates, and $\Psi_{\text{A}} = c^2 \ln A$ is the fifth force contribution to the metric potential Φ . To study the spherical collapse before shell crossing, it is convenient to label each shell by its Lagrangian radius q or enclosed mass M , and to introduce its normalized radius $y(t)$ by

$$y(t) = \frac{r(t)}{a(t)q} \quad \text{with} \quad q = \left(\frac{3M}{4\pi\bar{\rho}_0} \right)^{1/3}, \quad y(t=0) = 1. \quad (129)$$

In particular, the matter density contrast within radius $r(t)$ reads as

$$1 + \delta_{<}(r) = y(t)^{-3}. \quad (130)$$

Then, Eq.(128) gives for the evolution of the normalized radius y , or density contrast $\delta_{<} = y^{-3} - 1$,

$$\frac{d^2 y}{d(\ln a)^2} + \left(2 + \frac{1}{H^2} \frac{dH}{dt} \right) \frac{dy}{d \ln a} = -\frac{y}{H^2 r} \frac{\partial}{\partial r} (\Psi_{\text{N}} + \Psi_{\text{A}}). \quad (131)$$

The Newtonian potential is given by $\Psi_{\text{N}} = -\mathcal{G}\delta M/r$, with $\delta M(< r) = 4\pi\delta_{<}(r)\bar{\rho}r^3/3$, which yields

$$\frac{\partial \Psi_{\text{N}}}{\partial r} = \Omega_{\text{m}} \frac{H^2 r}{2} (y^{-3} - 1). \quad (132)$$

The derivative of the fifth force potential reads as

$$\frac{\partial \Psi_{\text{A}}}{\partial r} = c^2 \frac{\partial \ln A}{\partial r} = \frac{c^2}{r} \frac{d \ln A}{d \ln \rho} \frac{\partial \ln \rho}{\partial r}. \quad (133)$$

This gives the equation of motion

$$\frac{d^2 y}{d(\ln a)^2} + \left(2 + \frac{1}{H^2} \frac{dH}{dt} \right) \frac{dy}{d \ln a} + \frac{\Omega_{\text{m}}}{2} y(y^{-3} - 1) = -y \left(\frac{c}{Hr} \right)^2 \frac{d \ln A}{d \ln \rho} \frac{r}{1 + \delta} \frac{\partial \delta}{\partial r}. \quad (134)$$

In contrast with the Λ -CDM case, where the dynamics of different shells are decoupled before shell crossing, the fifth force introduces a coupling as it depends on the density profile, through the local density $\rho(r) = \bar{\rho}(1 + \delta(r))$ (which is different from the mean density $\bar{\rho}(1 + \delta_{<})$ within radius r) and its first derivative $\partial\delta/\partial r$.

To obtain a closed expression without solving simultaneously the dynamics of all shells (which would not be exact at late time when inner shells collapse and cross each other), we use an ansatz for the density profile. Following [18, 19], we use the density profile defined by

$$\begin{aligned} \delta(x') &= \frac{\delta_{<}(x)}{\sigma_x^2} \int_V \frac{d\mathbf{x}''}{V} \xi_L(\mathbf{x}', \mathbf{x}'') \\ &= \frac{\delta_{<}(x)}{\sigma_x^2} \int_0^{+\infty} dk 4\pi k^2 P_L(k) \tilde{W}(kx) \frac{\sin(kx')}{kx'}. \end{aligned} \quad (135)$$

Here $x(t) = a(t)r(t)$ is the comoving radius of the spherical shell of mass M that we are interested in while x' is any radius along the profile; ξ_L and P_L are the linear correlation function and power spectrum of the matter density contrast, $\sigma_x^2 = \langle \delta_{L<}(x)^2 \rangle$ its variance within radius x , which defines a sphere of volume V ; and $\tilde{W}(kx) = 3[\sin(kx) - kx \cos(kx)]/(kx)^3$ the Fourier transform of the 3D top hat of radius x . The choice (135) corresponds to the typical density profile around a spherical overdensity of amplitude $\delta_{L<}$ at radius x for a Gaussian field of power spectrum P_L . As the overdensity turns nonlinear the profile should be distorted but we neglect this effect. The ansatz (135) allows us to compute the local density contrast $\delta(x)$ and its derivative $\partial\delta/\partial x$ at radius x from $\delta_{<}(x)$ and to close the equation of motion (134).

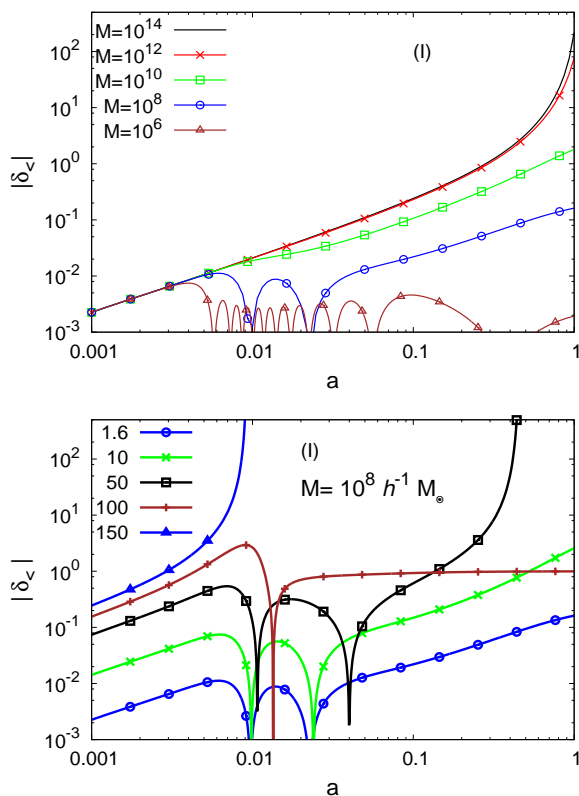


FIG. 6: Time evolution of the nonlinear density contrast $\delta_{<}$ given by the spherical dynamics, as a function of the scale factor a . *Upper panel:* $\delta_{<}(a)$ for several masses, from $M = 10^6$ to $10^{14} h^{-1} M_{\odot}$ from bottom to top, with the same initial condition that corresponds to the Λ -CDM linear density threshold today $\delta_{<L}^{\Lambda\text{-CDM}} = 1.6$. *Lower panel:* $\delta_{<}(a)$ for several initial conditions, from $\delta_{<L}^{\Lambda\text{-CDM}} = 1.6$ to 150 from bottom to top, for the fixed mass $M = 10^8 h^{-1} M_{\odot}$.

B. Model (I)

We show in Fig. 6 the evolution with time of the nonlinear density contrast within a shell of mass M given by the spherical dynamics, for the model (I). In the upper panel, we consider the curves obtained for different masses M with a common normalization for the linear density contrast $\delta_{<L}$ at a very high redshift, $z_i \gtrsim 10^3$. In the case of the Λ -CDM cosmology, this corresponds to a linear density contrast today, at $z = 0$, of $\delta_{<L}^{\Lambda\text{-CDM}} = 1.6$, and to a nonlinear density contrast $\delta_{<} \simeq 200$, hence to a collapsed and just-virialized halo. In agreement with the results of Sec. VII B and Fig. 3, we find that for large masses, $M \gtrsim 10^{12} h^{-1} M_{\odot}$, which correspond to large scales, we remain close to the Λ -CDM behavior (which cannot be distinguished from the curves for $M \geq 10^{14} h^{-1} M_{\odot}$), whereas the collapse is delayed for smaller masses. Because the density contrast is still in the linear regime around $a_{\alpha} \sim 0.01$, where the fifth force

is important (on small scales), the spherical dynamics follows the behavior of the linear growing mode displayed in Fig. 3. For large mass it keeps growing as in the Λ -CDM scenario whereas for small mass it shows oscillations with an amplitude that is about the same at the end of the oscillatory phase, a_+ , as at its beginning, a_- . This delays the collapse for small masses and leads to a density contrast today that is much smaller than 200. In fact, because the oscillations imply a change of sign of the density contrast, as was the case for the linear mode D_+ , an initially overdense perturbation can come out of the oscillatory phase as an underdensity, in which case it will never collapse but give rise to a void (neglecting shell crossing).

In the lower panel of Fig. 6, we show the spherical dynamics for the fixed mass $M = 10^8 h^{-1} M_{\odot}$ and several values of the initial linear density contrast, which in the Λ -CDM cosmology would give rise today to a linear density contrast of $\delta_{<L}^{\Lambda\text{-CDM}} = 1.6$ to 150. For $\delta_{<L}^{\Lambda\text{-CDM}} \lesssim 10$ the dynamics remains in the linear regime until $z = 0$ and the curves are simply a rescaled copy of the result obtained for $\delta_{<L}^{\Lambda\text{-CDM}} = 1.6$. As $\delta_{<}$ only shows two changes of sign (for $M = 10^8 h^{-1} M_{\odot}$ the oscillation frequency is still low) the perturbation comes out of the oscillatory phase as an overdensity, which then resumes its growth. Because of the delay of the collapse around $a_{\alpha} \sim 0.01$ the final nonlinear density contrast does not go much beyond unity at $z = 0$. For the greater initial density contrast $\delta_{<L}^{\Lambda\text{-CDM}} = 50$, the overdensity has a higher amplitude at the beginning of the oscillatory phase. It exits with a similar and positive density contrast and it has time to reach a nonlinear density contrast greater than 200 before $z = 0$. However, we can see from the curve obtained for $\delta_{<L}^{\Lambda\text{-CDM}} = 100$ that the final nonlinear density contrast is not a monotonic function of the initial condition at high initial overdensities, $\delta_{<L}^{\Lambda\text{-CDM}} > 50$. Indeed, for the higher initial density $\delta_{<L}^{\Lambda\text{-CDM}} = 100$ there is a single oscillation, which implies that the perturbation becomes an underdensity with a nonlinear density contrast that converges to -1 at late time, when the fifth force no longer plays a significant role. Increasing further the initial density contrast, $\delta_{<L}^{\Lambda\text{-CDM}} \gtrsim 150$, the perturbation collapses before the oscillatory phase and remains highly overdense.

For smaller masses, where the oscillatory phase shows numerous oscillations in the linear regime, we obtain a similarly non-monotonic behavior as a function of the initial condition. In these cases, to obtain a collapsed halo today the overdensity needs to have already collapsed before the oscillatory phase begins, which leads to a much more stringent condition than for the Λ -CDM cosmology. The linear density contrast today, extrapolated from very early times by the Λ -CDM growth factor, needs to be greater than about 100 today, instead of about 1.6.

We show in Fig. 7 the linear density contrast threshold, measured by $\delta_{<L}^{\Lambda\text{-CDM}}$ (i.e., the extrapolation up to $z = 0$ of the linear initial density contrast by the Λ -CDM growth rate), required to reach a nonlinear density

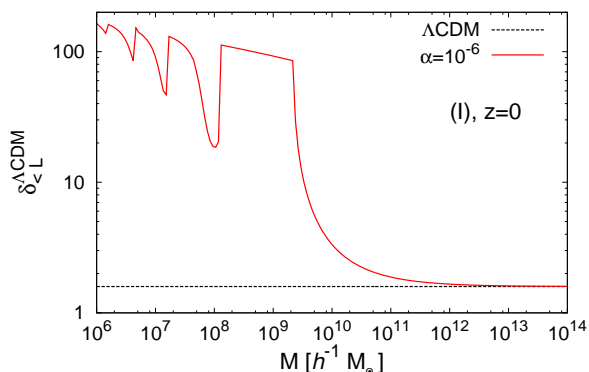


FIG. 7: Initial linear density contrast, as measured by $\delta_{<L}^{\Lambda\text{-CDM}}$, that gives rise to a nonlinear density contrast $\delta_{<} = 200$ at $z = 0$, as a function of the halo mass M . The lower dashed line is the mass-independent linear density threshold obtained for the Λ -CDM cosmology.

contrast $\delta_{<} = 200$ today. In agreement with Fig. 6, at large mass we recover the Λ -CDM linear density threshold, $\delta_{<L}^{\Lambda\text{-CDM}} \simeq 1.6$, whereas at small mass we obtain a much greater linear density threshold $\delta_{<L}^{\Lambda\text{-CDM}} \sim 100$. We also find a non-monotonic curve, which is due to the oscillation phase and the complex behavior found in Fig. 6. Moving towards smaller masses, from $M \sim 10^{11}$ down to $M \sim 2 \times 10^9 h^{-1} M_{\odot}$, the linear density threshold shows a steep rise as it must compensate for the delay around $a_{\alpha} \sim 0.01$ of structure growth (this corresponds to the curve $M = 10^{10}$ in the upper panel in Fig. 6). The threshold grows until $\delta_{<L}^{\Lambda\text{-CDM}} \sim 100$ at $M \sim 2 \times 10^9 h^{-1} M_{\odot}$, which corresponds to perturbations that have collapsed just at a_{-} , just before the beginning of the oscillatory phase (this behavior corresponds to the curve labeled “150” in the lower panel in Fig. 6). Next, down to $M \sim 2 \times 10^8 h^{-1} M_{\odot}$ the linear density threshold keeps slowly increasing as the oscillatory phase expands and a_{-} decreases (see the upper panel in Fig. 6). At these masses the oscillatory phase displays a zero and next one change of sign (so that overdensities emerge as underdensities and never collapse, as for the curve labeled “100” in the lower panel in Fig. 6). At $M \sim 2 \times 10^8 h^{-1} M_{\odot}$ there is a sudden drop in the linear density threshold. This is because the oscillatory phase now shows two changes of sign, and it is possible for overdensities that have not yet collapsed before a_{-} to emerge as overdensities and resume their collapse (this corresponds to the curve labeled “50” in the lower panel in Fig. 6). Moving to lower masses the linear threshold smoothly increases as a_{-} decreases (so that the delay grows) until we again reach the plateau around ~ 100 , and next encounter a second drop at $M \sim 2 \times 10^7 h^{-1} M_{\odot}$ at the transition from three to four changes of sign. The second drop is smaller than the first, because the width of the oscillatory phase has increased so that it needs a higher initial linear density

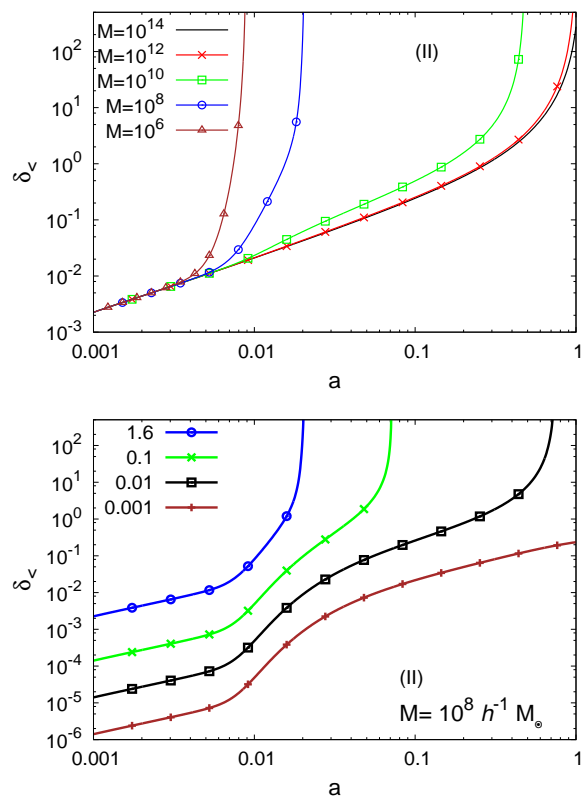


FIG. 8: Time evolution of the nonlinear density contrast $\delta_{<}$ given by the spherical dynamics, as a function of the scale factor a . Upper panel: $\delta_{<}(a)$ for several masses, from $M = 10^{14}$ to $10^6 h^{-1} M_{\odot}$ from bottom to top, with the same initial condition that corresponds to the Λ -CDM linear density threshold today $\delta_{<L}^{\Lambda\text{-CDM}} = 1.6$. Lower panel: $\delta_{<}(a)$ for several initial conditions, from $\delta_{<L}^{\Lambda\text{-CDM}} = 1.6$ to 0.001 from top to bottom, for the fixed mass $M = 10^8 h^{-1} M_{\odot}$.

contrast to eventually reach $\delta_{<} = 200$ today.

In any case, the formation of low mass halos, $M \lesssim 2 \times 10^9 h^{-1} M_{\odot}$, is strongly suppressed as compared with the Λ -CDM scenario. In fact, rather than forming in the usual bottom-up hierarchical fashion of CDM models, low-mass halos may form later in a top-down fashion, by fragmentation of larger-mass halos, as in Warm Dark Matter (WDM) scenarios.

C. Model (II)

We show in Fig. 8 the evolution with time of the nonlinear density contrast within a shell of mass M given by the spherical dynamics, for the model (II). As in Fig. 6, in the upper panel, we consider the curves obtained for different masses M with a common normalization for the linear density contrast $\delta_{<L}$ at a very high redshift, $z_i \gtrsim 10^3$. In the case of the Λ -CDM cosmology, this cor-

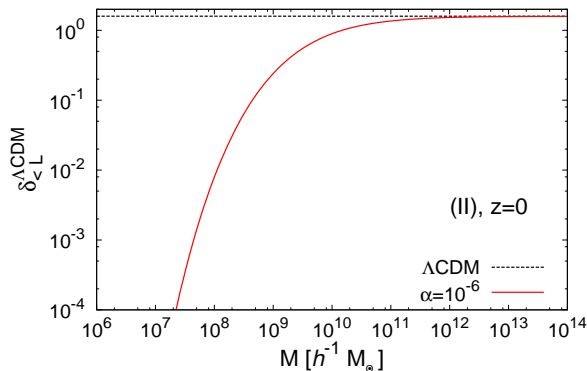


FIG. 9: Initial linear density contrast, as measured by $\delta_{<L}^{\Lambda\text{-CDM}}$, that gives rise to a nonlinear density contrast $\delta_{<} = 200$ at $z = 0$, as a function of the halo mass M . The upper dashed line is the mass-independent linear density threshold obtained for the $\Lambda\text{-CDM}$ cosmology.

responds to a linear density contrast today, at $z = 0$, of $\delta_{<L}^{\Lambda\text{-CDM}} = 1.6$, and to a nonlinear density contrast $\delta_{<} \simeq 200$, hence to a collapsed and just virtualized halo. In agreement with the results of Sec. VII C and Fig. 4, we find that for large masses, $M \gtrsim 10^{12} h^{-1} M_{\odot}$, which correspond to large scales, we remain close to the $\Lambda\text{-CDM}$ behavior (which cannot be distinguished from the curves for $M \geq 10^{14} h^{-1} M_{\odot}$), whereas the collapse is accelerated for smaller masses and can occur as soon as $a \sim 0.01$.

In the lower panel of Fig. 8, we show the spherical dynamics for the fixed mass $M = 10^8 h^{-1} M_{\odot}$ and several values of the initial linear density contrast, which in the $\Lambda\text{-CDM}$ cosmology would give rise today to a linear density contrast of $\delta_{<L}^{\Lambda\text{-CDM}} = 1.6$ to 0.001. We can clearly see the accelerated growth during the phase, $a_- < a < a_+$, where the fifth force is important. This implies that linear density contrasts as low as $\delta_{<L}^{\Lambda\text{-CDM}} \simeq 0.05$ can give rise to a collapsed halo today.

We show in Fig. 9 the linear density contrast threshold, measured by $\delta_{<L}^{\Lambda\text{-CDM}}$ (i.e., the extrapolation up to $z = 0$ of the linear initial density contrast by the $\Lambda\text{-CDM}$ growth rate), required to reach a nonlinear density contrast $\delta_{<} = 200$ today. In agreement with Fig. 8, at large mass we recover the $\Lambda\text{-CDM}$ linear density threshold, $\delta_{<L}^{\Lambda\text{-CDM}} \simeq 1.6$, whereas at small mass we obtain a much smaller linear density threshold $\delta_{<L}^{\Lambda\text{-CDM}} \ll 1$. This means that small scales have turned nonlinear at $a_-(M) \lesssim 0.01$, much before than in the $\Lambda\text{-CDM}$ cosmology.

D. Model (III)

The model (III) shows a behavior that is very close to the model (II), as was the case for the linear growing modes studied in Sec. VII D. Therefore, we only show the

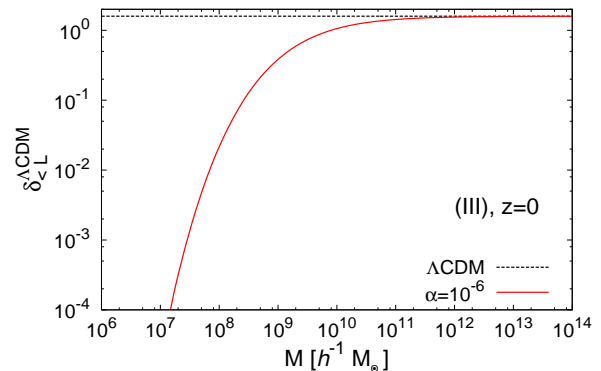


FIG. 10: Initial linear density contrast, as measured by $\delta_{<L}^{\Lambda\text{-CDM}}$, that gives rise to a nonlinear density contrast $\delta_{<} = 200$ at $z = 0$, as a function of the halo mass M . The upper dashed line is the mass-independent linear density threshold obtained for the $\Lambda\text{-CDM}$ cosmology.

linear density threshold $\delta_{<L}^{\Lambda\text{-CDM}}$ required for the nonlinear density contrast $\delta_{<} = 200$ at $z = 0$, in Fig. 10. We can check that this is close to the result displayed in Fig. 9 for the model (II). Again, at large mass we recover the standard $\Lambda\text{-CDM}$ result whereas at small mass the accelerated growth leads to a much smaller linear threshold $\delta_{<L}^{\Lambda\text{-CDM}} \ll 1$.

IX. HALO MASS FUNCTION

A. Model (I)

As for the $\Lambda\text{-CDM}$ cosmology, we write the comoving halo mass function as [20]

$$n(M) \frac{dM}{M} = \frac{\bar{\rho}_0}{M} f(\nu) \frac{d\nu}{\nu}, \quad (136)$$

where the scaling variable $\nu(M)$ is defined as

$$\nu(M) = \frac{\delta_L^{\Lambda\text{-CDM}}(M)}{\sigma(M)}, \quad (137)$$

and $\delta_L^{\Lambda\text{-CDM}}(M)$ is again the initial linear density contrast (extrapolated up to $z = 0$ by the $\Lambda\text{-CDM}$ linear growth factor) that is required to build a collapsed halo (which we define here by a nonlinear density contrast of 200 with respect to the mean density of the Universe). The variable ν measures whether such an initial condition corresponds to a rare and very high overdensity in the initial Gaussian field ($\nu \gg 1$) or to a typical fluctuation ($\nu \lesssim 1$). In the Press-Schechter approach, we have $f(\nu) = \sqrt{2/\pi} \nu e^{-\nu^2/2}$. Here we use the same function as in [21]. Then, the impact of the modified gravity only arises through the linear threshold $\delta_L^{\Lambda\text{-CDM}}(M)$, as we assume the same initial matter density power spectrum as for the $\Lambda\text{-CDM}$ reference at high redshift.

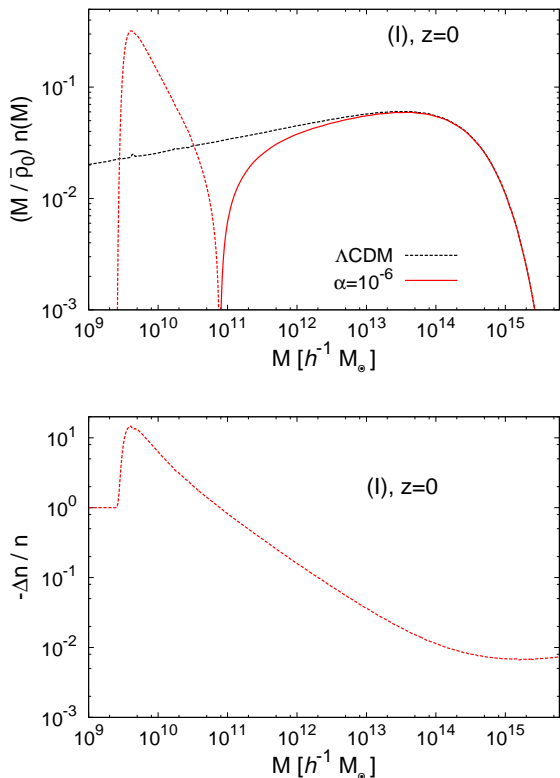


FIG. 11: *Upper panel:* halo mass function at $z = 0$ for the model (I) (red line with a downward spike at $M \simeq 10^{11} h^{-1} M_{\odot}$) and for the Λ -CDM reference (smooth black dashed line). The red solid line shows the range where $n_{(I)} > 0$ and the red dashed line the range where $n_{(I)} < 0$. *Lower panel:* relative deviation of the halo mass function from the Λ -CDM reference, for the model (I). We show $-\Delta n/n$ as $n_{(I)} < n_{\Lambda\text{CDM}}$.

We show our results for the halo mass function obtained for the model (I) in Fig. 11. In agreement with Fig. 7, at large masses the halo mass function is close to the Λ -CDM prediction whereas it is significantly lower at low masses, $M \sim 10^{11} - 10^{12} h^{-1} M_{\odot}$, because of the delay of the collapse on small scales. In fact, at $M \simeq 10^{11} h^{-1} M_{\odot}$ the mass function given by Eq.(136) becomes negative. In the usual Λ -CDM cosmology $\delta_L^{\Lambda\text{CDM}}(M)$ is actually mass independent while $\sigma(M)$ is a monotonic decreasing function of M . Then, $\nu(M)$ is a monotonic increasing function of M , which expresses the hierarchical bottom-up nature of the gravitational clustering: smaller scales and masses collapse first. As is well known from N-body simulations and semi-analytic modeling, this gives a mass function that can be described by Eq.(136), which is everywhere positive with an almost universal scaling function $f(\nu)$, and with a low-mass power-law tail and a large-mass exponential cutoff.

In contrast, in the case of the model (I), the linear threshold $\delta_L^{\Lambda\text{CDM}}(M)$ shows a strong mass dependence,

as displayed in Fig. 7. In particular, it shows a steep increase at lower masses from $M \simeq 10^{11} h^{-1} M_{\odot}$ down to $M \simeq 2 \times 10^9 h^{-1} M_{\odot}$. In this range, the variable $\nu(M)$ becomes a decreasing function of mass, so that the mass function (136) becomes negative because of the factor $d \ln \nu / d \ln M$. At small mass the mass function $n_{(I)}$ becomes very small because of the high values reached by the linear threshold $\delta_L^{\Lambda\text{CDM}}(M)$. Of course, this negative sign merely signals the breakdown of Eq.(136) as the exact mass function is always positive. The change of sign of $d \ln \nu / d \ln M$ means that at low mass and small scales gravitational clustering proceeds in an inverse hierarchy: smaller scales and masses collapse later. This corresponds to a top-down process as in the Hot Dark Matter (HDM) scenario. In practice, we can expect that small halos form in a very different manner than in the usual Λ -CDM cosmology, by the fragmentation of larger-mass halos. This very different mechanism implies that the halo mass function for low masses cannot be described by a rescaling of the form (136) and one must build a new modeling suited to this different process. We do not pursue this task here, which would require comparisons to numerical simulations.

It is interesting to note that this behavior is different from the modelization often used for the Warm Dark Matter (WDM) scenario, where the formation of low-mass halos is also suppressed as compared with the CDM scenario. Indeed, in the WDM case, the main effect comes from a cutoff of the linear power spectrum at high k , due to the free-streaming of the dark matter particles that have a non-negligible velocity dispersion after recombination. However, at low redshift their velocity dispersion is small (for typical candidates of particle mass $m \gtrsim 3$ keV) and the collapse proceeds as in the usual CDM case. Then, the linear threshold $\delta_L^{\Lambda\text{CDM}}(M)$ is identical to the Λ -CDM one and $\nu(M)$ is still a monotonic increasing function of M , but with a smaller decrease at low mass. Typically, σ goes to a finite constant for $M \rightarrow 0$. This pushes Eq.(136) to its limits, and the scaling function $f(\nu)$ may differ from the CDM one, but it remains positive and shows a reasonable shape. However, numerical simulations suggest that this recipe overestimates the low-mass tail and this is sometimes cured by using a window function $W(kR)$ [that defines the variance σ^2 in Eq.(137)] that is a top hat in Fourier space instead of configuration space [22] (but this involves introducing a free parameter to relate the wave number cutoff to the mass scale, which is fitted to the simulations). In contrast, in the case of the model (I), the initial linear power spectrum (that defines the initial conditions, e.g. at $z \sim 1000$) remains the same as in the Λ -CDM cosmology, but it is the linear threshold that is modified, because of the different dynamics around a_- . This leads to a dramatic decrease of the halo mass function at low mass, without the need to change the filter $W(kR)$, and it makes apparent the top-down hierarchy that can be expected from the analysis of the spherical dynamics.

An alternative modeling, which is closer to the one

often used for WDM, would be to define the initial conditions at sufficiently late time, after a_+ when the fifth force is no longer dominant. Then, the linear power spectrum would be modified from the Λ -CDM reference, and given by the lower panel in Fig. 3, whereas the spherical collapse and the linear density contrast threshold would be the same as for Λ -CDM. However, this would hide the inverted hierarchical process [$\nu(M)$ would again be a monotonic increasing function of mass] and would be likely to underestimate the decrease of the low-mass tail, as in the WDM case. In any case, a Press-Schechter-like modeling is unlikely to be meaningful in the low-mass regime for such scenarios, and obtaining a better match with the numerical simulations by changing the filter may not amount to much more than coincidence.

On the other hand, at large mass and in the exponential cutoff of the mass function, where the gravitational clustering proceeds in the usual bottom-up fashion and we probe rare events governed by the universal tail $e^{-\nu^2/2}$ associated with the Gaussian initial conditions, we expect our results to be robust.

B. Model (II)

We show our results for the halo mass function obtained for model (II) in Fig. 12. In agreement with Fig. 9, at large masses the halo mass function is close to the Λ -CDM prediction whereas it is significantly higher at low masses, $M \sim 10^8 - 10^{11} h^{-1} M_\odot$, because of the acceleration of the collapse on small scales. At low masses the mass function becomes smaller than in the Λ -CDM cosmology, because both mass functions are normalized to unity (the sum over all halos cannot give more matter than the mean matter density).

At large masses, $M > 10^{12} h^{-1} M_\odot$, where the formation of large-scale structures remains close to the Λ -CDM case, with only a modest acceleration, and the mass function is dominated by the Gaussian tail $\sim e^{-\nu^2/2}$, we can expect the results displayed in Fig. 12 to be robust. The relative deviation does not decrease from 10^{14} to $10^{15} h^{-1} M_\odot$ because the convergence towards Λ -CDM is counterbalanced by the Gaussian tail $e^{-\nu^2/2}$ which increasingly amplifies deviations from Λ -CDM at high mass.

At low masses, $M < 10^{12} h^{-1} M_\odot$, where the history of gravitational clustering is significantly different from the Λ -CDM scenario, as a large range of masses have collapsed together before a redshift of 100, and the halo mass function is no longer dominated by its universal Gaussian tail, these results are unlikely to be accurate. Indeed, there is no reason to expect that the exponent of the low- ν power-law tail remains the same as in Λ -CDM, and because of the rather different clustering history the mass function may show a significantly different behavior, even in terms of the scaling variable ν . Nevertheless, we can still expect the halo mass function to be significantly higher than in the Λ -CDM case for masses

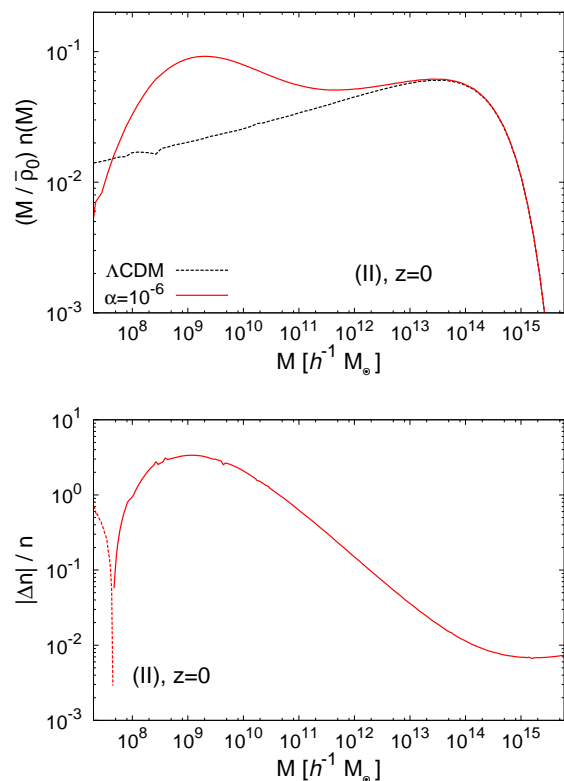


FIG. 12: *Upper panel:* halo mass function at $z = 0$ for the model (II) (solid line) and the Λ -CDM reference (dashed line). *Lower panel:* relative deviation of the halo mass function from the Λ -CDM reference, for the model (II). We show the absolute value $|\Delta n|/n$ (with a solid line for $n_{\text{(II)}} > n_{\Lambda\text{CDM}}$ and a dashed line otherwise).

$M \sim 10^8 - 10^{11} h^{-1} M_\odot$, although it is difficult to predict the maximum deviation and the transition to a negative deviation at very low masses.

C. Model (III)

We show our results for the halo mass function obtained for model (III) in Fig. 13. In agreement with Sec. VIII D, the results are very close to those obtained for model (II). The acceleration of the gravitational collapse by the fifth force leads to a higher halo mass function at moderate and large masses, with an amplification that grows towards smaller masses, from $M = 10^{13}$ down to $10^9 h^{-1} M_\odot$, and a convergence to the Λ -CDM falloff around $M \sim 10^{13} - 10^{15} h^{-1} M_\odot$. At very small masses, $M < 10^7 h^{-1} M_\odot$, the deviation from the Λ -CDM halo mass function becomes negative, in agreement with the constraint associated with the normalization of the halo mass function.

Again, these results should be robust at large mass,

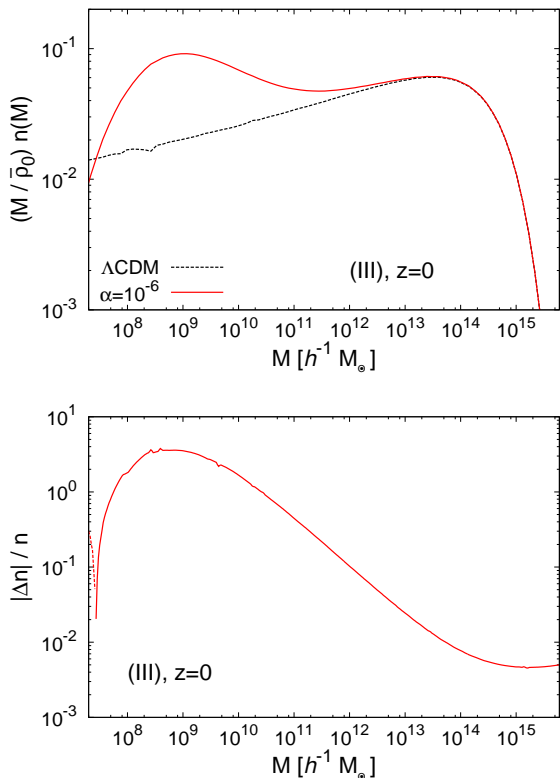


FIG. 13: *Upper panel:* halo mass function at $z = 0$ for the model (III) (solid line) and the Λ -CDM reference (dashed line). *Lower panel:* relative deviation of the halo mass function from the Λ -CDM reference, for the model (III). We show the absolute value $|\Delta n|/n$ (with a solid line for $n_{\text{(III)}} > n_{\Lambda\text{CDM}}$ and a dashed line otherwise).

$M > 10^{12} h^{-1} M_\odot$, where gravitational collapse remains similar to the usual Λ -CDM case, whereas the predictions are unlikely to be accurate at low masses, $M < 10^{12} h^{-1} M_\odot$, where the significant differences in the process of gravitational clustering could change the shape of the scaling function $f(\nu)$.

X. SCREENING OF THE FIFTH FORCE IN DENSE ENVIRONMENTS

So far we have focused on the impact of the modification of gravity on the background cosmology and the large-scale structures, including the linear regime and the formation of collapsed halos. In practice, we wish to recover General Relativity on small scales, especially in the Solar System where accurate measurements provide stringent constraints on a possible fifth force. Therefore, we compare in this section the magnitude of the fifth force with the Newtonian gravity on a variety of objects, from clusters of galaxies to galaxies and to the Solar System.

A. Screening within clusters or spherical halos

We first consider here how the ratio of the fifth force to Newtonian gravity behaves within spherical halos with a mean density profile such as the Navarro-Frenk-White (NFW) [23] density profile, often used to describe massive dark matter halos. In particular, we wish to find the conditions for the fifth force not to diverge at the center of the halos and to remain modest at all radii, to be consistent with observations of X-ray clusters. Within spherical halos, the Newtonian force reads as

$$F_N = -\frac{\mathcal{G}_N M(< r)}{r^2} = -\frac{\Omega_m}{2} \Delta(< r) r H^2, \quad (138)$$

where $\Delta(< r)$ is the mean overdensity within radius r . We can also write this as

$$F_N = -\frac{v_N^2(r)}{r}, \quad v_N^2 = \frac{\mathcal{G}_N M(< r)}{r}, \quad (139)$$

where v_N^2 is the circular velocity at radius r , which also measures the typical magnitude of the velocity dispersion when Newtonian gravity is dominant. The fifth force reads as

$$F_A = -c^2 \frac{d \ln A}{dr} = -\frac{c_s^2(r)}{r} = -\frac{c^2}{r} \frac{d \ln A}{d \ln \rho} \frac{d \ln \rho}{d \ln r}. \quad (140)$$

Therefore, the ratio of the fifth force to the Newtonian force is

$$\eta \equiv \frac{F_A}{F_N} = \frac{2}{\Omega_m \Delta(< r)} \left(\frac{c}{rH} \right)^2 \frac{d \ln A}{d \ln \rho} \frac{d \ln \rho}{d \ln r} \quad (141)$$

$$= \frac{c^2}{v_N^2} \frac{d \ln A}{d \ln \rho} \frac{d \ln \rho}{d \ln r}. \quad (142)$$

In agreement with the discussion in Secs. III B 2 and IV A, the second line (142) shows that we need a small amplitude for the coupling function $\ln A$ to compensate the large factor c^2/v_N^2 , for the ratio η not to be much greater than unity in typical astrophysical and cosmological structures. This is provided by the parameter $\alpha \sim 10^{-6}$. In agreement with Eq.(44) and the analysis of cosmological perturbations in Sec. VII, the first line (141) shows that the relative importance of the fifth force typically grows at smaller scales, as $1/r^2$ or k^2 , and that the factor α is again needed to ensure that the fifth force does not greatly exceed Newtonian gravity at scales $\sim 1 h^{-1} \text{Mpc}$.

From the Euler equation (36) or the expression (140) of the fifth force, we can also associate with the fifth force the velocity scale c_s , with

$$c_s^2 = |r F_A| = c^2 \left| \frac{d \ln A}{d \ln r} \right|, \quad (143)$$

in a fashion similar to v_N^2 for Newtonian gravity. Then, the force ratio η also reads as

$$|\eta| = \frac{c_s^2}{v_N^2}, \quad (144)$$

and it also measures the ratio of these two velocity scales.

On very small scales and high densities, the fifth force is also partly screened by the nonlinearities of the coupling function $\ln A$, as $d \ln A / d \ln \rho$ goes to zero at large densities (because $\ln A$ is monotonic and bounded).

From Eq.(86), we have at moderate densities

$$\rho \ll \frac{\mathcal{M}^4}{\alpha} : |\eta| \sim \frac{\alpha^2}{a^3} \left(\frac{c}{rH} \right)^2. \quad (145)$$

Thus, at low redshifts the ratio η is actually suppressed by a factor α^2 , for the models studied in this paper, so that η only reaches unity at $r \sim 3h^{-1}\text{kpc}$, i.e. at galaxy scales (see also Sec. X B below). At higher densities, we obtain for models (I) and (II), $|d \ln A / d \ln \rho| \sim \mathcal{M}^8 / \alpha \rho^2$ and

$$(I) \text{ and } (II), \quad \rho \gg \frac{\mathcal{M}^4}{\alpha} : |\eta| \sim \frac{a^6}{\alpha \Delta^3} \left(\frac{c}{rH} \right)^2, \quad (146)$$

and for model (III), $|d \ln A / d \ln \rho| \sim \sqrt{\alpha \mathcal{M}^4 / \rho}$ and

$$(III), \quad \rho \gg \frac{\mathcal{M}^4}{\alpha} : |\eta| \sim \sqrt{\frac{\alpha a^3}{\Delta^3}} \left(\frac{c}{rH} \right)^2. \quad (147)$$

Let us consider a power-law density profile, of exponent $\gamma > 0$ and critical radius r_α ,

$$\rho(r) \sim \frac{\bar{\rho}_0}{\alpha} \left(\frac{r}{r_\alpha} \right)^{-\gamma}. \quad (148)$$

Since $\mathcal{M}^4 = \bar{\rho}_{\text{de}0} \sim \bar{\rho}_0$, at radii greater than r_α we have the behavior (145),

$$r > r_\alpha : |\eta| \sim \frac{\alpha^2}{a^3} \left(\frac{c}{rH} \right)^2, \quad (149)$$

whereas at smaller radii we have

$$r < r_\alpha : (I) \text{ and } (II), \quad |\eta| \sim \frac{a^6}{\alpha \Delta^3} \left(\frac{c}{rH} \right)^2, \quad (150)$$

$$(III), \quad |\eta| \sim \sqrt{\frac{\alpha a^3}{\Delta^3}} \left(\frac{c}{rH} \right)^2. \quad (151)$$

From Eq.(149) we find that at large radius the relative importance of the fifth force decreases as $1/r^2$, independently of the shape of the halo profile. From Eqs.(150) and (151) we find that at small radii the ratio η behaves as $r^{3\gamma-2}$ for the models (I) and (II), and as $r^{3\gamma/2-2}$ for the model (III). Therefore, the conditions for the ratio to go to zero at the center are:

$$r \rightarrow 0 : \quad \eta \rightarrow 0 \quad \text{if} \quad \gamma > 2/3 \quad \text{for (I) and (II)}, \quad (152)$$

$$\gamma > 4/3 \quad \text{for (III)}. \quad (153)$$

If we consider halos with a mean Navarro-Frenk-White (NFW) density profile, which has $\gamma = 1$, we find that the relative importance of the fifth force vanishes at the center for the models (I) and (II) but diverges for the model (III). This means that the model (III) is ruled

out, unless the small-scale cutoff ℓ_s discussed in Sec. V B is of the order of $1 h^{-1} \text{kpc}$. If we do not wish to rely on the small-scale cutoff ℓ_s , Eq.(141) shows that, to obtain a negligible fifth force at the center of a halo of exponent γ , the coupling function must decay at large densities as

$$\text{for } \eta \rightarrow 0 : \quad \frac{d \ln A}{d \ln \rho} \sim \rho^{-\mu} \quad \text{with } \mu > \frac{2}{\gamma} - 1. \quad (154)$$

However, we shall come back to this point in section XI D and argue that the divergence of the fifth force at the center could actually disappear because of the non-linearities of the scalar field dynamics and its ultra-local character. Indeed, the result (153) was derived from dimensional analysis and assumes that the density field remains smooth. However, in the non-linear regime the density field can develop strong inhomogeneities and fragment, because of the fifth-force instability. This in turn leads to a screening mechanism as isolated subhalos do not exert a fifth force on each other because of its ultra-local character.

Keeping with the dimensional analysis in this section, the result (154) would suggest that the relative importance of the fifth force always diverges at the center of halos with a flat core, $\gamma = 0$, but this is not the case as Eq.(154) was derived for power-law profiles with $\gamma > 0$, where $d \ln \rho / d \ln r$ in Eq.(141) was assumed to be of order unity. For halos with a core radius r_c , we can write $\rho \simeq \rho_c [1 - (r/r_c)^2]$ at small radii $r \ll r_c$, hence $|d \ln \rho / d \ln r| \sim (r/r_c)^2$ and Eq.(141) gives the finite limit

$$r \ll r_c : \quad |\eta| \sim \frac{1}{\Delta_c} \left(\frac{c}{r_c H} \right)^2 \left| \frac{d \ln A}{d \ln \rho} \right|_{\rho_c}. \quad (155)$$

We show in Fig. 14 the radial profile of the force ratio η at $z = 0$, for several halo masses. Here we consider spherical halos with a mean NFW density profile, $\rho(r) = \rho_s / [(r/r_s)(1 + r/r_s)^2]$, and a concentration parameter, $c = R/r_s$ given by $c(M, z) = 11(M/10^{12} M_\odot)^{-0.1} (1 + z)^{-1.5}$. We define the halo radius R_{200c} by the mean overdensity threshold $\Delta_{200c} = 200$ with respect to the critical density ρ_{crit} . In agreement with Eq.(149) and Eqs.(150)-(151), the force ratio decreases as $1/r^2$ at large radii for all three models, it decreases as r at small radii for the models (I) and (II), while it increases as $r^{-1/2}$ for the model (III). The ratio η is maximum, for models (I) and (II), or shows a bend between the small-radius and large-radius regimes, at $r_\alpha \sim R_{200c}/100$ (for the cases considered here). The overall amplitude of η increases for smaller mass (hence smaller halo radius) because of the characteristic growth on small scale, as $1/r^2$, of the modification of gravity investigated in this paper.

As noticed above, the steady growth of the ratio η towards the center of the halo for the model (III) suggests that this model would lead to cluster or galaxy halos that are significantly different from those obtained in the Λ -CDM scenario. Then, this model would be ruled out by observations, which show that Λ -CDM cosmologies provide a reasonably good agreement with data for the

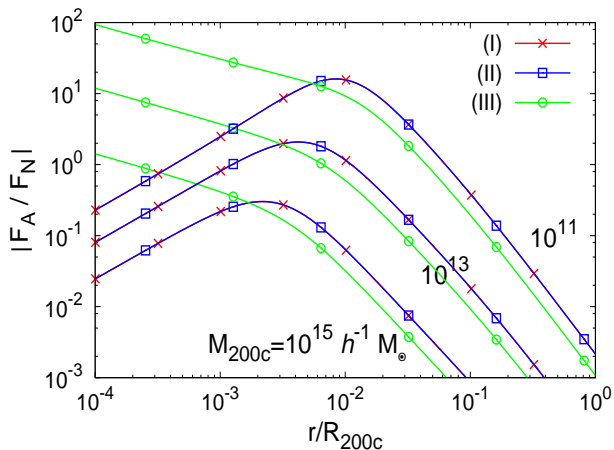


FIG. 14: Absolute value of the ratio $\eta = F_A/F_N$, as a function of the radius r , within spherical halos. We display the halo masses $M_{200c} = 10^{15}$, 10^{13} and $10^{11} h^{-1} M_{\odot}$, from bottom to top, at $z = 0$. We consider the models (I) (red line with crosses), (II) (blue line with squares) and (III) (green line with circles); $\eta < 0$ for the model (I); $\eta > 0$ for the models (II) and (III). The absolute values $|\eta|$ of models (I) and (II) are equal.

properties of clusters and galaxies. The ratio η becomes of order 10 (or greater) around $R_{200c}/100$ for the models (I) and (II) for halo masses $M \sim 10^{11} h^{-1} M_{\odot}$ (or lower). This suggests that these models may also be strongly constrained by observations, which would provide an upper bound on the model parameter α . However, obtaining a quantitative estimate of this constraint requires a dedicated study that we leave for future work. We would need to evaluate the impact of the fifth force on the final halo profile, which may require numerical simulations, and to estimate the observational accuracy of the halo profiles measured on the intermediary scale $\sim r_{\alpha}$. Moreover, as we discuss in section XIV D below, the results obtained above may break down in the regime dominated by the fifth force because it could lead to the formation of strong inhomogeneities that in turn screen the fifth force in the final configuration of the system.

B. Cosmological and astrophysical structures

We now estimate the fifth force to Newtonian gravity ratio η for a variety of astrophysical objects and environments, from clusters of galaxies to the laboratory on the Earth, at low redshift.

1. Clusters of galaxies

In a halo of mass M and radius R , the Newtonian potential and the Newtonian force are of order

$$\frac{\Psi_N}{c^2} \sim \frac{\mathcal{G}_N M}{c^2 R}, \quad \frac{F_N}{c^2} \sim \frac{\mathcal{G}_N M}{c^2 R^2}. \quad (156)$$

As in Eq.(128), the fifth force $\mathbf{F}_A = -\nabla\Psi_A = -c^2\nabla\ln A$ is of order

$$\frac{F_A}{c^2} \sim \frac{d\ln A}{dr} \sim \frac{1}{R} \frac{d\ln A}{d\ln\rho}, \quad (157)$$

where we assumed $d\ln\rho/d\ln r \sim 1$. As seen from Eq.(86), in the low-density regime we have:

$$\alpha\Delta \ll 1 : \quad \frac{d\ln A}{d\ln\rho} \sim \alpha^2\Delta, \quad (158)$$

where $\Delta = \rho/\bar{\rho}$ is the typical matter overdensity of the object. Then, for a cluster of galaxies, with $\Delta \sim 10^3$, $R \sim 1$ Mpc, $M \sim 10^{14} M_{\odot}$, we obtain

$$\begin{aligned} \frac{F_N}{c^2} &\sim 5 \times 10^{-6} \text{Mpc}^{-1}, & \frac{F_A}{c^2} &\sim \alpha^2 10^3 \text{Mpc}^{-1}, \\ \frac{F_A}{F_N} &\sim (10^4 \alpha)^2 \ll 1. \end{aligned} \quad (159)$$

Therefore, the fifth force is negligible on cluster scales. However, as seen in Sec. X A and Fig. 14, this is no longer the case far inside the cluster, at $r \lesssim R_{200c}/100$, for clusters of mass $M \lesssim 10^{13} h^{-1} M_{\odot}$.

2. Galaxies

We now consider a typical galaxy, such as the Milky Way, with $M \sim 10^{12} M_{\odot}$, $R \sim 10$ kpc, and $\Delta \sim 10^6$. This high value of the density contrast is at the limit of validity of the regime (158), but this should still provide the order of magnitude of the fifth force. Then, we obtain

$$\begin{aligned} \frac{F_N}{c^2} &\sim 5 \times 10^{-4} \text{Mpc}^{-1}, & \frac{F_A}{c^2} &\sim \alpha^2 10^8 \text{Mpc}^{-1}, \\ \frac{F_A}{F_N} &\sim (10^6 \alpha)^2 \sim 1. \end{aligned} \quad (160)$$

Thus, the fifth force is of the same order as the Newtonian gravity on galaxy scales. This suggests that interesting phenomena could occur in this regime and that galaxies could provide a useful probe of such models. On the other hand, since we are at the border of the regime (158), nonlinear effects may already come into play and partly screen the fifth force, depending on the details of the coupling function $A(\tilde{\chi})$.

3. Solar System

Many alternative theories to General Relativity are strongly constrained, or even ruled out, by Solar System

tests, based on the trajectories of planets around the Sun (measurements by the Cassini satellite [24]) or the motion of the Moon around the Earth (Lunar Laser Ranging experiment [16]). To remain consistent with these data, modified-gravity scenarios often involve nonlinear screening mechanisms that ensure convergence to General Relativity in small-scale and high-density environments (typically by suppressing the gradients of the scalar field or its coupling to matter). In our case, if we consider stars, planets and moons as isolated objects in the vacuum, the screening is provided by the definition of the model itself and is 100% efficient. Indeed, because the fifth force is exactly local, as $\mathbf{F}_A = -c^2 \nabla \ln A(\rho)$ only depends on the local density and its gradient, the impact of the Sun onto the motion of the Earth through the fifth force is exactly zero, unless if it creates a distant density gradient by other means (e.g. Newtonian gravity). However, the impact of the gradient of the Newtonian force from the Sun onto the matter distribution in the Earth is negligible and completely superseded by local geophysical sources (the radial structure of the Earth core and atmosphere and random variations associated with mountains and oceans for instance). Therefore, the Sun is completely “screened” as viewed from the Earth by the fifth force, as well as all planets and moons of the Solar System. Therefore, the trajectories of astrophysical objects in the Solar System are exactly given by the usual Newtonian gravity, or more accurately General Relativity, and all Solar Systems tests of gravity are satisfied, to the same accuracy as General Relativity.

Here we assumed that the small-scale cutoff ℓ_s of the theory, discussed in Sec. VB, is below the Solar System scales. If this is not the case, then one needs to explicitly consider the small-scale behavior of the complete theory. If the small-scale regularization is associated with a kinetic term in the scalar-field Lagrangian, as in Eq.(90), we recover a standard Dilaton model. Then, high-density regions, or compact objects such as stars, give rise to a long-range fifth force but the latter is screened in dense environments by the usual Damour-Polyakov mechanism, as the coupling function $\ln A$ goes to a constant at high-densities and the coupling strength $d \ln A / d\tilde{\chi}$ vanishes. The efficiency of this screening mechanism depends on the details of the model [the kinetic and potential terms in the original scalar-field Lagrangian $\tilde{\mathcal{L}}_\varphi(\varphi)$].

4. On the Earth and in the laboratory

Even though the fifth force on the Earth is not significantly influenced by the Sun and other planets, it does not vanish as it is sensitive to the local gradient of the matter density. Then, we must check that this local force is small enough to have avoided detection in the laboratory or on the Earth (e.g., at its surface or in the atmosphere). Here we first assume that the cutoff ℓ_s is smaller than the scales we consider.

So far we have assumed that the scalar field is cou-

pled in the same manner to the dark matter and to the ordinary baryonic matter. For the analysis of cosmological structures, from the background dynamics down to galaxies, we are dominated by dark matter so we mostly probed the coupling to the dark matter and it made no difference whether the coupling to baryons is the same or not. However, on smaller scales, such as in the Solar System or on Earth, we are dominated by baryonic matter. Then, a simple manner to ensure that we satisfy observations and experiments performed in the laboratory or on the Earth is to assume that ordinary matter is not coupled to the scalar field.

A second alternative is that screening mechanisms are sufficiently efficient to make the fifth force negligible on the Earth. We now investigate whether this is the case, assuming dark matter and baryons couple in the same fashion to the scalar field. As seen in Eq.(36), the local nature of the scalar field configuration makes the fifth force appear as a polytropic pressure $p_A(\rho)$, given by Eq.(37), where ρ is now the baryonic matter density as the dark matter density and its gradient can be neglected. Since $\bar{A} \simeq 1$ and $\mathcal{M}^4 \simeq \bar{\rho}_{\text{de}0}$, we obtain for a typical density of 1 g/cm^3 ,

$$\rho \sim 1 \text{ g.cm}^{-3} : \quad \frac{p_A}{\rho} \sim 3 \times 10^{-13} \tilde{\chi} \text{ (m/s)}^2. \quad (161)$$

For $\tilde{\chi} \sim 1$, as in the models (I) and (II) where $\tilde{\chi}$ has a finite range of order unity, this corresponds to small velocities and motions. To compare this pressure with the thermal motions found on the Earth or in the laboratory, we write Eq.(161) as a temperature,

$$\frac{m_p p_A}{\rho k_B} \sim 3 \times 10^{-17} \tilde{\chi} \text{ K}, \quad (162)$$

where again we chose $\rho \sim 1 \text{ g/cm}^3$, m_p is the proton mass and k_B the Boltzmann constant. For the models (I) and (II) where $\tilde{\chi}$ has a finite range of order unity, this gives a very low temperature of order 10^{-17} K , which is much smaller than the temperature reached by cold-atoms experiments in the laboratory, $T \sim 10^{-7} \text{ K}$. Thus, for such models where $\tilde{\chi} \sim 1$ the fifth force can be neglected in the laboratory and on the Earth (and in other astrophysical objects).

More generally, Eq.(162) gives the local upper bound for $|\tilde{\chi}|$:

$$\rho \sim 1 \text{ g.cm}^{-3} : \quad |\tilde{\chi}| < 10^{10}. \quad (163)$$

For the model (III) where $|\tilde{\chi}|$ is not bounded, we obtain from Eq.(76) $\tilde{\chi} \sim -6 \times 10^{14} \alpha^{1/2} \sim -6 \times 10^{11}$, which violates the upper bound (163). Therefore, this model would appear to be ruled out by such cold-atoms experiments. Models where $|\tilde{\chi}|$ is not bounded are still allowed but their function $\tilde{\chi}(\rho)$ should be somewhat smaller than Eq.(76) for $\rho \sim 1 \text{ g/cm}^3$.

However, as noticed in Sec. VB, the local model (5) considered in this paper is not expected to apply down to arbitrarily small scales, but only above a small-scale

cutoff ℓ_s . This may arise for instance from a nonzero kinetic term in the scalar-field Lagrangian. In any case, we should have $\ell_s > 1$ m in the cosmological background (i.e., in the intergalactic space). The cutoff scale ℓ_s generically depends on the environment, e.g. on the local value of the scalar field through the change of variable (4). On the Earth, the result (162) suggests that the theory could be valid down to somewhat smaller scales, as long as we remain above the atomic scale and we can still define a continuum limit to the density field. In any case, this small-scale regularization suggests that the cold-atom bound (163) can be relaxed and the result (162) shows that the fifth force is negligible on the Earth and in the laboratory, and hence it is consistent with local experiments.

C. Fifth-force dominated regime

In the previous section, we estimated the fifth force to Newtonian gravity ratio η and the impact of the scalar field for a variety of objects and environments. It is useful to make this analysis more general and to determine the domain of length, density and mass scales where the fifth force is dominant. Thus, using for instance Eq.(141) and taking $d \ln \rho / d \ln r \sim 1$, we write for structures of typical radius R , density ρ and mass $M = 4\pi\rho R^3/3$,

$$|\eta| \sim \frac{2}{\Omega_{m0}} \frac{\bar{\rho}_0}{\rho} \left(\frac{c}{RH_0} \right)^2 \left| \frac{d \ln A}{d \ln \rho} \right|. \quad (164)$$

Then, the fifth force is greater than Newtonian gravity if we have

$$|\eta| \geq 1: \quad R^2 \leq \left(\frac{c}{H_0} \right)^2 \frac{2}{\Omega_{m0}} \frac{\bar{\rho}_0}{\rho} \left| \frac{d \ln A}{d \ln \rho} \right|. \quad (165)$$

Although for convenience we write the right-hand side in terms of the cosmological quantities H_0 , $\bar{\rho}_0$ and Ω_{m0} at $z = 0$, this expression does not depend on redshift nor on cosmology. Moreover, it is only a function of the density ρ , as any coupling function $\ln A(\tilde{\chi})$ also defines the functions $\tilde{\chi}(\rho)$ and $\ln A(\rho)$ through the scalar-field equation (50). Therefore, in a density-radius plane, the domain where $|\eta| \geq 1$ is given by the area under the curve $R_\eta(\rho)$, where $R_\eta(\rho)$ is the density-dependent radius defined by the right-hand side in Eq.(165).

We display this domain in the (ρ, R) -plane in Fig. 15. At low densities, using Eqs.(86) and (88), we obtain

$$\rho \ll \frac{\mathcal{M}^4}{\alpha}: \quad R_\eta(\rho) \sim R_\alpha \quad \text{with} \quad R_\alpha \equiv \frac{c}{H_0} \frac{\alpha}{\sqrt{\Omega_{de0}}}. \quad (166)$$

Thus, at low densities we obtain a constant radius threshold, of order $R_\alpha \sim 0.01$ Mpc for $\alpha = 10^{-6}$, as we can check in Fig. 15. At high densities, we have the behav-

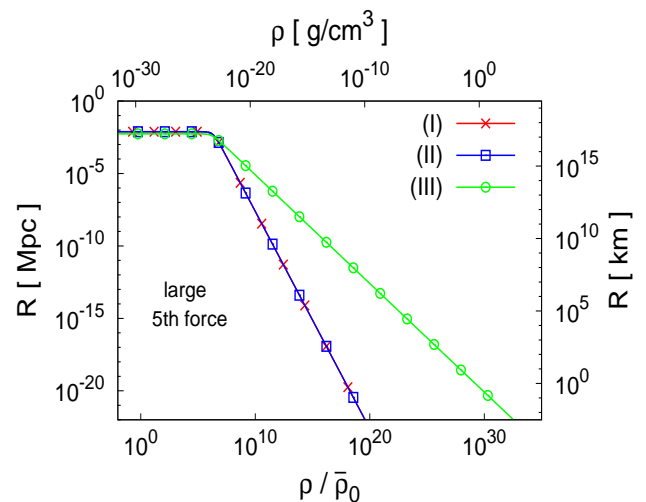


FIG. 15: Domain in the density-radius plane where the fifth force is greater than Newtonian gravity. This domain is identical for the models (I) and (II), and greater for the model (III). The horizontal axis is the typical density of the structure, ρ , given in units of the mean matter cosmological density today, $\bar{\rho}_0$, in the bottom-border scale, and in units of $\text{g}\cdot\text{cm}^{-3}$ in the top-border scale. The vertical axis is the typical radius of the structure, R , given in Mpc in the left-border scale and in km in the right-border scale.

iors

$$\begin{aligned} \text{(I) and (II),} \quad \rho \gg \frac{\mathcal{M}^4}{\alpha}: \quad \left| \frac{d \ln A}{d \ln \rho} \right| &\sim \frac{\mathcal{M}^8}{\alpha \rho^2}, \\ R_\eta(\rho) &\sim \frac{c}{H_0} \frac{\Omega_{de0}}{\sqrt{\alpha \Omega_{m0}^3}} \frac{\bar{\rho}_0^{3/2}}{\rho^{3/2}}, \end{aligned} \quad (167)$$

and

$$\begin{aligned} \text{(III),} \quad \rho \gg \frac{\mathcal{M}^4}{\alpha}: \quad \frac{d \ln A}{d \ln \rho} &\sim \sqrt{\frac{\alpha \mathcal{M}^4}{\rho}}, \\ R_\eta(\rho) &\sim \frac{c}{H_0} \left(\frac{\alpha \Omega_{de0}}{\Omega_{m0}^3} \right)^{1/4} \frac{\bar{\rho}_0^{3/4}}{\rho^{3/4}}. \end{aligned} \quad (168)$$

Thus, at high densities the upper boundary of the fifth-force domain decreases as $R_\eta \propto \rho^{-3/2}$ for the models (I) and (II) and as $\rho^{-3/4}$ for the model (III). As in previous sections, we find that the effects of the fifth force are greater for the model (III). This screening of the fifth force at high densities ensures that it becomes negligible at the center of halos with sufficiently steep density profiles and for astrophysical objects such as stars and planets. On the other hand, we find that, independently of the density, the fifth force is always negligible on scales greater than $R_\alpha \sim \alpha c / H_0$, of order 0.01 Mpc. This confirms again that the fifth force is small on cluster scales and beyond.

To facilitate the comparison with astrophysical structures, it is convenient to display the fifth-force domain

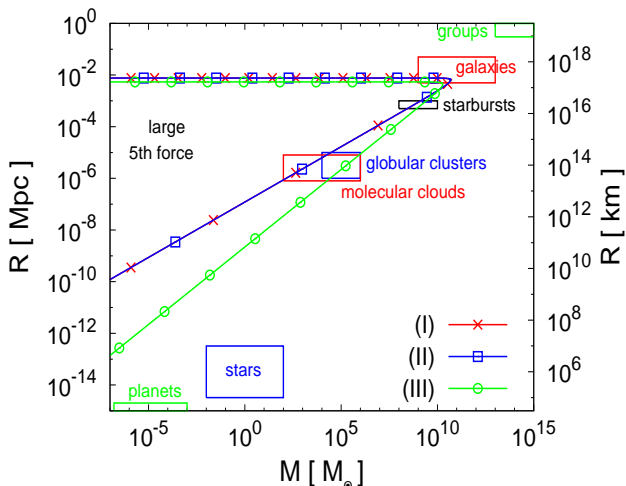


FIG. 16: Domain in the mass-radius plane where the fifth force is greater than Newtonian gravity. This domain is identical for the models (I) and (II), and greater for the model (III). The horizontal axis is the typical mass of the structure, M , given in units of the solar mass. The vertical axis is the typical radius of the structure, R , given in Mpc in the left-border scale and in km in the right-border scale. The rectangles show the typical scales of various astrophysical structures.

(165) in the mass-radius plane (M, R). This is shown in Fig. 16, as the curve $R_\eta(\rho)$ provides a parametric definition of the boundary $R_\eta(M)$, defining the mass of the structure as $M = 4\pi\rho R^3/3$. We obtain a triangular domain, with a constant-radius upper branch and a lower branch that goes towards small radius and mass with a slope that depends on the model. The upper branch corresponds to the regime (166), with

$$\text{upper branch: } R = R_\alpha \text{ for } M < M_\alpha, \quad (169)$$

and

$$M_\alpha \equiv \frac{\alpha^2 \bar{\rho}_0}{\Omega_{m0} \sqrt{\Omega_{de0}}} \left(\frac{c}{H_0} \right)^3, \quad (170)$$

where $M_\alpha = \rho_\alpha R_\alpha^3$ with $\rho_\alpha = \mathcal{M}^4/\alpha$. For $\alpha = 10^{-6}$ this yields $M_\alpha \sim 10^{10} M_\odot$. The lower branch corresponds to the regimes (167) and (168), which yield

lower branch for $M < M_\alpha$:

$$\text{(I) and (II) : } R = R_\alpha \left(\frac{M}{M_\alpha} \right)^{3/7}, \quad (171)$$

$$\text{(III) : } R = R_\alpha \left(\frac{M}{M_\alpha} \right)^{3/5}. \quad (172)$$

We also show in Fig. 16 the regions in this (M, R)-plane occupied by various astrophysical objects. From

left-bottom to right-top, we show planets, stars, molecular clouds, globular clusters, extended starburst regions, galaxies and groups of galaxies. In agreement with Secs. X A and X B, we find that the fifth force is negligible for clusters and groups (at their global scale) and Solar-System objects, while it is of the same order as Newtonian gravity for galaxies. In particular, it appears that various galactic structures, from the molecular clouds and extended starburst regions, where star formation takes place, to the overall extent of low-mass galaxies, as well as the small old globular clusters, all lie close to the boundary of the fifth-force domain. Therefore, they may provide strong constraints on the models considered in this paper. In fact, the model (III) might be ruled out by galaxy observations, independently of the issue found in Sec. X A with the divergence of the fifth force at the center of NFW halos (153). However, we leave a detailed study of molecular clouds and globular clusters to future works to check the quantitative constraints they can provide on the scalar-field theories (3).

XI. HISTORY AND PROPERTIES OF THE FORMATION OF COSMOLOGICAL STRUCTURES

In the previous sections we have studied the evolution of the linear perturbations and of the spherical collapse by assuming that the density field remains smooth and that the fifth force on cosmological scales x is set by the density gradient smoothed on these large scales. However, in the ultra-local models that we study in this paper the fifth force is directly sensitive to the local density gradient, as $\nabla \ln A = (d \ln A / d\rho) \nabla \rho$. As compared with the Λ -CDM cosmology, the models of the type (II) and (III) accelerate the growth of small-scale perturbations, and increasingly so on smaller scales because of the k^2 term in Eq.(44), as seen in Figs. 4 and 5 of the linear growing mode. This suggests that very small scales can develop strong inhomogeneities at early times and the local density gradient could always be set by such very small scales (actually the small-scale cutoff of the theory) rather than by the cosmological scales of interest. Then, the fifth force would be screened as in the Solar System, see the discussion in section X B 3, because of this ultra-local property, and there would be no effect left on cosmological scales. In this case, the universe would be made of small high-density clumps (set by the cutoff of the theory), built at high redshift, while perturbations on cosmological scales would evolve according to General Relativity. To address this issue, we need to go beyond perturbation theory and spherical dynamics, as this is a highly non-linear and inhomogeneous problem. In this article, we consider a thermodynamic analysis that provides a simple analytic framework, which we present in section XI B below.

However, before we tackle this problem, we first de-

scribe in section XI A the evolution with redshift of the scales that enter the non-linear regime. This allows us to distinguish various regimes: while at high redshift the non-linear transition is set by the fifth force, more precisely by the pressure-like term $\propto \nabla^2 \delta$ in Eq.(42) associated with the ultra-local potential $\ln A$, at low redshift it is set by the standard Newtonian gravity [the right-hand side in Eq.(42)].

In this section we focus on models (II) and (III), because model (I) actually damps small-scale perturbations, so that the issue of a possible sensitivity to small scales does not arise. Moreover, we have seen in section V A 1 that such scenarios are disfavored on theoretical grounds because they are not stable with respect to a small kinetic term.

A. Evolution of the cosmological non-linear transition for the model (II)

As explained in previous sections for models (II) and (III), at high redshift the fifth force amplifies the growth of structures and the non-linear transition $x_{\text{coll}}(z)$ is much greater than for the Λ -CDM cosmology, as seen from the linear power spectrum in Fig. 4. Using comoving coordinates, we define this non-linear scale by

$$\Delta_L^2(\pi/x_{\text{coll}}, z) = 1.5 \quad (173)$$

and we show $x_{\text{coll}}(z)$ in the upper panel of Fig. 17. The factor 1.5, which should be order unity, is chosen to give a scale of order $8h^{-1}\text{Mpc}$ at $z = 0$, when the Newtonian gravity dominates and we recover the usual Λ -CDM behavior. We define the non-linear scale $x_{\text{coll}}(z)$ by the condition (173) on the Fourier-space power spectrum $\Delta_L^2(k)$ rather than the real-space linear variance $\sigma_L^2(x)$ because of the steep growth of the linear growing mode $D_+(k, t)$ at high k . This makes the linear variance σ_L^2 divergent or ill-defined, dominated by a small-scale cutoff, but this is not physical because the linear theory cannot be trusted in the non-linear regime. Using $\Delta_L^2(k)$ allows us to avoid this problem (in contrast, for the Λ -CDM cosmology, where the slope of the linear power spectrum decreases at higher k , using either $\Delta_L^2(k)$ or $\sigma_L^2(x)$ gives similar results).

To perform the thermodynamic analysis presented in section XI B below, we shall need the initial kinetic energy or typical velocity of the collapsing region. From the evolution equation (42) of the linear density, we define an effective velocity scale c_{coll} by

$$c_{\text{coll}}^2(z) = c_s^2 + c_N^2, \quad (174)$$

with

$$c_s^2 = \epsilon_1 c^2, \quad c_N^2 = (1 + \epsilon_1) \frac{3\Omega_m}{2\pi^2} (H a x_{\text{coll}})^2. \quad (175)$$

The factor c_s^2 comes from the pressure-like term $\epsilon_1 c^2 \nabla^2 \delta$ in Eq.(42) while the term c_N^2 comes from the right-hand

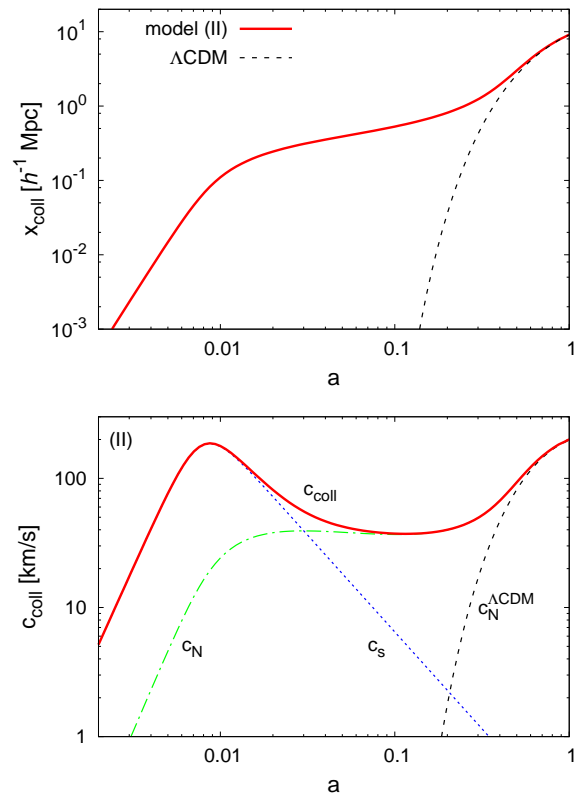


FIG. 17: *Upper panel:* collapse radius $x_{\text{coll}}(z)$ (in comoving coordinates) as a function of the scale factor a . The solid line is for the model (II) while the dashed line is for the Λ -CDM cosmology. *Lower panel:* collapse velocity scale $c_{\text{coll}}(z)$ (solid line) as a function of the scale factor a for the model (II). The dotted and dot-dashed lines are c_s and c_N whereas the dashed line on the right is the result $c_{\text{coll}}^{\Lambda\text{-CDM}} = c_N^{\Lambda\text{-CDM}}$ in the case of the Λ -CDM cosmology.

side, associated with the usual gravitational force (where the Newton constant is amplified by the negligible factor $\epsilon_1 \ll 1$). We show our results in the lower panel of Fig. 17. We also display the case of the Λ -CDM cosmology where $c_{\text{coll}}^{\Lambda\text{-CDM}} = c_N^{\Lambda\text{-CDM}}$ as there is no pressure-like term. It gives $c_{\text{coll}}^{\Lambda\text{-CDM}} \sim 200 \text{ km/s}$ at $z = 0$, which is indeed of the order of the velocities associated with collapsed structures today. It is a bit low, by a factor two if we compare with large clusters of galaxies, which is not surprising as the relation (175) is only an order of magnitude estimate, but this is sufficient for our purposes.

The component c_s , associated with the pressure-like term associated with the fifth-force potential $\ln A$, dominates at high redshift. Its amplitude follows the rise and fall of $\epsilon_1(z)$ displayed in Fig. 2, with a peak at $z_\alpha \sim \alpha^{-1/3} \sim 100$. The component c_N , associated with the Newtonian gravity, explicitly depends on the scale $r_{\text{coll}}(z)$. It grows with time, along with $r_{\text{coll}}(z)$, and dominates at late times, $a \gtrsim 0.03$. The plateau for $0.01 \lesssim a \lesssim 0.2$ follows from the very slow growth of

$r_{\text{coll}}(z)$ found in the upper panel in this redshift range. This can be understood from the peak at $z_\alpha \sim 100$ of the fifth-force characteristic amplitude ϵ_1 and from the analysis of the linear growing modes and of the spherical collapse shown in Figs. 4 and 8. As seen in the previous sections, the fifth force amplifies the growth of structures with a peak at z_α and a strong dependence on scales, following the k^2 factor in Eq.(44). As can be seen in Fig. 8, the main effect is that wave numbers higher than the characteristic value $k_\alpha^{\text{min}} \sim 3h\text{Mpc}^{-1}$ of Eq.(119) become strongly amplified and reach the non-linear regime at z_α , with a steep scale dependence of $D_+(k)$. This leads to the steady rise of $r_{\text{coll}}(z)$ and $c_{\text{coll}}(z)$ until z_α and its subsequent stop as the fifth force declines and the steep scale dependence imprinted on the linear perturbations implies that it requires a very long time for the usual gravitational instability to push the non-linear regime towards greater scales. We recover the standard Λ -CDM behavior at late times, $a > a_{\Lambda\text{-CDM}} \simeq 0.2$, when the Newtonian gravity dominates and the scales that turn non-linear had not been significantly impacted by the fifth force at z_α (i.e. $x \gtrsim 1/k_\alpha^{\text{min}}$).

Thus, we can distinguish three regimes from Fig. 17, defining $a_{c_s/c_N} \simeq 0.03$ as the transition where $c_s = c_N$ and $a_{\Lambda\text{-CDM}} \sim 0.2$ as the time when we recover the Λ -CDM behavior. At early times, $a < a_\alpha = 0.01$, the fifth force dominates and increasingly large scales enter the non-linear regime. This is the period when the thermodynamic analysis of section XIB below applies and allows us to estimate the behavior of the system in the non-linear regime. For $a_\alpha < a < a_{c_s/c_N}$, the fifth force remains dominant but $r_{\text{coll}}(z)$ does not significantly grow so that no new structures form. For $a_{c_s/c_N} < a < a_{\Lambda\text{-CDM}}$, the Newtonian gravity becomes dominant but again $r_{\text{coll}}(z)$ does not significantly grow so that no larger structures form. However, some top-down structure formation might occur (in the range where gravity remains dominant), as in hot dark matter scenarios. Finally, for $a_{\Lambda\text{-CDM}} < a < 1$, we recover the Λ -CDM behavior as Newtonian gravity is dominant and the linear power spectrum on the large scales that now turn non-linear has not been strongly modified by earlier fifth-force effects.

We can note that this history singles out a characteristic mass and velocity scale, associated with the plateau found in Fig. 17 over $0.02 \lesssim a \lesssim 0.2$. This yields

$$\begin{aligned} x_* &\sim 0.355 h^{-1}\text{Mpc}, & M_* &\sim 2 \times 10^{10} h^{-1}M_\odot, \\ c_* &\sim 50 \text{ km/s}. \end{aligned} \quad (176)$$

As in Fig. 16, we recover galaxy scales, more precisely here the scales associated with small galaxies. Again, it is tempting to wonder whether this could help alleviate some of the problems encountered on galaxy scales by the standard Λ -CDM scenario. However, this would require detailed numerical studies that are beyond the scope of this paper.

B. Thermodynamic equilibrium in the fifth-force regime for the model (II)

As explained above, we have so far implicitly assumed that during the initial phase $a < a_\alpha$ of structure formation governed by the fifth force the density field remains smooth on cosmological scales. In other words, we assumed for the computation of the fifth force in linear theory and for the spherical collapse dynamics that the gradient of the fifth force potential, $\nabla \ln A$, is set by the density field smoothed on cosmological scales. This is not obvious because small scales, $x \leq x_{\text{coll}}(z)$, have already turned non-linear at high redshift, $z > z_\alpha$, as seen in the upper panel in Fig. 17. Then, the density field could have become strongly inhomogeneous, made of objects of mass $M_{\text{coll}}(z_{\text{cutoff}})$ formed at a high cutoff redshift z_{cutoff} amid empty space. Then, the gradient of the fifth force potential $\nabla \ln A$ at a given location in space would be unrelated with the gradient of the density field smoothed on cosmological scales. This strong sensitivity to the small-scale distribution of the density field does not arise for the Newtonian gravitational force, because the force at a distance d explicitly depends on the density smoothed over a size of the same order, through the integral $\mathbf{F} = \mathcal{G}_N \int d^3r \rho(\mathbf{r})\mathbf{r}/r^3$. This comes from the fact that the Newtonian potential is given by the Poisson equation (28), $\Psi_N \propto \nabla^{-2}\rho$, which regularizes the density field, whereas the fifth force potential $\ln A$ is a direct function of the local density through Eq.(50). Thus, this issue only arises in the first stage $a < a_\alpha$ found in Fig. 17, where new scales enter the non-linear regime and are dominated by the fifth force.

To address this question we need to go beyond perturbation theory and spherical dynamics, as this is a highly non-linear and inhomogeneous problem. We use a thermodynamic analysis, which provides a simple analytic framework, and we leave dedicated numerical studies for future works. Assuming that the scales that turn non-linear because of the fifth force at high redshift reach a statistical equilibrium through the rapidly changing effects of the fluctuating potential, in a fashion somewhat similar to the violent relaxation that takes place for gravitational systems [25], we investigate the properties of this thermodynamic equilibrium. This first requires the study of the phase transitions and of the phase diagram associated with the potential $\ln A(\rho)$ that defines our models. Because this issue arises from the behavior of the fifth force in the regime where it dominates over Newtonian gravity, we can neglect the latter to investigate this problem. Note that contrary to the usual gravitational case, the potential $\ln A$ is both bounded and short-ranged, so that we cannot build infinitely large negative (or positive) potential energies and a stable thermodynamic equilibrium always exists, and it is possible to work with either micro-canonical, canonical or grand-canonical ensembles. In this respect, a thermodynamic analysis is better suited for such systems than for standard 3D gravitational systems, where the potential energy is unbounded from be-

low and stable equilibria do not always exist, and different statistical ensembles are not equivalent [26].

1. Thermodynamic phase transition and phase diagram

We work in the grand-canonical ensemble, where the dark matter particles are confined in a box of size x (the scale that reaches the non-linear regime at a given redshift) with a mean temperature $T = 1/\beta$ and chemical potential μ . These two thermodynamic quantities will be set by the initial energy and density at the non-linear transition $x_{\text{coll}}(z)$. If the potential $\ln A(\rho)$ were constant, there would be no fifth force and as usual the potential would disappear as an irrelevant constant in the statistical analysis. Then, we would recover the homogeneous equilibrium of the perfect gas, without interactions. However, because of the variations of $\ln A$ we expect inhomogeneities to develop. For the models (II) and (III), where the potential $\ln A(\rho)$ decreases at higher density, see Eqs.(65) and (73)-(77), the fifth force generates instabilities, as already seen from the behavior of linear perturbations, and the medium can be expected to become strongly inhomogeneous, with small high-density clumps amid large voids. However, this outcome depends on the temperature $1/\beta$. At high temperature, we are dominated by the kinetic energy and the potential energy is negligible as $\ln A$ is bounded. Then, we recover the perfect gas with an homogeneous distribution. At low temperature, the potential becomes important and we expect the system to present strong inhomogeneities. As for the thermodynamics of many standard systems, we shall find that there is a phase transition between the homogeneous and the inhomogeneous phases at a critical temperature $T_c = 1/\beta_c$. We do not need to consider cases such as model (I), where $\ln A(\rho)$ increases at higher density and the fifth force has a stabilizing influence that prevents the formation of small-scale inhomogeneities, as already seen from the behavior of linear perturbations.

In the continuum limit, where the mass m of the dark matter particles goes to zero, we describe the system by the smooth phase-space distribution function $f(\mathbf{x}, \mathbf{v})$. The mass M , the energy E and the entropy S of the system read as [26-28]

$$M = \int d^3x d^3v f(\mathbf{x}, \mathbf{v}), \quad (177)$$

$$E = \int d^3x d^3v f(\mathbf{x}, \mathbf{v}) \left(\frac{v^2}{2} + c^2 \ln A[\rho(\mathbf{x})] \right), \quad (178)$$

$$S = - \int d^3x d^3v f(\mathbf{x}, \mathbf{v}) \ln \frac{f(\mathbf{x}, \mathbf{v})}{f_0}, \quad (179)$$

where f_0 is a normalization constant and we used the fact that the potential $\ln A$ is a function of the local density. In the grand-canonical ensemble the statistical equilibrium is obtained by minimizing the grand-canonical potential Ω , which is given by

$$\Omega = E - S/\beta - \mu M, \quad (180)$$

where β and μ are the inverse temperature and the chemical potential. With our notations β has units of inverse squared velocity and μ has units of squared velocity. The equilibrium phase-space distribution is given by the minimum of the grand potential, $\mathcal{D}\Omega/\mathcal{D}f = 0$. This yields

$$f(\mathbf{x}, \mathbf{v}) = f_0 e^{-\beta(v^2/2 + c^2 \ln A + c^2 d \ln A/d \ln \rho) + \beta\mu - 1}. \quad (181)$$

Since $\ln A$ only depends on the positions of the particles but not on their velocities, we recover as expected the Maxwellian distribution over velocities, $f(\mathbf{x}, \mathbf{v}) \propto \rho(\mathbf{x}) e^{-\beta v^2/2}$. The proportionality factor is obtained by integrating over velocities, which gives the usual result

$$f(\mathbf{x}, \mathbf{v}) = \left(\frac{\beta}{2\pi} \right)^{3/2} \rho(\mathbf{x}) e^{-\beta v^2/2}, \quad (182)$$

and Eq.(181) yields

$$\rho(\mathbf{x}) = f_0 \left(\frac{2\pi}{\beta} \right)^{3/2} e^{-\beta c^2 (\ln A + d \ln A/d \ln \rho) + \beta\mu - 1}. \quad (183)$$

Because of the specific form of the potential $\ln A$, which is local and only depends on the local density $\rho(\mathbf{x})$, the thermodynamic equilibrium condition (183) factorizes over different positions \mathbf{x} . The different space locations are thus decoupled and we can omit the space coordinate \mathbf{x} : the equilibrium condition (183), which was a functional equation over the field $\rho(\mathbf{x})$, simplifies to an ordinary function of the local density ρ . As noticed in section IV A 2, it is convenient to introduce the rescaled dimensionless potential and density λ and $\hat{\rho}$, from Eqs.(51) and (52). Defining also the rescaled dimensionless inverse temperature $\hat{\beta}$ and chemical potential $\hat{\mu}$,

$$\hat{\beta} = \alpha c^2 \beta, \quad (184)$$

$$\hat{\mu} = \ln \left[\frac{\alpha f_0 c^3}{\mathcal{M}^4} \left(\frac{2\pi}{\beta c^2} \right)^{3/2} \right] + \beta\mu - 1, \quad (185)$$

the equilibrium condition (183) reads as

$$\hat{\mu} = \theta + \hat{\beta} \nu(\theta), \quad (186)$$

where we introduced

$$\theta = \ln \hat{\rho}, \quad \nu(\theta) = \lambda + \frac{d\lambda}{d\theta}. \quad (187)$$

For a given value of the rescaled inverse temperature $\hat{\beta}$ and chemical potential $\hat{\mu}$, this gives the equilibrium density θ as the solution of the implicit equation (186). In terms of these dimensionless variables, the grand-canonical potential (180) reads as

$$\Omega = \frac{\mathcal{M}^4 c^2 V}{\hat{\beta}} \hat{\Omega} \quad \text{with} \quad \hat{\Omega} = e^\theta \left[\hat{\beta} \lambda - \hat{\mu} - 1 + \theta \right], \quad (188)$$

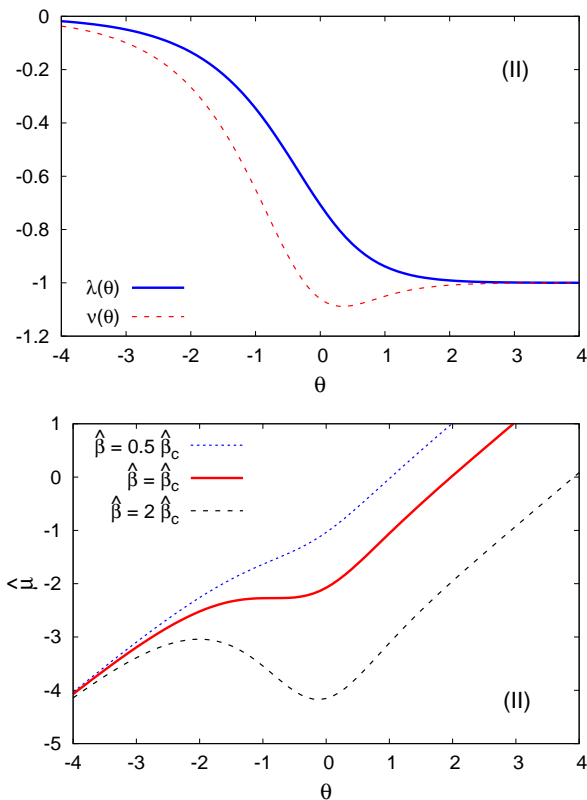


FIG. 18: *Upper panel*: fifth-force potential functions $\lambda(\theta)$ and $\nu(\theta)$ for the model (II). *Lower panel*: thermodynamic equilibrium relation $\hat{\mu} = \hat{\mu}(\theta, \hat{\beta})$ as a function of θ , fixing $\hat{\beta} = 0.5\hat{\beta}_c, \hat{\beta}_c$ and $2\hat{\beta}_c$.

where V is the total volume of the system. Thus, the equilibrium equation (186) is the condition $d\hat{\Omega}/d\theta = 0$, as the thermodynamic equilibrium corresponds to the minimization of the grand-potential.

It is convenient to analyse the system at a fixed temperature, which corresponds to a given initial velocity dispersion, as a function of the chemical potential $\hat{\mu}$ or of the density $\hat{\rho}$, seen as conjugate variables. At high temperature, $\hat{\beta} \rightarrow 0$, Eq.(186) becomes $\hat{\mu} = \theta$ and there is a unique density for each $\hat{\mu}$. This corresponds to the high-temperature homogeneous phase where we recover the perfect gas as the potential energy is negligible. At low temperature, $\hat{\beta} \rightarrow \infty$, the right hand side of Eq.(186) can become non-monotonic so that for some values of the chemical potential $\hat{\mu}$ there are several solutions θ_i . This corresponds to the inhomogeneous phase, where the system splits over several regions of different densities θ_i , with an admixture such that the mean density over the large scale $x = V^{1/3}$ is the initial density $\bar{\rho}$, see [29] for an analysis of such phase transitions.

We first consider the model (II) defined in Eq.(63).

From Eq.(65), with again $\chi_* = -2$, we obtain

$$(II) : \lambda(\theta) = -\frac{1}{\sqrt{1+e^{-2\theta}}}, \quad \nu(\theta) = -\frac{1+2e^{-2\theta}}{(1+e^{-2\theta})^{3/2}}. \quad (189)$$

We show these two functions in the upper panel of Fig. 18. From Eq.(186), the function $\hat{\mu}(\theta)$, at fixed inverse temperature $\hat{\beta}$, is strictly monotonic if $d\hat{\mu}/d\theta = 1 + \hat{\beta}d\nu/d\theta > 0$. Therefore, the function $\hat{\mu}(\theta)$ becomes non-monotonic below the temperature $1/\hat{\beta}_c$, where $\hat{\beta}_c$ is given by the most negative value of $d\nu/d\theta$,

$$\hat{\beta}_c = \frac{-1}{\min(d\nu/d\theta)} = \frac{(15 + \sqrt{105})^{5/2}}{16(51 + 5\sqrt{105})} \simeq 1.96 \quad (190)$$

We display in the lower panel of Fig. 18 the function $\hat{\mu}(\theta)$ for three values of $\hat{\beta}$. As explained above, for low $\hat{\beta}$ (i.e. high temperature) the function $\hat{\mu}(\theta)$ is monotonic while for high $\hat{\beta}$ (i.e. low temperature) it is non-monotonic over some range of densities, with a first-order phase transition at $\hat{\beta}_c$. Then, for $\hat{\beta} < \hat{\beta}_c$, we always have a single solution $\theta(\hat{\mu})$ for any chemical potential $\hat{\mu}$. For $\hat{\beta} > \hat{\beta}_c$, in a finite range $[\hat{\mu}_1, \hat{\mu}_2]$ and $[\theta_1, \theta_2]$, we have three solutions, $\theta_- < \theta_m < \theta_+$, for a given chemical potential $\hat{\mu}$. Both θ_- and θ_+ are local minima of the grand-potential $\hat{\Omega}$ whereas θ_m is a local maximum. Then, the physical solution $\theta(\hat{\mu})$ is the global minimum among $\{\theta_-, \theta_+\}$ (i.e. the deepest minimum). For $\hat{\mu} \simeq \hat{\mu}_1$, where we are close to the bottom left monotonic branch in the lower panel of Fig. 18 (i.e. the low-density branch), this global minimum is the lowest-density one θ_- . For $\hat{\mu} \simeq \hat{\mu}_2$, where we are close to the upper right monotonic branch (i.e. the high-density branch), this global minimum is the highest-density one θ_+ . Then, there is a critical value $\hat{\mu}_s$ in between, $\hat{\mu}_1 < \hat{\mu}_s < \hat{\mu}_2$, where we make the transition from θ_- to θ_+ . This happens at the crossing of their values of the grand-potential, when $\hat{\Omega}(\theta_-; \hat{\mu}_s) = \hat{\Omega}(\theta_+; \hat{\mu}_s)$ [29]. This condition allows us to compute $\hat{\mu}_s$, as a function of $\hat{\beta}$, from Eqs.(186) and (188). At leading order for large $\hat{\beta}$ we obtain

$$\hat{\beta} \rightarrow \infty : \hat{\mu}_s \sim -\hat{\beta}, \quad \theta_- \sim -\hat{\beta}, \quad \theta_+ \sim \frac{\ln \hat{\beta}}{2}. \quad (191)$$

This means that the transition occurs close to the low-density boundary $(\theta_1, \hat{\mu}_1)$ of the multi-valued region. Thus, we have a first-order phase transition, as the density of the system jumps from $\theta_-(\hat{\mu}_s)$ to $\theta_+(\hat{\mu}_s)$ when the chemical potential goes through $\hat{\mu}_s$. At $\hat{\mu}_s$, where $\hat{\Omega}_- = \hat{\Omega}_+$, there is a coexistence of the two phases. One part of the volume V is at the low density θ_- and the other part at the high density θ_+ . The relative fraction between the two phases is set by the mean density θ of the full volume, $\theta_- \leq \theta \leq \theta_+$, which is given by the initial condition of the system (the constraint on the average density of the full system).

The thermodynamic phase diagram of the system, in the inverse temperature - density plane, is shown by the

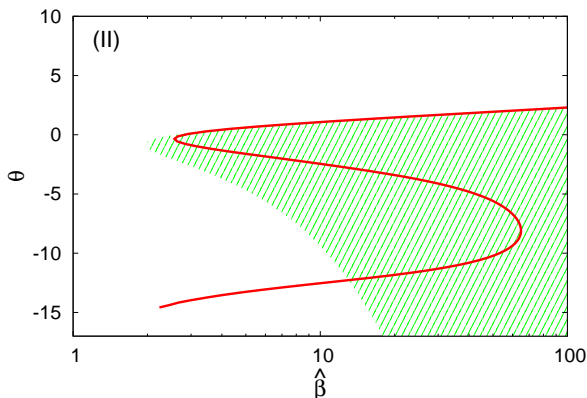


FIG. 19: Thermodynamic phase diagram of model (II). The shaded area is the region of initial inverse temperature $\hat{\beta}$ and density θ where the system reaches an inhomogeneous thermodynamic equilibrium. The white area corresponds to the homogeneous phase. The solid line is the cosmological trajectory $(\hat{\beta}_{\text{coll}}(z), \theta_{\text{coll}}(z))$.

shaded area in Fig. 19. This domain is limited at low $\hat{\beta}$ by the critical temperature $\hat{\beta}_c$. The lower and upper limits of the domain are the curves $\theta_-(\hat{\beta}) \equiv \theta_-(\hat{\mu}_s(\hat{\beta}), \hat{\beta})$ and $\theta_+(\hat{\beta}) \equiv \theta_+(\hat{\mu}_s(\hat{\beta}), \hat{\beta})$, which obey the asymptotes (191). We choose the $(\hat{\beta}, \theta)$ plane to display the phase diagram, rather than $(\hat{\beta}, \hat{\mu})$ for instance, because the density is a more direct physical variable than the chemical potential, while the temperature $1/\hat{\beta}$ is also directly related to the initial kinetic energy. Whereas in the $(\hat{\beta}, \hat{\mu})$ plane the transition appears as a critical line $\hat{\mu}_s(\hat{\beta})$, in the $(\hat{\beta}, \theta)$ plane it appears as an extended domain, because the critical line $\hat{\mu}_s(\hat{\beta})$ corresponds to the jump from θ_- to θ_+ over the density. The meaning of the diagram in Fig. 19 is the following. If the average initial temperature and density, $(1/\hat{\beta}, \theta)$, fall outside of the shaded region, the system remains in the homogeneous phase. If the initial condition falls inside the shaded region, the system becomes inhomogeneous and splits over domains with density θ_- or θ_+ , with a proportion such that the total mass over the full volume is conserved.

2. Cosmological trajectory in the phase diagram

Using the phase diagram of Fig. 19, we can now consider the behavior of the collapsing scales $r_{\text{coll}}(z)$ obtained in Fig. 17, in the time interval $a < a_\alpha$ where the new structures that reach the non-linear regime are governed by the fifth-force potential $\ln A$. For the typical density associated with the non-linearity transition we simply take $\rho_{\text{coll}}(z) = \bar{\rho}(z)$, as the transition corresponds

to density contrasts of order unity, hence

$$\rho_{\text{coll}}(z) = \bar{\rho}(z), \quad \theta_{\text{coll}}(z) = \ln \left[\frac{\alpha \bar{\rho}(z)}{\mathcal{M}^4} \right]. \quad (192)$$

At the thermodynamic equilibrium (182) the kinetic energy reads as $E_{\text{kin}} = 3MT/2 = 3M/2\beta$. From the typical velocity scale $c_{\text{coll}}(z)$ of Eq.(174) we use the simple estimate

$$\beta_{\text{coll}}(z) = \frac{1}{c_{\text{coll}}^2(z)} \quad \text{hence} \quad \hat{\beta}_{\text{coll}}(z) = \frac{\alpha c^2}{c_{\text{coll}}^2(z)}. \quad (193)$$

We show in Fig. 19 the cosmological trajectory $(\hat{\beta}_{\text{coll}}(z), \theta_{\text{coll}}(z))$ over the phase space diagram of the system defined by the fifth-force potential $\ln A$ of the model (II). The curve runs downwards to lower densities θ_{coll} as cosmic time grows. In agreement with the lower panel of Fig. 17, the inverse temperature $\hat{\beta}_{\text{coll}}$ first decreases until a_α , as the velocity $c_{\text{coll}}(z)$ grows. Next, $\hat{\beta}_{\text{coll}}$ increases while $c_{\text{coll}}(z)$ decreases until $a_{\Lambda\text{-CDM}}$, when we recover the Λ -CDM behavior, and $\hat{\beta}_{\text{coll}}$ decreases again thereafter. We are interested in the first era, $a < a_\alpha$, and we find that the cosmological trajectory is almost indistinguishable from the upper boundary $\theta_+(\hat{\beta})$ of the inhomogeneous thermodynamic phase. Indeed, from Eq.(174) and Fig. 17 we have at early times $c_{\text{coll}} \simeq c_s$, hence $\hat{\beta}_{\text{coll}} \simeq \alpha/\epsilon_1$. Using Eq.(67) we have at high densities, which also correspond to $a < a_\alpha$, $\epsilon_1 \simeq \alpha \hat{\rho}^{-2} = \alpha e^{-2\theta}$, hence

$$a \ll a_\alpha : \quad \theta_{\text{coll}} \sim \frac{1}{2} \ln \hat{\beta}_{\text{coll}}, \quad (194)$$

and we recover the asymptote (191) of $\theta_+(\hat{\beta})$. Depending on the choice of some numerical factors, e.g. whether we modify Eq.(193) as $\beta_{\text{coll}}(z) = 2/c_{\text{coll}}^2(z)$ or $\beta_{\text{coll}}(z) = 1/2c_{\text{coll}}^2(z)$, we can push θ_{coll} slightly above or below θ_+ . If $\theta_{\text{coll}} > \theta_+$ we are in the homogeneous phase and the system remains at the initial density $\bar{\rho}$. If $\theta_{\text{coll}} < \theta_+$ we are in the inhomogeneous phase and the system splits over regions of densities θ_+ and θ_- . However, as we remain close to θ_+ most of the volume is at the density $\theta_+ \simeq \theta_{\text{coll}}$ and only a small fraction of the volume is at the low density θ_- . Neglecting these small regions, we can consider that in both cases the system remains approximately homogeneous. This means that, according to this thermodynamic analysis, the cosmological density field does not develop strong inhomogeneities that are set by the cutoff scale of the theory when it enters the fifth-force non-linear regime. Therefore, density gradients remain set by the large-scale cosmological density gradients and the analysis of the linear growing modes in section VII and of the spherical collapse in section VIII are valid. Of course, on small non-linear scales and at late times, where Newtonian gravity becomes dominant, we recover the usual gravitational instability that we neglected in this analysis and structure formation proceeds as in the standard Λ -CDM case.

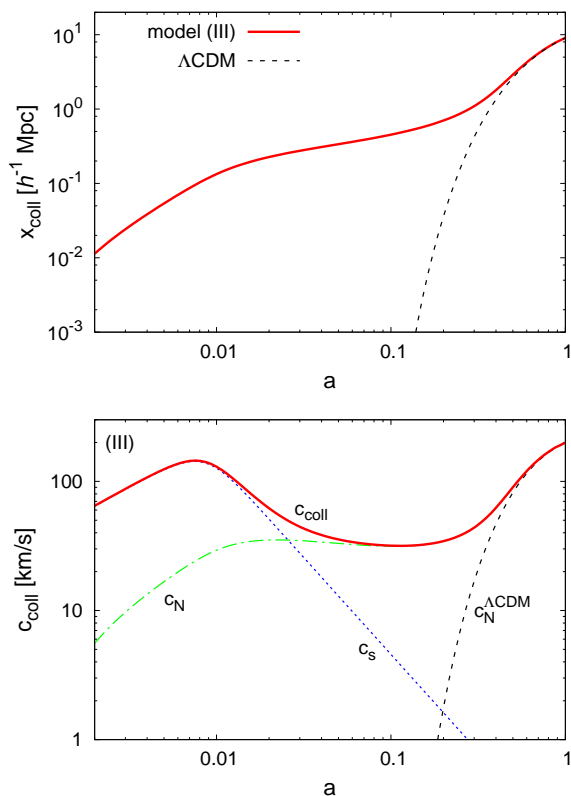


FIG. 20: *Upper panel:* collapse radius $x_{\text{coll}}(z)$ (in comoving coordinates) as a function of the scale factor a . The solid line is for the model (II) while the dashed line is for the Λ -CDM cosmology. *Lower panel:* collapse velocity scale $c_{\text{coll}}(z)$ (solid line) as a function of the scale factor a for the model (II). The dotted and dashed lines are c_s and c_N whereas the dashed line on the right is the result $c_{\text{coll}}^{\Lambda\text{-CDM}} = c_N^{\Lambda\text{-CDM}}$ in the case of the Λ -CDM cosmology.

C. Cosmological trajectory in the phase diagram for the model (III)

We can repeat the previous analysis for the model (III), which also amplifies density perturbations and is similar to the model (II) in many respects. We show the evolution of the non-linearity scale $r_{\text{coll}}(z)$ and of the velocity scale $c_{\text{coll}}(z)$ in Fig. 20. We can see that the behavior is similar to the one obtained in Fig. 17 for the model (II), except that $r_{\text{coll}}(z)$ and $c_{\text{coll}}(z)$ decrease more slowly at high redshift, $z \gg z_\alpha$. This is because the amplitude of the fifth force, as measured by ϵ_1 , decreases more slowly at high z for this model, as found in Fig. 2 and explained in section VI. At lower redshifts, $z < z_\alpha$, the models behave in the same fashion, as was also seen in Fig. 2. This leads to the same characteristic mass and velocity scales (176), associated with the intermediate redshift plateau, $z_{\Lambda\text{-CDM}} \ll z \ll z_\alpha$.

The thermodynamic behavior is similar to the one obtained for the model (II) in section XIB 1. As in the

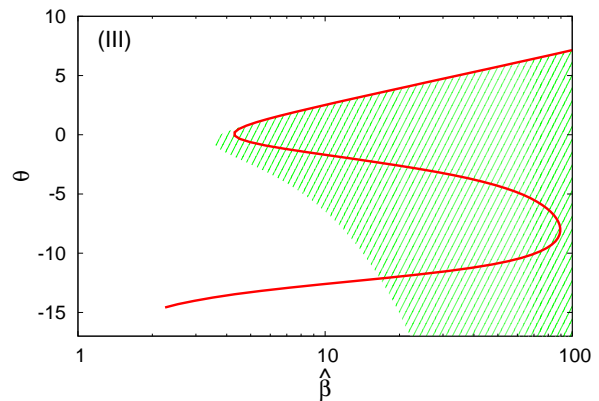


FIG. 21: Thermodynamic phase diagram of model (III). The shaded area is the region of initial inverse temperature $\hat{\beta}$ and density θ where the system reaches an inhomogeneous thermodynamic equilibrium. The white area corresponds to the homogeneous phase. The solid line is the cosmological trajectory $(\hat{\beta}_{\text{coll}}(z), \theta_{\text{coll}}(z))$.

upper panel of Fig. 18, the fifth-force potential functions $\lambda(\theta)$ and $\nu(\theta)$ again decrease from 0 at low density to -1 at high density, except that $\nu(\theta)$ is now strictly decreasing and does not show a local minimum at $\theta \simeq 0$ (which did not play a significant role anyway). We again obtain a first-order phase transition as described in the lower panel of Fig. 18. The inverse critical temperature is now

$$\hat{\beta}_c \simeq 3.53, \quad (195)$$

and at low temperature we obtain the asymptotic behaviors

$$\hat{\beta} \rightarrow \infty : \hat{\mu}_s \sim -\hat{\beta}, \quad \theta_- \sim -\hat{\beta}, \quad \theta_+ \sim 2 \ln \hat{\beta}. \quad (196)$$

We show the thermodynamic phase diagram of the model (III) in Fig. 21. We recover the same features as for the model (II) shown in Fig. 19, with a somewhat higher inverse critical temperature $\hat{\beta}_c$ and upper boundary θ_+ of the inhomogeneous phase. The cosmological trajectory $(\hat{\beta}_{\text{coll}}(z), \theta_{\text{coll}}(z))$ again roughly follows the upper boundary θ_+ at high redshift, $z > z_\alpha$. Indeed, using again $\hat{\beta}_{\text{coll}} \simeq \alpha c^2 / c_s^2 = \alpha / \epsilon_1$ and Eq.(79), we obtain at high densities and redshifts $\epsilon_1 \simeq \alpha / \sqrt{8\hat{\rho}} = \alpha e^{-\theta/2} / \sqrt{8}$, hence

$$a \ll a_\alpha : \theta_{\text{coll}} \sim 2 \ln \hat{\beta}_{\text{coll}}, \quad (197)$$

and we again recover the asymptote (196) of $\theta_+(\hat{\beta})$. Therefore, as for model (II), we can conclude that during the fifth-force era of structure formation, $a < a_\alpha$, density gradients up to the linear transition remain set by large scales and do not suffer from cutoff-scale dependence, so that the analysis of the linear growing modes in section VII and of the spherical collapse in section VIII are valid.

D. Halo centers

It is interesting to apply the thermodynamic analysis presented above to the inner radii of clusters and galaxies. Indeed, we have seen in section X A that the fifth force can become large inside spherical halos and the ratio F_A/F_N can actually diverge at the center for shallow density profiles, see Fig. 14 and Eqs.(152)-(153). However, this analysis was based on dimensional and scaling arguments and it fails if the density field becomes strongly inhomogeneous so that the typical density inside the halo is very different from the global average density. The thermodynamic analysis presented in section X B 1 neglected Newtonian gravity. However, we can also apply its conclusions to a regime dominated by Newtonian gravity where at radius r inside the halo the structures built by gravity and the density gradients are on scale r . Then, we can ask whether at this radius r fifth-force effects may lead to a fragmentation of the system on much smaller scales $\ell \ll r$. To study this small-scale behavior we can neglect the larger-scale gravitational gradients r and discard gravitational forces.

Within a radius r inside the halo the averaged reduced density is

$$\theta_r = \ln \left[\frac{\alpha \rho(< r)}{\mathcal{M}^4} \right] = \ln \left[\frac{\alpha 3M(< r)}{4\pi r^3 \mathcal{M}^4} \right]. \quad (198)$$

We write the reduced inverse temperature as

$$\hat{\beta}_r = \frac{\alpha c^2}{\text{Max}(c_s^2, v_N^2)}, \quad (199)$$

where v_N is the circular velocity (139) associated with the Newtonian gravity while c_s is the velocity scale (143) associated with the fifth force. As noticed in Eq.(144), the maximum $\text{Max}(c_s^2, v_N^2)$ shifts from one velocity scale to the other when the associated force becomes dominant. Here we choose the non-analytic interpolation $\text{Max}(c_s^2, v_N^2)$ instead of the smooth interpolation $c_s^2 + v_N^2$ that we used in Eq.(174) for the cosmological analysis for illustrative convenience. Indeed, the discontinuous changes of slope in Fig. 22 below will show at once the location of the transition $|\eta| = 1$ between the fifth-force and Newtonian gravity regimes.

If the density grows at small radii as a power law, $\rho \propto r^{-\gamma}$, we have seen in Eqs.(150) and (151) that the fifth-force to gravity ratio η behaves as $\eta_{(\text{II})} \sim r^{3\gamma-2}$ for the model (II) and $\eta_{(\text{III})} \sim r^{3\gamma/2-2}$ for the model (III). This led to the bounds (152) and (153) over γ for the fifth force to become negligible at the center. From Eqs.(198) and (199) we obtain in this power-law regime $\theta_r \sim -\gamma \ln r$ and

$$v_N^2 \sim r^{2-\gamma}, \quad c_{s(\text{II})}^2 \sim r^{2\gamma}, \quad c_{s(\text{III})}^2 \sim r^{\gamma/2}, \quad (200)$$

where we used Eqs.(65) and (77). In the Newtonian gravity regime this gives for both models

$$|\eta| < 1 : \quad \theta_r \sim \frac{\gamma}{2-\gamma} \ln \hat{\beta}_r, \quad (201)$$

and in the fifth-force regime

$$|\eta| > 1 : \quad \theta_{r(\text{II})} \sim \frac{1}{2} \ln \hat{\beta}_r, \quad \theta_{r(\text{III})} \sim 2 \ln \hat{\beta}_r. \quad (202)$$

For $\gamma > 2$ we are in the Newtonian regime for both models and $v_N^2 \rightarrow \infty$, $\hat{\beta}_r \rightarrow 0$, so that we are in the homogeneous phase of the thermodynamic phase diagram as $\hat{\beta}_r < \hat{\beta}_c$. Let us now consider the case $\gamma < 2$. For model (II), Newtonian gravity dominates at small radii if $\gamma > 2/3$ from Eq.(152). In this regime Eq.(201) yields $\theta_r > (1/2) \ln \hat{\beta}_r$, so that we are above the upper boundary θ_+ of the inhomogeneous phase obtained in Eq.(191). For shallower density profiles, $\gamma < 2/3$, the fifth force dominates and we obtain $\theta_r \sim \theta_+ \sim (1/2) \ln \hat{\beta}_r$. The model (III) shows a similar behavior. Newtonian gravity now dominates for $\gamma > 4/3$ from Eq.(153), this gives $\theta_r > 2 \ln \hat{\beta}_r$ hence $\theta_r > \theta_+$. In the fifth-force regime, $\gamma < 4/3$, we obtain $\theta_r \sim \theta_+ \sim 2 \ln \hat{\beta}_r$. Therefore, in both models in the Newtonian gravity regime we are far in the homogeneous phase of the thermodynamic diagram whereas in the fifth-force regime we are along the upper boundary of the inhomogeneous phase domain. This means that the dimensional analysis of section X A is valid as the fifth force does not push towards a fragmentation of the system down to very small scales.

The previous results were obtained in the small-radius limit $r \rightarrow 0$. In Fig. 22 we show the full radial trajectories ($\hat{\beta}_r, \theta_r$) over the thermodynamic phase diagram, from R_{200c} inward, for the NFW halos that were displayed in Fig. 14 at $z = 0$. As we move inside the halo, towards smaller radii r , the density θ_r grows. The turnaround of $\hat{\beta}_r$ at $\theta_r \simeq -4$ corresponds to the NFW radius r_s where the local slope of the density goes through $\gamma = 2$ and the circular velocity is maximum. At smaller radii, $r \ll r_s$, the NFW profile goes to $\rho \propto r^{-1}$, hence $\gamma = 1$. For model (II) (upper panel) this corresponds to the Newtonian regime and we move farther away above the inhomogeneous phase. However, for low-mass halos, $M \lesssim 10^{13} h^{-1} M_\odot$, at intermediate radii we are in the fifth force regime, as seen in Fig. 14, and the trajectory converges towards the upper boundary of the inhomogeneous phase. These behaviors agree with the discussion above and Eqs.(201)-(202). The transitions between the Newtonian-gravity and fifth-force regimes correspond to the discontinuous changes of slope in the figure. For $M = 10^{15} h^{-1} M_\odot$ there is no intermediate fifth-force regime, for $M = 10^{13} h^{-1} M_\odot$ it corresponds to $-1 \lesssim \theta_r \lesssim 2$, while for $M = 10^{11} h^{-1} M_\odot$ the low-radius boundary of the intermediate fifth-force regime is beyond the scales shown in the figure. For model (III) (lower panel) the small-radius density slope $\gamma = 1$ is in the fifth-force domain and we can see that for the three masses the trajectory converges to the upper boundary θ_+ of the inhomogeneous domain, in agreement with Eqs.(201)-(202).

The results found in Fig. 22 suggest that for large-mass halos, $M \gtrsim 10^{13} h^{-1} M_\odot$ at $z = 0$, the dimensional analysis of section X A is valid. In the case of

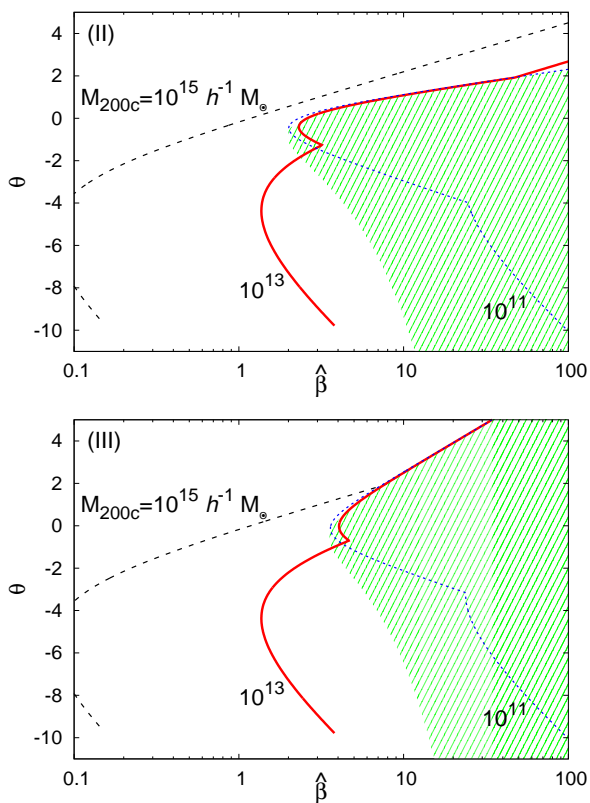


FIG. 22: Radial trajectory $(\hat{\beta}_r, \theta_r)$ over the thermodynamic phase diagram inside halos of mass $M_{200c} = 10^{15}$, 10^{13} and $10^{11} h^{-1} M_{\odot}$, at $z = 0$. We show our results for the models (II) (upper panel) and (III) (lower panel).

model (III) this would lead to an increasingly dominant fifth force at small radii and characteristic velocities that are higher than the Newtonian circular velocity. This is likely to rule out this scenario. For low-mass halos, $M \lesssim 10^{11} h^{-1} M_{\odot}$ at $z = 0$, we find that a significant part of the halo is within the inhomogeneous thermodynamic phase for both models II and III. This may leave some signature as a possible fragmentation of the system on these intermediate scales into higher-density structures. This process would next lead to a screening of the fifth force, as discussed for the Solar System and the Earth in sections XB3 and XB4, because of the ultra-local character of the fifth force. Indeed, because it is set by the local density gradients, the fragmentation of the system leads to a disappearance of large-scale collective effects and the fifth force behaves like a surface tension at the boundaries of different domains. Such a process may also happen in the case of massive halo at earlier stages of their formation, which could effectively screen the fifth force in the case of model (III) where a simple static analysis leads to a dominant fifth force at small radii. However, a more precise analysis to follow such evolutionary tracks and check the final outcomes of the

system requires numerical studies that are beyond the scope of this paper.

XII. DEPENDENCE ON THE PARAMETER α

It is interesting to investigate how the results obtained in the previous sections change when we vary the parameter α that measures the amplitude of the modification to General Relativity. For illustration, we consider the model (II) defined by Eq.(63), keeping $\tilde{\chi}_* = -2$. We show our results in Fig. 23, where we compare the case $\alpha = 10^{-6}$ considered in the previous sections with the two cases $\alpha = 10^{-7}$ and $\alpha = 10^{-8}$.

In agreement with the discussion in Sec. VIA, the factor ϵ_1 shown in the upper left panel, which measures the amplitude of the modification of gravity at linear order over field fluctuations, decreases linearly with α while its peak is pushed towards higher redshift as $z_{\alpha} \sim \alpha^{-1/3}$.

The smaller value of ϵ_1 implies that the effect of the scalar field on gravitational clustering is pushed to smaller scales, as $k_{\alpha} \propto \epsilon_1^{-1/2}$ from Eq.(117), and hence $k_{\alpha} \propto \alpha^{-1/2}$. We can check in the upper right panel that the deviation from the Λ -CDM linear power spectrum is indeed pushed towards smaller scales as α decreases. This also means that the deviation of the halo mass function is repelled to smaller masses, as we can see in the lower left panel. At a given mass, the relative deviation $\Delta n/n$ decreases with α , but one can still reach deviations of order unity by going to small enough masses.

As expected, the area in the (M, R) plane where the fifth force is greater than Newtonian gravity shrinks as α decreases, as we can see in the lower right panel. The upper branch at constant radius is pushed towards smaller scales, as $R_{\alpha} \propto \alpha$ from Eq.(166). The lower branch keeps the same slope and goes down at the very slow rate $R \propto \alpha^{1/7}$ at fixed mass [as can be seen from Eq.(171) and the expressions of R_{α} and M_{α}]. Because the lower branch is almost insensitive to α , the various galactic structures shown in the figure remain along the border of the fifth-force dominated region. They only progressively leave this region, starting from the largest and most massive objects, as the upper branch is pushed downward. Therefore, globular clusters and molecular clouds remain sensitive to the modification of gravity until α becomes smaller than about 10^{-10} .

XIII. COMPARISON WITH SCALAR-FIELD MODELS WITH A KINETIC TERM AND TOMOGRAPHIC RECONSTRUCTION

The ultra-local models introduced in this paper can be easily compared to models of modified gravity of the chameleon type. These models are defined by two functions, the potential $V(\phi)$ and the conformal coupling $A(\phi)$ of a scalar field ϕ . They can be reconstructed from two functions $m^2(\rho)$ and $\beta(\rho)$, which are respectively the

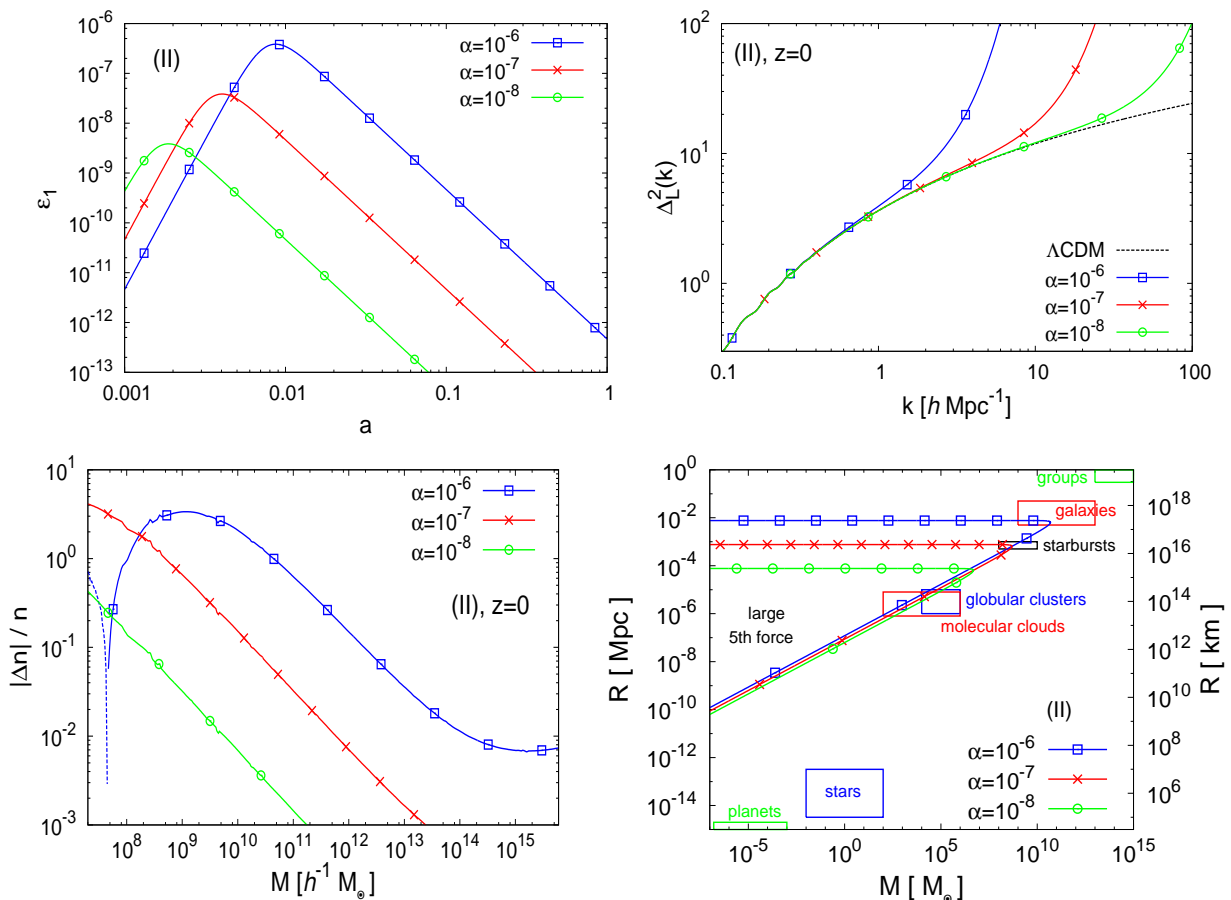


FIG. 23: Dependence on the parameter α of the deviations from the Λ -CDM predictions. We plot models of the type (II) with $\alpha = 10^{-6}$, 10^{-7} and 10^{-8} . *Upper left panel:* $\epsilon_1(a)$ as a function of the scale factor, as in Fig. 2. *Upper right panel:* linear logarithmic power spectrum $\Delta_L^2(k)$ at redshift $z = 0$, as in Fig. 4. *Lower left panel:* absolute value $|\Delta n|/n$ of the relative deviation of the halo mass function from the Λ -CDM result, as in Fig. 12. *Lower right panel:* domain in the mass-radius plane where the fifth force is greater than Newtonian gravity, as in Fig. 16.

mass squared and the coupling to matter in an environment of density ρ , using the tomographic mapping [6, 19]

$$\frac{\phi(\rho)}{M_{\text{Pl}}^2} = \frac{\phi_{\text{BBN}}}{M_{\text{Pl}}^2} - \int_{\rho_{\text{BBN}}}^{\rho} d\rho \frac{\beta(\rho)}{M_{\text{Pl}}^2 m^2(\rho)}, \quad (203)$$

and we have

$$\ln A(\rho) = - \int_{\rho_{\text{BBN}}}^{\rho} d\rho \frac{\beta^2(\rho)}{M_{\text{Pl}}^2 m^2(\rho)} \quad (204)$$

where we assumed that $A_{\text{BBN}}(\rho)$ is close to one, and

$$V(\rho) = V_{\text{BBN}} + \int_{\rho_{\text{BBN}}}^{\rho} d\rho \frac{\beta^2(\rho)\rho}{M_{\text{Pl}}^2 m^2(\rho)}. \quad (205)$$

This parametric mapping defines all the models of the chameleon-type such as $f(R)$ models, chameleons, dilatons and symmetrons.

In the case of the ultra-local models, as the rescaling $A(\chi)$ between the Einstein and the Jordan frames is constrained to vary cosmologically by less than 10^{-6} , the dynamics of the models can be equally understood in the Einstein frame. Then, we can write the ultra-local model in the same form as Eqs.(203)-(205), where $\tilde{\chi}$ plays the role of the reduced scalar field ϕ/M_{Pl} . The effective potential reads

$$V_{\text{eff}}(\tilde{\chi}) = -\mathcal{M}^4 \tilde{\chi} + \rho \ln A(\tilde{\chi}), \quad (206)$$

where ρ is the conserved matter density, and the equation of motion (50) corresponds to the minimum of the effective potential,

$$\left. \frac{\partial V_{\text{eff}}(\tilde{\chi})}{\partial \tilde{\chi}} \right|_{\tilde{\chi}_{\text{min}}(\rho)} = 0. \quad (207)$$

Thus, we recover the behavior of models of the chameleon-type, where the field is stuck at the minimum of the ef-

fective potential since Big Bang Nucleosynthesis. At this minimum one can define the effective coupling to matter

$$\beta_1(\rho) \equiv \left. \frac{d \ln A}{d \tilde{\chi}} \right|_{\tilde{\chi}_{\min}(\rho)} \quad (208)$$

and the effective mass

$$m^2(\rho) \equiv \left. \frac{1}{M_{\text{Pl}}^2} \frac{\partial^2 V_{\text{eff}}}{\partial \tilde{\chi}^2} \right|_{\tilde{\chi}_{\min}(\rho)} = \frac{\rho \beta_2(\rho)}{M_{\text{Pl}}^2}. \quad (209)$$

From $\beta_2 \equiv d\beta_1/d\tilde{\chi} = -\beta_1 d \ln \rho / d\tilde{\chi}$, where we used the equation of motion $\beta_1 = \mathcal{M}^4/\rho$, we obtain $d\tilde{\chi} = -(\beta_1/\beta_2)d \ln \rho$. With Eq.(209) this yields

$$\tilde{\chi}(\rho) = \tilde{\chi}_{\text{BBN}} - \int_{\rho_{\text{BBN}}}^{\rho} d\rho \frac{\beta_1(\rho)}{M_{\text{Pl}}^2 m^2(\rho)}. \quad (210)$$

Thus, we recover the same tomographic mapping as for chameleon-type models, where $\tilde{\chi}$ plays the role of the rescaled field ϕ/M_{Pl} and β_1 that of β in Eq.(203). We can also write $d \ln A / d\rho = \beta_1 d\tilde{\chi} / d\rho = -\beta_1^2 / \beta_2 \rho$, which yields

$$\ln A(\rho) = - \int_{\rho_{\text{BBN}}}^{\rho} d\rho \frac{\beta_1^2(\rho)}{M_{\text{Pl}}^2 m^2(\rho)}, \quad (211)$$

which also coincides with Eq.(204). Finally, writing $V = -\mathcal{M}^4 \tilde{\chi}$ and using $\mathcal{M}^4 = \rho \beta_1$, we recover Eq.(205). This completes the equivalence, at the background level, of the ultra-local models with a subclass of the chameleon-type models. Thus, the ultra-local models are defined by the specific choice

$$\text{ultra-local} \sim \text{chameleon with } \beta(\rho) = \frac{\mathcal{M}^4}{\rho}, \quad (212)$$

while the squared-mass $m^2(\rho)$, or equivalently the coupling $\beta_2(\rho)$, remains a free function. We recover the fact that all ultra-local models can be defined by a single function of the matter density, as was already seen in section IV.

At the linear perturbation level, the chameleon-type models modify the growth of structure as Newton's constant becomes space and time dependent [6, 18]

$$\mathcal{G}_{\text{eff}} = \mathcal{G}_{\text{N}} (1 + \epsilon(k, t)), \quad (213)$$

with

$$\epsilon_{\text{cham}}(k, t) = \frac{2\beta^2(a)}{1 + \frac{a^2 m^2(a)}{k^2}}. \quad (214)$$

On large scales beyond the Compton radius (but still below the horizon) we have

$$H \ll \frac{k}{a} \ll m : \quad \epsilon_{\text{cham}}(k, t) = \frac{2\beta^2(a)k^2}{a^2 m^2(a)}. \quad (215)$$

On the other hand, from Eq.(44) we find that on sub-horizon scales the ultra-local models also exhibit a modified Newton constant with

$$H \ll \frac{k}{a} : \quad \epsilon_{\text{ultra}}(k, t) = \epsilon_1(a) \frac{2k^2}{3\Omega_{\text{m}} a^2 H^2} = \frac{2\beta_1^2 k^2}{a^2 m^2}, \quad (216)$$

where in the second equality we used the definition (41), $\epsilon_1 = \beta_1^2/\beta_2$, and the identification (209), $\beta_2 = M_{\text{Pl}}^2 m^2/\bar{\rho}$. Thus, we recover the result (215) of the chameleon models, over the intermediate scales $H \ll k/a \ll m$.

So we find that the ultra-local models can be seen as chameleon-type models when their mass terms are much larger than the kinetic energy outside the Compton wavelength of the scalar field. We will give an explicit model with such a large mass in a companion paper where we discuss the supersymmetric chameleons. However, we should note that the correspondence found in Eq.(216) is not complete as it breaks down inside the Compton wavelength. From Eq.(209) and the estimate (108) we obtain at low redshift

$$z \lesssim 1 : \quad m^2 \sim \frac{\bar{\rho}}{\alpha^2 M_{\text{Pl}}^2} \sim \frac{H^2}{\alpha^2}. \quad (217)$$

This means that the correspondence with the chameleon models, in the low- k regime (215), applies up to $m \sim H/\alpha$. Since $\alpha \ll 1$ this means that it holds down to scales that are much below the horizon, $1/m \sim 3h^{-1} \text{ kpc}$ for $\alpha \sim 10^{-6}$. However, for the ultra-local models that we consider in this paper the rise with k of ϵ in Eq.(44) goes on to much higher k , until we reach the cutoff of the theory. Therefore, ultra-local models go beyond chameleon models with a relatively large squared-mass m^2 ; taking the kinetic terms in the Lagrangian or the unit factor in Eq.(214) to zero is not exactly the same as taking m large in Eq.(214). This is also clear from the phenomenology presented in this paper, which shows many different qualitative features from usual chameleon models at short enough scale inside the Compton wavelength of the chameleon scalar field.

XIV. CONCLUSIONS

We have introduced in this paper ultra-local models, a class of modified gravity theories where we add a scalar field with a negligible kinetic term to the Einstein-Hilbert action and a conformal coupling to matter. This gives rise to a new screening mechanism, which is not mainly due to the non-linearity of the scalar field potential or coupling function but to the absence of kinetic term. Indeed, it is this feature that leads to the ultra-local character of the model, where the fifth force potential only depends on the local density. This removes any fifth force between isolated objects in vacuum. Another property of this class of models is that the scalar field potential and coupling function are degenerate, so that predictions only depend on a single free function. We have then presented a cosmological analysis of these scenarios.

We have shown the ultra-local models recover the Λ -CDM expansion history at a level of accuracy which is set by a free parameter α of the theory but is always smaller than $\alpha \lesssim 10^{-6}$. Moreover we have demonstrated that, for some of the models considered in this paper, the results obtained for the expansion history are stable if we add a small initial kinetic term to the Lagrangian. We have also checked that the non-linearities of the models do not lead to strong back-reaction effects on the cosmological background. In addition to the dark energy density today, $\bar{\rho}_{\text{de}0}$, these models single out a characteristic density $\rho_\alpha \sim \bar{\rho}_{\text{de}0}/\alpha$ and redshift $z_\alpha \sim \alpha^{-1/3} \gtrsim 100$ where the fifth force is the greatest.

At the linear level of cosmological perturbations, the presence of the ultra-local scalar field has a major impact on the growth rate of structures at small scales, enhancing or diminishing it, even though the last case corresponds to a model that is found to be unstable if we add a small initial kinetic term to its Lagrangian.

We have studied the spherical collapse in this framework showing that, due to the modification of the growth rate at small scales, the halo mass function is substantially modified in the low mass tail. However, it must be taken into account that we have used a Press-Schechter-like approach without considering qualitative modifications to the spherical collapse, which we may be taken into account in future studies.

We have shown that due to the ultra-local behavior of the theory, very dense environments such as the Solar System are completely screened but on the other hand the importance of the fifth force in astrophysical systems with a continuous distribution of matter, such as galaxies or clusters of galaxies, may or may not diminish going towards the center of the objects depending on the shape of the coupling function. This could provide very stringent constraints on the latter, which may require a better understanding of the possible modifications of the halo profile for this theory and/or the use of numerical simulations.

To study the non-linear and inhomogeneous regime of the fifth force, which requires to go beyond perturba-

tion theory or the spherical collapse, we have presented a thermodynamic analysis. This leads to a phase diagram with a first-order phase transition. At low temperature (i.e. low initial kinetic energy) and intermediate density, the system becomes inhomogeneous and splits over domains of either larger or smaller density. We have checked that this inhomogeneous transition does not invalidate our cosmological analysis. On the other hand, for small masses $M \lesssim 10^{11} M_\odot$, the ultra-local force may alter significantly the landscape of inhomogeneities inside the object. The study of this effect requires numerical methods beyond the present work.

Then, we have briefly considered the dependence of our results on the main free parameter α of these models. As it decreases we slowly converge to the Λ -CDM scenario. However, from $\alpha \sim 10^{-6}$ down to $\alpha \sim 10^{-8}$ we expect some signatures on galactic or subgalactic scales. Indeed, it is a peculiar feature of these modified gravity scenarios that the fifth force appears to be most significant on galactic scales, 1 pc – 10 kpc, whereas clusters of galaxies and astrophysical compact objects (stars or planets) show no significant fifth force or are screened.

In the last section we have compared the ultra-local models to chameleon-type models with a mass term that is much greater than the potential one. Both scenarios are similar outside the Compton wave-length of the scalar but differ otherwise. We shall discuss a supersymmetric implementation of ultra-local models in a companion paper [30, 31].

Acknowledgments

This work is supported in part by the French Agence Nationale de la Recherche under Grant ANR-12-BS05-0002. This project has received funding from the European Unions Horizon 2020 research and innovation programme under the Marie Skłodowska-Curie grant agreement No 690575.

-
- [1] S. Perlmutter et al. (Supernova Cosmology Project), *Astrophys.J.* **517**, 565 (1999), astro-ph/9812133.
 - [2] A. G. Riess et al. (Supernova Search Team), *Astron.J.* **116**, 1009 (1998), astro-ph/9805201.
 - [3] L. Amendola et al. (Euclid Theory Working Group), *Living Rev.Rel.* **16**, 6 (2013), 1206.1225.
 - [4] C. M. Will, *Living Rev.Rel.* **4**, 4 (2001), gr-qc/0103036.
 - [5] J. Khoury (2010), 1011.5909.
 - [6] P. Brax, A.-C. Davis, and B. Li, *Physics Letters B* **715**, 38 (2012), 1111.6613.
 - [7] P. Brax, *Class.Quant.Grav.* **30**, 214005 (2013).
 - [8] T. Damour and A. M. Polyakov, *Nucl. Phys.* **B423**, 532 (1994), hep-th/9401069.
 - [9] J. Khoury and A. Weltman, *Phys.Rev.Lett.* **93**, 171104 (2004), astro-ph/0309300.
 - [10] A. Vainshtein, *Phys.Lett.* **B39**, 393 (1972).
 - [11] P. Brax and P. Valageas, *Phys. Rev. D* **90**, 023508 (2014), 1403.5424.
 - [12] S. M. Carroll, I. Sawicki, A. Silvestri, and M. Trodden, *New J. Phys.* **8**, 323 (2006), astro-ph/0607458.
 - [13] V. Faraoni, E. Gunzig, and P. Nardone, *Fundam. Cosmic Phys.* **20**, 121 (1999), gr-qc/9811047.
 - [14] J.-P. Uzan, *Living Rev.Rel.* **14**, 2 (2011), 1009.5514.
 - [15] M. Alvarez, D. D’Armiento, G. Agnetta, A. Alberdi, A. Antonelli, A. Argan, P. Assis, E. A. Baltz, C. Bambi, G. Barbiellini, et al. (2007), 0712.1548, URL <http://arxiv.org/abs/0712.1548>.
 - [16] J. G. Williams, S. G. Turyshev, and D. H. Boggs,

- Phys.Rev.Lett. **93**, 261101 (2004), gr-qc/0411113.
- [17] Planck Collaboration, P. A. R. Ade, N. Aghanim, M. Arnaud, M. Ashdown, J. Aumont, C. Baccigalupi, A. J. Banday, R. B. Barreiro, J. G. Bartlett, et al., ArXiv e-prints (2015), 1502.01589.
- [18] P. Brax and P. Valageas, Phys. Rev. D **86**, 063512 (2012), 1205.6583.
- [19] P. Brax and P. Valageas, Phys. Rev. D **88**, 023527 (2013), 1305.5647.
- [20] W. H. Press and P. Schechter, Astrophys. J. **187**, 425 (1974).
- [21] P. Valageas, *Astr. & Astrophys.* **508**, 93 (2009), 0905.2277.
- [22] A. Schneider, R. E. Smith, and D. Reed, *Mon. Not. R. Astr. Soc.* **433**, 1573 (2013), 1303.0839.
- [23] J. F. Navarro, C. S. Frenk, and S. D. M. White, *Astrophys. J.* **462**, 563 (1996), astro-ph/9508025.
- [24] B. Bertotti, L. Iess, and P. Tortora, *Nature* **425**, 374 (2003).
- [25] D. Lynden-Bell, *Mon. Not. R. Astr. Soc.* **136**, 101 (1967).
- [26] T. Padmanabhan, *Phys. Rep.* **188**, 285 (1990).
- [27] P. H. Chavanis, J. Vatteville, and F. Bouchet, *European Physical Journal B* **46**, 61 (2005), arXiv:cond-mat/0408117.
- [28] P. Valageas, *Astr. & Astrophys.* **450**, 445 (2006), arXiv:astro-ph/0601390.
- [29] R. Balian, *From Microphysics to Macrophysics*, Theoretical and Mathematical Physics (Springer-Verlag, Berlin, Germany, 2007), ISBN 978-3-540-45469-4, URL <http://www.springer.com/fr/book/9783540454694>.
- [30] P. Brax, A.-C. Davis, and J. Sakstein, *Phys. Lett.* **B719**, 210 (2013), 1212.4392.
- [31] P. Brax, A.-C. Davis, and J. Sakstein, *JCAP* **1310**, 007 (2013), 1302.3080.

Article C

Supersymmetric chameleons and ultra-local models

Supersymmetric chameleons and ultra-local models

Philippe Brax, Luca Alberto Rizzo, and Patrick Valageas

*Institut de Physique Théorique,
Université Paris-Saclay CEA, CNRS,
F-91191 Gif-sur-Yvette, Cédex, France*

(Dated: May 20, 2016)

Super-chameleon models where all types of matter belong to three secluded sectors, i.e. the dark, supersymmetry breaking and matter sectors, are shown to be dynamically equivalent to ultra-local models of modified gravity. In the dark sector, comprising both dark matter and dark energy, the interaction range between the dark energy field and dark matter is constrained to be extremely short, i.e. shorter than the inverse gravitino mass set by supersymmetry breaking. This realises an extreme version of chameleon screening of the dark energy interaction. On the other hand, the baryonic matter sector decouples from the dark energy in a Damour-Polyakov way. These two mechanisms preclude the existence of any modification of gravity locally in the Solar System due to the presence of the super-chameleon field. On larger scales, the super-chameleon can have effects on the growth of structure and the number of dark matter halos. It can also affect the dynamics of galaxies where the fifth force interaction that it induces can have the same order of magnitude as Newton's interaction.

PACS numbers: 98.80.-k

I. INTRODUCTION

Dark energy [1–3] is still as mysterious now as it was when the first observations of its existence appeared more than fifteen years ago. Moreover it has been realized over the last ten years that very often dark energy and a modification of gravity on large scales are intimately connected [4]. This is the case for models as diverse as $f(R)$ theories [5] or Galileons [6]. These models utilise a scalar field as the simplest way of going beyond a mere cosmological constant. Such theories where the dynamical equations of motion are of second order have been classified [7]. Their dynamics depend on the coupling of the scalar degree of freedom to matter. In the most general case [8], this coupling can be either conformal or disformal with different physical consequences. For conformal couplings, the resulting scalar-induced fifth force needs to be screened locally. This appears to be feasible in only a few ways: chameleon [9], Damour-Polyakov [10], K-mouflage [11, 12] and Vainshtein [13]. Another mechanism, associated with the ultra-local models introduced in a companion paper [14], arises from the absence of kinetic terms and the locality of the theory. We will find in this paper that this case can be related, outside the Compton wavelength, to the chameleon models with a large mass. For disformal couplings, no fifth force is present in (quasi)-static situations [15] precluding the need for a specific screening mechanism.

All these theories involve non-linearities, either in the potential or kinetic terms and as such appear as low-energy effective field theories. In particular, the issue of the structure of the radiative corrections to the bare Lagrangian is a thorny one, only alleviated in some cases by non-renormalisation theorems, e.g. for Galileons [6] or K-mouflage [16]. For this reason, and because of its radiative stability, supersymmetry might be a promising

setting for dark energy models [17, 18]. In this paper, we will consider the super-chameleon models [19, 20] where the chameleon model is embedded in a supersymmetric setting. This requires the existence of three separate sectors. The dark sector where both dark matter and dark energy live. The matter sector which should include the standard model of particle physics and finally a supersymmetry breaking sector which shifts the masses of the matter superpartners compared to their standard model counterparts. The analysis of this model was already presented in [19, 20]. Here we recall the salient features and emphasize two facts. First of all, the interaction between dark matter particles mediated by dark energy is of extremely short range, shorter than the inverse gravitino mass. Nevertheless, dark matter will see its dynamics modified, i.e. a modification of gravity, on very large scales where collective phenomena for the coarse-grained dark matter fluid can be present. Second, we also recall that ordinary matter decouples from dark energy due to the Damour-Polyakov mechanism leading to no modification of gravity in the Solar System.

In this paper we point out that on cosmological and astrophysical scales these super-chameleon models can be identified to the ultra-local models introduced in a companion paper [14]. These ultra-local models correspond to modified source models [21] where the coupling to matter has a magnitude of order $|\ln A| \lesssim 10^{-6}$ to guarantee that the contribution of modified gravity to Newton's potential is at most of order one. Ultra-local models are such that the value of the dark energy field depends algebraically on the local dark matter density. This leads to a certain number of important properties. First, the growth of structure in the linear to quasi-linear regime has an instability at short scales which is eventually tamed by the absence of fifth forces on short distances like the Solar System. This screening mechanism

is quite different from the usual screening mechanisms encountered in other modified-gravity scenarios as it directly follows from the locality of the fifth-force interaction. The intermediate region between the very large and very small scales is not amenable to our analysis and would require numerical simulations which go beyond our analysis, although we present a thermodynamic approach to investigate the fifth-force non-linear regime. We find that the number of intermediate dark matter halos is affected by the presence of the super-chameleon. This is all the more true for galactic size and mass halos where the fifth force is of the same magnitude as Newton's force. A more complete analysis would require numerical simulations which are left for future work.

This paper is organized as follows. In section II we describe the supersymmetric chameleon models and the dark and baryonic sectors. Next, in section III we show that these models can be identified with ultra-local models introduced in a companion paper, over the scales that are relevant for cosmological purposes. We describe the background dynamics and the growth of large-scale structures in section IV, considering both linear perturbation theory and the spherical collapse dynamics. In section V we estimate the magnitude of the fifth force within spherical halos and on cluster and galaxy scales. In section VI we use a thermodynamic approach to investigate the non-linear fifth-force regime for the cosmological structures that turn non-linear at high redshift and for the cores of dark matter halos. We briefly investigate the dependence on the parameter α of our results in section VII and we conclude in section VIII.

II. SUPERSYMMETRIC CHAMELEONS

A. Super-chameleons

The nature of the dark part of the Universe, i.e. dark matter and dark energy, is still unknown. It is not ruled out that both types of dark elements belong to a secluded sector of the ultimate theory of physics describing all the interactions of the Universe. In this paper, we will use a supersymmetric setting at low energy and assume that the theory comprises three sectors with only gravitational interaction between each other. We will assume that the standard model of particles to which baryons belong is one of them. We will also add a supersymmetry breaking sector \mathcal{SG} and a dark sector comprising both the dark energy field, which will turn out to be a supersymmetric version of a chameleon dark energy model, and dark matter represented by fermions in separate superfields from the super-chameleon one. For details about supersymmetry and its relation to cosmology, see for instance [22].

Baryons are introduced in a secluded sector defined by the Kähler potential K_M and the superpotential W_M . This is the matter sector which complements the dark sector and the supersymmetry breaking one. Assuming

no direct interaction between the super-chameleon Φ and matter, we take for the total Kähler potential which governs the kinetic terms of the model

$$K = K(\Phi\Phi^\dagger) + K_{\mathcal{SG}} + K_M \quad (1)$$

and similarly for the superpotential which is responsible for the interactions between the fields

$$W = W(\Phi) + W_{\mathcal{SG}} + W_M. \quad (2)$$

The kinetic terms for the complex scalar fields ϕ^i of the model obtained as the scalar components of the superfields Φ^i are given by

$$\mathcal{L}_{\text{kin}} = -K_{i\bar{j}} \partial_\mu \phi^i \partial^\mu \bar{\phi}^{\bar{j}} \quad (3)$$

where we have defined

$$K_{i\bar{j}} = \frac{\partial^2 K}{\partial \Phi^i \partial \bar{\Phi}^{\bar{j}}} \equiv \partial_i \bar{\partial}_{\bar{j}} K \quad (4)$$

and its matrix inverse such that $K^{i\bar{j}} K_{k\bar{j}} = \delta_k^i$. The scalar potential obtained from the F -terms of the superfields is given by

$$V_F = K^{i\bar{j}} \partial_i W \bar{\partial}_{\bar{j}} \bar{W}, \quad (5)$$

where \bar{W} is the complex conjugate of W . This is the only term in the scalar potential when the fields are not charged under gauge groups.

We will also need to add a D -term potential to the scalar potential when some extra fields in the dark sector are charged under a gauge symmetry. We will also consider the corrections due to supergravity induced by the presence of the supersymmetry breaking sector. This will be dealt with in the corresponding sections.

B. The supersymmetric model

We consider supersymmetric models where the scalar potential and the coupling to Cold Dark Matter (CDM) arise from a particular choice of the Kähler potential for the dark energy superfield Φ which is non-canonical whilst the dark matter superfields Φ_\pm have a canonical normalisation

$$K(\Phi\Phi^\dagger) = \frac{\Lambda_1^2}{2} \left(\frac{\Phi^\dagger \Phi}{\Lambda_1^2} \right)^\gamma + \Phi_+^\dagger \Phi_+ + \Phi_-^\dagger \Phi_-. \quad (6)$$

The self-interacting part of the superpotential is

$$W = \frac{\gamma}{\sqrt{2}\omega} \left(\frac{\Phi^\omega}{\Lambda_0^{\omega-3}} \right) + \frac{1}{\sqrt{2}} \left(\frac{\Phi^\gamma}{\Lambda_2^{\gamma-3}} \right), \quad 0 < \omega < \gamma, \quad (7)$$

where Φ contains a complex scalar ϕ whose modulus acts as super-chameleon and Φ_\pm are chiral superfields containing dark matter fermions ψ_\pm . Defining the super-chameleon field as $\phi(x) = |\phi|e^{i\theta}$ and identifying $\phi \equiv |\phi|$,

one can minimise the potential over the angular field θ and after introducing the new scales

$$\Lambda = \Lambda_2 \left(\frac{\Lambda_1}{\Lambda_2} \right)^{(\gamma-1)/2}, \quad \phi_{\min} = \Lambda_2 \left(\frac{\Lambda_2}{\Lambda_0} \right)^{(\omega-3)/(\gamma-\omega)}, \quad (8)$$

the scalar potential becomes

$$V_{\text{F}}(\phi) = K^{\Phi\Phi^\dagger} \left| \frac{dW}{d\Phi} \right|^2 = \Lambda^4 \left[1 - \left(\frac{\phi_{\min}}{\phi} \right)^{\frac{n}{2}} \right]^2, \quad (9)$$

with

$$n = 2(\gamma - \omega) \quad \text{for } n \geq 2, \quad \gamma \geq \omega + 1. \quad (10)$$

When $\phi \ll \phi_{\min}$ equation (9) reduces to the Ratra-Peebles potential [23]

$$\phi \ll \phi_{\min} : \quad V_{\text{F}}(\phi) \approx \Lambda^4 \left(\frac{\phi_{\min}}{\phi} \right)^n, \quad (11)$$

which has been well studied in the context of dark energy and used to define chameleons. This is the reason why this model is called super-chameleon. At larger field values the potential has a minimum at $\phi = \phi_{\min}$ where $V_{\text{F}}(\phi_{\min}) = 0$ and $dW/d\phi = 0$. Supersymmetry is therefore broken whenever $\phi \neq \phi_{\min}$ and restored at the minimum where the supersymmetric minimum always has a vanishing energy (this follows from the supersymmetry algebra). Then, a new mechanism must be introduced in order to have a non-vanishing cosmological constant at the minimum of the potential.

C. The Fayet-Iliopoulos mechanism

An effective cosmological constant can be implemented by introducing two new scalars $\Pi_{\pm} = \pi_{\pm} + \dots$ with charges $\pm q$ under a local U(1) gauge symmetry in the dark sector. These have the canonical Kähler potential

$$K(\Pi_{\pm}) = \Pi_+^\dagger e^{2qX} \Pi_+ + \Pi_-^\dagger e^{-2qX} \Pi_-, \quad q > 0, \quad (12)$$

where X is the U(1) vector multiplet containing the U(1) gauge field A_μ . They are chosen to couple to the super-chameleon via the superpotential

$$W_\pi = g' \Phi \Pi_+ \Pi_- \quad (13)$$

where $g' = \mathcal{O}(1)$ is a coupling constant. This construction gives rise to new terms in the scalar potential. The first contribution is the D-term potential coming from the fact that the Π_{\pm} fields are charged

$$V_{\text{D}} = \frac{1}{2} (q\pi_+^2 - q\pi_-^2 - \xi^2)^2, \quad (14)$$

where we have included a Fayet-Iliopoulos term ξ^2 which will later play the role of the cosmological constant. The

second part of the new scalar potential is far more complicated with the addition of these new fields but when $\langle \pi_- \rangle = 0$ it simplifies and the sum of both terms yields

$$V(\pi_+) = \frac{1}{2} (q\pi_+^2 - \xi^2)^2 + g'^2 \phi^2 \pi_+^2; \quad \langle \pi_- \rangle = 0, \quad (15)$$

where we have put $\pi_+ = |\pi_+|$. It can be shown [19] that $\langle \pi_- \rangle = 0$ minimises the whole potential so we only consider the effects of the new term $V(\pi_+)$. In particular, the mass of the charged scalar π_+ is

$$m_{\pi_+}^2 = 2g'^2 \phi^2 - 2q\xi^2. \quad (16)$$

At early times the super-chameleon is small ($\phi \ll \phi_{\min}$) and this mass is negative. The U(1) symmetry is therefore broken ($\langle \pi_+ \rangle \neq 0$). However, as the cosmological field evolves towards its minimum this mass increases until it reaches zero, restoring the symmetry so that $\langle \pi_+ \rangle = 0$. Minimising (15) with respect to π_+ one finds

$$\phi < \frac{\sqrt{q}}{g'} \xi : \quad V_{\min} = -\frac{m_{\pi_+}^4}{8q^2} + \frac{\xi^4}{2}, \quad (17)$$

$$\phi > \frac{\sqrt{q}}{g'} \xi : \quad V_{\min} = \frac{\xi^4}{2}. \quad (18)$$

Therefore, at late times we recover the present-day dark energy density by taking

$$\xi^4 = 2\bar{\rho}_{\text{de}0}, \quad (19)$$

which gives $\xi \sim 10^{-3} \text{eV}$. This mechanism requires that $\phi_{\min} > \sqrt{q}\xi/g'$, which imposes restrictions on the parameter space,

$$\Lambda_2 \left(\frac{\Lambda_2}{\Lambda_0} \right)^{(\omega-3)/(\gamma-\omega)} > \frac{\sqrt{q}}{g'} (2\bar{\rho}_{\text{de}0})^{1/4}. \quad (20)$$

D. The coupling to Cold Dark Matter

Dark energy in the form of Φ is coupled to dark matter. The coupling function between the two dark sides of the model is found by considering the interaction of Φ and Φ_{\pm}

$$W_{\text{int}} = m \left[1 + \frac{g\Phi^\sigma}{m\Lambda_3^{\sigma-1}} \right] \Phi_+ \Phi_-, \quad \sigma > 0, \quad (21)$$

which gives a super-chameleon dependent mass to the dark matter fermions

$$\mathcal{L} \supset \frac{\partial^2 W_{\text{int}}}{\partial \Phi_+ \partial \Phi_-} \psi_+ \psi_-. \quad (22)$$

When the dark matter condenses to a finite density, $\rho = m\langle \psi_+ \psi_- \rangle$, this term gives a density-dependent contribution to the scalar potential

$$\mathcal{L} \supset A(\phi)\rho, \quad (23)$$

from which one can read off the coupling function

$$A(\phi) = 1 + \frac{g \phi^\sigma}{m \Lambda_3^{\sigma-1}}. \quad (24)$$

This function reappears in the form of the conformal coupling between dark matter and dark energy considered as a scalar-tensor theory

E. The normalised dark-energy scalar field φ

Because $K_{\phi\bar{\phi}} \neq 1$ the field ϕ is not canonically normalised, since the kinetic term in the Lagrangian reads

$$\mathcal{L}_{\text{kin}} = -K_{\phi\bar{\phi}} \partial_\mu \phi \partial^\mu \bar{\phi} = -\frac{\gamma^2}{2} \left(\frac{|\phi|}{\Lambda_1} \right)^{2(\gamma-1)} \partial_\mu \phi \partial^\mu \bar{\phi}. \quad (25)$$

The normalised field is then easily defined by

$$\varphi = \Lambda_1 \left(\frac{\phi}{\Lambda_1} \right)^\gamma, \quad (26)$$

and the coupling function (24) becomes

$$A(\varphi) = 1 + \alpha \left(\frac{\varphi}{\varphi_{\text{min}}} \right)^{\sigma/\gamma} \quad \text{with} \quad \alpha \equiv \frac{g \phi_{\text{min}}^\sigma}{m \Lambda_3^{\sigma-1}}, \quad (27)$$

and

$$\varphi_{\text{min}} = \Lambda_1 \left(\frac{\phi_{\text{min}}}{\Lambda_1} \right)^\gamma = \Lambda_1 \left(\frac{\Lambda_2}{\Lambda_1} \right)^\gamma \left(\frac{\Lambda_2}{\Lambda_0} \right)^{\gamma(\omega-3)/(\gamma-\omega)}, \quad (28)$$

while the effective potential $V_{\text{F}}(\varphi) + \rho(A(\varphi) - 1)$ is

$$V_{\text{eff}}(\varphi) = \Lambda^4 \left[\left(\frac{\varphi_{\text{min}}}{\varphi} \right)^{n/2\gamma} - 1 \right]^2 + \alpha \rho \left(\frac{\varphi}{\varphi_{\text{min}}} \right)^{\sigma/\gamma}. \quad (29)$$

Notice that the effective potential in this model coincides with the one obtained in a scalar tensor theory with the potential $V_{\text{F}}(\varphi)$ and the coupling function $A(\varphi)$. We will exploit this fact below. Since we require the cosmology to remain close to the Λ -CDM scenario, i.e. the fifth force must not be much greater than Newtonian gravity, within this framework we can infer that the coupling function $A(\varphi)$ must remain close to unity. This provides the constraint

$$\alpha \ll 1 \quad (30)$$

on the parameter combination α of Eq.(27).

The dynamics of the model can be determined by minimizing the effective potential. This leads to the minimum φ of the theory in the presence of matter (CDM)

$$\left(\frac{\varphi_{\text{min}}}{\varphi} \right)^{(n+\sigma)/\gamma} - \left(\frac{\varphi_{\text{min}}}{\varphi} \right)^{(n+2\sigma)/2\gamma} = \frac{\rho}{\rho_\infty}, \quad (31)$$

where we have defined the energy density

$$\rho_\infty = \frac{n}{\alpha \sigma} \Lambda^4 = \bar{\rho}_0 (1 + z_\infty)^3, \quad \text{and} \quad 0 < \varphi \leq \varphi_{\text{min}}, \quad (32)$$

where z_∞ is the redshift below which the field becomes close to its supersymmetric minimum φ_{min} [34].

As in scalar tensor theories, such as dilaton models or $f(R)$ theories, it is convenient to introduce the coupling $\beta(\varphi)$ defined by

$$\beta(\varphi) = M_{\text{Pl}} \frac{d \ln A}{d \varphi} \quad (33)$$

$$= \frac{\alpha \sigma}{\gamma} \frac{M_{\text{Pl}}}{\varphi_{\text{min}}} \left[1 + \alpha \left(\frac{\varphi}{\varphi_{\text{min}}} \right)^{\sigma/\gamma} \right]^{-1} \left(\frac{\varphi}{\varphi_{\text{min}}} \right)^{\sigma/\gamma-1} \quad (34)$$

and the effective mass $m_{\text{eff}}^2 = \partial^2 V_{\text{eff}} / \partial \varphi^2$ at the minimum of the effective potential,

$$m_{\text{eff}}^2(\varphi) = \frac{\alpha \sigma \rho_\infty}{\gamma \varphi^2} \left(\frac{\varphi}{\varphi_{\text{min}}} \right)^{\sigma/\gamma} \left[\frac{n}{\gamma} \left(\frac{\varphi_{\text{min}}}{\varphi} \right)^{(n+\sigma)/\gamma} - \frac{n}{2\gamma} \left(\frac{\varphi_{\text{min}}}{\varphi} \right)^{(n+2\sigma)/2\gamma} + \frac{\sigma}{\gamma} \frac{\rho}{\rho_\infty} \right], \quad (35)$$

where we used Eq.(31). The quasi-static approximation (32) applies if $m_{\text{eff}}^2 \gg H^2$. This holds for redshifts $z \leq z_\infty$ provided

$$\frac{\alpha \rho_\infty}{\varphi_{\text{min}}^2} \gg H_\infty^2, \quad \text{whence} \quad \left(\frac{\varphi_{\text{min}}}{M_{\text{Pl}}} \right)^2 \ll \alpha, \quad (36)$$

where in the second inequality we assumed $z_\infty \leq z_{\text{eq}}$. At higher redshifts, $m_{\text{eff}}(z)$ grows at least as fast as $H(z)$ in both the matter and radiation eras if we have

$$\text{matter era: } \sigma \leq 2\gamma, \quad \text{radiation era: } \sigma \leq \gamma + \omega/2. \quad (37)$$

F. Supersymmetry breaking

Supersymmetry is broken by values much larger than the energy density of CDM. This is achieved in a dedicated sector of the theory which we do not need to specify here. Gravitational interactions lead to a correction to the scalar potential coming from supersymmetry breaking [20]

$$\Delta V_{\text{S}\mathcal{E}} = \frac{m_{3/2}^2 |K_\Phi|^2}{K_{\Phi\Phi^\dagger}} \sim \frac{m_{3/2}^2 \phi^{2\gamma}}{\Lambda_1^{2\gamma-2}}, \quad (38)$$

where $m_{3/2}$ is the gravitino mass. This competes with the density dependent term in the effective potential (29). This correction does not upset the dynamics of the model as long as

$$\left(\frac{\varphi_{\text{min}}}{M_{\text{Pl}}} \right)^2 \ll \frac{\alpha \rho_\infty}{M_{\text{Pl}}^2 m_{3/2}^2}. \quad (39)$$

This is typically much more stringent than the quasi-static condition (36). Using Eq.(35) this can also be shown to correspond to a condition on the mass of the scalar field φ at the supersymmetric minimum, for $z \leq z_\infty$,

$$m_{\text{eff}}^2(\varphi_{\text{min}}) \sim \frac{\alpha \rho_\infty}{\varphi_{\text{min}}^2} \gg m_{3/2}^2. \quad (40)$$

As the gravitino mass is always greater than 10^{-5} eV in realistic models of supersymmetry breaking [24], we deduce that the range of the scalar interaction mediated by φ is very small, at most at the cm level. Because the scalar interaction has such a short range, we call these models ultra-local. In fact, we shall see below that they can be related to the so-called ‘‘ultra-local models’’ introduced in the companion paper [14].

G. Coupling to baryons

We consider that matter fermions ψ belong to a superfield Φ_M . The mass of the canonically normalised matter fermions becomes

$$m_\psi = e^{K(\Phi, \Phi^\dagger)/2M_{\text{Pl}}^2} m_\psi^{(0)}, \quad (41)$$

where $m_\psi^{(0)}$ is the bare mass of the baryons $\frac{\partial^2 W}{\partial \Phi_M^2}$. The exponential prefactor is at the origin of the coupling function between the matter fields and the super-chameleon in the Einstein frame. This leads to the identification of coupling function in the matter sector

$$A_M(\varphi) = e^{\varphi^2/2M_{\text{Pl}}^2} \quad (42)$$

for the canonically normalised super-chameleon, and the coupling to baryons

$$\beta_M(\varphi) = \frac{\varphi}{M_{\text{Pl}}}, \quad (43)$$

which is the coupling of a dilaton to matter. As long as $\varphi_{\text{min}} \ll M_{\text{Pl}}$, which is already required to suppress the supergravity corrections to the scalar potential, the coupling to baryons is negligible. Hence this model describes a scenario where dark energy essentially couples to dark matter and decouples from ordinary matter.

III. THE SUPERSYMMETRIC CHAMELEON AS AN ULTRA-LOCAL MODEL

A. Definition of ultra-local models

We define ultra-local scalar field models by the action [14]

$$S = \int d^4x \sqrt{-\tilde{g}} \left[\frac{\tilde{M}_{\text{Pl}}^2}{2} \tilde{R} + \tilde{\mathcal{L}}_\varphi(\varphi) \right] + \int d^4x \sqrt{-g} \mathcal{L}_m(\psi_m^{(i)}, g_{\mu\nu}), \quad (44)$$

where the dark matter fields $\psi_m^{(i)}$ follow the Jordan-frame metric $g_{\mu\nu}$, with determinant g , which is related to the Einstein-frame metric $\tilde{g}_{\mu\nu}$ by

$$g_{\mu\nu} = A^2(\varphi) \tilde{g}_{\mu\nu}. \quad (45)$$

We explicitly take no coupling between baryons and the scalar field to make possible the equivalence with the supersymmetric chameleon models. In this paper we restrict ourselves to large cosmological scales, which are dominated by the dark matter, and we neglect the impact of baryons. Ultra-local models are defined by the property that their scalar-field kinetic term is negligible,

$$\tilde{\mathcal{L}}_\varphi(\varphi) = -V(\varphi). \quad (46)$$

Introducing the characteristic energy scale \mathcal{M}^4 of the potential and the dimensionless field $\tilde{\chi}$ as

$$\tilde{\chi} \equiv -\frac{V(\varphi)}{\mathcal{M}^4}, \quad \text{and} \quad A(\tilde{\chi}) \equiv A(\varphi), \quad (47)$$

these models are fully specified by a single function, $A(\tilde{\chi})$, which is defined from the initial potential $V(\varphi)$ and coupling function $A(\varphi)$ through Eq.(47). In other words, because the kinetic term is negligible there appears a degeneracy between the potential $V(\varphi)$ and the coupling function $A(\varphi)$. The change of variable (47) absorbs this degeneracy and we are left with a single free function $A(\tilde{\chi})$.

B. Cosmological background of ultra-local models

Because the matter fields follow the geodesics set by the Jordan frame and satisfy the usual conservation equations in this frame, we mostly work in the Jordan frame. We introduce the time dependent coupling

$$\epsilon_2(t) \equiv \frac{d \ln \bar{A}}{d \ln a}, \quad (48)$$

such that, as shown in the companion paper, the Friedmann equation reads as

$$3M_{\text{Pl}}^2 \mathcal{H}^2 = (1 - \epsilon_2)^{-2} a^2 (\bar{\rho} + \bar{\rho}_{\text{rad}} + \bar{\rho}_{\tilde{\chi}}), \quad (49)$$

where τ is the conformal time, \mathcal{H} the conformal Hubble expansion rate, and the Jordan-frame Planck mass is

$$M_{\text{Pl}}^2(t) = \bar{A}^{-2}(t) \tilde{M}_{\text{Pl}}^2, \quad (50)$$

while $\bar{\rho}$, $\bar{\rho}_{\text{rad}}$ and $\bar{\rho}_{\tilde{\chi}}$ are the matter, radiation and scalar field energy densities. In particular, the background matter and radiation densities evolve as usual as

$$\bar{\rho} = \frac{\bar{\rho}_0}{a^3}, \quad \bar{\rho}_{\text{rad}} = \frac{\bar{\rho}_{\text{rad}0}}{a^4}, \quad (51)$$

while the scalar field energy density is given by

$$\bar{\rho}_{\tilde{\chi}} = -\bar{A}^{-4} \mathcal{M}^4 \tilde{\chi}, \quad (52)$$

and the equation of motion of the background scalar field is

$$\mathcal{M}^4 = \bar{A}^4 \bar{\rho} \frac{d \ln \bar{A}}{d \tilde{\chi}} \quad \text{hence} \quad \frac{d \tilde{\chi}}{d \tau} = \bar{A}^4 \frac{\bar{\rho}}{\mathcal{M}^4} \epsilon_2 \mathcal{H}. \quad (53)$$

It is convenient to write the Friedmann equation (49) in a more standard form by introducing the effective dark energy density $\bar{\rho}_{\text{de}}$ defined by

$$3M_{\text{Pl}}^2 \mathcal{H}^2 = a^2 (\bar{\rho} + \bar{\rho}_{\text{rad}} + \bar{\rho}_{\text{de}}), \quad (54)$$

which gives

$$\bar{\rho}_{\text{de}} = \bar{\rho}_{\tilde{\chi}} + \frac{2\epsilon_2 - \epsilon_2^2}{(1 - \epsilon_2)^2} (\bar{\rho} + \bar{\rho}_{\text{rad}} + \bar{\rho}_{\tilde{\chi}}). \quad (55)$$

C. Cosmological perturbations of ultra-local models

We write the Newtonian gauge metric as

$$ds^2 = a^2 [-(1 + 2\Phi)d\tau^2 + (1 - 2\Psi)d\mathbf{x}^2], \quad (56)$$

so that the Einstein- and Jordan-frame metric potentials are related by

$$1 + 2\Phi = \frac{A^2}{\bar{A}^2} (1 + 2\tilde{\Phi}), \quad 1 - 2\Psi = \frac{A^2}{\bar{A}^2} (1 - 2\tilde{\Psi}), \quad (57)$$

while the Jordan-frame Newtonian potential is defined by

$$\frac{\nabla^2}{a^2} \Psi_{\text{N}} \equiv \frac{\delta\rho + \delta\rho_{\tilde{\chi}}}{2M_{\text{Pl}}^2}. \quad (58)$$

Because we wish the deviations of Φ and Ψ from the Newtonian potential Ψ_{N} to remain modest, and we typically have $|\Psi_{\text{N}}| \lesssim 10^{-5}$ for cosmological and astrophysical structures, we require $|\delta \ln A| \lesssim 10^{-5}$ and $|\delta\rho_{\tilde{\chi}}| \lesssim |\delta\rho|$. This first constraint is fulfilled by choosing coupling functions $A(\tilde{\chi})$ that are bounded and deviate from unity by less than 10^{-5} , which reads as

$$|\ln A(\tilde{\chi})| \lesssim 10^{-5}, \quad (59)$$

while the second constraint will follow naturally because the characteristic scalar field energy density is the dark energy density today. Then, we can linearize Eq.(57) in $\delta \ln A$. This leads to

$$\Phi = \Psi_{\text{N}} + \delta \ln A, \quad \Psi = \Psi_{\text{N}} - \delta \ln A, \quad (60)$$

while the dark energy density fluctuations read as

$$\delta\rho_{\tilde{\chi}} = -\mathcal{M}^4 \delta\tilde{\chi}. \quad (61)$$

In Eq.(61) and in the following we use the characteristic property (59) of ultra-local models to write $A \simeq 1$ whenever this approximation is valid within a 10^{-5} accuracy

(the only place where deviations of A from unity are important is for the computation of the fifth force through the gradient $\nabla \ln A$).

In general configurations including perturbations, the equation of motion of the scalar field reads as

$$\frac{d \ln A}{d \tilde{\chi}} = \frac{\mathcal{M}^4}{\rho}. \quad (62)$$

The dark matter component obeys the continuity and Euler equations

$$\frac{\partial \rho}{\partial \tau} + (\mathbf{v} \cdot \nabla) \rho + (3\mathcal{H} + \nabla \cdot \mathbf{v}) \rho = 0, \quad (63)$$

and

$$\frac{\partial \mathbf{v}}{\partial \tau} + (\mathbf{v} \cdot \nabla) \mathbf{v} + \mathcal{H} \mathbf{v} = -\nabla \Phi. \quad (64)$$

From Eq.(60) we have $\nabla \Phi = \nabla \Psi_{\text{N}} + \nabla \ln A$, and then the scalar field equation (62) gives

$$\nabla \ln A = \frac{\mathcal{M}^4}{\rho} \nabla \tilde{\chi}. \quad (65)$$

Thus in terms of matter dynamics, the scalar field appears via the modification of the Poisson equation (58), because of the additional source associated to the scalar field and the time dependent Planck mass, and via the appearance of the ‘‘new’’ term (65) in the Euler equation (64), which is due to the spatial variation of $\ln A$.

On large scales we may linearize the equations of motion. Expanding the coupling function $A(\tilde{\chi})$ as

$$\ln A(\tilde{\chi}) = \ln \bar{A} + \sum_{n=1}^{\infty} \frac{\beta_n(t)}{n!} (\delta\tilde{\chi})^n, \quad (66)$$

the scalar field equation (62) gives at the background and linear orders

$$\beta_1 = \frac{\mathcal{M}^4}{\bar{\rho}}, \quad \delta\tilde{\chi} = -\frac{\beta_1}{\beta_2} \delta. \quad (67)$$

Defining

$$\epsilon_1(t) \equiv \frac{\beta_1}{\beta_2} \frac{\mathcal{M}^4}{\bar{\rho}} = \frac{\beta_1^2}{\beta_2}, \quad (68)$$

we have for the linear matter density contrast δ

$$\frac{\partial^2 \delta}{\partial \tau^2} + \mathcal{H} \frac{\partial \delta}{\partial \tau} + \epsilon_1 c^2 \nabla^2 \delta = \frac{\bar{\rho} a^2}{2M_{\text{Pl}}^2} (1 + \epsilon_1) \delta, \quad (69)$$

which also reads in Fourier space as

$$\frac{\partial^2 \delta}{\partial \tau^2} + \mathcal{H} \frac{\partial \delta}{\partial \tau} - \frac{3}{2} \Omega_{\text{m}}(\tau) \mathcal{H}^2 [1 + \epsilon(k, \tau)] \delta = 0, \quad (70)$$

where $\epsilon(k, \tau)$, which corresponds to the deviation from the Λ -CDM cosmology, is given by

$$\epsilon(k, \tau) = \epsilon_1(\tau) \left[1 + \frac{2}{3\Omega_{\text{m}}} \frac{c^2 k^2}{a^2 H^2} \right]. \quad (71)$$

The k -dependent term dominates when $ck/aH > 1$, i.e. on sub-horizon scales. Moreover, we have $(ck/aH)^2 \sim 10^7$ today at scales of about $1 h^{-1}\text{Mpc}$. Therefore, we must have

$$|\epsilon_1| \lesssim 10^{-7} \quad (72)$$

to ensure that the growth of large-scale structures is not too significantly modified. This small value does not require introducing additional small parameters as it will follow from the constraint (59), which already leads to the introduction of a small parameter $\alpha \lesssim 10^{-5}$ that gives the amplitude of the coupling function $\ln A$.

The quantity ϵ_2 introduced in Eq.(48) is related to the quantity ϵ_1 defined in Eq.(68) by

$$\epsilon_2 = 3\epsilon_1, \quad \text{hence } |\epsilon_2| \lesssim 10^{-7}. \quad (73)$$

This implies that at the background level the ultra-local model behaves like the Λ -CDM cosmology, see Eqs.(52)-(55), as the scalar field and dark energy densities coincide and are almost constant at low z , within an accuracy of 10^{-6} .

D. Super-chameleon identification

Super-chameleon models are such that the mass of the scalar field is so large that the kinetic terms are negligible. They behave like ultra-local models on distances $r \gtrsim m_{\text{eff}}^{-1}$. It is only on very short distances, which are negligible on astrophysical and cosmological scales, that the kinetic terms play a role. The identification with an ultra-local model is therefore valid on scales

$$\frac{k}{a} \lesssim m_{\text{eff}}; \quad \text{this includes the range } \frac{k}{a} \lesssim m_{3/2} \ll m_{\text{eff}}, \quad (74)$$

where we used Eq.(40). Even as early as $a_{\text{BBN}} \sim 10^{-10}$, the model is equivalent to an ultra-local model on comoving scales larger than 10 km, well below the distances of interest in the growth of cosmological structures. As a result, for all practical purposes super-chameleon models can be identified with ultra-local models. Thus, the coupling function $A(\varphi)$ and the potential $V(\varphi)$ defined in Eqs.(45)-(46) for the ultra-local model can be read from the effective potential (29) of the super-chameleon model, to which we must add the cosmological constant contribution (18). Using the mapping (47) in terms of the dimensionless field $\tilde{\chi}$ this yields

$$A(\tilde{\chi}) = 1 + \alpha \left(\frac{\varphi}{\varphi_{\text{min}}} \right)^{\sigma/\gamma} \quad (75)$$

and

$$-\mathcal{M}^4 \tilde{\chi} = V = \Lambda^4 \left[\left(\frac{\varphi_{\text{min}}}{\varphi} \right)^{n/2\gamma} - 1 \right]^2 + \frac{\xi^4}{2}. \quad (76)$$

We have seen in Eq.(19) that $\xi^4 = 2\bar{\rho}_{\text{de}0}$ to recover the cosmological constant associated with the current expansion of the Universe. We can also take $\mathcal{M}^4 = \bar{\rho}_{\text{de}0}$ without loss of generality, as this only sets the choice of normalization of $\tilde{\chi}$. To simplify the model we also take $\Lambda^4 = \bar{\rho}_{\text{de}0}$, which avoids introducing another scale. This gives

$$\mathcal{M}^4 = \Lambda^4 = \bar{\rho}_{\text{de}0} : \quad \tilde{\chi} = -1 - \left[\left(\frac{\varphi_{\text{min}}}{\varphi} \right)^{n/2\gamma} - 1 \right]^2 \quad (77)$$

and

$$A(\tilde{\chi}) = 1 + \alpha \left(1 + \sqrt{-1 - \tilde{\chi}} \right)^{-2\sigma/n} \quad \text{with } \tilde{\chi} \leq -1, \quad (78)$$

which is the expression of the coupling function in terms of the ultra local scalar field. The comparison with the supersymmetric model can be completed by verifying that the cosmological perturbations also obey the same dynamics.

The coupling of dark energy to dark matter implies that the growth of the density contrast of CDM is modified [25-27] and the linear density contrast $\delta = \delta\rho/\rho$ of the super-chameleon model in the conformal Newtonian Gauge evolves on sub-horizon scales according to

$$\frac{\partial\delta}{\partial\tau^2} + \mathcal{H} \frac{\partial\delta}{\partial\tau} - \frac{3}{2} \Omega_{\text{m}}(\tau) \mathcal{H}^2 \left(1 + \frac{2\beta^2(\varphi)}{1 + \frac{m_{\text{eff}}^2 a^2}{k^2}} \right) \delta = 0. \quad (79)$$

Physically, the last term in (79) corresponds to a scale dependent enhancement of Newton's constant. As the mass of the scalar field is always very large compared to astrophysical wave numbers, we can simplify (79) to find

$$\frac{\partial\delta}{\partial\tau^2} + \mathcal{H} \frac{\partial\delta}{\partial\tau} - \frac{3}{2} \Omega_{\text{m}}(\tau) \mathcal{H}^2 \left(1 + \frac{2k^2\beta^2(\varphi)}{m_{\text{eff}}^2 a^2} \right) \delta = 0 \quad (80)$$

for $k/a \ll m_{\text{eff}}$. This equation is the same as the equation (70) obtained for the ultra-local models, on sub-horizon scales where we can neglect the unit factor in Eq.(71). Indeed, the chameleon coupling $\beta(\varphi)$ defined in Eq.(33), $\beta = M_{\text{Pl}} d \ln A / d\varphi$, and the ultra-local coupling $\beta_1(\tilde{\chi})$ defined in Eq.(66), $\beta_1 = d \ln A / d\tilde{\chi}$, are related by

$$\beta = \beta_1 M_{\text{Pl}} \frac{d\tilde{\chi}}{d\varphi}. \quad (81)$$

From the identification (76) we can write the effective chameleon potential of Eq.(29) as

$$V_{\text{eff}}(\varphi) = -\mathcal{M}^4 \tilde{\chi} + \rho(A - 1) - \bar{\rho}_{\text{de}0}, \quad (82)$$

where we explicitly subtract the cosmological constant. Then, the quasi-static equation (31) for φ , which corresponds to the minimum of the potential $\partial V_{\text{eff}} / \partial\varphi = 0$, yields $\beta_1 = \mathcal{M}^4 / \rho$, where we used Eq.(81) and $A \simeq 1$, and we recover the ultra-local equation of motion (62)-(67). Next, from the definition of the chameleon effective

mass, $m_{\text{eff}}^2 = \partial^2 V_{\text{eff}} / \partial \varphi^2$, we obtain using Eq.(82) and the result $\beta_1 = \mathcal{M}^4 / \rho$,

$$m_{\text{eff}}^2(\varphi) = \frac{\rho \beta_2 \beta^2}{M_{\text{Pl}}^2 \beta_1^2}, \quad (83)$$

where the ultra-local factor $\beta_2 = d^2 \ln A / d\tilde{\chi}^2 = d\beta_1 / d\tilde{\chi}$ was introduced in Eq.(66). This gives $2\beta^2 / m_{\text{eff}}^2 = 2M_{\text{Pl}}^2 \beta_1^2 / \rho \beta_2$ and we find that Eq.(80) coincides with Eq.(70) over the range $H \ll k/a \ll m_{\text{eff}}$, using the second expression (68) for $\epsilon_1(t)$.

This identification of the super-chameleon model with the ultra-local model shows that on cosmological scales, $H \ll k/a \ll m_{\text{eff}}$, the dynamics is set by the single function $A(\tilde{\chi})$ obtained in Eq.(78). This implies that structure formation is only sensitive to two combinations of the parameters introduced in the supersymmetric chameleon setting, namely the exponent ratio σ/n and the ratio $\Lambda^4 / \bar{\rho}_{\text{de}0}$ (which we set to unity in this paper), in addition to the cosmological constant $\xi^4/2 = \bar{\rho}_{\text{de}0}$. Conversely, there is a wide model degeneracy and the same coupling function (78) corresponds to many different chameleon models.

We can note here that in the context of usual chameleon models such as $f(R)$ theories, where $\beta \sim 1$, having a very large effective mass m_{eff}^2 , with $m_{\text{eff}}^{-1} \ll 10^{-4} \text{mm}$, would lead to negligible departure from the Λ -CDM cosmology for the formation of large scale structures, as seen from Eq.(80). This is not the case for the super-chameleon models studied in this paper because the coupling β is also very large and much greater than unity. Indeed, from Eq.(34) we have $\beta \sim \alpha M_{\text{Pl}} / \varphi_{\text{min}} \gg 1$, whereas from Eq.(35) we have $m_{\text{eff}}^2 \sim \alpha \rho_{\infty} / \varphi_{\text{min}}^2$. This yields

$$\frac{\beta^2}{m_{\text{eff}}^2} \sim \frac{\alpha^2 M_{\text{Pl}}^2}{\Lambda^4}, \quad (84)$$

and $\beta^2 k^2 / m_{\text{eff}}^2 a^2$ can be of order unity on kpc to Mpc scales, even with $\alpha \ll 1$, as we typically have $\Lambda^4 \sim M_{\text{Pl}}^2 H_0^2$.

E. Example of models

It is interesting to consider templates for ultra-local models coming from super-chameleons.

A good set of models can be obtained for instance by taking the cut-off of the theory $\Lambda_1 = M_{\text{Pl}}$ in the Kähler potential (6). To obtain $\Lambda^4 = \bar{\rho}_{\text{de}0}$ as in Eq.(77) this requires the non-renormalised scale in the superpotential W of Eq.(7) to be $\Lambda_2 = M_{\text{Pl}} (\bar{\rho}_{\text{de}0} / M_{\text{Pl}}^4)^{1/(6-2\gamma)}$. A simple choice for the exponents ω and γ is $\omega = 1$ and $\gamma = 2$, which gives $n = 2$ and the Kähler potential becomes

$$K(\Phi \Phi^\dagger) = \frac{M_{\text{Pl}}^2}{2} \left(\frac{\Phi^\dagger \Phi}{M_{\text{Pl}}^2} \right)^2 + \Phi_+^\dagger \Phi_+ + \Phi_-^\dagger \Phi_- \quad (85)$$

while the self-interacting part of the superpotential is

$$W = \sqrt{2} \Lambda_0^2 \Phi + \sqrt{\frac{3\Omega_{\text{de}0}}{2}} H_0 \Phi^2, \quad (86)$$

which contains a linear term and a mass term, with $\Lambda_2 = \sqrt{3\Omega_{\text{de}0}} H_0$. Both Λ_0 and H_0 are protected by supersymmetry under renormalisation.

The supersymmetric minimum ϕ_{min} of Eq.(8) becomes

$$\phi_{\text{min}} = \frac{\Lambda_0^2}{\Lambda_2}. \quad (87)$$

Requiring that $\phi_{\text{min}} > \sqrt{q\xi}/g'$ to recover the late cosmological constant behavior (18) and using Eq.(19) we obtain the lower bound on Λ_0

$$\Lambda_0^2 \gtrsim M_{\text{Pl}}^2 \left(\frac{H_0}{M_{\text{Pl}}} \right)^{3/2}. \quad (88)$$

The normalized chameleon field φ of Eq.(26) reads as

$$\frac{\varphi}{M_{\text{Pl}}} = \frac{\phi^2}{M_{\text{Pl}}^2}, \quad \frac{\varphi_{\text{min}}}{M_{\text{Pl}}} = \frac{\Lambda_0^4}{3\Omega_{\text{de}0} M_{\text{Pl}}^2 H_0^2}, \quad (89)$$

while the characteristic density ρ_{∞} of Eq.(32) is

$$\rho_{\infty} = \frac{2}{\alpha \sigma} \bar{\rho}_{\text{de}0} \sim \frac{\bar{\rho}_{\text{de}0}}{\alpha}. \quad (90)$$

We must also satisfy the constraint (39), which yields the upper bound on Λ_0

$$\Lambda_0^2 \ll M_{\text{Pl}}^2 \left(\frac{H_0}{M_{\text{Pl}}} \right)^{3/2} \left(\frac{M_{\text{Pl}}}{m_{3/2}} \right)^{1/2}. \quad (91)$$

As we always have $m_{3/2} \ll M_{\text{Pl}}$, the comparison of Eq.(91) with Eq.(88) shows that the range of values for Λ_0 is fairly large.

The scales m and Λ_3 of the dark matter interaction W_{int} in Eq.(21) are only constrained through their combination with ϕ_{min} in the coupling parameter α of Eq.(27), which must be small as noticed in Eq.(30). In fact, the identification with the ultra-local model and the study presented in the companion paper shows that we must require $\alpha \lesssim 10^{-6}$ to keep the formation of large cosmological structures close to the Λ -CDM behavior. From Eq.(37) the exponent σ should satisfy $\sigma \leq 5/2$ if we wish to ensure that the quasi-static approximation remains valid up to arbitrarily high redshifts, which gives $0 < \sigma/n \leq 5/4$. More generally, combining Eqs.(10) and (37) we have

$$0 < \frac{\sigma}{n} \leq \frac{\gamma + \omega/2}{2(\gamma - \omega)} \quad \text{hence} \quad 0 < \frac{\sigma}{n} \leq \frac{3\gamma - 1}{4}. \quad (92)$$

It is interesting to obtain the characteristic scales of the coupling β and effective mass m_{eff} of these super-chameleon models. Using the bounds (88) and (91) we obtain

$$\beta \sim \frac{\alpha M_{\text{Pl}}^2 H_0^2}{\Lambda_0^4} \quad \text{hence} \quad \frac{\alpha m_{3/2}}{H_0} \ll \beta \lesssim \frac{\alpha M_{\text{Pl}}}{H_0}, \quad (93)$$

and

$$m_{\text{eff}}^2 \sim \frac{M_{\text{Pl}}^4 H_0^5}{\Lambda_0^8} \quad \text{hence} \quad m_{3/2}^2 \ll m_{\text{eff}}^2 \lesssim M_{\text{Pl}}^2. \quad (94)$$

We can check that both β and m_{eff} are large in these super-chameleon models.

As noticed above from Eq.(78), eventually we will study the super-chameleon models of this type where the only parameters are α , which will be chosen to be 10^{-6} or lower, and $\zeta = \sigma/n$, of order unity.

IV. ULTRA-LOCAL DYNAMICS

A. Chameleon and ultra-local potentials and coupling functions

As the total variation of $A(\tilde{\chi})$ is bounded by $\alpha \lesssim 10^{-6}$, we can approximate Eq.(78) as

$$\ln A(\tilde{\chi}) = \alpha \left(1 + \sqrt{-1 - \tilde{\chi}} \right)^{-2\zeta}, \quad \zeta > 0, \quad (95)$$

where we defined $\zeta = \sigma/n$. Equation (95) fully defines the ultra-local model that corresponds to the super-chameleon models considered in this paper. For the numerical applications below we take $\alpha = 10^{-6}$ and ζ among $\{1/2, 1, 3/2\}$. The first two choices can be obtained with $\sigma = 1$ and $\sigma = 2$ for the explicit super-chameleon model described in section III E with $\gamma = n = 2$. The choice $\zeta = 3/2$ requires a model with $\gamma \geq 7/3$ or corresponds to a model with $\gamma < 7/3$ where the field φ has not yet reached the quasi-static equilibrium (31) at very high redshift (which is not very important as the dark energy and the fifth force do not play a significant role at high redshifts far in the radiation era).

Using Eq.(95), the equation for the evolution of the scalar field (62) becomes

$$\frac{\rho}{\rho_\alpha} = \frac{1}{\zeta} \sqrt{-1 - \tilde{\chi}} \left(1 + \sqrt{-1 - \tilde{\chi}} \right)^{2\zeta+1}, \quad (96)$$

where we introduced

$$\rho_\alpha = \frac{\mathcal{M}^4}{\alpha} = \frac{\bar{\rho}_{\text{de}0}}{\alpha}. \quad (97)$$

This explicitly shows that, because of the small parameter α , such models introduce a second density scale $\rho_\alpha \gtrsim 10^6 \bar{\rho}_{\text{de}0}$ in addition to the current dark energy density $\bar{\rho}_{\text{de}0}$.

Eq.(96) can be used to express $\tilde{\chi}$ as a function of the density in the high- and low-density limits,

$$\rho \gg \rho_\alpha : \quad \tilde{\chi}(\rho) \sim - \left(\frac{\zeta \rho}{\rho_\alpha} \right)^{1/(1+\zeta)}, \quad (98)$$

$$\rho \ll \rho_\alpha : \quad \tilde{\chi}(\rho) \simeq -1 - \left(\frac{\zeta \rho}{\rho_\alpha} \right)^2. \quad (99)$$

At the background level, we switch from the high-density regime (98) to the low-density regime (99) at the redshift z_α , with

$$a_\alpha = \alpha^{1/3} \lesssim 0.01, \quad z_\alpha = \alpha^{-1/3} \gtrsim 100, \quad \bar{\rho}(z_\alpha) = \rho_\alpha. \quad (100)$$

Thus, together with the density scale ρ_α these ultra-local models also select a particular redshift $z_\alpha \gtrsim 100$. This is the redshift where the fifth force effects are the strongest, in terms of the formation of cosmological structures, even though at the background level the scalar field energy density only becomes dominant at low z as a dark energy contribution. Up to factors of order unity, the density ρ_α and redshift z_α also correspond to the density ρ_∞ and redshift z_∞ introduced in Eq.(32), where the super-chameleon field φ reaches the supersymmetric minimum φ_{min} (we chose $\Lambda^4 = \bar{\rho}_{\text{de}0}$). Thus, within this supersymmetric setting the density and redshift (ρ_α, z_α) obtain an additional physical meaning.

From Eqs.(98) and (99) we also obtain the behavior of the coupling function $\ln A(\rho)$ in terms of the matter density,

$$\rho \gg \rho_\alpha : \quad \ln A(\rho) \sim \alpha \left(\frac{\zeta \rho}{\rho_\alpha} \right)^{-\zeta/(1+\zeta)}, \quad (101)$$

$$\rho \ll \rho_\alpha : \quad \ln A(\rho) \simeq \alpha \left(1 - 2\zeta^2 \frac{\rho}{\rho_\alpha} \right). \quad (102)$$

As shown in the companion paper, the derived function $\ln A(\rho)$ is particularly important when applied to static configurations and can be used to probe the existence of a screening mechanism for this theory as we will show in sec.V A.

We show in Fig. 1 the characteristic functions that define the super-chameleon models and the associated ultra-local models, for the choice of chameleon exponents $\gamma = 2, \omega = 1, n = 2$ for the Kähler potential K and the superpotential W , and $\sigma = 1, 2, 3$ for the interaction potential W_{int} . This gives $\zeta = 1/2, 1, 3/2$ for the ultra-local coupling function $\ln A(\tilde{\chi})$. The left panel shows the normalized chameleon potential V/\mathcal{M}^4 , which is also equal to the opposite of the ultra-local field $\tilde{\chi}$ from Eq.(76). It is identical for the three models that we consider in the numerical computations presented in this paper. The middle panel shows the chameleon coupling function $\ln A(\varphi)$ for the three choices for the exponent σ . The right panel shows the ultra-local coupling function $\ln A(\tilde{\chi})$ for the corresponding three choices of the exponent ζ . In terms of the ultra-local model, or for the dynamics of cosmological perturbation in the chameleon model over scales $H \ll k/a \ll m_{\text{eff}}$, this function $\ln A(\tilde{\chi})$ fully defines the system.

In the right panel of Fig. 1 we show the coupling function $\ln A$ as a function of the normalized scalar field φ for different values of the parameter ζ . For all the models we have $|\bar{\Lambda} - 1| \lesssim 10^{-6} \ll 1$ which means that we recover the Λ -CDM cosmology at the background level to

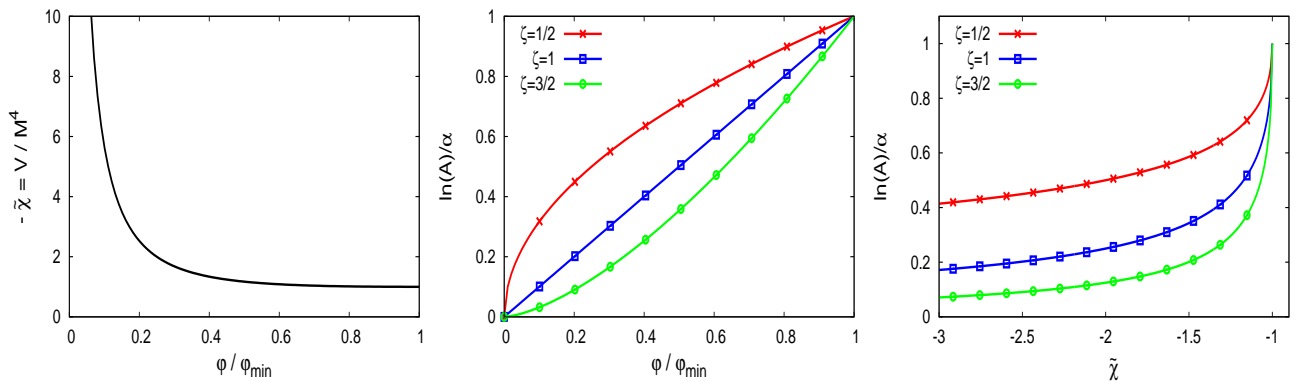


FIG. 1: *Left panel:* ultra-local scalar field or chameleon potential, $-\tilde{\chi} = V/M^4$, as a function of the chameleon scalar field φ/φ_{\min} , as in Eq.(77) for $\gamma = 2, n = 2$. *Middle panel:* coupling function $\ln A(\varphi)$ as a function of the chameleon scalar field from Eq.(27), with $\gamma = 2, \sigma = 1, 2, 3$, which corresponds to $\zeta = 1/2, 1, 3/2$ with $n = 2$. *Right panel:* coupling function $\ln A(\tilde{\chi})$ as a function of the ultra-local scalar field $\tilde{\chi}$ from Eq.(95), for $\zeta = 1/2, 1, 3/2$.

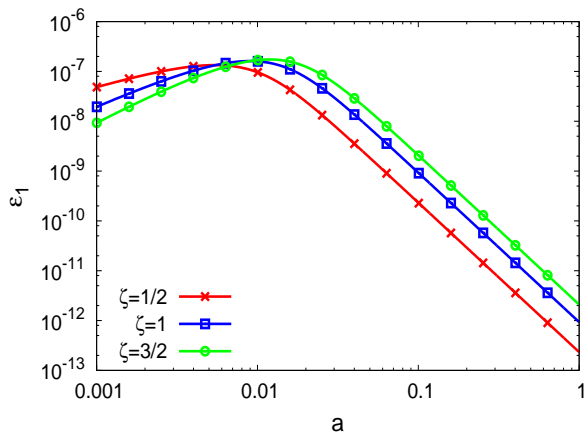


FIG. 2: Time evolution of the factor $\epsilon_1(a)$ as a function of the scale factor for $\zeta = 1/2, 1, 3/2$.

a 10^{-6} accuracy: in particular as we increase ζ the coupling function becomes steeper making the effect of the presence of the scalar field on the growth of structure more relevant, as we will demonstrate in section IV B.

B. Cosmological background and perturbations

For all the models we have $|\bar{A} - 1| \lesssim 10^{-6} \ll 1$, which means that we recover the Λ -CDM cosmology at the background level to a 10^{-6} accuracy. Therefore, to distinguish such models from the Λ -CDM scenario we must consider the dynamics of cosmological perturbations. As we can see from Eq.(70), the linear growth $D_+(k, t)$ of the dark matter density contrast is modified with respect to the Λ -CDM case only by the presence of the factor $\epsilon(k, t)$,

which for the models presented in the previous sections is equal to

$$\epsilon_1 = 2\alpha\zeta \frac{\sqrt{-1-\tilde{\chi}}(1+\sqrt{-1-\tilde{\chi}})^{-2\zeta}}{1+2(\zeta+1)\sqrt{-1-\tilde{\chi}}}, \quad (103)$$

where we used the definition (68). From Eq.(98) and (99) we have the following simplified expressions for ϵ_1 as function of the density

$$\rho \gg \rho_\alpha : \epsilon_1(\rho) \sim \frac{\alpha\zeta}{1+\zeta} \left(\frac{\zeta\rho}{\rho_\alpha} \right)^{-\zeta/(1+\zeta)}, \quad (104)$$

$$\rho \ll \rho_\alpha : \epsilon_1(\rho) \sim 2\alpha\zeta^2 \frac{\rho}{\rho_\alpha}. \quad (105)$$

This explicitly shows that ϵ_1 decreases both at high and low densities and peaks around ρ_α . This also gives the evolution of $\epsilon_1(t)$ as a function of the scale factor $a(t)$ using $\bar{\rho} = \bar{\rho}_0 a^{-3}$,

$$a \ll a_\alpha = \alpha^{1/3} : \epsilon_1(a) \sim \alpha \left(\frac{a}{a_\alpha} \right)^{3\zeta/(1+\zeta)}, \quad (106)$$

$$a \gg a_\alpha = \alpha^{1/3} : \epsilon_1(a) \sim \alpha \left(\frac{a}{a_\alpha} \right)^{-3}, \quad (107)$$

which peaks at the scale factor a_α that corresponds to $\bar{\rho} = \rho_\alpha$. In Fig. 2 we show the evolution of ϵ_1 , for $\zeta = 1/2, 1, 3/2$, as a function of the scale factor. It is always positive for these models leading to an amplification of the Newtonian gravity. We can check that ϵ_1 has a maximum around $a_\alpha = \alpha^{1/3}$, which for this paper corresponds to a value of $a_\alpha = 0.01$. At low redshifts we recover the same decrease as $\epsilon_1 \propto a^{-3}$ of Eq.(107), whereas at high redshift the decrease is stronger for higher exponent ζ , in agreement with Eq.(106). At its peak at

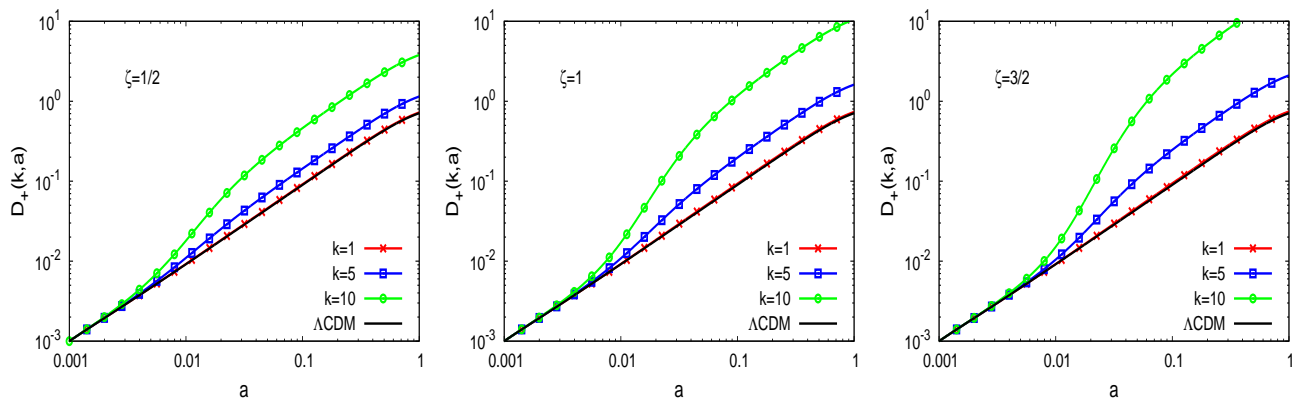


FIG. 3: Linear growing mode $D_+(k, a)$ for the models defined by Eq.(95), as a function of the scale factor for $k = 1, 5$ and $10 h\text{Mpc}^{-1}$, and for the Λ -CDM cosmology. We consider the cases $\zeta = 1/2, 1$ and $3/2$ (respectively left, center and right panel).

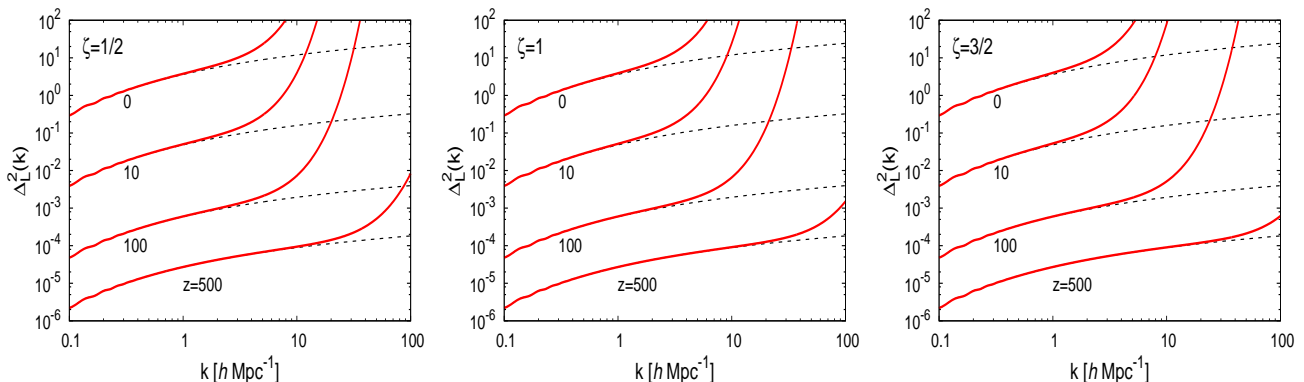


FIG. 4: Logarithmic linear power spectra $\Delta_L^2(k, z)$ at redshifts $z = 0, 10, 100$ and 500 (from top to bottom) at fixed $\zeta = 1/2, 1$ and $3/2$ (respectively left, center and right panel).

a_α , we have $\epsilon_1 \sim \alpha = 10^{-6}$, whereas today we have $\epsilon_1 \sim \alpha^2 = 10^{-12}$.

As shown in the companion paper, the growth of structure is vastly enhanced by the presence of the scalar field when $\epsilon(k, a) \gg 1$ in Eq.(70). Because $\epsilon(k, a)$ grows as k^2 at high k , there exists a time dependent scale $k_\alpha(a)$ such that for any scale smaller than the latter $D_+(k, a)$ deviates significantly from the Λ -CDM one. This threshold $k_\alpha(a)$ can be computed from the condition $\epsilon[k_\alpha(a), a] = 1$ in Eq.(71), to obtain

$$k_\alpha(a) = \frac{aH}{c\sqrt{\epsilon_1}} \sim \frac{H_0}{c\sqrt{\epsilon_1 a}}, \quad (108)$$

where we used $H^2 \propto a^{-3}$ in the matter era. Because ϵ_1 decreases at both high and low redshifts, with a peak at a_α , the threshold $k_\alpha(a)$ is minimum at the scale factor a_α ,

$$k_\alpha^{\min} = k_\alpha(a_\alpha) \sim \frac{H_0}{c a_\alpha^{2/3}} \sim 3h\text{Mpc}^{-1}, \quad (109)$$

Therefore, low wave numbers $k < k_\alpha^{\min}$ are never sensitive to the fifth force whereas high wave numbers $k > k_\alpha^{\min}$ are sensitive to the fifth force around a_α . The range of scale factors $[a_-(k), a_+(k)]$ where a wave number k feels the fifth force broadens at higher k . From Eq.(108) we obtain

$$k > k_{\min} : a_-(k) \sim a_\alpha \left(\frac{k}{k_{\min}} \right)^{-(2\zeta+2)/(4\zeta+1)}, \quad (110)$$

$$a_+(k) \sim a_\alpha \frac{k}{k_{\min}}. \quad (111)$$

In Fig. 3 we show the evolution of the linear growing mode $D_+(k, a)$ obtained numerically solving Eq.(70) at three different scales, for the models considered in this paper. In agreement with the discussion of Eq.(109) above, low wave numbers $k < k_\alpha^{\min}$ are never sensitive to the fifth force and follow the Λ -CDM growth. Higher wave numbers depart from the Λ -CDM behavior around

$a_\alpha \sim 0.01$ and show a faster growth over a limited time range $[a_-, a_+]$, resuming the Λ -CDM growth at later times. This transient speed-up increases with k . This effect becomes stronger at higher ζ because of the higher amplitude of ϵ_1 found in Fig. 2.

The presence of the scalar field leads to a very steep increase of $D_+(k, a)$ at $k \gg 1 h \text{ Mpc}^{-1}$ and so these scales enter the nonlinear regime much earlier than in the Λ -CDM cosmology, at $z \sim z_\alpha$. This can be seen in Fig. 4 where we plot the logarithmic linear power spectrum $\Delta_L^2(k, z) = 4\pi k^3 P_L(k, z)$.

C. Spherical collapse

On large scales where the baryonic pressure is negligible, the particle trajectories $\mathbf{r}(t)$ follow the equation of motion

$$\frac{d^2 \mathbf{r}}{dt^2} - \frac{1}{a} \frac{d^2 a}{dt^2} \mathbf{r} = -\nabla_{\mathbf{r}} (\Psi_N + \Psi_A), \quad (112)$$

where $\mathbf{r} = a\mathbf{x}$ is the physical coordinate, Ψ_N the Newtonian potential and $\Psi_A = c^2 \ln A$ the fifth-force potential. To study the spherical collapse before shell crossing, it is convenient to label each shell by its Lagrangian radius q or enclosed mass M , and to introduce its normalized radius $y(t)$ by

$$y(t) = \frac{r(t)}{a(t)q} \quad \text{with} \quad q = \left(\frac{3M}{4\pi\bar{\rho}_0} \right)^{1/3}, \quad y(t=0) = 1. \quad (113)$$

In particular, the matter density contrast within radius $r(t)$ reads as

$$1 + \delta_{<}(r) = y(t)^{-3}. \quad (114)$$

The equation of motion becomes

$$\frac{d^2 y}{d(\ln a)^2} + \left(2 + \frac{1}{H^2} \frac{dH}{dt} \right) \frac{dy}{d \ln a} + \frac{\Omega_m}{2} y(y^{-3} - 1) = -y \left(\frac{c}{Hr} \right)^2 \frac{d \ln A}{d \ln \rho} \frac{r}{1 + \delta} \frac{\partial \delta}{\partial r}. \quad (115)$$

The fifth force introduces a coupling as it depends on the density profile, through the local density $\rho(r) = \bar{\rho}(1 + \delta(r))$.

In the following, we use the density profile defined by

$$\begin{aligned} \delta(x') &= \frac{\delta_{<}(x)}{\sigma_x^2} \int_V \frac{d\mathbf{x}''}{V} \xi_L(\mathbf{x}', \mathbf{x}'') \\ &= \frac{\delta_{<}(x)}{\sigma_x^2} \int_0^{+\infty} \frac{dk}{k} \Delta_L^2(k) \tilde{W}(kx) \frac{\sin(kx')}{kx'}. \end{aligned} \quad (116)$$

Here $x(t) = a(t)r(t)$ is the comoving radius of the spherical shell of mass M that we are interested in while x' is any radius along the profile; ξ_L and Δ_L^2 are the linear correlation function and logarithmic power spectrum

of the matter density contrast, $\sigma_x^2 = \langle \delta_{L<}(x)^2 \rangle$ its variance within radius x , which defines a sphere of volume V ; and $\tilde{W}(kx) = 3[\sin(kx) - kx \cos(kx)]/(kx)^3$ the Fourier transform of the 3D top hat of radius x . The profile (116) is the typical profile around a density fluctuation at scale x in the initial Gaussian field and provides a convenient ansatz (here we use the initial linear power spectrum or its Λ -CDM amplified value at the redshift of interest).

We show in Fig. 5 the time evolution of the nonlinear density contrast $\delta_{<}(r)$ within a shell of mass M , given by the spherical dynamics (115), for different values of the mass M , fixing the initial linear density contrast so that $\delta_L^{\Lambda\text{-CDM}} = 1.6$ today (the initial condition is set at high redshift before the onset of the fifth force and it is common to all models and the Λ -CDM cosmology; as usual it is convenient to describe this initial condition by its value today using the Λ -CDM linear growth factor). In agreement with what we found by studying the evolution of linear perturbations, we can see that at large masses, $M \gtrsim 10^{12} h^{-1} M_\odot$, the evolution of $\delta_{<}(r)$ closely follows the Λ -CDM one, whereas the collapse of small masses is strongly accelerated around a_α . This faster growth occurs earlier for smaller mass, as $a_-(k)$ decreases on smaller scales.

We show in Fig. 6 the spherical dynamics for a fixed value of the mass $M = 10^8 h^{-1} M_\odot$ and several initial density contrasts. The acceleration of the growth of structure due to the presence of the scalar field makes halos collapse before $a = 1$, even starting from $\delta_L^{\Lambda\text{-CDM}} \simeq 0.1$. In agreement with previous figures, the acceleration of the collapse occurs around a_α . For sufficiently high initial conditions this leads to a collapse at high redshift around z_α . For lower initial conditions the dynamics is still in the linear regime after the fifth force has vanished, at low redshift, but with a higher amplitude than in the Λ -CDM cosmology and a higher final collapse redshift. Again, we can see that the effect of the fifth force increases with ζ .

We show in the upper panel of Fig. 7 the linear density contrast threshold, measured by $\delta_L^{\Lambda\text{-CDM}}$ (i.e., the extrapolation up to $z = 0$ of the linear initial density contrast by the Λ -CDM growth rate), required to reach a nonlinear density contrast $\delta_{<} = 200$ today. In agreement with Figs. 5 and 6, at large mass we recover the Λ -CDM linear density threshold, $\delta_L^{\Lambda\text{-CDM}} \simeq 1.6$, whereas at small mass we obtain a much smaller linear density threshold, $\delta_L^{\Lambda\text{-CDM}} \ll 1$, because of the acceleration of the collapse by the fifth force. Again, at small masses the threshold δ_L becomes smaller for larger exponent ζ as the effect of the fifth force increases.

D. Halo mass function

As for the Λ -CDM cosmology, we write the comoving halo mass function as

$$n(M) \frac{dM}{M} = \frac{\bar{\rho}_0}{M} f(\nu) \frac{d\nu}{\nu}, \quad (117)$$

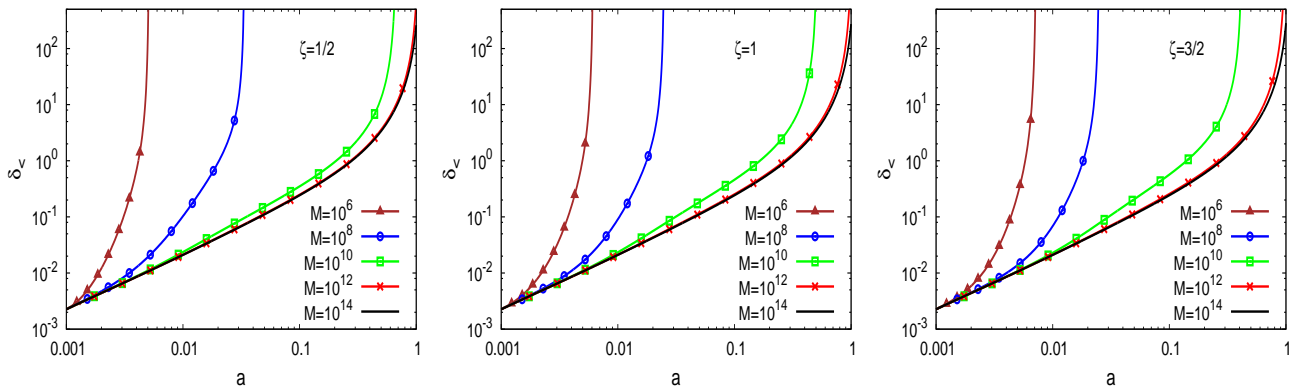


FIG. 5: Time evolution of the nonlinear density contrast $\delta(<r)$ given by the spherical dynamics, as a function of the scale factor, for several masses (in units of $h^{-1}M_{\odot}$) at fixed $\zeta = 1/2, 1, 3/2$ (respectively left, center and right panel). The initial condition corresponds to the same linear density contrast $\delta_L^{\Lambda\text{-CDM}} = 1.6$ today, using the Λ -CDM growth factor.

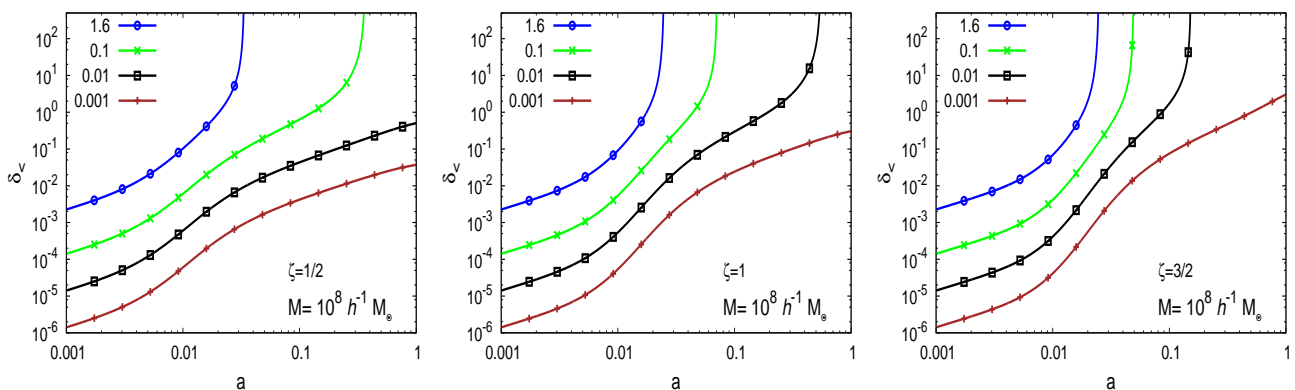


FIG. 6: Time evolution of the nonlinear density contrast $\delta(<r)$ given by the spherical dynamics, as a function of the scale factor, for several values of the initial density contrast and for a mass of $M = 10^8 h^{-1}M_{\odot}$ at fixed $\zeta = 1/2, 1, 3/2$ (respectively left, center and right panel). We show our results for different initial conditions, which correspond to $\delta_L^{\Lambda\text{-CDM}} = 1.6, 0.1, 0.01$ and 0.001 from top to bottom.

where the scaling variable $\nu(M)$ is defined as

$$\nu(M) = \frac{\delta_L^{\Lambda\text{-CDM}}(M)}{\sigma^{\Lambda\text{-CDM}}(M)}, \quad (118)$$

and $\delta_L^{\Lambda\text{-CDM}}(M)$ is again the initial linear density contrast (extrapolated up to $z = 0$ by the Λ -CDM linear growth factor) that is required to build a collapsed halo (which we define here by a nonlinear density contrast of 200 with respect to the mean density of the Universe) and $\sigma^{\Lambda\text{-CDM}}$ its variance. The variable ν measures whether such an initial condition corresponds to a rare and very high overdensity in the initial Gaussian field ($\nu \gg 1$) or to a typical fluctuation ($\nu \lesssim 1$). In the Press-Schechter approach, we have $f(\nu) = \sqrt{2/\pi}\nu e^{-\nu^2/2}$. Here we use the same function as in [28]. Then, the impact of the modified gravity only arises through the linear threshold $\delta_L^{\Lambda\text{-CDM}}(M)$, as we assume the same initial matter den-

sity power spectrum as for the Λ -CDM reference at high redshift.

The threshold $\delta_L^{\Lambda\text{-CDM}}(M)$ was shown in the upper panel of Fig. 7. We show the mass function in the lower panel of Fig. 7. Once again, we can notice that at large mass all the mass functions are close to the Λ -CDM prediction whereas at smaller masses, $M \sim 10^8 - 10^{10} h^{-1}M_{\odot}$, they are higher. This is because the fifth force has no effect on very large scales and accelerates the formation of structures on small scales. At lower mass, $M \lesssim 10^7 h^{-1}M_{\odot}$, the mass function becomes smaller than in the Λ -CDM cosmology, because both mass functions are normalized to unity (the sum over all halos cannot give more matter than the mean matter density).

At large masses, $M > 10^{12} h^{-1}M_{\odot}$, where the formation of large-scale structures remains close to the Λ -CDM

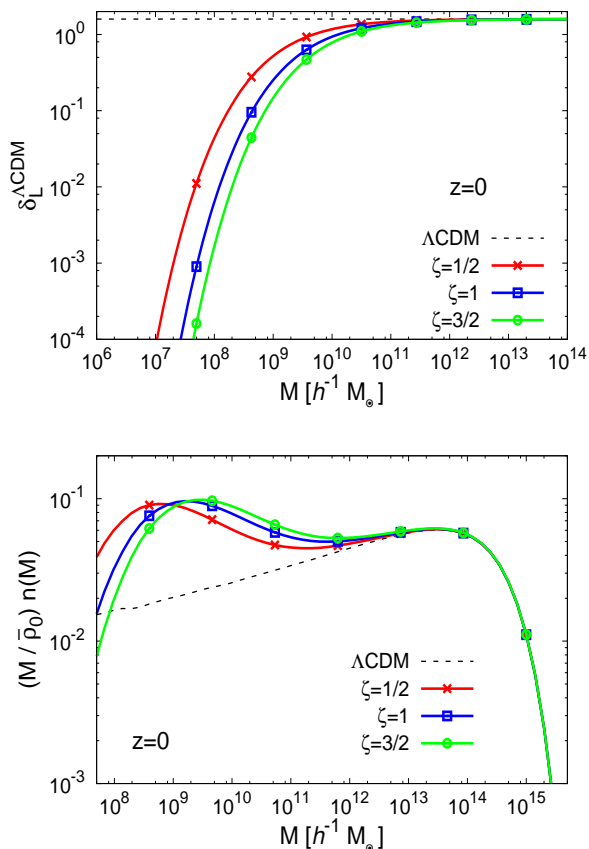


FIG. 7: *Upper panel:* Initial linear density contrast, as measured by $\delta_L^{\Lambda\text{-CDM}}$, that gives rise to a nonlinear density contrast $\delta_{<} = 200$ at $z = 0$, as a function of the halo mass M for fixed $\zeta = 1/2, 1$ and $3/2$. *Lower panel:* Halo mass function at $z = 0$ for fixed $\zeta = 1/2, 1$ and $3/2$, and for the Λ -CDM cosmology.

case, with only a modest acceleration, and the mass function is dominated by the Gaussian tail $\sim e^{-\nu^2/2}$, we can expect that the results obtained are robust, since in this regime the shape of the halo mass function is dominated by the exponential tail $e^{-\nu^2/2}$. At low masses, $M < 10^{12} h^{-1} M_\odot$, where the history of gravitational clustering is significantly different from the Λ -CDM scenario, as a large range of masses have collapsed together before a redshift of 100, and the halo mass function is no longer dominated by its universal Gaussian tail, these results are unlikely to be accurate. Nevertheless, we can still expect the halo mass function to be significantly higher than in the Λ -CDM case for masses $M \sim 10^8 - 10^{11} h^{-1} M_\odot$, although it is difficult to predict the maximum deviation and the transition to a negative deviation at very low masses.

V. ASTROPHYSICAL EFFECTS

A. Screening within spherical halos

1. Radial profiles

We first consider here how the ratio of the fifth force to Newtonian gravity behaves within spherical halos with a mean density profile such as the Navarro-Frenk-White (NFW) [29] density profile. In particular, we wish to find the conditions for the fifth force not to diverge at the center of the halos and to remain modest at all radii, to be consistent with observations of X-ray clusters. Within spherical halos, the Newtonian force reads as

$$F_N = -\frac{\mathcal{G}_N M(<r)}{r^2} = -\frac{\Omega_m}{2} \Delta(<r) r H^2, \quad (119)$$

where $\Delta(<r)$ is the mean overdensity within radius r . The fifth force reads

$$F_A = -c^2 \frac{d \ln A}{dr} = -\frac{c^2}{r} \frac{d \ln A}{d \ln \rho} \frac{d \ln \rho}{d \ln r}. \quad (120)$$

We can also use F_N and F_A to define characteristic velocity scales,

$$F_N = -\frac{v_N^2(r)}{r}, \quad F_A = -\frac{c_s^2(r)}{r}, \quad (121)$$

with

$$v_N^2 = \frac{\mathcal{G}_N M(<r)}{r}, \quad c_s^2 = c^2 \frac{d \ln A}{d \ln r}, \quad (122)$$

where v_N is the Newtonian circular velocity. Therefore, the ratio of the fifth force to the Newtonian force is

$$\eta \equiv \frac{F_A}{F_N} = \frac{c_s^2}{v_N^2} = \frac{2}{\Omega_m \Delta(<r)} \left(\frac{c}{rH}\right)^2 \frac{d \ln A}{d \ln \rho} \frac{d \ln \rho}{d \ln r}. \quad (123)$$

From Eq.(102), we have at moderate densities, $\rho \sim \bar{\rho}(z)$,

$$\rho \ll \rho_\alpha : |\eta| \sim \frac{\alpha^2 \zeta^2}{a^3} \left(\frac{c}{rH}\right)^2. \quad (124)$$

Thus, in the late Universe the ratio η is suppressed by a factor α^2 so that η only reaches unity at $r \sim 3h^{-1} \text{kpc}$, i.e. at galaxy scales (see also Sec. V A 3 below). At higher densities, we obtain from Eq.(101)

$$\rho \gg \rho_\alpha : |\eta| \sim \frac{\alpha^2 \zeta}{a^3} \left(\frac{a^3}{\alpha \zeta \Delta}\right)^{(1+2\zeta)/(1+1\zeta)} \left(\frac{c}{rH}\right)^2. \quad (125)$$

We plot the ratio η for several halo masses, with an NFW density profile in Fig. 8. In agreement with the results obtained in previous sections, we can see that the fifth force is more important for smaller halos, which also correspond to smaller scales. For a power-law density profile, of exponent $\gamma_p > 0$ and critical radius r_α ,

$$\rho(r) = \rho_\alpha \left(\frac{r}{r_\alpha}\right)^{-\gamma_p}, \quad (126)$$

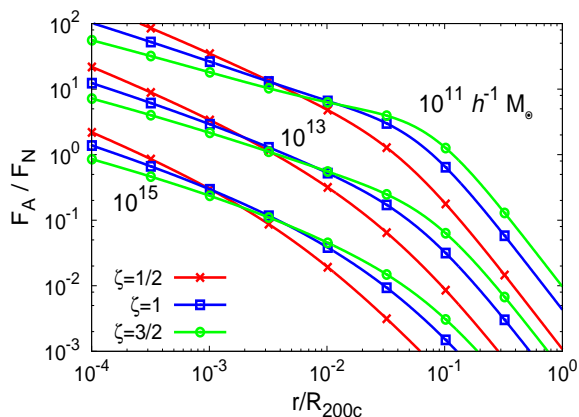


FIG. 8: Ratio $\eta = F_A/F_N$ as a function of the radius r , within spherical halos with an NFW profile. We display the cases of halo masses $M = 10^{11}, 10^{13}$ and $10^{15} h^{-1} M_{\odot}$ from top to bottom, for the ultra-local model exponent $\zeta = 1/2, 1$ and $3/2$.

we have

$$r < r_{\alpha}, \quad \eta \sim r^{\gamma_p(1+2\zeta)/(1+\zeta)-2}. \quad (127)$$

If we consider halos with a mean NFW density profile, which has $\gamma_p = 1$, we find that $\eta \sim r^{-1/(1+\zeta)}$ and the relative importance of the fifth force does not vanish at the center for the models, whatever the value of the exponent ζ , in agreement with Fig. 8. This suggests that these models would lead to significant modifications in the cluster dynamics with respect to the Λ -CDM model and so would be ruled out by the observations, which show a good agreement with the Λ -CDM cosmology. However, as we can see from Fig. 8, for typical cluster masses η only becomes of the order of unity far within the virial radius, $r \lesssim 0.01 R_{200c}$ for $M \gtrsim 10^{13} h^{-1} M_{\odot}$. Because at these scales clusters have significant substructures the approximation of a smooth profile is not any more correct. Then, deeper analyses are needed to unravel the dynamics of clusters of galaxies considering the ultra-local behaviour of the theory. We leave these analysis for future studies when we may need to use numerical simulations and to estimate the observational accuracy of the measured halo profiles. On the other hand, we will perform a thermodynamic analysis of the system in VI where we find that for large enough clusters, the mean density approximation is valid.

2. Clusters of galaxies

We now estimate the fifth force to Newtonian gravity ratio η on a global scale, for clusters and for galaxies. In contrast with the companion paper, we do not need to study the Solar System, the Earth or the labo-

ratory, because within the supersymmetric setting considered in this paper baryons do not couple to the fifth force. Therefore, astrophysical systems which are dominated by baryons do not feel the effect of the fifth force and we automatically recover the General Relativity or Newtonian dynamics in these systems.

We have seen in Eq.(123) that $\eta = c_s^2/v_N^2$, whence $\eta \sim (c/v_N)^2 |d \ln A/d \ln \rho|$ if we take $d \ln \rho/d \ln r \sim 1$. From Eq.(102), we also have at moderate densities below $\rho_{\alpha} \sim 10^6 \bar{\rho}_0$, $d \ln A/d \ln \rho \sim -\alpha^2 \Delta$ at redshift $z = 0$. This gives

$$z = 0 : \quad \eta \sim \left(\frac{\alpha c}{v_N} \right)^2 \Delta. \quad (128)$$

For clusters of galaxies, with $\Delta \sim 10^3$ and $v_N \sim 500$ km/s, this yields

$$\text{clusters: } \eta \sim (10^4 \alpha)^2 \ll 1. \quad (129)$$

Therefore, the fifth force is negligible on cluster scales. However, as seen in Fig. 8, this is no longer the case far inside the cluster, where the characteristic scales are smaller and the density greater, which gives rise to a greater fifth force.

3. Galaxies

We now consider a typical galaxy, such as the Milky Way, with $\Delta \sim 10^6$, which is at the upper limit of the regime $\rho \lesssim \rho_{\alpha}$, and $v_N \sim 200$ km/s. This gives

$$\text{galaxies: } \eta \sim (10^6 \alpha)^2 \sim 1. \quad (130)$$

Thus, the fifth force is of the same order as the Newtonian gravity on galaxy scales. This suggests that interesting phenomena could occur in this regime and that galaxies could provide a useful probe of such models, as we can see from Fig. 8 for low-mass halos $M \lesssim 10^{11} h^{-1} M_{\odot}$.

B. Fifth-force dominated regime

It is useful to reformulate the analysis presented above for clusters and galaxies and to determine the domain of length, density and mass scales where the fifth force is dominant. Taking $d \ln \rho/d \ln r \sim 1$, we write for structures of typical radius R , density ρ and mass $M = 4\pi R^3/3$,

$$|\eta| \sim \frac{2}{\Omega_{m0}} \frac{\bar{\rho}_0}{\rho} \left(\frac{c}{RH_0} \right)^2 \left| \frac{d \ln A}{d \ln \rho} \right|. \quad (131)$$

Then, the fifth force is greater than Newtonian gravity if we have

$$|\eta| \geq 1 : \quad R^2 \leq R_{\eta}^2 \equiv \left(\frac{c}{H_0} \right)^2 \frac{2}{\Omega_{m0}} \frac{\bar{\rho}_0}{\rho} \left| \frac{d \ln A}{d \ln \rho} \right|. \quad (132)$$

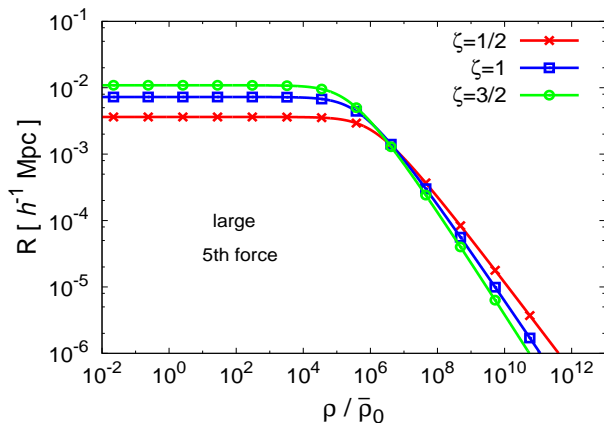


FIG. 9: Domain in the density-radius plane where the fifth force is greater than Newtonian gravity (bottom left area below the curves), for the ultra-local exponents $\zeta = 1/2, 1$ and $3/2$.

At low densities, using Eq.(102) we obtain

$$\rho \ll \rho_\alpha : R_\eta(\rho) \sim R_\alpha \text{ with } R_\alpha \equiv \frac{\alpha \zeta c}{H_0}. \quad (133)$$

Thus, at low densities we obtain a constant radius threshold, of order $R_\alpha \sim 3h^{-1} \text{ kpc}$ for $\alpha = 10^{-6}$, which grows with ζ as we can check in Fig. 9. At high densities, we have the behaviour

$$\rho \gg \rho_\alpha : R_\eta \sim R_\alpha \left(\frac{\rho}{\rho_\alpha} \right)^{-(2\zeta+1)/(2\zeta+2)}. \quad (134)$$

Thus, at high densities the upper boundary of the fifth-force domain decreases and the fifth force becomes negligible in the center of halos with sufficiently steep profiles, as seen in Eq.(127).

To facilitate the comparison with astrophysical structures, it is convenient to display the fifth-force domain (132) in the mass-radius plane (M, R) . This is shown in Fig. 10, as the curve $R_\eta(\rho)$ provides a parametric definition of the boundary $R_\eta(M)$, defining the mass of the structure as $M = 4\pi\rho R^3/3$. We obtain a triangular domain, with a constant-radius upper branch and a lower branch that goes towards small radius and mass with a slope that depends on ζ . The upper branch corresponds to the regime (133), with

$$R_\eta \sim R_\alpha \text{ for } M < M_\alpha, \quad (135)$$

and

$$M_\alpha \equiv \alpha^2 \zeta^3 \bar{\rho}_0 \left(\frac{c}{H_0} \right)^3. \quad (136)$$

For $\alpha = 10^{-6}$ this yields $M_\alpha \sim 10^{10} M_\odot$. The lower branch corresponds to the regime (134), which yields for

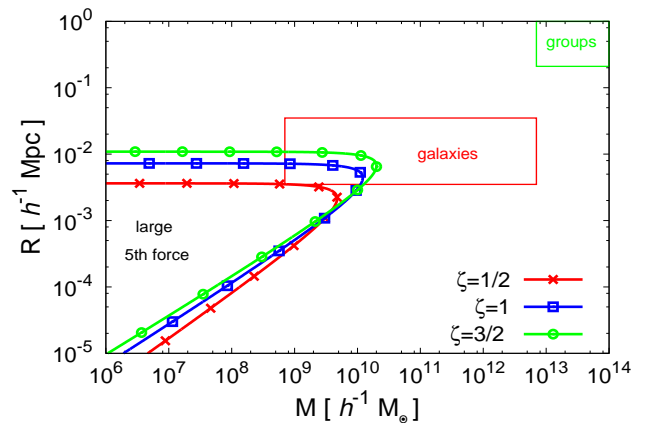


FIG. 10: Domain in the mass-radius plane where the fifth force is greater than Newtonian. The horizontal axis is the typical mass M of the structure and the vertical axis its typical radius R . The rectangles show the typical scales of galaxies and groups of galaxies.

$$M < M_\alpha$$

$$R \sim R_\alpha \left(\frac{M}{M_\alpha} \right)^{(2\zeta+1)/(4\zeta+1)}. \quad (137)$$

We also show in Fig. 10 the regions in this (M, R) -plane occupied by groups and clusters of galaxies and by galaxies. We only show astrophysical objects whose dynamics is due to the presence of dark matter since for this model the coupling of the scalar field with baryons is negligible, as shown in section II G. In agreement with section V A, we find that the fifth force is negligible for clusters and groups (at their global scale), while it is of the same order as Newtonian gravity for galaxies. Therefore galaxies may provide strong constraints on the models considered in this paper.

VI. HISTORY AND PROPERTIES OF THE FORMATION OF COSMOLOGICAL STRUCTURES

To study the evolution of cosmological perturbations in the previous sections, either through linear theory or the spherical collapse, we assumed that the density field remains smooth and that the fifth force on cosmological scale x is set by the density gradient on the same scale. However, the ultra-local fifth force is directly sensitive to the local density gradient, $\nabla \ln A = (d \ln A / d \ln \rho) \nabla \rho$, in contrast with the Newtonian force which involves an average over scale x , $F_N \propto \int d\mathbf{x}' \rho(\mathbf{x}') / |\mathbf{x} - \mathbf{x}'|^2$. Moreover, smaller scales are increasingly unstable because of the k^2 factor in the factor $\epsilon(k, \tau)$ in Eq.(71) that amplifies the gravitational attraction in the linear evolution equation (70). This could invalidate the analysis presented

above as small scales could develop strong instabilities. This would lead to a fragmentation of the system down to very small scales so that the local density gradient, hence the fifth force, is nowhere related to cosmological scale gradients. This would in turn lead to an effective screening mechanism as isolated overdensities no longer interact. Note that this mechanism, due to the ultra-local character of the theory, is the key to the screening of the fifth force in local environments, such as in the Solar System, which is required in the theories studied in the companion paper where both the baryons and the dark matter feel the fifth force. In the supersymmetric setting considered in this paper, we do not need to invoke this mechanism to ensure that the theory is consistent with Solar System tests as the baryons do not feel the fifth force. However, it could still play a role in case it leads to a fragmentation of the dark matter density field at high redshift, when the fifth force is dominant, and makes a “mean field” approach inadequate.

As described in details in the companion paper [14], we can investigate this issue by using a thermodynamic approach, which allows us to go beyond perturbation theory and spherical dynamics. Thus, we assume that at high redshift, when the fifth force is dominant, regions that collapse and turn non-linear because of the fifth-force interaction relax towards the thermodynamic equilibrium. Then, if this equilibrium is strongly inhomogeneous the mean field approach used in the previous sections breaks down, whereas if this equilibrium is homogeneous we can conclude that the system does not develop strong small-scale inhomogeneities and the previous analysis is correct.

A. Cosmological non-linear transition

We first study in this section the evolution with redshift of the comoving cosmological scales $x_{\text{coll}}(z)$ that enter the non-linear regime, which we define by

$$\Delta_L^2(\pi/x_{\text{coll}}, z) = 1.5 \quad (138)$$

where Δ_L^2 is the logarithmic linear power spectrum. (The factor 1.5 is chosen so that we obtain $x_{\text{coll}} \simeq 8h^{-1}\text{Mpc}$ at $z = 0$ in the Λ -CDM scenario.) As seen in the upper panel in Fig. 11, $x_{\text{coll}}(z)$ is much greater than in the Λ -CDM cosmology at high redshift because the fifth force amplifies the growth of structure. After a_α the fifth force fastly decreases, as seen in Fig. 2. This leads to the plateau for $x_{\text{coll}}(z)$ over $a_\alpha \leq a \leq a_{\Lambda\text{-CDM}}$, with $a_\alpha = \alpha^{1/3} \sim 0.01$ associated with the peak of the fifth force and $a_{\Lambda\text{-CDM}} \simeq 0.2$ associated with the convergence to the Λ -CDM prediction for $x_{\text{coll}}(z)$. The reason why $a_\alpha \ll a_{\Lambda\text{-CDM}}$ is that after a_α the fast decrease of the fifth force implies that structure formation due to the fifth force stalls, and we need to wait until $a_{\Lambda\text{-CDM}}$ for Newtonian gravity to take over at the scale $x_{\text{coll}}(z_\alpha)$, because at a_α Newtonian gravity was much weaker than the fifth force at the comoving scale $x_{\text{coll}}(z_\alpha)$. Thus, from the point of view of cosmological structure formation, we have three

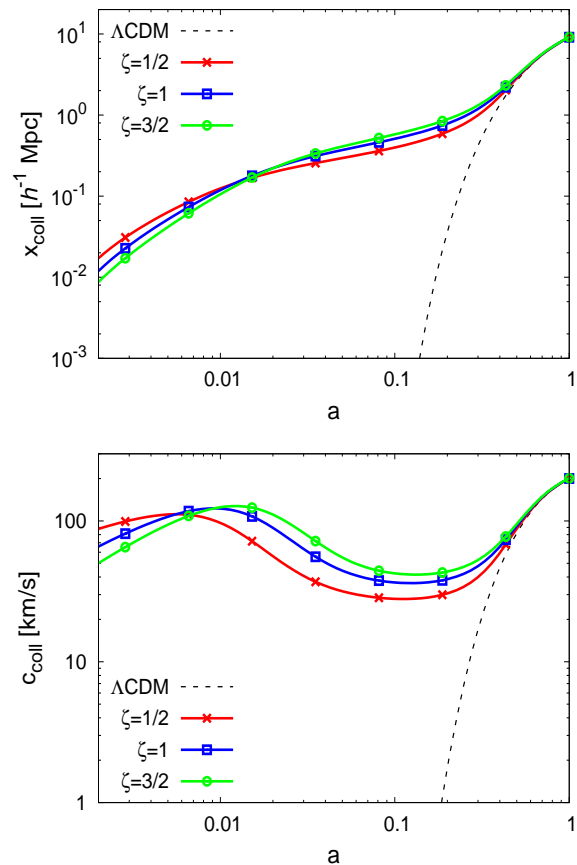


FIG. 11: *Upper panel:* collapse radius $x_{\text{coll}}(z)$ (in comoving coordinates) as a function of the scale factor, for the ultra-local models and the Λ -CDM cosmology. *Lower panel:* collapse velocity scale $c_{\text{coll}}(z)$.

eras. For $a < a_\alpha$, the non-linear transition $x_{\text{coll}}(z)$ of the cosmological density field is due to the fifth force and occurs at scales much greater than in the Λ -CDM scenario. For $a_\alpha < a < a_{\Lambda\text{-CDM}}$, structure formation stalls as the fifth force decreases and Newtonian gravity is still weak on these scales. For $a_{\Lambda\text{-CDM}} < a$, we recover the growth predicted by the Λ -CDM cosmology, due to Newtonian gravity.

For the thermodynamic analysis presented in the next section we also need the initial kinetic energy or typical velocity of the collapsing domains. Thus, we define the effective velocity $c_{\text{coll}}(z)$ by

$$c_{\text{coll}}^2(z) = c_s^2 + c_N^2, \quad (139)$$

with

$$c_s^2 = \epsilon_1 c^2, \quad c_N^2 = (1 + \epsilon_1) \frac{3\Omega_m}{2\pi^2} (H a x_{\text{coll}})^2. \quad (140)$$

The term c_s^2 comes from the pressure-like term $\epsilon_1 c^2 \nabla^2 \delta$ in Eq.(69) while the term c_N^2 comes from the right-hand side

in Eq.(69), associated with Newtonian gravity (amplified by the negligible factor ϵ_1). In the case of the Λ -CDM cosmology we only have $c_{\text{coll}}^{\Lambda\text{-CDM}} = c_{\text{N}}^{\Lambda\text{-CDM}}$ as there is no fifth-force pressure-like term. As seen in the lower panel in Fig. 11, at high redshift, $a < a_{\Lambda\text{-CDM}}$, we have $c_{\text{coll}} \gg c_{\text{coll}}^{\Lambda\text{-CDM}}$, whereas at low redshift, $a_{\Lambda\text{-CDM}} < a$, we have $c_{\text{coll}} \simeq c_{\text{coll}}^{\Lambda\text{-CDM}}$ as we recover the Λ -CDM behavior. Between a_α and $a_{\Lambda\text{-CDM}}$ the velocity scale first decreases until $a_{c_s/c_N} \simeq 0.1$ with the decline of the fifth force, as $c_{\text{coll}} \simeq c_s$, and next grows again with Newtonian gravity as $c_{\text{coll}} \simeq c_N$.

This history singles out a characteristic mass and velocity scale, associated with the plateau found in Fig. 11 over $0.02 \lesssim a \lesssim 0.2$. This yields

$$\begin{aligned} x_* &\sim 0.355 h^{-1} \text{Mpc}, & M_* &\sim 2 \times 10^{10} h^{-1} M_\odot, \\ c_* &\sim 50 \text{ km/s}. \end{aligned} \quad (141)$$

As in Fig. 10, we recover galaxy scales, more precisely here the scales associated with small galaxies. It is tempting to wonder whether this could help alleviate some of the problems encountered on galaxy scales by the standard Λ -CDM scenario. However, this would require detailed numerical studies that are beyond the scope of this paper.

B. Thermodynamic equilibrium on cosmological scales

We can now study the non-linear dynamics of the cosmological scales $x_{\text{coll}}(z)$ that enter the non-linear regime found in Fig. 11. More precisely, we use a thermodynamic approach to investigate whether these regions develop a fragmentation process and show strong small-scale inhomogeneities [30, 31]. Because we are interested in the evolution at high redshift, $z \geq z_\alpha$, when the fifth force is dominant, we neglect the Newtonian gravity and we consider the thermodynamic equilibrium of systems defined by the energy E and entropy S given by

$$E = \int d^3x d^3v f(\mathbf{x}, \mathbf{v}) \left(\frac{v^2}{2} + c^2 \ln A[\rho(\mathbf{x})] \right), \quad (142)$$

$$S = - \int d^3x d^3v f(\mathbf{x}, \mathbf{v}) \ln \frac{f(\mathbf{x}, \mathbf{v})}{f_0}. \quad (143)$$

Here $f(\mathbf{x}, \mathbf{v})$ is the phase-space distribution function, f_0 is an irrelevant normalization constant, and we used the fact that the fifth-force potential $\ln A$ is a function of the local density. Then, assuming that the scales that turn non-linear because of the fifth force at high redshift reach a statistical equilibrium through the rapidly changing effects of the fluctuating potential, in a fashion somewhat similar to the violent relaxation that takes place for gravitational systems [32], we investigate the properties of this thermodynamic equilibrium.

Contrary to the usual gravitational case, the potential $\ln A$ is both bounded and short-ranged, so that we

cannot build infinitely large negative (or positive) potential energies and a stable thermodynamic equilibrium always exists, and it is possible to work with either micro-canonical, canonical or grand-canonical ensembles. In this respect, a thermodynamic analysis is better suited for such systems than for standard 3D gravitational systems, where the potential energy is unbounded from below and stable equilibria do not always exist, and different statistical ensembles are not equivalent [33].

We work in the grand-canonical ensemble, where the dark matter particles are confined in a box of size x (the scale $x_{\text{coll}}(z)$ that is turning non-linear at redshift z), with a mean temperature $T = 1/\beta$ and chemical potential μ that are set by the initial velocity scale $c_{\text{coll}}(z)$ and mean density $\bar{\rho}(z)$. The analysis of the thermodynamic equilibria and phase transitions is described in details in the companion paper [14]. The main result is that at high temperature, $T > T_c$ and $\beta < \beta_c$, the thermodynamic equilibrium is homogeneous, whereas at low temperature, $T < T_c$ and $\beta > \beta_c$, the equilibrium is inhomogeneous. Indeed, at high temperature the system is dominated by its kinetic energy and the potential energy associated with the fifth force (which is bounded) is negligible, so that we recover a perfect gas without interactions, whereas at low temperature the fifth-force potential becomes important and leads to strong inhomogeneities as it corresponds to an attractive force. In terms of the rescaled dimensionless variables θ and $\hat{\beta}$,

$$\theta = \ln \left(\frac{\rho}{\rho_\alpha} \right), \quad \hat{\beta} = \alpha c^2 \beta, \quad (144)$$

this leads to the phase diagram shown in Fig. 12. The equilibrium is inhomogeneous inside the shaded region, which is limited at low $\hat{\beta}$ by the inverse critical temperature $\hat{\beta}_c$, with $\hat{\beta}_c \simeq \{6.85, 5.58, 5.14\}$ for $\zeta = \{1/2, 1, 3/2\}$. The upper and lower limits of the domain are the curves $\theta_+(\hat{\beta})$ and $\theta_-(\hat{\beta})$, which obey the low-temperature asymptotes

$$\hat{\beta} \rightarrow \infty : \quad \theta_+ \sim \frac{1+\zeta}{\zeta} \ln \hat{\beta}, \quad \theta_- \sim -\hat{\beta}. \quad (145)$$

Then, if the average initial temperature and density ($1/\hat{\beta}, \theta$) fall outside the shaded domain the system remains homogeneous. If they fall inside the shaded domain the system becomes inhomogeneous and splits over two domains with density θ_- and θ_+ , with a proportion such that the total mass is conserved. Because of the ultra-local property [i.e. $\ln A$ is a local function through $\rho(\mathbf{x})$], the equilibrium factorizes over space \mathbf{x} so that the two domains at density θ_\pm are not necessarily connected and can take any shape.

The solid curves in Fig. 12 are the cosmological trajectories associated with the scale and velocity $\{x_{\text{coll}}(z), c_{\text{coll}}(z)\}$ displayed in Fig. 11, which correspond to

$$\theta_{\text{coll}}(z) = \ln \left(\frac{\bar{\rho}(z)}{\rho_\alpha} \right), \quad \hat{\beta}_{\text{coll}}(z) = \frac{\alpha c^2}{c_{\text{coll}}^2(z)}. \quad (146)$$

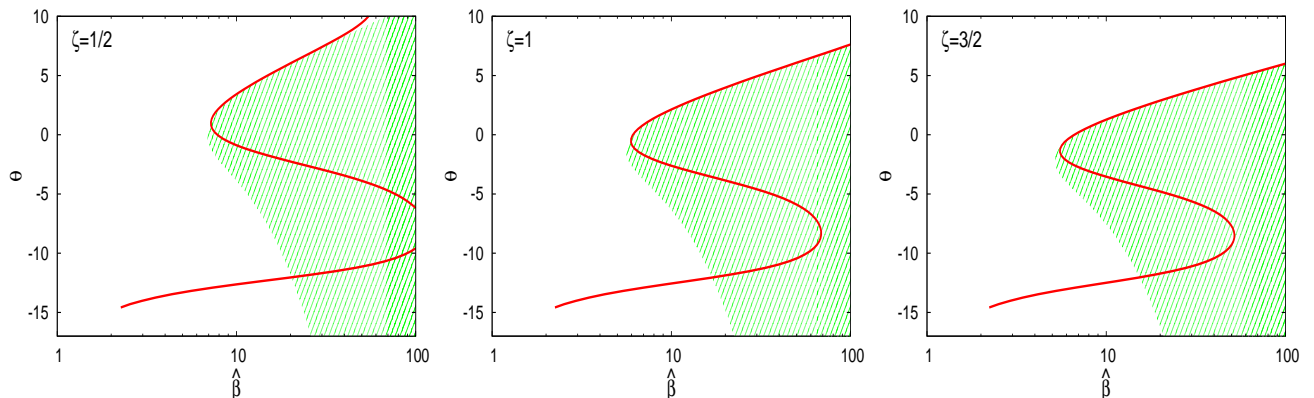


FIG. 12: Thermodynamic phase diagram for the ultra-local models with $\zeta = 1/2, 1$ and $3/2$. The shaded area is the region of initial inverse temperature $\hat{\beta}$ and density θ where the thermodynamic equilibrium is inhomogeneous. The solid line is the cosmological trajectory $(\hat{\beta}_{\text{coll}}(z), \theta_{\text{coll}}(z))$.

This trajectory moves downward to lower densities with cosmic time, following $\bar{\rho}(z)$. In agreement with the lower panel of Fig. 11, the inverse temperature $\hat{\beta}_{\text{coll}}$ first decreases until a_α , as the velocity $c_{\text{coll}}(z)$ grows. Next, $\hat{\beta}_{\text{coll}}$ increases while $c_{\text{coll}}(z)$ decreases along with the fifth force, until we recover the Λ – CDM behavior at late times and $\hat{\beta}_{\text{coll}}$ decreases again thereafter. We are interested in the first era, $a < a_\alpha$, and we find that the cosmological trajectory is almost indistinguishable from the upper boundary $\theta_+(\hat{\beta})$ of the inhomogeneous thermodynamic phase. Indeed, at early times we have $c_{\text{coll}} \simeq c_s$, hence $\hat{\beta}_{\text{coll}} \simeq \alpha/\epsilon_1$ from Eq.(140). Using Eq.(104) we have at high densities, which also correspond to $a < a_\alpha$, $\epsilon_1 \sim \alpha(\rho/\rho_\alpha)^{-\zeta/(1+\zeta)} = \alpha e^{-\zeta\theta/(1+\zeta)}$, hence

$$a \ll a_\alpha : \quad \theta_{\text{coll}} \sim \frac{1+\zeta}{\zeta} \ln \hat{\beta}_{\text{coll}}, \quad (147)$$

and we recover the asymptote (145) of $\theta_+(\hat{\beta})$.

If $\theta_{\text{coll}} > \theta_+$ we are in the homogeneous phase and the system remains at the initial density $\bar{\rho}$. If $\theta_{\text{coll}} \lesssim \theta_+$ we are in the inhomogeneous phase and the system splits over regions of densities θ_+ and θ_- . However, as we remain close to θ_+ most of the volume is at the density $\theta_+ \simeq \theta_{\text{coll}}$ and only a small fraction of the volume is at the low density θ_- . Neglecting these small regions, we can consider that in both cases the system remains approximately homogeneous. This means that, according to this thermodynamic analysis, the cosmological density field does not develop strong inhomogeneities that are set by the cutoff scale of the theory when it enters the fifth-force non-linear regime. Therefore, density gradients remain set by the large-scale cosmological density gradients and the analysis of the linear growing modes and of the spherical collapse presented in previous sections are valid. On small non-linear scales and at late times, where Newtonian gravity becomes dominant, we recover the usual gravitational instability that we neglected in this analy-

sis and structure formation proceeds as in the standard Λ -CDM case.

C. Halo centers

It is interesting to apply the thermodynamic analysis presented above to the inner radii of clusters and galaxies. Indeed, we have seen in section V A 1 that the fifth force becomes large inside spherical halos and the ratio F_A/F_N actually diverges at the center for shallow density profiles, see Fig. 8 and Eq.(127). However, this analysis was based on dimensional and scaling arguments and it fails if the density field becomes strongly inhomogeneous so that the typical density inside the halo is very different from the global averaged density. The thermodynamic analysis used to derive the phase space diagram shown in Fig. 12 neglected Newtonian gravity. However, we can also apply its conclusions to a regime dominated by Newtonian gravity where at radius r inside the halo the structures built by gravity and the density gradients are on scale r . Then, we can ask whether at this radius r fifth-force effects may lead to a fragmentation of the system on much smaller scales $\ell \ll r$. To study this small-scale behavior we can neglect the larger-scale gravitational gradients r and discard gravitational forces.

Within a radius r inside the halo the averaged reduced density and inverse temperature are

$$\theta_r = \ln \left(\frac{\rho_{<(r)}}{\rho_\alpha} \right), \quad \hat{\beta}_r = \frac{\alpha c^2}{\text{Max}(c_s^2, v_N^2)}, \quad (148)$$

where v_N is the Newtonian circular velocity and c_s is the fifth-force velocity scale defined in Eq.(122). As seen in Eq.(123), the maximum $\text{Max}(c_s^2, v_N^2)$ shifts from one velocity scale to the other when the associated force becomes dominant. Here we choose the non-analytic interpolation $\text{Max}(c_s^2, v_N^2)$ instead of the smooth interpolation

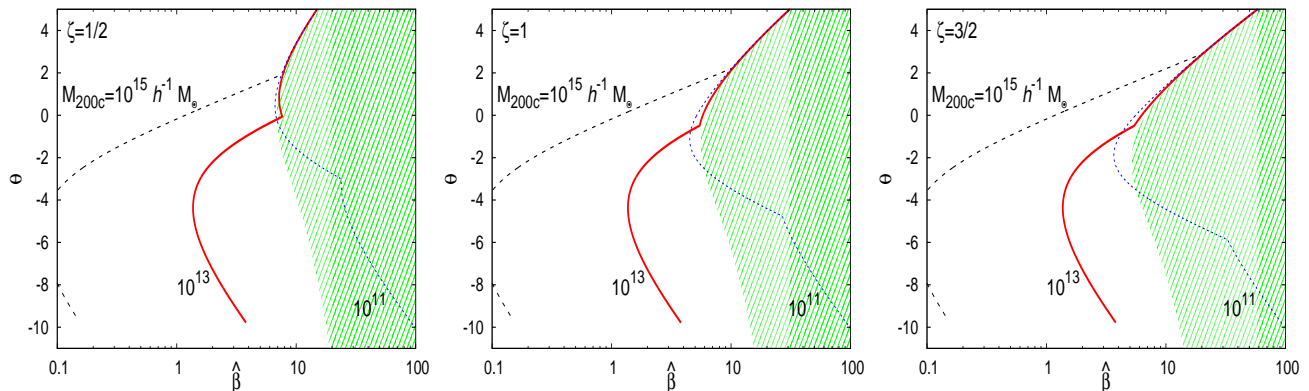


FIG. 13: Radial trajectory $(\hat{\beta}_r, \theta_r)$ over the thermodynamic phase diagram inside NFW halos of mass $M = 10^{15}, 10^{13}$ and $10^{11} h^{-1} M_\odot$. at $z = 0$.

$c_s^2 + v_N^2$ that we used in Eq.(139) for the cosmological analysis for illustrative convenience. Indeed, the discontinuous changes of slope in Fig. 13 show at once the location of the transitions $|\eta| = 1$ between the fifth-force and Newtonian gravity regimes.

When the density grows at small radii as a power law, $\rho \propto r^{-\gamma_p}$, we have seen in Eq.(127) that the fifth-force to gravity ratio η behaves as $\eta \sim r^{\gamma_p(1+2\zeta)/(1+\zeta)-2}$ with

$$v_N^2 \sim r^{2-\gamma_p}, \quad c_s^2 \sim r^{\gamma_p \zeta / (1+\zeta)}, \quad (149)$$

at high density $\rho \gg \rho_\alpha$, where we used Eq.(101). This gives in the Newtonian gravity and fifth-force regimes

$$|\eta| < 1: \quad \theta_r \sim \frac{\gamma_p}{2 - \gamma_p} \ln \hat{\beta}_r, \quad (150)$$

$$|\eta| > 1: \quad \theta_r \sim \frac{1 + \zeta}{\zeta} \ln \hat{\beta}_r. \quad (151)$$

For $\gamma_p > 2$ we are in the Newtonian regime $v_N^2 \rightarrow \infty$, $\hat{\beta}_r \rightarrow 0$, so that we are in the homogeneous phase of the thermodynamic phase diagram as $\hat{\beta}_r < \hat{\beta}_c$. For $(2 + 2\zeta)/(1 + 2\zeta) < \gamma_p < 2$ Newtonian gravity still dominates at small radii and we have the asymptote (150) with $\gamma_p/(2 - \gamma_p) > (1 + \zeta)/\zeta$, so that the radial trajectory $(\hat{\beta}_r, \theta_r)$ moves farther above from the upper bound θ_+ of Eq.(145) of the inhomogeneous phase and small radii are within the homogeneous phase. For $\gamma_p < (2 + 2\zeta)/(1 + 2\zeta)$ we are in the fifth-force regime and we obtain $\theta_r \sim \theta_+$, so that the radial trajectory $(\hat{\beta}_r, \theta_r)$ follows the upper boundary of the inhomogeneous phase domain. This means that the dimensional analysis of section V A 1 is valid as the fifth force does not push towards a fragmentation of the system down to very small scales.

These asymptotic results apply to the small-radius limit $r \rightarrow 0$. In Fig. 13 we show the full radial trajectories $(\hat{\beta}_r, \theta_r)$ over the thermodynamic phase diagram, from R_{200c} inward, for the NFW halos that were displayed in

Fig. 8 at $z = 0$. As we move inside the halo, towards smaller radii r , the density θ_r grows and the trajectory moves upward in the figure. The turn-around of $\hat{\beta}_r$ at $\theta_r \simeq -4$ corresponds to the NFW radius r_s where the local slope of the density goes through $\gamma = 2$ and the circular velocity is maximum. At smaller radii, $r \ll r_s$, the NFW profile goes to $\rho \propto r^{-1}$, hence $\gamma_p = 1$. In agreement with the asymptotic analysis above, this implies that we move farther into the fifth-force regime and we follow the upper boundary θ_+ of the inhomogeneous phase domain, so that the dimensional analysis of section V A 1 is valid. This also leads to an increasingly dominant fifth force at small radii and characteristic velocities that are higher than the Newtonian circular velocity. This may rule out these ultra-local scenarios. However, on small scales the baryonic component is non-negligible and it actually dominates on kpc scales inside galaxies. Since the baryons do not feel the fifth force this could keep these models consistent with observations. On the other hand, for low-mass halos, $M \lesssim 10^{11} h^{-1} M_\odot$ at $z = 0$, we find that a significant part of the halo is within the inhomogeneous thermodynamic phase. This may leave some signature as a possible fragmentation of the system on these intermediate scales into higher-density structures. This process would next lead to a screening of the fifth force, because of the ultra-local character of the fifth force. Indeed, because it is set by the local density gradients, the fragmentation of the system leads to a disappearance of large-scale collective effects and the fifth force behaves like a surface tension at the boundaries of different domains. Such a process may also happen in the case of massive halos at earlier stages of their formation, which could effectively screen the fifth force whereas the simple static analysis leads to a dominant fifth force at small radii. However, a more precise analysis to follow such evolutionary tracks and check the final outcomes of the systems requires numerical studies that are beyond the scope of this paper.

VII. DEPENDENCE ON THE α PARAMETER

In this section we investigate how the results obtained in the previous sections change when we vary the parameter α . As a matter of example, we consider the model with $\zeta = 1$ and we show our results in Fig. 14, where we compare the case $\alpha = 10^{-6}$ considered in the previous sections with the two cases $\alpha = 10^{-7}$ and $\alpha = 10^{-8}$.

In agreement with the discussion in section IV B, as α decreases the maximum amplitude of ϵ_1 decreases as $\epsilon_1(a_\alpha) \sim \alpha$ while the associated scale factor decreases as $a_\alpha \sim \alpha^{1/3}$. This implies that the effect of the fifth force is shifted to higher redshift with a lower amplitude, whence a smaller impact of the scalar field on the matter power spectrum, $P(k, z)$, and on the halo mass function, as we can check in the upper right and lower left panels in Fig. 14. The area in the (M, R) plane where the fifth force is greater than Newtonian gravity also shrinks as α decreases, as we can see in the lower right panel. This is because $R_\alpha \propto \alpha$, which moves the upper branch down towards small radii, whereas the lower branch slowly moves upward because at fixed mass we have $R(M) \sim \alpha^{-1/(4\zeta+1)}$. Therefore, galaxies are no longer sensitive to the modification of gravity if $\alpha \lesssim 5 \times 10^{-7}$.

VIII. CONCLUSION

We have considered in this paper supersymmetric chameleon models with a very large mass, $1/m_{\text{eff}} \ll 10^{-4}\text{mm}$, and coupling $\beta \gg 1$. This makes the range of the fifth force very small and leads to an equivalence between these supersymmetric chameleon models and the ultra-local models studied in a companion paper, for cosmological scales with $H \ll k/a \ll m_{\text{eff}}$. The background remains very close to the Λ -CDM cosmology in both sets of models. However, in contrast with the more general ultra-local models, in this supersymmetric context only the dark matter is sensitive to the fifth force. Therefore, although the ultra-local character of the models gives rise to an automatic screening mechanism that ensures that we satisfy Solar System tests of gravity in that more general framework, in the context studied in this paper this mechanism is not so critical as baryons, which dominate on small scales and in the Solar System, never feel the fifth force (except through its effects on the dark matter Newtonian potential) and follow General Relativity.

We have first described how to build such chameleon models in this supersymmetric context. This involves several characteristic functions that enter the Kähler potential K , which governs the kinetic terms of the model, the superpotential W responsible for the interactions between the fields, and the coupling between the dark matter and the dark energy. This also introduces several energy scales that may be different. We have shown in details how these models are equivalent to ultra-local models for cosmological purposes. This leads to a great

simplification as the latter involve a single free function, $\ln A(\tilde{\chi})$. As in most dark energy and modified gravity models, we also need to introduce a cosmological constant and the associated energy scale. In addition, we need a small parameter $\alpha \lesssim 10^{-6}$, which however appears as a ratio of several energy scales. This provides a natural setting to explain why this quantity can be significantly different from unity.

Next, we have used the ultra-local models identification to study the cosmological properties of these scenarios. We have considered both the background dynamics and the evolution of linear perturbations. Whereas the background remains very close to the Λ -CDM evolution, within an accuracy of 10^{-6} , the growth of cosmological structures is significantly amplified on scales below $1h^{-1}\text{Mpc}$. This fifth-force effect shows a fast increase at high k as it corresponds to a pressure-like term in the linearized equations of motion. Another property that is peculiar to these models, as opposed to most dark energy or modified gravity models, is that the fifth force is the greatest at a high redshift $z_\alpha \sim \alpha^{-1/3} \sim 100$ and for galaxies (among cosmological structures).

We have also considered the modifications to the spherical collapse of cosmological structures. The faster growth of structures at $z \sim z_\alpha$ leads to an acceleration of the collapse at these early times and to a lower linear density threshold $\delta_L^{\Lambda\text{-CDM}}$ required to reach a non-linear density contrast of 200 today, especially on smaller scales where the fifth force is greater. This leads to a higher halo mass function at intermediate masses, $10^8 \lesssim M < 10^{14}h^{-1}M_\odot$, as compared with the Λ -CDM cosmology. Next, we have considered the behavior of the fifth force inside spherical halos. We find that the fifth force increasingly dominates at smaller radii in halos with a shallow density profile, $\gamma_p \lesssim 1$, as for NFW profiles. On the other hand, the fifth force is negligible on cluster scales and of the same order as Newtonian gravity on galaxy scales. This suggests that galaxies could be the best probes of such models.

To investigate the non-linear fifth force regime, and to check that the previous cosmological analysis is not violated by small-scale non-linear effects, we have used the thermodynamic analysis developed in the companion paper. Again, we find that for these supersymmetric chameleon models the cosmological scales that turn non-linear at high redshift because of the fifth force are at the boundary of the inhomogeneous domain in the thermodynamic phase diagram. This suggests that they do not develop strong small-scale inhomogeneities and that the standard mean field cosmological analysis is valid. The same behavior is found at small radii in spherical halos, which again suggests that the spherically averaged analysis applies. However, for low-mass halos, $M \lesssim 10^{11}h^{-1}M_\odot$ at $z = 0$, intermediate radii fall within the inhomogeneous phase. This could lead to some fragmentation of the system with the formation of intermediate mass clumps. On the other hand, this same process leads to a self-screening of the fifth force as isolated

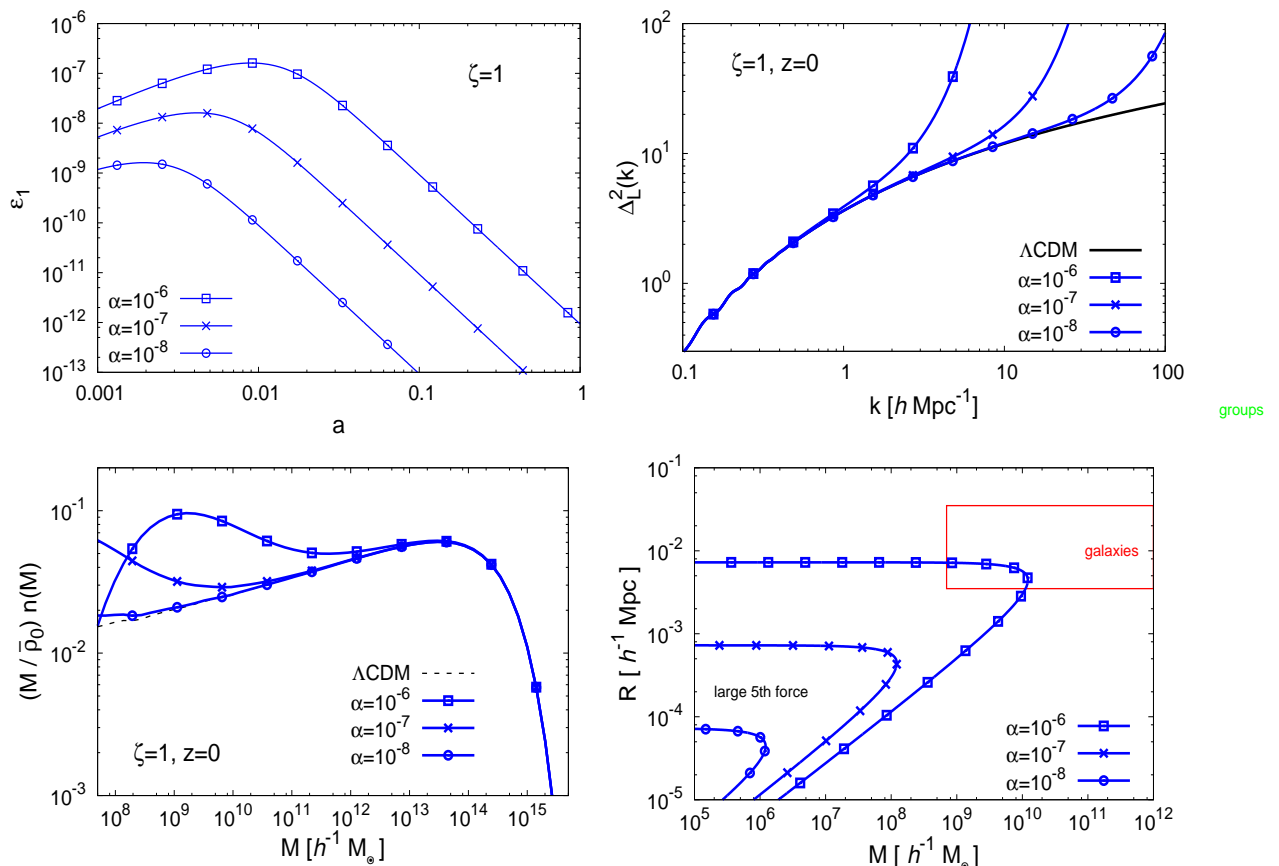


FIG. 14: Dependence on the parameter α of the deviations from the Λ -CDM predictions. We plot models with $\zeta = 1$ and $\alpha = 10^{-6}$, 10^{-7} and 10^{-8} . *Upper left panel:* $\epsilon_1(a)$ as a function of the scale factor, as in Fig. 2. *Upper right panel:* logarithmic linear power spectrum $\Delta_L^2(k, z)$ at redshift $z = 0$, as in Fig. 4. *Lower left panel:* halo mass function as in the lower panel of Fig. 7. *Lower right panel:* domain in the mass-radius plane where the fifth force is greater than Newtonian gravity, as in Fig. 10.

clumps no longer interact through the fifth force because of its ultra-local character. Finally, we have considered the dependence of our results on the value of the parameter α . We find that for $\alpha \ll 10^{-7}$ the deviations from the Λ -CDM cosmology are likely to be negligible (contrary to the models studied in the companion paper) because they have a lower amplitude and are pushed to lower scales where baryons are dominant.

Thus, we find that although such models follow the Λ -CDM behavior at the background level they display a non-standard behavior for the dark matter perturbations on small scales, below $1h^{-1}\text{Mpc}$. At the level of the preliminary analysis presented in this paper they appear to remain globally consistent with observational constraints. However, the effects of the fifth force deep inside halos, on kpc scales, may provide strong constraints and rule out this models. In particular, the thermodynamic anal-

ysis presented in this paper may not be sufficient as the systems may not reach this equilibrium because of incomplete relaxation. To go beyond the analytic approaches used in this paper and to make an accurate comparison with data on galaxy scales requires numerical simulations, which we leave to future work.

Acknowledgments

This work is supported in part by the French Agence Nationale de la Recherche under Grant ANR-12-BS05-0002. This project has received funding from the European Unions Horizon 2020 research and innovation programme under the Marie Skłodowska-Curie grant agreement No 690575.

-
- [1] A. G. Riess et al. (Supernova Search Team), *Astron.J.* **116**, 1009 (1998), astro-ph/9805201.
- [2] S. Perlmutter et al. (Supernova Cosmology Project), *Bull.Am.Astron.Soc.* **29**, 1351 (1997), astro-ph/9812473.
- [3] E. J. Copeland, M. Sami, and S. Tsujikawa, *Int.J.Mod.Phys.* **D15**, 1753 (2006), hep-th/0603057.
- [4] A. Joyce, B. Jain, J. Khoury, and M. Trodden, *Phys. Rept.* **568**, 1 (2015), 1407.0059.
- [5] W. Hu and I. Sawicki, *Phys. Rev.* **D76**, 064004 (2007), 0705.1158.
- [6] A. Nicolis, R. Rattazzi, and E. Trincherini, *Phys.Rev.* **D79**, 064036 (2009), 0811.2197.
- [7] G. W. Horndeski, *Int.J.Theor.Phys.* **10**, 363 (1974).
- [8] J. D. Bekenstein, *Phys. Rev.* **D48**, 3641 (1993), gr-qc/9211017.
- [9] J. Khoury and A. Weltman, *Phys. Rev.* **D69**, 044026 (2004), astro-ph/0309411.
- [10] T. Damour and A. M. Polyakov, *Nucl. Phys.* **B423**, 532 (1994), hep-th/9401069.
- [11] E. Babichev, C. Deffayet, and R. Ziour, *Int.J.Mod.Phys.* **D18**, 2147 (2009), 0905.2943.
- [12] P. Brax and P. Valageas, *Phys. Rev. D* **90**, 023507 (2014), 1403.5420.
- [13] A. Vainshtein, *Phys.Lett.* **B39**, 393 (1972).
- [14] P. Brax, L. A. Rizzo, and P. Valageas (2016), 1605.02938.
- [15] P. Brax, *Phys.Lett.* **B712**, 155 (2012), 1202.0740.
- [16] C. de Rham and R. H. Ribeiro, *JCAP* **1411**, 016 (2014), 1405.5213.
- [17] P. Brax and J. Martin, *Phys. Lett.* **B468**, 40 (1999), astro-ph/9905040.
- [18] P. Brax, C. van de Bruck, J. Martin, and A.-C. Davis, *JCAP* **0909**, 032 (2009), 0904.3471.
- [19] P. Brax, A.-C. Davis, and J. Sakstein, *JCAP* **1310**, 007 (2013), 1302.3080.
- [20] P. Brax, A.-C. Davis, and J. Sakstein, *Phys. Lett.* **B719**, 210 (2013), 1212.4392.
- [21] S. M. Carroll, I. Sawicki, A. Silvestri, and M. Trodden, *New J. Phys.* **8**, 323 (2006), astro-ph/0607458.
- [22] P. Binetruy, *Supersymmetry: Theory, experiment and cosmology* (2006).
- [23] B. Ratra and P. J. E. Peebles, *Phys. Rev.* **D37**, 3406 (1988).
- [24] P. Fayet, *Phys. Lett.* **B175**, 471 (1986).
- [25] P. Brax, C. van de Bruck, A.-C. Davis, J. Khoury, and A. Weltman, *Phys. Rev.* **D70**, 123518 (2004), astro-ph/0408415.
- [26] P. Brax, C. van de Bruck, A.-C. Davis, and A. M. Green, *Phys.Lett.* **B633**, 441 (2006), astro-ph/0509878.
- [27] P. Brax, A.-C. Davis, B. Li, and H. A. Winther (2012), 1203.4812.
- [28] W. H. Press and P. Schechter, *Astrophys. J.* **187**, 425 (1974).
- [29] J. F. Navarro, C. S. Frenk, and S. D. M. White, *Astrophys. J.* **462**, 563 (1996), astro-ph/9508025.
- [30] P. H. Chavanis, J. Vatteville, and F. Bouchet, *European Physical Journal B* **46**, 61 (2005), arXiv:cond-mat/0408117.
- [31] R. Balian, *From Microphysics to Macrophysics*, Theoretical and Mathematical Physics (Springer-Verlag, Berlin, Germany, 2007), ISBN 978-3-540-45469-4, URL <http://www.springer.com/fr/book/9783540454694>.
- [32] D. Lynden-Bell, *Mon. Not. R. Astr. Soc.* **136**, 101 (1967).
- [33] T. Padmanabhan, *Phys. Rep.* **188**, 285 (1990).
- [34] Although the vacuum energy due to V_D lifts the vanishing energy density of a true supersymmetric minimum and therefore supersymmetry is broken by ξ , we will still refer to φ_{\min} as the supersymmetric minimum as it minimises V_F .

Article D

Testing Modified Gravity with Cosmic Shear

Testing Modified Gravity with Cosmic Shear

J. Harnois-Déraps¹, D. Munshi², P. Valageas^{3,4}, L. van Waerbeke¹, P. Brax^{3,4}, P. Coles²,
L. Rizzo^{3,4}

¹Department of Physics and Astronomy, University of British Columbia, 6224 Agricultural Road, Vancouver, B.C., V6T 1Z1, Canada

²Astronomy Centre, School of Mathematical and Physical Sciences, University of Sussex, Brighton BN1 9QH, United Kingdom

³CEA, IPhT, F-91191, Gif-sur-Yvette, Cedex, France

⁴CNRS, URA, 2306, F-91191, Gif-sur-Yvette, Cedex, France

23 June 2015

ABSTRACT

We use the cosmic shear data from the Canada-France-Hawaii Telescope Lensing Survey to place constraints on $f(R)$ and *Generalized Dilaton* models of modified gravity. This is highly complementary to other probes since the constraints mainly come from the non-linear scales: maximal deviations with respects to the General-Relativity + Λ CDM scenario occurs at $k \sim 1h\text{Mpc}^{-1}$. At these scales, it becomes necessary to account for known degeneracies with baryon feedback and massive neutrinos, hence we place constraints jointly on these three physical effects. To achieve this, we formulate these modified gravity theories within a common tomographic parameterization, we compute their impact on the clustering properties relative to a GR universe, and propagate the observed modifications into the weak lensing ξ_{\pm} quantity. Confronted against the cosmic shear data, we reject the $f(R)$ $\{|f_{R_0}| = 10^{-4}, n = 1\}$ model with more than 99.9% confidence interval (CI) when assuming a Λ CDM dark matter only model. In the presence of baryonic feedback processes and massive neutrinos with total mass up to 0.2eV, the model is disfavoured with at least 94% CI in all different combinations studied. Constraints on the $\{|f_{R_0}| = 10^{-4}, n = 2\}$ model are weaker, but nevertheless disfavoured with at least 89% CI. We identify several specific combinations of neutrino mass, baryon feedback and $f(R)$ or Dilaton gravity models that are excluded by the current cosmic shear data. Notably, universes with three massless neutrinos and no baryon feedback are strongly disfavoured in all modified gravity scenarios studied. These results indicate that competitive constraints may be achieved with future cosmic shear data.

Key words: : Cosmology– Modified Gravity Theories – Methods: analytical, statistical, numerical

1 INTRODUCTION

Explaining the late-time acceleration of the Universe first reported in Riess et al. (1998); Perlmutter et al. (1999) represents a major challenge in modern cosmology, and current interpretations mostly rely on the inclusion of dark energy components and/or modifications to the theory of General Relativity (GR). One important difficulty encountered in solving this puzzle relates to the fact that, by construction, the background dynamics in viable dark energy and modified gravity models are almost indistinguishable (Bertschinger 2006; Song, Hu & Sawicki 2007; Brax et al. 2008). These two frameworks only really decouple when considering the evolution of matter density fluctuations and of perturbations associated with the metric. In addition, there are various ways in which a modification of gravity on large scales could account for the apparent acceleration (Clifton et al. 2013; Joyce et al. 2014). Exploiting this, many observational probes based on large scale structure formation have been proposed to test theories of modified gravity, including galaxy clustering (Pogosian & Silvestri 2008; Oyazu, Lima & Hu 2008), integrated Sachs-Wolfe effect in the cosmic microwave background (CMB) anisotropies and its

cross-correlation with galaxy density (Song, Peiris, Hu 2007), cluster abundance (Jain & Zhang 2008; Lombriser et al. 2010), peculiar velocities (Li et al. 2000; Johnson et al. 2014, 2015), redshift-space distortions from spectroscopic surveys (Guzzo et al. 2008; Jennings et al. 2012; Asaba et al. 2013), 21cm observations (Hall et al. 2013) and weak gravitation lensing (Heavens, Kitching & Verde 2007; Schimd 2008; Tsujikawa & Tatekawa 2008; Simpson et al. 2013; Wilcox et al. 2015).

In this paper we investigate the extent to which current weak lensing surveys can constrain departures from GR. In particular, we study the signatures of two specific classes of parametrized modified gravity theories, the $f(R)$ and the generalized Dilaton models, on the cosmic shear measurement extracted from the CFHTLenS (Erben et al. 2013). These models are known to cause an enhancement of structure formation over scales in the range $[0.2 - 20] \text{Mpc}h^{-1}$, an effect which could be detectable with current lensing surveys. In addition, the departure of these models from General Relativity is maximal at scales of $k \sim 1h^{-1}\text{Mpc}$, which are difficult to interpret with other clustering data due to the large uncertainty in the galaxy bias. This

makes the weak lensing approach special, probing modified gravity models at the scale of influence of the ‘fifth’ force.

In its approach, this paper is an extension of Harnois-Déraps, van Waerbeke, Viola & Heymans (2015, hereafter HWVH), where the same data was used to place joint constraints on baryon feedback models and on the sum of neutrino mass. The general idea can be understood as follows: on the one hand, the accuracy achieved by modern CMB experiments (Hinshaw et al. 2013; Planck Collaboration 2015) on most Λ CDM parameters is at the percent level; on the other hand, the modified gravity effects we are looking for affect the baseline signal by up to 20 percent at small scales. It is therefore justified to assume a fixed cosmology and search for possible deviations. Any residual uncertainty in the cosmology can thereafter be treated as systematic uncertainty in the analysis. While next generation weak lensing experiments such as RCSLenS¹, DES², KiDS³, Euclid⁴ and LSST⁵ will have enough statistical power to repeat this analysis in a full MCMC pipeline, we demonstrate here that we can find interesting results with simpler tools and existing data.

This paper is organized as follows: In §2 we review the theoretical formulation of structure formation in $f(R)$ and Dilaton gravity theories; §3 describes the theoretical and numerical modelling of the weak lensing signal, and details our cosmic shear measurement from the CFHTLenS data. In §4 we present and discuss our results, and conclude in §5. The baseline cosmological parameters that are used throughout our study correspond to the WMAP9 + BAO + SN Λ CDM cosmology: $h = 0.6898$, $\Omega_m = 0.2905$, $\Omega_\Lambda = 0.7095$, $\Omega_K = 0$, $w = -1$, $\sigma_8 = 0.831$ and $n_s = 0.969$. The reason why we did not opt for the *Planck* cosmology is to minimize the effect of the known cosmological tension in our model rejection strategy. Otherwise this would involve a full MCMC calculation including all cosmological parameters and both data sets as in MacCrann et al. (2014), which is not necessary in our approach. In the end however, we do marginalize over this cosmological discrepancy.

2 MODIFIED GRAVITY THEORIES

Modified theories of gravity can be distinguished by their screening properties in dense environments. Indeed, given the strong Solar System constraints, these theories need to have a built-in screening mechanism, suppressing the deviations from GR. Three types of such mechanisms have emerged in the last few years: the *Chameleon*, *K-mouflage* and *Vainshtein* models (see Brax & Valageas 2014, for a comparison between these different screening mechanisms). On the one hand, K-mouflage and Vainshtein models involve non-linear kinetic terms describing additional scalar fields whose presence modifies GR predictions. On the other hand, modifications of the Chameleon type can be broadly categorized as either containing additional couplings between the metric and new scalar fields, or involving extra geometric terms. These two equivalent descriptions can be captured by the *tomographic* parameterization, which will be used throughout this paper (Brax, Davis & Li 2012; Brax, Davis, Li & Winther 2012).

In all Chameleon cases, modifications of gravity induce a global enhancement of the effective force of gravity, due to the ‘fifth force’, which directly translates into an increase of structure formation. In this Section, we review two different types of modified gravity,

namely the *Dilaton* and the $f(R)$ models; we describe their distinct screening mechanisms, and detail their parameterization in the context of large scale structure formation.

2.1 Gravity in Dilaton models

The *Dilaton* and *Symmetron*⁶ theories of modified gravity are Chameleon models that exhibit the *Damour-Polyakov* property (Damour & Polyakov 1994), according to which the coupling between the scalar field φ and the rest of the matter components approaches zero in dense environments (Pietroni 2005; Olive & Pospelov 2008; Hinterbichler & Khoury 2010). In contrast to the case of $f(R)$ theories, described in Sec. 2.2 below, the scalar field here takes on a small mass everywhere and thus mediates a long-range (screened) force.

These Dilaton models are scalar-tensor theories, where the action defining the system takes the general form

$$S = \int d^4x \sqrt{-g} \left[\frac{M_{\text{Pl}}^2}{2} R - \frac{1}{2} (\nabla\varphi)^2 - V(\varphi) - \Lambda_0^4 \right] + \int d^4x \sqrt{-\tilde{g}} \tilde{\mathcal{L}}_m(\psi_m^{(i)}, \tilde{g}_{\mu\nu}), \quad (1)$$

where $M_{\text{Pl}} = (8\pi\mathcal{G}_N)^{-1/2}$ is the reduced Planck mass (in natural units), Λ_0^4 is the cosmological constant term today, g is the determinant of the Einstein-frame metric tensor $g_{\mu\nu}$ and \tilde{g} the determinant of the Jordan-frame metric tensor $\tilde{g}_{\mu\nu}$. The two metrics are connected via a conformal rescaling

$$\tilde{g}_{\mu\nu} = A^2(\varphi) g_{\mu\nu}. \quad (2)$$

The various matter fields $\psi_m^{(i)}$ are governed by the Jordan-frame Lagrangian density $\tilde{\mathcal{L}}_m$ and the scalar field φ by the Einstein-frame Lagrangian density $\mathcal{L}_\varphi = -1/2(\nabla\varphi)^2 - V(\varphi)$, where $V(\varphi)$ is the potential of the scalar field⁷. There is no explicit coupling between matter and the scalar fields, and the fifth force on matter particles due to φ arises from the conformal transformation given by equation (2) (more precisely, through gradients of A).

In the original Dilaton model, the potential $V(\varphi)$ and the coupling⁸ $A(\varphi)$ with the metric have the following functional forms:

$$V(\varphi) = V_* \exp\left(-\frac{\varphi}{M_{\text{Pl}}}\right), \quad (3)$$

$$A(\varphi) = 1 + \frac{1}{2} \frac{A_2}{M_{\text{Pl}}^2} \varphi^2, \quad (4)$$

where $\{V_*, A_2\}$ are the two free parameters. In regions where $\varphi \approx 0$, the coupling to matter is negligible, and gravity converges to GR. However, the field nevertheless mediates a long range gravitational force that has an effect elsewhere, i.e. in less dense environments. This model can be generalized to a greater class of Dilaton models, by keeping the coupling function as in equation (4) but considering more general potentials. Then, instead of specifying the model by

⁶ We do not further investigate the Symmetron, K-mouflage nor Vainshtein models in this paper.

⁷ In equation (1), we explicitly added the cosmological constant term Λ_0^4 , so that the minimum of $V(\varphi)$ is zero and is reached for $\varphi \rightarrow \infty$. Alternatively, this term could also be interpreted as the non-zero minimum of the scalar field potential.

⁸ This coupling is often defined as $A(\varphi) = 1 + \frac{1}{2} \frac{A_2}{M_{\text{Pl}}^2} (\varphi - \varphi_*)^2$, where φ_* is some free parameter of the model. We opted to absorb φ_* into φ in equation (4), a choice that has no physical impact anyway.

¹ <http://www.rcslens.org>

² <http://www.darkenergysurvey.org>

³ <http://kids.strw.leidenuniv.nl>

⁴ <http://sci.esa.int/euclid>

⁵ <http://www.lsst.org/lsst>

its potential $V(\varphi)$, it is re-casted in the tomographic parametrization $\{\beta(a), m(a)\}$ in terms of the cosmological scale factor $a(t)$, where the coupling $\beta(a)$ and the scalar field mass $m(a)$ are defined as (Brax, Davis & Li 2012; Brax & Valageas 2013):

$$\beta(a) \equiv \beta[\bar{\varphi}(a)] = M_{\text{Pl}} \frac{d \ln A}{d\varphi}(\bar{\varphi}), \quad (5)$$

$$m^2(a) \equiv m^2[\bar{\varphi}(a), \bar{\rho}(a)] = \frac{1}{c^2} \left[\frac{d^2 V}{d\varphi^2}(\bar{\varphi}) + \bar{\rho} \frac{d^2 A}{d\varphi^2}(\bar{\varphi}) \right]. \quad (6)$$

Hereafter, we denote with an overbar unperturbed cosmological background quantities, and with a subscript ‘0’ quantities evaluated today. For instance, $\bar{\rho}(a) = 3\Omega_{\text{m}0} H_0^2 M_{\text{Pl}}^2 / a^3$ is the background matter density, $\bar{\varphi}$ is the mean value of the field, H_0 is the current value of the Hubbles parameter, and $\Omega_{\text{m}0}$ is the current matter density. Also, c is the speed of light in vacuum. In this paper we consider the simple forms

$$m(a) = m_0 a^{-r}, \quad \beta(a) = \beta_0 \exp \left[-s \frac{a^{2r-3} - 1}{3 - 2r} \right], \quad (7)$$

with

$$s = \frac{9A_2 \Omega_{\text{m}0} H_0^2}{c^2 m_0^2}. \quad (8)$$

In this framework, the Yukawa potential given by equation (3) corresponds to $r = 3/2$. The values of the free parameters $\{m_0, r, \beta_0, s\}$ that enter equation (7) are displayed in Table 1. The models {A, B, C, D} were chosen such as to correspond to those studied in Brax & Valageas (2013) and Brax et al. (2012), where detailed comparisons between numerical and analytical calculations are presented. More specifically, the models {A, B, C} probe the dependence on $\{s, \beta_0, r\}$ respectively, all other parameters being fixed, while models D probe the dependence on m_0 at fixed A_2 . We added the models E that probe the dependence on the parameter m_0 at fixed $\{s, \beta_0, r\}$. These models probe deviations from the Λ CDM cosmology of less than 20%, in terms of the matter power spectrum. Let us now explore the detailed mechanism through which the power spectrum of matter fluctuations is affected by this theory.

In these Dilaton models, the coupling function A is always very close to unity, so that most Einstein-frame and Jordan-frame quantities (e.g., Hubble expansion rates or densities) are almost identical. Indeed, using $|\bar{A} - 1| \ll 1$, we can see from equations (4) and (5) that $\bar{A} \simeq 1 + \beta^2 / (2A_2)$. From equation (8) we also obtain $A_2 \sim (cm_0/H_0)^2$. Solar System tests of gravity such as that analysed in Chiba (2003) imply that $m_0 \gtrsim 10^3 H_0/c$, whence $A_2 \gtrsim 10^6$ and

$$|\bar{A} - 1| \lesssim 10^{-6}. \quad (9)$$

Therefore, the Jordan-frame and Einstein-frame scale factors and background matter densities, related by $\tilde{a} = \bar{A}a$ and $\tilde{\rho} = \bar{A}^{-4}\bar{\rho}$, can be considered equal, as well as the cosmic times and Hubble expansion rates. In the rest of this Section we work in the Einstein frame, where the analysis of the gravitational dynamics are simpler.

In the Einstein frame, the Friedmann equation takes the usual form

$$3M_{\text{Pl}}^2 H^2 = \bar{\rho} + \bar{\rho}_\varphi + \bar{\rho}_\Lambda, \quad (10)$$

where we explicitly separate contributions from the matter ($\bar{\rho}$) and scalar field ($\bar{\rho}_\varphi$) components and from the cosmological constant $\bar{\rho}_\Lambda$. The background value of the scalar field potential is given by

$$\frac{d\bar{V}}{d\bar{\varphi}} + \frac{\beta}{M_{\text{Pl}}} \bar{\rho} = 0. \quad (11)$$

Combining with equation (6), and writing $m = m(a)$, this leads to

$$\frac{d\bar{\varphi}}{da} = \frac{3\beta\bar{\rho}}{c^2 M_{\text{Pl}} a m^2}, \quad \frac{d\bar{V}}{da} = -\frac{3\beta^2 \bar{\rho}^2}{c^2 M_{\text{Pl}}^2 a m^2}, \quad (12)$$

whence

$$\frac{\dot{\bar{\varphi}}^2}{2\bar{\rho}} \sim \left(\frac{H}{cm} \right)^4 \sim 10^{-12}, \quad \frac{\bar{V}}{\bar{\rho}} \sim \left(\frac{H}{cm} \right)^2 \sim 10^{-6}. \quad (13)$$

Thus, the scalar field energy density is dominated by its potential term, which is negligible as compared with the matter density. Therefore, the Friedmann equation (10) is governed by the matter density and the cosmological constant and we recover the Λ CDM cosmological expansion, $3M_{\text{Pl}}^2 H^2 = \bar{\rho} + \bar{\rho}_\Lambda$, up to an accuracy of 10^{-6} .

We now briefly consider the behaviour of metric and density fluctuations. In the quasi-static limit, the scalar field is given by the Klein-Gordon equation,

$$\frac{c^2}{a^2} \nabla^2 \varphi = \frac{dV}{d\varphi} + \rho \frac{dA}{d\varphi}, \quad (14)$$

and at linear order over the matter density and scalar field fluctuations we obtain

$$\frac{\delta\varphi}{M_{\text{Pl}}} = -\frac{\beta}{c^2 M_{\text{Pl}}^2} \frac{\delta\rho}{m^2 + k^2/a^2}, \quad (15)$$

where k is the comoving wave number. Using equation (11) this gives

$$|\delta A| \sim \frac{|\delta\rho|}{\bar{\rho}} \left(\frac{H}{cm} \right)^2 \frac{1}{1 + k^2/a^2 m^2} \lesssim 10^{-6}, \quad (16)$$

so that the perturbations of the conformal factor A^2 are negligible compared to unity. Also,

$$\frac{\delta\rho_\varphi}{\delta\rho} \sim \left(\frac{H}{cm} \right)^2 \frac{1}{1 + k^2/a^2 m^2} \lesssim 10^{-6}, \quad (17)$$

hence fluctuations of the scalar field energy density are negligible compared with the matter density fluctuations.

Therefore, the main source that drives modifications to structure growth is not a different background evolution, nor perturbations in the scalar field energy density, but really the action of the fifth force on the matter field. In the Newtonian gauge, the perturbed metric can be written as

$$ds^2 = -(1 + 2\Phi)dt^2 + a^2(t)(1 - 2\Psi)\delta_{ij}dx^i dx^j, \quad (18)$$

where Φ and Ψ are the Einstein-frame metric gravitational potentials. Using equations (15) and (17), we can check that the impact of the scalar field fluctuations on the metric potentials are negligible, and we have within a 10^{-6} accuracy

$$\Phi = \Psi = \Psi_{\text{N}}, \quad (19)$$

where Ψ_{N} is the Newtonian potential given by the Poisson equation,

$$\frac{\nabla^2}{a^2} \Psi_{\text{N}} = 4\pi\mathcal{G}_{\text{N}}\delta\rho = \frac{3\Omega_{\text{m}0} H_0^2}{2a^3} \delta. \quad (20)$$

In the above expression, $\delta = \delta\rho/\bar{\rho}$ is the matter density contrast. However, the dynamics of matter particles are modified by the scalar field, which gives rise to the fifth force given by $\mathbf{F} = -c^2 \nabla \ln A$. That is, in the Euler equation we must add a fifth-force potential, $\Psi_A = c^2 \ln A$, that is not negligible. When solving for structure growth given the parameters listed in Table 1, the new term can lead to 10 – 20% deviations in the matter density power spectrum.

2.2 Gravity in $f(R)$ theories

In models based on $f(R)$ gravity, the Einstein-Hilbert action is modified by promoting the Ricci scalar R to a function of R (Buchdahl

1970; Starobinsky 1980, 2007; Hu & Sawicki 2007). The new action S in $f(R)$ gravity theories can be written as:

$$S = \int d^4x \sqrt{-g} \left[\frac{M_{\text{Pl}}^2}{2} [R + f(R)] - \Lambda_0^4 + \mathcal{L}_m(\psi_m^{(i)}) \right], \quad (21)$$

where we explicitly added the cosmological constant contribution⁹. The $f(R)$ models are most easily described in the Jordan frame, which is why, in this Section, we denote with a tilde Einstein-frame quantities instead of Jordan-frame ones, contrary to the notation of §2.1. In the parameterization of Hu & Sawicki (2007), the functional form $f(R)$ can be expressed in the high curvature limit as:

$$f(R) = -\frac{f_{R_0}}{n} \frac{R_0^{n+1}}{R^n}, \quad f_R \equiv \frac{df(R)}{dR} = f_{R_0} \frac{R_0^{n+1}}{R^{n+1}}. \quad (22)$$

The two independent parameters, f_{R_0} and n , can be constrained by observations. In the above expression, R_0 is the present value of the Ricci scalar for the cosmological background. Note that this parametrization and that of Starobinsky (2007) both reproduce the same results in the large curvature regime.

The $f(R)$ theories of gravity also invoke the Chameleon mechanism to screen modifications of GR in dense environments such as in our Solar System. Specifically, this occurs by requiring that all extra terms vanish in high curvature environment, such that $f(|R| \gg |R_0|) \rightarrow 0$. The background expansion otherwise follows the Λ CDM dynamics and the growth of structure is only affected on intermediate and quasi-linear scales.

There is an essential connection between the formulation of the $f(R)$ theory presented above and scalar-tensor theories of modified gravity. Upon the coordinate rescaling $\tilde{g}_{\mu\nu} = A^{-2}(\varphi)g_{\mu\nu}$ (recall that in this Section $\tilde{g}_{\mu\nu}$ is the Einstein-frame metric) with $A(\varphi) = \exp[\beta\varphi/M_{\text{Pl}}]$ and $\beta = 1/\sqrt{6}$, the $f(R)$ modifications to GR are recasted as arising from contributions of an extra scalar field φ , subject to a potential $V(\varphi)$ given by:

$$V(\varphi) = \frac{M_{\text{Pl}}^2}{2} \left(\frac{Rf_R - f(R)}{(1 + f_R)^2} \right), \quad f_R = \exp \left[-\frac{2\beta\varphi}{M_{\text{Pl}}} \right] - 1. \quad (23)$$

In that sense, $f(R)$ theories are equivalent to a scalar-tensor theory expressed in the Einstein frame (Chiba 2003; Nunez & Solgnaik 2004). In this new formulation, the screening mechanism takes another form: the mass of the scalar field grows with matter density, and a Yukawa-like potential suppresses the fifth force in dense environments. This can be conveniently reformulated by saying that screening takes place wherever the scalar field is small compared to the ambient Newtonian potential.

It turns out that all Chameleon-like models such as $f(R)$ theories can again be parameterized by the value of the mass $m(a)$ and the coupling $\beta(a)$ of the scalar field, in terms of the scale factor a and the associated background matter density $\bar{\rho}(a)$. With the specific functional form of $f(R)$ given by equation (22), we can directly relate $\{n, f_{R_0}\}$ to $\{\beta(a), m(a)\}$ via:

$$m(a) = m_0 \left(\frac{4\Omega_{\Lambda 0} + \Omega_{m 0} a^{-3}}{4\Omega_{\Lambda 0} + \Omega_{m 0}} \right)^{(n+2)/2}, \quad (24)$$

$$m_0 = \frac{H_0}{c} \sqrt{\frac{\Omega_{m 0} + 4\Omega_{\Lambda 0}}{(n+1)|f_{R_0}|}}, \quad \beta(a) = \frac{1}{\sqrt{6}}.$$

In this paper, we consider values of $n = \{1, 2\}$ and $|f_{R_0}| = \{10^{-4}, 10^{-5}, 10^{-6}\}$. The larger value of $|f_{R_0}|$ is currently ruled

out by other independent probes, so this serves as a consistency test. The numerical values for $\{\beta(a), m(a)\}$ corresponding to these three models are listed in Table 1.

As for the Dilaton models described in §2.1, the $f(R)$ models that we consider in this paper follow very closely the Λ CDM cosmology at the background level, mainly because $|f_{R_0}| \ll 1$. Indeed, from the action (equation 21) one obtains the Friedmann equation as (Tsujiikawa 2007);

$$3M_{\text{Pl}}^2 \left[H^2 - \bar{f}_R(H^2 + \dot{H}) + \bar{f}/6 + \bar{f}_{RR}H\dot{\bar{R}} \right] = \bar{\rho} + \bar{\rho}_\Lambda, \quad (25)$$

where the dot denotes the derivative with respect to cosmic time t and $f_{RR} = d^2f/dR^2$. In the background we have $\bar{R} = 12H^2 + 6\dot{H}$ and we can check that all extra terms in the brackets in equation (25) are of order $|f_{R_0}|H^2$, so that we recover the Λ CDM expansion, $3M_{\text{Pl}}^2H^2 = \bar{\rho} + \bar{\rho}_\Lambda$, up to an accuracy of 10^{-4} for $|f_{R_0}| \lesssim 10^{-4}$. Moreover, the conformal factor $A(\varphi)$ is given by $A = (1 + f_R)^{-1/2}$, so that $|\bar{A} - 1| \lesssim 10^{-4}$ and the background quantities associated with the Einstein and Jordan frames can be considered equal (and equal to the Λ CDM reference) up to an accuracy of 10^{-4} .

Considering the metric and density perturbations, we can again write the Newtonian gauge metric as in equation (18) (but this is now the Jordan-frame metric). Then, in the small-scale sub-horizon limit $k/a \gg H/c$, the modified Einstein equations lead to (Tsujiikawa & Tatekawa 2008)

$$\frac{\nabla^2}{a^2} \Phi = -\frac{c^2 \nabla^2}{2a^2} \delta f_R + 4\pi \mathcal{G}_N \delta \rho, \quad (26)$$

$$\frac{\nabla^2}{a^2} \Psi = \frac{c^2 \nabla^2}{2a^2} \delta f_R + 4\pi \mathcal{G}_N \delta \rho, \quad (27)$$

where $\delta f_R = f_R - \bar{f}_R$ and $\delta \rho = \rho - \bar{\rho}$. Therefore, in terms of the Newtonian gravitational potential Ψ_N defined as in GR by equation (20), we have

$$\Phi = \Psi_N - \frac{c^2}{2} \delta f_R, \quad \Psi = \Psi_N + \frac{c^2}{2} \delta f_R. \quad (28)$$

Thus, because we work in the Jordan frame (in contrast with the Dilaton case presented in §2.1), the modification of gravity directly appears through the metric potentials. The fluctuations of the new degree of freedom δf_R are given by:

$$\frac{3c^2 \nabla^2}{a^2} \delta f_R = \delta R - 8\pi \mathcal{G}_N \delta \rho. \quad (29)$$

Finally, the dynamics of the matter particles is given by the geodesic equation, where the Newtonian potential that appears in GR is replaced by the potential Φ given in equation (28).

3 WEAK LENSING

3.1 Theory

3.1.1 Weak lensing convergence power spectrum

In all the cosmologies considered in this paper, we work in the Newtonian gauge with the perturbed metric given by equation (18), where Φ and Ψ are the metric gravitational potentials¹⁰. In practice, we measure the statistical properties of weak lensing distortions by summing over many galaxy images. This means that the measured signal is an integral over selected sources with a broad redshift distribution

⁹ The terms R and Λ_0^4 are often included within the function $f(R)$. Written in the form of equation (21), $f(R)$ describes deviations from both GR and the Λ CDM cosmology.

¹⁰ In the Dilaton models, this is understood as the Einstein-frame metric while in the $f(R)$ models this is the Jordan-frame metric, following the approach described in §2. In any case, we can work in either frame as the observational results do not depend on this computational choice.

Table 1. Parameters describing the modified gravity theories considered in our study, mapped on the $\{\beta(a), m(a)\}$ surface, parameterized with $\{m_0, r, \beta_0, s\}$ following equation (7). The first five rows correspond to different realizations of the generalized Dilaton theories. The last two rows show $f(R)$ theories with $n = 1$ and 2 respectively, in which m_0 is given by equation (24), while $r \equiv 3(n+2)/2$, $\beta_0 = 1/\sqrt{6}$ and $s = 0$.

Model	m_0 (h/Mpc)	r	β_0	s
(A1, A2, A3)	(0.334, 0.334, 0.334)	(1.0, 1.0, 1.0)	(0.5, 0.5, 0.5)	(0.6, 0.24, 0.12)
(B1, B3, B4)	(0.334, 0.334, 0.334)	(1.0, 1.0, 1.0)	(0.25, 0.75, 1.0)	(0.24, 0.24, 0.24)
(C1, C3, C4)	(0.334, 0.334, 0.334)	(1.33, 0.67, 0.4)	(0.5, 0.5, 0.5)	(0.24, 0.24, 0.24)
(D1, D3, D4)	(0.667, 0.167, 0.111)	(1.0, 1.0, 1.0)	(0.5, 0.5, 0.5)	(0.06, 0.96, 2.16)
(E1, E3, E4)	(0.667, 0.167, 0.111)	(1.0, 1.0, 1.0)	(0.5, 0.5, 0.5)	(0.24, 0.24, 0.24)
$n = 1, \log_{10} f_{R_0} = (-4, -5, -6)$	(0.042, 0.132, 0.417)	(4.5, 4.5, 4.5)	(0.408, 0.408, 0.408)	(0, 0, 0)
$n = 2, \log_{10} f_{R_0} = (-4, -5, -6)$	(0.034, 0.108, 0.340)	(6.0, 6.0, 6.0)	(0.408, 0.408, 0.408)	(0, 0, 0)

$n(z_s)dz_s$ (mapped to $n(\chi)d\chi$ in terms of the radial distance, given the Jacobian $d\chi/dz$) that we normalize to unity. Thus, introducing the kernel $g(\chi)$ that defines the radial depth of the survey:

$$g(\chi) = \int_{\chi}^{\infty} d\chi_s n(\chi_s) \frac{\chi_s - \chi}{\chi_s}, \quad (30)$$

the integrated convergence field at a position θ on the sky reads as:

$$\kappa(\theta) = \int_0^{\infty} d\chi \frac{\chi}{c^2} g(\chi) \nabla^2 \Phi_{\text{wl}}(\chi, \chi\theta). \quad (31)$$

We assumed a flat background universe in the above equation, and introduced the weak lensing potential, defined by

$$\Phi_{\text{wl}} = \frac{\Phi + \Psi}{2}, \quad (32)$$

which is convenient when computing weak lensing modifications to GR. Solving equation (31) in multipole space and taking the ensemble average of the squared complex norm, we obtain the convergence power spectrum:

$$C_{\ell}^{\kappa} = \int_0^{\infty} d\chi \frac{g(\chi)^2}{c^4} \frac{\ell^4}{\chi^4} P_{\Phi_{\text{wl}}}(\ell/\chi; z) \quad (33)$$

as an integral over the weak lensing power spectrum $P_{\Phi_{\text{wl}}}(k; z)$. Note that the above also assumes both Limber and Born approximations. From this, we also derive predictions for the cosmic shear two-point correlation functions $\xi_{\pm}(\theta)$, computed as:

$$\xi_{\pm}(\theta) = \frac{1}{2\pi} \int C_{\ell}^{\kappa} J_{0/4}(\ell\theta) \ell d\ell \quad (34)$$

where $J_{0/4}(x)$ are Bessel functions of the first kind.

3.1.2 C_{ℓ}^{κ} in General Relativity

In the Λ CDM cosmology + GR case, we can exactly express the weak lensing convergence power spectrum (33) in terms of the total matter power spectrum $P(k)$ via Poisson equation. Indeed, we can safely neglect the anisotropic stress, and General Relativity gives:

$$\Phi_{\text{wl}} = \Phi = \Psi = \Psi_{\text{N}}, \quad (35)$$

where Ψ_{N} is the Newtonian potential given by Poisson equation (equation 20). Therefore, we recover

$$P_{\Phi_{\text{wl}}}(k; z) = \left(\frac{3\Omega_{\text{m}0}H_0^2}{2ak^2} \right)^2 P(k; z), \quad (36)$$

and the convergence power spectrum (33) becomes:

$$C_{\ell}^{\kappa} = \int_0^{\infty} d\chi W(\chi)^2 P(\ell/\chi; z), \quad (37)$$

with

$$W(\chi) = \frac{3\Omega_{\text{m}0}H_0^2}{2c^2} g(\chi)(1+z). \quad (38)$$

3.1.3 C_{ℓ}^{κ} in theories of modified gravity

For the Dilaton models, we have seen in equation (19) and in §2.1 that the two Einstein-frame metric potentials are equal to the Newtonian potential up to order 10^{-6} accuracy, and that background cosmological quantities such as the Hubble expansion rate and the radial comoving distances are equal to those of the Λ CDM reference within that same accuracy. This means that equations (35)-(36) apply as in GR, and that C_{ℓ}^{κ} is again given by equations (37)-(38). Therefore, in terms of this weak lensing statistics, the modification of gravity and the departures from the Λ CDM+GR results only appear through the modified matter density power spectra $P(k; z)$, which we describe in §3.2.3.

In the case of $f(R)$ models, we have seen in equation (28) that the two Jordan-frame potentials are different from the Newtonian potentials, receiving contributions from terms linear in δf_R . However, these two extra terms exactly cancel in the weak lensing potential (equation 32) such that $\Phi_{\text{wl}} = \Psi_{\text{N}}$. Therefore, we recover equations (36)-(38) in $f(R)$ models too. Moreover, we have seen that both the Jordan-frame and Einstein-frame background quantities are equal to the reference Λ CDM background quantities up to an accuracy of 10^{-4} for $|f_{R_0}| \lesssim 10^{-4}$. This means that weak lensing statistics can again be computed in the reference background cosmology, so long as the modified matter density power spectrum is used.

3.2 Non-linear matter power spectrum

The choice of non-linear power spectrum to insert in equation (37) depends on the cosmology under investigation. In this paper, we are interested in constraining modified gravity models, but with respect to a Λ CDM baseline, these are strongly degenerate with universes that include baryon feedbacks and/or massive neutrinos. In the context of cosmic shear, these phenomenas are therefore intrinsically connected and must be jointly analysed. We detail in this Section how we combine all these effects in the construction of our theoretical predictions.

3.2.1 Dark matter only

The first choice we make concerns the dark matter model $P^{\text{DM}}(k)$, which is a delicate issue that has been thoroughly investigated in HWVH in a very similar context. Following this work, we choose the dark matter only model that best reproduces the results from a number of N -body simulations, then implement the combined effect

of modified gravity, baryon feedback and massive neutrinos relative to this dark matter only baseline. Our dark matter only prediction is a hybrid model that combines the Extended Cosmic Emulator (Heitmann et al. 2013) with the recalibrated HALOFIT code by Takahashi et al. (2012). Its convergence properties have been well examined in HWVH, and it was shown to have the best agreement with independent high-resolution simulation suites, compared with other models. In addition, HWVH examined the scatter across multiple models, and estimated the theoretical uncertainty on the global dark matter only prediction for ξ_{\pm} . In this paper, we also incorporate this model uncertainty in the analysis pipeline, at the level of the χ^2 calculation (see §4.1).

3.2.2 Neutrino and baryon feedback

Following HWVH, we model the impact of massive neutrinos and baryon feedback on the matter power spectrum as separate effects that can be expressed with multiplicative feedback terms, namely:

$$P^{\text{DM}+\nu+b(m)}(k, z) = P^{\text{DM}}(k, z) \times b_{M\nu}^2(k, z) \times b_m^2(k, z). \quad (39)$$

The underlying assumption is that both biases are independent, which is reasonable since baryons were found to have a one percent effect on the neutrinos bias for $k < 8h\text{Mpc}^{-1}$ (Bird et al. 2012).

We compute the *neutrino feedback bias* term $b_{M\nu}^2$ with the CAMB cosmological code (Lewis et al. 2000), which is reported to be accurate to better than 10 percent at $k = 10h\text{Mpc}^{-1}$ (Bird et al. 2012). We assume one massive neutrino flavour, and fix the cosmology at high redshift – i.e. we keep the primordial amplitude A_s fixed but let σ_8 vary. We justify this choice from the fact that the former quantity is measured very accurately by CMB observations, whereas our estimation of the latter quantity is much less accurate due to galactic and cluster bias. We construct the neutrino bias as

$$b_{M\nu}^2(k, z) \equiv \frac{P_{\text{CAMB}}^{\text{DM}+M\nu}(k, z)}{P_{\text{CAMB}}^{\text{DM}}(k, z)}, \quad (40)$$

where the $M\nu$ ($= 0.0, 0.2, 0.4$, or 0.6 eV) superscript specifies the total neutrino mass considered, and the subscript ‘CAMB’ specifies that both quantities are measured from this cosmological numerical code.

The *baryonic feedback bias* is estimated from two hydrodynamical simulations ran in the context of the OverWhelmingly Large (OWL) Simulation Project (Schaye et al. 2010). The dark matter only run (DM-ONLY) is a purely collision-less N -body calculation and acts as the baseline for this baryon feedback measurement only. The AGN simulation run contains gas dynamics with physical prescriptions for cooling, heating, star formation and evolution, chemical enrichment, supernovae feedback and active galactic nuclei feedback (see van Daalen et al. 2011, for details about these simulations). Following van Daalen et al. (2011); Semboloni et al. (2011), we measure the baryonic feedback bias by taking the ratio between the AGN and the DM-ONLY models¹¹:

$$b_m^2(k, z) \equiv \frac{P_{\text{OWL}}^{\text{DM}+b(m)}(k, z)}{P_{\text{OWL}}^{\text{DM}}(k, z)}, \quad (41)$$

where the index $b(m)$ refers to either DM-ONLY or AGN, and the subscript ‘OWL’ specifies that these quantities were measured specifically from the OWL simulation suite.

Fig. 1 shows the impact of different combinations of baryons and massive neutrinos on the matter power spectrum. Fig. 2 and 3

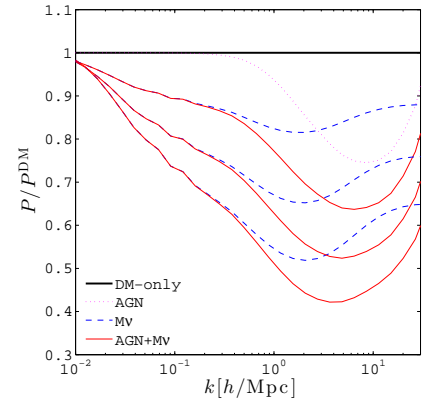


Figure 1. Combined effect from baryon feedback and massive neutrinos on the matter power spectrum $P(k)$, evaluated at $z = 1$. Results are shown with respect to the dark matter only non-linear predictions (thick solid line). From top to bottom, the (blue) dashed lines represent the effect of massive neutrinos with $M_\nu = 0.2, 0.4$ and 0.6eV respectively. The combinations of massive neutrinos with baryon feedback are shown with the thin (red) solid lines.

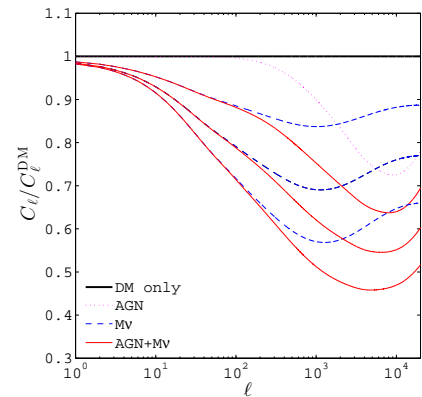


Figure 2. Combined effect from baryon feedback and massive neutrinos on the weak lensing power spectrum, assuming the source redshift distribution given by equation (45) and the baseline *WMAP9* cosmology. As for Fig. 1, results of different combinations are shown with respect to the dark matter only non-linear predictions (thick solid line), and the sum of neutrino masses shown are, from top to bottom, $M_\nu = 0.2, 0.4$ and 0.6eV .

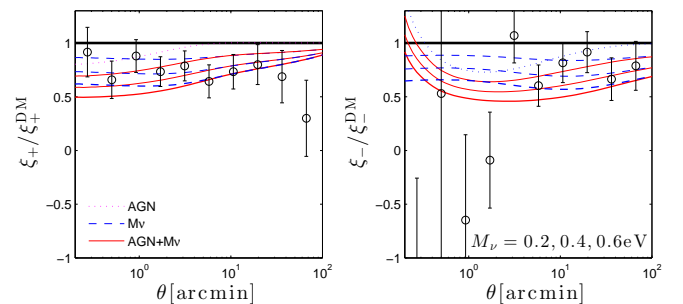


Figure 3. (left:) Combined effect from baryon feedback and massive neutrinos on the weak lensing two-point correlation function ξ_+ . The open symbols represent our measurements from CFHTLenS data, shown with 1σ error bars. (right:) Same as the left panel, but for the ξ_- estimator. We used the same y -axis range for both panels to emphasize on the differences across the models, hence the leftmost point falls outside the frame, at $\xi_- / \xi_-^{\text{DM}} = -3.8$.

¹¹ The power spectrum measurements from the OWL simulation suite are publicly available at: <http://vd11.strw.leidenuniv.nl>

show the equivalent effects on the weak lensing power spectrum C_ℓ^{κ} and on the shear two-point correlation function $\xi_{\pm}(\theta)$, respectively. We can see from the three figures that all models converge to DM-ONLY at large scales (low k , low ℓ and high θ), and that the combined effect can suppress more than 50% of the power, depending on the models and neutrino mass. Also, it becomes clear that surveys probing small patches (restricted to $\ell > 500$ for example) would have difficulties to distinguish between the two feedback processes. This degeneracy can only be broken with the inclusion of lower ℓ multipoles, where baryon feedback is minimal but massive neutrinos still leaves a signature (Natarajan et al. 2014).

3.2.3 Combined feedback with modified gravity

The evolution of perturbations in the context of large-scale structures has been carefully studied in $f(R)$ and scalar-tensors theories gravity (Zhang 2006; Koivisto 2006; Bean et al. 2007; Song, Hu & Sawicki 2007; Hu & Sawicki 2007; Song, Peiris, Hu 2007; Pogosian & Silvestri 2008; Carloni, Dunsby & Troisi 2008; Koyama, Taruya & Hiramatsu 2009; Motohashi, Starobinsky & Yokoyama 2009; Li & Hu 2011; Brax et al. 2011; Li, Zhao & Koyama 2012; Linares & Mota 2013; Taddei, Catena & Pietroni 2013; Brax & Valageas 2013). In this paper, we focus on the matter density power spectrum $P(k; z)$, or more precisely, on the weak lensing convergence power spectrum C_ℓ^{κ} , which can be computed from $P(k; z)$ through the modified Poisson equations that relate the metric gravitational potentials to the matter density fluctuations.

Therefore, before computing weak lensing statistics, we first need to describe gravitational clustering and the 3D matter density power spectrum for all cosmological scenarios that we investigate. We use the approach first developed in Valageas, Nishimichi & Taruya (2013) for the Λ CDM cosmology, generalized afterwards to various modified-gravity scenarios in Brax & Valageas (2013, 2014). This is an analytical approach that combines perturbation theory up to one-loop order (i.e., up to order P_L^2 , where P_L is the linear matter density power spectrum) with a phenomenological halo model. Namely, we are splitting the matter power spectrum as:

$$P(k) = P_{2H}(k) + P_{1H}(k), \quad (42)$$

where $P_{2H}(k)$ is the ‘two-halo’ term associated with pairs of particles that are enclosed in two different halos, whereas $P_{1H}(k)$ is the ‘one-halo’ term associated with pairs enclosed in the same halo. This construction allows us to obtain predictions for the non-linear matter power spectrum covering the linear, quasi-linear and highly non-linear scales. We refer the reader to the work cited above for complete details and validations of equation (42), but nevertheless provide an overview of the method in the Appendix for quick reference. We note that other prescriptions exist for modelling $P(k)$ in modified gravity scenarios, i.e. Zhao (2014) for the $f(R)$ model. However the modelling we adopt here applies also to $f(R)$ with $n \neq 1$ gravity, to Dilaton gravity, and in fact to any modified gravity model expressed in the tomographic parameterization, which makes it general and accurate at the same time.

In analogy with equations (40) and (41), we define the *modified gravity bias*:

$$b_{\text{MG}(\alpha)}^2(k, z) \equiv \frac{P_{\text{VNT}}^{\text{MG}(\alpha)}(k, z)}{P_{\text{VNT}}^{\text{DM}}(k, z)}, \quad (43)$$

where $\text{MG}(\alpha)$ refers to the gravity model, with $\alpha=0$ corresponding to GR, $\alpha= [1, 2, 3, \dots, 15]$ specifying dilation models [A1, A2, A3, ..., E4], $\alpha= [16, 17, 18]$ specifying $f(R)$ models with $n = 1$ and $|f_{R0}| = 10^{-4}, 10^{-5}, 10^{-6}$, and finally $\alpha= [19, 20, 21]$ the $f(R)$ models with $n = 2$ and the same $|f_{R0}|$ values. The subscript ‘VNT’

indicates quantities that are computed in the framework of Valageas, Nishimichi & Taruya (2013), i.e. with equation (42).

Bringing all the pieces together, we construct the matter power spectrum for any combination of baryon feedback, neutrino mass and modified gravity by multiplying the DM-ONLY model by the corresponding biases:

$$P^{\text{DM}+\nu+b(m)+\text{MG}} = P^{\text{DM}} \times b_{M_\nu}^2 \times b_m^2 \times b_{\text{MG}(\alpha)}^2. \quad (44)$$

We have removed the dependences on scale and redshift for each of these terms to clarify the notation. This modelling assumes that the effect of modified gravity on the baryon and neutrino feedbacks can be neglected, allowing for the convenient factorization presented in equation (44). This seems to be a valid approximation for some models, as it was shown in Hammami et al. (2015) that the modified gravity bias measured in dark matter only matched to better than 5% the same measurement done in full hydrodynamical simulations, for $f(R)$ models with $n = 1$ and $|f_{R0}| \in [10^{-4} - 10^{-6}]$. However, the same group also observed larger deviations in many symmetron models, up to 20% by $k = 10h\text{Mpc}^{-1}$ in some cases. This places a limit on the accuracy of equation (44), and calls for more hydrodynamical simulation runs where b_m and $b_{\text{MG}(\alpha)}$ are merged into one term, $b_{m, \text{MG}(\alpha)}$, measured for each combination of $\{\alpha, m\}$. This is unfortunately not available at the moment, hence equation (44) is currently our best shot at this joint measurement. On the neutrino sector, results by Baldi (2014) are further encouraging: they looked at joint simulations of modified gravity and massive neutrinos and came to the conclusion that one could consider the effect of each almost independently, supporting the validity of equation (44).

For each combination, we compute predictions for the weak lensing quantity with equations (37) and (34). We report our results on $P(k)$ and C_ℓ^{κ} in Fig. 4 and 5 respectively. Whereas modified gravity is generally boosting the clustering compared to a Λ CDM universe, the inclusion of massive neutrinos and/or baryonic feedback is working in the opposite direction. It becomes clear that a precise distinction between these three feedback contributions poses a challenge to clustering and weak lensing experiments.

3.3 Data

Our measurement of the shear correlation functions ξ_{\pm} is based on the public release of the Canada France Hawaii Telescope Lensing Survey (CFHTLenS¹²). The CFHTLenS covers a total area of 154 deg², which is reduced to 128 deg² after masking bright stars, foreground moving objects and faulty CCD rows. Full details about the data reduction pipeline are provided in Erben et al. (2013). Source redshifts are obtained from the five bands *u'griz* photometric observations (Hildebrandt et al. 2012) and were carefully tested in Benjamin et al. (2013); shape measurements are performed on the *r*-band images with the *lensfit* Bayesian code described in Miller et al. (2013). A detailed assessment of the residual systematics is provided in Heymans et al. (2012), and we refer the reader to these references for more information on the CFHTLenS data.

As described in Heymans et al. (2012), the public shear data must be recalibrated with additive and multiplicative factors, commonly referred to as the *c* and *m* corrections. In contrast with this reference, we use a different *c* correction, as detailed in HWVH, which is less model dependent. Although the overall change on the correction is marginal, the number of CFHTLenS pointings that are flagged as *bad* is reduced by almost a half.

Following the recommendations of Heymans et al. (2012) and

¹² CFHTLenS: www.cfhtlens.org

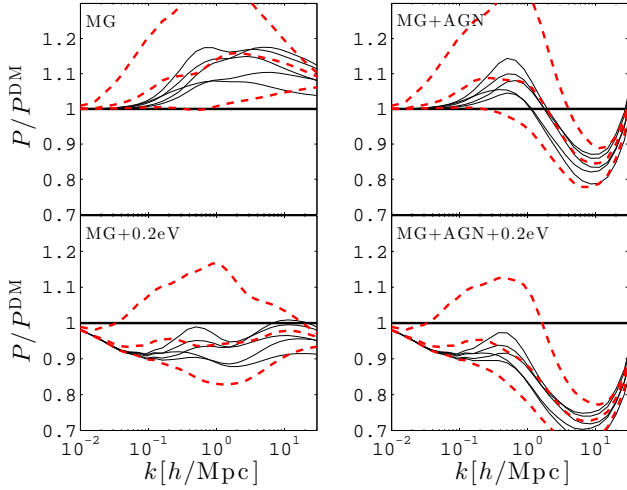


Figure 4. Combined effect from baryon feedback and massive neutrinos on the matter power spectrum $P(k)$ assuming different modified gravity models, again evaluated at $z = 1$. Results are shown with respect to the dark matter only non-linear predictions (thick horizontal solid line). From top to bottom at $k = 0.2h\text{Mpc}$, the solid lines represent Dilaton models B4, A3, E3, D1 and C1 respectively. The thick red dashed lines correspond to $f(R)$ gravity with $n = 1$. Top to bottom are for $|f_{R0}| = 10^{-4}, 10^{-5}$ and 10^{-6} respectively. We do not show the $n = 2$ results to avoid over-crowding the figure, but they are qualitatively similar in shape to the $n = 1$ case, albeit with a smaller departure from ΛCDM . Different panels show different combinations of massive neutrinos and baryon feedback on these same models, all computed with equation (44).

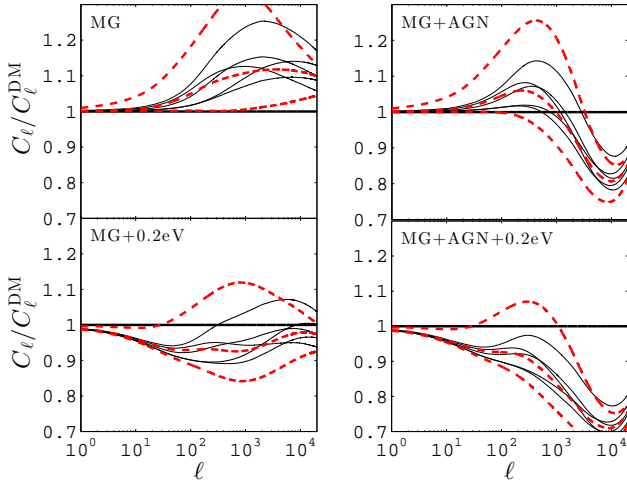


Figure 5. Same as Fig. 4, but for the weak lensing power spectrum.

Benjamin et al. (2013), we minimize the systematic contamination from badly reconstructed photometric redshifts by applying the selection cut $0.4 < z_{\text{phot}} < 1.3$. We construct the redshift distribution $n(z)$ for the selected galaxies from the *lensfit*-weighted stacked probability distribution functions of the galaxy sample. As shown in HWMH, the distribution is well described by the following analytical expression:

$$n(z) = N_0 e^{-(z-z_0)^2/\sigma_0^2} + N_1 e^{-(z-z_1)^2/\sigma_1^2} + \frac{N_2 e^{-(z-z_2)^2/\sigma_2^2}}{1.0 + e^{-10.0(z-0.6)}}, \quad (45)$$

where $(N_0, z_0, \sigma_0, N_1, z_1, \sigma_1, N_2, z_2, \sigma_2) = (0.14438, 0.760574,$

0.14594, 0.514894, 0.498379, 0.15608, 1.74435, 0.445019, 0.684098). There is a 0.4 percent difference in the mean redshift between the fit and the distribution, which yields a small error well below the other sources of error in our analysis. We therefore neglected this contribution to the systematic budget.

We construct our shear correlation function estimator following Kilbinger et al. (2013):

$$\xi_{\pm}(\theta) = \frac{\sum_{i,j} w_i w_j [e_t(\theta_i) e_t(\theta_j) \pm e_r(\theta_i) e_r(\theta_j)]}{\sum_{i,j} w_i w_j}. \quad (46)$$

All galaxy pairs (i, j) separated with angular distance $|\theta_i - \theta_j| \in \theta$ contribute to the same bin, with their contribution weighted by the product of their *lensfit* weights $w_i w_j$ (Miller et al. 2013). The shear quantities e_t and e_r are the tangential and cross-component of the galaxy ellipticity, measured in the coordinate system of the galaxy pair. We account for the shear calibration by measuring

$$1 + K(\theta) = \frac{\sum_{i,j} w_i w_j (1 + m_i)(1 + m_j)}{\sum_{i,j} w_i w_j} \quad (47)$$

and dividing ξ_{\pm} by $1 + K$. As a rule of thumb, K is ~ -0.11 at all angular scales, with variations smaller than 0.1%. We finally exclude all pairs with $\theta < 12$ arcseconds in order to minimize contamination by post stamp leakage across *lensfit* templates. We perform this measurement with ATHENA¹³, and show our results in Fig. 3.

3.4 Simulations

In order to achieve a high precision cosmic shear measurement, not only must the data be thoroughly tested for subtle systematics residuals, but the sampling variance must be accurately estimated, a quantity that is very hard to assess from the data. To overcome this difficulty, we rely on a suite of weak lensing simulations based on *WMAP9* + SN + BAO cosmology. As detailed in Harnois-Déraps & van Waerbeke (2015), the SLICS-LE suite consists of 60 sq. degrees light cones extracted from 500 independent N -body realizations. The numerical weak lensing signal is precise to better than 10 percent for ξ_+ with $\theta > 0.4'$ (and $\theta > 5'$ for ξ_-). We construct the mock maps by combining the different redshift planes with a redshift source distribution that mimics that of the data. We then sample the simulated shear maps with 10^5 points randomly located, and compute the shear two-point correlation functions ξ_{\pm} of these mock ‘galaxies’ with the same pipeline as the data (i.e. from equation 46).

4 RESULTS

In this Section, we first review our error budget, we then describe how different components combine in our model rejection procedure, and finally present our results.

4.1 Error budget

This analysis closely follows that of HWHV; we summarize here the main ingredients, and refer the reader to the reference for more details. The sources of error in this analysis can be broken into three terms: 1- uncertainty on the cosmic shear measurement, 2- uncertainty in the theoretical model describing the non-linear regime of structure formation, and 3- uncertainty on the fiducial cosmology.

1- The error on our cosmic shear measurement is dominated by shape noise at small angles and sampling variance at large angles.

¹³ ATHENA: <http://cosmostat.org/athena.html>

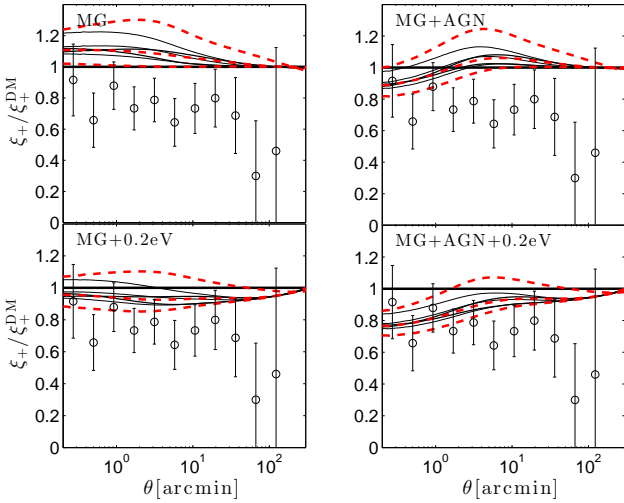


Figure 6. Same as Fig. 4, but for ξ_+ . The open symbols represent our measurements from the CFHTLenS data, exactly as in the right panel of Fig. 3. Shown are the 1σ error bars.

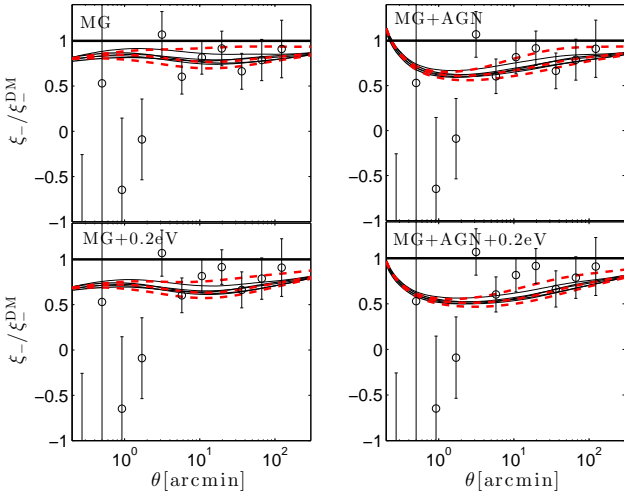


Figure 7. Same as Fig. 6, but for ξ_- . Note the different y -axis range compared to Fig. 6.

The angular scales at which these two errors contribute equally occur at $\theta = 2$ and 30 arc minutes for ξ_+ and ξ_- , respectively. In addition, the variance-shape noise mixed term contributes to about a third of the error on ξ_+ at large angles, but is negligible in ξ_- , as seen in Kilbinger et al. (2013). We have estimated the sampling variance from the SLICS-LE weak lensing simulations, and added an extra contribution from the *halo sampling variance*, following the modelling of Sato et al. (2009), which provides at most a 10 percent correction on the overall error. Our measurement is minimally affected by intrinsic alignment of galaxies, since we do not perform tomographic analysis (see Heymans et al. 2013, for more details on intrinsic alignments in the CFHTLenS data). The error from shape reconstruction is already included in the statistical term, hence does not require an extra term. Photometric redshift uncertainty enters the measurement through modification of the source distribution $n(z)$, but this effect is negligible compared with other sources of error hence is not included.

2- The uncertainty on the dark matter only non-linear model has been carefully assessed in HWVH by comparing five different predictions: HALOFIT2012, HALOFIT2011 + small scale empirical re-

calibration, Cosmic Emulator + power law graft, Cosmic Emulator + HALOFIT2012 graft and, finally, the mean over five independent high resolution simulations – the SLICS-HR suite described in Harnois-Déraps & van Waerbeke (2015). These five models agree very well over most angular scales, and the 1σ scatter among them is taken as the (θ -dependent) theoretical error.

3- The uncertainty in the cosmological parameters is set by the WMAP9 precision (Hinshaw et al. 2013), whose dominant contribution on the weak lensing uncertainty arises via the parameters Ω_M and A_s . With the inclusion of the BAO and SN external data, these two parameters are allowed a 3.4 and 3.3 percent variation about their mean values (1σ). Since the amplitude of ξ_{\pm} roughly scales as $(A_s \Omega_M)^2$, we expect the combined error to be of the order 5 percent of the Λ CDM baseline signal, assuming no prior on the joint contour.

Note that the cosmological error and the modelling error (terms 2 and 3) enter in our analysis as systematic uncertainties, therefore we add them in quadrature and marginalize over them (see details in §4.2). Also note that the Planck cosmology $\{\Omega_M, A_s\}$ falls within our 3σ search limits, although closer to the edge of the search zone.

4.2 Model rejection strategy

As seen in Fig. 6 and 7, the effects of baryons, massive neutrinos and modified gravity are significantly degenerate on ξ_{\pm} . Given the noise levels in the current data and the number of internal parameters that describe these different mechanisms, performing a full MCMC analysis is not convenient to extract meaningful constraints. A more appropriate and direct way is to sample a finite set of model combinations and examine their agreement with the data. This case-by-case strategy has the potential to reject models that are inconsistent with the data, which can then be translated into constraints on the underlying free parameters.

The metric we adopt for this type of analysis is the p -value, which measures the probability that the data is consistent with the model, *if the model is true*. It is given by the integral over the χ^2 probability density function, where the lower bound is the measured χ^2 and the upper bound is infinity. As a rule of thumb, models with p -values $< 10\%$ are rejected with more than 90% confidence, and $1\sigma, 2\sigma, 3\sigma, \dots$ rejection measurements are obtained for p -values of 0.317, 0.046, 0.003.... Our strategy therefore consists to measure the χ^2 and p -value associated with each combination of baryon feedback, neutrino mass and modified gravity model, and to flag every combination with $p < 0.1$ as being disfavoured.

The uncertainty arising from statistical and sampling variance naturally enters this calculation through the evaluation of the χ^2 , which involves the inversion of the cosmic shear covariance matrix. The systematic uncertainty, however, is trickier to capture. In our cosmic shear measurement, it mainly manifests itself as shifts in the amplitude of the signal, as described in §4.1. The systematic error is higher at smaller angles and represents at most an error of $\sim 9\%$ on the ξ_{\pm} model amplitude. In order to marginalize over this effect, for each model, we allow the theoretical signal to shift up and down by $3\sigma_{\text{sys}}$, corresponding to vertical excursion of 27% in Fig. 6 and 7, keeping the error bars (statistical + sampling) fixed. We then compute an array of p -values in this excursion range, and record only the largest measurement (i.e. the least restrictive).

The exact number of degrees of freedom ($d.o.f.$) that enters the χ^2 distribution function must be carefully chosen. To begin with, each of the two cosmic shear observables is organized in 11 angular bins, yielding a maximum of 22 $d.o.f.$ However, assigning one $d.o.f.$ per angular bin would be incorrect, for the following reason. In a statistical sense, our model rejection method is completely equivalent to fitting the parameter combination $(A_s^2 \Omega_M^{1.8})$ from the amplitude of

the ξ_{\pm} signals, followed by an extraction of the most likely neutrino mass for each baryon feedback and modified gravity model from the largest p -value. This implies that the number of degrees of freedom should be reduced by two (one for fitting $A_s^2 \Omega_M^{1.8}$, one for fitting M_{ν}) in the conversion between χ^2 and p -values.

Note that for a given angular scale, both ξ_+ and ξ_- probe different physical scales, the latter focusing on structures about five times smaller. It is therefore relevant to examine the constraining power of ξ_+ first, and to add ξ_- to the data vector as a second step. When both are combined, the full data covariance matrix involves the cross-correlation region, as described in HWVH. The resulting p -values are summarized for all our results in Table 2, for $M_{\nu} \leq 0.2$ eV. No conclusions can be drawn from models with higher total neutrino masses, as the p -values for any combination is always greater than 0.175. The models rejected at more than 1.64σ (i.e. 90% CI) are highlighted in bold font.

4.3 Discussion

One of the main results recovered from Table 2 is that the $f(R)$ model with $\{|f_{R_0}|, n\} = \{10^{-4}, 1\}$ is strongly disfavoured by the cosmic shear data, regardless of the baryonic feedback model or sum of neutrino mass, consistent with independent constraints. The $f(R)$ and $f(R) + \text{AGN}$ models are rejected by at least 3σ , but combinations including massive (0.2eV) neutrinos tend to weaken this constraints. This can be understood by the fact that massive neutrinos and modified gravity partly compensate for one another, reducing the global departure from ΛCDM . Also, $f(R, n=2)$ models are generally in better agreement with the data compared to their ($n=1$) counterpart. This is so simply because higher values of n rapidly suppress the $f(R)$ term, hence deviations from GR, as seen in equation (22).

The next important result is that the rejection of massless neutrinos + DM-ONLY is robust against all modified gravity models we have tested, and typically made stronger. The cosmic shear data clearly prefers lower values of ξ_{\pm} at small angular scales, and modified gravity pulls the other way.

The inclusion of baryon feedback reduces to about two thirds the number of models rejected with 90% CI. For instance, dilation models A2, A3, B3, B4, C1, C3, D1, E3 and E4 are disfavoured; these are the most discrepant with $\text{GR} + \Lambda\text{CDM}$. Referring to Table 1 and the model descriptions in §2.1, this can be interpreted as follow. In a tomographic parameterization of modified gravity centred on $\{m_0, r, \beta_0, s\} = \{0.334, 1.0, 0.5, 0.24\}$, excursion in the s , β_0 and r directions are studied with models A, B and C respectively, and the data favours lower parameters values. Model E explores the m_0 direction, and the data prefers higher values. Model D explores the diagonal direction in the $\{m_0, s\}$ plane at fixed A_2 (see equation 8), where here we observe instead that the data prefers lower m_0 values.

We note that there is a mild effect seen in the ‘AGN’ column of Table 2, where the addition of ξ_- to the data vector sometimes increases the p -value by a small amount. This can be attributed to the fact that at small angles, ξ_- prefers amplitude even lower than ξ_+ , compared to the DM-ONLY model. Adding baryon feedback therefore produces a lower rejection rate in the former than in the latter quantity.

When neutrino masses are allowed to reach 0.2eV, only the $f(R)\{10^{-4}, 1\}$, $f(R)\{10^{-4}, 2\}$ and the Dilaton B4 and E4 models remain in tension with the data. With $\text{AGN} + M_{\nu}=0.2\text{eV}$, no models are rejected, aside from the most extreme case considered in this paper: $f(R)\{10^{-4}, 1\}$.

This means that given the current cosmic shear data and levels of systematics, it is possible to accommodate most models, as long as either massive neutrinos or strong baryon feedback mechanisms

counter-balance the effect of the fifth force on the matter clustering. As upcoming independent cosmological probes will tighten the uncertainty on neutrino masses and significantly improve the statistical and sampling errors, we expect the next generation of such analysis to be much more constraining. Once at this stage, it will be instructive to propagate our measurements onto $\{m(a), \beta(a)\}$ contours and provide a Fisher matrix for joint probes analyses. If, for instance, the total mass turns out to be much smaller than 0.2eV, then the current AGN column should give a very good approximation of the rejection power from the CFHTLenS cosmic shear data. Precise modelling of the baryon feedback is likely to take more time to reach, due to the higher level of complexity intrinsic to these astrophysical phenomena. Intermediate solutions will involve a series of tuneable parameters, also to be constrained.

On a separate note, we stress that the constraints can be further tightened using additional information about the weak-lensing observables, such as the non-Gaussian features (Munshi, van Waerbeke, Smidt & Coles 2012), or by combining the results with external probes such as redshift distortions, peculiar velocity, etc.

5 CONCLUSION

Cosmic shear is a promising tool for probing deviations from GR, since these are maximal at scales of a few Mpc, where the lensing signal-to-noise ratio is the highest. These same scales are very challenging to probe with other types of large scale structure observables, mainly because of the galaxy bias that is largely unknown. At the same time, this complementarity offers a number of opportunities for strong constraints based on joint data sets.

One of the main challenge in working with these non-linear scales is the large theoretical uncertainties due to the unknown neutrino masses, the precise baryonic feedback mechanisms and, to a lesser extend, inaccuracies in the clustering of dark matter. However, a lot of effort is invested in all these areas, such that it becomes possible to place joint constraints on these degenerate physical effects.

This paper presents the first constraints on modified gravity obtained from cosmic shear measurements alone; the results are derived by studying the impact of modified gravity on matter clustering and comparing the predictions with the public CFHTLenS data. Limiting the background ΛCDM cosmology to the 3σ range in $\{A_s, \Omega_M\}$ allowed by *WMAP9* + SN + BAO, we compared the ξ_{\pm} data against predictions including $f(R)$ and Dilaton models in a number of parameter configurations. We carried a model rejection analysis accounting for possible degeneracies with massive neutrinos and baryonic feedback mechanisms, and investigated which combinations of models were mostly disfavoured by the data. As summarized in Table 2, the $f(R)$ model with $|f_{R_0}| = 10^{-4}$ is strongly disfavoured even in the presence of realistic levels of baryonic feedback and massive neutrinos reaching $M_{\nu}=0.2\text{eV}$. A universe with no baryonic feedback and massless neutrinos is also rejected with 2σ or above in most modified gravity scenarios. We are not yet able to identify a preferred model with the current level of statistical accuracy, but we expect future weak lensing experiments to improve significantly in this direction.

In our analyses, we have use the simplifying assumption that the biases due to massive neutrinos, baryon feedback and modified gravity were uncorrelated, which is justified to some extend based on the several numerical results. However, precise correlations will need to be studied for a number of models, a task that involves suites of large cosmological hydrodynamical simulations including all the ingredients at once.

One important future tasks will be to map observational detec-

Table 2. Distribution of p -values for different combination of baryon feedback models, neutrino masses and gravity models (see main text for details). The parameters listed in the leftmost column of the $f(R)$ models are $\{n, |f_{R_0}|\}$. Dilaton models are described in Table 1. For this calculation, we fit all data in the range $0.2 < \theta < 167$ arcminutes. Specifically, each entry in this Table represents the largest p -value probed inside a $3\sigma_{\text{sys}}$ region about the mean of the model. Values in bold face highlight the model combinations that are excluded by the data with more than 1.64σ significance (p -value < 0.1 , equivalent to a confidence interval (CI) of 90%). Models with $M_\nu > 0.2$ eV are not listed, as none has value lower than 0.176.

Model	DM-ONLY		AGN		0.2eV		AGN+0.2eV	
	ξ_+	$\xi_+\xi_-$	ξ_+	$\xi_+\xi_-$	ξ_+	$\xi_+\xi_-$	ξ_+	$\xi_+\xi_-$
General Relativity								
Λ CDM	0.132	0.065	0.119	0.150	0.331	0.297	0.289	0.444
Generalized Dilaton								
A1	0.126	0.058	0.116	0.141	0.323	0.282	0.284	0.431
A2	0.088	0.030	0.093	0.099	0.269	0.203	0.256	0.363
A3	0.037	0.008	0.060	0.051	0.184	0.105	0.207	0.265
B1	0.120	0.054	0.113	0.135	0.315	0.273	0.281	0.424
B3	0.043	0.010	0.064	0.054	0.195	0.113	0.212	0.272
B4	0.008	0.001	0.032	0.019	0.107	0.037	0.150	0.161
C1	0.080	0.022	0.100	0.098	0.259	0.171	0.271	0.365
C3	0.104	0.040	0.098	0.111	0.293	0.239	0.261	0.385
C4	0.114	0.049	0.104	0.122	0.307	0.259	0.267	0.402
D1	0.063	0.013	0.100	0.085	0.232	0.132	0.276	0.347
D3	0.127	0.060	0.115	0.141	0.325	0.286	0.282	0.431
D4	0.131	0.064	0.119	0.149	0.331	0.295	0.288	0.441
E1	0.118	0.049	0.117	0.135	0.314	0.260	0.289	0.425
E3	0.047	0.013	0.053	0.049	0.200	0.132	0.186	0.257
E4	0.026	0.007	0.032	0.027	0.156	0.094	0.138	0.188
$f(R)$								
$\{1, 10^{-4}\}$	0.001	0.000	0.005	0.003	0.051	0.018	0.054	0.057
$\{1, 10^{-5}\}$	0.058	0.013	0.072	0.062	0.222	0.134	0.222	0.292
$\{1, 10^{-6}\}$	0.129	0.054	0.125	0.145	0.328	0.271	0.298	0.437
$\{2, 10^{-4}\}$	0.011	0.003	0.020	0.014	0.112	0.056	0.104	0.131
$\{2, 10^{-5}\}$	0.095	0.030	0.094	0.097	0.277	0.200	0.254	0.354
$\{2, 10^{-6}\}$	0.137	0.063	0.126	0.154	0.338	0.292	0.299	0.449

tions of modifications to GR onto parameter constraints such as the $\{m(a), \beta(a)\}$ pair. However, the current data is not quite there yet. Several theories can accommodate similar phenomenological effects, and model-independent parameterizations such as that presented in Leonard, Baker & Ferreira (2015) might prove helpful for this.

This paper used the impact of modified gravity on the clustering properties of matter and their propagation onto the weak lensing cosmic shear signal. Other avenues of probing deviations from GR with weak lensing data are complementary, including direct combinations with baryonic probes or tomographic decomposition, and worth exploring in the near future.

ACKNOWLEDGEMENTS

We would like to thank Alexander Mead for his comments on the manuscript, and to acknowledge useful discussions with Alexei Starobinsky, Alan Heavens, Catherine Heymans and Massimo Viola. We are deeply grateful to all the CFHTLenS team for having made public their high quality shear data. Computations for the N -body simulations were performed on the GPC supercomputer at the SciNet HPC Consortium. SciNet is funded by: the Canada Foundation for Innovation under the auspices of Compute Canada; the Government of Ontario; Ontario Research Fund - Research Excellence; and the University of Toronto. This work is based on observations obtained with MegaPrime/MegaCam, a joint project of CFHT and CEA/IRFU, at the Canada-France-Hawaii Telescope (CFHT) which is operated by the National Research Council (NRC) of Canada, the Institut National des Sciences de l'Univers of the Centre National de la Recherche Scientifique (CNRS) of France, and the University of

Hawaii. This research used the facilities of the Canadian Astronomy Data Centre operated by the National Research Council of Canada with the support of the Canadian Space Agency. CFHTLenS data processing was made possible thanks to significant computing support from the NSERC Research Tools and Instruments grant program. JHD and LvW are funded by the NSERC and Canadian Institute for Advanced Research Cifar; DM and PC acknowledge support from the Science and Technology Facilities Council (grant numbers ST/L000652/1; LR and PV receive support from the French Agence Nationale de la Recherche under Grant ANR-12-BS05-0002; PB acknowledges partial support from the European Union FP7 ITN INVISIBLES (Marie Curie Actions, PITN- GA-2011- 289442) and from the Agence Nationale de la Recherche under contract ANR 2010 BLANC 0413 01.

REFERENCES

- Asaba S., Hikage C., Koyama K., Zhao G.-B., Hojjati A. & Pogosian L., JCAP, 2013, 08, 029
 Baldi M., 2014, PDU, 3, 4
 Bean R., Bernat D., Pogosian L., Silvestri A. & Trodden M., 2007, PRD, 75, 064020
 Benjamin, J., van Waerbeke L., Heymans C. et al., 2013, MNRAS, 431, 1547
 Bernardeau F., Colombi S., Gaztanaga E. & Scoccimarro R., 2002, Phys. Rep. 367, 1
 Bertschinger E., 2006, ApJ, 648, 797
 Bird S., Viel M. & Haehnelt M. G. 2012, MNRAS, 420, 2551

- Brax P., van de Bruck C., Davis A.-C., Li B., Schmauch B. et al., 2011, PRD, 84, 123524
- Brax P., Davis A.-C. & Li B., 2012, PhLB, 715, 38B
- Brax P., Davis A.-C., Li B., Winther H. A. & Zhao G.-B., 2012, JCAP, 10, 002
- Brax P., C. van de Bruck, Davis A. C. & Shaw D.J., 2008, PRD, 78, 104021
- Brax P., Davis A.-C. & Li B., 2012, PRD, 86, 044015
- Brax P. & Valageas P., 2013, PRD, 88, 023527
- Brax P. & Valageas P., 2014, PRD, 90, 023507
- Brax P. & Valageas P., 2014, PRD, 90, 023508
- Buchdahl H. A., 1970, MNRAS, 150, 1
- Carlioni S., Dunsby P. & Troisi A., 2008, PRD, 77, 024024
- Chiba T., 2003, PhLB, 575, 1
- Clifton T., Ferreira P. G., Padilla A. & Skordis C., 2012, Phys. Rep., 513, 1, 1
- Damour T. & Polyakov A. M., 1994, Nucl. Phys. B, 423, 532
- Erben T., Hildebrandt H., Miller L. et al. 2013, MNRAS, 433, 2545
- Guzzo L. et al., 2008, Nature, 451, 541
- Hall A., Bonvin C. & Challinor A., 2013, PRD, 87, 064026
- Hammami A., Llinares C., Mota D. F. & Winther, H. A., 2015, Arxiv e-prints, 1503.02004
- Harnois-Déraps J. & van Waerbeke L., 2015, MNRAS, 450, 2857
- Harnois-Déraps J., van Waerbeke L., Viola M. & Heymans C., 2015, MNRAS, 450, 1212
- Heitmann K., Lawrence E., Kwan J., Habib S. & Higdon D., 2013, arXiv e-prints, 1304.7849
- Heavens A. F., Kitching T.D. & Verde L., 2007, MNRAS, 380, 1029
- Heymans C., van Waerbeke L., Miller L. et al., 2012, MNRAS, 427, 146
- Heymans C., Groot E., Heavens A. F. et al., 2013, MNRAS, 432, 2433
- Hildebrandt H., Erben T., Kuijken K. et al., 2012, MNRAS, 421, 2355
- Hinshaw G., Larson D., Komatsu E. et al., 2013, ApJ, 208, 19
- Hinterbichler K. & Khoury J., 2010, PRL, 104, 231301
- Hu W. & Sawicki I., 2007, PRD, 76, 064004
- Jain B. & Zhang P., 2008, PRD, 78, 063503
- Jennings E., Baugh C. M., Li B., Zhao G.-B. & Koyama K., 2012, arXiv:1205.2698
- Johnson, A., Blake, C., Dossett, J., Koda, J., Parkinson, D. & Joudaki, S., 2015, eprint arXiv:1504.06885
- Johnson A., Blake C., Koda J., Ma Y.-Z. et al., 2014, MNRAS, 444, 3926
- Joyce A., Jain B., Khoury J. & Trodden M., arXiv:1407.0059
- Kilbinger M., Fu L., Heymans C. et al. 2013, MNRAS, 430, 2200
- Koivisto T., 2006, PRD, 73, 083517
- Koyama K., Taruya A. & Hiramoto T., 2009, PRD, 79, 123512
- Leonard D., Baker T. & Ferreira P. G., arXiv:1501.03509
- Lewis A., Challinor A. & Lasenby A., 2000, ApJ, 538, 473
- Li Y. & Hu W., 2011, PRD, 84, 084033
- Li B., Hellwing W.A., Koyama K., Zhao G.-B., Jennings E. & Baugh C. M., 2013, MNRAS, 428, 743
- Li B., Zhao G.-B. & Koyama K., 2012, MNRAS, 421, 3481
- Llinares C. & Mota D. F., 2013, PRL, 110, 151104
- Lombriser L., Slosar A., Seljak U. & Hu W., arXiv e-prints, 1003.3009
- Lombriser L., Koyama K., Zhao G.-B. & Li B., 2012, PRD, 85, 124054
- Lombriser L., Li B., Koyama K. & Zhao G.-B., 2013, PRD, 87, 123511
- MacCrann N., Zuntz J., Bridle S., Jain B. & Becker M. R., arXiv e-prints, 1408.4742
- Miller L., Heymans C., Kitching T. D. et al. 2013, MNRAS, 429, 2858
- Motohashi H., Starobinsky A. & Yokoyama J., 2009, Int. J. Mod. Phys. D, 18, 1731
- Munshi D., van Waerbeke L., Smidt J. & Coles P., 2012, MNRAS, 419, 536
- Natarajan A., Zentner A. R., Battaglia N. & Trac H., 2014, arXiv e-prints, 1405.6205
- Nunez A. & Solganik S., arXiv eprints (hep-th), 0403159
- Olive K.A. & Pospelov M., 2008, PRD, 77, 043524
- Oyaizu H., Lima M. & Hu W., 2008, PRD, 78, 123524
- Perlmutter S. et al., 1999, ApJ, 517, 565
- Pietroni M., 2005, PRD, 72, 043535
- Planck Collaboration, 2015, arXiv e-prints, 1502.01589
- Pogosian L. & Silvestri A., 2008, PRD, 77, 023503
- Riess A. G. et al., 1998, Astron J., 116, 1009
- Sato M., Hamana T., Takahashi R. et al., 2009, ApJ, 701, 945
- Schaye, J. et al., 2010, MNRAS, 402, 1536
- Schmidt F., 2008, PRD, 78, 3002
- Semboloni E., Hoekstra H., Schaye J., van Daalen M. P. & McCarthy I. G., 2011, MNRAS, 417, 2020
- Simpson F., Heymans C., Parkinson D., Blake C. et al., 2013, MNRAS, 429, 2249
- Song Y.-S., Hu W. & Sawicki I., 2007, PRD, 75, 044004
- Song Y.-S., Peiris H. & Hu W., 2007, PRD, 76, 063517
- Starobinsky A. A., 1980, PhLB, 91, 99
- Starobinsky A. A., 2007, JETP Lett., 86, 157
- Taddei L., Catena R. & Pietroni M., arXiv e-prints, 1310.6175
- Takahashi R., Sato M., Nishimichi T., Taruya A. & Oguri M., 2012, ApJ, 761, 152
- Tsujikawa S., 2007, PRD, 76, 023514
- Tsujikawa S. & Tatekawa T., 2008, PhLB, 665, 325
- Valageas P. & Nishimichi T., 2011, A&A, 527, A87
- Valageas P., Nishimichi T. & Taruya A., 2013, PRD, 87, 083522
- Valageas P., 2013, PRD, 88, 083524
- van Daalen M. P., Schaye J., Booth C. M. & Dalla Vecchia C., 2011, MNRAS, 415, 3649
- Wilcox H., Bacon D., Nichol R. C., Rooney P. J., Terukina A. et al., 2015, arXiv e-prints, 1504.03937
- Zhao G.-B., 2014, ApJS, 211, 23
- Zhang P., 2006, PRD, 73, 123504
- Zentner A. R., Semboloni E., Dodelson S., Eifler T., Krause E. & Hearin A. P., 2013, PRD, 87, 043509

APPENDIX: Details on the Theoretical Modelling of $P(k)$ in Modified Gravity Scenarios

This Appendix discusses the construction strategy of the matter density power spectrum $P(k; z)$ in the presence of $f(R)$ or Dilaton modifications to General Relativity; full details are provided in the references contained herein.

1 Two-halo term: $P_{2H}(k)$

The power spectrum analytical prediction is constructed from a halo model approach, following equation (42). The two-halo term, which dominates on large scales, is computed from a Lagrangian-space resummation of standard perturbation theory that is exact up to order P_L^2 and contains partial resummations of higher order terms. It is also supplemented with non-perturbative contributions that take into

account some aspects of shell crossing and ensure that all particle pairs are counted only once in the sum. Within this framework, the large-scale term $P_{2H}(k)$ essentially contains no free parameter. It can therefore be computed in Λ CDM and modified-gravity scenarios by using perturbation theory up to order P_L^2 (which requires going to order δ_L^3 in terms of the density field itself).

In the case of the Λ CDM cosmology, this perturbative expansion follows the standard approach (Bernardeau, Colombi, Gaztanaga & Scoccimarro 2002), where the density and velocity fields are written as perturbative expansions over powers of the linear density field δ_L ; subsequent orders are computed by substituting into the continuity and Euler-Poisson equations. In the case of the modified-gravity scenarios considered in this paper, we follow the same approach but require an additional expansion to write the fifth force in terms of the non-linear density fluctuations. Indeed, using the quasi-static approximation, we can relate the scalar field φ to the matter density field ρ , typically through a non-linear Klein-Gordon equation. Then, we can solve for φ as an expansion over the non-linear density fluctuations $\delta\rho$. This allows us to obtain both the Newtonian potential and the fifth-force potential as functionals of the non-linear matter density fluctuations. However, while the Newtonian potential is given by the linear Poisson equation, the fifth-force potential is usually given by a non-linear equation that involves new time and scale dependences. In terms of the diagrammatic expansion of the non-linear power spectrum $P(k)$ over $P_L(k)$, this implies that the linear propagators and the vertices are modified with new diagrams associated with the new non-linearity of the modified Poisson equation. See Brax & Valageas (2013) for more explanations.

2 One-halo term: $P_{1H}(k)$

The one-halo term is obtained from the halo mass function and the halo density profile, with the addition of a counter-term first introduced in Valageas & Nishimichi (2011) that arises from mass conservation. This also ensures that $P_{1H}(k)$ decays at low k and becomes subdominant as compared with $P_{2H}(k)$, whereas the usual formulation gives a spurious white-noise tail that dominates on very large scales. We take into account the impact of modified gravity through its effect on the halo mass function (i.e., through the acceleration or slowing down of the spherical collapse), but neglect the impact on the halo shape and profile. This should be sufficient for our purposes, because we only consider cosmologies that remain close to the Λ CDM reference, and these modified gravity models have a much stronger impact on the halo mass function, especially on its large-mass tail, than on the halo profile. As shown in Valageas (2013), at $z = 0$, a 10% change to the mass-concentration relation only yields a 2% change of $P(k)$ at $1h\text{Mpc}^{-1}$, whereas a 10% change to the halo mass function yields a 2% change of $P(k)$ at $0.35h\text{Mpc}^{-1}$ and a 7.5% change at $1h\text{Mpc}^{-1}$. Generally, the concentration parameter always remains in the range 3 – 10 for typical halos and does not vary by much more than 10% for realistic scenarios, whereas the mass function at $M \sim 5 \times 10^{14} h^{-1} M_\odot$ can vary by more than 50% (Lombriser, Koyama, Zhao & Li 2012; Lombriser, Li, Koyama & Zhao 2013). The interior of haloes are mostly affected by screening anyway, further justifying this approximation.

3 Comparison with numerical simulations

The modelling described above for the matter density power spectrum has been checked in details against numerical simulations in Valageas, Nishimichi & Taruya (2013) for Λ CDM cosmologies, and in Brax & Valageas (2013) for the class of modified gravity models that we consider in this paper. In the case of Λ CDM, it provides

an accuracy of 2% up to comoving wavenumber $k \sim 0.9h\text{Mpc}^{-1}$, and 15% up to $k = 15h\text{Mpc}^{-1}$ down to $z = 0.35$. In terms of the real-space correlation function, this translates into an accuracy of 5% down to the comoving scale $r = 0.15h^{-1}\text{Mpc}$. For the $f(R)$ theories, it is able to reproduce very well the deviations from the Λ CDM scenarios up to $k = 3h\text{Mpc}^{-1}$ (the highest wave number available from the simulations) at $z = 0$, for $|f_{R0}| = 10^{-4}, 10^{-5}$, and 10^{-6} . In particular, it accurately captures the relative effect on the power compared to the Λ CDM reference due to the non-linear Chameleon mechanism. For the Dilaton models, the agreement with the numerical simulations depends somewhat on the model parameters but it typically gives a good quantitative estimate of the deviations from Λ CDM up to $k = 5h\text{Mpc}^{-1}$ (the highest wave number available from the simulations). When there is a noticeable departure from the simulations, it corresponds to an underestimation of the amplification of the power spectrum at $k \gtrsim 2h\text{Mpc}^{-1}$, which may be due to our neglect of the impact of modified gravity on the halo concentration parameter. Therefore, in such cases our approach provides a conservative estimate of the deviations from Λ CDM. Again, this modelling is able to capture the decrease of the deviations from the Λ CDM reference due to the non-linear Damour-Polyakov mechanism.

Article E

Nonzero Density-Velocity Consistency Relations for Large Scale Structures

Nonzero Density-Velocity Consistency Relations for Large Scale Structures

Luca Alberto Rizzo,^{1,2,3} David F. Mota,³ and Patrick Valageas^{1,2}

¹*Institut de Physique Théorique, CEA, IPhT, F-91191 Gif-sur-Yvette, Cédex, France*

²*Institut de Physique Théorique, CNRS, URA 2306, F-91191 Gif-sur-Yvette, Cédex, France*

³*Institute of Theoretical Astrophysics, University of Oslo, 0315 Oslo, Norway*

(Received 12 June 2016; published 15 August 2016)

We present exact kinematic consistency relations for cosmological structures that do not vanish at equal times and can thus be measured in surveys. These rely on cross correlations between the density and velocity, or momentum, fields. Indeed, the uniform transport of small-scale structures by long-wavelength modes, which cannot be detected at equal times by looking at density correlations only, gives rise to a shift in the amplitude of the velocity field that could be measured. These consistency relations only rely on the weak equivalence principle and Gaussian initial conditions. They remain valid in the nonlinear regime and for biased galaxy fields. They can be used to constrain nonstandard cosmological scenarios or the large-scale galaxy bias.

DOI: 10.1103/PhysRevLett.117.081301

Introduction.—Cosmological structures can be described on large scales by perturbative methods while smaller scales are described by phenomenological models or studied with numerical simulations. This makes it difficult to obtain accurate predictions on the full range of scales probed by galaxy or weak lensing surveys. Moreover, if we consider galaxy density fields, theoretical predictions remain sensitive to the galaxy bias (galaxies do not exactly follow the matter density field), which involves some phenomenological modeling of star formation.

This makes exact analytical results that go beyond low-order perturbation theory and apply to biased tracers very rare. However, such exact results have recently been obtained [1–9] in the form of “kinematic consistency relations.” They relate the $(\ell + n)$ -density (or velocity divergence) correlations, with ℓ large-scale wave numbers and n small-scale wave numbers, to the n -point small-scale correlation. These relations, obtained at the leading order over the large-scale wave numbers, arise from the equivalence principle. It ensures that small-scale structures respond to a large-scale perturbation (which at leading order corresponds to a constant gravitational force over the extent of the small-sized object) by a uniform displacement. Therefore, these relations express a kinematic effect that vanishes for equal-time statistics, as a uniform displacement has no impact on the statistical properties of the density field observed at a given time.

In practice, it is difficult to measure different-time correlations and it is useful to obtain relations that remain nonzero at equal times. This is possible by going to the next order and taking into account tidal effects, which at their leading order are given by the response of small-scale structures to a change of the background density. However, in order to derive expressions that apply to our Universe one needs to introduce some additional approximations [10–12].

In this Letter, we show that it is possible to derive exact kinematic consistency relations that do not vanish at equal times by considering cross correlations between the density and velocity, or momentum, fields. Indeed, the uniform displacement due to the long-wavelength mode also gives rise to a shift in the amplitude of the velocity field that does not vanish at equal times and can thus be observed. These consistency relations have the same degree of validity as the previously derived density (or velocity divergence) relations and only rely on the weak equivalence principle and Gaussian initial conditions.

Correlation and response functions.—The consistency relations that apply to large-scale structures assume that the system is fully defined by Gaussian initial conditions (the primordial fluctuations that are found at the end of the inflationary epoch). Thus, the dynamics is fully determined by the Gaussian linear matter growing mode $\delta_{L0}(\mathbf{x})$ (which we normalize today as usual) that directly maps the initial conditions and can be observed on very large linear scales. Then, any dependent quantities $\{\rho_1, \dots, \rho_n\}$, such as the dark matter or galaxy densities at space-time positions (\mathbf{x}_i, τ_i) , are functionals of the field $\delta_{L0}(\mathbf{x})$ and we can write the mixed correlation functions over δ_{L0} and $\{\rho_i\}$ as Gaussian averages,

$$\begin{aligned} C^{1,n}(\mathbf{x}) &= \langle \delta_{L0}(\mathbf{x}) \rho_1 \dots \rho_n \rangle \\ &= \int \mathcal{D}\delta_{L0} e^{-\delta_{L0} C_{L0}^{-1} \delta_{L0} / 2} \delta_{L0}(\mathbf{x}) \rho_1 \dots \rho_n, \end{aligned} \quad (1)$$

where $C_{L0}(\mathbf{x}_1, \mathbf{x}_2) = \langle \delta_{L0}(\mathbf{x}_1) \delta_{L0}(\mathbf{x}_2) \rangle$ is the two-point correlation function of the Gaussian field δ_{L0} . Integrating by parts over δ_{L0} gives

$$C^{1,n}(\mathbf{x}) = \int d\mathbf{x}' C_{L0}(\mathbf{x}, \mathbf{x}') R^{1,n}(\mathbf{x}'), \quad (2)$$

where we introduced the mean response function

$$R^{1,n}(\mathbf{x}) = \left\langle \frac{\mathcal{D}[\rho_1 \dots \rho_n]}{\mathcal{D}\tilde{\delta}_{L0}(\mathbf{x})} \right\rangle. \quad (3)$$

Equation (2) describes how the mixed correlation (1) between the initial Gaussian field δ_{L0} and the dependent quantities $\{\rho_i\}$ is related to the response function of the latter to this Gaussian field. Going to Fourier space, which we denote with a tilde, with the normalizations $\delta_{L0}(\mathbf{x}) = \int d\mathbf{k} e^{i\mathbf{k}\cdot\mathbf{x}} \tilde{\delta}_{L0}(\mathbf{k})$ and $\langle \tilde{\delta}_{L0}(\mathbf{k}_1) \tilde{\delta}_{L0}(\mathbf{k}_2) \rangle = P_{L0}(k_1) \delta_D(\mathbf{k}_1 + \mathbf{k}_2)$, Eq. (2) gives

$$\tilde{C}^{1,n}(\mathbf{k}) = P_{L0}(k) \tilde{R}^{1,n}(-\mathbf{k}), \quad (4)$$

where we defined the Fourier-space correlation and response functions as

$$\tilde{C}^{1,n}(\mathbf{k}) = \langle \tilde{\delta}_{L0}(\mathbf{k}) \rho_1 \dots \rho_n \rangle, \quad \tilde{R}^{1,n}(\mathbf{k}) = \left\langle \frac{\mathcal{D}[\rho_1 \dots \rho_n]}{\mathcal{D}\tilde{\delta}_{L0}(\mathbf{k})} \right\rangle.$$

Consistency relations for the density contrast.—If we consider the quantities $\{\rho_i\}$ to be the nonlinear matter density contrasts $\tilde{\delta}(\mathbf{k}_i, \tau_i)$ at wave number \mathbf{k}_i and conformal time τ_i , Eq. (4) is written as

$$\begin{aligned} & \langle \tilde{\delta}_{L0}(\mathbf{k}') \tilde{\delta}(\mathbf{k}_1, \tau_1) \dots \tilde{\delta}(\mathbf{k}_n, \tau_n) \rangle \\ &= P_{L0}(k') \left\langle \frac{\mathcal{D}[\tilde{\delta}(\mathbf{k}_1, \tau_1) \dots \tilde{\delta}(\mathbf{k}_n, \tau_n)]}{\mathcal{D}\tilde{\delta}_{L0}(-\mathbf{k}')} \right\rangle. \end{aligned} \quad (5)$$

On large scales the density field is within the linear regime, $\tilde{\delta}(\mathbf{k}', \tau') \rightarrow D_+(\tau') \tilde{\delta}_{L0}(\mathbf{k}')$; then for $k' \rightarrow 0$,

$$\begin{aligned} & k' \rightarrow 0: \langle \tilde{\delta}(\mathbf{k}', \tau') \tilde{\delta}(\mathbf{k}_1, \tau_1) \dots \tilde{\delta}(\mathbf{k}_n, \tau_n) \rangle \\ &= D_+(\tau') P_{L0}(k') \left\langle \frac{\mathcal{D}[\tilde{\delta}(\mathbf{k}_1, \tau_1) \dots \tilde{\delta}(\mathbf{k}_n, \tau_n)]}{\mathcal{D}\tilde{\delta}_{L0}(-\mathbf{k}')} \right\rangle. \end{aligned} \quad (6)$$

This relation can serve as a basis to derive consistency relations for the squeezed limit of the $n+1$ density correlations (i.e., the limit $k' \rightarrow 0$) if we obtain an explicit expression for the response function in the right-hand side. It turns out that this is possible because the response of the matter distribution to a long-wavelength mode $\tilde{\delta}_{L0}(\mathbf{k}')$ takes a simple form in the limit $k' \rightarrow 0$ [1–3]. Such a change $\Delta\delta_{L0}$ of the initial condition is associated with a change of both the linear density and velocity fields, because we change the linear growing mode where the density and velocity fields are coupled [1],

$$\begin{aligned} \delta_L(\mathbf{q}, \tau) &\rightarrow \hat{\delta}_L = \delta_L + D_+(\tau) \Delta\delta_{L0}, \\ \mathbf{v}_L(\mathbf{q}, \tau) &\rightarrow \hat{\mathbf{v}}_L = \mathbf{v}_L - \frac{dD_+}{d\tau} \nabla_{\mathbf{q}}^{-1} \Delta\delta_{L0}. \end{aligned} \quad (7)$$

Then, in the limit $k' \rightarrow 0$ for the support of $\Delta\delta_{L0}(\mathbf{k}')$, the trajectories of the particles are simply modified as [7]

$$\mathbf{x}(\mathbf{q}, \tau) \rightarrow \hat{\mathbf{x}}(\mathbf{q}, \tau) = \mathbf{x}(\mathbf{q}, \tau) + D_+(\tau) \Delta\Psi_{L0}(\mathbf{q}), \quad (8)$$

where \mathbf{q} is the Lagrangian coordinate of the particles and Ψ_{L0} is the linear displacement field,

$$\Delta\Psi_{L0} = -\nabla_{\mathbf{q}}^{-1} \Delta\delta_{L0}, \quad \mathbf{x}_L(\mathbf{q}, \tau) = \mathbf{q} + \Psi_L. \quad (9)$$

The transformation (8) simply means that in the limit $k' \rightarrow 0$ smaller-scale structures are displaced by the uniform translation Ψ_{L0} as all particles fall at the same rate in the additional constant force field $\Delta\mathbf{F} \propto \nabla_{\mathbf{q}}^{-1} \Delta\delta_{L0}$. In other words, in the limit $k' \rightarrow 0$ we add an almost constant force perturbation (i.e., a change of the gravitational potential that is linear over \mathbf{q} for small-scale subsystems) that gives rise to a uniform displacement, thanks to the weak equivalence principle [3,7]. Then, the density field $\delta(\mathbf{x}, \tau)$ at time τ is merely displaced by the shift $D_+(\tau) \Delta\Psi_{L0}$, which gives in Fourier space

$$\begin{aligned} \tilde{\delta}(\mathbf{k}, \tau) &\rightarrow \hat{\tilde{\delta}}(\mathbf{k}, \tau) = \tilde{\delta}(\mathbf{k}, \tau) e^{-i\mathbf{k}\cdot D_+(\tau) \Delta\Psi_{L0}} \\ &= \tilde{\delta}(\mathbf{k}, \tau) - iD_+(\mathbf{k}\cdot\Delta\Psi_{L0}) \tilde{\delta}(\mathbf{k}, \tau), \end{aligned} \quad (10)$$

where in the last expression we expanded up to linear order over $\Delta\Psi_{L0}$. The reader may note that in Eq. (10) we do not see the additive effect seen at the linear level in the first Eq. (7). This is because although the small change of the mean overdensity over a small structure also leads to a faster (or slower) collapse and distorts the small-scale clustering, this is a higher-order effect than the kinematic effect studied in this Letter [10,11]. Indeed, we check in Eqs. (11) and (12) that this kinematic effect gives rise to factors $\sim 1/k'$ that diverge as $k' \rightarrow 0$. This is because the linear displacement field is proportional to the inverse gradient of the linear density field, $\Psi_L = -\nabla_{\mathbf{q}}^{-1} \delta_L$. In contrast, the distortions of the small-scale structure (i.e., changes to the shape and amplitude of the small-scale clustering) are higher-order effects and do not exhibit this factor $1/k'$ [10,11]. Using the expression $\Psi_{L0}(\mathbf{q}) = \int d\mathbf{k} e^{i\mathbf{k}\cdot\mathbf{q}} i(\mathbf{k}/k^2) \tilde{\delta}_{L0}(\mathbf{k})$, we obtain

$$\begin{aligned} k' \rightarrow 0: \quad & \frac{\mathcal{D}\Psi_{L0}(\mathbf{q})}{\mathcal{D}\tilde{\delta}_{L0}(\mathbf{k}')} = i \frac{\mathbf{k}'}{k'^2}, \\ & \frac{\mathcal{D}\tilde{\delta}(\mathbf{k})}{\mathcal{D}\tilde{\delta}_{L0}(\mathbf{k}')} = D_+ \frac{\mathbf{k}\cdot\mathbf{k}'}{k'^2} \tilde{\delta}(\mathbf{k}). \end{aligned} \quad (11)$$

Using this result in the relation (6) gives

$$\begin{aligned} & \langle \tilde{\delta}(\mathbf{k}', \tau') \tilde{\delta}(\mathbf{k}_1, \tau_1) \dots \tilde{\delta}(\mathbf{k}_n, \tau_n) \rangle'_{k' \rightarrow 0} \\ &= -P_L(k', \tau') \\ & \times \langle \tilde{\delta}(\mathbf{k}_1, \tau_1) \dots \tilde{\delta}(\mathbf{k}_n, \tau_n) \rangle' \sum_{i=1}^n \frac{D_+(\tau_i) \mathbf{k}_i \cdot \mathbf{k}'}{D_+(\tau') k'^2}, \end{aligned} \quad (12)$$

which is the density consistency relation in the subhorizon Newtonian regime [1–9]. Here the prime in $\langle \dots \rangle'$ denotes

that we removed the Dirac factors $\delta_D(\sum \mathbf{k}_i)$. The remarkable property of Eq. (12) is that it does not require the wave numbers \mathbf{k}_i to be in the linear or perturbative regimes. In particular, it still applies when \mathbf{k}_i are in the highly nonlinear regime governed by shell-crossing effects and affected by baryonic and galactic processes such as star formation and cooling. In fact, under the approximation of the squeezed limit, the long-wavelength fluctuation $\tilde{\delta}_{L0}(\mathbf{k}')$ merely transports the small-scale structure of the system. This also leads to another key property of Eq. (12), namely, that it vanishes at equal times, $\tau_1 = \dots = \tau_n$.

Consistency relations for velocity and momentum fields.—The leading-order effect of a long-wavelength perturbation is to move smaller structures by a uniform shift and single-time statistics that only probe the density field cannot see any effect. However, it is clear that we may detect an effect if we consider the velocity field, as the latter

is again displaced but also has its amplitude modified. Thus, the transformation law (10) becomes

$$\tilde{\mathbf{v}}(\mathbf{k}, \tau) \rightarrow \hat{\tilde{\mathbf{v}}}(\mathbf{k}, \tau) = \tilde{\mathbf{v}}(\mathbf{k}, \tau) - iD_+(\mathbf{k} \cdot \Delta\Psi_{L0})\tilde{\mathbf{v}}(\mathbf{k}, \tau) + \frac{dD_+}{d\tau}\Delta\Psi_{L0}\delta_D(\mathbf{k}), \quad (13)$$

where the last factor is the new term, as compared with Eq. (10), that is associated with the shift of the amplitude. This yields

$$k' \rightarrow 0: \frac{\mathcal{D}\tilde{\mathbf{v}}(\mathbf{k})}{\mathcal{D}\tilde{\delta}_{L0}(\mathbf{k}')} = D_+ \frac{\mathbf{k} \cdot \mathbf{k}'}{k'^2} \tilde{\mathbf{v}}(\mathbf{k}) + \frac{dD_+}{d\tau} i \frac{\mathbf{k}'}{k'^2} \delta_D(\mathbf{k}). \quad (14)$$

Using again the general relation (4), as in Eq. (6) but where the quantities $\{\rho_1, \dots, \rho_n\}$ are a combination of density contrasts and velocities, we obtain

$$\begin{aligned} \left\langle \tilde{\delta}(\mathbf{k}', \tau') \prod_{j=1}^n \tilde{\delta}(\mathbf{k}_j, \tau_j) \prod_{j=n+1}^{n+m} \tilde{\mathbf{v}}(\mathbf{k}_j, \tau_j) \right\rangle'_{k' \rightarrow 0} &= -P_L(k', \tau') \left\langle \left\langle \prod_{j=1}^n \tilde{\delta}(\mathbf{k}_j, \tau_j) \prod_{j=n+1}^{n+m} \tilde{\mathbf{v}}(\mathbf{k}_j, \tau_j) \right\rangle' \sum_{i=1}^{n+m} \frac{D_+(\tau_i)}{D_+(\tau')} \frac{\mathbf{k}_i \cdot \mathbf{k}'}{k'^2} \right. \\ &+ \sum_{i=n+1}^{n+m} \left\langle \prod_{j=1}^n \tilde{\delta}(\mathbf{k}_j, \tau_j) \prod_{j=n+1}^{i-1} \tilde{\mathbf{v}}(\mathbf{k}_j, \tau_j) \right. \\ &\left. \times \left[\frac{(dD_+/d\tau)(\tau_i)}{D_+(\tau')} i \frac{\mathbf{k}'}{k'^2} \delta_D(\mathbf{k}_i) \right] \prod_{j=i+1}^{n+m} \tilde{\mathbf{v}}(\mathbf{k}_j, \tau_j) \right\rangle' \left. \right\rangle. \quad (15) \end{aligned}$$

If we take $\mathbf{k}_i \neq 0$, as usual for studies of Fourier-space polyspectra, the last term vanishes and we recover the same form as for the consistency relation (12) of the density field. However, this new Dirac term gives a nonzero contribution in configuration space. Therefore, real-space correlation functions obey consistency relations that differ from those of the density field if we include cross correlations with the velocity field. The correlation functions in Eq. (15) are 3^m -component quantities, as the velocity field is a 3-component vector. One may obtain scalar relations by taking for instance the divergence of the velocity field or considering the components along Cartesian coordinates. The divergence $\theta = \nabla \cdot \mathbf{v}$ was considered in [2,5]. We recover the fact that it obeys relations similar to the density field because the new Dirac term $\delta_D(\mathbf{k}_i)$ disappears as $\tilde{\theta}_i = i\mathbf{k}_i \cdot \tilde{\mathbf{v}}_i$. We rather focus on the divergence of the momentum field in this Letter, as it yields new terms in the consistency relations and it satisfies a direct relationship with the density field, which may provide useful checks.

One simple way to make the last term in Eq. (13) relevant in Fourier space at nonzero wave numbers is to consider composite operators, that is, products of the velocity field with other fields. Therefore, we define the momentum \mathbf{p} as

$$\mathbf{p} = (1 + \delta)\mathbf{v}, \quad (16)$$

which reads in Fourier space as

$$\tilde{\mathbf{p}}(\mathbf{k}) = \tilde{\mathbf{v}}(\mathbf{k}) + \int d\mathbf{k}_1 d\mathbf{k}_2 \delta_D(\mathbf{k}_1 + \mathbf{k}_2 - \mathbf{k}) \tilde{\delta}(\mathbf{k}_1) \tilde{\mathbf{v}}(\mathbf{k}_2). \quad (17)$$

Using Eqs. (11) and (14) we obtain

$$k' \rightarrow 0: \frac{\mathcal{D}\tilde{\mathbf{p}}(\mathbf{k})}{\mathcal{D}\tilde{\delta}_{L0}(\mathbf{k}')} = D_+ \frac{\mathbf{k} \cdot \mathbf{k}'}{k'^2} \tilde{\mathbf{p}}(\mathbf{k}) + \frac{dD_+}{d\tau} i \frac{\mathbf{k}'}{k'^2} [\delta_D(\mathbf{k}) + \tilde{\delta}(\mathbf{k})]. \quad (18)$$

The first term, which is common with Eqs. (11) and (14), corresponds to the translation of the system, whereas the second term corresponds to the additional velocity generated by the long-wavelength mode. Thanks to the convolution in Eq. (17) it is now nonzero for $\mathbf{k} \neq 0$. However, in contrast to the translation term, it transforms the field because the functional derivative of the momentum $\tilde{\mathbf{p}}$ now gives rise to a factor that is proportional to the density contrast $\tilde{\delta}$. In a fashion similar to Eqs. (12) and (15), we obtain the consistency relation

$$\begin{aligned}
\left\langle \tilde{\delta}(\mathbf{k}', \tau') \prod_{j=1}^n \tilde{\delta}(\mathbf{k}_j, \tau_j) \prod_{j=n+1}^{n+m} \tilde{\mathbf{p}}(\mathbf{k}_j, \tau_j) \right\rangle'_{k' \rightarrow 0} &= -P_L(k', \tau') \left\langle \left\langle \prod_{j=1}^n \tilde{\delta}(\mathbf{k}_j, \tau_j) \prod_{j=n+1}^{n+m} \tilde{\mathbf{p}}(\mathbf{k}_j, \tau_j) \right\rangle' \sum_{i=1}^{n+m} \frac{D_+(\tau_i) \mathbf{k}_i \cdot \mathbf{k}'}{D_+(\tau')} \frac{1}{k'^2} \right. \\
&+ \sum_{i=n+1}^{n+m} \frac{(dD_+/d\tau)(\tau_i)}{D_+(\tau')} \left\langle \prod_{j=1}^n \tilde{\delta}(\mathbf{k}_j, \tau_j) \prod_{j=n+1}^{i-1} \tilde{\mathbf{p}}(\mathbf{k}_j, \tau_j) \right. \\
&\left. \left. \times \left(i \frac{\mathbf{k}'}{k'^2} [\delta_D(\mathbf{k}_i) + \tilde{\delta}(\mathbf{k}_i, \tau_i)] \right) \prod_{j=i+1}^{n+m} \tilde{\mathbf{p}}(\mathbf{k}_j, \tau_j) \right\rangle' \right\rangle. \quad (19)
\end{aligned}$$

The first term, which has the same form as the density and velocity consistency relations (12) and (15), is due to the translation of smaller-scale structures by the long-wavelength mode k' . The new second term is due to the additional velocity and arises from the second term in Eq. (18). This term has a different form as it transforms one small-scale momentum mode, $\tilde{\mathbf{p}}(\mathbf{k}_i)$, into a small-scale density mode, $\tilde{\delta}(\mathbf{k}_i)$. Moreover, this new term no longer automatically vanishes at equal times. This leads to a nontrivial consistency relation at equal times, when $\tau' = \tau_1 = \dots = \tau_{n+m}$,

$$\left\langle \tilde{\delta}(\mathbf{k}') \prod_{j=1}^n \tilde{\delta}(\mathbf{k}_j) \prod_{j=n+1}^{n+m} \tilde{\mathbf{p}}(\mathbf{k}_j) \right\rangle'_{k' \rightarrow 0} = -iP_L(k') \frac{d \ln D_+}{d\tau} \sum_{i=n+1}^{n+m} \left\langle \prod_{j=1}^n \tilde{\delta}(\mathbf{k}_j) \prod_{j=n+1}^{i-1} \tilde{\mathbf{p}}(\mathbf{k}_j) \left(\frac{\mathbf{k}'}{k'^2} [\delta_D(\mathbf{k}_i) + \tilde{\delta}(\mathbf{k}_i)] \right) \prod_{j=i+1}^{n+m} \tilde{\mathbf{p}}(\mathbf{k}_j) \right\rangle', \quad (20)$$

where we did not write the common time τ of all fields. We can also obtain a consistency relation that involves both the density and velocity fields $\tilde{\delta}$ and $\tilde{\mathbf{v}}$, together with the momentum field $\tilde{\mathbf{p}}$, and it shows the same behaviors.

To obtain a scalar quantity from the momentum field \mathbf{p} we consider its divergence,

$$\lambda \equiv \nabla \cdot [(1 + \delta)\mathbf{v}], \quad \tilde{\lambda}(\mathbf{k}) = i\mathbf{k} \cdot \tilde{\mathbf{p}}(\mathbf{k}). \quad (21)$$

Then, the consistency relation for the divergence $\tilde{\lambda}$ follows from Eq. (19). This gives

$$\begin{aligned}
\left\langle \tilde{\delta}(\mathbf{k}', \tau') \prod_{j=1}^n \tilde{\delta}(\mathbf{k}_j, \tau_j) \prod_{j=n+1}^{n+m} \tilde{\lambda}(\mathbf{k}_j, \tau_j) \right\rangle'_{k' \rightarrow 0} &= -P_L(k', \tau') \left\langle \left\langle \prod_{j=1}^n \tilde{\delta}(\mathbf{k}_j, \tau_j) \prod_{j=n+1}^{n+m} \tilde{\lambda}(\mathbf{k}_j, \tau_j) \right\rangle' \sum_{i=1}^{n+m} \frac{D_+(\tau_i) \mathbf{k}_i \cdot \mathbf{k}'}{D_+(\tau')} \frac{1}{k'^2} \right. \\
&- \sum_{i=n+1}^{n+m} \left\langle \tilde{\delta}(\mathbf{k}_i, \tau_i) \prod_{j=1}^n \tilde{\delta}(\mathbf{k}_j, \tau_j) \prod_{\substack{j=n+1 \\ j \neq i}}^{n+m} \tilde{\lambda}(\mathbf{k}_j, \tau_j) \right\rangle' \frac{(dD_+/d\tau)(\tau_i) \mathbf{k}_i \cdot \mathbf{k}'}{D_+(\tau')} \frac{1}{k'^2} \left. \right\rangle. \quad (22)
\end{aligned}$$

At equal times this gives the relation

$$\left\langle \tilde{\delta}(\mathbf{k}') \prod_{j=1}^n \tilde{\delta}(\mathbf{k}_j) \prod_{j=n+1}^{n+m} \tilde{\lambda}(\mathbf{k}_j) \right\rangle'_{k' \rightarrow 0} = P_L(k') \frac{d \ln D_+}{d\tau} \sum_{i=n+1}^{n+m} \frac{\mathbf{k}_i \cdot \mathbf{k}'}{k'^2} \left\langle \tilde{\delta}(\mathbf{k}_i) \prod_{j=1}^n \tilde{\delta}(\mathbf{k}_j) \prod_{\substack{j=n+1 \\ j \neq i}}^{n+m} \tilde{\lambda}(\mathbf{k}_j) \right\rangle', \quad (23)$$

where we did not write the common time τ of all fields. We can easily check the relation (22) by noticing that the divergence λ is related to the density field through the continuity equation, $(\partial\delta/\partial\tau) + \nabla \cdot [(1 + \delta)\mathbf{v}] = 0$, which implies $\lambda = -\partial\delta/\partial\tau$. Therefore, Eq. (22) can be directly obtained from the density consistency relation (12) by taking partial derivatives with respect to the times τ_j .

Applications.—As for the density contrast relation (12), the new consistency relations that we have obtained in this Letter are valid beyond the perturbative regime, after shell crossing, and also apply to baryons, gas, and galaxies, independently of the bias of the objects that are used.

Indeed, they only use the property (8), which states that at leading order the effect of a long-wavelength mode is to move smaller-scale structures without disturbing them. This relies on the equivalence principle, which states that all particles (and astrophysical objects) fall at the same rate in a gravitational potential well (the inertial mass is also the gravitational mass) [3,7,8].

After shell crossing we enter a multistreaming regime where the velocity field is multivalued: at a given position there are several streams with different velocities as they cross each other and build a nonzero velocity dispersion, as within virialized halos. Nevertheless, our results remain

valid. In that case, \mathbf{v} can be taken as any of these streams or as any given linear combination of them, because all stream velocities are modified in the same way. In multistreaming regions, such as high-density nonlinear environments like clusters or filaments, it is more practical to work with the mean momentum \mathbf{p} , where Eq. (16) reads in the case of several streams i as $\mathbf{p} = \sum_{\text{streams}} (1 + \delta_i) \mathbf{v}_i$, or in terms of a phase-space distribution function as $\mathbf{p} = \int d\mathbf{v} f(\mathbf{x}, \mathbf{v}) \mathbf{v}$. This is also more convenient for observational purposes as we only observe velocities where there is baryonic matter, so that it is easier to build momentum maps than velocity maps, which are difficult to measure in voids. The expression (18) remains valid in these multistreaming regions, as the first term simply expresses the translation of the smaller-scale system while the second term expresses the large-scale constant additive term that is added to all velocities. Thus, these consistency relations only rely on (1) Gaussian initial conditions [Eq. (4)]; (2) the weak equivalence principle [Eq. (8)]. Therefore, a detection of a violation would be a signature of non-Gaussian initial conditions or of a modification of gravity (or a fifth force). In practice, we also need to make sure the large-scale wave number k' is within the linear regime and far below the other wave numbers k_i , so that the limit $k' \rightarrow 0$ is reached.

The simplest relation that does not vanish at equal times is the bispectrum with one momentum field. From Eqs. (20) and (23) we obtain for $\mathbf{k} \neq 0$

$$\begin{aligned} \langle \tilde{\delta}(\mathbf{k}') \tilde{\delta}(\mathbf{k}) \tilde{\mathbf{p}}(-\mathbf{k}) \rangle'_{k' \rightarrow 0} &= -i \frac{\mathbf{k}' \cdot d \ln D_+}{k'^2 d\tau} P_L(k') P(k), \\ \langle \tilde{\delta}(\mathbf{k}') \tilde{\delta}(\mathbf{k}) \tilde{\lambda}(-\mathbf{k}) \rangle'_{k' \rightarrow 0} &= -\frac{\mathbf{k} \cdot \mathbf{k}' d \ln D_+}{k'^2 d\tau} P_L(k') P(k). \end{aligned}$$

Here $P(k)$ is the nonlinear density power spectrum and these relations remain valid in the nonperturbative nonlinear regime. For galaxies these relations are

$$\langle \tilde{\delta}(\mathbf{k}') \tilde{\delta}_g(\mathbf{k}) \tilde{\mathbf{p}}_g(-\mathbf{k}) \rangle'_{k' \rightarrow 0} = -i \frac{\mathbf{k}' \cdot d \ln D_+}{k'^2 d\tau} P_L(k') P_{\delta_g \delta_g}(k), \quad (24)$$

$$\langle \tilde{\delta}(\mathbf{k}') \tilde{\delta}_g(\mathbf{k}) \tilde{\lambda}_g(-\mathbf{k}) \rangle'_{k' \rightarrow 0} = -\frac{\mathbf{k} \cdot \mathbf{k}' d \ln D_+}{k'^2 d\tau} P_L(k') P_{\delta_g \delta_g}(k), \quad (25)$$

where $\tilde{\delta}$ and P_L are again the matter density field and linear power spectrum, $\tilde{\delta}_g$ and $\tilde{\mathbf{p}}_g$ the galaxy density contrast and momentum, and $P_{\delta_g \delta_g}$ the galaxy density power spectrum. In Eqs. (24) and (25) we kept the long mode k' as the matter

density contrast $\tilde{\delta}$ because the actual consistency relation is with respect to the initial condition δ_{L0} , as in Eq. (5), and $\delta(\mathbf{k}')$ merely stands for $D_+(\tau') \delta_{L0}(\mathbf{k}')$ in the limit $k' \rightarrow 0$. If we wish to write Eqs. (24) and (25) in terms of galaxy fields only, we need to assume that the matter and galaxy density fields are related by a finite bias b_1 in the limit $k' \rightarrow 0$. Then, Eq. (25) becomes

$$\begin{aligned} b_1 \langle \tilde{\delta}_g(\mathbf{k}') \tilde{\delta}_g(\mathbf{k}) \tilde{\lambda}_g(-\mathbf{k}) \rangle'_{k' \rightarrow 0} &= -\frac{\mathbf{k} \cdot \mathbf{k}' d \ln D_+}{k'^2 d\tau} P_{\delta_g \delta_g}(k') \\ &\times P_{\delta_g \delta_g}(k), \end{aligned} \quad (26)$$

where we assumed a deterministic large-scale limit b_1 for the galaxy bias, $k' \rightarrow 0: \delta_g(\mathbf{k}') = b_1 \delta(\mathbf{k}')$. Then, Eq. (26) can be used as a measurement of the large-scale bias b_1 .

Conclusions.—We have obtained in this Letter very general and exact consistency relations for cosmological structures that do not vanish at equal times by taking cross correlations with the velocity or momentum fields. These relations, which are nonperturbative and also apply to galaxy fields, could be useful to constrain the Gaussianity of the initial conditions, deviations from general relativity, or large-scale galaxy bias.

This work is supported in part by the French Agence Nationale de la Recherche under Grant No. ANR-12-BS05-0002. D. F. M. is supported by the Norwegian Research Council.

-
- [1] A. Kehagias and A. Riotto, *Nucl. Phys.* **B873**, 514 (2013).
 - [2] M. Peloso and M. Pietroni, *J. Cosmol. Astropart. Phys.* **5** (2013) 031.
 - [3] P. Creminelli, J. Noreña, M. Simonović, and F. Vernizzi, *J. Cosmol. Astropart. Phys.* **12** (2013) 025.
 - [4] A. Kehagias, J. Noreña, H. Perrier, and A. Riotto, *Nucl. Phys.* **B883**, 83 (2014).
 - [5] M. Peloso and M. Pietroni, *J. Cosmol. Astropart. Phys.* **4** (2014) 011.
 - [6] P. Creminelli, J. Gleyzes, M. Simonović, and F. Vernizzi, *J. Cosmol. Astropart. Phys.* **2** (2014) 051.
 - [7] P. Valageas, *Phys. Rev. D* **89**, 083534 (2014).
 - [8] B. Horn, L. Hui, and X. Xiao, *J. Cosmol. Astropart. Phys.* **9** (2014) 044.
 - [9] B. Horn, L. Hui, and X. Xiao, *J. Cosmol. Astropart. Phys.* **9** (2015) 068.
 - [10] P. Valageas, *Phys. Rev. D* **89**, 123522 (2014).
 - [11] A. Kehagias, H. Perrier, and A. Riotto, *Mod. Phys. Lett. A* **29**, 1450152 (2014).
 - [12] T. Nishimichi and P. Valageas, *Phys. Rev. D* **90**, 023546 (2014).

Article F

Consistency relations for
large-scale structures:
applications to the integrated
Sachs-Wolfe effect and the
kinematic Sunyaev-Zeldovich
effect

Consistency relations for large-scale structures: applications to the integrated Sachs-Wolfe effect and the kinematic Sunyaev-Zeldovich effect

Luca Alberto Rizzo¹, David F. Mota², and Patrick Valageas¹

¹ Institut de Physique Théorique, CEA, IPhT, F-91191 Gif-sur-Yvette, Cédex, France

² Institute of Theoretical Astrophysics, University of Oslo, 0315 Oslo, Norway

January 17, 2017

ABSTRACT

Consistency relations of large-scale structures provide exact nonperturbative results for cross-correlations of cosmic fields in the squeezed limit. They only depend on the equivalence principle and the assumption of Gaussian initial conditions, and remain nonzero at equal times for cross-correlations of density fields with velocity or momentum fields, or with the time derivative of density fields. We show how to apply these relations to observational probes that involve the integrated Sachs-Wolfe effect or the kinematic Sunyaev-Zeldovich effect. In the squeezed limit, this allows us to express the three-point cross-correlations, or bispectra, of two galaxy or matter density fields, or weak lensing convergence fields, with the secondary CMB distortion in terms of products of a linear and a nonlinear power spectrum. In particular, we find that cross-correlations with the integrated Sachs-Wolfe effect show a specific angular dependence. These results could be used to test the equivalence principle and the primordial Gaussianity, or to check the modeling of large-scale structures.

Key words. Cosmology – large-scale structure of the Universe

1. Introduction

Measuring statistical properties of cosmological structures is not only an efficient tool to describe and understand the main components of our Universe, but also it is a powerful probe of possible new physics beyond the standard Λ CDM concordance model. However, on large scales cosmological structures are described by perturbative methods, while smaller scales are described by phenomenological models or studied with numerical simulations. It is therefore difficult to obtain accurate predictions on the full range of scales probed by galaxy and lensing surveys. Furthermore, if we consider galaxy density fields, theoretical predictions remain sensitive to the galaxy bias which involves phenomenological modeling of star formation, even if we use cosmological numerical simulations. As a consequence, exact analytical results that go beyond low-order perturbation theory and also apply to biased tracers are very rare.

Recently, some exact results have been obtained (Kehagias & Riotto 2013; Peloso & Pietroni 2013; Creminelli et al. 2013; Kehagias et al. 2014a; Peloso & Pietroni 2014; Creminelli et al. 2014; Valageas 2014b; Horn et al. 2014, 2015) in the form of “kinematic consistency relations”. They relate the $(\ell + n)$ -density correlation, with ℓ large-scale wave numbers and n small-scale wave numbers, to the n -point small-scale density correlation. These relations, obtained at the leading order over the large-scale wave numbers, arise from the Equivalence Principle (EP) and the assumption of Gaussian initial conditions. The equivalence principle ensures that small-scale structures respond to a large-scale perturbation by a uniform displacement while primordial Gaussianity provides a simple relation between correlation and response functions (see Valageas et al. (2016) for the additional terms associated with

non-Gaussian initial conditions). Hence, such relations express a kinematic effect that vanishes for equal-times statistics, as a uniform displacement has no impact on the statistical properties of the density field observed at a given time.

In practice, it is however difficult to measure different-times density correlations and it would therefore be useful to obtain relations that remain nonzero at equal times. One possibility to overcome such problem, is to go to higher orders and take into account tidal effects, which at leading order are given by the response of small-scale structures to a change of the background density. Such an approach, however, introduces some additional approximations (Valageas 2014a; Kehagias et al. 2014b; Nishimichi & Valageas 2014).

Fortunately, it was recently noticed that by cross-correlating density fields with velocity or momentum fields, or with the time derivative of the density field, one obtains consistency relations that do not vanish at equal times (Rizzo et al. 2016). Indeed, the kinematic effect modifies the amplitude of the large-scale velocity and momentum fields, while the time derivative of the density field is obviously sensitive to different-times effects.

In this paper, we investigate the observational applicability of these new relations. We consider the lowest-order relations, which relate three-point cross-correlations or bispectra in the squeezed limit to products of a linear and a nonlinear power spectrum. To involve the non-vanishing consistency relations, we study two observable quantities, the secondary anisotropy Δ_{ISW} of the cosmic microwave background (CMB) radiation due to the integrated Sachs-Wolfe effect (ISW), and the secondary anisotropy Δ_{kSZ} due to the kinematic Sunyaev-Zeldovich (kSZ) effect. The first process, associated with the motion of CMB photons through time-dependent gravitational potentials, depends on the time derivative of the matter density field. The second pro-

cess, associated with the scattering of CMB photons by free electrons, depends on the free electrons velocity field. We investigate the cross correlations of these two secondary anisotropies with both galaxy density fields and the cosmic weak lensing convergence.

This paper is organized as follows. In section 2 we recall the consistency relations of large-scale structures that apply to density, momentum and momentum-divergence (i.e., time derivative of the density) fields. We describe the various observational probes that we consider in this paper in section 3. We study the ISW effect in section 4 and the kSZ effect in section 5. We conclude in section 6.

2. Consistency relations for large-scale structures

2.1. Consistency relations for density correlations

As described in recent works (Kehagias & Riotto 2013; Peloso & Pietroni 2013; Creminelli et al. 2013; Kehagias et al. 2014a; Peloso & Pietroni 2014; Creminelli et al. 2014; Valageas 2014b; Horn et al. 2014, 2015), it is possible to obtain exact relations between density correlations of different orders in the squeezed limit, where some of the wavenumbers are in the linear regime and far below the other modes that may be strongly nonlinear. These “kinematic consistency relations”, obtained at the leading order over the large-scale wavenumbers, arise from the equivalence principle and the assumption of Gaussian primordial perturbations. They express the fact that, at leading order where a large-scale perturbation corresponds to a linear gravitational potential (hence a constant Newtonian force) over the extent of a small-size structure, the latter falls without distortions in this large-scale potential.

Then, in the squeezed limit $k \rightarrow 0$, the correlation between one large-scale density mode $\tilde{\delta}(\mathbf{k})$ and n small-scale density modes $\tilde{\delta}(\mathbf{k}_j)$ can be expressed in terms of the n -point small-scale correlation, as

$$\begin{aligned} \langle \tilde{\delta}(\mathbf{k}, \eta) \prod_{j=1}^n \tilde{\delta}(\mathbf{k}_j, \eta_j) \rangle'_{k \rightarrow 0} &= -P_L(k, \eta) \langle \prod_{j=1}^n \tilde{\delta}(\mathbf{k}_j, \eta_j) \rangle' \\ &\times \sum_{i=1}^n \frac{D(\eta_i)}{D(\eta)} \frac{\mathbf{k}_i \cdot \mathbf{k}}{k^2}, \end{aligned} \quad (1)$$

where the tilde denotes the Fourier transform of the fields, η is the conformal time, $D(\eta)$ is the linear growth factor, the prime in $\langle \dots \rangle'$ denotes that we factored out the Dirac factor, $\langle \dots \rangle = \langle \dots \rangle' \delta_D(\sum \mathbf{k}_j)$, and $P_L(k)$ is the linear matter power spectrum. It is worth stressing that these relations are valid even in the nonlinear regime and for biased galaxy fields $\tilde{\delta}_g(\mathbf{k}_j)$. The right-hand side gives the squeezed limit of the $(1+n)$ correlation at the leading order, which scales as $1/k$. It vanishes at this order at equal times, because of the constraint associated with the Dirac factor $\delta_D(\sum \mathbf{k}_j)$.

The geometrical factors $(\mathbf{k}_i \cdot \mathbf{k})$ vanish if $\mathbf{k}_i \perp \mathbf{k}$. Indeed, the large-scale mode induces a uniform displacement along the direction of \mathbf{k} . This has no effect on small-scale plane waves of wavenumbers \mathbf{k}_i with $\mathbf{k}_i \perp \mathbf{k}$, as they remain identical after such a displacement. Therefore, the terms in the right-hand side of Eq.(1) must vanish in such orthogonal configurations, as we can check from the explicit expression.

The simplest relation that one can obtain from Eq.(1) is for the bispectrum with $n = 2$,

$$\begin{aligned} \langle \tilde{\delta}(\mathbf{k}, \eta) \tilde{\delta}_g(\mathbf{k}_1, \eta_1) \tilde{\delta}_g(\mathbf{k}_2, \eta_2) \rangle'_{k \rightarrow 0} &= -P_L(k, \eta) \frac{\mathbf{k}_1 \cdot \mathbf{k}}{k^2} \\ &\times \langle \tilde{\delta}_g(\mathbf{k}_1, \eta_1) \tilde{\delta}_g(\mathbf{k}_2, \eta_2) \rangle' \frac{D(\eta_1) - D(\eta_2)}{D(\eta)}, \end{aligned} \quad (2)$$

where we used that $\mathbf{k}_2 = -\mathbf{k}_1 - \mathbf{k} \rightarrow -\mathbf{k}_1$. For generality, we considered here the small-scale fields $\tilde{\delta}_g(\mathbf{k}_1)$ and $\tilde{\delta}_g(\mathbf{k}_2)$ to be associated with biased tracers such as galaxies. The tracers associated with \mathbf{k}_1 and \mathbf{k}_2 can be different and have different bias. At equal times the right-hand side of Eq.(2) vanishes, as recalled above.

2.2. Consistency relations for momentum correlations

The density consistency relations (1) express the uniform motion of small-scale structures by large-scale modes. This simple kinematic effect vanishes for equal-time correlations of the density field, precisely because there are no distortions, while there is a nonzero effect at different times because of the motion of the small-scale structure between different times. However, as pointed out in Rizzo et al. (2016), it is possible to obtain non-trivial equal-times results by considering velocity or momentum fields, which are not only displaced but also see their amplitude affected by the large-scale mode. Let us consider the momentum \mathbf{p} defined by

$$\mathbf{p} = (1 + \delta)\mathbf{v}, \quad (3)$$

where \mathbf{v} the peculiar velocity. Then, in the squeezed limit $k \rightarrow 0$, the correlation between one large-scale density mode $\tilde{\delta}(\mathbf{k})$, n small-scale density modes $\tilde{\delta}(\mathbf{k}_j)$, and m small-scale momentum modes $\tilde{\mathbf{p}}(\mathbf{k}_j)$ can be expressed in terms of $(n+m)$ small-scale correlations, as

$$\begin{aligned} \langle \tilde{\delta}(\mathbf{k}, \eta) \prod_{j=1}^n \tilde{\delta}(\mathbf{k}_j, \eta_j) \prod_{j=n+1}^{n+m} \tilde{\mathbf{p}}(\mathbf{k}_j, \eta_j) \rangle'_{k \rightarrow 0} &= -P_L(k, \eta) \\ &\times \left\{ \langle \prod_{j=1}^n \tilde{\delta}(\mathbf{k}_j, \eta_j) \prod_{j=n+1}^{n+m} \tilde{\mathbf{p}}(\mathbf{k}_j, \eta_j) \rangle' \sum_{i=1}^{n+m} \frac{D(\eta_i)}{D(\eta)} \frac{\mathbf{k}_i \cdot \mathbf{k}}{k^2} \right. \\ &+ \sum_{i=n+1}^{n+m} \frac{(dD/dn)(\eta_i)}{D(\eta)} \langle \prod_{j=1}^n \tilde{\delta}(\mathbf{k}_j, \eta_j) \prod_{j=n+1}^{i-1} \tilde{\mathbf{p}}(\mathbf{k}_j, \eta_j) \\ &\left. \times \left(i \frac{\mathbf{k}}{k^2} [\delta_D(\mathbf{k}_i) + \tilde{\delta}(\mathbf{k}_i, \eta_i)] \prod_{j=i+1}^{n+m} \tilde{\mathbf{p}}(\mathbf{k}_j, \eta_j) \right) \right\}. \end{aligned} \quad (4)$$

These relations are again valid in the nonlinear regime and for biased galaxy fields $\tilde{\delta}_g(\mathbf{k}_j)$ and $\tilde{\mathbf{p}}_g(\mathbf{k}_j)$. As for the density consistency relation (1), the first term vanishes at this order at equal times. The second term however, which arises from the $\tilde{\mathbf{p}}$ fields only, remains nonzero. This is due to the fact that $\tilde{\mathbf{p}}$ involves the velocity, the amplitude of which is affected by the motion induced by the large-scale mode.

The simplest relation associated with Eq.(4) is the bispectrum among two density-contrast fields and one momentum field,

$$\begin{aligned} \langle \tilde{\delta}(\mathbf{k}, \eta) \tilde{\delta}_g(\mathbf{k}_1, \eta_1) \tilde{\mathbf{p}}_g(\mathbf{k}_2, \eta_2) \rangle'_{k \rightarrow 0} &= -P_L(k, \eta) \\ &\times \left(\frac{\mathbf{k}_1 \cdot \mathbf{k}}{k^2} \langle \tilde{\delta}_g(\mathbf{k}_1, \eta_1) \tilde{\mathbf{p}}_g(\mathbf{k}_2, \eta_2) \rangle' \frac{D(\eta_1) - D(\eta_2)}{D(\eta)} + \right. \\ &\left. + i \frac{\mathbf{k}}{k^2} \langle \tilde{\delta}_g(\mathbf{k}_1, \eta_1) \tilde{\delta}_g(\mathbf{k}_2, \eta_2) \rangle' \frac{1}{D(\eta)} \frac{dD}{d\eta}(\eta_2) \right). \end{aligned} \quad (5)$$

For generality, we considered here the small-scale fields $\tilde{\delta}_g(\mathbf{k}_1)$ and $\tilde{\mathbf{p}}_g(\mathbf{k}_2)$ to be associated with biased tracers such as galaxies, and the tracers associated with \mathbf{k}_1 and \mathbf{k}_2 can again be different and have different bias. At equal times Eq.(5) reads as

$$\langle \tilde{\delta}(\mathbf{k}) \tilde{\delta}_g(\mathbf{k}_1) \tilde{\mathbf{p}}_g(\mathbf{k}_2) \rangle'_{k \rightarrow 0} = -i \frac{\mathbf{k}}{k^2} \frac{d \ln D}{d\eta} P_L(k) P_g(k_1), \quad (6)$$

where $P_g(k)$ is the galaxy nonlinear power spectrum and we omitted the common time dependence. This result does not vanish thanks to the term generated by $\tilde{\mathbf{p}}$ in the consistency relation (5).

2.3. Consistency relations for momentum-divergence correlations

In addition to the momentum field \mathbf{p} , we can consider its divergence λ , defined by

$$\lambda \equiv \nabla \cdot [(1 + \delta)\mathbf{v}] = -\frac{\partial \delta}{\partial \eta}. \quad (7)$$

The second equality expresses the continuity equation, that is, the conservation of matter. In the squeezed limit we obtain from Eq.(4) (Rizzo et al. 2016)

$$\begin{aligned} \langle \tilde{\delta}(\mathbf{k}, \eta) \prod_{j=1}^n \tilde{\delta}(\mathbf{k}_j, \eta_j) \prod_{j=n+1}^{n+m} \tilde{\lambda}(\mathbf{k}_j, \eta_j) \rangle'_{k \rightarrow 0} &= -P_L(k, \eta) \\ &\times \left\{ \left\langle \prod_{j=1}^n \tilde{\delta}(\mathbf{k}_j, \eta_j) \prod_{j=n+1}^{n+m} \tilde{\lambda}(\mathbf{k}_j, \eta_j) \right\rangle' \sum_{i=1}^{n+m} \frac{D(\eta_i)}{D(\eta)} \frac{\mathbf{k}_i \cdot \mathbf{k}}{k^2} \right. \\ &\quad - \sum_{i=n+1}^{n+m} \langle \tilde{\delta}(\mathbf{k}_i, \eta_i) \prod_{j=1}^n \tilde{\delta}(\mathbf{k}_j, \eta_j) \prod_{\substack{j=n+1 \\ j \neq i}}^{n+m} \tilde{\lambda}(\mathbf{k}_j, \eta_j) \rangle' \\ &\quad \left. \times \frac{(dD/d\eta)(\eta_i)}{D(\eta)} \frac{\mathbf{k}_i \cdot \mathbf{k}}{k^2} \right\}. \quad (8) \end{aligned}$$

These relations can actually be obtained by taking derivatives with respect to the times η_j of the density consistency relations (1), using the second equality (7). As for the momentum consistency relations (4), these relations remain valid in the nonlinear regime and for biased small-scale fields $\tilde{\delta}_g(\mathbf{k}_j)$ and $\tilde{\lambda}_g(\mathbf{k}_j)$. The second term in Eq.(8), which arises from the $\tilde{\lambda}$ fields only, remains nonzero at equal times. This is due to the fact that λ involves the velocity or the time-derivative of the density, which probes the evolution between (infinitesimally close) different times.

The simplest relation associated with Eq.(8) is the bispectrum among two density-contrast fields and one momentum-divergence field,

$$\begin{aligned} \langle \tilde{\delta}(\mathbf{k}, \eta) \tilde{\delta}_g(\mathbf{k}_1, \eta_1) \tilde{\lambda}_g(\mathbf{k}_2, \eta_2) \rangle'_{k \rightarrow 0} &= -P_L(k, \eta) \frac{\mathbf{k}_1 \cdot \mathbf{k}}{k^2} \\ &\times \left(\langle \tilde{\delta}_g(\mathbf{k}_1, \eta_1) \tilde{\lambda}_g(\mathbf{k}_2, \eta_2) \rangle' \frac{D(\eta_1) - D(\eta_2)}{D(\eta)} + \right. \\ &\quad \left. + \langle \tilde{\delta}_g(\mathbf{k}_1, \eta_1) \tilde{\delta}_g(\mathbf{k}_2, \eta_2) \rangle' \frac{1}{D(\eta)} \frac{dD}{d\eta}(\eta_2) \right). \quad (9) \end{aligned}$$

At equal times, Eq.(9) reads as

$$\langle \tilde{\delta}(\mathbf{k}) \tilde{\delta}_g(\mathbf{k}_1) \tilde{\lambda}_g(\mathbf{k}_2) \rangle'_{k \rightarrow 0} = -\frac{\mathbf{k}_1 \cdot \mathbf{k}}{k^2} \frac{d \ln D}{d\eta} P_L(k) P_g(k_1). \quad (10)$$

3. Observable quantities

To test cosmological scenarios with the consistency relations of large-scale structures we need to relate them with observable quantities. We describe in this section the observational probes that we consider in this paper. We use the galaxy numbers counts or the weak lensing convergence to probe the density field. To apply the momentum consistency relations (6) and (10), we use the ISW effect to probe the momentum divergence λ (more precisely the time derivative of the gravitational potential and matter density) and the kSZ effect to probe the momentum \mathbf{p} .

3.1. Galaxy number density contrast δ_g

From galaxy surveys we can typically measure the galaxy density contrast within some redshift bin, smoothed with some finite-size window on the sky,

$$\delta_g^s(\boldsymbol{\theta}) = \int d\theta' W_\Theta(|\boldsymbol{\theta}' - \boldsymbol{\theta}|) \int d\eta I_g(\eta) \delta_g[r, r\boldsymbol{\theta}'; \eta], \quad (11)$$

where $W_\Theta(|\boldsymbol{\theta}' - \boldsymbol{\theta}|)$ is a 2D symmetric window function centered on the direction $\boldsymbol{\theta}$ on the sky, of characteristic angular radius Θ , $I_g(\eta)$ is the radial weight along the line of sight associated with a normalized galaxy selection function $n_g(z)$,

$$I_g(\eta) = \left| \frac{dz}{d\eta} \right| n_g(z), \quad (12)$$

$r = \eta_0 - \eta$ is the radial comoving coordinate along the line of sight, and η_0 is the conformal time today. Here and in the following we use the flat sky approximation, and $\boldsymbol{\theta}$ is the 2D vector that describes the direction on the sky of a given line of sight. The superscript ‘‘s’’ in δ_g^s denotes that we smooth the galaxy density contrast with the finite-size window W_Θ . Expanding in Fourier space the galaxy density contrast we can write

$$\begin{aligned} \delta_g^s(\boldsymbol{\theta}) &= \int d\theta' W_\Theta(|\boldsymbol{\theta}' - \boldsymbol{\theta}|) \int d\eta I_g(\eta) \\ &\quad \times \int d\mathbf{k} e^{i\mathbf{k}_\parallel r + i\mathbf{k}_\perp \cdot r\boldsymbol{\theta}'} \tilde{\delta}_g(\mathbf{k}, \eta) \end{aligned} \quad (13)$$

where k_\parallel and \mathbf{k}_\perp are respectively the parallel and the perpendicular components of the 3D wavenumber $\mathbf{k} = (k_\parallel, \mathbf{k}_\perp)$ (with respect to the reference direction $\boldsymbol{\theta} = 0$, and we work in the small-angle limit $\theta \ll 1$). Defining the 2D Fourier transform of the window W_Θ as

$$\tilde{W}_\Theta(|\boldsymbol{\ell}|) = \int d\boldsymbol{\theta} e^{-i\boldsymbol{\ell} \cdot \boldsymbol{\theta}} W_\Theta(|\boldsymbol{\theta}|), \quad (14)$$

we obtain

$$\delta_g^s(\boldsymbol{\theta}) = \int d\eta I_g(\eta) \int d\mathbf{k} \tilde{W}_\Theta(k_\perp r) e^{i\mathbf{k}_\parallel r + i\mathbf{k}_\perp \cdot r\boldsymbol{\theta}} \tilde{\delta}_g(\mathbf{k}, \eta). \quad (15)$$

3.2. Weak lensing convergence κ

From weak lensing surveys we can measure the weak lensing convergence, given in the Born approximation by

$$\kappa^s(\boldsymbol{\theta}) = \int d\theta' W_\Theta(|\boldsymbol{\theta}' - \boldsymbol{\theta}|) \int d\eta r g(r) \nabla^2 \frac{\Psi + \Phi}{2}[r, r\boldsymbol{\theta}'; \eta], \quad (16)$$

where Ψ and Φ are the Newtonian gauge gravitational potentials and the kernel $g(r)$ that defines the radial depth of the survey is

$$g(r) = \int_r^\infty dr_s \frac{dz_s}{dr_s} n_g(z_s) \frac{r_s - r}{r_s}, \quad (17)$$

where $n_g(z_s)$ is the redshift distribution of the source galaxies. Assuming no anisotropic stress, i.e. $\Phi = \Psi$, and using the Poisson equation,

$$\nabla^2 \Psi = 4\pi \mathcal{G}_N \bar{\rho}_0 \delta / a, \quad (18)$$

where \mathcal{G}_N is the Newton constant, $\bar{\rho}_0$ is the mean matter density of the Universe today, and a is the scale factor, we obtain

$$\kappa^s(\boldsymbol{\theta}) = \int d\eta I_\kappa(\eta) \int d\mathbf{k} \tilde{W}_\Theta(k_\perp r) e^{i\mathbf{k}_\parallel r + i\mathbf{k}_\perp \cdot r\boldsymbol{\theta}} \tilde{\delta}(\mathbf{k}, \eta), \quad (19)$$

with

$$I_\kappa(\eta) = 4\pi \mathcal{G}_N \bar{\rho}_0 \frac{rg(r)}{a}. \quad (20)$$

3.3. ISW secondary anisotropy Δ_{ISW}

From Eq.(7) λ can be obtained from the momentum divergence or from the time derivative of the density contrast. These quantities are not as directly measured from galaxy surveys as density contrasts. However, we can relate the time derivative of the density contrast to the ISW effect, which involves the time derivative of the gravitational potential. Indeed, the secondary cosmic microwave background temperature anisotropy due to the integrated Sachs-Wolfe effect along the direction $\boldsymbol{\theta}$ reads as (Garriga et al. 2004)

$$\begin{aligned} \Delta_{\text{ISW}}(\boldsymbol{\theta}) &= \int d\eta e^{-\tau(\eta)} \left(\frac{\partial \Psi}{\partial \eta} + \frac{\partial \Phi}{\partial \eta} \right) [r, r\boldsymbol{\theta}; \eta] \\ &= 2 \int d\eta e^{-\tau(\eta)} \frac{\partial \Psi}{\partial \eta} [r, r\boldsymbol{\theta}; \eta], \end{aligned} \quad (21)$$

where $\tau(\eta)$ is the optical depth, which takes into account the possibility of late reionization, and in the second line we assumed no anisotropic stress, i.e. $\Phi = \Psi$. We can relate Δ_{ISW} to λ through the Poisson equation (18), which reads in Fourier space as

$$-k^2 \tilde{\Psi} = 4\pi \mathcal{G}_N \bar{\rho}_0 \tilde{\delta} / a. \quad (22)$$

This gives

$$\frac{\partial \tilde{\Psi}}{\partial \eta} = \frac{4\pi \mathcal{G}_N \bar{\rho}_0}{k^2 a} (\tilde{\lambda} + \mathcal{H} \tilde{\delta}), \quad (23)$$

where $\mathcal{H} = d \ln a / d\eta$ is the conformal expansion rate. Integrating the ISW effect δ_{ISW} over some finite-size window on the sky, we obtain as in Eq.(15)

$$\begin{aligned} \Delta_{\text{ISW}}^s(\boldsymbol{\theta}) &= \int d\eta I_{\text{ISW}}(\eta) \int d\mathbf{k} \tilde{W}_\Theta(k_\perp r) e^{i\mathbf{k}_\parallel r + i\mathbf{k}_\perp \cdot r\boldsymbol{\theta}} \\ &\quad \times \frac{\tilde{\lambda} + \mathcal{H} \tilde{\delta}}{k^2}, \end{aligned} \quad (24)$$

with

$$I_{\text{ISW}}(\eta) = 8\pi \mathcal{G}_N \bar{\rho}_0 \frac{e^{-\tau}}{a}. \quad (25)$$

3.4. Kinematic SZ secondary anisotropy Δ_{kSZ}

Thomson scattering of CMB photons off moving free electrons in the hot galactic or cluster gas generates secondary anisotropies (Sunyaev & Zeldovich 1980; Gruzinov & Hu 1998; Knox et al.

1998). The temperature perturbation, $\Delta_{\text{kSZ}} = \delta T / T$, due to this kinematic Sunyaev Zeldovich (kSZ) effect, is

$$\Delta_{\text{kSZ}}(\boldsymbol{\theta}) = - \int d\mathbf{l} \cdot \mathbf{v}_e \sigma_T n_e e^{-\tau} = \int d\eta I_{\text{kSZ}}(\eta) \mathbf{n}(\boldsymbol{\theta}) \cdot \mathbf{p}_e, \quad (26)$$

where τ is again the optical depth, σ_T the Thomson cross section, \mathbf{l} the radial coordinate along the line of sight, n_e the number density of free electrons, \mathbf{v}_e their peculiar velocity, and $\mathbf{n}(\boldsymbol{\theta})$ the radial unit vector pointing to the line of sight. We also defined the kSZ kernel by

$$I_{\text{kSZ}}(\eta) = -\sigma_T \bar{n}_e a e^{-\tau}, \quad (27)$$

and the free electrons momentum \mathbf{p}_e as

$$n_e \mathbf{v}_e = \bar{n}_e (1 + \delta_e) \mathbf{v}_e = \bar{n}_e \mathbf{p}_e. \quad (28)$$

Because of the projection $\mathbf{n} \cdot \mathbf{p}_e$ along the line of sight, some care must be taken when we smooth $\Delta_{\text{kSZ}}(\boldsymbol{\theta})$ over some finite size angular window $W_\Theta(|\boldsymbol{\theta}' - \boldsymbol{\theta}|)$. Indeed, because the different lines of sight $\boldsymbol{\theta}'$ in the conical window are not perfectly parallel, if we define the longitudinal and transverse momentum components by the projection with respect to the mean line of sight $\mathbf{n}(\boldsymbol{\theta})$ of the circular window, e.g. $p_{e\parallel} = \mathbf{n}(\boldsymbol{\theta}) \cdot \mathbf{p}_e$, the projection $\mathbf{n}(\boldsymbol{\theta}') \cdot \mathbf{p}_e$ receives contributions from both $p_{e\parallel}$ and $\mathbf{p}_{e\perp}$. In the limit of small angles we could a priori neglect the contribution associated with $\mathbf{p}_{e\perp}$, which is multiplied by an angular factor and vanishes for a zero-size window. However, for small but finite angles, we need to keep this contribution because fluctuations along the lines of sight are damped by the radial integrations and vanish in the Limber approximation, which damps the contribution associated with $p_{e\parallel}$.

For small angles we write at linear order $\mathbf{n}(\boldsymbol{\theta}) = (\theta_x, \theta_y, 1)$, close to a reference direction $\boldsymbol{\theta} = 0$. Then, the integration over the angular window gives for the smoothed kSZ effect

$$\begin{aligned} \Delta_{\text{kSZ}}^s(\boldsymbol{\theta}) &= \int d\eta I_{\text{kSZ}}(\eta) \int d\mathbf{k} e^{i\mathbf{k} \cdot \mathbf{nr}} \left[\tilde{p}_{e\parallel} \tilde{W}_\Theta(k_\perp r) \right. \\ &\quad \left. - i \frac{\mathbf{k}_\perp \cdot \tilde{\mathbf{p}}_{e\perp}}{k_\perp} \tilde{W}'_\Theta(k_\perp r) \right]. \end{aligned} \quad (29)$$

Here we expressed the result in terms of the longitudinal and transverse components of the wave numbers and momenta with respect to the mean line of sight $\mathbf{n}(\boldsymbol{\theta})$ of the circular window W_Θ . Thus, whereas the radial unit vector is $\mathbf{n}(\boldsymbol{\theta}) = (\theta_x, \theta_y, 1)$, we can define the transverse unit vectors as $\mathbf{n}_{\perp x} = (1, 0, -\theta_x)$ and $\mathbf{n}_{\perp y} = (0, 1, -\theta_y)$, and we write for instance $\mathbf{k} = k_{\perp x} \mathbf{n}_{\perp x} + k_{\perp y} \mathbf{n}_{\perp y} + k_\parallel \mathbf{n}$. We denote $\tilde{W}'_\Theta(\ell) = d\tilde{W}_\Theta/d\ell$. The last term in Eq.(29) is due to the finite size Θ of the smoothing window, which makes the lines of sight within the conical beam not strictly parallel. It vanishes for an infinitesimal window, where $W_\Theta(\boldsymbol{\theta}) = \delta_D(\boldsymbol{\theta})$ and $\tilde{W}'_\Theta = 0$.

4. Consistency relation for the ISW temperature anisotropy

In this section we consider cross correlations with the ISW effect. This allows us to apply the consistency relation (9), which involves the momentum divergence λ and remains nonzero at equal times.

4.1. Galaxy-galaxy-ISW correlation

To take advantage of the consistency relation (9), we must consider three-point correlations ξ_3 (in configuration space) with one observable that involves the momentum divergence λ . Here, using the expression (24), we study the cross-correlation between two galaxy density contrasts and one ISW temperature anisotropy,

$$\xi_3(\delta_g^s, \delta_{g_1}^s, \Delta_{\text{ISW}_2}^s) = \langle \delta_g^s(\boldsymbol{\theta}) \delta_{g_1}^s(\boldsymbol{\theta}_1) \Delta_{\text{ISW}_2}^s(\boldsymbol{\theta}_2) \rangle. \quad (30)$$

The subscripts g , g_1 , and ISW_2 denote the three lines of sight associated with the three probes. Moreover, the subscripts g and g_1 recall that the two galaxy populations associated with δ_g^s and $\delta_{g_1}^s$ can be different and have different bias. As we recalled in section 2, the consistency relations rely on the undistorted motion of small-scale structures by large-scale modes. This corresponds to the squeezed limit $k \rightarrow 0$ in the Fourier-space equations (1) and (8), which writes more precisely as

$$k \ll k_L, \quad k \ll k_j, \quad (31)$$

where k_L is the wavenumber associated with the transition between the linear and nonlinear regimes. The first condition ensures that $\tilde{\delta}(k)$ is in the linear regime, while the second condition ensures the hierarchy between the large-scale mode and the small-scale modes. In configuration space, these conditions correspond to

$$\Theta \gg \Theta_L, \quad \Theta \gg \Theta_j, \quad |\boldsymbol{\theta} - \boldsymbol{\theta}_j| \gg |\boldsymbol{\theta}_1 - \boldsymbol{\theta}_2|. \quad (32)$$

The first condition ensures that $\delta_g^s(\boldsymbol{\theta})$ is in the linear regime, whereas the next two conditions ensure the hierarchy of scales.

The expressions (15) and (24) give

$$\begin{aligned} \xi_3 = & \int d\eta d\eta_1 d\eta_2 I_g(\eta) I_{g_1}(\eta_1) I_{\text{ISW}_2}(\eta_2) \\ & \times \int d\mathbf{k} d\mathbf{k}_1 d\mathbf{k}_2 \tilde{W}_\Theta(k_\perp r) \tilde{W}_{\Theta_1}(k_{1\perp} r_1) \tilde{W}_{\Theta_2}(k_{2\perp} r_2) \\ & \times e^{i(k_{\parallel} r + k_{\parallel 1} r_1 + k_{\parallel 2} r_2 + \mathbf{k}_\perp \cdot r \boldsymbol{\theta} + \mathbf{k}_{1\perp} \cdot r_1 \boldsymbol{\theta}_1 + \mathbf{k}_{2\perp} \cdot r_2 \boldsymbol{\theta}_2)} \\ & \times \langle \tilde{\delta}_g(\mathbf{k}, \eta) \tilde{\delta}_{g_1}(\mathbf{k}_1, \eta_1) \frac{\tilde{\lambda}(\mathbf{k}_2, \eta_2) + \mathcal{H}_2 \tilde{\delta}(\mathbf{k}_2, \eta_2)}{k_2^2} \rangle. \end{aligned} \quad (33)$$

The configuration-space conditions (32) ensure that we satisfy the Fourier-space conditions (31) and that we can apply the consistency relations (2) and (9). This gives

$$\begin{aligned} \xi_3 = & - \int d\eta d\eta_1 d\eta_2 b_g(\eta) I_g(\eta) I_{g_1}(\eta_1) I_{\text{ISW}_2}(\eta_2) \\ & \times \int d\mathbf{k} d\mathbf{k}_1 d\mathbf{k}_2 \tilde{W}_\Theta(k_\perp r) \tilde{W}_{\Theta_1}(k_{1\perp} r_1) \tilde{W}_{\Theta_2}(k_{2\perp} r_2) \\ & \times e^{i(k_{\parallel} r + k_{\parallel 1} r_1 + k_{\parallel 2} r_2 + \mathbf{k}_\perp \cdot r \boldsymbol{\theta} + \mathbf{k}_{1\perp} \cdot r_1 \boldsymbol{\theta}_1 + \mathbf{k}_{2\perp} \cdot r_2 \boldsymbol{\theta}_2)} \\ & \times P_L(k, \eta) \frac{\mathbf{k}_1 \cdot \mathbf{k}}{k^2} \delta_D(\mathbf{k} + \mathbf{k}_1 + \mathbf{k}_2) \\ & \times \left(\langle \tilde{\delta}_{g_1} \frac{\tilde{\lambda}_2 + \mathcal{H}_2 \tilde{\delta}_2}{k_2^2} \rangle' \frac{D(\eta_1) - D(\eta_2)}{D(\eta)} \right. \\ & \left. + \langle \tilde{\delta}_{g_1} \frac{\tilde{\delta}_2}{k_2^2} \rangle' \frac{1}{D(\eta)} \frac{dD}{d\eta}(\eta_2) \right). \end{aligned} \quad (34)$$

Here we assumed that on large scales the galaxy bias is linear,

$$k \rightarrow 0: \quad \tilde{\delta}_g(\mathbf{k}) = b_g(\eta) \tilde{\delta}(\mathbf{k}) + \tilde{\epsilon}(\mathbf{k}), \quad (35)$$

where $\tilde{\epsilon}$ is a stochastic component that represents shot noise and the effect of small-scale (e.g., baryonic) physics on galaxy formation. From the decomposition (35), it is uncorrelated with the large-scale density field (Hamaus et al. 2010), $\langle \tilde{\delta}(\mathbf{k}) \tilde{\epsilon}(\mathbf{k}) \rangle = 0$. Then, in Eq.(34) we neglected the term $\langle \tilde{\epsilon} \tilde{\delta}_{g_1}(\tilde{\lambda}_2 + \mathcal{H}_2 \tilde{\delta}_2) \rangle$. Indeed, the small-scale local processes within the region $\boldsymbol{\theta}$ should be very weakly correlated with the density fields in the distant regions $\boldsymbol{\theta}_1$ and $\boldsymbol{\theta}_2$, which at leading order are only sensitive to the total mass within the large-scale region $\boldsymbol{\theta}$. Therefore, $\langle \tilde{\epsilon} \tilde{\delta}_{g_1}(\tilde{\lambda}_2 + \mathcal{H}_2 \tilde{\delta}_2) \rangle$ should exhibit a fast decay at low k , whereas the term in Eq.(34) associated with the consistency relation only decays as $P_L(k)/k \sim k^{n_s-1}$ with $n_s \simeq 0.96$. In Eq.(34), we also assumed that the galaxy bias b_g goes to a constant at large scales, which is usually the case, but we could take into account a scale dependence [by keeping the factor $b_g(k, \eta)$ in the integral over k].

The small-scale two-point correlations $\langle 1 \cdot 2 \rangle'$ are dominated by contributions at almost equal times, $\eta_1 \simeq \eta_2$, as different redshifts would correspond to points that are separated by several Hubble radii along the lines of sight and density correlations are negligible beyond Hubble scales. Therefore, ξ_3 is dominated by the second term that does not vanish at equal times. The integrals along the lines of sight suppress the contributions from longitudinal wavelengths below the Hubble radius c/H , while the angular windows only suppress the wavelengths below the transverse radii $c\Theta/H$. Then, for small angular windows, $\Theta \ll 1$, we can use Limber's approximation, $k_{\parallel} \ll k_\perp$ hence $k \simeq k_\perp$. Integrating over k_{\parallel} through the Dirac factor $\delta_D(k_{\parallel} + k_{\parallel 1} + k_{\parallel 2})$, and next over $k_{1\parallel}$ and $k_{2\parallel}$, we obtain the Dirac factors $(2\pi)^2 \delta_D(r_1 - r) \delta_D(r_2 - r)$. This allows us to integrate over η_1 and η_2 and we obtain

$$\begin{aligned} \xi_3 = & -(2\pi)^2 \int d\eta b_g(\eta) I_g(\eta) I_{g_1}(\eta) I_{\text{ISW}_2}(\eta) \frac{d \ln D}{d\eta} \\ & \times \int d\mathbf{k}_\perp d\mathbf{k}_{1\perp} d\mathbf{k}_{2\perp} \delta_D(\mathbf{k}_\perp + \mathbf{k}_{1\perp} + \mathbf{k}_{2\perp}) \tilde{W}_\Theta(k_\perp r) \\ & \times \tilde{W}_{\Theta_1}(k_{1\perp} r) \tilde{W}_{\Theta_2}(k_{2\perp} r) e^{i r(\mathbf{k}_\perp \cdot \boldsymbol{\theta} + \mathbf{k}_{1\perp} \cdot \boldsymbol{\theta}_1 + \mathbf{k}_{2\perp} \cdot \boldsymbol{\theta}_2)} \\ & \times P_L(k_\perp, \eta) \frac{\mathbf{k}_{1\perp} \cdot \mathbf{k}_\perp}{k_\perp^2 k_{2\perp}^2} P_{g_1, m}(k_{1\perp}, \eta), \end{aligned} \quad (36)$$

where $P_{g_1, m}$ is the galaxy-matter power spectrum. The integration over $\mathbf{k}_{2\perp}$ gives

$$\begin{aligned} \xi_3 = & -(2\pi)^2 \int d\eta b_g I_g I_{g_1} I_{\text{ISW}_2} \frac{d \ln D}{d\eta} \int d\mathbf{k}_\perp d\mathbf{k}_{1\perp} \tilde{W}_\Theta(k_\perp r) \\ & \times \tilde{W}_{\Theta_1}(k_{1\perp} r) \tilde{W}_{\Theta_2}(k_{1\perp} r) P_L(k_\perp, \eta) P_{g_1, m}(k_{1\perp}, \eta) \\ & \times e^{i r(\mathbf{k}_\perp \cdot (\boldsymbol{\theta} - \boldsymbol{\theta}_2) + \mathbf{k}_{1\perp} \cdot (\boldsymbol{\theta}_1 - \boldsymbol{\theta}_2))} \frac{\mathbf{k}_{1\perp} \cdot \mathbf{k}_\perp}{k_{1\perp}^2 k_\perp^2}, \end{aligned} \quad (37)$$

and the integration over the angles of \mathbf{k}_\perp and $\mathbf{k}_{1\perp}$ gives

$$\begin{aligned} \xi_3 = & \frac{(\boldsymbol{\theta} - \boldsymbol{\theta}_2) \cdot (\boldsymbol{\theta}_1 - \boldsymbol{\theta}_2)}{|\boldsymbol{\theta} - \boldsymbol{\theta}_2| |\boldsymbol{\theta}_1 - \boldsymbol{\theta}_2|} (2\pi)^4 \int d\eta b_g I_g I_{g_1} I_{\text{ISW}_2} \frac{d \ln D}{d\eta} \\ & \times \int_0^\infty dk_\perp dk_{1\perp} \tilde{W}_\Theta(k_\perp r) \tilde{W}_{\Theta_1}(k_{1\perp} r) \tilde{W}_{\Theta_2}(k_{1\perp} r) \\ & \times P_L(k_\perp, \eta) P_{g_1, m}(k_{1\perp}, \eta) J_1(k_\perp r |\boldsymbol{\theta} - \boldsymbol{\theta}_2|) \\ & \times J_1(k_{1\perp} r |\boldsymbol{\theta}_1 - \boldsymbol{\theta}_2|), \end{aligned} \quad (38)$$

where J_1 is the first-order Bessel function of the first kind.

As the expression (38) arises from the kinematic consistency relations, it expresses the response of the small-scale two-point correlation $\langle \delta_{g_1}^s(\boldsymbol{\theta}_1) \Delta_{\text{ISW}_2}^s(\boldsymbol{\theta}_2) \rangle$ to a change of the initial condition associated with the large-scale mode $\delta_g^s(\boldsymbol{\theta})$. The kinematic effect

given at the leading order by Eq.(38) is due to the uniform motion of the small-scale structures by the large-scale mode. This explains why the result (38) vanishes in the two following cases

1. $(\theta - \theta_2) \perp (\theta_1 - \theta_2)$. There is a nonzero response of $\langle \delta_1 \lambda_2 \rangle$ if there is a linear dependence on $\delta(\theta)$ of $\langle \delta_1 \lambda_2 \rangle$, so that its first derivative is nonzero. A positive (negative) $\delta(\theta)$ leads to a uniform motion at θ_2 towards (away from) θ , along the direction $(\theta - \theta_2)$. From the point of view of θ_1 and θ_2 , there is a reflection symmetry with respect to the axis $(\theta_1 - \theta_2)$. For instance, if $\delta_1 > 0$ the density contrast at a position θ_3 typically decreases in the mean with the radius $|\theta_3 - \theta_1|$, and for $\Delta\theta_2 \perp (\theta_1 - \theta_2)$ the points $\theta_3^\pm = \theta_2 \pm \Delta\theta_2$ are at the same distance from θ_1 and have the same density contrast δ_3 in the mean, with typically $\delta_3 < \delta_2$ as $|\theta_3^\pm - \theta_1| > |\theta_2 - \theta_1|$. Therefore, the large-scale flow along $(\theta - \theta_2)$ leads to a positive $\lambda_2 = -\Delta\delta_2/\Delta\eta_2$ independently of whether the matter moves towards or away from θ (here we took a finite deviation $\Delta\theta_2$). This means that the dependence of $\langle \delta_1 \lambda_2 \rangle$ on $\delta(\theta)$ is quadratic [it does not depend on the sign of $\delta(\theta)$] and the first-order response function vanishes. Then, the leading-order contribution to ξ_3 vanishes. [For infinitesimal deviation $\Delta\theta_2$ we have $\lambda_2 = -\partial\delta_2/\partial\eta_2 = 0$; by this symmetry, in the mean δ_2 is an extremum of the density contrast along the orthogonal direction to $(\theta_1 - \theta_2)$.]
2. $\theta_1 = \theta_2$. This is a particular case of the previous configuration. Again, by symmetry from the viewpoint of δ_1 , the two points $\delta(\theta_2 + \Delta\theta_2)$ and $\delta(\theta_2 - \Delta\theta_2)$ are equivalent and the mean response associated with the kinematic effect vanishes.

This also explains why Eq.(38) changes sign with $(\theta_1 - \theta_2)$ and $(\theta - \theta_2)$. Let us consider for simplicity the case where the three points are aligned and $\delta(\theta) > 0$, so that the large-scale flow points towards θ . We also take $\delta_1 > 0$, so that in the mean the density is peaked at θ_1 and decreases outwards. Let us take θ_2 close to θ_1 , on the decreasing radial slope, and on the other side of θ_1 than θ . Then, the large-scale flow moves matter at θ_2 towards θ_1 , so that the density at θ_2 at a slightly later time comes from more outward regions (with respect to the peak at θ_1) with a lower density. This means that $\lambda_2 = -\partial\delta_2/\partial\eta_2$ is positive so that $\xi_3 > 0$. This agrees with Eq.(38), as $(\theta - \theta_2) \cdot (\theta_1 - \theta_2) > 0$ in this geometry, and we assume the integrals over wavenumbers are dominated by the peaks of $J_1 > 0$. If we flip θ_2 to the other side of θ_1 , we find on the contrary that the large-scale flow brings higher-density regions to θ_2 , so that we have the change of signs $\lambda_2 < 0$ and $\xi_3 < 0$. The same arguments explain the change of sign with $(\theta - \theta_2)$. In fact, it is the relative direction between $(\theta - \theta_2)$ and $(\theta_1 - \theta_2)$ that matters, measured by the scalar product $(\theta - \theta_2) \cdot (\theta_1 - \theta_2)$.

This geometrical dependence of the leading-order contribution to ξ_3 could provide a simple test of the consistency relation, without even computing the explicit expression in the right-hand side of Eq.(38).

4.2. Three-point correlation in terms of a two-point correlation

The three-point correlation ξ_3 in Eq.(38) cannot be written as a product of two-point correlations because there is only one integral along the line of sight that is left. However, if the linear power spectrum $P_L(k, z)$ is already known, we may write ξ_3 in terms of some two-point correlation ξ_2 . For instance, the small-scale cross-correlation between one galaxy density contrast and one weak lensing convergence,

$$\xi_2(\delta_{g_1}^s, \kappa_2^s) = \langle \delta_{g_1}^s(\theta_1) \kappa_2^s(\theta_2) \rangle \quad (39)$$

reads as

$$\xi_2 = (2\pi)^2 \int d\eta I_{g_1} I_{\kappa_2} \int_0^\infty dk_{1\perp} k_{1\perp} \tilde{F}_{\Theta_1}(k_{1\perp} r) \times \tilde{F}_{\Theta_2}(k_{1\perp} r) J_0(k_{1\perp} r |\theta_1 - \theta_2|) P_{g_1, m}(k_{1\perp}), \quad (40)$$

where we again used Limber's approximation. Here we denoted the angular smoothing windows by \tilde{F} to distinguish ξ_2 from ξ_3 . Then, we can write

$$\xi_3 = \frac{(\theta - \theta_2) \cdot (\theta_1 - \theta_2)}{|\theta - \theta_2| |\theta_1 - \theta_2|} \xi_2, \quad (41)$$

if the angular windows of the two-point correlation are chosen such that

$$\begin{aligned} \tilde{F}_{\Theta_1}(k_{1\perp} r) \tilde{F}_{\Theta_2}(k_{1\perp}) &= (2\pi)^2 \frac{I_g I_{\text{ISW}_2}}{I_{\kappa_2}} b_g \frac{d \ln D}{d\eta} \\ &\times \left(\int_0^\infty dk_{\perp} \tilde{W}_{\Theta}(k_{\perp} r) J_1(k_{\perp} r |\theta - \theta_2|) P_L(k_{\perp}, \eta) \right) \\ &\times \frac{\tilde{W}_{\Theta_1}(k_{1\perp} r) \tilde{W}_{\Theta_2}(k_{1\perp} r) J_1(k_{1\perp} r |\theta_1 - \theta_2|)}{k_{1\perp} J_0(k_{1\perp} r |\theta_1 - \theta_2|)}. \end{aligned} \quad (42)$$

This implies that the angular windows \tilde{F}_{Θ_1} and \tilde{F}_{Θ_2} of the two-point correlation ξ_2 have an explicit redshift dependence.

In practice, the expression (42) may not be very convenient. Then, to use the consistency relation (38) it may be more practical to first measure the power spectra P_L and $P_{g_1, m}$ independently, at the redshifts needed for the integral along the line of sight (38), and next compare the measure of ξ_3 with the expression (38) computed with these power spectra.

4.3. Lensing-lensing-ISW correlation

From Eq.(38) we can directly obtain the lensing-lensing-ISW three-point correlation,

$$\xi_3(\kappa^s, \kappa_1^s, \Delta_{\text{ISW}_2}^s) = \langle \kappa^s(\theta) \kappa_1^s(\theta_1) \Delta_{\text{ISW}_2}^s(\theta_2) \rangle, \quad (43)$$

by replacing the galaxy kernels $b_g I_g$ and I_{g_1} by the lensing convergence kernels I_{κ} and I_{κ_1} ,

$$\begin{aligned} \xi_3 &= \frac{(\theta - \theta_2) \cdot (\theta_1 - \theta_2)}{|\theta - \theta_2| |\theta_1 - \theta_2|} (2\pi)^4 \int d\eta I_{\kappa} I_{\kappa_1} I_{\text{ISW}_2} \frac{d \ln D}{d\eta} \\ &\times \int_0^\infty dk_{\perp} dk_{1\perp} \tilde{W}_{\Theta}(k_{\perp} r) \tilde{W}_{\Theta_1}(k_{1\perp} r) \tilde{W}_{\Theta_2}(k_{1\perp} r) \\ &\times P_L(k_{\perp}, \eta) P(k_{1\perp}, \eta) J_1(k_{\perp} r |\theta - \theta_2|) \\ &\times J_1(k_{1\perp} r |\theta_1 - \theta_2|). \end{aligned} \quad (44)$$

As compared with Eq.(38), the advantage of the cross-correlation with the weak lensing convergence κ is that Eq.(44) involves the matter power spectrum $P(k_{1\perp})$ instead of the more complicated galaxy-matter cross power spectrum $P_{g_1, m}(k_{1\perp})$.

5. Consistency relation for the kSZ effect

In this section we consider cross correlations with the kSZ effect. This allows us to apply the consistency relation (5), which involves the momentum \mathbf{p} and remains nonzero at equal times.

5.1. Galaxy-galaxy-kSZ correlation

In a fashion similar to the galaxy-galaxy-ISW correlation studied in section 4.1, we consider the three-point correlation between two galaxy density contrasts and one kSZ CMB anisotropy,

$$\xi_3(\delta_g^s, \delta_{g_1}^s, \Delta_{\text{kSZ}_2}^s) = \langle \delta_g^s(\boldsymbol{\theta}) \delta_{g_1}^s(\boldsymbol{\theta}_1) \Delta_{\text{kSZ}_2}^s(\boldsymbol{\theta}_2) \rangle, \quad (45)$$

in the squeezed limit given by the conditions (31) in Fourier space and (32) in configuration space. The expressions (15) and (29) give

$$\xi_3 = \xi_{3\parallel} + \xi_{3\perp} \quad (46)$$

with

$$\begin{aligned} \xi_{3\parallel} = & \int d\eta d\eta_1 d\eta_2 I_g(\eta) I_{g_1}(\eta_1) I_{\text{kSZ}_2}(\eta_2) \int d\mathbf{k} d\mathbf{k}_1 d\mathbf{k}_2 \\ & \times e^{i(\mathbf{k}\cdot\mathbf{n}r + \mathbf{k}_1\cdot\mathbf{n}_1 r_1 + \mathbf{k}_2\cdot\mathbf{n}_2 r_2)} \tilde{W}_\Theta(k_\perp r) \tilde{W}_{\Theta_1}(k_{1\perp} r_1) \\ & \times \tilde{W}_{\Theta_2}(k_{2\perp} r_2) \langle \tilde{\delta}_g(\mathbf{k}, \eta) \tilde{\delta}_{g_1}(\mathbf{k}_1, \eta_1) \tilde{p}_{e\parallel}^{(n_2)}(\mathbf{k}_2, \eta_2) \rangle \end{aligned} \quad (47)$$

and

$$\begin{aligned} \xi_{3\perp} = & -i \int d\eta d\eta_1 d\eta_2 I_g(\eta) I_{g_1}(\eta_1) I_{\text{kSZ}_2}(\eta_2) \int d\mathbf{k} d\mathbf{k}_1 d\mathbf{k}_2 \\ & \times e^{i(\mathbf{k}\cdot\mathbf{n}r + \mathbf{k}_1\cdot\mathbf{n}_1 r_1 + \mathbf{k}_2\cdot\mathbf{n}_2 r_2)} \tilde{W}_\Theta(k_\perp r) \tilde{W}_{\Theta_1}(k_{1\perp} r_1) \\ & \times \tilde{W}'_{\Theta_2}(k_{2\perp} r_2) \langle \tilde{\delta}_g(\mathbf{k}, \eta) \tilde{\delta}_{g_1}(\mathbf{k}_1, \eta_1) \frac{\mathbf{k}_{2\perp}^{(n_2)} \cdot \tilde{\mathbf{p}}_{e\perp}^{(n_2)}}{k_{2\perp}^{(n_2)}}(\mathbf{k}_2, \eta_2) \rangle, \end{aligned} \quad (48)$$

where we split the longitudinal and transverse contributions to Eq.(29). Here $\{\mathbf{n}, \mathbf{n}_1, \mathbf{n}_2\}$ are the radial unit vectors that point to the centers $\{\boldsymbol{\theta}, \boldsymbol{\theta}_1, \boldsymbol{\theta}_2\}$ of the three circular windows, and $\{(k_\parallel^{(n)}, \mathbf{k}_\perp^{(n)}), (k_{1\parallel}^{(n_1)}, \mathbf{k}_{1\perp}^{(n_1)}), (k_{2\parallel}^{(n_2)}, \mathbf{k}_{2\perp}^{(n_2)})\}$ are the longitudinal and transverse wave numbers with respect to the associated central lines of sight [e.g., $k_\parallel^{(n)} = \mathbf{n} \cdot \mathbf{k}$].

The computation of the transverse contribution (48) is similar to the computation of the ISW three-point correlation (34), using again Limber's approximation. At lowest order we obtain

$$\begin{aligned} \xi_{3\perp} = & \frac{(\boldsymbol{\theta} - \boldsymbol{\theta}_1) \cdot (\boldsymbol{\theta}_2 - \boldsymbol{\theta}_1)}{|\boldsymbol{\theta} - \boldsymbol{\theta}_1| |\boldsymbol{\theta}_2 - \boldsymbol{\theta}_1|} (2\pi)^4 \int d\eta b_g I_g I_{g_1} I_{\text{kSZ}_2} \frac{d \ln D}{d\eta} \\ & \times \int_0^\infty dk_\perp dk_{2\perp} k_{2\perp} \tilde{W}_\Theta(k_\perp r) \tilde{W}_{\Theta_1}(k_{2\perp} r) \tilde{W}'_{\Theta_2}(k_{2\perp} r) \\ & \times P_L(k_\perp, \eta) P_{g_1, e}(k_{2\perp}, \eta) J_1(k_\perp r |\boldsymbol{\theta} - \boldsymbol{\theta}_1|) \\ & \times J_1(k_{2\perp} r |\boldsymbol{\theta}_2 - \boldsymbol{\theta}_1|), \end{aligned} \quad (49)$$

where $P_{g_1, e}$ is the galaxy-free electrons cross power spectrum.

The computation of the longitudinal contribution (47) requires slightly more care. Applying the consistency relation (5) gives

$$\begin{aligned} \xi_{3\parallel} = & - \int d\eta d\eta_1 d\eta_2 b_g(\eta) I_g(\eta) I_{g_1}(\eta_1) I_{\text{kSZ}_2}(\eta_2) \\ & \times \int d\mathbf{k} d\mathbf{k}_1 d\mathbf{k}_2 \tilde{W}_\Theta(k_\perp r) \tilde{W}_{\Theta_1}(k_{1\perp} r_1) \tilde{W}_{\Theta_2}(k_{2\perp} r_2) \\ & \times e^{i(\mathbf{k}\cdot\mathbf{n}r + \mathbf{k}_1\cdot\mathbf{n}_1 r_1 + \mathbf{k}_2\cdot\mathbf{n}_2 r_2)} D(\eta) P_{L0}(k) \frac{dD}{d\eta}(\eta_2) \\ & \times i \frac{\mathbf{n}_2 \cdot \mathbf{k}}{k^2} \langle \tilde{\delta}_{g_1} \tilde{\delta}_{e_2} \rangle' \delta_D(\mathbf{k} + \mathbf{k}_1 + \mathbf{k}_2), \end{aligned} \quad (50)$$

where we only kept the contribution that does not vanish at equal times, as it dominates the integrals along the lines of sight, and

we used $P_L(k, \eta) = D(\eta)^2 P_{L0}(k)$. If we approximate the three lines of sight as parallel, we can write $\mathbf{n}_2 \cdot \mathbf{k} = k_\parallel$, where the longitudinal and transverse directions coincide for the three lines of sight. Then, Limber's approximation, which corresponds to the limit where the radial integrations have a constant weight on the infinite real axis, gives a Dirac term $\delta_D(k_\parallel)$ and $\xi_{3\parallel} = 0$ [more precisely, as we recalled above Eq.(36), the radial integration gives $k_\parallel \lesssim H/c$ while the angular window gives $k_\perp \lesssim H/(c\Theta)$ so that $k_\parallel \ll k_\perp$]. Taking into account the small angles between the different lines of sight, as for the derivation of Eq.(29), the integration over \mathbf{k}_2 through the Dirac factor gives at leading order in the angles

$$\begin{aligned} \xi_{3\parallel} = & - \int d\eta d\eta_1 d\eta_2 b_g(\eta) I_g(\eta) D(\eta) I_{g_1}(\eta_1) I_{\text{kSZ}_2}(\eta_2) \frac{dD}{d\eta}(\eta_2) \\ & \times \int dk_\parallel d\mathbf{k}_\perp dk_{1\parallel} d\mathbf{k}_{1\perp} \tilde{W}_\Theta(k_\perp r) \tilde{W}_{\Theta_1}(k_{1\perp} r_1) \tilde{W}_{\Theta_2}(k_{1\perp} r_2) \\ & \times e^{i[k_\parallel(r-r_2) + \mathbf{k}_\perp \cdot (\boldsymbol{\theta} - \boldsymbol{\theta}_2) r_2 + k_{1\parallel}(r_1 - r_2) + \mathbf{k}_{1\perp} \cdot (\boldsymbol{\theta}_1 - \boldsymbol{\theta}_2) r_2]} \\ & \times P_{L0}(k_\perp) P_{g_1, e}(k_{1\perp}; \eta_1, \eta_2) i \frac{k_\parallel + \mathbf{k}_\perp \cdot (\boldsymbol{\theta}_2 - \boldsymbol{\theta})}{k_\perp^2}. \end{aligned} \quad (51)$$

We used Limber's approximation to write for instance $P_{L0}(k) \simeq P_{L0}(k_\perp)$, but we kept the factor k_\parallel in the last term, as the transverse factor $\mathbf{k}_\perp \cdot (\boldsymbol{\theta}_2 - \boldsymbol{\theta})$, due to the small angle between the lines of sight \mathbf{n} and \mathbf{n}_2 , is suppressed by the small angle $|\boldsymbol{\theta}_2 - \boldsymbol{\theta}|$. We again split $\xi_{3\parallel}$ over two contributions, $\xi_{3\parallel} = \xi_{3\parallel}^{\parallel} + \xi_{3\parallel}^{\perp}$, associated with the factors k_\parallel and $\mathbf{k}_\perp \cdot (\boldsymbol{\theta}_2 - \boldsymbol{\theta})$ of the last term. Let us first consider the contribution $\xi_{3\parallel}^{\parallel}$. Writing $ik_\parallel e^{ik_\parallel(r-r_2)} = \frac{\partial}{\partial r} e^{ik_\parallel(r-r_2)}$, we integrate by parts over η . For simplicity we assume that the galaxy selection function I_g vanishes at $z = 0$,

$$I_g(\eta_0) = 0, \quad (52)$$

so that the boundary term at $z = 0$ vanishes. Then, the integrations over k_\parallel and $k_{1\parallel}$ give a factor $(2\pi)^2 \delta_D(r - r_2) \delta_D(r_1 - r_2)$, and we can integrate over η and η_1 . Finally, the integration over the angles of the transverse wave numbers yields

$$\begin{aligned} \xi_{3\parallel}^{\parallel} = & -(2\pi)^4 \int d\eta \frac{d}{d\eta} [b_g I_g D] I_{g_1} I_{\text{kSZ}_2} \frac{dD}{d\eta} \\ & \times \int_0^\infty dk_\perp dk_{1\perp} \tilde{W}_\Theta(k_\perp r) \tilde{W}_{\Theta_1}(k_{1\perp} r) \tilde{W}_{\Theta_2}(k_{1\perp} r) \\ & \times \frac{k_{1\perp}}{k_\perp} P_{L0}(k_\perp) P_{g_1, e}(k_{1\perp}, \eta) J_0(k_\perp r |\boldsymbol{\theta} - \boldsymbol{\theta}_2|) \\ & \times J_0(k_{1\perp} r |\boldsymbol{\theta}_1 - \boldsymbol{\theta}_2|), \end{aligned} \quad (53)$$

where J_0 is the zeroth-order Bessel function of the first kind. For the transverse contribution $\xi_{3\parallel}^{\perp}$ we can proceed in the same fashion, without integration by parts over η . This gives

$$\begin{aligned} \xi_{3\parallel}^{\perp} = & -(2\pi)^4 \int d\eta b_g I_g I_{g_1} I_{\text{kSZ}_2} D \frac{dD}{d\eta} \\ & \times \int_0^\infty dk_\perp dk_{1\perp} \tilde{W}_\Theta(k_\perp r) \tilde{W}_{\Theta_1}(k_{1\perp} r) \tilde{W}_{\Theta_2}(k_{1\perp} r) \\ & \times k_{1\perp} P_{L0}(k_\perp) P_{g_1, e}(k_{1\perp}, \eta) |\boldsymbol{\theta} - \boldsymbol{\theta}_2| J_1(k_\perp r |\boldsymbol{\theta} - \boldsymbol{\theta}_2|) \\ & \times J_0(k_{1\perp} r |\boldsymbol{\theta}_1 - \boldsymbol{\theta}_2|). \end{aligned} \quad (54)$$

Comparing Eq.(54) with Eq.(53), we find $\xi_{3\parallel}^{\perp} / \xi_{3\parallel}^{\parallel} \sim k_\perp r |\boldsymbol{\theta} - \boldsymbol{\theta}_2|$. If the cutoff on k_\perp is set by the Bessel functions, we obtain $\xi_{3\parallel}^{\perp} \sim \xi_{3\parallel}^{\parallel}$. For very small angles, $|\boldsymbol{\theta} - \boldsymbol{\theta}_2| \rightarrow 0$, the cutoff over k is set by the angular window $\tilde{W}_\Theta(k_\perp r)$ or by the falloff of the linear power spectrum $P_{L0}(k_\perp)$, and $\xi_{3\parallel}^{\perp} \ll \xi_{3\parallel}^{\parallel}$.

In contrast with Eq.(38), the kSZ three-point correlation, given by the sum of Eqs.(49), (53) and (54), does not vanish for orthogonal directions between the small-scale separation $(\theta_1 - \theta_2)$ and the large-scale separation $(\theta - \theta_2)$. Indeed, the leading order contribution in the squeezed limit to the response of $\langle \delta_1 \mathbf{p}_2 \rangle$ to a large-scale perturbation δ factors out as $\langle \delta_1 \delta_2 \rangle \mathbf{v}_2$, where we only take into account the contribution that does not vanish at equal times (and we discard the finite-size smoothing effects). The intrinsic small-scale correlation $\langle \delta_1 \delta_2 \rangle$ does not depend on the large-scale mode δ , whereas \mathbf{v}_2 is the almost uniform velocity due to the large-scale mode, which only depends on the direction to $\delta(\theta)$ and is independent of the orientation of the small-scale mode $(\theta_1 - \theta_2)$.

Because the measurement of the kSZ effect only probes the radial velocity of the free electrons gas along the line of sight, which is generated by density fluctuations almost parallel to the line of sight over which we integrate and are damped by this radial integration, the result (53) is suppressed as compared with the ISW result (38) by the radial derivative $d \ln(b_g I_g D) / d\eta \sim 1/r$. Also, the contribution (53), associated with transverse fluctuations that are almost orthogonal to the second line of sight, is suppressed as compared with the ISW result (38) by the small angle $|\theta - \theta_2|$ between the two lines of sight.

One drawback of the kSZ consistency relation, (49) and (53)-(54), is that it is not easy to independently measure the galaxy-free electrons power spectrum $P_{g_1, e}$, which is needed if we wish to test this relation. Alternatively, Eqs.(53)-(54) may be used as a test of models for the free electrons distribution and the cross power spectrum $P_{g_1, e}$.

5.2. Lensing-lensing-kSZ correlation

Again, from Eqs.(49) and (53)-(54) we can directly obtain the lensing-lensing-kSZ three-point correlation,

$$\xi_3(\kappa^s, \kappa_1^s, \Delta_{\text{kSZ}_2}^s) = \langle \kappa^s(\theta) \kappa_1^s(\theta_1) \Delta_{\text{kSZ}_2}^s(\theta_2) \rangle, \quad (55)$$

by replacing the galaxy kernels $b_g I_g$ and I_{g_1} by the lensing convergence kernels I_k and I_{k_1} . This gives $\xi_3 = \xi_{3\perp} + \xi_{3\parallel}^{\parallel} + \xi_{3\parallel}^{\perp}$ with

$$\begin{aligned} \xi_{3\perp} &= \frac{(\theta - \theta_1) \cdot (\theta_2 - \theta_1)}{|\theta - \theta_1| |\theta_2 - \theta_1|} (2\pi)^4 \int d\eta I_k I_{k_1} I_{\text{kSZ}_2} \frac{d \ln D}{d\eta} \\ &\times \int_0^\infty dk_\perp dk_{2\perp} k_{2\perp} \tilde{W}_{\Theta}(k_\perp r) \tilde{W}_{\Theta_1}(k_{2\perp} r) \tilde{W}'_{\Theta_2}(k_{2\perp} r) \\ &\times P_L(k_\perp, \eta) P_{m, e}(k_{2\perp}, \eta) J_1(k_\perp r |\theta - \theta_1|) \\ &\times J_1(k_{2\perp} r |\theta_2 - \theta_1|), \end{aligned} \quad (56)$$

$$\begin{aligned} \xi_{3\parallel}^{\parallel} &= -(2\pi)^4 \int d\eta \frac{d}{d\eta} [I_k D] I_{k_1} I_{\text{kSZ}_2} \frac{dD}{d\eta} \int_0^\infty dk_\perp dk_{1\perp} \\ &\times \tilde{W}_{\Theta}(k_\perp r) \tilde{W}_{\Theta_1}(k_{1\perp} r) \tilde{W}_{\Theta_2}(k_{1\perp} r) \frac{k_{1\perp}}{k_\perp} P_{L0}(k_\perp) \\ &\times P_{m, e}(k_{1\perp}, \eta) J_0(k_\perp r |\theta - \theta_2|) J_0(k_{1\perp} r |\theta_1 - \theta_2|), \end{aligned} \quad (57)$$

and

$$\begin{aligned} \xi_{3\parallel}^{\perp} &= -(2\pi)^4 \int d\eta I_k I_{k_1} I_{\text{kSZ}_2} D \frac{dD}{d\eta} \int_0^\infty dk_\perp dk_{1\perp} \\ &\times \tilde{W}_{\Theta}(k_\perp r) \tilde{W}_{\Theta_1}(k_{1\perp} r) \tilde{W}_{\Theta_2}(k_{1\perp} r) k_{1\perp} P_{L0}(k_\perp) \\ &\times P_{m, e}(k_{1\perp}, \eta) |\theta - \theta_2| J_1(k_\perp r |\theta - \theta_2|) J_0(k_{1\perp} r |\theta_1 - \theta_2|). \end{aligned} \quad (58)$$

This now involves the matter-free electrons cross power spectrum $P_{m, e}$.

The application of the relations above is, unfortunately, a nontrivial task in terms of observations: to test those relations one would require the mixed galaxy (matter) - free electrons power spectrum. One possibility would be to do a stacking analysis of several X-rays observations of the hot ionised gas by measuring the bremsstrahlung effect. For instance, one could infer $n_e n_p T^{-1/2}$, by making some reasonable assumptions about the plasma state, as performed in Fraser-McKelvie et al. (2011), with the aim to measure n_e in filaments. We would of course need to cover a large range of scales. For kpc scales, inside galaxies and in the intergalactic medium, one could use for instance silicon emission line ratios (Kwitter & Henry 1998; Henry et al. 1996). For Mpc scales, or clusters, one may use the SZ effect (Rossetti et al. 2016). Nevertheless, all these proposed approaches are quite speculative at this stage.

6. Conclusions

In this paper, we have shown how to relate the large-scale consistency relations with observational probes. Assuming the standard cosmological model (more specifically, the equivalence principle and Gaussian initial conditions), nonzero equal-times consistency relations involve the cross-correlations between galaxy or matter density fields with the velocity, momentum or time-derivative density fields. We have shown that these relations can be related to actual measurements by considering the ISW and kSZ effects, which indeed involve the time derivative of the matter density field and the free electrons momentum field. We focused on the lowest-order relations, which apply to three-point correlation functions or bispectra, because higher-order correlations are increasingly difficult to measure.

The most practical relation obtained in this paper is probably the one associated with the ISW effect, more particularly its cross-correlation with two cosmic weak lensing convergence statistics. Indeed, it allows one to write this three-point correlation function in terms of two matter density field power spectra (linear and nonlinear), which can be directly measured (e.g., by two-point weak lensing statistics). Moreover, the result, which is the leading-order contribution in the squeezed limit, shows a specific angular dependence as a function of the relative angular positions of the three smoothed observed statistics. Then, both the angular dependence and the quantitative prediction provide a test of the consistency relation, that is, of the equivalence principle and of primordial Gaussianity. If we consider instead the cross-correlation of the ISW effect with two galaxy density fields, we obtain a similar relation but it now involves the mixed galaxy-matter density power spectrum $P_{g, m}$ and the large-scale galaxy bias b_g . These two quantities can again be measured (e.g., by two-point galaxy-weak lensing statistics) and provide another test of the consistency relation.

The relations obtained with the kSZ effect are more intricate. They do not show a simple angular dependence, which would provide a simple signature, and they involve the galaxy-free electrons or matter-free electrons power spectra. These power spectra are more difficult to measure. One can estimate the free electron density in specific regions, such as filaments or clusters, through X-ray or SZ observations, or around typical structures by stacking analysis of clusters. This could provide an estimate of the free electrons cross power spectra and a check of the consistency relations. Although we can expect significant error bars, it would be interesting to check that the results remain consistent with the theoretical predictions.

A violation of these consistency relations would signal either a modification of gravity on cosmological scales or non-

Gaussian initial conditions. We leave to future works the derivation of the deviations associated with various nonstandard scenarios.

Acknowledgements. This work is supported in part by the French Agence Nationale de la Recherche under Grant ANR-12-BS05-0002. DFM thanks the support of the Research Council of Norway.

References

- Creminelli, P., Gleyzes, J., Simonović, M., & Vernizzi, F. 2014, *J. Cosmology Astropart. Phys.*, 2, 051
- Creminelli, P., Noreña, J., Simonović, M., & Vernizzi, F. 2013, *J. Cosmology Astropart. Phys.*, 12, 025
- Fraser-McKelvie, A., Pimbblet, K. A., & Lazendic, J. S. 2011, *MNRAS*, 415, 1961
- Garriga, J., Pogosian, L., & Vachaspati, T. 2004, *Phys. Rev. D*, 69, 063511
- Gruzinov, A. & Hu, W. 1998, *ApJ*, 508, 435
- Hamaus, N., Seljak, U., Desjacques, V., Smith, R. E., & Baldauf, T. 2010, *Phys. Rev.*, D82, 043515
- Henry, R. B. C., Kwitter, K. B., & Howard, J. W. 1996, *ApJ*, 458, 215
- Horn, B., Hui, L., & Xiao, X. 2014, *J. Cosmology Astropart. Phys.*, 9, 044
- Horn, B., Hui, L., & Xiao, X. 2015, *J. Cosmology Astropart. Phys.*, 9, 068
- Kehagias, A., Noreña, J., Perrier, H., & Riotto, A. 2014a, *Nuclear Physics B*, 883, 83
- Kehagias, A., Perrier, H., & Riotto, A. 2014b, *Modern Physics Letters A*, 29, 1450152
- Kehagias, A. & Riotto, A. 2013, *Nuclear Physics B*, 873, 514
- Knox, L., Scoccimarro, R., & Dodelson, S. 1998, *Physical Review Letters*, 81, 2004
- Kwitter, K. B. & Henry, R. B. C. 1998, *ApJ*, 493, 247
- Nishimichi, T. & Valageas, P. 2014, *Phys. Rev. D*, 90, 023546
- Peloso, M. & Pietroni, M. 2013, *J. Cosmology Astropart. Phys.*, 5, 031
- Peloso, M. & Pietroni, M. 2014, *J. Cosmology Astropart. Phys.*, 4, 011
- Rizzo, L. A., Mota, D. F., & Valageas, P. 2016, *Phys. Rev. Lett.*, 117, 081301
- Rossetti, M., Gastaldello, F., Ferioli, G., et al. 2016, *Mon. Not. Roy. Astron. Soc.*, 457, 4515
- Sunyaev, R. A. & Zeldovich, I. B. 1980, *MNRAS*, 190, 413
- Valageas, P. 2014a, *Phys. Rev. D*, 89, 123522
- Valageas, P. 2014b, *Phys. Rev. D*, 89, 083534
- Valageas, P., Taruya, A., & Nishimichi, T. 2016, *ArXiv e-prints* [arXiv:1610.00993]